THÈSE

En vue de l'obtention du

DOCTORAT DE L'UNIVERSITÉ DE TOULOUSE

Délivré par :

Institut National Polytechnique de Toulouse (INP Toulouse)

Discipline ou spécialité :

Science et Génie des Matériaux

Présentée et soutenue par :

M. AURELIEN PRILLIEUX

le vendredi 30 juin 2017

Titre :

Hydrogen and water vapour effects on oxygen solubility and diffusivity in high temperature Fe-Ni alloys

---

Ecole doctorale :

Sciences de la Matière (SDM)

Unité de recherche :

Centre Interuniversitaire de Recherche et d'Ingénierie des Matériaux (C.I.R.I.M.A.T.)

Directeur(s) de Thèse :

M. DANIEL MONCEAU

M. DAVID YOUNG

Rapporteurs :

M. DOMINIQUE MANGELINCK, AIX-MARSEILLE UNIVERSITE

Mme LAURE MARTINELLI, CEA SACLAY

Membre(s) du jury :

M. MARC LEGROS, CEMES TOULOUSE, Président

M. DANIEL MONCEAU, INP TOULOUSE, Membre

M. DAVID YOUNG, UNIVERSITY OF NEW SOUTH WALES SYDNEY, Membre

Mme CLARA DESGRANGES, GROUPE SAFRAN, Membre

Hydrogen and water vapour effects on oxygen solubility and diffusivity in high temperature Fe-Ni alloys

by

Aurélien Prillieux

A thesis in fulfilment of the requirements for the degree of

Doctor of Philosophy

School of Materials Science and Engineering,

University of New South Wales Sydney,

Sydney, Australia

Faculty of Science

CIRIMAT,

Institut polytechnique de Toulouse,

Toulouse, France

September 2017

ORIGINALITY STATEMENT

'I hereby declare that this submission is my own work and to the best of my knowledge it contains no materials previously published or written by another person, or substantial proportions of material which have been accepted for the award of any other degree or diploma at UNSW or any other educational institution, except where due acknowledgement is made in the thesis. Any contribution made to the research by others, with whom I have worked at UNSW or elsewhere, is explicitly acknowledged in the thesis. I also declare that the intellectual content of this thesis is the product of my own work, except to the extent that assistance from others in the project's design and conception or in style, presentation and linguistic expression is acknowledged.'

Signed .....

Date 04/09/2017

COPYRIGHT STATEMENT

'I hereby grant the University of New South Wales or its agents the right to archive and to make available my thesis or dissertation in whole or part in the University libraries in all forms of media, now or here after known, subject to the provisions of the Copyright Act 1968. I retain all proprietary rights, such as patent rights. I also retain the right to use in future works (such as articles or books) all or part of this thesis or dissertation.
I also authorise University Microfilms to use the 350 word abstract of my thesis in Dissertation Abstract International (this is applicable to doctoral theses only).
I have either used no substantial portions of copyright material in my thesis or I have obtained permission to use copyright material; where permission has not been granted I have applied/will apply for a partial restriction of the digital copy of my thesis or dissertation.'

Signed .....

Date 11/09/2017

AUTHENTICITY STATEMENT

'I certify that the Library deposit digital copy is a direct equivalent of the final officially approved version of my thesis. No emendation of content has occurred and if there are any minor variations in formatting, they are the result of the conversion to digital format.'

Signed .....

Date 11/09/2017

PLEASE TYPE

THE UNIVERSITY OF NEW SOUTH WALES
Thesis/Dissertation Sheet

Surname or Family name: Prillieux

First name: Aurélien Other name/s: François, Gerard

Abbreviation for degree as given in the University calendar: PhD

School: Material Science and Engineering Faculty: Science

Title: Hydrogen and water vapour effects on oxygen solubility and diffusivity in high temperature Fe-Ni alloys

Abstract 350 words maximum: (PLEASE TYPE)

One solution to reduce greenhouse gases emissions is to improve efficiency of energy production units by increasing their operating temperature. Therefore, new austenitic materials based on the Fe-Ni-Cr system should be designed. These materials require good protection against high temperature oxidation, which is achieved by forming a slow growing chromium oxide. However, to predict the formation of a protective scale, knowledge of the oxygen permeability in the base alloy is required.

This study aimed to measure the effect of water vapour on oxygen permeability, solubility and diffusivity in Fe-Ni alloys at temperatures above 1000°C. Two atmospheres were used: one dry and one wet.

The maximum oxygen solubility was found in pure iron, and decreased with addition of nickel. The dependence of solubility on alloy composition is non-ideal, and cannot be predicted from simple models. The presence of water vapour in the atmosphere seems to increase the solubility by a factor of 2 in alloys with nickel content lower than 80 at.%, at temperatures near 1000°C. At 1150°C, the oxygen solubility is independent of the environment.

The oxygen permeability was determined by measuring the internal oxidation kinetics of Fe-Ni-Cr alloy. The oxygen permeability exhibits the same variation with alloy composition as the oxygen solubility, independent of the atmosphere. Specifically, no significant effect of water vapour on oxygen permeability values was observed. For temperature above 1000°C, the variation of oxygen diffusion coefficient with alloy composition is similar in all environments, and a maximum is observed for alloys with a nickel content of 40 at.%. For a nickel content up to 60 at.%, the presence of water vapour in the atmosphere decreases the value of oxygen diffusion coefficient by a factor of 2-3 at 1000°C. The difference between diffusion coefficients measured in a dry and wet atmosphere increases as temperature decreases. It was found that the water vapour has no effect on the variation of oxygen permeability, solubility and diffusivity with alloy composition. The presence of water vapour in the environment appears to increase the oxygen solubility and decrease the oxygen diffusivity in iron-rich alloys, the effect being more significant at low temperatures.

Declaration relating to disposition of project thesis/dissertation

I hereby grant to the University of New South Wales or its agents the right to archive and to make available my thesis or dissertation in whole or in part in the University libraries in all forms of media, now or here after known, subject to the provisions of the Copyright Act 1968. I retain all property rights, such as patent rights. I also retain the right to use in future works (such as articles or books) all or part of this thesis or dissertation.

I also authorise University Microfilms to use the 350 word abstract of my thesis in Dissertation Abstracts International (this is applicable to doctoral theses only).

Prillieux 04/09/2017

Signature Witness Signature Date

The University recognises that there may be exceptional circumstances requiring restrictions on copying or conditions on use. Requests for restriction for a period of up to 2 years must be made in writing. Requests for a longer period of restriction may be considered in exceptional circumstances and require the approval of the Dean of Graduate Research.

FOR OFFICE USE ONLY Date of completion of requirements for Award:

Acknowledgements

Firstly, I would like to thank Gerald MEIER and Gordon TATLOCK for accepting to review this thesis.

I would like to express my sincere gratitude to my supervisor David YOUNG for the continuous support during my PhD study, for his patience, motivation and immense knowledge. He kept me on the right path during the time of research and writing of this thesis and learning from him was a real privilege.

My sincere thanks also goes to Jianqiang ZHANG who helped me in my first steps in the School of Material Sciences and for his invariability in answering all my questions despite a busy agenda. I also would like to thank Brynn HIBBERT for his insightful comments and his precious help to give a sense to the large number of data we had.

I thank Rahmat KARTONO for his incommensurable help when we were trying to find a solution almost every day to be able to carry out experiments in the new Material Sciences building. I can clearly say that without his help I would not have been able to do half of the work I did.

I am indebted to my teammate Domingo JULLIAN who did stunning work to make quartz capsules. It was a real pleasure to share ideas and results with him.

I also would like to thank my fellow labmates: Maggie, Sonia, Mahsa, Irene, Carina, Tom, Fred, Patrick C., Neil, Stuart, Patrick T., Felix, Kaan, Daniel, Scott and Viet. I really appreciated being part of the Postgraduate Association with these people for their ideas and good humour. I have a special thanks to Akhila MUKKAVILLI and Caitlin HEALY who gave me strong support in the last months of my PhD and tried to keep me sane as much as they could.

Finally, I will always remember my housemates of the 109 Commonwealth Street and the trivia group who showed me around Sydney and made my stay in Australia a very enjoyable experience.

Remerciements

Je tiens tout d'abord à remercier Marc LEGROS pour avoir présidé mon jury de thèse, ainsi que Laure MARTINELLI et Dominique MANGELINCK pour avoir accepté d'être rapporteur de mon travail. Je souhaite également remercier Clara DESGRANGES et Alain GALERIE pour avoir pris part à mon jury lors de ma soutenance à Toulouse.

Mes remerciements vont également à mon directeur de thèse Daniel MONCEAU pour son aide sur les questions scientifiques mais également pour les nombreux conseils qu'il m'a prodigués tout au long de ma thèse et notamment pour m'avoir toujours poussé à plus de "pédagogie" dans mes explications.

Durant mes différents séjours au laboratoire CIRIMAT, j'ai reçu l'aide de nombreuses personnes. Je remercie les différents permanents pour leur disponibilité à répondre à mes nombreuses interrogations. Je tiens tout particulièrement à remercier Dominique POQUILLION qui, malgré un emploi du temps chargé, a toujours pris le temps pour s'occuper de mes problèmes logistiques tels que la plomberie "capricieuse" du laboratoire. Je souhaite également remercier Damien CONNETABLE avec qui j'ai appris énormément sur ce domaine obscur qu'est le calcul DFT.

La réalisation de mes expériences au CIRIMAT a été un réel challenge et je souhaite remercier Ronan MANGUY et Alexandre FREULON pour leurs précieux conseils techniques et pratiques qui m'ont permis d'obtenir de nombreux résultats.

Au cours de mes différents passages au CIRIMAT, j'ai eu la chance de côtoyer différentes générations de thésards avec qui je partage de nombreux souvenirs. Il y a tout d'abord ceux que j'appellerai les "anciens" et qui m'ont chaleureusement accueilli lors de mes débuts au laboratoire. Je pense à Maxime et nos discussions de codeur, à Clément et nos parties de squash après "le boulot", à Aneesha et nos heures de discussion en salle métallo, ainsi qu'à Bertrand, Pierre G., Mathilde, Pauline, Jean, Aurélien F. Il y a ensuite ceux que je considère comme "la nouvelle génération" : Alexandra, Elodie, Coralie, Charlotte, Marie-Laetitia, Rosanne,

Héloïse, Pierre P., Loïc, Alexandre M., Romain, Alexandre P., Bruno, Tom, Mathieu, André, Ugras, Jacques, Franck, Clément R., Nathan, Rémi que je souhaite remercier pour l'atmosphère de camaraderie et d'entraide qu'ils entretiennent au laboratoire et qui ont rendu mes séjours au CIRIMAT très agréables.

Finalement, je souhaite remercier ma famille ainsi que mes amis de Cherbourg, Paris, Grenoble et d'ailleurs qui n'ont jamais cessé de m'encourager et de me soutenir durant cette aventure. Ces personnes ont toutes participé, chacune à leur manière, à faire de moi ce que je suis aujourd'hui et je n'aurai pas assez de place ici pour leur exprimer toute ma gratitude.

Contents

Introduction **1**

1 Literature review **7**

1.1 Oxidation of pure metals 8

1.1.1 Thermodynamic approach to oxidation 9

1.1.2 Oxidation kinetics 11

1.1.3 Oxidation of pure iron 15

1.2 Diffusion in metals 17

1.2.1 Thermodynamic approach to diffusion 17

1.2.2 Diffusion in alloys 20

1.2.2.1 Cross-effects 20

1.2.2.2 Interdiffusion coefficient 21

1.3 Oxidation of alloys 22

1.3.1 Selective oxidation of one component 24

1.3.2 Internal oxidation 26

1.3.2.1 Steps of internal oxidation 26

1.3.2.2 Wagner's model for internal oxidation kinetics in the absence of external scale formation 27

1.3.2.3 Kinetics of internal oxidation under an external scale 31

1.3.2.4 Gesmundo's model for internal oxidation kinetics measured by weight gain measurement 33

1.3.2.5 Transition between internal and external oxidation . 34

1.3.2.6 Internal oxidation leading to the formation of multiple internal oxides . . . 36
1.3.2.7 Nucleation and growth of precipitates . . . 38
1.4 Examples of Internal Oxidation . . . 43
1.4.1 Fe based alloys . . . 43
1.4.2 Ni based alloys . . . 50
1.4.3 Prediction of internal oxidation with Wagner's analysis . . . 56
1.4.3.1 Chromium diffusion coefficient in Fe-Cr alloys . . . 57
1.4.3.2 Chromium diffusion coefficient in Ni-Cr alloys . . . 59
1.4.3.3 Critical chromium concentration calculation . . . 61
1.4.4 Fe-Ni based alloys . . . 65
1.5 Oxygen solubility in metal . . . 68
1.5.1 Oxygen solubility in iron . . . 70
1.5.2 Oxygen solubility in nickel . . . 73
1.5.3 Oxygen solubility in binary alloys . . . 75
1.5.3.1 Quasichemical model . . . 75
1.5.3.2 Wagner's model . . . 77
1.5.4 Expression of first order interaction parameter . . . 80
1.6 Oxygen diffusion in alloys . . . 81
1.6.1 Diffusion in iron . . . 81
1.6.2 Diffusion in nickel . . . 83
1.7 General summary . . . 86

2 Materials and experimental methods 89

2.1 Materials . . . 90
2.1.1 Solubility experiments . . . 90
2.1.2 Internal oxidation experiment . . . 91
2.2 Sample preparation . . . 95
2.3 Gas compositions . . . 98
2.3.1 Rhines pack experiment . . . 98

2.3.2 H_2/H_2O . . . 101
2.4 Solubility experiment duration . . . 103
2.5 Experimental protocol . . . 104
2.5.1 Rhines pack experiments . . . 104
2.5.2 Flowing gas experiments . . . 107
2.6 Oxygen analysis . . . 110
2.7 Internal oxidation zone characterisation . . . 115
2.7.1 IOZ depth measurement . . . 115
2.7.2 Volume fraction measurement . . . 116
2.8 characterisation technique . . . 118
2.8.1 Scanning Electron Microscopy/Energy Dispersive Spectroscopy (SEM/EDS) . . . 118
2.8.2 X-Ray Diffraction (XRD) . . . 118

3 Oxygen solubility 121
3.1 Determination of the oxygen solubility . . . 122
3.1.1 Evaluation of the excess Gibbs free energy of oxygen dissolution reaction . . . 123
3.1.2 Oxygen solubility in dry environment . . . 124
3.1.3 Oxygen solubility measured in H_2/H_2O gases . . . 132
3.2 Discussion on oxygen solubility in pure metals . . . 136
3.2.1 Oxygen solubility in pure iron . . . 137
3.2.2 Oxygen solubility in nickel . . . 140
3.3 Effect of water vapour on the oxygen solubility . . . 142
3.4 Prediction of oxygen solubility in binary alloy . . . 146
3.5 Summary . . . 150

4 Internal oxidation kinetics 153
4.1 Internal oxidation kinetics in Fe/FeO Rhines packs . . . 154
4.1.1 Internal oxidation zone characterisation . . . 154

4.1.2 Internal oxidation kinetics 163
4.2 Internal oxidation in H_2/H_2O gas 170
4.2.1 Internal oxidation zone microstructure 170
4.2.2 Internal oxidation kinetics in H_2/H_2O gases with 13% water vapour 176
4.2.2.1 Penetration measurement 176
4.2.2.2 Discontinuous TGA 182
4.2.2.3 Comparison of kinetics in term of weight gain and penetration 185
4.2.3 Internal oxidation in H_2/H_2O gases with 3% water vapour . . 187
4.2.3.1 Continuous TGA 187
4.2.3.2 Penetration measurement 192
4.2.3.3 Comparison between penetration and weight gain measurement 193
4.3 Effect of water vapour and hydrogen on internal oxidation rates . . . 195
4.4 Summary 202

5 Oxygen permeability 205

5.1 $k_p^{(i)}$ with consideration of volume expansion 207
5.2 Enrichment factor 208
5.2.1 Diffusional approach for enrichment factor calculation 209
5.2.1.1 IOZ expansion due to internal oxide precipitation . . 210
5.2.1.2 Enrichment factor calculated from diffusional approach214
5.2.2 Estimation of the enrichment factor by internal oxide volume fraction measurement 221
5.2.2.1 Definition of volume fractions in the case of the pre-cipitations of 2 oxides for estimation of enrichment factor. 221
5.2.2.2 Calculation of enrichment factor from volume fraction measurement 224

5.3 Determination of internal oxide stoichiometry 228
5.3.1 Definition of the effective stoichiometry 228
5.3.2 Determination of the effective stoichiometric coefficient by coupling TGA and penetration measurement 230
5.3.3 Matrix chromium content at $X = X_{(t)}$ 234
5.3.3.1 Chromium oxide solubility product in Fe-Cr alloys . 235
5.3.3.2 Chromium oxide solubility product in Ni-Cr alloys . 237
5.3.3.3 Calculation of the matrix chromium content at $X = X_{(t)}$ 238
5.3.4 Distribution of volume fraction through the IOZ 240
5.3.5 Orhiner and Morral model for distribution of internal oxide in subzone 2 244
5.3.6 Effect of water content on the effective stoichiometry 253
5.4 Oxygen permeability 255
5.4.1 Oxygen permeability measured in Fe/FeO Rhines packs 255
5.4.1.1 Determination of oxygen permeability at 1,000 and 1,050°C 256
Calculation of F_A^{ox} and F_A^{int} 259
Effective oxygen diffusion coefficient 261
Calculation of oxygen permeability 267
5.4.1.2 Determination of oxygen permeability at 1,100 and 1,150°C 270
5.4.1.3 Matrix oxygen permeability 272
5.4.2 Oxygen permeability in H_2/H_2O gases 276
5.4.2.1 Oxygen permeability measured in gases with 13% water vapour 276
Determination of oxygen permeability at 1,000 and 1,050°C 277

Determination of oxygen permeability at 1,100 and 1,150°C 277
Matrix oxygen permeability 280
5.4.2.2 Oxygen permeability measured in gases with 3% water vapour by penetration measurement 282
5.4.3 Effect of H_2/H_2O gases on matrix oxygen permeability 285
5.4.4 Effect of water vapour on the parameter λ 286
5.4.5 Iron Oxygen permeability 287
5.4.6 Oxygen permeability of Fe-Ni alloys from internal/external oxidation transition 290
5.5 Summary 292

6 Oxygen Diffusion **297**
6.1 Oxygen diffusion coefficient measured in Rhines pack 298
6.2 Oxygen diffusion coefficient measured in H_2/H_2O 307
6.2.1 Gases with 13% of water vapour 307
6.2.2 Gases with 3% water vapour 310
6.3 Effects of water vapour and hydrogen on the oxygen diffusion coefficient311
6.4 Summary 318

7 Conclusions **323**

Appendices **333**

A Analysis certificate from raw materials **335**

B Etchants **339**

C LECO analyser parameters **341**

D Standards for oxygen analysis **343**

E Error for functions of 2 variables **345**

Résumé étendu **349**

1 Introduction 350

2 Solubilité de l'oxygène 353

3 Oxydation interne 356

3.1 Microstructure de la zone d'oxydation interne 356

3.2 Cinétique d'oxydation interne 358

4 Perméabilité de l'oxygène 360

4.1 Facteur d'enrichissement 360

4.2 Stoechiométrie effective 361

4.3 Calcul de la perméabilité de l'oxygène 363

5 Diffusion de l'oxygène 364

6 Conclusion 365

List of Figures

1.1 Dissociation pressure of wustite, nickel oxide and chromium oxide. . . 10

1.2 Atomic transport in a growing oxide scale, where $C_{B(1)}$ and $C_{B(2)}$ are the concentrations of the diffusing species B at the boundaries. 12

1.3 Optical microscopic observation of an oxide layer on pure iron oxidised in air at 700°C. 15

1.4 Oxidation kinetics of iron in various environments. 16

1.5 Schematic representation of the different types of oxidation. © IOP Publishing. Reproduced with permission. All rights reserved. 23

1.6 Internal oxidation steps in the absence of an outer scale. 27

1.7 Schematic representation of concentration profiles in the IOZ and in the alloy during internal oxidation if $N_O^{(s)} D_O >> N_B^{(0)} D_B$. 30

1.8 Schematic representation of concentration profiles in the IOZ and in the alloy during internal oxidation in combination with external scale formation. 31

1.9 Transition from internal to external oxidation for Ag-In alloys at 550°C. Transition started (○), Transition complete (●). $N_{In}^{(0)*}$ value calculated for transition between internal and external oxidation (- - -). 36

1.10 Schematic representation of oxygen concentration profiles in the IOZ when multiple internal oxides precipitate. 37

1.11 Concentration profiles at the oxidation front during internal oxidation process. Situations (a),(b),(c) described in text. 40

1.12 Free energy of a spherical nucleus. 42

1.13 Oxygen permeability in γ-iron after reaction in Fe/FeO Rhines pack, Fe-Si alloys (open symbols), Fe-Al alloys (filled symbols). 45

1.14 Internal oxidation of Fe-5Cr alloys at $p_{O_2} = 8.7 \times 10^{-17}$ atm in Ar-H_2-H_2O at 900°C. 47

1.15 Oxygen permeability of iron measured in γ and α iron in different atmospheres, Fe/FeO Rhines pack (open symbols), H_2/H_2O gas mixtures (filled symbols). 49

1.16 Internal oxides in Ni-Al alloys after oxidation in Ni/NiO Rhines pack for 10h at 1,100°C. Reprinted by permission of the publisher Taylor & Francis Ltd. 51

1.17 Oxygen permeability in various Ni based alloys at 1,100°C (open symbols) and 1,000°C (filled symbols). 53

1.18 Oxygen permeability in nickel from Rhines pack experiment (open symbols) and H_2/H_2O experiment (filled symbols). 56

1.19 Chromium diffusion coefficient in Fe-Cr alloys. Calculated from tracer experiment (filled symbols), measured with interdiffusion couple (open symbols) for different chromium contents: 0-28 at.% (–○–). 58

1.20 Chromium diffusion coefficient in Ni-Cr alloys. Calculated from tracer experiment (filled symbols), measured from interdiffusion couple (open symbols) for different chromium contents: 0-13 at.% (○), 5 at.% (□), 10 at.% (⬠), 5-30 at.% (◇). 60

1.21 Critical chromium concentration to observe the transition between internal and external oxidation in γ-iron at the Fe/FeO equilibrium pressure, calculated with different permeability; Meijering (——) and Takada *et al.* (- - -). Essuman *et al.*'s observation on Fe-Cr alloy exposed in H_2/H_2O; (○) Internal oxidation, (●) External oxidation. . . 61

1.22 Critical chromium concentration for transition between internal and external oxidation in nickel at the Ni/NiO equilibrium pressure, calculated with Schwarzkopf's permeability. Essuman *et al.*'s observation on Ni-Cr alloy; (○) Internal oxidation, (●) External oxidation. 63

1.23 Section of the iron-nickel-chromium-oxygen phase diagram at 1,000°C and a constant oxygen concentration equal to the solubility of oxygen in alloy matrix. It shows the limit of appearance of internal oxidation in various alloy compositions. Internal oxidation (○), no internal oxidation (●). 65

1.24 Chromium interdiffusion coefficient measured in Fe-Cr and Ni-Cr and in Fe-Ni-Cr. 66

1.25 Permeability measured from the chromium critical content for transition between internal and external oxidation observed by Croll and Wallwork at 1,000°C and calculated for the Fe/FeO dissociation pressure. Takada(□), Eq.(1.118)(△). 67

1.26 Variation of the oxygen content in iron with the ratio H_2/H_2O at 1,350°C in Ar-H_2-H_2O gas. 72

1.27 Partial molar excess of Gibbs free energy for oxygen dissolved in pure nickel calculated from data in Table 1.10 and Eq.(1.135). 74

1.28 Oxygen activity in Fe-Ni melts at 1,600°C. Eq.(1.144) with $h = 2.08$ kJ mol^{-1} (——), Eq.(1.147) with $h_1 = 6.41$ kJ mol^{-1} and $h_2 = -2.32$ kJ mol^{-1} (- - -). 79

1.29 Oxygen diffusion coefficients in iron determined from internal oxidation experiments in Rhines pack (open symbols) and H_2/H_2O gas mixture (filled symbols) and independent solubility measurements. . . 81

1.30 Oxygen diffusion in nickel measured by different experimental techniques. 84

2.1 Fe-Cr phase diagram. 92

2.2 Optical observations of samples after annmealing 72h at 1,100°C under Ar-5%H_2. Etchants specified in sub-captions. 96
2.3 Button cutting pattern. 97
2.4 Slice cutting directions. 98
2.5 Iron oxide equilibrium pressures (——) and partial pressure set in the reaction furnace by the equilibrium H_2/H_2O (- - -). 100
2.6 Comparison of the oxygen partial pressure set by the H_2/H_2O gas mixture in the different apparatus with the Fe/FeO dissociation pressure. Horizontal furnace (▮▮), Thermobalance (▯▯). 102
2.7 Pure Fe surface after 4h of exposure at 1,150°C in H_2/H_2O 103
2.8 Rhines pack capsule 104
2.9 Gas experiment steps. 108
2.10 Schematic representation of experimental setup for TGA under H_2/H_2O gas mixtures. 109
2.11 Calibration line for ultra low oxygen content. 111
2.12 Test for ultra low oxygen calibration. Certified values (–▲–), measured values (-■-). 111
2.14 Amount of oxygen from oxidised impurities, with Cr_2O_3(–■–),no Cr_2O_3 (–□–). 115
2.15 Measurement of the IOZ depth for alloy Fe-20Ni-7.5Cr reacted 60h at 1,000°C in H_2/H_2O with 3% water vapour content. 116
2.16 Optical micrograph, x1000, Fe-20Ni-7.5Cr exposed 4h at 1,150°C in H_2/H_2O gas with 13% water vapour. 117
2.17 Internal oxide volume fraction as function of IOZ depth measured for Fe-20Ni-7.5Cr alloy exposed for 4h at 1,150°C in H_2/H_2O mixtures containing 13% of water vapour. 117

3.1 Excess Gibbs free energy evaluated from oxygen concentration measurement for different temperature after reaction in Fe/FeO packs, assuming no impurity Cr oxidation (○) and with Cr oxidation (+). . . 126

3.2 Difference between excess Gibbs free energy for oxygen dissolution if chromium impurities remains in solution or form Cr_2O_3: 1,000°C (▯▯), 1,050°C (▮▮). 127

3.3 Variation of excess enthalpy and entropy with the alloy composition after exposure in Fe/FeO Rhines packs. 128

3.4 Excess Gibbs free energy measured after exposure in Fe/FeO Rhines packs at several temperatures, 1,000°C (–△–), 1,050°C (–□–), 1,100°C (–○–), 1,150°C (–◇–). 129

3.5 Variation of the oxygen solubility measured in Fe/FeO Rhines pack with the alloy composition. 130

3.6 Solubility at high temperature of carbon and nitrogen in Fe-Ni alloys measured in various conditions. 131

3.7 Excess Gibbs free energy evaluated from oxygen concentration measurement for different temperatures after reaction in H_2/H_2O gases containing 13% water vapour with the oxygen partial pressure set at the Fe/FeO equilibrium. 133

3.8 Variation of excess enthalpy and entropy with the alloy composition after exposure in H_2/H_2O gases containing 13% water vapour and the oxygen partial pressure set at the Fe/FeO dissociation pressure. . . . 134

3.9 Variation of $\overline{G}_O^{xs}$ with the alloy composition, measured after exposure in H_2/H_2O gases containing 13% water vapour with the oxygen partial pressure set at the Fe/FeO equilibrium for several temperatures: 1,000°C (extrapolation) (–△–), 1,050°C (–□–), 1,100°C (–○–), 1,150°C (–◇–). 135

3.10 Variation of the oxygen solubility with the alloy composition. Sample exposed to H_2/H_2O gases containing 13% water vapour and the oxygen partial pressure set at the Fe/FeO dissociation pressure. . . . 136

3.11 Excess Gibbs free energy for oxygen dissolution in pure Fe 137

3.12 Excess free energy for oxygen dissolution in pure Ni. 141

3.13 Comparison of the excess of Gibbs free energy for oxygen dissolution in pure Fe, Ni and several Fe-Ni alloys measured in Fe/FeO Rhines packs (–○–) and H_2/H_2O gases containing 13 % water vapour and oxygen partial pressure set at the Fe/FeO equilibrium (–●–). 144

3.14 Comparison of oxygen solubility calculated from Gibbs free energy measured in Fe/FeO Rhines pack,N_O^{RP} and H_2/H_2O gas mixtures ,$N_O^{H_2/H_2O}$ at different temperature: 1,000°C (▯▯), 1,050°C (▯▯), 1,100°C (▯▯), 1,150°C (▮▮). 145

3.15 Oxygen solubility measured in Fe/FeO Rhines packs and calculated with Alcock and Richardson's model (- - -) and Wagner's model(——). 148

3.16 Oxygen solubility measured in H_2/H_2O gases and calculated with Alcock and Richardson model's (- - -) and Wagner's model(——). . . . 149

4.1 Micrographs of IOZ after exposure in Fe/FeO Rhines pack at 1,000°C: 48 h for Fe, Fe-20Ni, Fe-40Ni; 100 h for Fe-60Ni, Fe-80Ni. 155

4.2 SEM observation of the IOZ after 48h of reaction at 1,150°C in Fe/FeO Rhines pack. 158

4.3 EDS scan in a composite oxide particle. 159

4.4 Variation of f with alloy nickel content. f measured for alloys with 7.5 at.% Cr reacted in Fe/FeO Rhines packs (4 at.% Cr for $\frac{N_{Ni}}{N_{Fe}+N_{Ni}}$=0.8). 1,000°C (–△–), 1,050°C (–□–), 1,100°C (–○–), 1,150°C (–◇–). 160

4.5 Variation of f (open symbols) and $p_{O_2}^{(t)}$ (filled symbols) with the alloy composition : 1,000°C (–△–,–▲–), 1,150°C (–◇–,–●–). 162

4.6 Internal oxidation kinetics measured in Fe/FeO Rhines packs at 1,000°C, $p_{O_2} = (1.2 \pm 0.2) \times 10^{-15}$ atm. 164

4.7 Internal oxidation kinetics measured in Fe/FeO Rhines packs at 1,150°C, $p_{O_2} = (2.3 \pm 0.4) \times 10^{-13}$ atm. 165

4.8 Variation of the internal oxidation constant measured in Fe/FeO Rhines pack with the alloy composition: 2 at.% Cr (–△–), 4 at.% Cr (–□–), 7.5 at.% Cr (–○–). 167

4.9 Arrhenius plots of internal oxidation rate constant measured in Fe/FeO Rhines pack. 169

4.10 Pre-exponential factor and activation energy for the internal oxidation rate constant, $k_p^{(i)}$, measured in Rhines Pack: 1 at.% (–◇–,▮▮), 2 at.% (–△–,▯▯), 4 at.% (–□–,▮▮), 7.5 at.% (–○–,▮▮). 170

4.11 Micrographs of IOZ after exposure in H_2/H_2O gas with 13% water vapour at 1,000°C for 150h. 171

4.12 BSE osbervation of Fe-60Ni-7.5Cr exposed for 100h at 1,150°C in H_2/H_2O gases containing 13% water vapour and oxygen partial pressure set at Fe/FeO equilibrium. 172

4.13 Variation of the parameter f with the alloy nickel content. f measured in alloy with 7.5 at.% Cr reacted in H_2/H_2O gases with 13% water vapour and oxygen partial pressure set at the Fe/FeO equilibrium. 1,000°C (–△–), 1,050°C (–□–), 1,100°C (–○–), 1,150°C (–◇–). . . 174

4.14 Fe-60Ni-7.5Cr after exposure at 1,000°C in Ar-H_2-H_2O for 24 h. . . . 174

4.15 Internal oxidation kinetics measured in H_2/H_2O gas at 1,000°C and oxygen partial pressure set at the Fe/FeO equilibrium. 177

4.16 Internal oxidation rate constants measured in H_2/H_2O gas with 13% of water vapour and oxygen partial pressure set at the Fe/FeO equilibrium as a function of the alloy composition: 2 at.% Cr (–△–), 4 at.% Cr (–□–), 7.5 at.% Cr (–○–). 179

4.17 Arrhenius plot of internal oxidation rate constant measured in H_2/H_2O gases with 13% water vapour and oxygen partial pressure set at the Fe/FeO equilibrium. 181

4.18 Pre-exponential factor and activation energy for $k_p^{(i)}$ measured in H_2/H_2O gases with 13% of water vapour and oxygen partial pressure set at the Fe/FeO equilibrium: 1 at.% (–◇–,▮▮), 2 at.% (–△–,▯▯), 4 at.% (–□–,▮▮), 7.5 at.% (–○–,▮▮). 182

4.19 Weigh change of sample measured in H_2/H_2O gas with 13% water vapour at 1,000°C, $p_{O_2} = (1.2 \pm 0.2) \times 10^{-15}$ atm. 183

4.20 $k_w^{(i)}$ measured in H_2/H_2O gas with 13% water vapour and oxygen partial pressure set at the Fe/FeO equilibrium as a function of the alloy composition: 2 at.% Cr (–△–), 4 at.% Cr (–□–), 7.5 at.% Cr (–○–).184

4.21 $\frac{k_w^{(i)}}{k_p^{(i)}}$ calculated from weight change and penetration: 1,000°C (△), 1,050°C (□) or calculated from $N_{Cr}^{(0)}$ and ν for two different internal oxides : $Fe_{0.5}CrO_2$ (——), $CrO_{1.5}$ (- - -). 186

4.22 Internal oxidation kinetics measured at 1,050°C in H_2/H_2O gas with 3% water vapour and oxygen partial pressure set at the Fe/FeO equilibrium, $p_{O_2} = (1.1 \pm 0.2) \times 10^{-15}$ atm. 188

4.23 Determination of the internal oxidation constant using the complete parabolic law: $t = C\left(\frac{\Delta w}{S}\right)^2 + B\frac{\Delta w}{S} + A$ and $k_w^{(i)} = 1/2C$ in $g^2\ cm^{-4}\ s^{-1}$. 189

4.24 Arrhenius plot of $k_w^{(i)}$ measured in H_2/H_2O gases with 3% water vapour and oxygen partial pressure set at the Fe/FeO equilibrium. . . 190

4.25 Pre-exponential factor and activation energy for $k_w^{(i)}$ measured in H_2/H_2O gases with 3% water vapour and oxygen partial pressure set at the Fe/FeO equilibrium: 1 at.% (–◇–,▮▮), 2 at.% (–△–,▯▯), 7.5 at.% (–○–,▮▮). 191

4.26 $\frac{k_w^{(i)}}{k_p^{(i)}}$ calculated from weight change and penetration: 1,000°C (△), 1,050°C (□), 1,150°C (◇) or calculated from $N_{Cr}^{(0)}$ and ν for two different internal oxides: $Fe_{0.5}CrO_2$ (——), $CrO_{1.5}$ (- - -). 194

4.27 Values of f measured at 1,150°C in various environment with the oxygen partial set at the Fe/FeO equilibrium : Fe/FeO Rhines packs (–○–), 3% H_2O (–●–), 13% H_2O (–●–). 197

4.28 Comparison of activation energy for $k_p^{(i)}$ measured in various environment : Fe/FeO Rhines packs (▯▯), 3% H_2O (▯▯), 13% H_2O (▯▯) 199

4.29 Comparison of internal oxidation constant evaluated by IOZ depth measurement in Rhines pack, $k_p^{(i)\,(\mathrm{RP})}$, and in flowing Ar-H_2-H_2O with 13% water vapour, $k_p^{(i)(13\%\ H_2O)}$: 1 at.% Cr (▯▯), 2 at.% Cr (▯▯), 4 at.% Cr (▯▯), 7.5 at.% Cr (▯▯). 201

4.30 Comparison of internal oxidation constant evaluated by weight gain measurement in H_2/H_2O gases with 3% water vapour, $k_w^{(i)(3\%H_2O)}$, and in H_2/H_2O gases with 13% water, $k_w^{(i)(13\%H_2O)}$. Oxygen partial pressure set at the Fe/FeO equilibrium in all environments: 1 at.% Cr (▯▯), 2 at.% Cr (▯▯), 7.5 at.% Cr (▯▯). 202

5.1 Internal oxide distribution in the internal oxidation zone. 210

5.2 Variation of Γ calculated for different values of enrichment factor and chromium content : 2 at.% (——), 4 at.% (——), 7.5 at.% (——). 213

5.3 Variation of the enrichment factor with alloy composition and temperature for alloys with 2 and 7.5 at.% of chromium. 1,000°C (–△–), 1,050°C (–□–), 1,100°C (–○–), 1,150°C (–◇–). 218

5.4 Effect of volume expansion on the value of the enrichment factor measured in Fe/FeO Rhines packs: 2 at.% (▯▯), 4 at.% (▯▯), 7.5 at.% (▯▯).219

5.5 Internal oxide distribution in the internal oxidation zone. 222

5.6 Comparison of total volume fraction measured by image analysis (▯▯,▯▯) and calculated with equation (5.42) (▯▯,▯▯) for alloys with 7.5 at.% Cr: Fe/FeO Rhines pack (▯▯,▯▯) and H_2/H_2O gases containing 13% of water vapour (▯▯,▯▯). 225

5.7 Comparison of enrichment factor calculated from the diffusional approach (Eq.5.15,–▲–) and from volume fraction measurement (Eq.5.53,–○–) for alloys containing 7.5 at.% Cr reacted in Fe/FeO Rhines packs 227

5.8 Comparison of enrichment factor calculated from the diffusional approach (Eq.5.15,–▲–) and from volume fraction measurement (Eq.5.53,–○–) for alloys containing 7.5 at.% Cr reacted H_2/H_2O gases containing 13% water vapour. 228

5.9 Effective stoichiometry calculated from internal oxidation rate (Eq.5.57) measured in H_2/H_2O gases containing 13% of water vapour as a function of the alloy chromium content. Fe (–△–), Fe-20Ni (–○–), Fe-40Ni (–□–), Fe-60Ni (–◇–). 232

5.10 Comparison of effective stoichiometric coefficient evaluated by kinetic measurements (Eq.5.57,▯▯)and SEM observations (Eq.5.54,▮▮) in alloys with 7.5 at.% Cr exposed to H_2/H_2O gases with 13% of water vapour. 233

5.11 Internal oxide volume fraction as function of the IOZ depht for alloys reacted at 1,000°C in H_2/H_2O gases with 13% of water vapour. 241

5.12 Estimation of y for different values of α 247

5.13 Schematic representation of internal oxide distribution in the IOZ when multiple internal oxides precipitate. 248

5.14 Variation of ν_{eff} in the case of incomplete precipitation in subzone 2 with f calculated for different values of y. 251

5.15 Comparison of ν_{eff} calculated with Equation (5.54) or (5.103). 252

5.16 Comparison of effective stoichiometry calculated from kinetics measured for alloys with 7.5 at.% Cr in flowing H_2/H_2O gases containing 13% (▯▯)and 3% (▮▮) water vapour. 253

5.17 Comparison of effective stoichiometric coefficient evaluated by kinetics measurement (Eq.5.57,□□) in alloys exposed to humid gas with 3% water vapour and SEM observation (Eq.5.54,▮▮) carried out in alloys exposed to wet gases with 13% water vapour both at 1,150°C. 254

5.18 Plot of the parameter $k_p^{(i)\prime}$ measured at 1,000 and 1,050°C in Fe/FeO Rhines packs versus the inverse of the alloy chromium concentration. 257

5.19 Geometry for area calculation. 259

5.20 Ratio $\frac{D_O^{eff}}{D_O^{mat}}$ calculated for different internal oxide volume fractions. . . 264

5.21 Plot of the parameter $k_p^{(i)\prime}$ measured at 1,000 and 1,050°C in Fe/FeO Rhines packs versus the inverse of the alloy chromium concentration. Values corrected for chromium-rich alloys using Equation (5.138) (–▲–,–■–). 270

5.22 Plot of the parameter $k_p^{(i)\prime}$ measured at 1,100 and 1,150°C in Fe/FeO Rhines packs versus the inverse of the chromium. 271

5.23 Matrix oxygen permeability measured in Fe/FeO Rhines packs at different temperature: 1,000°C (△), 1,050°C (□), 1,100°C (○), 1,150°C (◇). Values in pure nickel extrapolated with equation (5.143) from data published by Guo *et al.* (filled symbols). Note log scale. 273

5.24 Arrhenius plots of matrix permeability evaluated in Fe/FeO Rhines pack. Fe (△), Fe-20Ni (□), Fe-40Ni (□), Fe-60Ni (◇), Fe-80Ni (⬠). . . . 275

5.25 Plot of the parameter $k_p^{(i)\prime}$ measured at 1,000 and 1,050°C in H_2/H_2O gases containing 13% water vapour and the oxygen partial pressure set at the Fe/FeO equilibrium versus the inverse of the chromium. . . 278

5.26 Plot of the parameter $k_p^{(i)\prime}$ measured at 1,100 and 1,150°C in H_2/H_2O gases containing 13% water vapour and the oxygen partial pressure set at the Fe/FeO equilibrium versus the inverse of the chromium. . . 279

5.27 Matrix oxygen permeability measured in H_2/H_2O gases containing 13% water vapour and the oxygen partial pressure set at Fe/FeO equilibrium: 1,000°C (△), 1,050°C (□), 1,100°C (○), 1,150°C (◇). Values in pure nickel extrapolated with equation (5.143) from data published by Guo *et al.* (filled symbols). Note log scale. 280

5.28 Arrhenius plots of matrix oxygen permeability measured in H_2/H_2O gases containing 13% water vapour and the oxygen partial pressure set at the Fe/FeO equilibrium.Fe (△), Fe-20Ni (□), Fe-40Ni (□), Fe-60Ni (◇), Fe-80Ni (⬠). 282

5.29 $k_p^{(i)'}$ measured at different temperatures in H_2/H_2O gases containing 3% water vapour and oxygen partial pressure set at the Fe/FeO equilibrium. 283

5.30 Comparison of matrix oxygen permeability measured in Fe/FeO Rhines packs (○), H_2/H_2O gases with 13% water vapour (▲) and H_2/H_2O gases with 3% water vapour (◆). Values in pure nickel extrapolated with Equation (5.143) from data published by Guo *et al.* (□, ■, ■). Note log scale. 285

5.31 Comparison of λ estimated from experiments carried out in Fe/FeO Rhines packs (▯▯) and H_2/H_2O (▮▮) gas with 13% of water vapour. . . 287

5.32 Arrhenius plots for iron matrix permeability with data from Fe/FeO Rhines pack and H_2/H_2O gas mixtures with 13 and 3% water vapour considered as a single set of data 288

5.33 Oxygen permeability of γ-iron measured in different atmospheres, Fe/FeO Rhines pack (open symbols), H_2/H_2O gas mixtures (filled symbols), ◐ combined data RP+H_2/H_2O. 289

5.34 Permeability measured from the chromium critical content for transition between internal and external oxidation observed by Croll and Wallwork at 1,000°C and calculated for the Fe/FeO dissociation pressure (–●–,–■–). Oxygen permeability measured by internal oxidation in Fe/FeO Rhines pack (○), H_2/H_2O with 13% water vapour (▲), H_2/H_2O with 3% water vapour (♦). 291

6.1 Matrix oxygen diffusion coefficient measured in Fe/FeO Rhines packs at different temperature: 1,000°C (–△–), 1,050°C (–□–), 1,100°C (–○–), 1,150°C (–◇–). Values for pure nickel extrapolated with Equation (5.143) from data published by Guo *et al.* (filled symbols). . . . 300

6.2 Carbon diffusion coefficient in Fe-Ni alloys with a fix concentration $N_C^{(0)} = 1 \times 10^3$ at.ppm : 1,000°C (–△–), 1,050°C (–□–), 1,100°C (–○–). 302

6.3 Lattice parameter at high temperature for Fe-Ni alloys : 950°C (–△–); 1,050°C (–□–). 302

6.4 Excess enthalpy as a function of the number of iron atoms surrounding an octahedral site. 304

6.5 Arrhenius plots of internal oxidation rate constant measured in Fe/FeO Rhines pack. 305

6.6 Matrix oxygen diffusion coefficient measured in H_2/H_2O gases containing 13% water vapour and oxygen partial pressure set at the Fe/FeO equilibrium pressure at different temperature: 1,000°C (–△–), 1,050°C (–□–), 1,100°C (–○–), 1,150°C (–◇–). Values in pure nickel extrapolated with Equation (5.143) from data published by Guo *et al.* (filled symbols). 308

6.7 Arrhenius plots of internal oxidation rate constant measured in H_2/H_2O gases containing 13% water vapour and oxygen partial pressure set at the Fe/FeO equilibrium pressure. 309

6.8 Matrix oxygen diffusion coefficient measured in H_2/H_2O gases with 3% water vapour at 1,150°C (–◇–). Values in pure nickel extrapolated with Equation (5.143) from data published by Guo *et al.* (filled symbols) 311

6.9 Comparison of matrix oxygen diffusion coefficient measured in Fe/FeO Rhines packs (–○–), H_2/H_2O gas with 3% water vapour (–◍–), H_2/H_2O gas with 13% water vapour (–●–). Values in pure nickel extrapolated with Equation (5.143) from data published by Guo *et al.* Note log scale. 312

6.10 Activation energy for oxygen diffusion coefficient measured in Fe/FeO Rhines packs (▯▯) and H_2/H_2O gases containing 13% of water vapour with the oxygen partial pressure set at the Fe/FeO equilibrium pressure (▮▮). Value for nickel determined in Section 1.6.2 from several internal oxidation experiments at Ni/NiO dissociation pressure (▮▮). . 314

List of Tables

1.1 Formation reaction standard free energies of Fe, Ni, Cr oxides. 10

1.2 Comparison of interdiffusion coefficient ($cm^2\ s^{-1}$) measured and calculated for the Ag-Au system. 22

1.3 Enrichment factor measured in Fe-Al and Fe-Si alloys at 1,050°C after internal oxidation in Rhines pack. 44

1.4 Oxygen permeability in γ-iron measured by internal oxidation of Fe-Cr alloys. 48

1.5 Activation energy of the internal oxidation parabolic constant for Ni-Cr alloys. 54

1.6 Volume of one mole of alloy and one mole of Cr in oxides. 57

1.7 Pre-exponential factor and activation energy for the Fe-Cr alloy diffusion coefficient calculation. 59

1.8 Pre-exponential factor and activation energy for the Ni-Cr alloy diffusion coefficient calculation. 60

1.9 Oxygen solubility in γ-iron equilibrated in H_2/H_2O mixtures. 71

1.10 Oxygen solubility in nickel measured at the Ni/NiO dissociation pressure. 74

1.11 Value of the Wagner parameter and the two parameters model for the Fe-Ni-O system. 79

1.12 Pre-exponential factor and activation energy for oxygen diffusion in γ-iron. 82

1.13 Pre-exponential factor and activation energy for oxygen diffusion in α-iron. 82

1.14 Pre-exponential factor and activation energy for oxygen diffusion in nickel. 84

2.1 Alloy compositions for solubility experiment. 91

2.2 Critical chromium content to observe the transition between internal and external oxidation in Fe-Ni-Cr alloys at 1,000°C with the oxygen partial pressure set at the Fe/FeO equilibrium, extrapolated from Croll and Wallwork's measurement. 93

2.3 Alloy compositions for internal oxidation experiments. 95

2.4 Grain sizes after annealing for 72h at 1,100°C. 97

2.5 Standard free energy of formation of wüstite and Fe/FeO equilibrium pressure. 99

2.6 Gas composition and oxygen partial pressure for experiments in horizontal furnace. 101

2.7 Gas composition and oxygen partial pressure for experiments in thermobalance. 101

2.8 Predicted and selected duration for Rhines pack experiment ($\frac{M_t}{M_\infty} = 0.97$). 104

2.9 SiO partial pressure in Fe/FeO Rhines packs. 106

2.10 Evaluation of the maximum silicon contamination after 150h in Fe/FeO Rhines packs. 107

2.11 Material impurity level in at.ppm and oxidation reaction considered. . 112

3.1 Excess enthalpy and entropy determined by non-linear fitting of oxygen solubility (Eq.3.9) measured in Fe/FeO Rhines packs. 128

3.2 Oxygen solubility values calculated using Equation (3.9) with values of $\overline{H}_O^{xs}$ and $\overline{S}_O^{xs}$ determined in Fe/FeO Rhines packs. 131

3.3 Excess enthalpy and Entropy for oxygen dissolution from H_2/H_2O gases containing 13% water vapour with the oxygen partial pressure set at the Fe/FeO dissociation pressure. 132

3.4 Oxygen solubility values calculated using Equation (3.9) with values of $\overline{H}_O^{xs}$ and $\overline{S}_O^{xs}$ determined in H_2/H_2O gases containing 13% of water vapour and the oxygen partial pressure set at the Fe/FeO equilibrium pressure. 135

3.5 Excess enthalpy and entropy for oxygen dissolution in iron. 137

3.6 Calculation of $\frac{M_t}{M_\infty}$ with oxygen diffusion coefficient published by Takada *et al.* and corrected for higher oxygen solubility 138

3.7 Calculation of $\frac{M_t}{M_\infty}$ with oxygen diffusion coefficient published by Swisher and Turkdogan. 139

3.8 Excess enthalpy and entropy for oxygen dissolution in nickel. 141

3.9 Calculation of hydrogen partial pressure in Fe/FeO Rhines packs. . . 143

3.10 Energetic parameter h (kJ mol^{-1}) evaluated by fitting solubility calculated with Eq.(3.22) to experimental solubility. 149

4.1 f evaluated from measure of $X_{(t)}$ for alloys with 7.5 at.% Cr (4 at.% Cr for $\frac{N_{Ni}}{N_{Fe}+N_{Ni}}$=0.8) reacted in Fe/FeO Rhines packs. Error considered: ±0.1. 159

4.2 Iron activity calculated using $a_{Fe} = N_{Fe}\gamma_{Fe}$ and activity coefficient computed from Equation (4.11). 162

4.3 Evaluation of the oxygen partial pressure, $p_{O_2}^{(t)}$ (atm), at the location $X = X_{(t)}$. 162

4.4 $k_p^{(i)}$ measured after exposure in Fe/FeO Rhines Pack. 166

4.5 Pre-exponential factor and activation energy for internal oxidation rate constant: $k_p^{(i)} = k_p^{(0)} \exp(-Q/RT)$. 168

4.6 f evaluated from measurements of $X_{(t)}$ for alloys with 7.5 at.% Cr (2 at.% Cr for $\frac{N_{Ni}}{N_{Fe}+N_{Ni}}$=0.8)reacted in H_2/H_2O gas with 13% of water vapour and oxygen partial pressure set at the Fe/FeO equilibrium. Error considered: ±0.1. 173

4.7 f evaluated from measurements of $X_{(t)}$ for alloys with 7.5 at.% Cr (2 at.% Cr for $\frac{N_{Ni}}{N_{Fe}+N_{Ni}}$=0.8) reacted in H_2/H_2O gas with 3% water vapour and oxygen partial pressure set at the Fe/FeO equilibrium. Error considered: ±0.1. 175

4.8 $k_p^{(i)}$ measured after exposure in flowing H_2/H_2O gas containing 13% H_2O and oxygen partial pressure set at the Fe/FeO equilibrium. . . . 178

4.9 Pre-exponential factor and activation energy for internal oxidation rate constant measured in H_2/H_2O gases with 13% water vapour and oxygen partial pressure set at the Fe/FeO equilibrium: $k_p^{(i)} = k_p^{(0)} \exp(-Q/RT)$. 180

4.10 $k_w^{(i)}$ measured by discontinuous TGA in H_2/H_2O gas with 13% water and the oxygen partial pressure set at the Fe/FeO equilibrium. 184

4.11 Internal oxidation constant measured by continuous TGA in H_2/H_2O gas with 3% water and oxygen partial pressure set at the Fe/FeO equilibrium. 189

4.12 Pre-exponential factor and activation energy for internal oxidation rate constant measured in H_2/H_2O gases with 3% of water vapour and oxygen partial pressure set at the Fe/FeO equilibrium: $k_w^{(i)} = k_w^{(0)} \exp(-Q/RT)$. 191

4.13 $k_p^{(i)}$ measured after exposition in H_2/H_2O gas with 3% water and the oxygen partial pressure set at the Fe/FeO equilibrium 192

4.14 Pre-exponential factor and activation energy for internal oxidation rate constant measured in H_2/H_2O gases with 3% water vapour and oxygen partial pressure set at the Fe/FeO equilibrium: $k_p^{(i)} = k_p^{(0)} \exp(-Q/RT)$. 193

4.15 Time required to diffuse out of the sample residual hydrogen at 1,000°C196

5.1 Fractional volume expansion calculated considering $Fe_{0.5}CrO_2$ or $CrO_{1.5}$ oxides in Fe-Cr or Ni-Cr alloys. 212

5.2 Interdiffusion coefficients of chromium for Fe-Cr and Fe-Ni-Cr alloys . 215

5.3 Alloy lattice parameters and molar volumes. 216

5.4 Enrichment factors calculated with Equation (5.15) from kinetics measured in Fe/FeO Rhines packs. 217

5.5 Enrichment factors calculated with Equation (5.15) from kinetics measured in H_2/H_2O gases containing 13% water vapour. 220

5.6 Enrichment factors calculated with Equation (5.15) from kinetics measured in H_2/H_2O gases containing 3% of water vapour. 221

5.7 Volume fraction measured for alloys with 7.5 at.% Cr, after exposure at 1,000°C in Fe/FeO Rhines packs and H_2/H_2O gases containing 13% of water vapour. 223

5.8 Volume fraction measured for alloys with 7.5 at.% Cr after exposure at 1,150°C in Fe/FeO Rhines packs and H_2/H_2O gases containing 13% water vapour. 224

5.9 Effective stoichiometric coefficient for alloys with 7.5 at.% Cr reacted in Fe/FeO Rhines packs calculated with the mixing law (Eq.5.54) with f measured in Rhines packs. 229

5.10 Effective stoichiometric coefficient for alloys with 7.5 at.% Cr reacted in H_2/H_2O gases containing 13% of water vapour calculated with the mixing law (Eq.5.54) with f measured in alloys reacted in H_2/H_2O gases. 229

5.11 Activity coefficient for chromium in iron at infinite dilution. 236

5.12 Solubility product of chromium oxide in iron. 237

5.13 Solubility product of chromium oxide in nickel 238

5.14 Evaluation of the matrix chromium content at $X = X_{(t)}$. 239

5.15 Mole fraction of chromium unoxidised in subzone 2 for alloys reacted at 1,000°C in H_2/H_2O gases with 13% of water vapour. 243

5.16 Comparison of $F_v^{(2)}$ required for $N_{Cr}^{(2)} = 0$ and the volume fraction measured. 243

5.17 Evaluation of the solubility parameter α in various alloys reacted at 1,000°C. 246

5.18 Average particle size, $\overline{R}_p$ (μm), measured at 3 locations in the IOZ. . 266

5.19 Ratio of parameters λ calculated for different particle sizes. 266

5.20 Matrix oxygen permeability measured in Fe/FeO Rhines packs. 272

5.21 Values of λ for alloys reacted in Fe/FeO Rhines packs. 275

5.22 Matrix oxygen permeability measured in H_2/H_2O gases containing 13% of water vapour and the oxygen partial pressure set at the Fe/FeO equilibrium 280

5.23 Values of λ for alloys reacted in H_2/H_2O gas mixture containing 13% water vapour and oxygen partial pressure set at the Fe/FeO equilibrium. 281

5.24 Matrix oxygen permeability measured in alloys exposed to H_2/H_2O gases with 3% water vapour. Error in oxygen permeability estimated at 30%. 284

6.1 Matrix oxygen diffusion coefficient measured in Fe/FeO Rhines packs. 298

6.2 Determination of $\frac{M_t}{M_\infty}$ to verify saturation of samples used for solubility experiment in Fe/FeO Rhines packs. 299

6.3 Pre-exponential factor and activation energy for oxygen diffusion measured in Fe/FeO Rhines pack. 306

6.4 Matrix oxygen diffusion coefficient measured in H_2/H_2O gases with 13% of water vapour and oxygen partial pressure set at the Fe/FeO equilibrium. 307

6.5 Determination of $\frac{M_t}{M_\infty}$ to verify saturation of samples used for solubility experiment in H_2/H_2O gases. 308

6.6 Pre-exponential factor and activation energy for oxygen diffusion measured in H_2/H_2O gases with 13% water vapour and oxygen partial pressure set at the Fe/FeO equilibrium. 310

6.7 Matrix oxygen diffusion coefficient measured in H_2/H_2O gases with 3% water vapour and oxygen partial pressure set at the Fe/FeO equilibrium. 311

6.8 Comparison of internal particle size measured at $X/X_{(i)} = 0.5$ after exposure in Fe/FeO Rhines packs and H_2/H_2O gas with 13% water vapour. Alloy exposed 48h at 1,000°C. 320

Abstract

It is a worldwide priority to reduce emissions of greenhouse gases such as CO_2. One solution for reducing these emissions is to improve the efficiency of energy production units by increasing their operating temperature. However, in order to increase operating temperature, new austenitic materials based on the Fe-Ni-Cr system have to be designed. In addition, these materials need to exhibit good protection against high temperature oxidation, which is achieved by the formation of a slow growing chromium oxide or alumina scale on the metal. However, to predict the formation of a protective scale, knowledge of the oxygen permeability, the product of oxygen solubility and diffusivity, in the base alloy is required.

The objective of this study is to measure the permeability, solubility and diffusivity of oxygen in Fe-Ni alloys at temperatures above 1,000°C. In order to obtain the best results, the formation of an external oxide layer during the experiment has to be avoided. To achieve this, the oxygen partial pressure was fixed at the Fe/FeO equilibrium pressure in all experiments. In addition, two types of atmospheres were used: one dry and one wet, in order to investigate the effect of water vapour on oxygen permeability, solubility and diffusivity. The dry atmosphere was achieved using the Rhines Pack technique. The samples were oxidised in vacuum-sealed quartz capsules, which contained a mixture of powdered iron and wüstite. The humid atmosphere was obtained by using H_2/H_2O gas mixtures with the appropriate water vapour to hydrogen ratio to fix oxygen partial pressure at the Fe/FeO equilibrium.

The maximum oxygen solubility was found in pure iron, and decreased continuously with nickel additions to the alloy. The dependence of solubility on alloy

composition is non-ideal, and cannot be predicted from simple models. Moreover, the presence of water vapour in the atmosphere seems to increase the solubility by a factor of 2 in alloys with nickel content lower than 80 at.% at temperatures near 1,000°C. However, at 1,150°C the solubility of the oxygen is independent of the environment. The oxygen permeability was determined by measuring the internal oxidation kinetics of Fe-Ni-Cr alloy. These kinetics were evaluated by measuring the internal oxidation zone depth by optical microscopy, or by continuous and discontinuous thermogravimetry. Results showed that the oxygen permeability exhibits the same variation with alloy composition as the oxygen solubility, independent of the atmosphere. In particular, no significant effect of water vapour on oxygen permeability values was observed. In the present study, the oxygen diffusion coefficient was also determined using permeability, in addition to the independent measurement of the oxygen solubility carried out in the present study. For temperature above 1,000°C, the variation of oxygen diffusion coefficient with the alloy composition is similar in all environments tested, and a maximum is observed for alloys with a nickel content of 40 at.%. However, for a given nickel content up to 60 at.%, the presence of water vapour in the atmosphere decreases the value of the oxygen diffusion coefficient by a factor of 2-3 at 1,000°C. In addition, this difference between diffusion coefficients measured in a dry and wet atmosphere increases as the temperature decreases.

Overall, it was found that the water vapour has no effect on the way in which oxygen permeability, solubility and diffusivity vary with the alloy composition. However, the presence of water vapour in the environment appears to increase the oxygen solubility and decrease the oxygen diffusivity in iron-rich alloys, the effect being more significant at low temperatures. These results suggest further research into interactions between O, H and metal vacancies, particularly for temperature around 1,000°C and below, as the latter defect is thought to change the diffusion and solubility properties of interstitial species.

Résumé

Les matériaux basés sur le système Fe-Ni-Cr utilisés à haute température doivent présenter une bonne résistance à l'oxydation, généralement obtenue par la croissance lente d'une couche d'oxyde de chrome à la surface de ces alliages. Pour prédire la formation d'une couche d'oxyde protectrice la perméabilité de l'oxygène dans l'alliage doit être connue, la perméabilité étant définie comme le produit de la solubilité et du coefficient de diffusion de l'oxygène.

L'objectif de nos travaux est de mesurer la perméabilité, la solubilité et la diffusivité de l'oxygène dans des alliages Fe-Ni pour des températures supérieures à 1000°C. Afin d'obtenir les meilleurs résultats, la formation d'une couche externe d'oxyde pendant les expériences doit être évitée. Pour cela, la pression partielle d'oxygène a été fixée à la pression d'équilibre Fe/FeO dans toutes les expériences. En outre, afin d'étudier l'effet de la vapeur d'eau sur la perméabilité, la solubilité et la diffusivité de l'oxygène, deux atmosphères ont été utilisées: l'une considérée comme sèche et l'autre comme humide. L'atmosphère sèche a été obtenue en utilisant la technique du « pack de Rhines » : les échantillons sont oxydés dans des capsules en quartz sous vide qui contiennent un mélange de poudre de fer et de wüstite. L'atmosphère humide a quant à elle été obtenue en utilisant des mélanges gazeux H_2/H_2O avec un ratio approprié de vapeur d'eau et d'hydrogène afin de fixer la pression partielle d'oxygène à la pression d'équilibre Fe/FeO.

Les mesures de solubilité réalisées dans ce travail ont montré que celle-ci atteint son maximum dans le fer pur et diminue avec l'ajout de nickel. Cependant, la dépendance de la solubilité avec la composition de l'alliage Fe-Ni n'est pas idéale et ne

peut être prédite à partir de modèles simples. De plus, les résultats obtenus sous atmosphère humide suggèrent que la présence de vapeur d'eau dans l'atmosphère augmente la solubilité de l'oxygène d'un facteur 2 dans les alliages avec une concentration en nickel inférieure ou égale à 60 at.% pour des températures proches de 1000°C, tandis qu'à 1150°C, la solubilité de l'oxygène est indépendante de l'environnement.

La perméabilité de l'oxygène a été déterminée en mesurant la cinétique d'oxydation interne d'alliages Fe-Ni-Cr. Les résultats ont montré que la perméabilité de l'oxygène présente les mêmes variations avec la composition de l'alliage que la solubilité de l'oxygène, indépendamment de l'atmosphère. De plus, aucun effet significatif de la vapeur d'eau sur les valeurs de perméabilité de l'oxygène n'a été observé. Le coefficient de diffusion de l'oxygène a également été déterminé en utilisant les résultats précédents, c'est à dire la perméabilité et la solubilité de l'oxygène mesurées dans notre étude. Pour une température supérieure à 1000°C, la variation du coefficient de diffusion de l'oxygène avec la composition de l'alliage est similaire dans tous les environnements testés et un maximum est observé pour les alliages avec une teneur en nickel de 40 at.%. Cependant, la présence de vapeur d'eau dans l'atmosphère diminue les valeurs du coefficient de diffusion de l'oxygène, par un facteur 2-3 à 1000°C, pour les alliages avec une concentration en nickel inférieure ou égal à 60 at.%. De plus, il a été trouvé que la différence entre les coefficients de diffusion mesurés dans l'atmosphère sèche et humide augmente à mesure que la température diminue.

En conclusion, il a été constaté que la vapeur d'eau n'a aucun effet sur la manière dont la perméabilité, la solubilité et la diffusivité de l'oxygène varient avec la composition des alliages Fe-Ni. Cependant, la présence de vapeur d'eau dans l'environnement semble augmenter la solubilité de l'oxygène et diminuer sa diffusivité dans les alliages riches en fer. De plus, l'effet de la vapeur d'eau apparaît plus important aux plus basses températures étudiées.

Introduction

Producing energy in our society has become a real challenge. Worldwide, states try to reduce their emissions of CO_2 and for that, renewable energies seem to provide a sustainable way. However they need further development to be able to answer the energy demand. At the moment, oil and coal provide 60% of the global production of energy, and it is forecast that the consumption of coal is going to increase by 20% by around 2020, to become the primary source of energy in the world. To reduce emissions from coal fired energy production plants, operating temperatures have to be increased in order to improve their efficiency. In several countries, new targets have been identified with the aim of using the steam temperatures between 700 and 800°C to achieve the best performance.

Today, ferritic-martensitic steels are widely used in power plants. They will need to be replaced by high temperature materials, based on the Fe-Ni system, in order to survive increased operating temperatures of these units. However, materials used in power generation units at high temperature are exposed to aggressive environments containing corrosive gases such as CO, CO_2, SO_2, H_2O etc., and therefore need to exhibit good protection against high temperature corrosion. This is usually achieved by the formation of a slow growing chromia or alumina scale on the alloy surface, which acts as a barrier to protect the underlying alloy of corrosive gases. Thus the Fe-Ni-Cr system is a good candidate for the design of new high temperature materials. However, to observe this protective oxidation, the alloy composition has to meet several criteria stated by Carl Wagner [1].

When Fe-Ni-Cr alloys are exposed to high temperatures in oxidising environments, in the early stage of the oxidation process, a competition between the inward flux of oxygen and the outward flux of chromium takes place. If the flux of oxygen is significantly larger than the chromium flux, only a small part of the oxygen flux is consumed to form Cr_2O_3 at the alloy surface. The remaining oxygen diffuses deeper into the material, oxidising chromium during its penetration and resulting in the formation of an internal oxidation zone. On the other hand, if the chromium flux is sufficiently high, all oxygen entering into the material is consumed at the

surface to form Cr_2O_3, and the formation of an external scale is observed. This scale greatly reduces the oxygen flux entering into the material and prevents further internal oxidation.

Internal oxidation may be desirable to the design of some materials, with small and scattered precipitates used in order to strengthen the alloy. However, in most cases this type of oxidation should be avoided when the alloy is used in service. Indeed, internal oxidation can weaken the alloy if strengthening elements are removed from the matrix and leads to dramatic failure of materials. One solution to prevent internal oxidation is to increase the chromium flux, therefore its concentration in the alloy. Wagner showed that the minimum amount of chromium to observe the transition between internal and external oxidation may be evaluated if the oxygen permeability, defined as the product of oxygen solubility and diffusivity, of the base metal is known.

Internal oxidation kinetics are controlled by the oxygen permeability. Thus, this property has been measured for pure Fe and Ni by internally oxidising Fe-Cr/Al or Ni-Cr/Al alloys. However, no data is available in the literature for Fe-Ni alloys. In addition, the effect of water vapour on oxygen permeability for pure metals has been investigated but is difficult to assess as the few studies available were carried out under different experimental conditions. Oxygen permeability measurements allow the evaluation of the oxygen diffusion coefficient in the base metal since an independent measure of oxygen solubility is available. However, as with the oxygen permeability, data for oxygen solubility in Fe-Ni alloys are not available and only 4 studies have provided reliable data for oxygen solubility for pure Fe or Ni.

The aim of this project was to measure the oxygen solubility, permeability and diffusivity for Fe and Fe-Ni model alloys of various compositions. The oxygen permeability was obtained by internal oxidation of Fe-Ni-Cr model alloys. However, it should be noted that determination of the oxygen permeability required evaluation of secondary parameters such as the internal oxide stoichiometry and an enrichment factor. The effect of water vapour and/or hydrogen on the oxygen solubility,

permeability and diffusivity was also investigated by using two atmospheres, one considered as dry, obtained with the Rhines packs technique, and the other humid, obtained from H_2/H_2O gas mixtures.

This present manuscript is divided into 7 Chapters. The first Chapter is devoted to a review of oxidation studies at high temperature of iron, nickel and Fe-Ni based alloys with a particular focus on internal oxidation. In addition, the few studies for oxygen solubility in iron and nickel are presented in one section of this Chapter. Chapter 2 describes the experimental protocol and characterisation techniques used in this study. In Chapter 3, results of oxygen solubility measurements are presented, along with a discussion of possible effects of water vapour on this property. Results for internal oxidation kinetics measured in various environments are presented in Chapter 4. In Chapter 5, values of oxygen permeability evaluated from internal oxidation kinetics are presented. In addition, a particular focus is given to the evaluation of secondary parameters required for oxygen permeability evaluation, in particular the internal oxide stoichiometry and chromium enrichment in the IOZ. In a section of Chapter 5, the question of the water vapour and/or hydrogen effect on the oxygen permeability is addressed. In Chapter 6, the oxygen diffusion coefficient is evaluated by combining the oxygen permeability and solubility measured in the present study. A final chapter summarises the findings made and conclusions arrived at in this thesis.

Chapter 1

Literature review

This chapter reviews the literature on internal oxidation at high temperature of iron, nickel and Fe-Ni alloys. These elements are major constituents of many commercial steels and superalloys, and knowledge of their behaviour relevant to high temperature corrosion is critical to proper alloy design. Firstly, concepts of the oxidation process are presented from a thermodynamic and kinetics point of view. A brief review of pure iron oxidation is added to illustrate these concepts. In the last part of this section, the basics of alloy diffusion are presented. In a second part, the alloy internal oxidation process described by Wagner [1] is reviewed. This development reveals that the alloy permeability, which is the product of oxygen solubility and diffusivity, is a critical parameter in predicting the kinetics of this particular oxidation and the general behaviour of alloys regarding oxidation. In addition, a selection of internal oxidation experimental results is presented to examine the effects of water vapour on oxygen permeability.

A second aim of this project was to measure oxygen solubility in Fe, Ni and Fe-Ni alloys. As is reviewed here, very little information is available in the literature. In addition, models for the prediction of oxygen solubility in liquid metals are introduced as a discussion base for model in the solid state.

Finally, knowledge of the oxygen permeability and solubility allows calculation of oxygen diffusion coefficients. Data present in the literature are reviewed in the last part of this chapter.

1.1 Oxidation of pure metals

This section concerns the oxidation of pure metals, and presents basic principles of oxidation at high temperature. Firstly, a thermodynamic approach to the oxidation is given, then kinetic laws of oxidation are described and the oxidation of iron is briefly presented.

1.1.1 Thermodynamic approach to oxidation

The oxidation of a pure metal M by oxygen is described by the general equation

$$x\mathrm{M} + \frac{y}{2}\mathrm{O}_2 \rightarrow \mathrm{M}_x\mathrm{O}_y \tag{1.1}$$

For an isobaric, isothermal system, the condition for equilibrium is given by the relation

$$\sum_{i=1}^{n} \nu_i \mu_i = \sum_{i=1}^{n} \nu_i [\mu_i^0 + RT \ln (a_i)] = 0 \tag{1.2}$$

where n is the number of constituents, μ_i^0 the reference chemical potential of the species i, a_i the activity of this species and ν_i the stoichiometric coefficient. If this relation is applied to Equation (1.1), and the gas species activity equated to its partial pressure, we obtain

$$x\mu_M^0 + \frac{y}{2}\mu_{O_2}^0 - \mu_{M_xO_y}^0 + RT \ln \left(\frac{a_M^x p_{O_2}^{\frac{y}{2}}}{a_{M_xO_y}} \right) = 0 \tag{1.3}$$

where p_{O_2} is the oxygen partial pressure. Equation (1.3) could be rewritten

$$K_{1.1} = \exp \left(\frac{-\Delta G_{1.1}^0}{RT} \right) = \frac{a_{M_xO_y}}{a_M^x p_{O_2}^{\frac{y}{2}}} \tag{1.4}$$

where $\Delta G_{1.1}^0 = \mu_{M_xO_y}^0 - x\mu_M^0 - \frac{y}{2}\mu_{O_2}^0$ is the standard free energy of the reaction and $K_{1.1}$ is the equilibrium constant of reaction 1.1. Assuming that oxidation of the pure metal leads to the formation of one single oxide phase, and putting the activity for condensed phases equal to unity, Equation (1.4) yields the equilibrium oxygen pressure,$p_{O_2,eq}$

$$\exp \left(\frac{-\Delta G_{1.1}^0}{RT} \right) = \frac{1}{p_{O_2,eq}^{\frac{y}{2}}} \tag{1.5}$$

This pressure, called the dissociation pressure of the oxide, is the minimum pressure to oxidise the metal M. To know if a metal could be oxidised, p_{O_2} in the system has to be compared to $p_{O_2,eq}$.

To calculate the equilibrium pressure, the free energy of the reaction is needed.

$$\Delta G^0(T) = \Delta H^0(T) - T\Delta S^0(T) \tag{1.6}$$

Here $\Delta H^0(T)$ is the standard enthalpy of the reaction and $\Delta S^0(T)$ the standard change of internal entropy. A common approximation is to assume that both terms are constant in a range of temperature where no phase transition takes place, according to Ellingham's approximation [2]. Table 1.1 gives values of the standard enthalpy of the reaction and the standard change of entropy for the formation of wustite, nickel and chromium oxides. Using values from Table 1.1 in Equation (1.5), the dissociation pressure of the different oxides can be calculated as shown in Figure 1.1.

Table 1.1: Formation reaction standard free energies of Fe, Ni, Cr oxides [3].

Reactions	ΔH^0 kJ mol^{-1}	ΔS^0 J mol^{-1} K^{-1}
$Fe + \frac{1}{2}O_2 \rightarrow FeO$	-264.890	-65.4
$Ni + \frac{1}{2}O_2 \rightarrow NiO$	-234.345	-84.3
$\frac{2}{3}Cr + \frac{1}{2}O_2 \rightarrow \frac{1}{3}Cr_2O_3$	-373.420	-86.0

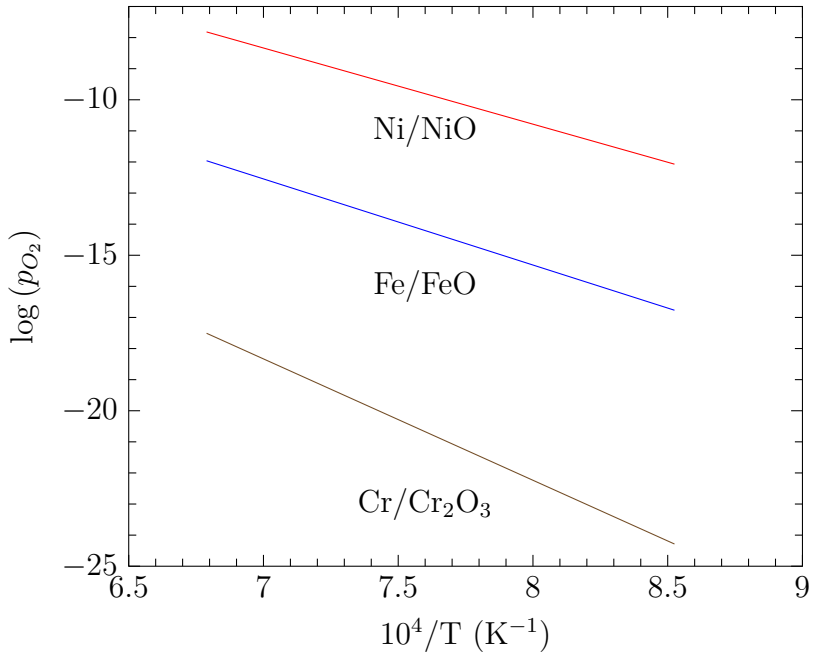

Figure 1.1: Dissociation pressure of wustite, nickel oxide and chromium oxide.

1.1.2 Oxidation kinetics

During oxide scale growth, metals and oxygen are ionised at their respective interfaces with the scale and one or both species diffuse across the scale to sustain the oxide growth. According to Wagner's theory [4], ionic species in an oxide scale can diffuse as a result of two driving forces: an electric field and chemical potential gradients. In order to predict the kinetic law for scale growth Pilling and Bedworth [5] classified metals into two groups: porous oxide formers and non-porous oxide formers. Their criterion is based on the ratio of the volume of metal oxide to the volume of the metal in this oxide (PBR). Most of the time this ratio is larger than 1 and metals form a dense oxide, while if this ratio is lower than 1, metals are likely to form porous oxide. This difference in oxide structure modifies the oxidation kinetics.

Linear Rate Law

According to Pilling and Bedworth [5], metals which form porous oxides undergo oxidation following kinetics described by a linear rate law.

$$X = k_l t + A \tag{1.7}$$

where X is the thickness of the scale, k_l the rate constant of the oxidation reaction and A another constant. This kind of oxide offers low protection and poor mechanical properties so they are often subject to spallation. In this case, the metal is always in contact with the atmosphere and the rate controlling process is an interfacial reaction. Since this is unaffected by the accumulation of porous scale, a constant rate and linear kinetics result. Only the alkali metals display this behaviour like K/K_2O with PBR= 0.45.

Parabolic rate law

In most cases, oxidation scaling kinetics are parabolic. This kinetics is controlled by the temperature and the oxygen partial pressure in the environment. On the other hand, the oxide structure and mechanical state can influence the oxidation kinetics.

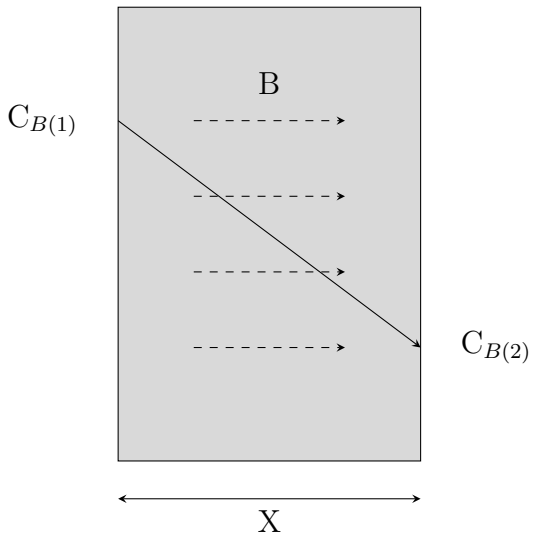

Figure 1.2: Atomic transport in a growing oxide scale, where $C_{B(1)}$ and $C_{B(2)}$ are the concentrations of the diffusing species B at the boundaries.

In the example where the oxidation rate is proportional to the flux of B, one can write

$$\frac{dX}{dt} = \Omega J_B \tag{1.8}$$

with Ω the volume of oxide formed per unit quantity of diffusing species, and J_B the flux of B going through a unit area of a plane perpendicular to the flux direction. The flux of B is given by Fick's first law

$$J_B = -\tilde{D}_B \frac{\partial C_B}{\partial X} \tag{1.9}$$

where C_B is the concentration of species B and $\tilde{D}_B$ the diffusion coefficient of B in the scale taking into account (1+z) charge of defect, with z, the charge of the species B. If the derivative is approximated by a linear concentration gradient as shown in

Figure 1.2, this yields

$$J_B = -\tilde{D}_B \frac{C_{B(2)} - C_{B(1)}}{X} \tag{1.10}$$

Combining Equations (1.8) and (1.10), the following relation is found

$$\frac{dX}{dt} = \Omega \tilde{D}_B \frac{C_{B(1)} - C_{B(2)}}{X} \tag{1.11}$$

The last step is to integrate to find the parabolic rate law

$$\int_{x=0}^{x=x} X \, \mathrm{d}X = \int_{t=0}^{t=t} k_p \, \mathrm{d}t \tag{1.12}$$

$$X^2 = 2k_p t \tag{1.13}$$

with $k_p = \Omega \tilde{D}_B \left(C_{B(1)} - C_{B(2)} \right)$. Wagner was the first to derive the expression of the oxidation parabolic constant and demonstrated that this parameter depends on different properties of the oxide, such as its composition or diffusion properties within the scale.

In practice, a common way to evaluate the parabolic constant is to measure the weight gain associated with oxygen uptaken. The parabolic rate law is then written as

$$\left(\frac{\Delta w}{S} \right)^2 = 2k_w t \tag{1.14}$$

where Δw is the mass variation recorded, S the surface area of the sample and k_w the gravimetric constant. This constant is linked to the parabolic constant by the relation

$$k_w = \left(\frac{y M_O}{V_{M_x O_y}} \right)^2 k_p \tag{1.15}$$

where y is the stoichiometric coefficient of oxygen in the oxide, M_O the atomic weight of oxygen and $V_{M_x O_y}$ the molar volume of the oxide. In addition, the variation of k_p

with temperature can be described by an Arrhenius relationship

$$k_p = k_p^{(0)} \exp\left(-\frac{Q}{RT}\right) \tag{1.16}$$

where $k_p^{(0)}$ is a constant and Q the activation energy which is also constant.

It must be emphasised that deviations from the parabolic law have often been observed during the early stage of alloy oxidation due to the simultaneous oxidation of more noble and less noble alloy components at the beginning of the oxidation process. On the other hand, low temperature deviations from the parabolic law have been observed after long terms because of grain growth that modifies diffrent properties of the oxide scale. In addition, Equation (1.14) is valid with the initial conditions $w = t = 0$. However, such conditions are difficult to obtain experimentally, and the sample oxidation may start during sample heating, for example. Monceau *et al.* [6] proposed a new analysis to evaluate the oxidation kinetics from thermogravimetric measurement without influence of initial conditions and/or oxidation mechanisms. These authors proposed to fit the experimental data to the following equation

$$t = A + B\frac{\Delta w}{S} + C\left(\frac{\Delta w}{S}\right)^2 \tag{1.17}$$

and demonstrated that the "true" parabolic constant is given by

$$k_w = \frac{1}{2C} \tag{1.18}$$

This analysis can be carried out on selected time-intervals through the entire set of data and make possible an investigation of the way in which the parabolic constant evolves with time. To test their analysis, Peraldi *et al.* [7] oxidised pure nickel in oxygen between 600 and 1,200°C. Results showed that the oxidation kinetics achieved a steady state after a transition time which decreases with increasing temperature, and the value found from (1.18) was in agreement with the value of k_w calculated with Equation (1.14).

1.1.3 Oxidation of pure iron

Oxidation of pure iron in air or oxygen has been studied in a wide range of temperatures by several authors [8–11]. Long term oxidation leads to the growth of a compact oxide scale, which is in reality composed of three layers. From the outer surface to the metal they are Fe_2O_3, Fe_3O_4 and FeO. In all reactions at temperatures between 700 and 1,250°C, it was found that the major part of the scale is FeO (95%) and other oxides Fe_2O_3, Fe_3O_4 account for 1% and 4% respectively, as Figure 1.3 shows. Each layer grows by a different diffusion mechanism. Davies *et al.* [8] described the growth mode for each iron oxide.

- Wüstite (FeO) grows almost entirely by iron ion lattice diffusion
- Magnetite (Fe_3O_4) grows by oxide ion and iron ion diffusion. However, the latter process accounts for 20% of the growth process.
- Hematite (Fe_2O_3) grows principally by oxide ion diffusion

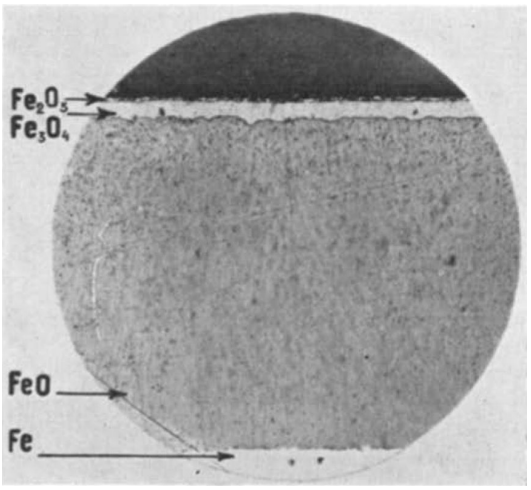

Figure 1.3: Optical microscopic observation of an oxide layer on pure iron oxidised in air at 700°C. Reprinted from [9] with permission from Elsevier.

Iron scaling kinetics were found to be independent of the oxygen pressure between 4×10^{-3} and 10 atm [10]. In addition, all authors found that the kinetics followed a parabolic rate law except in the early stage of oxidation. This deviation from the parabolic rate law was observed by Païdassi and Goursat *et al.* [9, 10],

who defined it as a transient state at the beginning of the oxidation process due to the exothermic reaction between iron and oxygen leading to a local increase of the temperature. At the beginning of iron oxidation, this over-temperature changed the oxidation rate which was faster than in isothermal oxidation. In this transient state, kinetics do not follow the parabolic rate law corresponding to long term oxidation.

Païdassi [9] carried out his experiments in air, where parameters like moisture were not controlled, compared to Davies *et al.* [8] who used purified oxygen. These differences in atmosphere might explain discrepancies between experimental results. However, taking into account these differences in experimental methods, results are consistent and are presented in Figure 1.4a. Chen and Yuen [12], using the previous data and other results for iron oxidation, obtained a good fit to Equation (1.16) in the range of 700-1,250°C and found an activation energy of 158 kJ.mol^{-1} for iron oxidation.

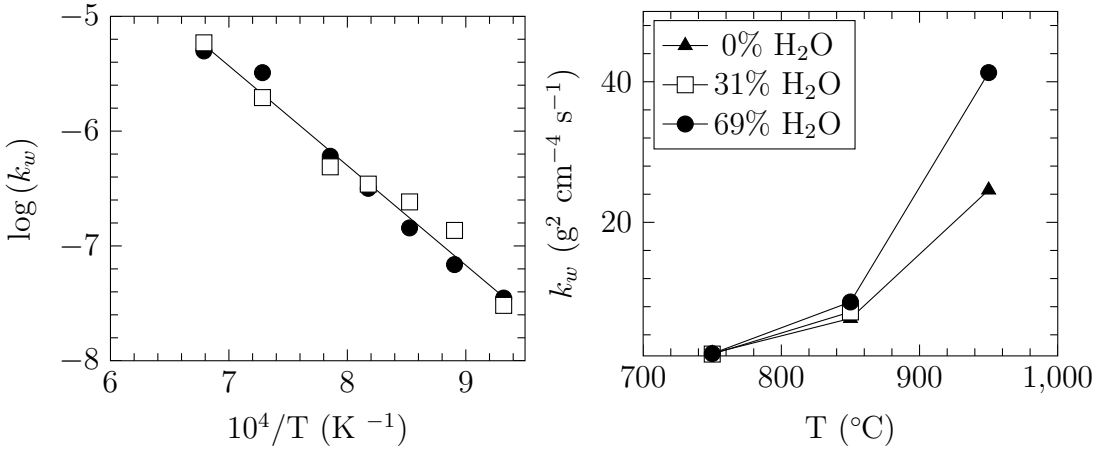

(a) iron oxidation kinetics: air [9] (●) purified oxygen [8] (□)

(b) Effect of temperature and gas composition on iron oxidation kinetics in O_2+steam [13]

Figure 1.4: Oxidation kinetics of iron in various environments.

The presence of humidity in the atmosphere has an impact on iron scaling kinetics. Rahmel and Tobolski [13] and Tuck *et al.* [14] studied oxidation of pure iron in oxygen plus steam environments, and all authors noted that for temperatures below 750°C, the presence of water vapour had no impact on kinetics. In addition, Rahmel and Tobolski observed that the iron oxidation rate was increasing with

temperature and water content of the gas as shown in Figure 1.4b. However, the two studies provided two different explanations, related to the microstructure of the oxide scales. Rahmel and Tobolski observed that in the presence of water vapour, the outer scale was compact while the inner scale was porous, and sometimes the contact between the metal and its oxide scale was lost. To explain the increased oxidation rates, they proposed that transport of oxygen was enhanced in pores where H_2O and H_2 were present. On the other hand, Tuck *et al.* observed an increase of the oxidation rate in steam environment, but the scales apparently stayed compact and contact between the alloy and the wüstite scale was never lost. They suggested that hydrogen dissolved in scales increased their plasticity, so they could easily be deformed, and the contact kept.

1.2 Diffusion in metals

The oxidation process at high temperature is often controlled by diffusion of ionic species in the scale or sometimes of solute in the alloy. In this section, a short review of the concept of diffusion in metals is presented. Diffusion laws were first announced by Adolph Fick [15], using similarities with heat transfer. Diffusion in a metal is a result of numerous small displacements of diffusing particles on the lattice, these movements being facilitated by the presence of point defects such as vacancies or interstitial atoms.

In this section a thermodynamic description of diffusion is given first, using a multi component approach and, in a second part, diffusion in alloys is presented.

1.2.1 Thermodynamic approach to diffusion

A first approach to diffusion in an alloy is to consider that when a concentration gradient is present, atoms move to homogenise the composition, from the part with the highest concentration to the region with the lowest.

If unidirectional diffusion by a vacancy mechanism in a binary alloy is consid-

ered, the flux of atom is defined by Fick's first law

$$J_1 = -D_1 \frac{\partial C_1}{\partial x} \tag{1.19}$$

where J_1 is the flux of atom in mol cm^{-2} s^{-1} and D_1 the diffusion coefficient of the corresponding species in cm^2 s^{-1}. The diffusion coefficient exhibits the same temperature dependency as k_p. One can write

$$D_1 = D_1^{(0)} \exp\left(\frac{-Q}{RT}\right) \tag{1.20}$$

where $D_1^{(0)}$ is a constant pre-exponential factor and Q the activation energy of diffusion.

In a thermodynamic approach for irreversible processes, a microscopic element of the alloy is considered to be at local equilibrium. The variation of entropy in this element is due to the flux of material under thermodynamic forces. If isothermal diffusion in a closed, isobaric, n-component system is considered, fluxes are expressed by linear equations given by the following equation [16]

$$J_i = -\sum_{j=1}^{n} L_{ij} \nabla \eta_j \tag{1.21}$$

where L_{ij} are the Osanger phenomenological coefficients and ∇ the gradient operator. If Equation (1.21) is compared to (1.19), the driving force corresponds to $\nabla \eta_j$ which is called the electrochemical potential gradient. This force is expressed by the addition of the chemical potential and electrostatic energy, Equation (1.11). However, in metallic alloys, matter is neutral so the driving force is only the chemical potential gradient. Osanger coefficients form a matrix with off diagonal terms which represent "cross-effects". These cross-effects can be due to thermodynamic or kinetic interaction between atoms. In a binary alloy, flux of the different species have the

following expression

$$J_1 = -L_{11}\frac{\partial \mu_1}{\partial x} - L_{12}\frac{\partial \mu_2}{\partial x} - L_{1v}\frac{\partial \mu_v}{\partial x} \tag{1.22}$$

$$J_2 = -L_{21}\frac{\partial \mu_1}{\partial x} - L_{22}\frac{\partial \mu_2}{\partial x} - L_{2v}\frac{\partial \mu_v}{\partial x} \tag{1.23}$$

$$J_v = -L_{v1}\frac{\partial \mu_1}{\partial x} - L_{v2}\frac{\partial \mu_2}{\partial x} - L_{vv}\frac{\partial \mu_v}{\partial x} \tag{1.24}$$

where the J_v is the flux of vacancies and J_1 and J_2 are the flux of species 1 and 2, respectively. A first approximation is to consider that vacancies are at any location in thermal equilibrium and yields $\mu_v \approx 0$. In addition, it is considered cross effect terms are negligible, $L_{12} = L_{21} \approx 0$. However, it should be emphasised that this assumption has to be considered with care because it is often not verified. The flux is therefore expressed by

$$J_1 = -L_{11}\frac{\partial \mu_1}{\partial x} \tag{1.25}$$

and $\mu_i = \mu_i^0 + RTln(a_i)$, as used in Equation (1.2). In the case of a non-ideal solution the relation between the activity and the mole fraction of a species, N_i, is given by

$$a_i = \gamma_i N_i \tag{1.26}$$

where γ_i is the activity coefficient and is equated to 1 in the case of an ideal solution. Finally, one can write

$$J_1 = -\frac{L_{11}RT}{N_1}\left(1 + \frac{\partial \ln(\gamma_1)}{\partial \ln(N_1)}\right)\frac{\partial N_1}{\partial x} \tag{1.27}$$

Comparing Equation (1.27) with (1.19) and using the relationship $C\partial N_1 = \partial C_1$ with C the average total molar concentration, the intrinsic diffusion coefficient is

found to be expressed as

$$D_1 = \frac{L_{11}RT}{C_1}\left(1 + \frac{\partial \ln(\gamma_1)}{\partial \ln(N_1)}\right) \tag{1.28}$$

Equation (1.28) shows that diffusion coefficient depends on thermodynamic properties of the alloys even if cross effects are neglected. In the literature, diffusion properties have often been measured by tracer technique. The intrinsic diffusion coefficient can be calculated from tracer diffusion coefficient using the following relationship if a binary alloy is considered

$$D_1 = D_1^*\left(1 + \frac{\partial \ln(\gamma_1)}{\partial \ln(N_1)}\right) \tag{1.29}$$

where D_1^* is the diffusion coefficient of 1 measured by tracer technique.

1.2.2 Diffusion in alloys

1.2.2.1 Cross-effects

In an alloy, as mentioned earlier, cross-effects can be due to thermodynamic or kinetic interactions between the different elements in the alloy. If Equation (1.21) is considered, it can be adopted to yield a generalisation of Fick's law in the form

$$J_i = -\sum_{j=1}^{n-1} D_{ij}\nabla C_j \tag{1.30}$$

Brown and Kirkaldy [17] in their work on carbon diffusion in dilute ternary austenites, assuming that kinetic cross-effects are negligible, found the following relation between diffusion coefficients

$$\frac{D_{12}}{D_{11}} = \frac{\frac{\partial \mu_1}{\partial N_2}}{\frac{\partial \mu_1}{\partial N_1}} \tag{1.31}$$

In addition, Wagner [18] examined the compositional dependence of activity coefficients (1.26) in an n-component system. He demonstrated that the activity coefficient can be expanded as a Taylor series which when limited to first order

terms for the component 1 is written

$$\ln(\gamma_1) = \ln(\gamma_1^0) + \sum_{k=1}^{n-1} \varepsilon_{1k} N_k \tag{1.32}$$

where γ_1^0 is the Henry's law coefficient, N_k the mole fraction of the species k, and ε_{1k} the first order free energy interaction parameter. The latter parameter is defined as

$$\varepsilon_{1k} = \left[\frac{\partial \ln(\gamma_1)}{\partial N_k} \right]_{N_k \longrightarrow 0} \tag{1.33}$$

Assuming a dilute solution limit and using the definition of the activity coefficient defined by Wagner (1.32), it is found that

$$\frac{D_{12}}{D_{11}} = \frac{\varepsilon_{12} N_1}{1 + \varepsilon_{11} N_1} \tag{1.34}$$

This relation enables us to determine the "off-diagonal" diffusion coefficients.

1.2.2.2 Interdiffusion coefficient

The protective oxidation of alloys relies on the diffusion of a solute, like aluminium or chromium, from the bulk alloy to its surface, there to be consumed and form an oxide scale. However, the solute and the base metal usually share the same lattice. Thus a composite mobility has to be defined taking into account interactions between the different species to predict the behaviour of alloys regarding oxidation. This diffusion coefficient is called the interdiffusion coefficient and is measured using a diffusion couple. Darken [19] showed that in a binary alloy, it is possible to estimate the interdiffusion coefficient from tracer diffusion coefficients as shown by Equation (1.35), known as the Darken-Hartley-Crank Equation.

$$\tilde{D} = (N_1 D_2^* + N_2 D_1^*) \left(1 + \frac{\partial \ln(\gamma_1)}{\partial \ln(N_1)} \right) \tag{1.35}$$

where D_1^* and D_2^* are diffusivities measured by tracer experiments. Darken checked Equation (1.35) calculating the interdiffusion coefficient in the Ag-Au system from

tracer measurements and compared its value to experimental data measured by Johnson [20] using the interdiffusion couple technique. Results of Darken's calculations and Johnson's experiments are presented in Table 1.2.

Table 1.2: Comparison of interdiffusion coefficient ($cm^2\ s^{-1}$) measured [20] and calculated [19] for the Ag-Au system.

	800°C	900°C	1,000°C
$\tilde{D} \times 10^{10}$ measured	4.5	24	97
$\tilde{D} \times 10^{10}$ (1.35)	3.8	21	93

Good agreement was found between measured and calculated values, confirming that Equation (1.35) is valid to calculate interdiffusion coefficient when the thermodynamics of the system are known.

Few data for intrinsic diffusion coefficient or interdiffusion coefficient are available in the literature, because most diffusion coefficients were measured by tracer diffusion technique. However, assuming ideal behaviour, Equation (1.29) can be rewritten as

$$D_1 \approx D_1^* \tag{1.36}$$

In addition, if only the interdiffusion coefficient is available and if the species of interest is dilute, the intrinsic diffusion coefficient can be approximated from (1.35) as

$$\tilde{D} \approx D_1 \tag{1.37}$$

1.3 Oxidation of alloys

Alloys used at high temperature are exposed to severe conditions and often highly corrosive environments containing water vapour, carbon dioxide, sulphur etc. Protection against high temperature oxidation is achieved by the formation of a thermodynamically stable, slow-growing oxide scale like chromia or alumina on the surface. If the oxidation of an alloy AB is considered, with B a less noble metal than A, different oxide structures can exist depending on the alloy composition and

experimental conditions . During oxidation, there is a competition between metallic atoms outward flux and the inward flux of oxygen in the alloy. If B is a minor element and the oxygen partial pressure is lower than the dissociation pressure of the oxide AO, no oxide scale forms on the alloy surface. As a result, the inward oxygen flux is greater than the outward flux of metallic atoms B and the formation of internal oxides beneath the alloy surface (Figure 1.5.(a)) is observed. This is usually observed for Fe-Cr and Ni-Cr alloys with low chromium content. If the alloy content of element B is increased, the flux of metallic atoms becomes larger and the alloy exhibits exclusive external oxidation with the formation of the oxide BO on the material surface, as with Fe-Cr or Ni-Cr alloys with large chromium content, which form a Cr_2O_3 scale (Figure 1.5.(b)). If now B is the major alloying element, B can

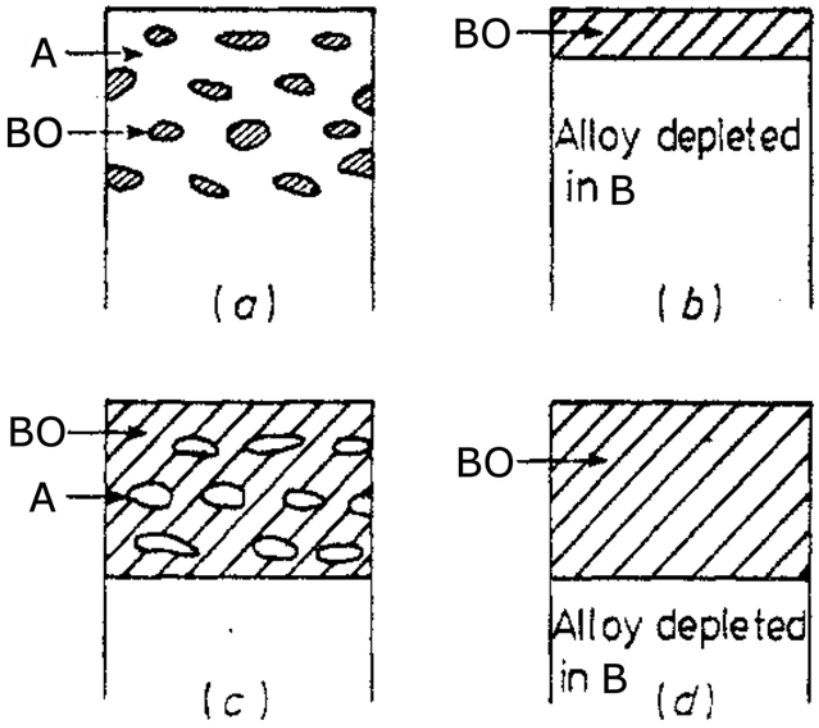

Figure 1.5: Schematic representation of the different types of oxidation in case of binary alloy A-B [21]. © IOP Publishing. Reproduced with permission. All rights reserved.

oxidise leaving some particles of pure metal A in the oxide (Figure 1.5.(c)) or the metal A is left in an enriched area beneath the scale BO (Figure 1.5.(d)). Wagner demonstrated that the selective oxidation of one component to obtain the formation

of a protective scale requires that the alloy composition meet certain criteria. In this section, selective oxidation of one component is examined with a particular focus on internal oxidation.

1.3.1 Selective oxidation of one component

Wagner [22] considered oxidation of Pt-Ni alloys in air to describe the selective oxidation of alloys. In these alloys, platinum is more noble than nickel, and a scale of NiO grows when this alloy is exposed to an oxidizing atmosphere. In addition, Wagner assumed that only diffusion controls the rate of oxidation, as described in section 1.1.2 on kinetics. The thickness of the NiO external scale is then given by

$$X^2 = 2k_p t \tag{1.38}$$

where X is the thickness of the external scale and k_p the alloy oxidation parabolic constant. Alloy diffusion is described by Fick's second law

$$\frac{\partial N_{Ni}}{\partial t} = \tilde{D}\frac{\partial^2 N_{Ni}}{\partial x^2} \tag{1.39}$$

where N_{Ni} is the mole fraction of nickel and $\tilde{D}$ the alloy interdiffusion coefficient. With the initial condition

$$N_{Ni} = N_{Ni}^{(0)} \text{ for } x > 0, t = 0 \tag{1.40}$$

where $N_{Ni}^{(0)}$ is the original mole fraction of nickel in the bulk alloy. Wagner showed that the steady state solution for the concentration profile of nickel from the initial surface could be written as below, under the assumptions that the movement of the oxide/alloy interface can be neglected and that the mole fraction of nickel at this interface is fixed

$$N_{Ni}(x,t) = N_{Ni}^{(i)} + (N_{Ni}^{(0)} - N_{Ni}^{(i)})\,\mathrm{erf}\left(\frac{x}{2\sqrt{\tilde{D}t}}\right) \tag{1.41}$$

where $N_{Ni}^{(i)}$ is the mole fraction of nickel at the metal/oxide interface. To ensure that enough Ni can diffuse to sustain the scale growth of the nickel oxide, the flux of nickel at the interface in the alloy has to be calculated. The flux is given by Fick's first law

$$J_{Ni} = -\frac{\tilde{D}}{V_{alloy}} \left.\frac{\partial N_{Ni}}{\partial x}\right|_{x=0} \tag{1.42}$$

where V_{alloy} is the molar volume of the alloy. Then, (1.42) combined with (1.41), yields

$$J_{Ni} = \left(\frac{\tilde{D}}{\pi t}\right)^{\frac{1}{2}} \frac{(N_{Ni}^{(0)} - N_{Ni}^{(i)})}{V_{alloy}} \tag{1.43}$$

To be able to sustain the scale growth, the flux of nickel has to be equal to the rate at which it is oxidised into the scale. Using the parabolic law of scale growth, Wagner found the following relation

$$(N_{Ni}^{(0)} - N_{Ni}^{(i)}) = \frac{V_{alloy}}{V_{NiO}} \left(\frac{\pi k_p}{2\tilde{D}}\right)^{\frac{1}{2}} \tag{1.44}$$

This equation enables us to calculate the minimum concentration required to sustain scale growth. The maximum alloy flux of atoms is reached when $N_{Ni}^{(i)} = 0$. In general, where B is the less noble metal, the alloy composition condition required to sustain the growth of an external scale is given by

$$N_B^{(0)} > \frac{V_{AB}}{V_{BO}} \left(\frac{\pi k_p}{2\tilde{D}}\right)^{\frac{1}{2}} \tag{1.45}$$

However, this expression is valid only if the growth of the scale is slow, otherwise the movement of the metal/oxide interface has to be considered. In addition, this condition is necessary but not sufficient to ensure that a scale of the less noble metal only will grow. At the beginning of the oxidation reaction, all alloying element oxides could nucleate and continue to grow and, another condition has to be fulfilled to totally control the selective oxidation process.

1.3.2 Internal oxidation

As it was described earlier in this section, internal oxidation consists of the oxidation beneath the alloy surface of less noble metals than the matrix. In some alloys, this phenomenon may have a significant effect on the alloy properties [23–25]. For example, interactions between these oxide particles and dislocations can influence mechanical properties such as tensile strength, creep behaviour or fatigue life. Controlling internal oxidation kinetics, internal oxide size or spacing between particles is necessary to design alloys with proper mechanical properties. In the following development, Wagner's model for internal oxidation kinetics and the fundamental work of Böhm and Kahlweit on internal oxide nucleation and growth are reviewed. In addition, special consideration is given to Gesmundo's work on the measurement of internal oxidation kinetics by a thermogravimetric technique.

1.3.2.1 Steps of internal oxidation

The process of internal oxidation, when no outer scale has grown, can be described by three different steps:

First the oxygen dissolution reaction at the alloy surface is described by

$$\frac{1}{2}\mathrm{O}_2 \rightarrow \underline{\mathrm{O}} \tag{1.46}$$

where underlining denotes solute species. The corresponding equilibrium expression is

$$N_O = K^{(s)} p_{O_2}^{1/2} \tag{1.47}$$

where $K^{(s)}$ is the Sievert constant and N_O the mole fraction of dissolved oxygen in the material at the equilibrium.

Second is oxygen diffusion through the alloy. According to Wagner's work [1], the velocity of internal oxidation front is controlled by the oxygen diffusion. Integration of Fick's laws, as in the first part of this chapter, yields a parabolic

rate law for the depth of the internal oxidation zone (IOZ).

$$X_{(i)}^2 = 2k_p^{(i)}t \tag{1.48}$$

where $X_{(i)}$ is the distance from the sample surface to the internal oxidation front and $k_p^{(i)}$ the internal oxidation parabolic constant.

Third the oxidation reaction at the internal oxidation front. The last step is the oxidation of metal by oxygen

$$x\underline{\mathrm{M}} + y\underline{\mathrm{O}} \rightarrow \mathrm{M}_x\mathrm{O}_y \tag{1.49}$$

with an equilibrium constant

$$K_{sp} = N_O^y N_{Cr}^x \tag{1.50}$$

where K_{sp} is the solubility product of the oxide.

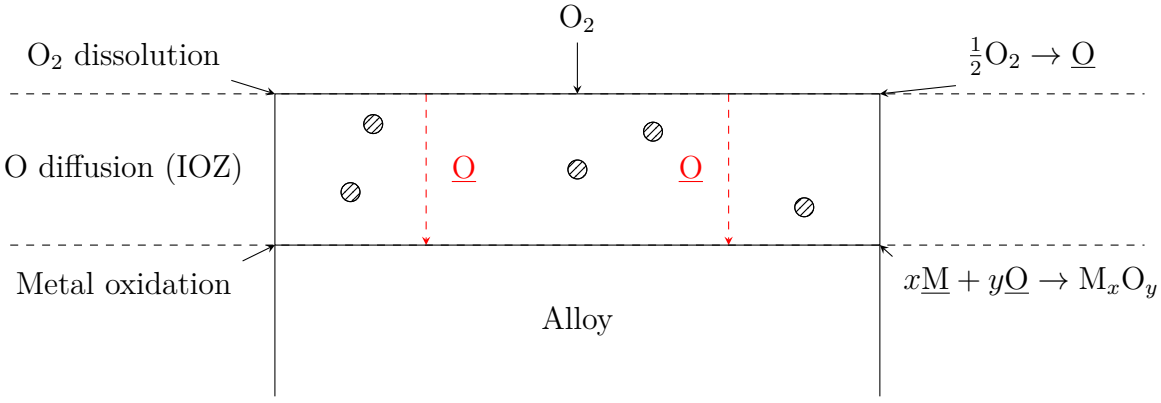

Figure 1.6: Internal oxidation steps in the absence of an outer scale.

1.3.2.2 Wagner's model for internal oxidation kinetics in the absence of external scale formation

Internal oxidation kinetics of several binary systems were reviewed by Rapp [26]. In this work, the author described the internal oxidation without or

under an oxide scale. In the following development, an alloy A-B is considered with B the less noble solute than A, and no outer scale is present.

According to Wagner, the internal oxidation obeys a parabolic law and the depth of the internal oxidation zone is defined by

$$X_{(i)}^2 = 4\gamma^2 D_O t = 2k_p^{(i)} t \tag{1.51}$$

that leads to

$$k_p^{(i)} = 2\gamma^2 D_O \tag{1.52}$$

where γ is a kinetic parameter introduced by Wagner and D_O the oxygen diffusion coefficient.

With the following boundary conditions

$$N_O = N_O^{(s)} \text{ for } x = 0, t > 0 \tag{1.53}$$

$$N_O = 0 \text{ for } x \geq X_{(i)}, t > 0 \tag{1.54}$$

the concentration profile for oxygen in the IOZ is given by

$$N_O(x) = N_O^{(s)} \left(1 - \frac{\text{erf}[x/(4D_O t)^{\frac{1}{2}}]}{\text{erf}(\gamma)} \right) \tag{1.55}$$

with x the distance from the alloy surface and $N_O^{(s)}$ the oxygen mole fraction at the alloy surface. Using the boundary conditions below

$$N_B = N_B^{(0)} \text{ for } x > 0, t = 0 \tag{1.56}$$

$$N_B = 0 \text{ for } x \leq X_{(i)}, t > 0 \tag{1.57}$$

the concentration profile of B for $x > X_{(i)}$ is expressed by

$$N_B(x) = N_B^{(0)} \left(1 - \frac{\mathrm{erfc}(x/(4D_B t)^{\frac{1}{2}})}{\mathrm{erfc}(hc)} \right) \tag{1.58}$$

where $N_B^{(0)}$ is the mole fraction of B in the bulk alloy and hc is equal to $\gamma \varphi_c^{\frac{1}{2}}$ with $\varphi_c = \frac{D_O}{D_B}$.

If it is assumed that B forms stoichiometric oxides B_xO_y, this could be rewritten as BO_ν with $\nu = \frac{y}{x}$. At the internal oxidation front, fluxes of B and O must balance, and using Fick's first law, the following equation is found

$$\frac{N_O^{(s)}}{\nu N_B^{(0)}} = \frac{\exp(\gamma^2)\,\mathrm{erf}(\gamma)}{\varphi^{\frac{1}{2}} \exp(hc^2)\,\mathrm{erfc}(hc)} \tag{1.59}$$

If all boundary conditions are valid, Equation (1.59) allows numerical or graphical evaluation of the parameter γ to calculate $k_p^{(i)}$. At this point some simplifications are used to evaluate the parameter γ. In most cases of internal oxidation without an external scale, $\gamma << 1$ and Equation (1.59) can be rewritten

$$\frac{N_O^{(s)}}{\nu N_B^{(0)}} \sim \frac{2\gamma^2}{\mathrm{F}(hc)} \tag{1.60}$$

with

$$\mathrm{F}(hc) = \sqrt{\pi} hc \exp\left(hc^2\right) \mathrm{erfc}(hc) \tag{1.61}$$

substitution of (1.60) in (1.52) yields

$$k_p^{(i)} \sim \frac{N_O^{(s)} D_O}{\nu N_B^{(0)}} \mathrm{F}(hc) \tag{1.62}$$

Equation (1.62) gives a general relation between the oxidation parabolic constant and the oxygen permeability. However, under specific conditions, the solute B may diffuse from the alloy to the IOZ. The extra amount of solute B in the IOZ can be calculated using the secondary function F. The degree of enrichment by the solute

B of the IOZ is defined by the following equation according to Wagner

$$\alpha = \frac{N_B^{BO_\nu}}{N_B^{(0)}} = [\mathrm{F}(hc)]^{-1} \tag{1.63}$$

where α is the enrichment factor and $N_B^{BO_\nu}$ the mole fraction of solute B present as BO_ν.

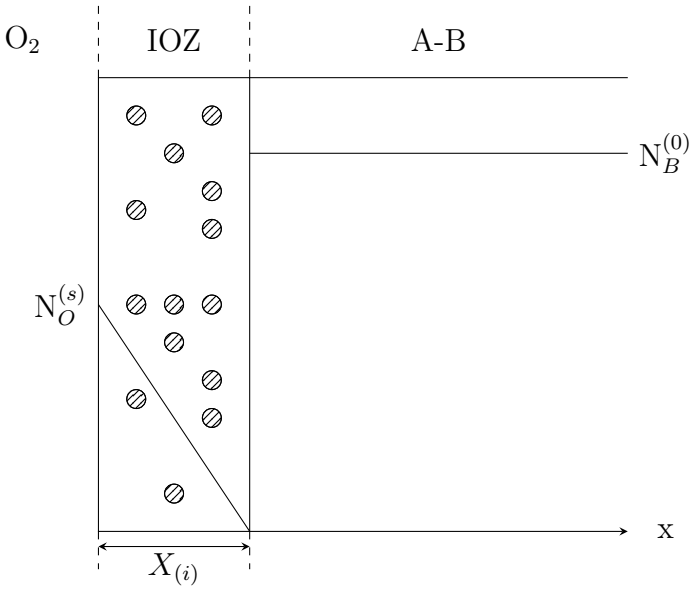

Figure 1.7: Schematic representation of concentration profiles in the IOZ and in the alloy during internal oxidation if $N_O^{(s)} D_O >> N_B^{(0)} D_B$.

From Equation (1.62) one limiting case can be studied. If $N_O^{(s)} D_O >> N_B^{(0)} D_B$, the oxygen diffusion is preponderant and controls internal oxidation kinetics. In Figure 1.7, concentration profiles of the different species are drawn under this condition. Here, the flux of oxygen is high enough to react with trapped solute atoms immobilising them, and no enrichment is observed. In that case hc tends to infinity and the limit of the secondary function F is

$$\lim_{hc \to +\infty} \mathrm{F}(hc) = 1 \tag{1.64}$$

Wagner's model for internal oxidation kinetics successfully predicts values for the depth of the internal oxidation zone under high temperature conditions and when the oxide has moderate stability. Nevertheless, to be able to predict the evolution

of the IOZ, parameters $N_O^{(s)}$, D_O, and D_B have to be known. Several authors have carried out internal oxidation experiments to determine the permeability, $N_O D_O$, of alloys as this parameter controls internal oxidation kinetics.

1.3.2.3 Kinetics of internal oxidation under an external scale

As internal oxidation obeys a parabolic rate law, the development begins with the same assumptions as in the case of internal oxidation without an external scale. One can write

$$X_{(i)}^2 = 4\gamma^2 D_O t = 2k_p^{(i)} t \tag{1.65}$$

If it is assumed that the external scale growth is diffusion controlled, a second parabolic law can be introduced

$$X^2 = 2k_c t \tag{1.66}$$

where k_c is the alloy corrosion constant and gives the rate of consumption of the alloy. Besides, $N_O^{(s)}$ now is equal to the mole fraction of oxygen at the metal/scale interface.

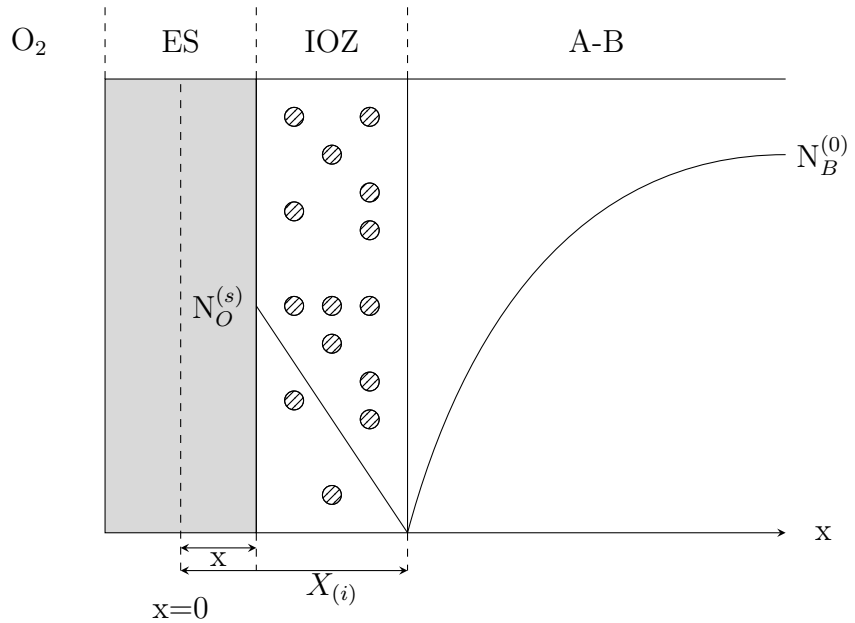

Figure 1.8: Schematic representation of concentration profiles in the IOZ and in the alloy during internal oxidation in combination with external scale formation.

Maak [27] solved Fick's second law for oxygen and for B in each corresponding zone with the following boundary conditions

$$N_O = 0 \text{ for } x \geq X_{(i)}, t > 0 \tag{1.67}$$

$$N_O = N_O^{(s)} \text{ for } x = X, t > 0 \tag{1.68}$$

$$N_B = 0 \text{ for } x \leq X_{(i)}, t > 0 \tag{1.69}$$

$$N_B = N_B^{(0)} \text{ for } x \geq 0, t = 0 \tag{1.70}$$

to obtain concentration profiles

$$N_O(x) = N_O^{(s)} \left(\frac{\text{erf}(\gamma) - \text{erf}[x/(4D_O t)^{\frac{1}{2}}]}{\text{erf}(\gamma) - \text{erf}[(k_c/2D_O)^{\frac{1}{2}}]} \right) \tag{1.71}$$

$$N_B(x) = N_B^{(0)} \left(1 - \frac{\text{erfc}[x/(4D_B t)^{\frac{1}{2}}}{\text{erfc}(hc)} \right) \tag{1.72}$$

with γ and hc defined as before. If B forms a stoichiometric oxide BO_ν then Equations (1.71) and (1.72) leads to a value of γ. To simplify the analysis, the usual case where $\gamma \ll 1$ and $X < X_{(i)}$ is considered. These assumptions lead to the expression

$$N_O^{(s)} D_O = N_B^{(0)} \frac{X_{(i)}(X_{(i)} - X)}{2t} \frac{1}{\text{F}[X_{(i)}/(4D_B t)^{\frac{1}{2}}]} \tag{1.73}$$

with F the secondary function defined by (1.61).

Several authors [27, 28] carried out internal oxidation experiments in which a scale also grew to determine the permeability of alloys. However, due to the presence of the external scale, the product $N_O^{(s)} D_O$ was found to increase with the solute content and values were lower than these found by exclusive internal oxidation [26]. To determine an unknown permeability, exclusive internal oxidation experiments

seem more reliable. Nevertheless, when the permeability is known, Equation (1.73) gives good estimates of $X_{(i)}$.

1.3.2.4 Gesmundo's model for internal oxidation kinetics measured by weight gain measurement

The internal oxidation of alloys is commonly studied by measuring the IOZ depth after oxidation reaction, but kinetics could also be measured by thermogravimetric analysis. However, only a few studies using this investigation technique are present in the literature [29, 30] due to technical difficulties of measuring small weight changes in dilute alloys. Gesmundo *et al.* [31] demonstrated the relation between internal oxidation kinetics, in term of weight change of a binary alloy A-B, and the oxygen permeability. In the alloy, the oxygen concentration profile is given by Equation (1.55) and using Fick's first law, the flux of oxygen at the sample surface is given by

$$J_O = -D_O \left.\frac{dN_O(x)}{dx}\right|_{x=0} = \frac{N_O^{(s)}}{V_{AB}\,\mathrm{erf}(\gamma)}\sqrt{\frac{D_O}{\pi t}} \tag{1.74}$$

The weight uptake per unit of surface can be evaluated by integrating Equation (1.74) from 0 to a time t, and introducing the atomic weight of oxygen, M_O,

$$\frac{\Delta w}{S} = \frac{2N_O^{(s)}M_O}{V_{AB}\,\mathrm{erf}(\gamma)}\sqrt{\frac{D_O t}{\pi}} \tag{1.75}$$

As mentioned previously, it is often assumed that $\gamma << 1$ and this yields at the first order

$$\mathrm{erf}(\gamma) \sim \frac{2\gamma}{\sqrt{\pi}} \tag{1.76}$$

Combining Equations (1.75) and (1.76), the following expression for the weight change per unit area is found

$$\left(\frac{\Delta w}{S}\right)^2 \sim \left(\frac{N_O^{(s)}M_O}{V_{AB}\gamma}\right)^2 D_O t \tag{1.77}$$

Gesmundo gave expressions for the internal oxidation rate constant for limiting cases

where the flux of oxygen or solute is predominant. Here, a general expression of the oxidation constant was obtained by combining Equations (1.60), (1.63) and (1.77).

$$\left(\frac{\Delta w}{S}\right)^2 \sim 2\left(\frac{M_O}{V_{AB}}\right)^2 \nu N_B^{(0)} \alpha N_O^{(s)} D_O t \tag{1.78}$$

then

$$k_w^{(i)} \sim \left(\frac{M_O}{V_{AB}}\right)^2 \nu N_B^{(0)} \alpha N_O^{(s)} D_O \tag{1.79}$$

Finally, the relation between the internal oxidation rate constant in term of thickness and weight gain is

$$\frac{k_w^{(i)}}{k_p^{(i)}} = \left[\frac{M_O}{V_{AB}} \nu N_B^{(0)} \alpha\right]^2 \tag{1.80}$$

The relation given by Equation (1.80) is independent of the oxygen permeability of the alloy and allows the determination of parameters like the enrichment factor or the internal oxide stoichiometry.

1.3.2.5 Transition between internal and external oxidation

The transition between internal and external oxidation was defined by Wagner [1] in the following way. An alloy exhibits a transition between internal and external oxidation when the internal oxide volume fraction reaches a critical value. If this value is reached, internal oxides could coalesce and form a compact layer which reduces the inward flux of oxygen. This decrease in oxygen flux promotes the growth of existing particles rather than the nucleation of new precipitates, and stops the progression of the oxidation front.

The volume fraction of internal oxide resulting from the internal oxidation of an alloy with a solute content $N_B^{(0)}$ is given by

$$F_v = \alpha N_B^{(0)} \left(\frac{V_{BO_\nu}}{V_{alloy}}\right) \tag{1.81}$$

If the critical internal oxide volume fraction is defined by F_v^*, the minimum amount

of solute required to observe the transition between internal and external oxidation can be calculated. This quantity is defined by

$$N_B^{(0)^*} = \frac{F_v^* V_{alloy}}{\alpha V_{BO_\nu}} \tag{1.82}$$

In addition, if the flux of oxygen is reduced by the formation of a compact oxide layer, the variable hc tends to 0 and the enrichment factor becomes

$$\alpha = [\mathrm{F}(hc)]^{-1} \sim \left[\sqrt{\pi} hc\right]^{-1} \tag{1.83}$$

This approximation yields a new expression for the parameter γ

$$\gamma \sim \frac{N_O^{(s)}}{2\nu N_B^{(0)}} \sqrt{\frac{\pi D_O}{D_B}} \tag{1.84}$$

Finally, combining Equations (1.82), (1.83) and (1.84), the minimum solute content to observe the transition between internal and external oxidation is given by

$$N_B^{(0)^*} = \left(\frac{F_v^* \pi V_{alloy} N_O^{(s)} D_O}{2\nu V_{BO_\nu} D_B} \right)^{\frac{1}{2}} \tag{1.85}$$

Rapp [32] used Ag-In alloys to test Wagner's criterion to predict when the transition occurs. He carried out internal oxidation experiments at 550°C under 1 atmosphere of pure oxygen. He observed that the transition occurred for $N_{In}^{(0)} = 0.15$ which was equivalent to an $InO_{1.5}$ volume fraction of 0.30. Assuming $F_v^* = 0.30$, Rapp calculated the critical value, $N_{In}^{(0)*}$, for oxygen pressure from 1.32×10^{-7} to 1 atm. As Figure 1.9 shows, the critical value of indium required for the transition decreases with the partial pressure of oxygen. Rough agreement is found between $N_{In}^{(0)*}$ calculated to achieve the transition between internal and external oxidation, using the critical density of 0.3, and experimental observations.

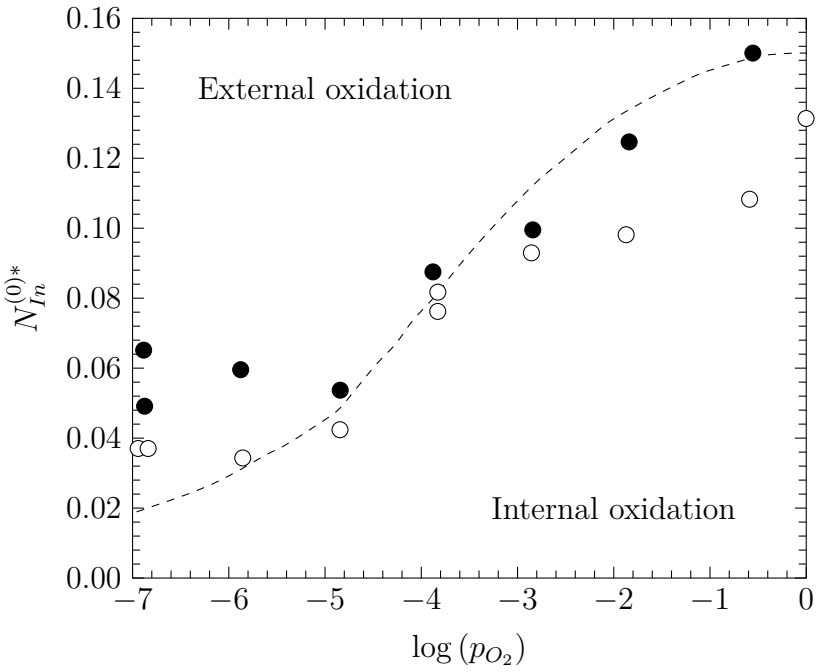

Figure 1.9: Transition from internal to external oxidation for Ag-In alloys at 550°C. Transition started (○), Transition complete (●). $N_{In}^{(0)*}$ calculated for transition between internal and external oxidation (- - -) [32].

1.3.2.6 Internal oxidation leading to the formation of multiple internal oxides

In the previous development, it was always considered that a single type of internal oxide precipitates in the IOZ. Nevertheless, internal oxidation of iron or nickel alloys containing chromium could result in the formation of different oxides such as $FeCr_2O_4$ and Cr_2O_3, due to the decrease of the oxygen activity through the IOZ as shown in Figure 1.10, where BO_{ν_1} is oxidised to BO_{ν_2} in the IOZ with $\nu_1 < \nu_2$.

Meijering [33] reviewed the case of internal oxidation with the formation of two precipitate zones within the IOZ under assumptions that the solute B is immobile, the two precipitates are extremely stable, the limit between the two zones is sharp and the reaction of oxidation of BO_{ν_1} to a higher oxide BO_{ν_2} is instantaneous. In addition, the former oxidation reaction takes place at $x = X_{(t)}$ and the oxygen concentration at this location is denoted $N_O^{(t)}$. The displacement of the two oxidation

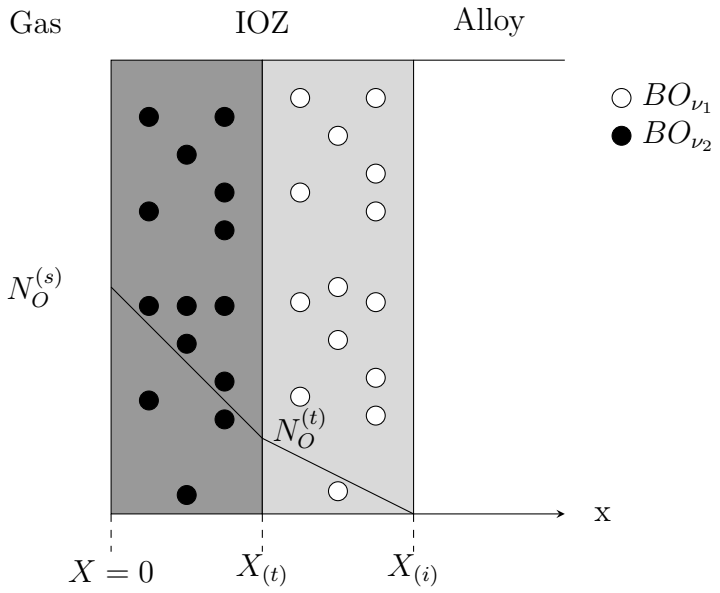

Figure 1.10: Schematic representation of oxygen concentration profiles in the IOZ when multiple internal oxides precipitate.

fronts at $x = X_i$ and $x = X_{(t)}$ are given by

$$\frac{N_O^{(t)} D_O}{X_{(i)} - X_{(t)}} = \nu_1 N_B^{(0)} \frac{dX_{(i)}}{dt} \tag{1.86}$$

$$\frac{\left(N_O^{(s)} - N_O^{(t)}\right) D_O}{X_{(t)}} = \nu_1 N_B^{(0)} \frac{dX_{(i)}}{dt} + (\nu_2 - \nu_1) N_B^{(0)} \frac{dX_{(t)}}{dt} \tag{1.87}$$

By dividing Equation (1.87) by (1.86), the following relation is found

$$\left(\frac{N_O^{(s)} - N_O^{(t)}}{N_O^{(t)}}\right) \frac{X_{(i)} - X_{(t)}}{X_{(t)}} = 1 + \frac{\nu_2 - \nu_1}{\nu_1} \frac{dX_{(t)}}{dX_{(i)}} \tag{1.88}$$

Assuming that both zones grow according to parabolic laws and at $t = 0$, $X_{(i)} = X_{(t)} = 0$, a constant f is defined by

$$f = \frac{X_{(t)}}{X_{(i)}} = \frac{dX_{(t)}}{dX_{(i)}} \tag{1.89}$$

Substitution of Equation (1.89) in (1.88) yields a second degree polynomial equation

$$\left(\frac{\nu_2}{\nu_1} - 1\right) f^2 + \frac{1}{m} f - \left(\frac{1}{m} - 1\right) = 0 \tag{1.90}$$

with $m = \frac{N_O^{(t)}}{N_O^{(s)}} = \sqrt{\frac{p_{O_2}^{(t)}}{p_{O_2}^{(s)}}}$. One solution of Equation (1.90) is

$$f = \frac{\left[1 + 4m(1-m)\left(\frac{\nu_2 - \nu_1}{\nu_1}\right)\right]^{1/2} - 1}{2m\left(\frac{\nu_2 - \nu_1}{\nu_1}\right)} \tag{1.91}$$

Then, assuming that the displacement of the internal oxidation front is proportional to $t^{\frac{1}{2}}$, one may write

$$k_p^{(i)} = \frac{N_O^{(s)} D_O}{\nu_{eff} N_B^{(0)}} \tag{1.92}$$

with

$$\nu_{eff} = \frac{\nu_1(1-f)}{m} \tag{1.93}$$

However, verification of the value given by Meijering's model is difficult as the value of $N_O^{(t)}$ can only be estimated from thermodynamic data and knowledge of $N_B^{(t)}$. In addition, Equation (1.93) is of limited use, as f and m are correlated. It should also be noted that Meijering's model only applies if no enrichment of the IOZ by the solute B is observed. To evaluate the effective stoichiometry in the case of a mobile solute B, Megusar *et al.* [34] proposed an analysis based on diffusion equations. These authors found that when multiple internal oxides with different stoichiometry precipitate and if the solute B is mobile, the relation between $k_p^{(i)}$ and $N_O^{(s)} D_O$ is given by

$$k_p^{(i)} = \frac{N_O^{(s)} D_O}{\nu_{eff} N_{Cr}^{(0)} \alpha} \tag{1.94}$$

where α is the enrichment factor defined by Equation (1.63) in Wagner's model and ν_{eff} is given by Equation (1.93).

1.3.2.7 Nucleation and growth of precipitates

During internal oxidation, oxides precipitate beneath the alloy surface and the particle morphologies and sizes are determined at the oxidation front. The main work describing the nucleation and growth of internal precipitates was carried out by Böhm and Kahlweit [35]. In this work, authors calculated oxygen and solute

concentration profiles and the internal oxidation front displacement, assuming that the internal oxide BO_ν has a finite solubility in the matrix defined by

$$K_{sp} = (N_B^{'})(N_O^{'})^{\nu} \tag{1.95}$$

where $(N_O^{'})$ and $(N_B^{'})$ are equilibrium oxygen and solute concentrations respectively. Figure 1.11 shows schematic representations of concentration profiles found by Böhm and Kahlweit for the diffusion controlled model for precipitate nucleation.

In the first step, the concentration N_O^* and N_B^* represent critical (supersatured) concentrations for the nucleation of a new particle at X. Figure 1.11.(a) shows that the nucleation of a new particle occurs in front of the oxidation front which is at the $X^{'}$ position. This continuous nucleation of new particles in advance of the oxidation front is necessary for its progress. In Figure 1.11.(b), oxygen and solute concentrations decrease at the X position due to the nucleation and growth of the new particle.

In Figure 1.11.(c), the supersaturated excess of solute B is consumed in the growth of the new particle, and its concentration profile reverts to that shown in Figure 1.11.(a) for the first step. Concerning oxygen, the totality of the oxygen flux is consumed to form an oxide BO_ν at the location $x = X'$. Therefore, the oxygen concentration for location $x > X'$ remains unchanged until all the metal B at the location $x = X'$ is consumed. Then when no metal is left at the location $x = X'$, the oxygen concentration for $x > X'$ increases and the process restarts as in Figure 1.11.(a).

Böhm and Kahlweit [35] gave an expression for the spacing between precipitates. They approximated this quantity as the distance between two successive nuclei $\Delta X = X - X'$, which leads to an expression for the quantity of precipitate per unit of volume $Z(X)$:

$$Z(X) \approx (\Delta X)^{-3} = \left(\frac{X}{\Delta X}\right)^3 \frac{1}{X^3} \tag{1.96}$$

In order to predict this quantity, the authors solved a system of equations to give an expression of $Z(X)$ with known parameters N_O^s, $N_B^{(0)}$, K_{sp} and $\frac{D_O}{D_B}$. Assuming that (N_O^*), (N_B^*) and diffusion coefficients are independent of the distance from the surface and $N_O^{(s)}$, they found

$$Z(X) = \beta \left(\frac{N_O^{(s)}}{X} \right)^3 \tag{1.97}$$

with

$$\beta = \left(\frac{1}{N_O^{(s)}} \frac{X}{\Delta X} \right)^3 = \left[\frac{D_O}{D_B} \frac{N_B^{(0)} - N_B^*}{\nu (N_B^{(0)} - N_B')(N_B^* - N_B')} \right]^3 \tag{1.98}$$

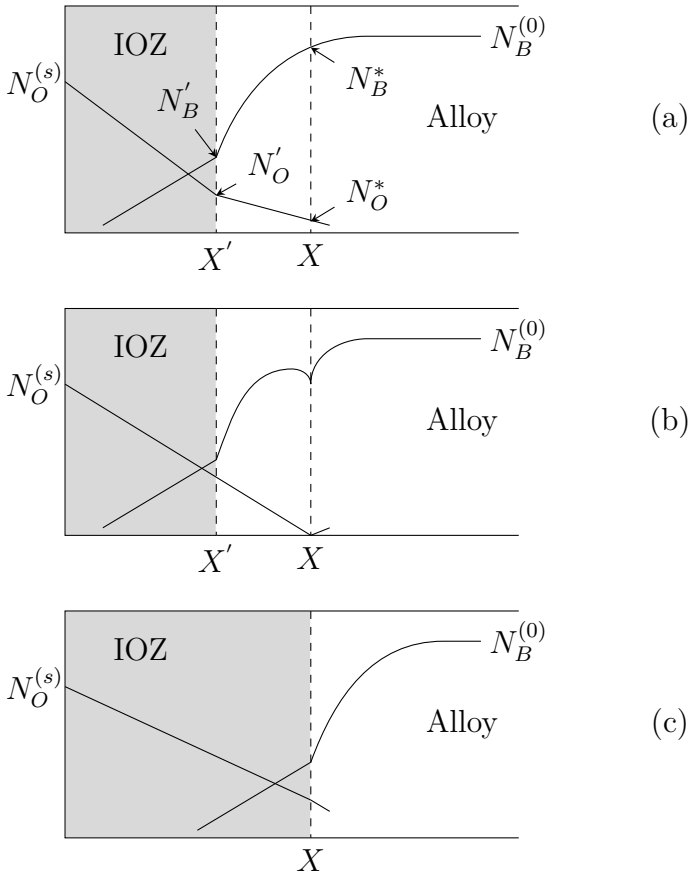

Figure 1.11: Concentration profiles at the oxidation front during internal oxidation process [26]. Situations (a),(b),(c) described in text.

For a system where all parameters are known, the density of oxide particles can be quantitatively predicted. The authors tested their equation by carrying out internal oxidation on Ag-Cd alloys. They estimated the particle density as a function of the penetration from the number of particles per unit of area and

observed that the particles density was varying with the inverse of X^3 as predicted by Equation (1.97). In addition, Böhm and Kahlweit expressed the particle size as a function of the distance from the surface, $R_p(X)$, assuming spherical shaped particles and negligible solute enrichment:

$$R_p(X) = \left(\frac{3V_{BO_\nu} N_B^{(0)}}{4\pi\beta} \right)^{\frac{1}{3}} \frac{X}{N_O^{(s)}} \tag{1.99}$$

This equation was tested by Wood [36] who studied the variation of internal aluminium oxide particles with penetration. He found a linear relation between the internal oxide radius and the depth as Böhm and Kahlweit predicted in Equation (1.99). However, some deviations from this equation are observed in case of very small or large precipitates. The smallest size this equation can predict is the critical size of a stable growing nucleus and the upper limit is when the density of particles is low due to the formation of large precipitates, usually no longer spherical in that case.

The critical size for the growth of a precipitate can be calculated using energetic considerations. If we assume the formation of a spherical nucleus of radius R_p in a homogeneous, isotropic alloy, and that the alloy and the oxide have the same volume, the free energy change is equal to

$$\Delta G = \frac{4}{3}\pi R_p^3 \Delta G_V + 4\pi R_p^2 \gamma \tag{1.100}$$

where the first term of the right side corresponds to the volume energy change with ΔG_V as the free energy per unit of volume of the precipitation reaction, and the second term is the change of surface energy with γ the precipitate-matrix interfacial tension. This equation gives the curve of Figure 1.12 which shows a maximum when $R_p = R_p^*$. This particular value is called the critical nucleus size. When a new precipitate nucleates, if $R_p < R_p^*$ this nucleus shrinks, while if $R_p > R_p^*$ the nucleus grows to decrease its energy according to the curve of Figure 1.12.

A more general description accounts for the fact that oxides generally do not

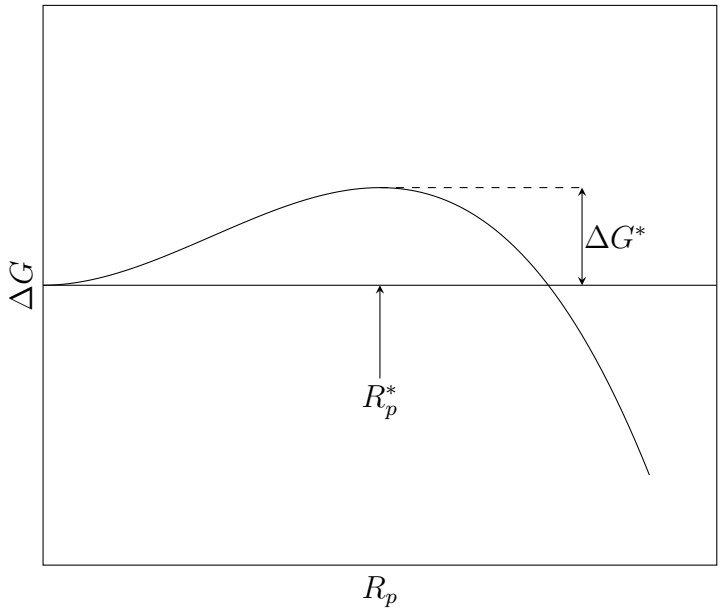

Figure 1.12: Free energy of a spherical nucleus [3].

have the same volume as the alloys, and nucleation site are usually local defects. Then (1.100) is rewritten for spherical precipitates as

$$\Delta G = \frac{4}{3}\pi R_p^3 \left(\Delta G_V + \Delta G_S\right) + 4\pi R_p^2 \gamma - \Delta G_d \tag{1.101}$$

where the two additional terms ΔG_S and ΔG_d are respectively, the strain energy from the volume change and the energy associated with defect site annihilation. From Equation (1.101), expressions for the critical radius and the surface energy barrier can be found by locating the maximum value of the energy change. Expressions of each term are given below

$$R_p^* = \frac{2\gamma}{\left(\Delta G_V - \Delta G_S\right)} \tag{1.102}$$

$$\Delta G^* = \frac{16\pi\gamma^3}{3\left(\Delta G_V - \Delta G_S\right)} - \Delta G_d \tag{1.103}$$

1.4 Examples of Internal Oxidation

In this section, the internal oxidation of iron, nickel and Fe-Ni based alloys is reviewed. Several authors measured the oxygen permeability using internal oxidation experiments. As previously mentioned, to achieve the best results for oxygen permeability measurement samples must exhibit exclusive internal oxidation. Rhines [37] used a technique, now known as the "Rhines pack", which allowed him to carry out internal oxidation experiment without the growth of an external scale. In these experiments, samples are put into a sealed capsule with a mixture of the base metal powder and its lowest oxide. This mixture sets the oxygen partial pressure in the capsule equal to the equilibrium pressure between the alloy base metal and its lowest oxide. In this case, the oxygen partial pressure is too low to oxidise the base metal of the alloy, but high enough to internally oxidise less noble alloying elements. The majority of internal oxidation experiments on Ni based alloys were carried out in Rhines packs due to the simplicity of the Ni/NiO system. However, for iron based alloys, few results from Rhines pack experiments are present in the literature due to the fact that the lowest iron oxide is wustite, which is difficult to synthesise. Instead of Rhines pack experiments, authors used a mix of H_2 and H_2O to reach low oxygen partial pressure.

In the further development described in this section, results of internal oxidation experiments carried out on Fe, Ni and Fe-Ni based alloys are presented. In addition, in all experiments reviewed in this section, it is assumed that all the solute present in the alloy precipitates as oxide once the oxidation front is passed. This assumption leads to the expression for $k_p^{(i)}$ given by Equation (1.62).

1.4.1 Fe based alloys

Different solutes such as Al, Cr and Si were used to design alloys for internal oxidation experiments. Internal oxidation of Fe-Al and Fe-Si alloys were investigated by Takada *et al.*, in α [38, 39] and γ [40, 41] alloys, using Fe/FeO and Fe/Fe_2O_3 Rhines packs in which the oxygen partial pressure was equal to the Fe/FeO disso-

ciation pressure. The authors identified $FeAl_2O_4$ and amorphous SiO_2 as internal oxides in Fe-Al and Fe-Si alloys, respectively. In addition, EPMA measurements in the IOZ showed that enrichment of the IOZ occurred during internal oxidation experiments. This enrichment in Fe-Si was small in γ iron and high in α. For Fe-Al, the opposite was observed. The value of the IOZ enrichment can be then used for permeability calculation in Equation (1.62) using (1.63). Values of the enrichment factor are given in Table 1.3.

Table 1.3: Enrichment factor measured in Fe-Al and Fe-Si alloys at 1,050°C after internal oxidation in Rhines pack.

Alloy	α	Ref.
Fe-0.069Al	1.61	
Fe-0.158Al	1.55	[40]
Fe-0.274Al	1.48	
Fe-0.070Si	1.03	
Fe-0.219Si	1.04	[41]
Fe-0.483Si	1.06	

To determine the oxygen permeability from internal oxidation kinetics a plot of $k_p^{(i)}$ versus the inverse of the solute alloy content is used. In Figure 1.13, values measured by Takada *et al.* in γ-iron are presented.

Good agreement is found between values measured for Fe-Al and Fe-Si alloys in Rhines packs. However, a discrepancy with Equation (1.62) is observed because regression lines do not pass through the origin as predicted by Wagner's model. The same deviation from Wagner's model was observed in α-iron by Takada *et al.* [38, 41] and Ani *et al.* [42].

This difference from Wagner's model is attributed to the fast oxygen diffusion at oxide/matrix interface and authors [38–42] considered that the oxygen permeability measured using Wagner's model was an effective permeability. To take into account the contribution of fast oxygen diffusion at matrix/oxide interface, an effective oxygen diffusion coefficient, D_O^{eff} is defined. Assuming that the oxygen solubility is not affected by the alloy solute content, the effective permeability is expressed by

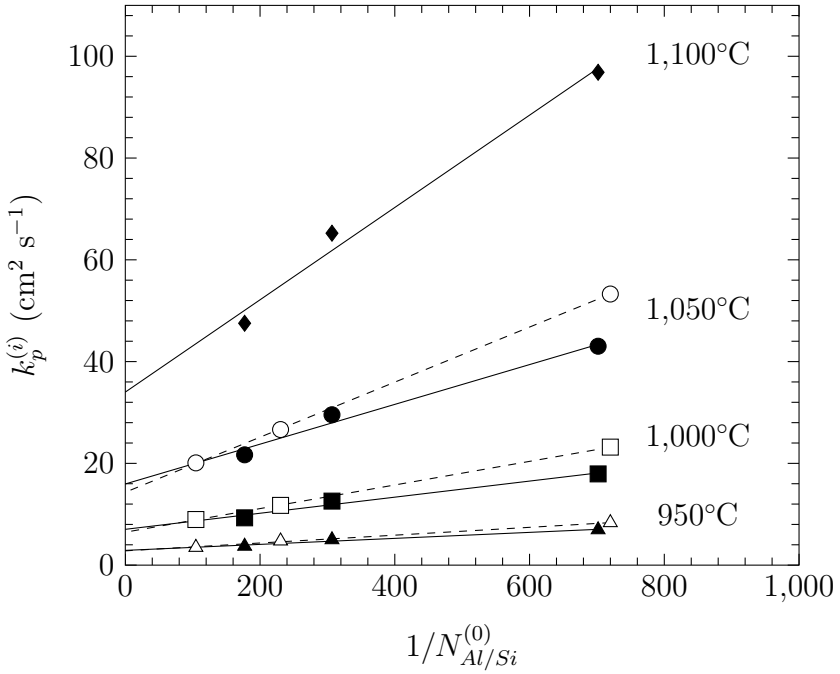

Figure 1.13: Oxygen permeability in γ-iron after reaction in Fe/FeO Rhines pack, Fe-Si alloys (open symbols), Fe-Al alloys (filled symbols).

$$N_O^{(s)} D_O^{eff} = N_O^{(s)} D_O^{mat} + N_B^{(0)} \lambda \tag{1.104}$$

where $N_O^{(s)} D_O^{mat}$ is the permeability of the matrix, λ a constant which represents the contribution of matrix/oxide interface diffusion and it is assumed that the amount of interface is proportional to $N_B^{(0)}$. Then Equation (1.62) becomes

$$\alpha\nu k_p^{(i)} = \frac{N_O^{(s)} D_O^{mat}}{N_B^{(0)}} + \lambda \tag{1.105}$$

Ani *et al.* [42] and Setiawan *et al.* [43], working in the same research group, obtained interesting results on the effect of water vapour and/or hydrogen on the oxygen permeability. To fix the oxygen partial pressure, they flushed Ar-5%H_2 over a buffer composed of a FeO/Fe powder mixture. Setiawan *et al.* measured kinetics in a dry and a wet atmosphere between 700 and 800°C while Ani *et al.* used a fix temperature of 800°C to investigate the effect of water content in the gas on internal oxidation kinetics. In these studies, the internal oxide was identified as iron chromium-spinel. However, Ani *et al.* carried out experiments on alloys with differ-

ent compositions, and observed that when the chromium content increases, Cr_2O_3 oxide started to precipitate close to the IOZ front. In both studies, it was observed that in humid atmosphere internal oxidation kinetics increased, and sometimes the precipitate shape changed from spheroidal to needle-like.

These authors found that there was no effect of water vapour and/or hydrogen on the matrix oxygen permeability. However, the constant λ was found to be larger after reaction in humid environment. In addition, the fact that the precipitate shape changed when humidity is present in the atmosphere may suggest that the properties of the matrix/oxide interface could be affected by hydrogen dissolved in the IOZ.

Others authors carried out internal oxidation experiments but they did not provide enough information to carry out the same analysis as with Takada's and Ani's data. For example, the Fe-Cr system was investigated by Young and Ahmed who carried out experiments in Ar-H_2-H_2O atmospheres at 900, 1,000 and 1,100°C [44, 45]. Five alloys with different compositions were exposed to oxidising conditions and internal oxidation kinetics were measured. Oxygen partial pressures in these experiments were 8.7×10^{-17} or 2.6×10^{-20} atm, which are at least 3 orders of magnitude lower than the Fe/FeO dissociation pressure. Under all conditions, alloys with a content of chromium above 17 wt.%, formed a chromia external scale. Alloys Fe-5Cr and Fe-7.5Cr at 1,000°C formed only internal oxides while the Fe-10Cr oxidized both internally and externally. At 1,100°C, alloys with chromium content lower than 10 wt.% exhibited exclusive internal oxidation. The major part of the oxide precipitates were Cr_2O_3, but the authors identified $FeCr_2O_4$ directly beneath the alloy surface under specific experimental conditions. They observed the precipitation of spinel in Fe-5Cr samples at all temperatures, in Fe-7.5Cr at 1,000 and 1,100°C and none of it in Fe-10Cr at all temperatures. The oxide shape was spheroidal in all conditions and authors also noted that the precipitate size increased and their volume fraction decreased when the depth increased, as Böhm and Kahlweit predicted [35]. This can be observed in Figure 1.14.

However, Young and Ahmed observed that the assumption in Wagner's model

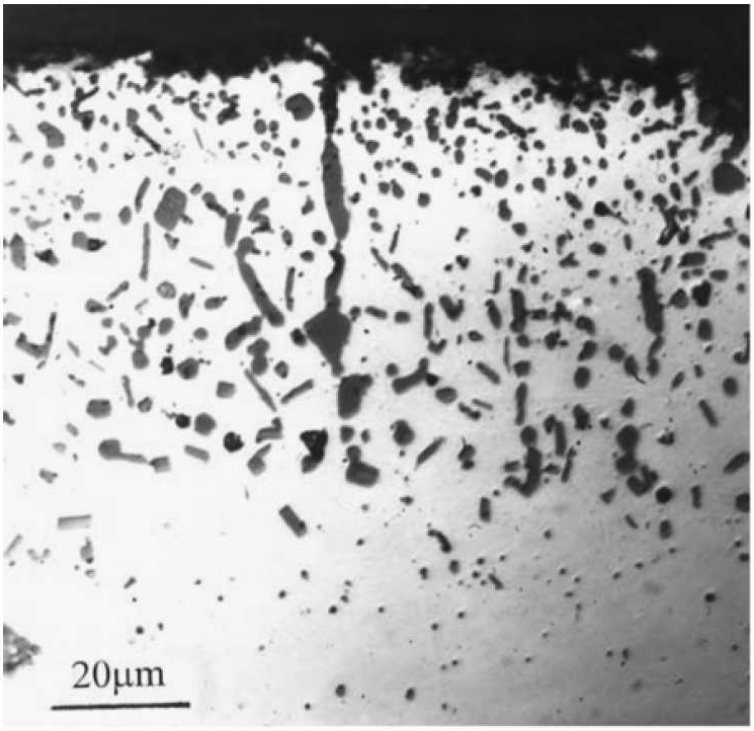

Figure 1.14: Internal oxidation of Fe-5Cr alloys at $p_{O_2} = 8.7 \times 10^{-17}$ atm in Ar-H_2-H_2O at 900°C [44].

that all chromium is precipitated as an oxide in the internal oxidation zone was not true when the oxygen partial pressure was significantly lower than the Fe/FeO dissociation pressure. This is due to the relatively high solubility product of the chromium oxide, which could cause an overestimation of permeability values measured. A theoretical treatment for internal oxidation in the case of incomplete solute precipitation was proposed by Ohriner and Morral [46] who introduced the solubility parameter α given by

$$\alpha = 1 - \frac{K_{sp}^{1/2}}{N_{Cr}^{(0)} \left(N_O^{(s)}\right)^{3/2}} \tag{1.106}$$

In Wagner's model, $\alpha \to 1$. However, Young and Ahmed showed that this condition is only fulfilled in Fe-10Cr at 1,000°C. Calculations for others alloys gave $\alpha \approx 0.5$. The theory of Ohriner and Morral [46] was used by Young and Ahmed with their α value to predict the $k_p^{(i)}$, and the result exceeds the value predicted by Wagner's model by a factor of 2.4 and permeability by a factor 6. Finally, no dependency of the permeability on the alloy chromium content was observed at any temperature investigated by these authors, corresponding to $D_O^{eff} = D_O^{mat}$. Permeability values

were measured at 1,000 and 1,100°C with samples in which all chromium were not oxidised in the IOZ. In Table 1.4, permeability values measured by Young and Ahmed were divided by 6 to consider Orhiner's calculation.

Table 1.4: Oxygen permeability in γ-iron measured by internal oxidation of Fe-Cr alloys [45].

Temperature °C	p_{O_2} atm	$\frac{N_O^{(s)} D_O^{mat}}{6}$ $cm^2\ s^{-1}$
1,000	2.6×10^{-20}	6.7×10^{-14}
1,100	8.7×10^{-17}	3.3×10^{-12}

Swisher *et al.* [47] carried out internal oxidation of Fe-Al alloys in H_2/H_2O gas mixtures with oxygen partial pressure slightly lower than the Fe/FeO oxygen partial pressure. These authors identified internal oxides as $FeAl_2O_4$ and Al_2O_3 depending on experimental conditions. In addition, as in the Young and Ahmed study, these authors did not report any variation of the permeability with the aluminium content, indicating $D_O^{eff} = D_O^{mat}$.

To be able to compare Swisher and Young's permeability values with other authors who did their experiments at the Fe/FeO equilibrium, Swisher and Young's values were extrapolated to the Fe/FeO dissociation pressure using the relation below

$$\frac{k_p^{(i)(Fe/FeO)}}{k_p^{(i)(exp)}} = \sqrt{\frac{p_{O_2}^{Fe/FeO}}{p_{O_2}^{exp}}} \tag{1.107}$$

where $k_p^{(i)(Fe/FeO)}$ is the internal oxidation constant extrapolated to the Fe/FeO dissociation pressure, $k_p^{(i)(exp)}$ the internal oxidation constant experimentally observed, $p_{O_2}^{Fe/FeO}$ the Fe/FeO dissociation pressure and $p_{O_2}^{exp}$ the oxygen partial pressure set during experiments.

Meijering also collected data on iron in his review of internal oxidation [33]. In his work, he reviewed data from authors who carried out experiments in H_2/H_2O with the partial pressure ratio set to yield an oxygen partial pressure equal to the dissociation pressure of wüstite. However, authors used Fe-Al and Fe-Si alloys in which it was observed that the oxygen permeability depends on the solute con-

centration [38–41, 48]. Therefore, it is likely that Equations (1.108) and (1.109), provided by Meijering for the oxygen permeability, only give a rough estimation of the effective oxygen permeability, $N_O^{(s)} D_O^{eff}$. The first equation is for BCC iron

$$\log(N_O^{(s)} D_O^{eff}) = \frac{-10,800}{T(K)} - 1.72 \ (\mathrm{cm}^2 \ \mathrm{s}^{-1}) \tag{1.108}$$

and one for FCC iron

$$\log(N_O^{(s)} D_O^{eff}) = \frac{-13,500}{T(K)} - 0.43 \ (\mathrm{cm}^2 \ \mathrm{s}^{-1}) \tag{1.109}$$

In Figure 1.15, oxygen permeability values measured in the different studies are plotted versus the inverse of the temperature.

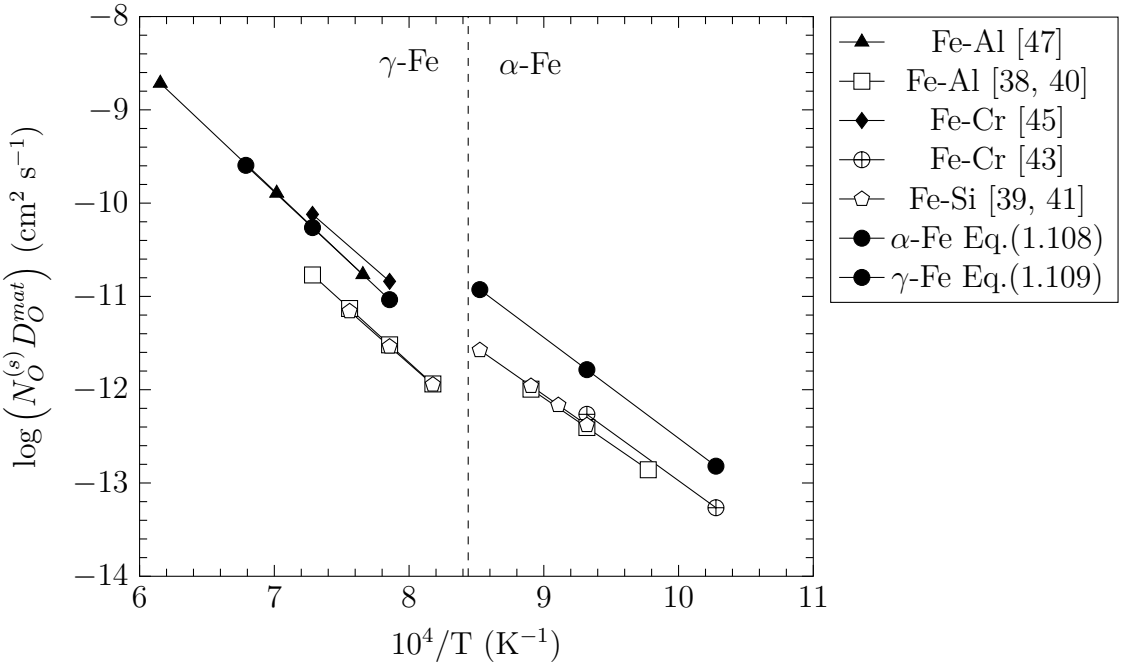

Figure 1.15: Oxygen permeability of iron measured in γ and α iron in different atmospheres, Fe/FeO Rhines pack (open symbols), H_2/H_2O gas mixtures (filled symbols).

Good agreement was found for the activation energy for the oxygen permeability, approximately 206 kJ mol^{-1} and 258 kJ mol^{-1} in α and γ iron, respectively. However, oxygen permeability measured in H_2/H_2O is always higher than permeability measured in Rhines packs. Nevertheless, the most careful studies were done

by Takada *et al.* [38–41] and Setiawan *et al.* [43]. In other works [33, 45, 47], some parameters were often not evaluated like the enrichment factor or the variation of oxygen permeability with solute concentration. For example, in γ-iron, Swisher and Turkdogan used Fe-Al alloys for their experiments and it was observed that aluminium internal oxide have a rod shape, which could help the oxygen diffusion through the internal oxidation zone. Permeability calculated with Equation (1.109) was added to Figure 1.15 and found relatively high compared to Takada *et al.*'s results. On the other hand Swisher and Turkdogan permeability is in good agreement with values calculated with Equation (1.109). This support the conclusion that Swisher and Turkdogan and Meijering reported the effective permeability, higher than the permeability of the matrix, in their work.

1.4.2 Ni based alloys

Internal oxidation of Ni based alloys has been studied by many authors [33, 49–52] due to the extensive use of nickel in alloys for high temperature application. Unlike iron, nickel forms only one oxide and this makes the achievement of Rhines pack experiment easier. On the other hand, little information is available in the literature concerning the internal oxidation of Ni based alloys in H_2/H_2O gas mixtures.

Whittle *et al.* [52] studied the internal oxidation of Ni-Cr and Ni-Al alloys in Ni/NiO Rhines packs, in 1 atm O_2 from 800 to 1,100°C. These authors observed that in Ni-Cr alloys, chromium oxides were spherical while aluminium internal oxides were rods extending from the sample surface to the internal oxidation front in Ni-Al alloys. They reported that the permeability was independent of the chromium content at temperature above 900°C. However, they found a strong dependency of the oxygen permeability on the aluminium content in Ni-Al alloys. This is thought to be due to the specific morphology of aluminium internal oxide. The IOZ microstructure of Ni-Al alloys was investigated with SEM observations carried out on deep etched samples as shown in Figure 1.16.

Stott and Wood [51] built a model more complex than Setiawan's Equa-

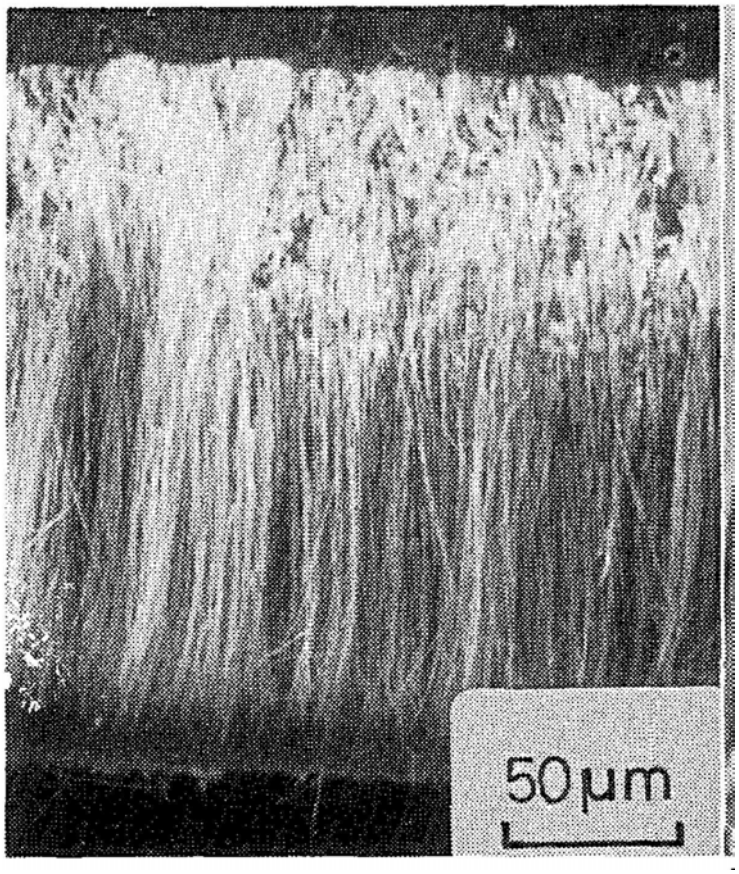

Figure 1.16: Internal oxides in Ni-Al alloys after oxidation in Ni/NiO Rhines pack for 10h at 1,100°C [51]. Reprinted by permission of the publisher Taylor & Francis Ltd.

tion (1.104) to calculate the oxygen permeability of the matrix taking into consideration fast oxygen diffusion at the matrix/oxide interface. Stott and Wood proposed several equations to calculate the effective oxygen permeability as a function of different parameters like the internal oxide size, the interface width and the oxygen diffusion coefficient at the metal/oxide interface. The basis of Stott and Wood's calculation are given in the following development. According to Hart's Equation [53], the effective oxygen diffusion coefficient is a linear combination of diffusivity of oxygen in the matrix, in the oxide and at the oxide/matrix interface. These diffusivities are weighted by the area fraction of each diffusion medium. The effective oxygen diffusion coefficient is expressed by the following equation

$$D_O^{eff} = F_A^{mat} D_O^{mat} + F_A^{int} D_O^{int} + F_A^{ox} D_O^{ox} \tag{1.110}$$

where

- F_A^{mat} is the area fraction of matrix.
- F_A^{int} is the area fraction of interface.
- F_A^{ox} is the area fraction of oxide.
- D_O^{mat} is the oxygen diffusion coefficient in the matrix.
- D_O^{int} is the oxygen diffusion coefficient at the interface oxide/matrix interface.
- D_O^{ox} is the oxygen diffusion coefficient in the oxide

Oxygen diffusion in the oxide is very slow compared to the oxygen diffusion in the matrix and at the metal/oxide interface. Therefore, Equation (1.110) becomes

$$D_O^{eff} = F_A^{mat} D_O^{mat} + F_A^{int} D_O^{int} \tag{1.111}$$

with

$$F_A^{mat} = 1 - F_A^{ox} - F_A^{int} \tag{1.112}$$

In the case of Ni-Al alloys, internal oxides are rods running from the surface to the oxidation front. The number of particles per unit area is given by

$$n^{particles} = \alpha N_{Al}^{(0)} \frac{V_{oxide}}{\pi R_P^2 V_{alloy}} \tag{1.113}$$

where R_p is the radius of a rod. Then the area fraction of interface is given by

$$F_A^{int} = n^{particles} 2\pi R_p \delta = 2\alpha N_{Al}^{(0)} \frac{\delta V_{oxide}}{R_P V_{alloy}} \tag{1.114}$$

where δ is the width of the matrix/oxide interface usually taken equal to 1 nm. The area fraction of oxide is expressed by

$$F_A^{ox} = n^{particles} \pi R_p^2 = \alpha N_{Al}^{(0)} \frac{V_{oxide}}{V_{alloy}} \tag{1.115}$$

finally, combining Equations (1.111), (1.112), (1.114) and (1.115) yields

$$D_O^{eff} = D_O^{mat}\left\{1 + \alpha N_{Al}^{(0)}\frac{V_{oxide}}{V_{alloy}}\left[\frac{2\delta}{R_p}\left(\frac{D_O^{int}}{D_O^{mat}} - 1\right) - 1\right]\right\} \tag{1.116}$$

It is also assumed that the oxygen diffusion at the matrix/oxide interface is faster than the diffusion in the matrix, and the ratio $\frac{D_O^{int}}{D_O^{mat}} >> 1$. In addition, if the oxygen solubility is unchanged by the solute content then Equation (1.116) becomes

$$N_O^{(s)} D_O^{eff} = N_O^{(s)} D_O^{mat}\left[1 + \alpha N_{Al}^{(0)}\frac{V_{oxide}}{V_{alloy}}\left(\frac{2\delta}{R_p}\frac{D_O^{int}}{D_O^{mat}} - 1\right)\right] \tag{1.117}$$

Stott and Wood tested their model by internally oxidising various Ni-Al, Ni-Cr and Ni-V alloys in Ni/NiO Rhines packs and observed that the oxygen permeability varies linearly with the solute content as illustrated in Figure 1.17.

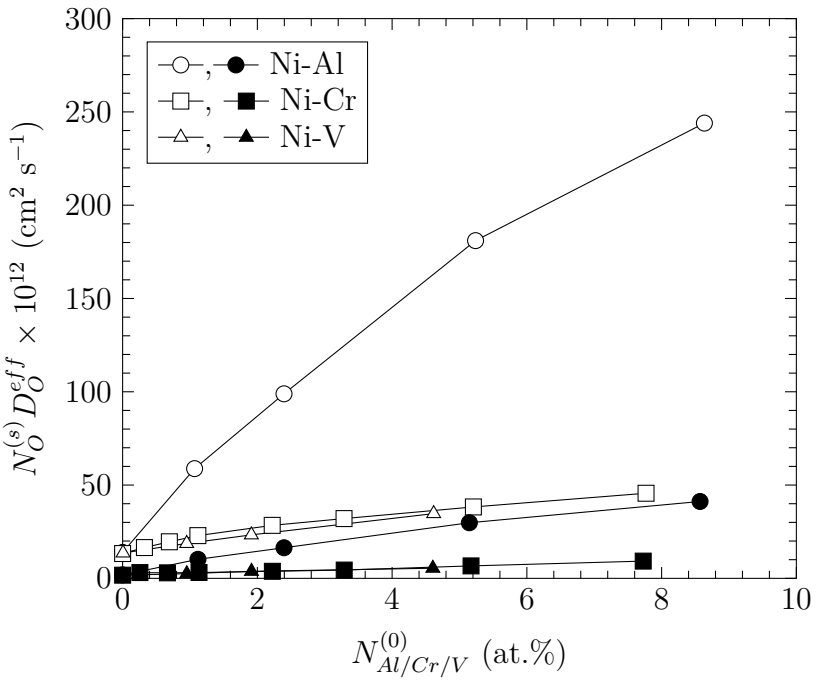

Figure 1.17: Oxygen permeability in various Ni based alloys at 1,100°C (open symbols) and 1,000°C (filled symbols) [51].

This linear dependency of the oxygen permeability with the solute content is in agreement with Equation (1.117) developed by Stott and Wood. In addition, these authors found good agreement for the matrix oxygen permeability in the different alloys when they extrapolated Equation (1.117) to $N_{Al/Cr/V} \to 0$, as shown in Fig-

ure 1.17. However, the authors noted that in Ni-Cr alloys, the oxygen permeability was less affected by the presence of internal oxides, due to the spherical shape of chromium internal oxides. Stott and Wood's development to calculate the matrix oxygen permeability also allows the evaluation of the oxygen diffusion coefficient at the interface matrix/oxide, D_O^{int}. However, the determination of this diffusion coefficient requires knowledge of δ and R_p which are often difficult to estimate.

Goto *et al.* [49] also studied the Ni-Cr system using the Rhines pack technique. They oxidised several alloys with chromium contents up to 4 wt.% at temperatures between 900 and 1,300°C to study the IOZ structure and growth kinetics. Their results showed that internal oxidation kinetics followed a parabolic law, corresponding to diffusion control and identified the internal oxides as Cr_2O_3. In Table 1.5, activation energies measured by Goto *et al.* for $k_p^{(i)}$ are given.

Table 1.5: Activation energy of the internal oxidation parabolic constant for Ni-Cr alloys [49].

N_{Cr} at.%	0.7	1.14	2.42	3.44	4.49
Q kJ mol^{-1}	289	276	264	255	251

Table 1.5 shows that the activation energy decreased when the solute mole fraction increased. This is due to the dependency of the oxygen diffusion coefficient on the chromium content as reported by Stott and Wood [51]. Increasing the chromium content increases the internal oxide volume fraction which promotes the interfacial oxygen diffusion provided that the internal oxide size is not altered by the alloy chromium content. Therefore, the contribution of the fast oxygen diffusion at matrix/oxide interface to the overall oxygen diffusion is larger in chromium-rich alloys. Under the assumption that the activation energy for oxygen diffusion at matrix/oxide interface is lower than the activation energy for oxygen diffusion in the matrix, larger alloy chromium content results in lower activation energy for the internal oxidation rate constant.

More recently, Guo *et al.* [50] internally oxidised Ni-Cr alloys in Ni/NiO packs and in flowing H_2/H_2O gas mixtures with the oxygen partial pressure, set at the Ni/NiO dissociation pressure to investigate the effect of water vapour and/or hydrogen on the oxygen permeability. They observed that the internal oxidation zone was mainly composed of chromium oxide, and some spinel particles were detected close to the sample surface in both environments. Guo reported that internal oxidation rates in Rhines pack were slightly faster than in H_2/H_2O environment, and attributed this to a change in internal oxide morphology. In Rhines pack, more needle shaped oxides precipitate, which can enhance oxygen diffusion more than spherical precipitate. In addition, they observed only a slight dependence of the oxygen permeability on alloy chromium content. Therefore, the oxygen permeability can be calculated using Equation (1.62).

Meijering [33] also collected permeability data in his review, using Schwarzkopft's data [54] to give an expression for the permeability of Ni-Cr alloys. In the Schwarzkopft experiments, Ni-Cr alloys were reacted in a Rhines pack with Ni/NiO powders, and then the depth of the IOZ measured. Alloys had chromium levels from 0.5 to 4 wt.% to give permeability values.

In Figure 1.18, permeability data measured by the different authors are plotted versus inverse temperature. Authors found good agreement between all values measured, regardless of the environment. Equation (1.118) was determined by least square regression over all data in Figure 1.18, and is represented by the continuous line

$$N_O^{(s)} D_O^{mat} = \left(0.57^{+1.2}_{-0.5}\right) \exp\left(\frac{-273 \pm 12 \text{ kJ mol}^{-1}}{RT}\right) (\text{cm}^2\text{s}^{-1}) \qquad (1.118)$$

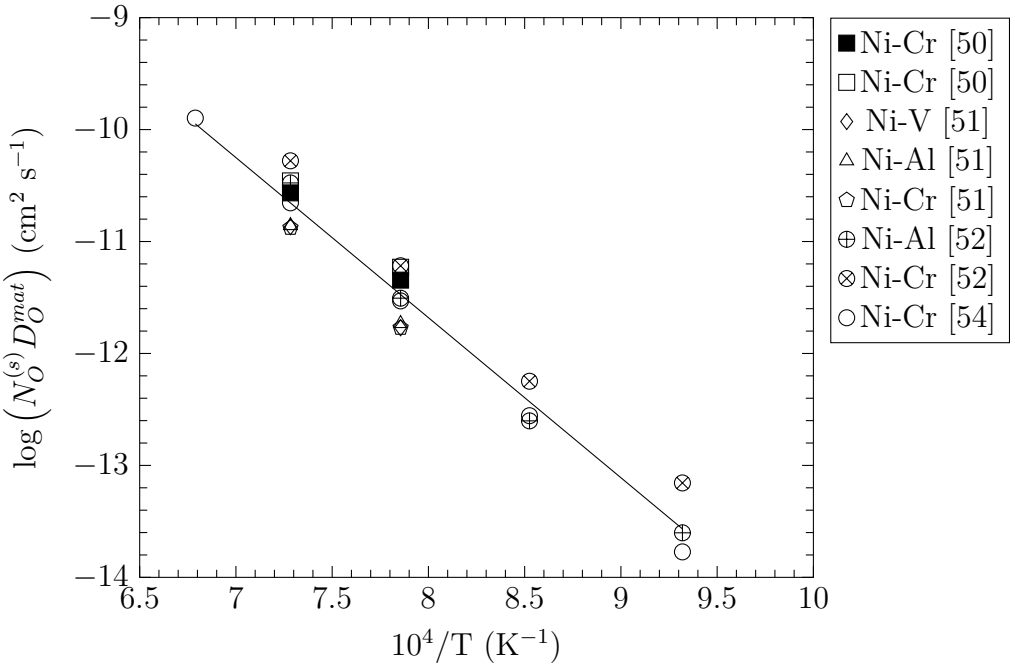

Figure 1.18: Oxygen permeability in nickel from Rhines pack experiment (open symbols) and H_2/H_2O experiment (filled symbols).

1.4.3 Prediction of internal oxidation with Wagner's analysis

As was described in Section 1.3, the behaviour of an alloy regarding the internal and external oxidation can be predicted using Wagner's Equation (1.85). Using permeabilities reviewed in the previous section for Fe-Cr and Ni-Cr alloys, the critical chromium concentration for the transition between internal and external oxidation under each oxidation conditions can be computed. To estimate this value the volume of one mole of chromium in solution in Fe and Ni or in oxide is required. These values are given by the alloy molar volume for Cr in solution in Fe and Ni and by the oxide molar volume for oxide species. However, for dilute Cr in solution in Fe and Ni, the effect of the small amount of chromium on the value of the alloy molar volume was ignored. Therefore, molar volumes for Fe-Cr and Ni-Cr alloys were considered equal to molar volumes of pure iron and nickel and are given in Table 1.6 along with oxide molar volumes.

Table 1.6: Volume of one mole of alloy and one mole of Cr in oxides.

V_{Fe}	V_{Ni}	$V_{CrO_{1.5}}$	$V_{Fe_{0.5}CrO_2}$
$cm^3\ mol^{-1}$			
7.1	6.6	14.6	23.8

In addition, the chromium diffusion coefficient is required to calculate the critical chromium concentration. In the next section, a brief review of chromium diffusion coefficient values in Fe-Cr and Ni-Cr alloys is presented.

1.4.3.1 Chromium diffusion coefficient in Fe-Cr alloys

As presented in Section 1.2, the chromium diffusion coefficient in Fe-Cr alloy can be calculated from tracer diffusion coefficient. In the literature, data for tracer diffusion coefficient are available but only a few values of the chromium diffusion coefficient were reported. The chromium diffusion coefficient in Fe-Cr is expressed by

$$D_{Cr} = D^*_{Cr}\left(1 + \frac{\partial \ln(\gamma_{Cr})}{\partial \ln(N_{Cr})}\right) \tag{1.119}$$

with D^*_{Cr} the tracer diffusion coefficient of chromium. In addition, Darken demonstrated that for the Fe-Cr system [19]

$$\frac{\partial \ln(\gamma_{Cr})}{\partial \ln(N_{Cr})} = \frac{\partial \ln(\gamma_{Fe})}{\partial \ln(N_{Fe})}. \tag{1.120}$$

Between 1,050°C and 1,390°C no variation of γ_{Cr} with the temperature was observed [55] and

$$\frac{\partial \ln(\gamma_{Fe})}{\partial \ln(N_{Fe})} = 0.08 \tag{1.121}$$

Finally, the chromium diffusion coefficient in iron can be approximated by

$$D_{Cr} = 1.08 D^*_{Cr} \tag{1.122}$$

In addition, some authors measured the interdiffusion coefficient Fe-Cr alloys with low chromium content. Therefore it was assumed that

$$D_{Cr} = \tilde{D} \tag{1.123}$$

Alberry and Haworth [56] measured chromium interdiffusion coefficient in Fe-Cr alloys, and compared their results to interdiffusion coefficients calculated from tracer experiments. They observed that high interdiffusion coefficients are found when calculated from tracer diffusion experiments and assumed that this resulted from a systematic error in tracer experiments. In addition, they observed no variation of the interdiffusion coefficient with the chromium content up to 28 at.%. Bowen and Leak [57] determined the tracer diffusion coefficient using tracer analysis and the alloy diffusion coefficient with EPMA measurements, using the Botzmann-Matano method. These authors found good agreement between values measured by both techniques.

In Figure 1.19, values of chromium diffusion coefficient measured and calculated with Equation (1.122) are plotted.

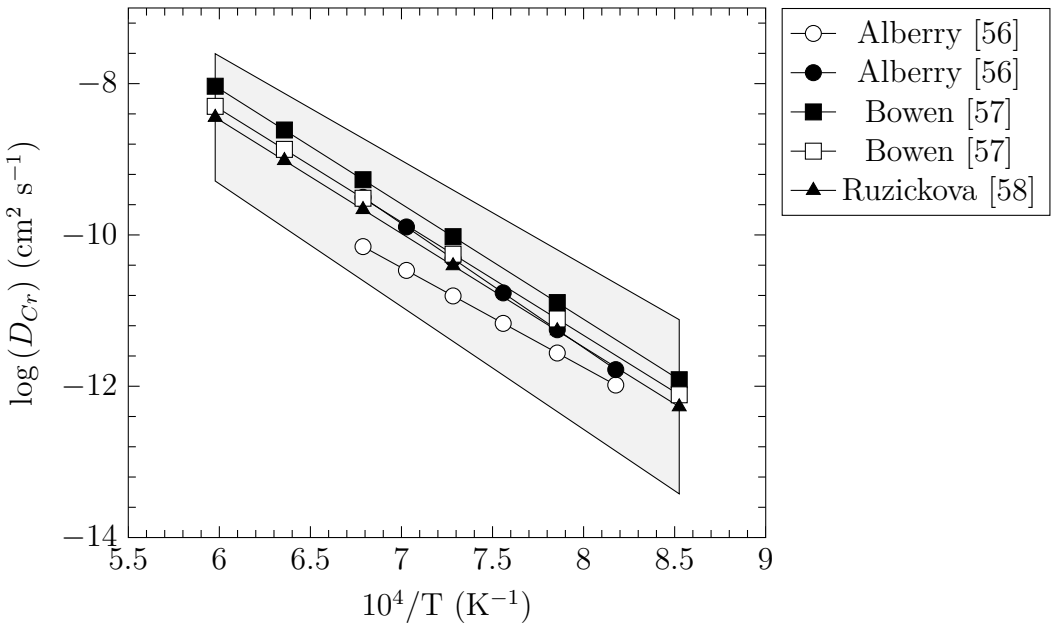

Figure 1.19: Chromium diffusion coefficient in Fe-Cr alloys. Calculated from tracer experiment (filled symbols), measured with interdiffusion couple (open symbols) for different chromium contents: 0-28 at.% (–○–).

The grey area represents possible value of the chromium diffusion coefficient according to errors reported by Ruzickova and Million [58]. In Figure 1.19, good agreement is found between values of chromium diffusion coefficient calculated from tracer diffusion and from interdiffusion experiments. In Table 1.7, values of activation energy and pre-exponential factor emerging from these measurements are reported.

Table 1.7: Pre-exponential factor and activation energy for the Fe-Cr alloy diffusion coefficient calculation.

Method	$D_{Cr}^{(0)} \times 10^2$ cm^2 s^{-1}	Q kJ mol^{-1}	Ref.
Tracer	4020^{+880}_{-780}	314 ± 28	[56]
Interdiff	$6.27^{+0.46}_{-0.42}$	252.3 ± 18.4	
Tracer	1080^{+335}_{-256}	291 ± 7	[57]
Tracer	313^{+254}_{-279}	287.3 ± 26.7	[58]

1.4.3.2 Chromium diffusion coefficient in Ni-Cr alloys

Some data on the chromium diffusion coefficient for the Ni-Cr system are present in the literature. However, as for the Fe-Cr system, it is possible to calculate the chromium diffusion coefficient from tracer diffusion coefficient. In addition, for low chromium content, the Ni-Cr system can be considered as an ideal solution. Therefore, the chromium diffusion coefficient is expressed by Equation (1.36)

$$D_{Cr} = D_{Cr}^{*} = \tilde{D} \tag{1.124}$$

Jung *et al.* [59] reported that the chromium interdiffusion coefficient slightly increases with alloy chromium content. In Figure 1.20, values of the chromium diffusion coefficient are presented. As in Figure 1.19, the grey area represents the uncertainty reported by Ruzickova and Million [58] in their review. A good agreement is found between the different chromium diffusion coefficients measured by the tracer technique and the diffusion coefficient measured by Ugaste [62] in alloys with

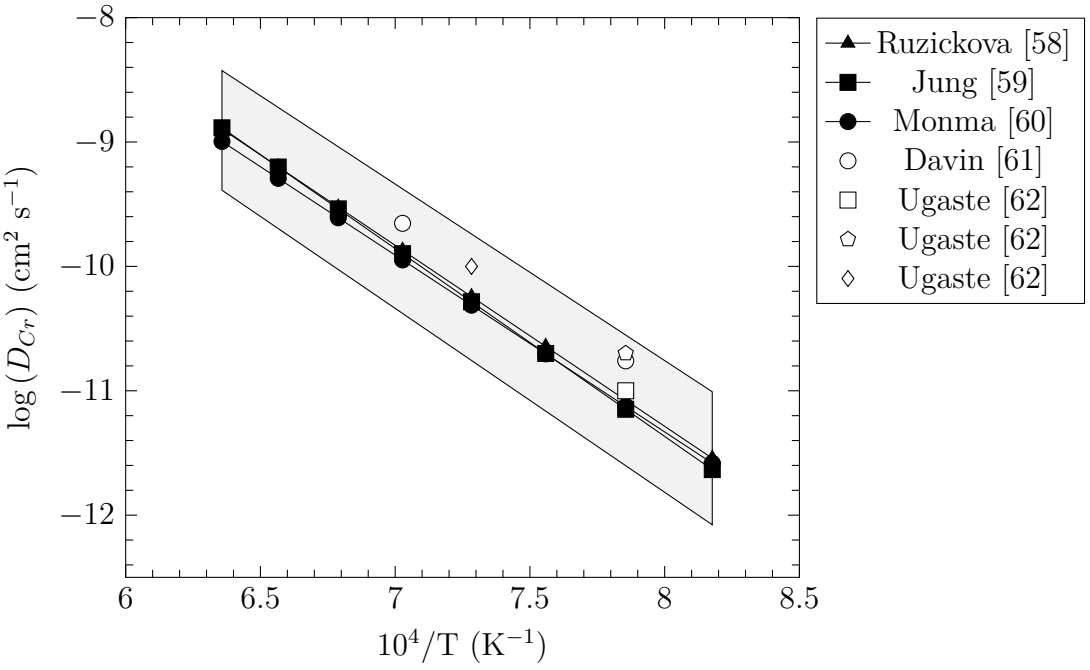

Figure 1.20: Chromium diffusion coefficient in Ni-Cr alloys. Calculated from tracer experiment (filled symbols), measured from interdiffusion couple (open symbols) for different chromium contents: 0-13 at.% (○), 5 at.% (□), 10 at.% (⬠), 5-30 at.% (◊).

a chromium content of 5 at.%. However, chromium diffusion coefficients estimated from interdiffusion couple for alloys with larger chromium content than 5 at.% are found to be slightly higher than diffusion coefficients measured by the tracer technique. These discrepancies suggest that the assumption of the dilute solution which yields Equation (1.124) may not be verified for alloys with chromium content larger than 5 at.%. In Table 1.8, the value of the pre-exponential factor and activation energy to calculate the different alloy diffusion coefficients are given.

Table 1.8: Pre-exponential factor and activation energy for the Ni-Cr alloy diffusion coefficient calculation.

Method	$D_{Cr}^{(0)}$ cm^2 s^{-1}	Q kJ mol^{-1}	Ref.
Tracer	$2.26^{+2.56}_{-1.20}$	278.4 ± 8.7	[58]
Interdiff	5.2 ± 1.2	289 ± 3	[59]
Tracer	1.1	272	[60]

1.4.3.3 Critical chromium concentration calculation

In Figure 1.21, the critical chromium content required for the transition between internal and external oxidation in γ-iron was calculated. For this calculation, Meijering's permeability measured in Fe-Cr alloys in H_2/H_2O gas mixtures with the oxygen partial pressure set at the Fe/FeO equilibrium pressure (solid lines) was considered. In addition, Takada's permeability measured in Fe/FeO Rhines pack in Fe-Al alloys (dashed lines) was used for comparison. Different internal oxides were considered in computing critical chromium concentration: Cr_2O_3 or $FeCr_2O_4$. It should be noted that the critical volume fraction of oxide was taken as 0.3 as determined by Rapp [32], and the chromium diffusion coefficient measured by Bowen and Leak with tracer was considered [57].

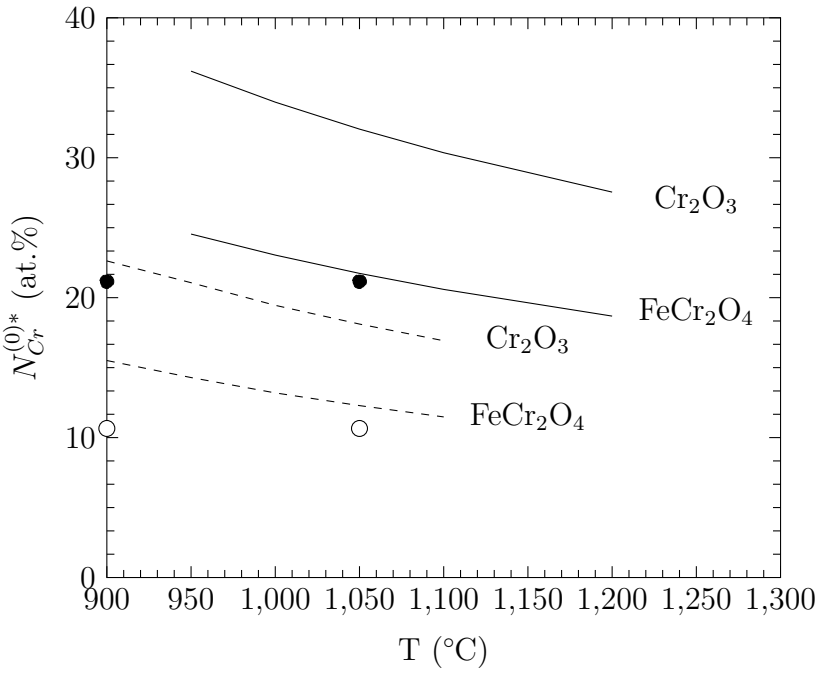

Figure 1.21: Critical chromium concentration to observe the transition between internal and external oxidation in γ-iron at the Fe/FeO equilibrium pressure, calculated with different permeability; Meijering [33] (——) and Takada *et al.* [38–41] (- - -). Essuman *et al.*'s [63] observation on Fe-Cr alloy exposed in H_2/H_2O; (○) Internal oxidation, (●) External oxidation.

Figure 1.21 shows that Meijering's permeability yields high value for the critical content of chromium for the transition between internal and external oxidation in iron because he published values of effective permeability as presented in Sec-

tion 1.4.1. This demonstrates that the oxygen solubility of the matrix has to be used for the calculation of the critical chromium concentration for transition between internal and external oxidation. Therefore, $N_{Cr}^{(0)*}$ calculated with oxygen permeability measured by Takada *et al.* is considered more reliable and compared to experimental observations.

Essuman *et al.* [63] investigated the effect of the water vapour on the transition between internal and external oxidation in Fe-Cr alloys. The authors exposed alloys containing 10 and 20 wt.% of chromium in different atmospheres with different oxygen partial pressures, and at two temperatures 900 and 1,050°C. However, alloys with 20 wt.% of chromium have a BCC structure at the two temperatures studied while alloys with 10 wt.% of chromium have an FCC structure. In one of their experiments, the authors used a H_2/H_2O gas mixture to set an oxygen partial pressure at a value slightly higher than the Fe/FeO dissociation pressure. However, when they examined their samples, no iron oxide was observed on the sample surface. It would seem that the oxygen partial pressure might have been lower than the Fe/FeO dissociation pressure during their experiments. After 72h of exposure at 900 and 1,050°C in this environment, the alloy with 10 wt.% of chromium exhibited exclusive internal oxidation, precipitating iron chromium spinel while a chromia scale growth on the alloy containing 20 wt.% of chromium at both temperatures. However, the formation of a chromia scale on α-iron, which has a BCC structure, is easier to achieve than for γ-iron, with a FCC lattice, because the diffusion of chromium is one order of magnitude faster in BCC than in FCC structures. In addition, the oxygen permeability of α-iron is only twice the permeability of γ-iron. Therefore, the critical chromium content to observe the transition between internal and external oxidation for α-iron alloys is related to $N_{Cr}^{(0)*}$ for γ-iron by

$$N_{Cr}^{(0)*}(\alpha) \approx 0.5 N_{Cr}^{(0)*}(\gamma) \tag{1.125}$$

In Figure 1.21, the dots represent the result of Essuman's observations at 900 and 1,050°C. The minimum chromium content to observe the transition between

internal and external oxidation for γ-iron at the Fe/FeO dissociation pressure and assuming spinel as internal oxide is around 22 and 12 at.% at 900 and 1,050°C, respectively. For alloys with 20 wt.% of chromium, which have a BCC structure, $N_{Cr}^{(0)*}$ is calculated with Equation (1.125). For α-iron with spinel as internal oxides, the critical chromium to observe the transition between internal and external oxidation is approximately 11 and 6 at.% at 900 and 1,050°C, respectively. Critical chromium content to observe the transition between internal and external oxidation calculated for γ-iron and α-iron with Takada's oxygen permeability are in agreement with Essuman's observations. However, Takada *et al.* measured the oxygen permeability in Fe/FeO Rhines pack while Essuman *et al.* carried out their experiments in H_2/H_2O gas mixture with the oxygen partial pressure set at the Fe/FeO equilibrium. This result may indicate that the presence of water vapour and/or hydrogen has no significant effect on the oxygen permeability in iron.

For alloys based on the Ni-Cr system, the same calculation is done and results are presented in Figure 1.22.

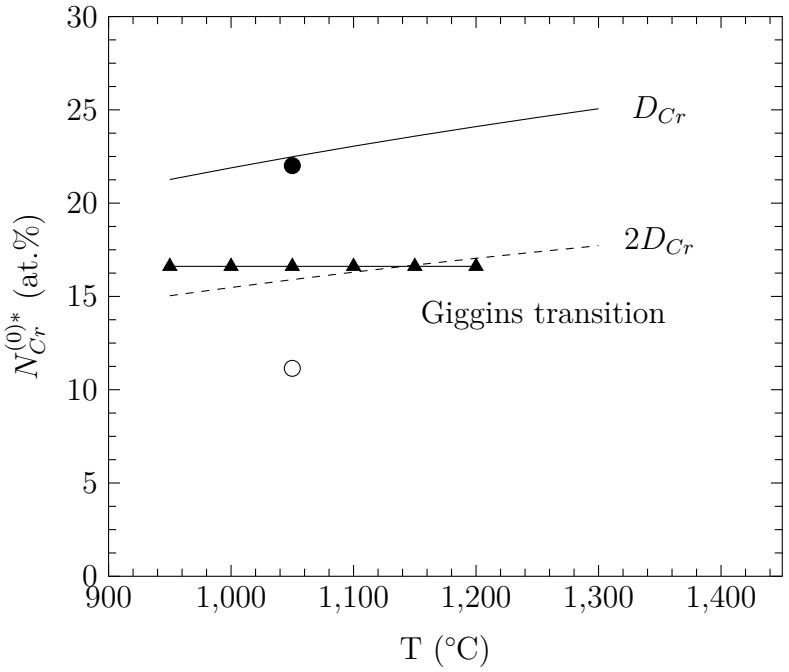

Figure 1.22: Critical chromium concentration for transition between internal and external oxidation in nickel at the Ni/NiO equilibrium pressure, calculated with Schwarzkopf's permeability [54]. Essuman *et al.*'s [64] observation on Ni-Cr alloy; (○) Internal oxidation, (●) External oxidation.

Giggins and Pettit [65] studied the oxidation of various Ni-Cr alloys in 0.1 atm of oxygen between 900°C and 1,200°C. At this oxygen partial pressure a NiO scale grows, and the oxygen partial pressure below the scale is equal to the Ni/NiO dissociation pressure. Therefore, Schwarzkopf's permeability [54] can be used to calculate the critical chromium content for the transition between external and internal oxidation. In addition, Giggins reported that only chromium oxides were detected in the IOZ and, the transition between internal and external oxidation took place for a chromium content greater than 15 wt.%. Essuman *et al.* oxidised Ni-Cr alloys at 1,050°C in different atmospheres [64]. For alloys containing 20 wt.% of chromium, no internal oxidation was observed under their experimental conditions. Internal oxidation occurred in alloys containing only 10 wt.%. In Figure 1.22, the 2 dots represent the results of Essuman *et al.*'s observations. In addition, Essuman *et al.* mentioned that the presence of water vapour associated with high oxygen partial pressure reduces the ability of Ni-Cr alloys to form a chromia scale on its surface. In Figure 1.22, the critical chromium content calculated with Schwarzkopf's permeability, Ruzickova's diffusion coefficient [58] and considering chromium oxide as internal oxides is presented. The calculation gave a higher chromium content to reach the transition between internal and external oxidation compared to observations of the different authors. However, Essuman *et al.*'s experiments were carried out at 1,050°C. At this temperature the chromium diffusion coefficients measured were 2 or 3 time higher than the tracer diffusion coefficient used for calculation in Figure 1.22 as presented in Section 1.4.3.2. The calculation of the critical chromium concentration for transition between internal and external oxidation were done again but the chromium diffusion coefficient was multiplied by a factor of two. The new result obtained is presented in Figure 1.22 by the dashed line. This correction gave a better agreement with observations reported in the literature. Nonetheless, Schwarzkopf's permeability used to calculate the critical chromium concentration was measured in Ni/NiO Rhines pack and Essuman's experiments were carried out in H_2/H_2O gas mixture but the prediction and observations are in agreement. This

may suggest that, as in iron, the presence of water vapour and/or hydrogen has no significant effect on the oxygen permeability.

1.4.4 Fe-Ni based alloys

The last example of this section is the internal oxidation of iron-nickel based alloys. This system provides the basis for many alloys used for high temperature applications in oxidising environments, for example commercial stainless steels and high nickel alloys currently used. Little information is available in the literature for the oxygen permeability of Fe-Ni alloys. One major work was carried out by Croll and Wallwork [66] who tried to define the boundary of the composition domain where internal oxidation did not occur at 1,000°C. In Figure 1.23, the solid line represents the stability of a chromic oxide layer and the dotted line denotes the transition between internal and external oxidation.

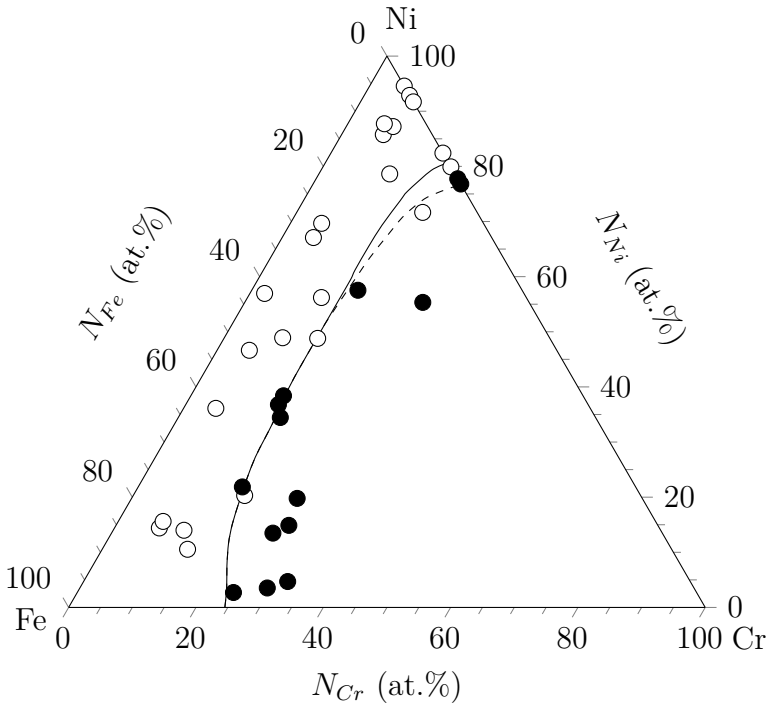

Figure 1.23: Section of the iron-nickel-chromium-oxygen phase diagram at 1,000°C and a constant oxygen concentration equal to the solubility of oxygen in alloy matrix. It shows the limit of appearance of internal oxidation in various alloy compositions. Internal oxidation (○), no internal oxidation (●) [66].

From Figure 1.23, the permeability of ternary alloys can be calculated, using

Equation (1.85). However the boundary between internal and external oxidation is well defined only for an iron content up to 60 at.%. At higher iron levels, the boundary could be anywhere between 15 at.% and 25 at.% of chromium. In addition, to calculate the permeability, chromium diffusion coefficients are calculated with data from Duh and Danayanda [67] who measured chromium coefficients for Fe-Ni-Cr alloys with different compositions at 1,100°C. From their results, it was possible to interpolate the value of the chromium diffusion coefficient for any composition. In addition, to calculate the value of the chromium diffusion coefficient at lower temperature, an activation energy of 300 kJ mol^{-1} was used with the following relation

$$D_{Cr}^{Fe-Ni}(T) = D_{Cr}^{Fe-Ni}(1,100°\text{C}\ )\exp\left(\frac{Q}{R}\left(\frac{1}{1373}-\frac{1}{T(K)}\right)\right) \tag{1.126}$$

In addition, cross-effects were neglected for the calculation. In Figure 1.24, the chromium diffusion coefficient calculated at different temperatures are presented versus the nickel content. For diffusion coefficient in the pure iron and nickel, chromium diffusion coefficients measured by Ruzickova and Million were added to Figure 1.24.

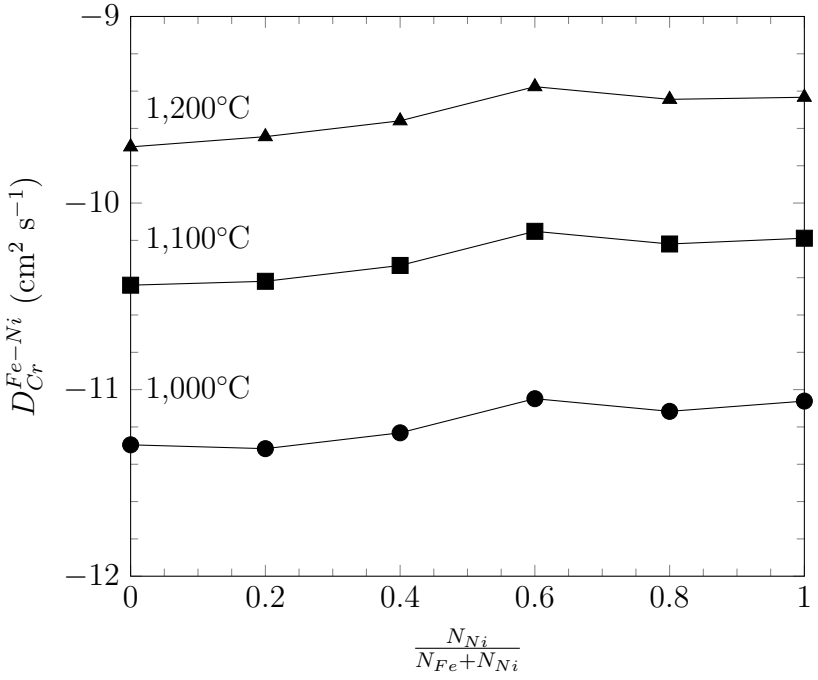

Figure 1.24: Chromium interdiffusion coefficient measured in Fe-Cr and Ni-Cr [58] and in Fe-Ni-Cr [67].

As mentioned before, Croll and Wallwork [66] carried out their experiments under conditions in which an oxide scale growth and the dissociation pressure under the scale depends on the alloy composition. Dalvi and Sridhar measured the dissociation pressure of the oxide in equilibrium with Fe-Ni alloys [68]. To be able to compare permeability values, Croll and Wallwork's results were extrapolated to the Fe/FeO dissociation pressure using Equation (1.107).

In Figure 1.25, permeability calculated from the critical chromium concentration for the transition between internal to external oxidation measured by Croll and Wallwork is plotted as a function of the ratio $\frac{N_{Ni}}{N_{Fe}+N_{Ni}}$. The critical volume fraction of oxide is taken equal to 0.3 for the calculation. For comparison, permeability values measured in iron by Takada *et al.* [38] and in nickel by Schwarzkopft [54] at the Fe/FeO dissociation pressure were added to Figure 1.25. The oxygen permeability is seen to decrease as the nickel content increases. In addition, values measured in pure iron and pure nickel are in rough agreement with values measured by Croll and Wallwork.

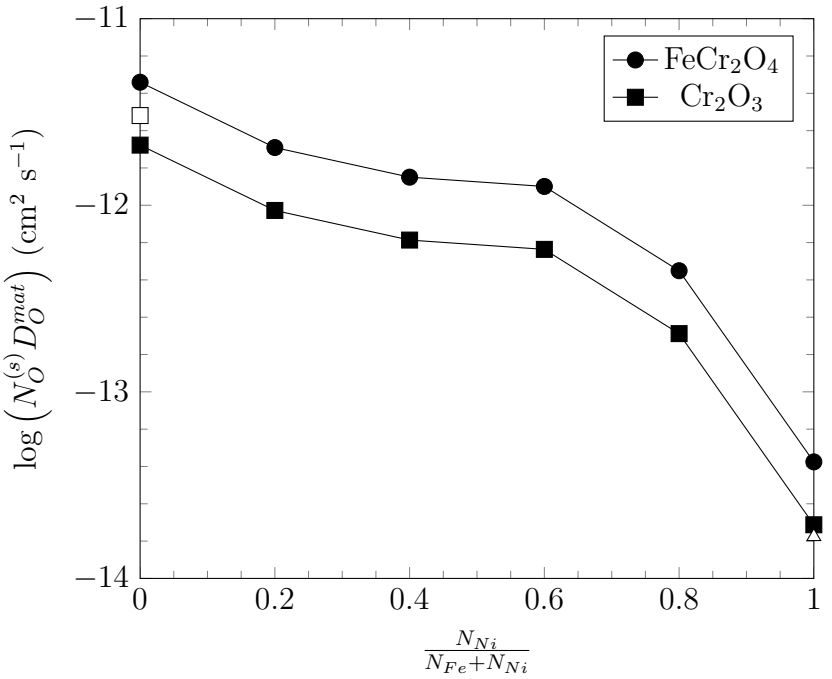

Figure 1.25: Permeability measured from the chromium critical content for transition between internal and external oxidation observed by Croll and Wallwork at 1,000°C and calculated for the Fe/FeO dissociation pressure. Takada [38] (□), Schwarzkopft [54] (△).

More recently, Ueda *et al.* [69] exposed Fe-30Ni based alloys in dry and wet environments at 800°C, with the oxygen partial pressure set at the Fe/FeO dissociation pressure. They found that the critical concentration for transition between external and internal oxidation was 30 at.% and 37 at.% in dry and wet environments, respectively. Careful study of the internal oxide distribution in Fe-30Ni-5Cr showed that under wet conditions the internal oxidation zone was mainly composed of $FeCr_2O_4$, while in dry conditions, both Cr_2O_3 and spinel were detected. Ueda *et al.* used the Meijering definition for the effective stoichiometry coefficient in Equation (1.93), and reported that in dry conditions the stoichiometry coefficient is a constant value of 1.7. Under wet conditions, the authors observed an increase of the effective stoichiometry coefficient with time until reaching a plateau with the value of 2. Considering the evolution of the effective stoichiometry coefficient, the authors calculated the oxygen permeability as 1.1×10^{-13} and 1.4×10^{-13} cm^2 s^{-1} in dry and wet conditions, respectively. The oxygen permeability was thus 30% higher during exposition in humid conditions. However, considering errors reported for both kinetics and effective stoichiometry values, which are scattered, the effect of water and/or hydrogen on the oxygen permeability is difficult to assess from their results.

1.5 Oxygen solubility in metal

In Section 1.3, it was demonstrated that oxygen solubility and diffusivity are two parameters which play a fundamental role in determining the internal oxidation rate, or whether it can be avoided. The oxygen solubility in a solid metal is defined as the oxygen concentration that a metal contains for a given oxygen partial pressure. In the case where the solute is a gas and the solvent a solid, the absorption of one solute atom by the alloy is described by Sievert's law.

$$\frac{1}{2}O_{2\left(g,\ p_{O_2}=1\ \mathrm{atm}\right)} = \underline{O}_{(N_O=1)} \tag{1.127}$$

The condition for equilibrium of reaction 1.127 is given by

$$\frac{1}{2}G^0_{O_2} - G^0_O = RT \ln \left(\frac{\gamma_O N_O}{p^{1/2}_{O_2}} \right) \tag{1.128}$$

where $G^0_{O_2}$ and G^0_O are the standard free energy of oxygen in gaseous phase and oxygen dissolved in the metal, respectively. In addition, γ_O is the activity coefficient of oxygen dissolved in the solution. Under the assumption of a Raoultian standard state for dissolved oxygen and 1 atm for oxygen in the gas phase. The standard free energy change at a temperature T for the dissolution of gaseous oxygen at 1 atm to the metal at the concentration $N_O = 1$ is given by

$$\Delta G^0_{1.127} = \frac{1}{2}G^0_{O_2} - G^0_O = 0 \tag{1.129}$$

Therefore, the equilibrium condition for reaction 1.127 becomes

$$1 = \frac{\gamma_O N_O}{p^{1/2}_{O_2}} \tag{1.130}$$

Finally, it is found that the oxygen mole fraction in the material is proportional to the square root of the oxygen partial pressure in the gas

$$N_O = \frac{p^{1/2}_{O_2}}{\gamma_O} = K^{(s)} p^{1/2}_{O_2} \tag{1.131}$$

with $K^{(s)} = \frac{1}{\gamma_O}$ and $K^{(s)}$ the Sievert constant.

A few authors [70–72] tried to predict oxygen solubility in liquid alloys using thermodynamic approaches. The interest in oxygen solubility in alloys arose because oxygen is a common impurity in metallurgical processes. Of interest here is that, these authors showed that the properties of the A-B-O system can be determined by separately studying the systems A-O and B-O.

In this section, firstly the oxygen solubility in iron and nickel are reviewed. Secondly, different models for predicting the solubility in liquid A-B alloys are presented. These are used as a basis for the prediction of oxygen solubility in solid

alloys. Finally, models are applied to the Fe-Ni system to predict their oxygen content.

1.5.1 Oxygen solubility in iron

Different techniques have been used to measure the oxygen level in iron: annealing of iron sample in hydrogen, measurement of the weight-change, vacuum fusion infrared method. It is necessary to recognise that solid iron can exist as different phases

α has a BCC structure and is stable up to 910°C;

γ has a FCC lattice and exists between 910 and 1,400°C;

δ has a BCC lattice and exists between 1,400 and 1,540°C.

In addition, iron equilibrates with different oxide phases at different temperatures, complicating the measurement still further.

Several authors [47, 73–77] reported solubility values in each phase. However, their values disagree, and are scattered from 21 at.% to 0.010-0.021 at.% for a temperature around 1,000°C. One reason for these discrepancies was given by Kitchener *et al.* [73], who highlighted the fact that if impurities, with a stronger affinity for oxygen, like Al or Si, were present in iron, they could internally oxidise, trapping the oxygen and increasing the apparent oxygen level. In order to reduce these impurities, they annealed their sample in hydrogen atmosphere. Nevertheless, some of these impurities formed very stable oxides, and could not be reduced by this treatment. Hepworth *et al.* [77], who published one of the latest papers, emphasised the fact that oxygen measurement below 350 at.ppm was very difficult.

Seybolt [74], to measure the oxygen solubility in α iron, oxidised pure iron in oxygen between 700 and 900°C, and then removed the oxide scale and analysed the iron by the vacuum fusion method. He measured oxygen contents of 300 and 1000 at.ppm at 700 and 900°C respectively. These values are orders of magnitude higher than those reported by Swisher and Turkdogan [47] in their work on γ iron. To

saturate iron with oxygen, they used an atmosphere of H_2/H_2O, with the appropriate ratio to obtain an oxygen partial pressure below the dissociation pressure of wüstite, avoiding iron oxidation. They carried out one measure on α iron and found an oxygen content of 12 ± 7 at.ppm at a temperature of 881°C.

Table 1.9: Oxygen solubility in γ-iron equilibrated in H_2/H_2O mixtures [47].

Temperature °C	p_{O_2} atm	N_O at.ppm
881	7.6×10^{-18}	12.2
951	1.6×10^{-16}	8.7
1,049	7.3×10^{-15}	17.4
1,250	3.3×10^{-12}	50.6
1,350	5.7×10^{-11}	87.2

In the same work, the authors measured the oxygen content of γ iron samples, and their results are reported in Table 1.9. These values are supported by the results of Kitchener *et al.* [73], who determined an average value of 105 at.ppm based on measurements between 1,325 and 1,425°C in a CO/CO_2 atmosphere.

Concerning the oxygen solubility in the δ phase, Hepworth *et al.* [77] carried out experiments on iron in equilibrium with molten oxide, and measured an oxygen solubility of 230 and 289 at.ppm at 1,450°C and 1,510°C, respectively. Their values are smaller than those reported by Tankins and Gokcen [76], who found at 1,450°C an oxygen solubility of 626 at.ppm, and 855 at.ppm at 1,510°C. However, their iron contained impurities which could account for 70 to 105 at.ppm excess oxygen.

In Figure 1.26, the variation of the oxygen content with the ratio $\frac{p_{H_2O}}{p_{H_2}}$ at 1,350°C is plotted [47]. Dashed lines on the plot represent the ratio to achieve an oxygen partial pressure of 3.3×10^{-12} atm at 1,350°C which is the oxygen pressure used for the solubility measurement at 1,250°C reported in Table 1.9. The corresponding oxygen level found from Figure 1.26 to be 20 at.ppm at 1,350°C. Comparing this value to the measurement at 1,250°C reported in Table 1.9, this shows that at a constant oxygen pressure, the solubility decreases when the temperature increases.

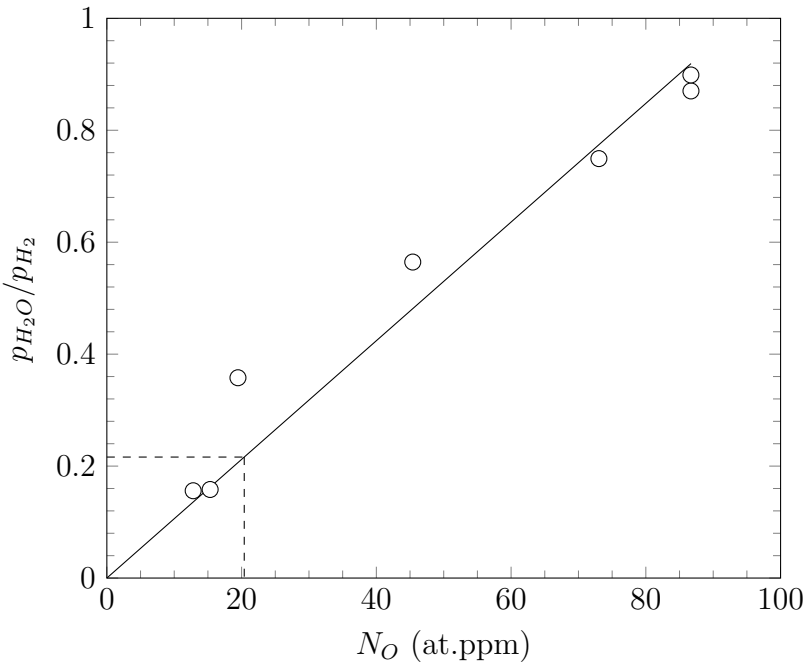

Figure 1.26: Variation of the oxygen content in iron with the ratio H_2/H_2O at 1,350°C in Ar-H_2-H_2O gas [47].

Swisher and Turkdogan [47] also derived free energy expressions for Sievert's constant from their data for BCC and FCC iron. For the α phase they extrapolated values obtained for δ iron. These free energies allow us to express oxygen content in iron as a function of pressure and temperature

BCC iron (α and δ)

$$N_O = 2.1 \times 10^{-4} (p_{O_2} \text{ (atm)})^{\frac{1}{2}} \exp\left(\frac{155454 \text{ J mol}^{-1}}{RT}\right) \tag{1.132}$$

FCC iron (γ)

$$N_O = 2.4 \times 10^{-5} (p_{O_2} \text{ (atm)})^{\frac{1}{2}} \exp\left(\frac{174975 \text{ J mol}^{-1}}{RT}\right) \tag{1.133}$$

1.5.2 Oxygen solubility in nickel

In the literature, there is little information on oxygen solubility in pure nickel. Seybolt [78] was the first to report such data. He oxidised pure nickel, then removed the oxide scale and chemically analysed the substrate for oxygen. Later, Alcock and Brown [79], using a thermogravimetric method, recorded the weight change of a pure nickel sample as a function of the oxygen partial pressure set by a CO/CO_2 mixture. To determine the oxygen solubility, they extrapolated their plot of the sample weight gain versus the oxygen partial pressure to the Ni/NiO dissociation pressure.

Park and Altstetter [80] used two electrochemical techniques to measure the oxygen solubility in nickel. Results from both techniques were close, and allowed them to give the following expression for the oxygen concentration in pure nickel.

$$N_O = 2.38 \times 10^{-6} (p_{O_2} \text{ (atm)})^{\frac{1}{2}} \exp\left(\frac{182 \text{ kJ mol}^{-1}}{RT}\right) \tag{1.134}$$

Oxygen solubility measured by the different authors at the Ni/NiO dissociation pressure are presented in Table 1.10, with the Ni/NiO equilibrium pressure. This equilibrium pressure was calculated using data in Table 1.1.

Remarkably, the results of Seybolt and Alcock and Brown's studies indicated that oxygen solubility decreased with rising temperature. In contrast, values found by Park and Altstetter [80] showed the oxygen solubility increased with temperature. However, in all the studied reviewed, oxygen solubility was measured at the Ni/NiO dissociation pressure which also vary with the temperature. Unlike for iron, as three different datasets are available in the literature, it is thoughtful to compare the partial molar excess of Gibbs free energy associated with oxygen dissolution in nickel. The partial molar excess of Gibbs free energy is given by

$$\overline{G}_O^{xs} = RT \ln(\gamma_O) \tag{1.135}$$

Combining Equations (1.135) and (1.131) yields

$$\overline{G}_O^{xs} = -RT \ln \left(\frac{N_O}{p_{O_2}^{1/2}} \right) \tag{1.136}$$

Table 1.10: Oxygen solubility in nickel measured at the Ni/NiO dissociation pressure.

Temperature	$p_{O_2}^{Ni/NiO}$	N_O (at.%)		
°C	atm	[78]	[79]	[80]*
800	9.6×10^{-15}	6.9×10^{-2}	-	1.7×10^{-2}
900	8.5×10^{-13}	6.0×10^{-2}	-	2.9×10^{-2}
1,000	3.7×10^{-11}	5.1×10^{-2}	-	4.6×10^{-2}
1,050	2.0×10^{-10}	-	$(3.6 \pm 0.2) \times 10^{-2}$	-
1,100	9.4×10^{-10}	4.8×10^{-2}	$(3.4 \pm 0.3) \times 10^{-2}$	-
1,150	4.0×10^{-9}	-	$(3.4 \pm 0.1) \times 10^{-2}$	-
1,200	1.5×10^{-8}	-	$(3.0 \pm 0.2) \times 10^{-2}$	-

*values calculated with (1.134) at the Ni/NiO dissociation pressure

Using data from Table 1.10, the free energy measured by the different authors were calculated and are presented in Figure 1.27.

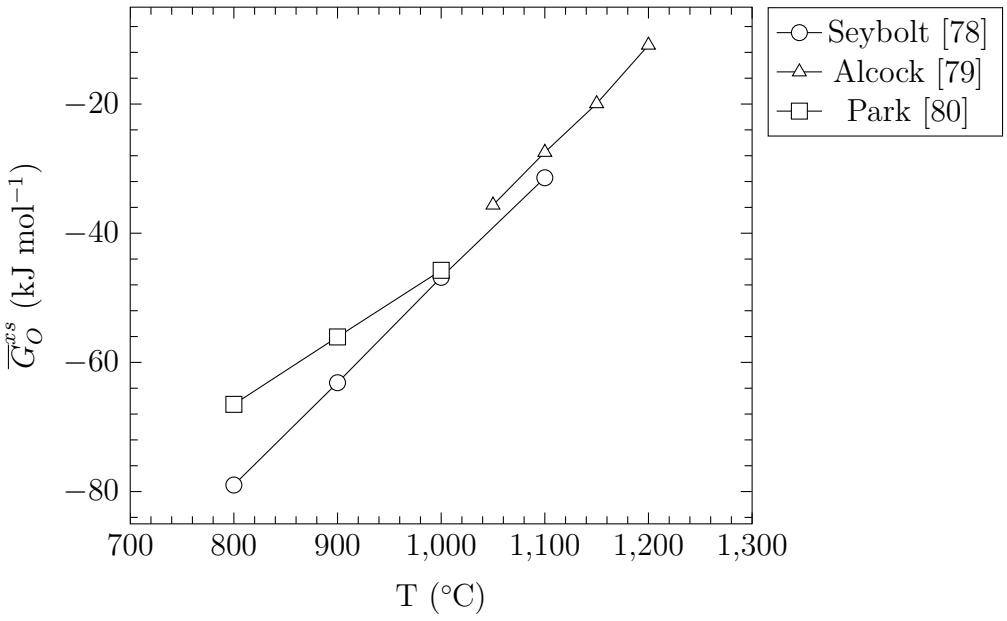

Figure 1.27: Partial molar excess of Gibbs free energy for oxygen dissolved in pure nickel calculated from data in Table 1.10 and Eq.(1.135).

Good agreement is found between Seybolt and Alcock and Brown's values while Park and Alstetter found higher free energy than Seybolt for temperature lower than 1,000°C. However, no explanation was found to account for discrepancies between values measured at low temperature.

1.5.3 Oxygen solubility in binary alloys

Several authors over the years have tried to predict gas solubilities in dilute solid or liquid solutions. One of the first models was proposed by Alcock and Richardson, called the Quasichemical model [70, 71]. The second reviewed in this section is Wagner's model [72] which was later modified by Chiang and Chang [81]. The various models are used to predict the activity coefficient of a solute S in an alloy A-B. Using the relation (1.131), the solute solubility can then be calculated.

1.5.3.1 Quasichemical model

In their first paper, Alcock and Richardson [70] provide an equation to predict the activity coefficient of a solute S in an alloy A-B. Equation (1.137) was determined by assuming that the atom distribution in the alloy and around the solute atom were the same, and the three species had the same coordination number. It was also assumed that the interaction energy between atom pairs is independent of their concentration. Then

$$\ln(\gamma_{S(A+B)}) = N_A \ln(\gamma_{S(A)}) + N_B \ln(\gamma_{S(B)}) - \left[N_A \ln(\gamma_{A(A+B)}) + N_B \ln(\gamma_{B(A+B)})\right] \tag{1.137}$$

where $\gamma_{S(A/B)}$ is the solute activity coefficient in the metal A or B, $\gamma_{S(A+B)}$ is the solute activity coefficient in the alloy A-B and $\gamma_{A/B(A+B)}$ the activity coefficient of A or B in the alloy A-B. This equation is very accurate in predicting the behaviour of a solute if the following condition is fulfilled

$$\ln\left[\frac{\gamma_{S(A)}}{\gamma_{A(A+B)}}\right] - \ln\left[\frac{\gamma_{S(B)}}{\gamma_{B(A+B)}}\right] \ll 1 \tag{1.138}$$

The two last terms of (1.137) are equal to the excess Gibbs energy of mixing for a binary alloy A-B, divided by RT. This yields

$$\ln(\gamma_{S(A+B)}) = N_A \ln(\gamma_{S(A)}) + N_B \ln(\gamma_{S(B)}) - \frac{G^E}{RT} \tag{1.139}$$

where G^E is the excess Gibbs energy of mixing. If the solution is an ideal mixture, $G^E = 0$, the solute activity is only dependent on the mole fraction of B and the relation is linear

$$\ln(\gamma_{S(A+B)}) = \ln(\gamma_{S(A)}) + N_B \ln\left(\frac{\gamma_{S(B)}}{\gamma_{S(A)}}\right) \tag{1.140}$$

Later, Alcock and Richardsons [71] revised their model to take into account the fact that a solute atom can be surrounded preferentially by atoms with a greater affinity for it. At this point, the atom distribution in the solute shell is no longer random. This aspect is important for solutes which have a great solubility in one of the alloy constituents. However, it is still assumed that the interaction energies A-S, B-S are independent of their concentration. For this case, the following equation was proposed by Alcock and Richardson

$$\gamma_{S(A+B)} = \left[N_A \left(\frac{\gamma_{A(A+B)}}{\gamma_{S(A)}}\right)^{\frac{1}{Z}} + N_B \left(\frac{\gamma_{B(A+B)}}{\gamma_{S(B)}}\right)^{\frac{1}{Z}} \right]^{-Z} \tag{1.141}$$

where Z is the number of nearest neighbours of S and $\gamma_{A(B)(A+B)}$ the activity coefficient of A or B in the alloy A-B.

Unfortunately, theoretical values were not in agreement with experimental results. These deviations resulted from strong assumptions in the Quasichemical model which were certainly not true. For example, the interactions A-S and B-S might not be the same in the bulk alloy and in the solvation shell of S. In addition, interaction energies should change with the proportions of A and B atoms around S, and finally, the coordination number of S may be less than the coordination number of A and B in the bulk alloys. The deviations exhibited by the Quasichemical model

encouraged others to refine models in order to better predict solute activity in binary alloys.

1.5.3.2 Wagner's model

Wagner [72] created a new model in order to predict oxygen gas solute activity in binary liquid. However, to developed his model, Wagner defined quasi interstitial sites in the liquid, and considered that there is a short range order which can be considered like a close-packed hexagonal or FCC structure in this state. Therefore, this model may also be applicable to solid Fe-Ni alloys. Wagner considered that oxygen is present in interstitial sites, and based on the size of octahedral and tetragonal sites, he considered that oxygen preferentially occupies octahedral sites which are larger, so the coordination number, Z, was chosen equal to 6. In addition, contrary to Alcock and Richardson who assumed a constant energy to change an atom in the solvation shell of the solute, Wagner proposed an increase of this energy with the addition of an atom, which has a greater affinity with the solute, in the shell. The binary alloy A-B is considered, and the solubility of S is assumed greater in B than in A. The change of solvation shell of S can be described by a jump of an atom S from a site surrounded by (Z-i) A and i B atoms to a quasi interstitial site with (Z-i-1) A atoms and (i+1) B atoms, and the enthalpy of this reaction is denoted by $\Delta H(i \rightarrow i+1)$. At this point, Wagner proposed a constant increase of the energy required to change an atom in the solvation shell at each occurrence. The value of this difference in energy is denoted by h.

$$\Delta H(i = 0 \rightarrow i = 1) < \Delta H(i = 1 \rightarrow i = 2) \text{ etc} \tag{1.142}$$

$$\Delta H(i+1 \rightarrow i+2) - \Delta H(i \rightarrow i+1) = h \tag{1.143}$$

Wagner then considered a random distribution of atoms A and B in the alloy and defined the probability of finding a quasi-interstitial site with a particular number

of atoms A and B by a combinatorial law. This led to an expression for the solute activity as a function of the alloy composition.

$$\frac{\gamma_S}{\left(\gamma_{S(A)}\gamma_{S(B)}\right)^{\frac{1}{2}}} = \left\{ \sum_{i=0}^{i-Z} \binom{Z}{i} \left[\frac{(1-N_B)}{\phi^{\frac{1}{2Z}}} \right]^{Z-i} \times \left[N_B \phi^{\frac{1}{2Z}} \right]^i \exp\left[\frac{(Z-i)ih}{2RT} \right] \right\}^{-1} \tag{1.144}$$

where $\binom{Z}{i}$ is the binomial factor and $\phi \equiv \left[\frac{N_{B(S)}}{N_{A(S)}}\right]_{p_{S_2}} = \frac{\gamma_{S(A)}}{\gamma_{S(B)}}$ with $N_{A(S)}$ and $N_{B(S)}$ the solubility of S in pure A and B, respectively. This calculation method gave good results in systems which do not exhibit strong deviation from ideality to be able to assume a random distribution of A and B atoms in the alloys. Total agreement with experimental values could not be expected because a great number of parameters are not taken into account. The greatest deviations were observed with solutions having strongly non ideal behaviour. The parameter h can be adjusted to adapt the model to different alloys, however it has to fulfil the following condition to achieve consistent results with (1.144)

$$\frac{h}{2RT} < \frac{1}{5}\ln(\phi) \tag{1.145}$$

Chiang and Chang [81] extended Wagner's model to predict the oxygen activity in binary solution which exhibited deviations from Equation (1.144). They introduced two energy parameters to more precisely define the variation of the energy required to change one atom in the solute shell. Indeed, instead of assuming that the energy increased by a constant value at each change of the solute coordination shell, they considered that the enthalpy varied linearly with the number of B atoms in the shell.

$$\Delta H(i+1 \rightarrow i+2) - \Delta H(i \rightarrow i+1) = h_1 + h_2 i \tag{1.146}$$

This leads to

$$\begin{aligned} \frac{\gamma_S}{\left(\gamma_{S(A)}\gamma_{S(B)}\right)^{\frac{1}{2}}} = & \left\{ \sum_{i=0}^{i-Z} \binom{Z}{i} \left[\frac{(1-N_B)}{\phi^{\frac{1}{2Z}}} \right]^{Z-i} \right. \\ & \left. \times \left[N_B \phi^{\frac{1}{2Z}} \right]^i \exp\left[\frac{(Z-i)i}{2RT}(h_1-h_2) + \frac{(Z^2-i^2)i}{6RT}h_2 \right] \right\}^{-1} \end{aligned} \tag{1.147}$$

in place of (1.144) the only term which changed is the energy term. If h_2=0 we find Wagner's model. In their work, Chiang and Chang compiled a large amount of thermodynamic data to compare both models. For the binary alloys Fe-Ni, models with one or two energetic parameters gave good results, as is shown in Figure 1.28. Table 1.11 below gives energetic parameter values of Wagner's model and its extension with two parameters for the Fe-Ni-O system at 1600°C.

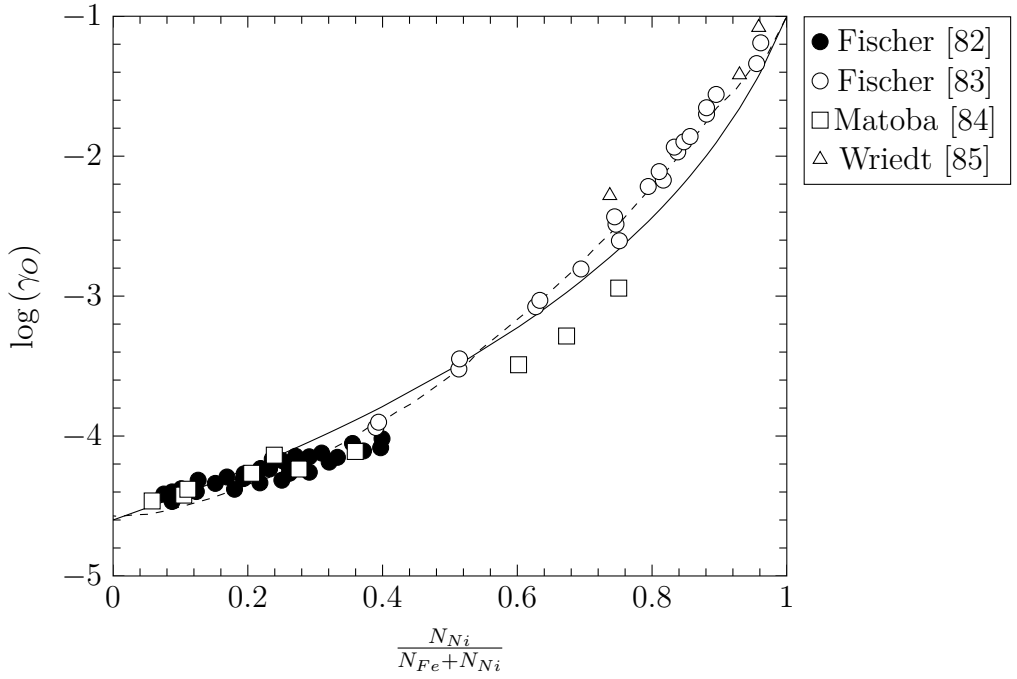

Figure 1.28: Oxygen activity in Fe-Ni melts at 1,600°C. Eq.(1.144) with $h = 2.08$ kJ mol^{-1} (——), Eq.(1.147) with $h_1 = 6.41$ kJ mol^{-1} and $h_2 = -2.32$ kJ mol^{-1} (- - -) [81].

Table 1.11: Value of the Wagner parameter [72] and the two parameters model [81] for the Fe-Ni-O system.

models	h kJ mol^{-1}	h_1 kJ mol^{-1}	h_2 kJ mol^{-1}	T °C	Ref.
Wagner	1.87	-	-	1,600	[72]
	2.08	-	-	1,600	[81]
Wagner's model extension	-	6.41	-2.32	1,600	[81]

In this system an equation with only one energy parameter seems sufficient. However, these data were reported for liquid alloys and changes are expected for solid solution.

1.5.4 Expression of first order interaction parameter

As presented in Section 1.2.2, Wagner [18] proposed an expression for the activity coefficients in an n-component system. If a system A-B-C-D with a solute S is considered, each parameter ε can be determined independently by studying the binary systems A-B, A-C, A-D with regard to the behaviour of the solute S.

According to the definition of the first order free energy interaction parameter in Eq (1.33), each model previously cited provides a different expression. Considering a binary system A-B, the parameter ε is expressed by the following equation from the Quasichemical model of Alcock and Richardson [71].

$$\varepsilon_{SB} = -Z(K-1) \quad \varepsilon_{SA} = \frac{-Z(K-1)}{K} \tag{1.148}$$

where $K = \left[\frac{\gamma_{S(A)}\gamma_{B(A+B)}}{\gamma_{S(B)}\gamma_{A(A+B)}}\right]^{\frac{1}{z}}$.

According to Wagner's model, the first order parameter is expressed as [86]

$$\varepsilon_{SB} = Z\left\{1-\phi^{\frac{1}{Z}}\exp\left[\left(\frac{Z-1}{2RT}\right)h\right]\right\} \quad \varepsilon_{SA} = Z\left\{1-\phi^{-\frac{1}{Z}}\exp\left[\left(\frac{Z-1}{2RT}\right)h\right]\right\} \tag{1.149}$$

According to the work of Chiang and Chang [81], the extension of Wagner's model leads to new expressions for ε

$$\varepsilon_{SB} = Z\left\{1-\phi^{\frac{1}{Z}}\exp\left[\frac{(Z-1)(h_1-h_2)}{2RT}+\frac{(Z^2-1)h_2}{6RT}\right]\right\} \tag{1.150}$$

$$\varepsilon_{SA} = Z\left\{1-\phi^{-\frac{1}{Z}}\exp\left[\frac{(Z-1)(h_1-h_2)}{2RT}+\frac{(Z-1)(2Z-1)h_2}{6RT}\right]\right\} \tag{1.151}$$

In addition, Chiang and Chang [81] found that first order interaction parameters vary linearly with the inverse of the temperature.

1.6 Oxygen diffusion in alloys

In Section 1.3, it was demonstrated that internal oxidation experiments allow the measurement of oxygen permeability. If the oxygen solubility in a material is known, the oxygen diffusion coefficient can then be calculated. In this section, values of oxygen diffusion coefficient measured in iron and in nickel are reviewed.

1.6.1 Diffusion in iron

To calculate the oxygen diffusivity, oxygen permeability reviewed in Section 1.4 on internal oxidation can be used in combination with oxygen solubility measured by Swisher and Turkdogan [47]. In Figure 1.29, values of the oxygen diffusion coefficient calculated for γ and α iron are presented.

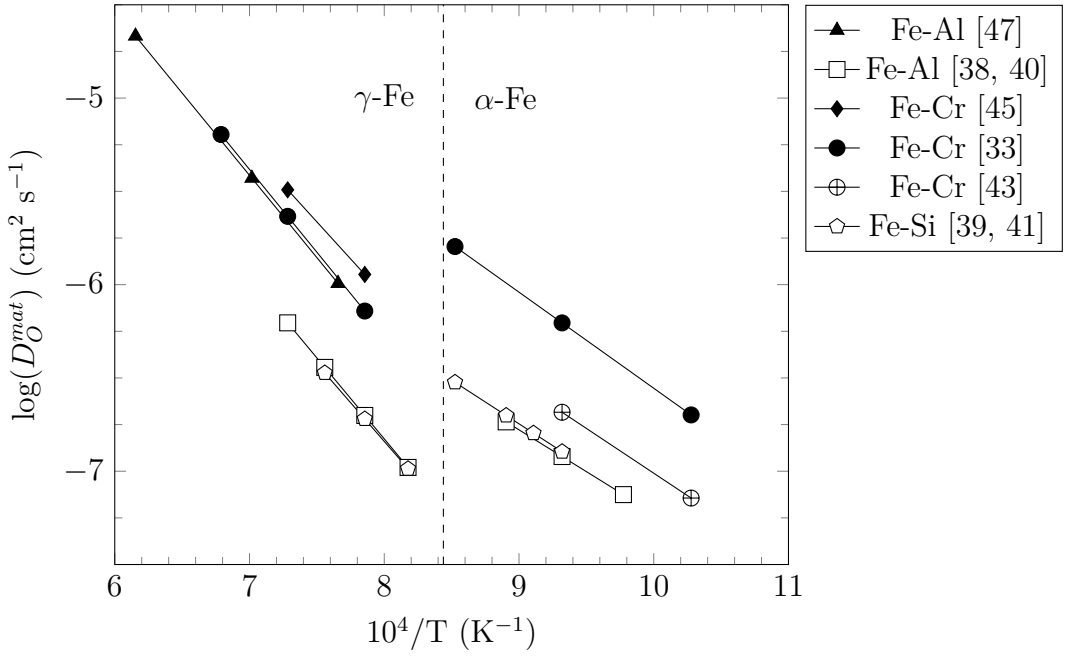

Figure 1.29: Oxygen diffusion coefficients in iron determined from internal oxidation experiments in Rhines pack (open symbols) and H_2/H_2O gas mixture (filled symbols) and independent solubility measurements [47].

From Figure 1.29, oxygen diffusion coefficients measured from exposure in wet conditions were found to be larger than coefficients measured from experiment in Rhines pack. However, as was highlighted in the section on oxygen permeability (1.4.1), authors who carried out internal oxidation experiment in H_2/H_2O did

not report variation of the oxygen permeability with the solute content. In that case, the oxygen permeability reported by those authors could be the effective IOZ oxygen permeability, higher than the matrix permeability measured by Takada *et al.* [38–41]. This leads to an overestimation of the oxygen permeability. Assuming that the solubility is independent of the solute content, this yields high values for oxygen diffusion coefficients, as observed in Figure 1.29. In addition, the oxygen solubility was measured after exposure in H_2/H_2O gas mixtures and no evidence that it remains the same in Rhines pack are available in the literature. However, good agreement is found for the activation energy of oxygen diffusion in both γ and α-iron. In Tables 1.12 and 1.13, values of the pre-exponential factor and activation energy measured in the different studies are reported.

Table 1.12: Pre-exponential factor and activation energy for oxygen diffusion in γ-iron.

Alloy	Alloy	$D_O^{(0)}$ $cm^2\ s^{-1}$	Q $kJ\ mol^{-1}$	Ref.
Fe-Al	Rhines pack	$1.3^{+0.8}_{-0.5}$	166 ± 5	Takada [40]
Fe-Al	H_2/H_2O	5.8	169	Swisher [47]
Fe-Si	Rhines pack	$0.64^{+0.44}_{-0.26}$	159 ± 5	Takada [41]
Fe-Cr	H_2/H_2O	6.7	170	Meijering [33]
Fe-Cr	H_2/H_2O	1.92	152	Young [45]

Table 1.13: Pre-exponential factor and activation energy for oxygen diffusion in α-iron.

Alloy	Alloy	$D_O^{(0)} \times 10^3$ $cm^2\ s^{-1}$	Q $kJ\ mol^{-1}$	Ref.
Fe-Al	Rhines pack	$1.79^{+1.76}_{-0.89}$	85.7 ± 6.1	Takada [38]
Fe-Si	Rhines pack	$2.91^{+3.4}_{-1.57}$	89.5 ± 7.2	Takada [39]
Fe-Cr	H_2/H_2O	39	98	Meijering [33]
Fe-Cr	H_2/H_2O	6.18	92	Setiawan [43]

In view of the different reaction conditions and data treatment methods used to calculate the oxygen diffusion coefficient, agreement between the different values

for D_O^{mat} is reasonably good. However, it is difficult to conclude from this dataset whether or not hydrogen and/or water vapour have an effect on this property.

1.6.2 Diffusion in nickel

The oxygen diffusion in nickel has been studied by internal oxidation experiments [52, 87, 88], an electrochemical method [80], a thermogravimetric technique [79] and in some studies [89–92] first principles simulation was used to find a value of D_O^{mat} by a computational method.

In internal oxidation experiments, authors found good agreement between the different values of oxygen permeability, as described in Section 1.4.2. The oxygen diffusivity was calculated using Equation (1.118) for the oxygen permeability values in Figure 1.18, and the Park and Alstetter solubility given by Equation (1.134). The value calculated is compared in Figure 1.30 with the oxygen diffusion coefficient measured by Park and Alstetter [80] using an electrochemical technique. Other techniques have been used to estimate the oxygen diffusivity. For example, Alcock and Brown [79] used a thermogravimetric technique to follow the weight change of a pure nickel sample. The time required to reach the equilibrium was recorded and a value of the oxygen diffusion coefficient calculated from this measurement.

Figure 1.30 shows that oxygen diffusion coefficients measured by internal oxidation are in rough agreement with values measured by electrochemical technique at high temperature. However, the activation energy deduced from internal oxidation experiments is high for interstitial diffusion, at a value of 220 kJ mol^{-1}, compared to the activation energy reported in iron of 150 kJ mol^{-1}. The activation energy of 164 kJ mol^{-1} measured by electrochemical technique is in agreement with the activation energy of interstitial diffusion. Values found by Alcock and Brown [79], calculating the oxygen diffusivity with time to reach the equilibrium, are also approximately consistent, though the authors reported that these coefficients contain a large uncertainty due to the difficulty in measuring small weight changes. Pre-exponential factor and activation energy values obtained from the different tech-

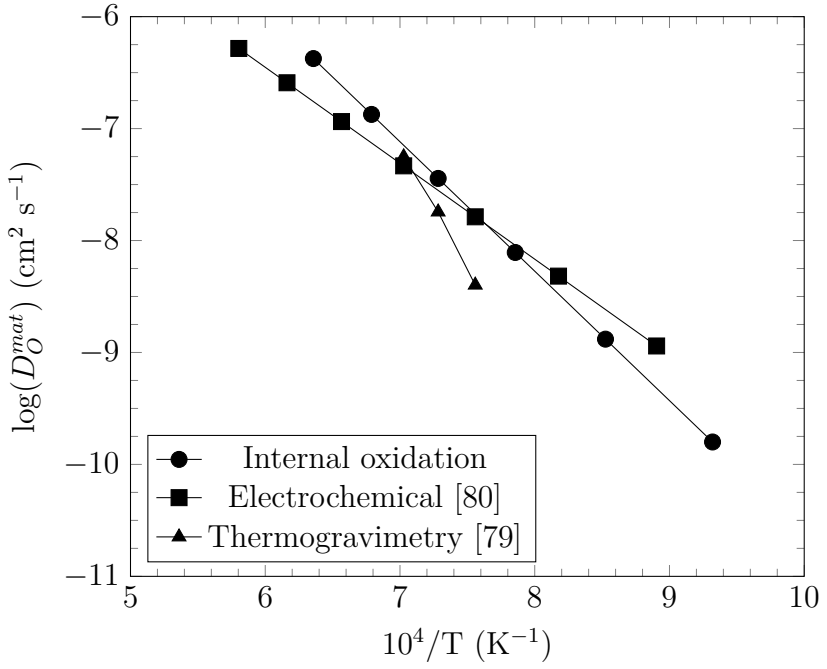

Figure 1.30: Oxygen diffusion in nickel measured by different experimental techniques.

niques are summarised in Table 1.14.

Table 1.14: Pre-exponential factor and activation energy for oxygen diffusion in nickel.

Technique	$D_O^{(0)}$ cm^2 s^{-1}	Q kJ mol^{-1}	Ref.
Internal oxidation	9.1	222	
Electrochemical	4.9×10^{-2}	164	[80]
Thermogravimetry	8.9×10^{7}	413	[79]

Discrepancies between activation energy for oxygen diffusion estimated from internal oxidation experiments and electrochemical method suggest that different mechanisms are involved for oxygen diffusion. Recently, groups of authors investigated how oxygen diffuses in nickel using computational techniques such as DFT calculations. Oxygen is assumed to diffuse through interstitial sites in the FCC lattice, since this structure has two interstitial sites: octahedral (O) and tetrahedral (T). It was reported that the most stable configuration for oxygen in nickel is in octahedral site [91, 92]. In addition, two migration mechanisms for oxygen atoms

in nickel were reported in the literature [92]. The first mechanism (O) → (O), corresponds to a direct jump from one octahedral site to the nearest octahedral site while the second mechanism involves an intermediate tetrahedral site, (O) → (T) → (O). However, the direct jump between octahedral sites exhibit a higher migration energy barrier than the migration path through a tetrahedral site. Therefore, the direct jump mechanism is not optimal for oxygen migration in nickel and the migration energy calculated for the mechanism (O) → (T) → (O) was found to range from 90 to 118 kJ mol^{-1}, lower than the activation energy of 164 kJ mol^{-1} reported by Park and Alstteter [80] for oxygen diffusion. It should be emphasised that the mechanisms discussed above do not take into account the presence of defects like vacancies in the material.

To investigate the effect of vacancies on oxygen diffusion, Fang *et al.* [91] introduced a vacancy near an oxygen atom and studied the path of this oxygen to move away from the vacancy. They found that the more favourable migration path had a migration energy barrier of 162 kJ mol^{-1} which is in agreement with the activation energy reported by Park and Alstteter [80]. In addition, a vacancy and oxygen atoms have strong attraction interaction and recent results have shown that a vacancy may interact with up to 6 oxygen atoms [93]. It is expected at high temperature that the vacancy concentration is extremely high, of a similar magnitude to the oxygen solubility [93]. Therefore, it is likely that a vacancy interacts with several oxygen atoms at high temperature and affects the oxygen diffusion. This idea is also supported by the work of Perusin *et al.* [94]. The authors oxidised pure nickel resulting in the formation of a nickel oxide scale and observed the formation of voids beneath the alloy surface. These voids result from condensation of vacancies injected in the material at the metal/scale interface. In addition, the authors observed that void walls were oxidised while no oxygen was detected in the matrix. This result supports the idea that oxygen diffusion is closely related to vacancy diffusion in nickel.

1.7 General summary

In this literature survey, alloy oxidation was reviewed with particular focus on internal oxidation. Wagner [1] demonstrated that the oxygen permeability is controlling internal oxidation kinetics. In addition, the oxygen permeability is a critical parameter to estimate the minimum content of chromium or aluminium required to achieve protective oxidation. The oxygen permeability was measured in Fe-Cr and Ni-Cr alloys and prediction of minimum chromium levels for transition between internal and external oxidation are in agreement with experimental observations. On the other hand, authors attempted to understand the effect of the water vapour on the transition between internal and external oxidation. Usually authors observed that when water vapour is present in the environment, internal oxidation is promoted and more chromium is required to observe the formation of an external scale of chromium. The determination of the critical chromium content to observe transition between internal and external oxidation is based on the following equation

$$N_{Cr}^{(0)^*} = \left(\frac{F_v^* \pi V_{alloy} N_O^{(s)} D_O}{2\nu V_{CrO_\nu} D_{Cr}} \right)^{\frac{1}{2}} \tag{1.152}$$

Authors often suggested that the higher chromium level required in wet condition is due to an effect of the water and/or hydrogen on the oxygen permeability. However, in Equation (1.152) many parameters like the critical volume of oxide, the chromium diffusion coefficient and the internal oxide stoichiometry may be affected by the presence of water vapour. Recent studies showed that the critical volume fraction [95, 96] or the internal oxide stoichiometry [69] may also be affected by the presence of humidity in the atmosphere. In the literature many experiments were carried out with different conditions and the effect of water vapour is difficult to assess.

Alloys based on the Fe-Cr and Ni-Cr two binary systems are used for high temperature applications. However, with environmental concerns, companies want to increase efficiency of energy production plants. This improvement requires to

increase operating temperatures, and new austenitic alloys based on the Fe-Ni-Cr system have to be designed. These alloys must have good resistance against oxidation which is achieved by the formation of a slow growing chromium oxide and the alloy surface. However, optimisation of the alloy composition to observe the formation of the chromia scale requires knowledge of oxygen permeability of the base metal. Unfortunately, no data are available for the Fe-Ni system. The internal oxidation of Fe-Cr and Fe-Ni-Cr alloys was selected as the technique to estimate the oxygen permeability because evaluation of internal oxidation kinetics allows a direct calculation of the product $N_O^{(s)} D_O$.

In addition, limited data on oxygen solubility in iron and nickel are available and seem reliable. These values provide a benchmark for the present investigation. However, no data is present in the literature in Fe-Ni alloys and were measured in the present work. Finally, knowing the oxygen permeability from internal oxidation of Fe-Cr alloys and Fe-Ni-Cr and with independent measurement of the oxygen solubility, oxygen diffusion coefficients were calculated as function of the alloy composition. However, it should be noted that this method is not a direct evaluation of oxygen diffusion coefficients and values of D_O are subject to large uncertainties due to their estimation from oxygen permeability and solubility measurements.

Chapter 2

Materials and experimental methods

The aim of this project was to compare the oxygen solubility in Fe, Ni and Fe-Ni alloys and internal oxidation kinetics in Fe-Cr and Fe-Ni-Cr alloys in 2 different atmospheres: one free of H_2 and H_2O and the other a H_2/H_2O gas mixture. To obtain the most accurate results, the formation of a scale must be avoided, experiments were conducted in Fe/FeO Rhines packs and in flowing H_2/H_2O with the oxygen partial pressure set at the Fe/FeO dissociation pressure. In this chapter, material and gas compositions together with experimental methods and procedures used in the different experiments are presented. In addition, a particular focus is directed to the oxygen solute analysis. It should be noted that all uncertainties reported in this chapter correspond to a 95% confidence interval.

2.1 Materials

2.1.1 Solubility experiments

All experiments concern reactions between Fe or Ni or Fe-Ni alloys and weakly oxidising gases. Oxygen solubility in these materials is difficult to measure because impurities which form stable oxides at very low oxygen partial pressure could be responsible for apparently high oxygen levels, as mentioned in Section 1.5. To minimise this effect, materials were cast from high purity iron (99.98%) supplied by Sigma-Aldrich and nickel (99.998%) from Alfa-Aesar. In Appendix A, results of elemental analyses provided by material manufacturers are given. The different materials were melted in an arc melter furnace using nonconsumable electrodes and under a flow of Ar-5%H_2. After casting, alloys were annealed for 72h at 1,100°C in a horizontal tubular furnace to ensure a homogeneous material.

The annealing duration was selected by comparing the characteristic length of diffusion, calculated with Equation (2.1) with the interdendritic space measured in the different alloys after casting

$$l = \sqrt{4\tilde{D}t} \tag{2.1}$$

Interdiffusion coefficients published by Ustad and Sørum [97] were used for Fe-Ni alloys. The smallest interdiffusion coefficient was measured in the alloy containing 20 at.% of nickel, with a value of 2×10^{-11} cm^2 s^{-1}. Using this coefficient in Equation (2.1) the characteristic length of diffusion is 45 μm for an exposure of 72h. The interdendritic space measured in the different alloys varied from 5 to 15 μm. Therefore the annealing duration was sufficient to homogenise the alloy. The atmosphere used to anneal samples was Ar-5%H_2. with a gas flow rate of 500 ml min^{-1}. Finally, the alloy composition was checked by Energy Dispersive Spectroscopy (EDS). Description of the EDS analysis is given in Section 2.8.1. Many buttons of the same composition were melted. In Table 2.1 the average composition measured over the different button melted is presented. In addition, the uncertainty reported takes into account composition dispersion between the different buttons melted for a given materials and the EDS measurement error.

Table 2.1: Alloy compositions for solubility experiment.

Material	N_{Fe} (at.%)	N_{Ni} (at.%)	$\frac{N_{Ni}}{N_{Fe}+N_{Ni}}$
Fe	100	-	0
Fe-20Ni	bal.	20 ± 1	0.20
Fe-40Ni	bal.	40 ± 2	0.40
Fe-60Ni	bal.	60 ± 2	0.60
Fe-80Ni	bal.	80 ± 1	0.80
Ni	-	100	1.0

2.1.2 Internal oxidation experiment

In this study, the binary Fe-Cr and ternary Fe-Ni-Cr system were investigated. Alloys were melted from the high purity iron and nickel used to melt alloys for solubility experiments plus high purity chromium (99.995%). In addition, these alloys were melted using the same technique as for materials for solubility experiments. However, it should be noted that the alloy chromium content has to be carefully chosen to meet the following criteria:

- the chromium content has to be low enough to avoid the formation of a chromia scale

- the chromium content has to be sufficiently high to observe a volume fraction of precipitate which allows measurement of the IOZ depth by optical microscopy

In addition, Fe-Ni-Cr alloys were designed to have same $\frac{N_{Ni}}{N_{Fe}+N_{Ni}}$ ratios as alloys used for solubility experiment because during internal oxidation, the chromium is consumed by the oxidation reaction and leaves an Fe-Ni matrix. Knowledge of the oxygen solubility of the matrix will enable us to calculate the oxygen diffusion coefficient from permeability measurements.

For Fe-Cr alloys, the value of the minimum chromium content for the transition between internal and external oxidation at the Fe/FeO dissociation pressure was calculated in Section 1.4.3.3 and results of calculations are presented in Figure 1.21. The critical chromium content for the transition is always found higher than 10 at.% from 950 to 1,100°C. In addition, the alloys are designed to have an FCC structure and a limiting factor is the small domain of stability of the γ phase at high temperature as shown by the Fe-Cr phase diagram presented in Figure 2.1.

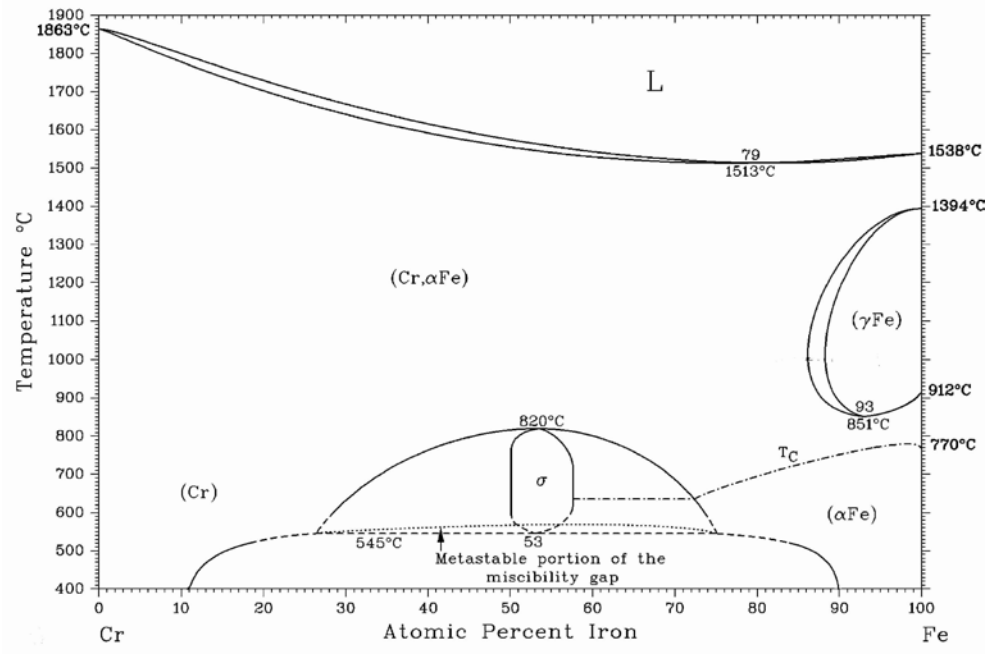

Figure 2.1: Fe-Cr phase diagram. Reprinted from [3] with permission from Elsevier.

To estimate the minimum chromium content required for the transition between internal and external oxidation in an environment where the oxygen partial pressure is set at the Fe/FeO equilibrium for Fe-Ni-Cr, Croll and Wallwork's observations presented in Section 1.4.4 can be used. The authors gave the boundary between internal oxidation as a function of the alloy composition but they carried out their experiments at 1,000°C under air. As previously mentioned, in this environment a scale growth on the alloy and the equilibrium pressure between the alloy and the oxide scale change with the alloy composition. These different equilibrium pressures were measured by Dalvi and Sridhar [68]. From Croll and Wallwork's measurements the critical chromium content required to observe the transition between internal and external oxidation at 1,000°C with the oxygen partial pressure set at the Fe/FeO equilibrium pressure can be estimated by

$$N_{Cr}^{*(Fe/FeO)} = N_{Cr}^{*(exp)} \left(\frac{p_{O_2}^{Fe/FeO}}{p_{O_2}^{exp}} \right)^{1/4} \tag{2.2}$$

where $N_{Cr}^{*(exp)}$ and $p_{O_2}^{exp}$ are the critical chromium content required for the transition between internal and external oxidation and, the oxygen partial pressure at the alloy/oxide interface in Croll and Wallwork's experiment, and $N_{Cr}^{*(Fe/FeO)}$ the critical chromium content required when the oxygen partial pressure set at the Fe/FeO equilibrium, $p_{O_2}^{Fe/FeO} = 1.2 \times 10^{-15}$ atm at 1,000°C. In Table 2.2, results of the calculation using Equation (2.2) are presented

Table 2.2: Critical chromium content to observe the transition between internal and external oxidation in Fe-Ni-Cr alloys at 1,000°C with the oxygen partial pressure set at the Fe/FeO equilibrium, extrapolated from Croll and Wallwork's measurement.

$\frac{N_{Ni}}{N_{Fe}+N_{Ni}}$	$N_{Cr}^{*(exp)}$	$p_{O_2}^{exp}$	$N_{Cr}^{*(Fe/FeO)}$
0.20	0.19	1.8×10^{-15}	0.17
0.40	0.17	2.9×10^{-15}	0.14
0.60	0.16	9.6×10^{-15}	0.10
0.80	0.18	1.4×10^{-13}	0.06

According to the different calculations, for pure iron and Fe-Ni based alloys with ratios $\frac{N_{Ni}}{N_{Fe}+N_{Ni}}$ lower or equal to 0.6, 3 chromium contents were selected: 2, 4 and 7.5 at.%. For alloy with $\frac{N_{Ni}}{N_{Fe}+N_{Ni}} = 0.8$, alloys with chromium content of 1, 2 and 4 at.% were used.

To carry out the same calculation for Ni-Cr alloys, at 1,000°C with the oxygen partial pressure equal to that of the Fe/FeO equilibrium, the oxygen permeability in pure nickel is calculated to be 2.0×10^{-14} cm^2 s^{-1}. Only Cr_2O_3 oxide can form if a Ni-Cr alloy is exposed to an atmosphere where the oxygen partial pressure is equal to the Fe/FeO equilibrium pressure. Using all these parameters and the chromium diffusion coefficient published by Ruzickova and Million [58] in Equation (1.85) gives a critical chromium concentration for the transition between internal and external oxidation at 1,000°C of 1.8 at.%. The design of ternary alloy compositions was such that their chromium levels were lower by a minimum of 2 at.% than the values calculated with Wagner's analysis, to ensure no formation of a chromia scale. In the case of nickel, such a design is clearly not possible. Moreover, since data are present in the literature [50] for the Ni-Cr system, it was decided that no Ni-Cr alloys would be used in this study.

After casting, metallographic observation revealed a similar interdendritic space as in binary Fe-Ni alloys. To estimate the characteristic length of diffusion interdiffusion coefficients published by Duh and Danayanda [67] were used for ternary alloys. First of all, Duh and Danayanda [67] and Ericsson *et al.* [98] observed that in the Fe-Ni-Cr system, the alloy chromium content has no major effect on the interdiffusion of Fe and Ni for chromium concentration up to 30 at.%. This allows us to neglect cross-effects. In addition, Duh and Dayananda calculated the binary interdiffusion coefficient for Fe-Ni alloys from their interdiffusion measurements on Fe-Ni-Cr alloys with low chromium content. They found good agreement with authors [97, 99] who measured interdiffusion coefficients in binary Fe-Ni alloys. Comparing the interdiffusion coefficient for chromium and for nickel in Fe-Ni-Cr alloys at 1,100°C, it is found that the smallest diffusion coefficient is for nickel diffusion. Therefore

the annealing procedure used for binary Fe-Ni alloys was used for ternary Fe-Ni-Cr alloys. However Fe-Ni-Cr alloys formed a chromia scale when they were annealed in Ar-5%H_2, hence the annealing atmosphere was changed to pure H_2. After annealing in pure H_2, neither internal nor external oxidation was observed. The gas flow rate used for annealing was 500 ml min^{-1}. Finally, the alloy composition was checked by Energy Dispersive Spectroscopy (EDS) technique. In Table 2.3, material designations and nominal compositions are reported. Uncertainty given is calculated as in Table 2.1.

Table 2.3: Alloy compositions for internal oxidation experiments.

Material	N_{Fe} at.%	N_{Ni} at.%	N_{Cr} at.%	$\frac{N_{Ni}}{N_{Fe}+N_{Ni}}$
Fe-2Cr	bal.	-	2.1 ± 0.3	0
Fe-4Cr	bal.	-	3.7 ± 0.3	0
Fe-7.5Cr	bal.	-	7.3 ± 0.5	0
Fe-20Ni-2Cr	bal.	19.0 ± 1.3	2.0 ± 0.2	0.19
Fe-20Ni-4Cr	bal.	19.0 ± 1.2	3.8 ± 0.3	0.20
Fe-20Ni-7.5Cr	bal.	18.0 ± 1.2	7.4 ± 0.6	0.19
Fe-40Ni-2Cr	bal.	38.4 ± 1.8	2.0 ± 0.2	0.39
Fe-40Ni-4Cr	bal.	37.5 ± 1.9	4.0 ± 0.3	0.39
Fe-40Ni-7.5Cr	bal.	36.4 ± 2.2	7.3 ± 0.7	0.39
Fe-60Ni-2Cr	bal.	57.8 ± 2.1	2.0 ± 0.2	0.59
Fe-60Ni-4Cr	bal.	56.4 ± 1.8	4.0 ± 0.3	0.59
Fe-60Ni-7.5Cr	bal.	54.3 ± 1.7	7.5 ± 0.5	0.59
Fe-80Ni-1Cr	bal.	79.2 ± 1.1	1.0 ± 0.1	0.80
Fe-80Ni-2Cr	bal.	78.5 ± 1.3	2.0 ± 0.2	0.80
Fe-80Ni-4Cr	bal.	76.1 ± 1.4	4.0 ± 0.5	0.79

2.2 Sample preparation

After annealing, metallographic cross-sections were produced to characterise the microstructure. In Figure 2.2, the different microstructures after annealing of binary alloys Fe-Ni are shown. Various etchants were used to reveal the alloy microstructure depending on the sample composition, and are listed in Appendix B. Pure Fe and Ni samples exhibit large grains with no particular orientation while

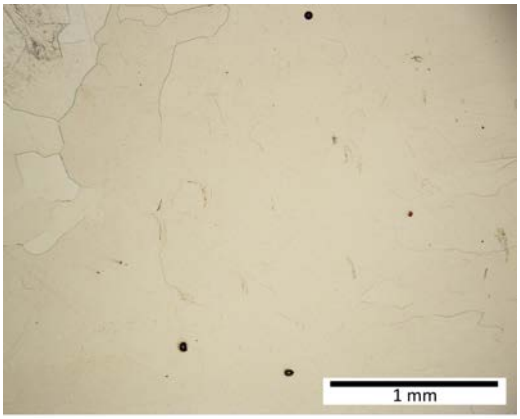

(a) Fe, Nital 5%

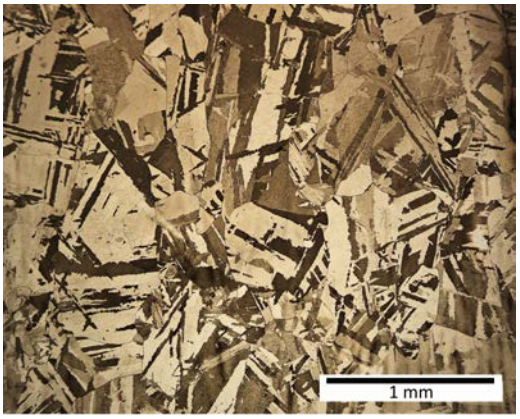

(b) Fe-20Ni, Marble

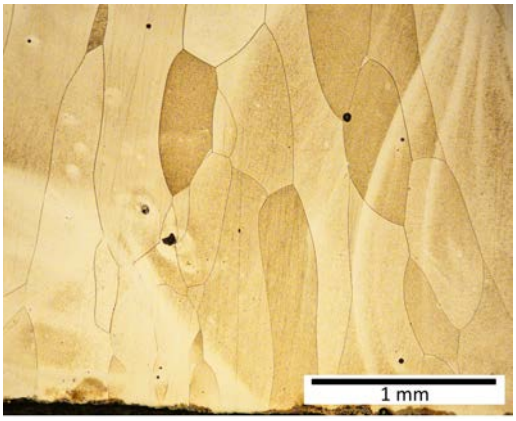

(c) Fe-40Ni, Marble

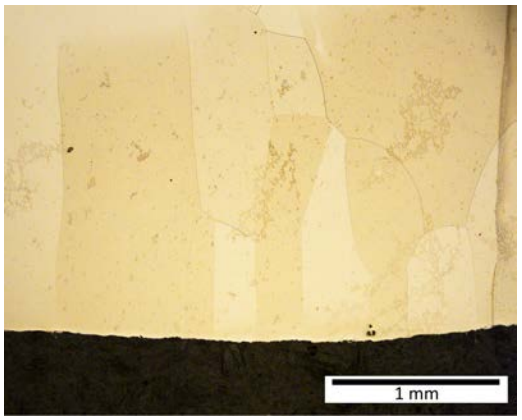

(d) Fe-60Ni, Marble

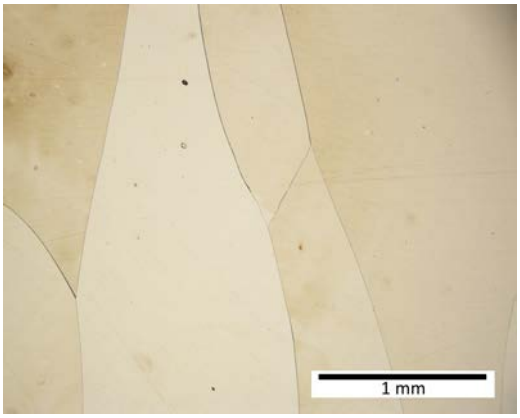

(e) Fe-80Ni, Marble

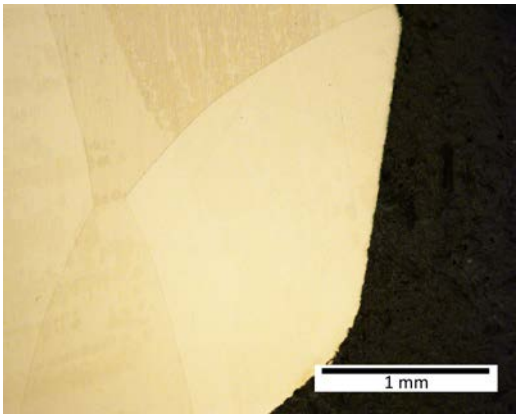

(f) Ni, 5% nitric acid + 95% acetic acid

Figure 2.2: Optical observations of samples after annmealing 72h at 1,100°C under Ar-5%H_2. Etchants specified in sub-captions.

Fe-40Ni, Fe-60Ni, Fe-80Ni alloys have similar microstructures. Grains are large and have a columnar orientation, resulting from the unidirectional heat transfer from the sample during solidification on a chilled copper plate. In Table 2.4, sample grain sizes are reported. To measure the grain size, two orientations, x and y, which represent

the horizontal and the vertical direction respectively, were selected. The Fe-20Ni alloy exhibits a martensitic structure at room temperature due to the high Ms point (210°C) in this alloy [100]. However, addition of sufficient chromium to this alloy prevents the formation of the martensite. An austenitic structure was observable in alloys containing 7.5 at% of chromium while the martensitic transformation took place in alloys with a chromium content of 2 and 4 at.%. This was the only noticeable difference between binary and ternary alloys.

Table 2.4: Grain sizes after annealing for 72h at 1,100°C.

$\frac{N_{Ni}}{N_{Fe}+N_{Ni}}$	x (μm)	y (μm)
0	>4626	>3606
0.2	-	-
0.4	374 ± 139	1261 ± 325
0.6	631 ± 202	1768 ± 612
0.8	>688	>2326
1	>2601	>4114

For solubility and internal oxidation experiments, slices were cut from an annealed alloy button following the pattern shown in Figure 2.3. For solubility, the sample thickness had to be smaller than 1.4 mm and the sample weight had to be close to 1 g. Lengths and widths of samples were variable, depending on the position on the button.

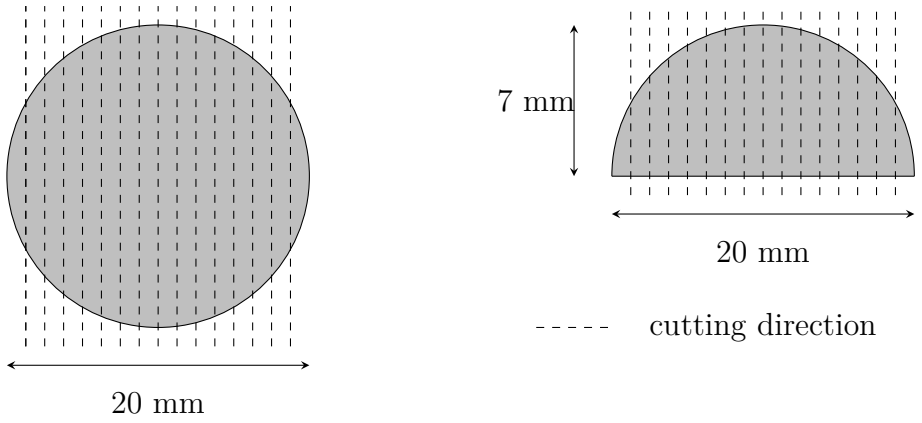

Figure 2.3: Button cutting pattern.

For internal oxidation experiments, an additional preparation step was added. Several samples were made from one slice and the cutting direction was parallel to the grain growth direction as illustrated in Figure 2.4. This cutting pattern was selected to maximise the number of grain boundaries observable after exposure when the sample was cross-sectioned in a direction perpendicular to the grain growth direction for metallographic observations as shown in Figure 2.4.

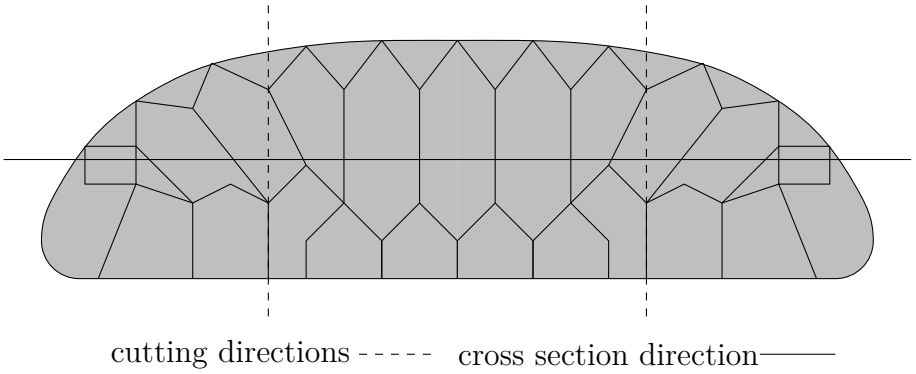

Figure 2.4: Slice cutting directions.

For solubility experiments, samples were then ground to a 1200 grit finish with SiC paper while samples used for internal oxidation experiments were ground to a 4000 grit finish to remove internal stress. Finally, samples were cleaned with ethanol in an ultrasonic bath and dried before exposure.

2.3 Gas compositions

2.3.1 Rhines pack experiment

In the Rhines pack experiment, the oxygen partial pressure is set by equilibrating an Fe/FeO powder mixture. The Fe/FeO dissociation pressure can be calculated considering the following reaction and reaction constant

$$\mathrm{Fe} + \frac{1}{2}\mathrm{O_2} \rightarrow \mathrm{FeO} \tag{2.3}$$

$$K_{2.3} = \frac{1}{p_{O_2}^{1/2}} \tag{2.4}$$

The free energy of the reaction was calculated using thermodynamic tables from NIST-JANAF [101]. In Table 2.5, the standard free energy of formation and the Fe/FeO dissociation pressure calculated using Equation (2.4) are given.

Table 2.5: Standard free energy of formation of wüstite and Fe/FeO equilibrium pressure.

Temperature °C	$\Delta G^0_{2.3}$ kJ mol^{-1}	$p_{O_2}^{Fe/FeO}$ atm
1,000	-181.6 ± 1.0	$(1.2 \pm 0.2) \times 10^{-15}$
1,050	-178.4 ± 1.0	$(8.0 \pm 1.5) \times 10^{-15}$
1,100	-175.2 ± 1.0	$(4.6 \pm 0.8) \times 10^{-14}$
1,150	-172.0 ± 1.0	$(2.3 \pm 0.4) \times 10^{-13}$

The Fe/FeO powder mixture was obtained by oxidising pure iron powder. To set the oxygen partial pressure to a higher value than the Fe/FeO equilibrium, a H_2/H_2O gas mixture was used and the following reaction considered

$$H_2 + \frac{1}{2}O_2 \rightarrow H_2O \tag{2.5}$$

$$K_{2.5} = \frac{p_{H_2O}}{p_{H_2} p_{O_2}^{1/2}} \tag{2.6}$$

At a given temperature, the oxygen partial pressure is set by the ratio $\frac{p_{H_2O}}{p_{H_2}}$. The H_2/H_2O gas mixture was generated by passing Ar-5%H_2 through a thermostatted water saturator set at a temperature to produce an excess of water vapour. The excess was then removed by passing the gas through a condenser set at a temperature corresponding to the desired water content [102]. To produce wüstite, the condenser was maintained at 58°C which corresponds to a water content of 17.9 % in the gas. The composition of the gas obtained after bubbling in the water was Ar-17.9%H_2O-4%H_2. Using Equation (2.6) and the standard free energy of reaction 2.5 from the NIST-JANAF thermodynamic table [101], the oxygen partial

pressure set in the furnace by the gas as a function of the furnace temperature is plotted in Figure 2.5, as are the indicated iron oxide equilibrium pressures.

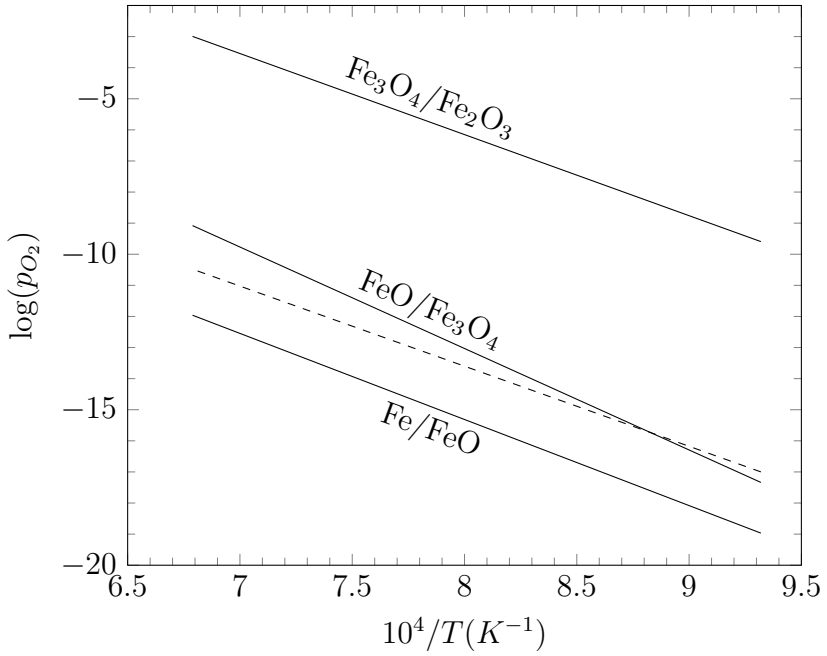

Figure 2.5: Iron oxide equilibrium pressures (——) and partial pressure set in the reaction furnace by the equilibrium H_2/H_2O (- - -).

The temperature of 950°C and a duration of 5 hours were selected for this experiment. After the reaction, the presence of Fe and FeO was checked by X-Ray Diffraction (XRD). No trace of magnetite was found in the powder mix. The resulting amount of Fe and FeO in the powder mixture was estimated by weight change measurement assuming that the surface of powder particle remains the same during the oxidation process. Weight change measured indicate that under the experimental conditions given above, the Fe/FeO powder mix had a ratio of 2:3. In the last step of the powder preparation, the Fe/FeO mix was sieved to have particle sizes in the powder larger than 100 μm and lower than 1.4 mm. This last step was introduced in the Fe/FeO powder mixture preparation to make insertion of the powder in the pack easier. In addition, After a few experiments in Rhines packs, the powder was analysed by XRD. Results showed that the powder mixture was still made of Fe and FeO, and no other phase was detected.

2.3.2 H_2/H_2O

Experiments in H_2/H_2O gas were carried out in a horizontal furnace and also in a thermobalance, both equipped with high purity alumina tube as their reaction chamber. In this environment, as for the wüstite synthesis, at a given temperature the oxygen partial pressure is set by controlling the ratio $\frac{p_{H_2O}}{p_{H_2}}$. To compare internal oxidation kinetics and oxygen solubility with experiments carried out in Fe/FeO Rhines packs, the oxygen partial pressure in H_2/H_2O mixture has to be set at the Fe/FeO dissociation pressure. For the two sets of experiments, horizontal furnace and thermobalance, different absolute water and hydrogen partial pressures were used, but for a given temperature the oxygen partial pressure was identical. In Tables 2.6 and 2.7, the different gas compositions and oxygen partial pressures are listed. The gas flow rate used was 500 ml.min^{-1} in the horizontal furnace

Table 2.6: Gas composition and oxygen partial pressure for experiments in horizontal furnace.

Temperature °C	$\Delta G^0_{2.5}$ kJ.mol^{-1}	H_2O %	H_2 %	p_{O_2} atm
1,000	-176.9 ± 0.1	13 ± 1	20.3 ± 0.1	$(1.2 \pm 0.2) \times 10^{-15}$
1,050	-174.2 ± 0.1	13 ± 1	19.5 ± 0.1	$(7.7 \pm 1.4) \times 10^{-15}$
1,100	-171.4 ± 0.1	13 ± 1	18.4 ± 0.1	$(4.4 \pm 0.8) \times 10^{-14}$
1,150	-168.7 ± 0.1	13 ± 1	17.2 ± 0.1	$(2.3 \pm 0.4) \times 10^{-13}$

Table 2.7: Gas composition and oxygen partial pressure for experiments in thermobalance.

Temperature °C	H_2O %	H_2 %	p_{O_2} atm
1,000	3.0 ± 0.2	4.8	$(1.1 \pm 0.2) \times 10^{-15}$
1,050	3.2 ± 0.2	4.8	$(7.7 \pm 1.0) \times 10^{-15}$
1,150	3.6 ± 0.2	4.8	$(2.4 \pm 0.3) \times 10^{-13}$

and 20 ml min^{-1} in the thermobalance, which corresponds to a linear velocity of 3.0 and 0.25 cm s^{-1}, respectively. Internal oxidation kinetics and oxygen permeability are proportional to the square root of the oxygen partial pressure. Therefore, it is

relevant to compare the square root of the oxygen partial pressure set by the Fe/FeO mixture, $p_{O_2}^{Fe/FeO}$, in the Rhines pack, and the value set by the different H_2/H_2O gas mixtures, $p_{O_2}^{H_2/H_2O}$. In Figure 2.6, the square root of the oxygen partial pressure ratio is given for the different temperature studied.

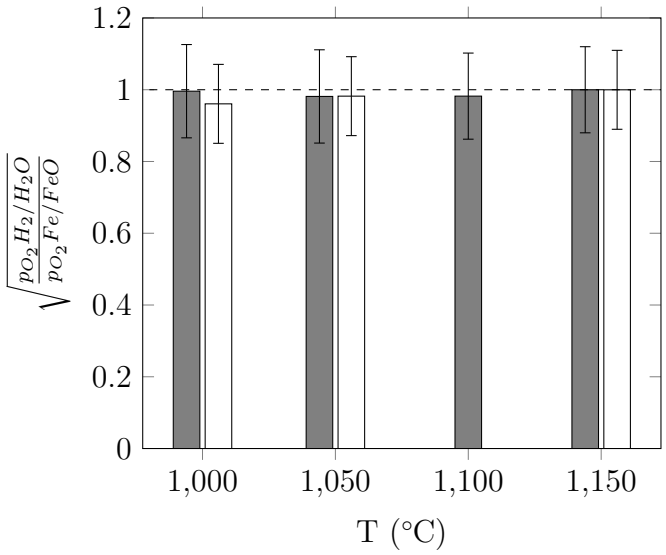

Figure 2.6: Comparison of the oxygen partial pressure set by the H_2/H_2O gas mixture in the different apparatus with the Fe/FeO dissociation pressure. Horizontal furnace (▮▮), Thermobalance (▯▯).

From Figure 2.6, the oxygen partial pressure in experiments using H_2/H_2O gas mixture is in close agreement with the Fe/FeO dissociation pressure, well within experimental error. Nevertheless, prior to running the experiment at a given temperature, the value of the oxygen partial pressure in the H_2/H_2O gas mixture was checked by exposing a sample of pure iron for 4 hours at the desired temperature. After exposure, the sample surface was examined to check the presence of oxide. The oxygen partial pressure was considered correct when only a few isolated nodules of wüstite were observed on the sample surface, as shown in Figure 2.7.

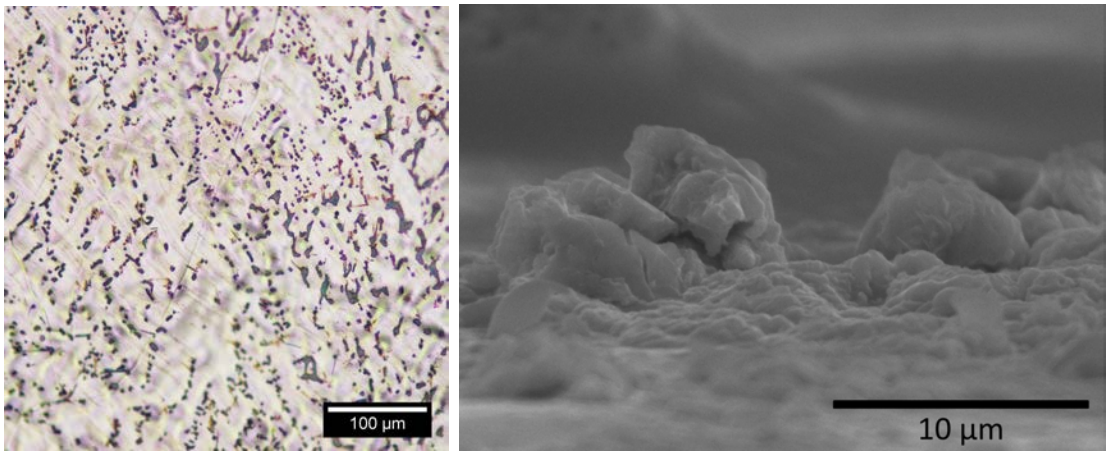

(a) Optical microscopy (b) SEM SE image

Figure 2.7: Pure Fe surface after 4h of exposure at 1,150°C in H_2/H_2O.

2.4 Solubility experiment duration

Before starting solubility experiments, it was necessary to estimate the time required to equilibrate a sample. Experimental durations were determined using Crank's Equation [103] for diffusion into a thin sheet with 2 parallel faces under assumptions of constant concentration at surfaces and an initial oxygen concentration in the material equal to 0. Crank calculated the kinetics of solute diffusion:

$$\frac{M_t}{M_\infty} = 1 - \sum_{n=0}^{\infty} \frac{8}{(2n+1)^2\pi^2} \exp\left(\frac{-D(2n+1)^2\pi^2 t}{4l^2}\right) \tag{2.7}$$

where M_t is the total solute amount at time t, M_∞ the total solute amount after infinite time, D the solute diffusion coefficient and l the half sheet thickness. No data is available in the literature for the oxygen diffusion in Fe-Ni alloys. However, as previously mentioned in Section 1.2, this is slower in nickel than in iron. To calculate the time to reach equilibrium in a slice at different temperatures, the case of oxygen diffusion in a nickel slice of 1.4 mm thickness was considered. Oxygen diffusion coefficient values measured by Park and Altstetter [80] were used for this calculation, and results are reported in Table 2.8. For safety in the alloy diffusion experiments, experimental durations were chosen to be approximatively twice the times given by Equation (2.7).

Table 2.8: Predicted and selected duration for Rhines pack experiment ($\frac{M_t}{M_\infty} = 0.97$).

Temperature °C	Estimated duration Eq.(2.7) hours	Selected duration hours
1,000	201	480
1,050	111	240
1,100	65	120
1,150	39	72

2.5 Experimental protocol

2.5.1 Rhines pack experiments

In a Rhines pack for a solubility experiment, 3 alloy samples of the same composition and 4.0 g of an Fe/FeO powder mix were put in a quartz capsule which was evacuated and filled with argon several times before being ultimately evacuated and sealed. To avoid interaction between the powder and the sample, the two were separated by a constriction in the capsule as shown in Figure 2.8.

Figure 2.8: Rhines pack capsule.

In the case of internal oxidation experiment, capsules were made with the same protocol except that only one sample was inserted in a capsule to avoid any reaction

between alloys of different compositions.

The experimental protocol was identical for solubility or internal oxidation experiment. Capsules were introduced into the hot furnace set at the experimental temperature, controlled by an R-type thermocouple within ±3°C, and remained for the selected experimental duration. Then capsules were quickly taken out from the hot furnace and directly dropped into cold water. Capsules were cold after 3 minutes in the water.

It should be noted that during experiments in Rhines packs, the silica capsule may release gaseous species and especially SiO under low oxygen partial pressure resulting in silicon contamination of sample surface. The formation of SiO in the capsule is the result of the following reaction

$$\mathrm{SiO_2} = \frac{1}{2}\mathrm{O_2} + \mathrm{SiO} \tag{2.8}$$

To estimate the amount of silicon transferred to the sample from the gaseous phase, the following relation is used [104]

$$\frac{dn_{SiO}}{dt} = 43.8\alpha_{sti}\left(\frac{p_{SiO}}{\sqrt{M_{SiO}T}}\right) \text{ (mol cm}^{-2}\text{ s}^{-1}\text{)} \tag{2.9}$$

with n_{SiO} the number of mole of SiO per unit area, p_{SiO} the SiO partial pressure, M_{SiO} the SiO molecular weight, T the absolute temperature and α_{sti} the sticking parameter. The latter parameter described the fraction of molecule hitting the surface which is adsorbed. Equation (2.9) is known at the Hertz-Knudsen relation and gives the number of mole of SiO added to the sample surface. However, this quantity is difficult to estimate because the value of the sticking parameter is unknown. It is likely that α_{sti} is extremely small because during exposure at high temperature the sample and the capsule wall are at the same temperature and there is no condition for preferential condensation on the sample surface. However, dissolution of Si into the metal might provide such a driving force.

To estimate the quantity of silicon that might be transferred to the sample

during exposure in Rhines packs, the flux of SiO molecules has to be evaluated with Equation (2.9). To do so, the SiO partial pressure is required. The formation of silicon monoxide in the pack results of the reaction 2.8 with an equilibrium constant

$$K_{2.8} = p_{SiO} p_{O_2}^{1/2} \tag{2.10}$$

The standard free energy of reaction 2.8 was calculated using thermodynamic data provided by Lamoreaux *et al.* [104] and is

$$\Delta G^0_{2.8} = 794,861 - 251T \text{ (J mol}^{-1}\text{)} \tag{2.11}$$

In addition, the oxygen partial pressure in the pack is fixed by the Fe/FeO powder mixture. Therefore, the SiO partial pressure is calculated with Equation (2.10) and results are presented in Table 2.9.

Table 2.9: SiO partial pressure in Fe/FeO Rhines packs.

Temperature °C	$K_{2.8}$	p_{O_2} atm	p_{SiO} atm
1,000	3.3×10^{-20}	1.2×10^{-15}	9.6×10^{-13}
1,050	5.7×10^{-19}	7.7×10^{-15}	6.5×10^{-12}
1,100	7.9×10^{-18}	4.4×10^{-14}	3.8×10^{-11}
1,150	9.1×10^{-17}	2.3×10^{-13}	1.9×10^{-10}

To evaluate the number of mole of silicon transferred to the sample, Equation (2.9) was used. However, as presented earlier in this section the value of the sticking parameter is difficult to assess. Here, to evaluate the maximum quantity of silicon which may transferred during exposure in the Rhines packs, it was considered that all SiO molecules hitting the sample surface remains stick on it. This assumption yields $\alpha_{sti} = 1$. In addition a sample surface of 1 cm^2 and the longest experimental duration for internal oxidation (150h) were considered.

In Table 2.10, the maximum number of moles of silicon transferred to the sample, calculated with Equation (2.9), are presented along with the possible thickness

of the SiO_2 scale if all the silicon transferred is oxidised. For this calculation, a molar volume of 27 cm^3 mol^{-1} was considered for SiO_2.

Table 2.10: Evaluation of the maximum silicon contamination after 150h in Fe/FeO Rhines packs.

Temperature °C	n_{SiO} mol	thickness SiO_2 μm
1,000	9.5×10^{-8}	2.6×10^{-2}
1,050	6.3×10^{-7}	1.7×10^{-1}
1,100	3.6×10^{-6}	9.8×10^{-1}
1,150	1.8×10^{-5}	4.8

Values in Table 2.10 show that the largest quantity of silicon is transferred at the highest temperature studied. However, no SiO_2 was detected on the sample surface using grazing angle XRD and no SiO_2 internal oxide was observed. These results support the idea that the silicon contamination is negligible and has no effect on internal oxidation kinetics.

2.5.2 Flowing gas experiments

For gas experiments in the horizontal furnace, between 6 and 15 samples were placed on a sample holder. First of all, high purity argon was flushed for 30 minutes to expel air from the tube, then a mix of Ar-5%H_2 was flushed continuously while the temperature was increased. Samples were held at the cold end of the tube until the furnace reached the target temperature, after approximatively 2 hours. When the temperature was stabilised, the proper argon and hydrogen mix was flushed through the water bath to set the desired oxygen partial pressure for the experiment. The temperature was controlled within ±3°C with an R-type thermocouple. Samples were introduced into the hot zone of the furnace, where they remained throughout the experiment. To stop the experiment, the same proportion of Ar and hydrogen used during the experiment was flushed directly into the furnace, and samples were pushed to the end of the tube into the cold area. The reducing atmosphere was maintained in the furnace during the cooling to avoid the formation of an oxide

scale on samples. The furnace cooling took approximately 10 hours, after which samples were taken out of the tube. Figure 2.9 is a schematic representation of the various steps.

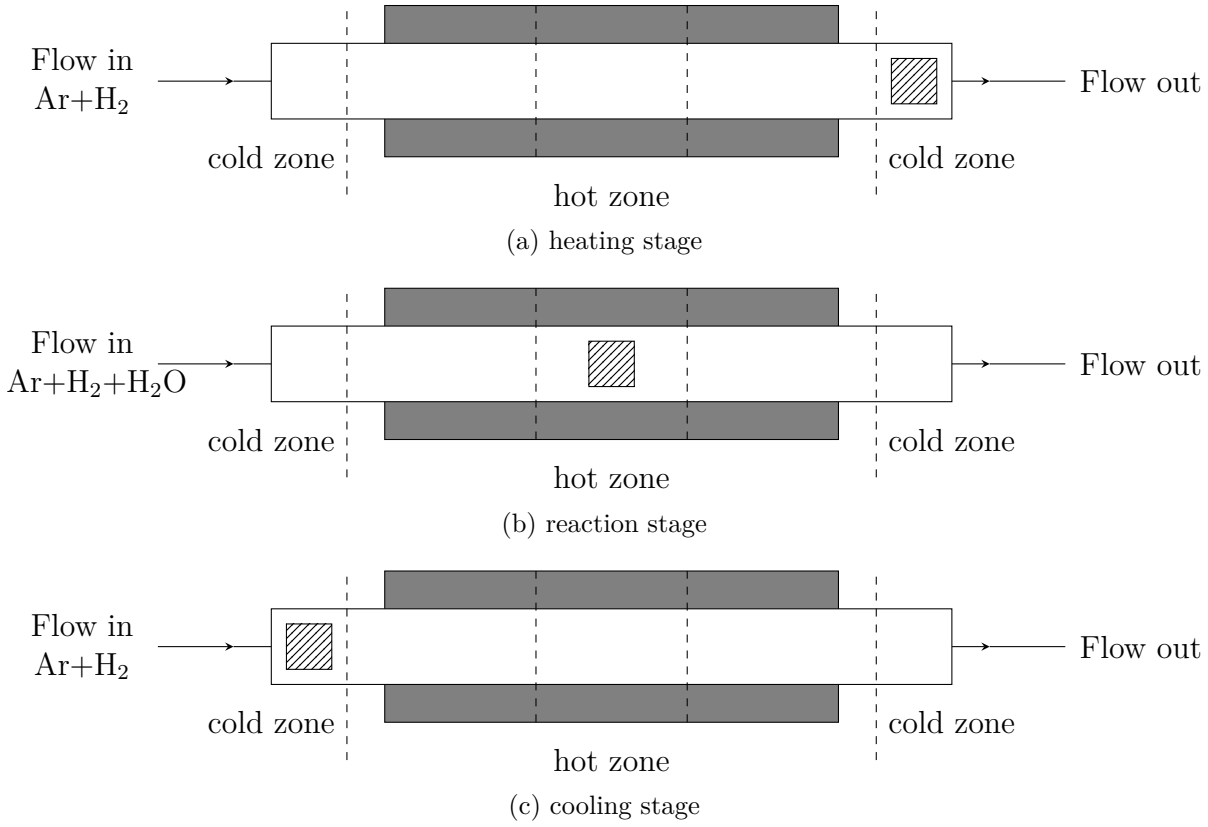

Figure 2.9: Gas experiment steps.

Thermogravimetric experiments were carried out in a SETARAM TAG24S thermobalance. This thermobalance is equipped with 2 symmetrical furnaces to compensate for the Archimedes force during heating and cooling steps. In addition, the balance sensitivity is 0.1 μg and the precision is estimated to be approximately 1 μg. In the classic balance configuration, reacting gases are introduced via the head of the balance and evacuated at the bottom of furnaces as shown in Figure 2.10. However, to avoid any damage to the balance due to the humid gas, the gas supply circuit for the balance was fully re-designed. The humid gas was introduced via the bottom of the furnace, argon was introduced via the head of the balance to protect it from humidity and gases were evacuated via the top of the furnace as illustrated in Figure 2.10.

Many tests were carried out to find the adequate flow rate ratio between the

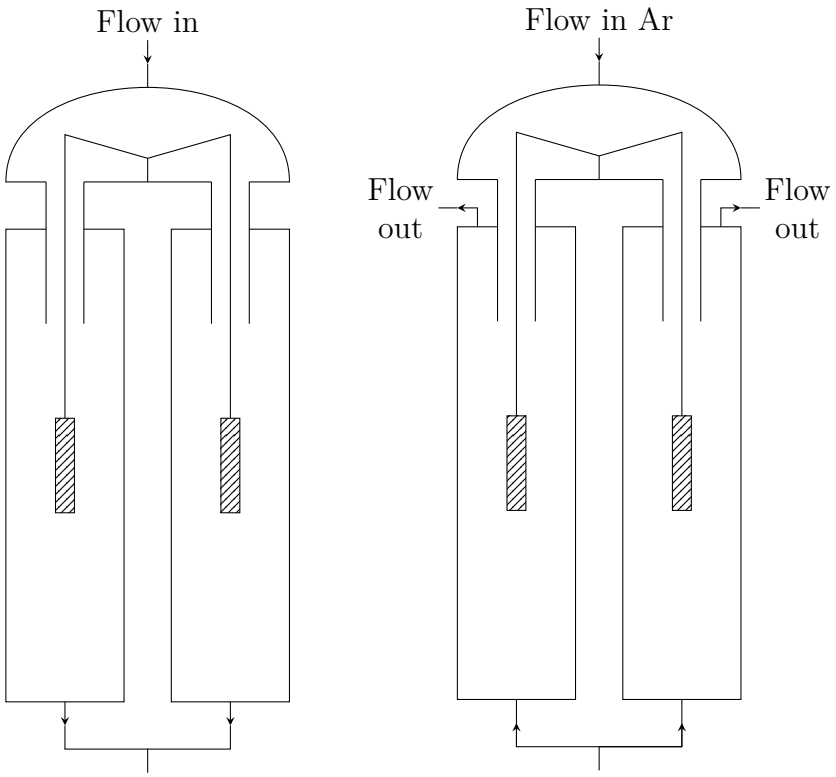

(a) Classic configuration (b) H_2/H_2O configuration

Figure 2.10: Schematic representation of experimental setup for TGA under H_2/H_2O gas mixtures.

reacting and the protection gas. In the thermobalance, only one sample at a time was exposed. The sample was hanging in the hot zone of the furnace during the whole experiment. Prior to starting the experiment, the furnace was evacuated and filled with Ar-5%H_2 twice.

The heating stage required 30 min at a heating rate of 60°C min^{-1}, and the atmosphere was Ar-5%H_2. When the furnace reached the required the temperature required for the experiment, the proper Ar-H_2-H_2O mixture was introduced and the sample weight change was recorded. At the end of the experiment, Ar-5%H_2 was flushed for 3 minutes before turning off the furnace. Room temperature was reached after 2 hours, and the sample was taken out.

2.6 Oxygen analysis

Prior to analysis, samples were grounded to a 1200 grit finish with a SiC paper to remove FeO nodules which nucleate on pure Fe during exposure at high temperature with the oxygen partial pressure set at the Fe/FeO equilibrium as shown in Figure 2.7, and also to remove possible surface contamination from handling samples in the furnace or from silicon evaporation for experiments in Fe/FeO Rhines packs. Finally, samples were cleaned with acetone in an ultrasonic bath and dried before analysis. Samples were analysed for oxygen in a LECO TCH600 by the inert gas fusion infrared method. The method used for oxygen analysis was as approved in ASTME-1019 of 2003, and was published by LECO in a technical note [105]. Few parameters were changed to adapt the method to our instrument and they are given in Appendix C. Low oxygen level values were expected, and to analyse the solubility experiment samples, a special calibration of the instrument for "ultra low oxygen content" was created, based on LECO standards. Five standards were used for the calibration and their reference are given in Appendix D. A linear calibration was used to convert the area under the curve drawn using the signal received by the detector to an oxygen concentration [106] as shown in Figure 2.11.

The concentration range of this calibration is 0-70 wt.ppm or 0-150 at.ppm. Samples weighed 1 g, which was shown to be the optimal sample weight for oxygen analysis [107]. An Sn accelerator was used to improve heat transfer and ensure a total melt of the sample. To test the calibration, 3 standards provided by the China National Analysis Centre with 3 different oxygen levels: 6.2 ± 0.6, 38 ± 2 and 66 ± 3 wt.ppm were used. In Figure 2.12, results of the analysis of the standard samples are presented and compared with the supplier certified values. In addition standards were analysed in a specific order to investigate the effect on the subsequent measurement. Results of the test showed that the calibration gave good results for the oxygen concentration measurement and each measurement was independent of the previous one.

First oxygen level measurements were done on raw materials. For these mea-

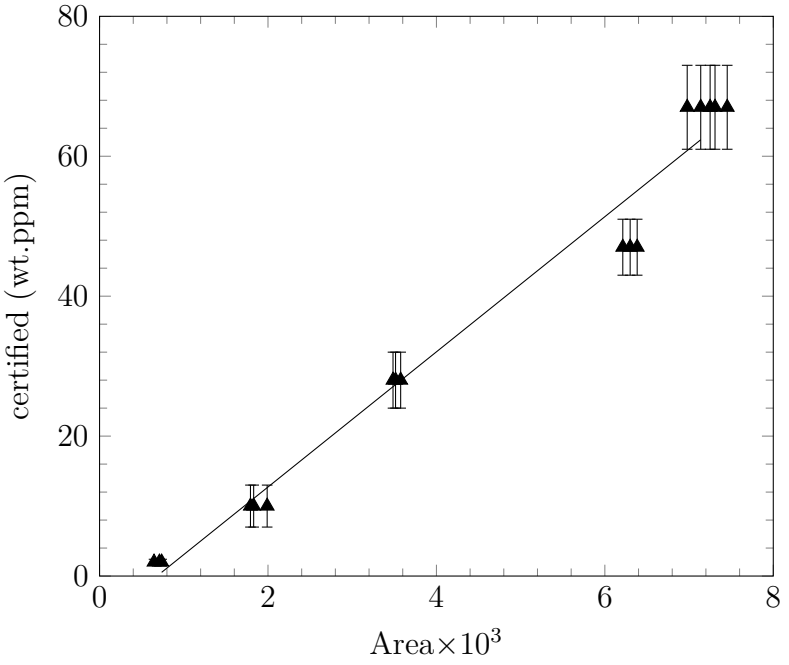

Figure 2.11: Calibration line for ultra low oxygen content.

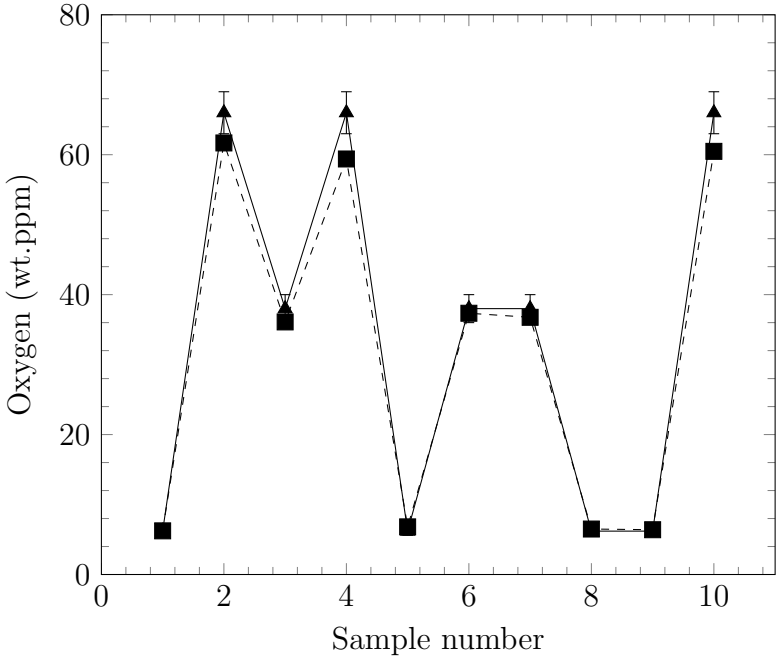

Figure 2.12: Test for ultra low oxygen calibration. Certified values (–▲–), measured values (-■-).

surements a standard calibration for "low oxygen content" was used. These measurements showed that iron contained more than 800 at.ppm of oxygen and nickel had an oxygen level of roughly 36 at.ppm. To be able to start solubility exper-

iments with the lowest oxygen level possible, oxygen in raw materials has to be reduced. Reduction of the oxygen level occurs during the casting of materials in the arc melter and during the annealing because both operations were carried out in reducing environment.

In addition, raw materials contain impurities which could form more thermodynamically stable oxides than iron. Since impurity levels from elemental analyses and the oxygen partial pressure in the reaction atmosphere are known, the oxygen amount coming from oxidised impurities can be evaluated. Small levels of Mg, Ca and Na were detected in the raw materials (Appendix A). However, these impurities should be in a gaseous form during melting of the alloys. As the melting is done under flowing Ar-H_2, it is assumed that these impurities are no longer present in alloys after melting. In addition, Si is present in nickel. However, SiO_2 is vaporised in SiO at high temperature and under low oxygen partial pressure [104]. Therefore, like the alkali and alkali earth metals, the silicon level would be extremely low in alloys after melting. In Table 2.11, main impurities levels are reported with the possible thermodynamically stable oxide that the impurity may form.

Table 2.11: Material impurity level in at.ppm and oxidation reaction considered.

impurity	N_{imp}^{Fe}	N_{imp}^{Ni}	Oxidation reaction
Al	3.5	0.15	$\frac{2}{3}Al_{(l)} + \frac{1}{2}O_{2(g)} \rightarrow \frac{1}{3}Al_2O_{3(s)}$
Cr	8.7	0.21	$\frac{2}{3}Cr_{(s)} + \frac{1}{2}O_{2(g)} \rightarrow \frac{1}{3}Cr_2O_{3(s)}$
Mn	24.2	0.006	$Mn_{(s)} + \frac{1}{2}O_{2(g)} \rightarrow MnO_{(s)}$
Ti	-	0.38	$\frac{1}{2}Ti_{(s)} + \frac{1}{2}O_{2(g)} \rightarrow \frac{1}{2}TiO_{2(s)}$

To investigate the stability of the different oxide the dissociation pressure of each oxide was calculated from thermodynamic data from NIST-JANAF [101] and using Equation (1.4). In addition, the level of impurity in the different alloys is extremely low. Therefore, assumptions of a dilute solution can be made to compute values of the oxide dissociation pressure. This assumption yields

$$a_{imp} = \gamma_{imp}^{0} N_{imp} \tag{2.12}$$

where a_{imp} and N_{imp} are the activity and the mole fraction of the impurity *imp* considered (*imp* =Al/Cr/Mn/Ti), respectively and γ^0_{imp} is the Henry's law coefficient for the impurity *imp*. However, due to the lack of thermodynamic data to evaluate γ^0_{imp} in the different alloys, it was considered in a first approximation, that impurities exhibit an ideal behaviour and Equation (2.12) becomes

$$a_{imp} = N_{imp} \tag{2.13}$$

To calculate the amount of impurities in the Fe-Ni alloys, the following relation was used:

$$N^{Fe-Ni}_{imp} = N_{Fe}N^{Fe}_{imp} + N_{Ni}N^{Ni}_{imp} \tag{2.14}$$

where N^{Fe-Ni}_{imp} is the amount of the impurity *imp* in the binary alloy, N^{Fe}_{imp} and N^{Ni}_{imp} the mole fraction of the impurity *imp* in pure iron and nickel, and N_{Fe} and N_{Ni} the mole fraction of iron and nickel in the alloy. In addition, the activity of the oxide is considered equal to 1. In Figure 2.13, the dissociation pressures of the different oxide are plotted and compared to the Fe/FeO dissociation pressure.

Figure 2.13 shows that at all temperatures studied, aluminium and titanium form stable oxides. It should be noted that no titanium impurities was reported in the analysis certificate of iron (Appendix A). Thus, this impurity does not appear in Figure 2.13 for iron. However at 1,000°C, in alloys with nickel content lower than 80 at.%, and lower than 40 at.% at 1,050°C, the dissociation pressure of the chromium oxide is close to the Fe/FeO equilibrium pressure. Therefore, it is difficult to conclude on the stability of the chromium oxide under the experimental conditions. To calculate the total amount of oxygen coming from oxidised impurity, it was assumed that if the impurity can form a stable oxide, the total amount of the impurity would be oxidised. The oxygen mole fraction from oxidised impurities is given by

$$N^{impurities}_{O} = \sum_{imp} \nu_{imp} N^{Fe-Ni}_{imp} \tag{2.15}$$

where $N^{impurities}_{O}$ is the mole fraction of oxygen from oxidised impurities and $\nu_{imp} = \frac{y}{x}$

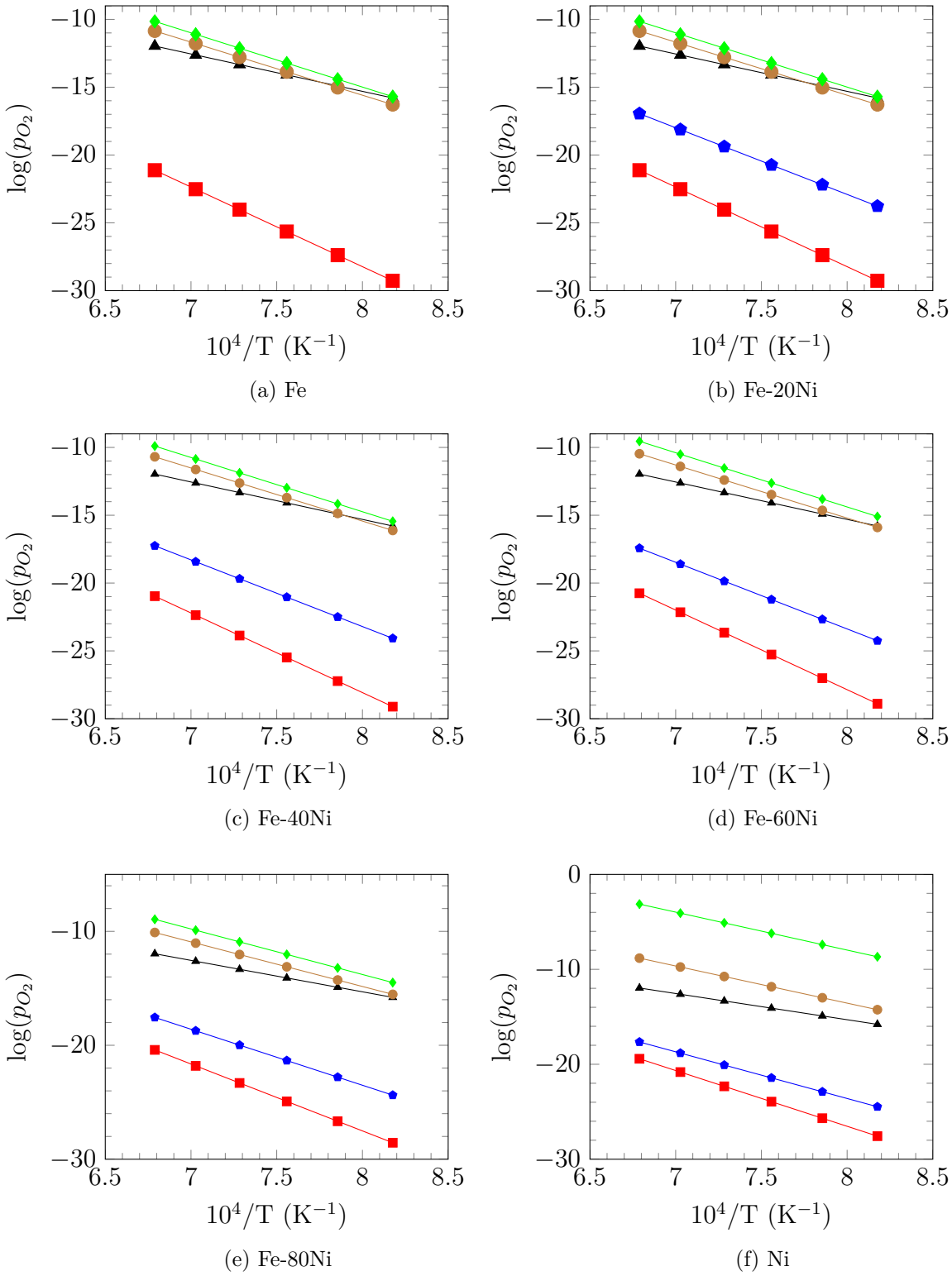

(a) Fe

(b) Fe-20Ni

(c) Fe-40Ni

(d) Fe-60Ni

(e) Fe-80Ni

(f) Ni

Figure 2.13: Dissociation pressure of impurities present in the different alloys compared with the Fe/FeO (—▲—) dissociation pressure.
Al/Al_2O_3 (—■—),Cr/Cr_2O_3 (—●—), Mn/MnO (—◆—), Ti/TiO_2 (—⬟—).

for and oxidised impurity M_xO_y. In addition, for alloys where it is impossible to conclude if chromium is oxidised, the total amount of oxygen was calculated with and without the presence of chromium oxide. In Figure 2.14, the total amount of oxygen from impurities are plotted versus the alloy composition.

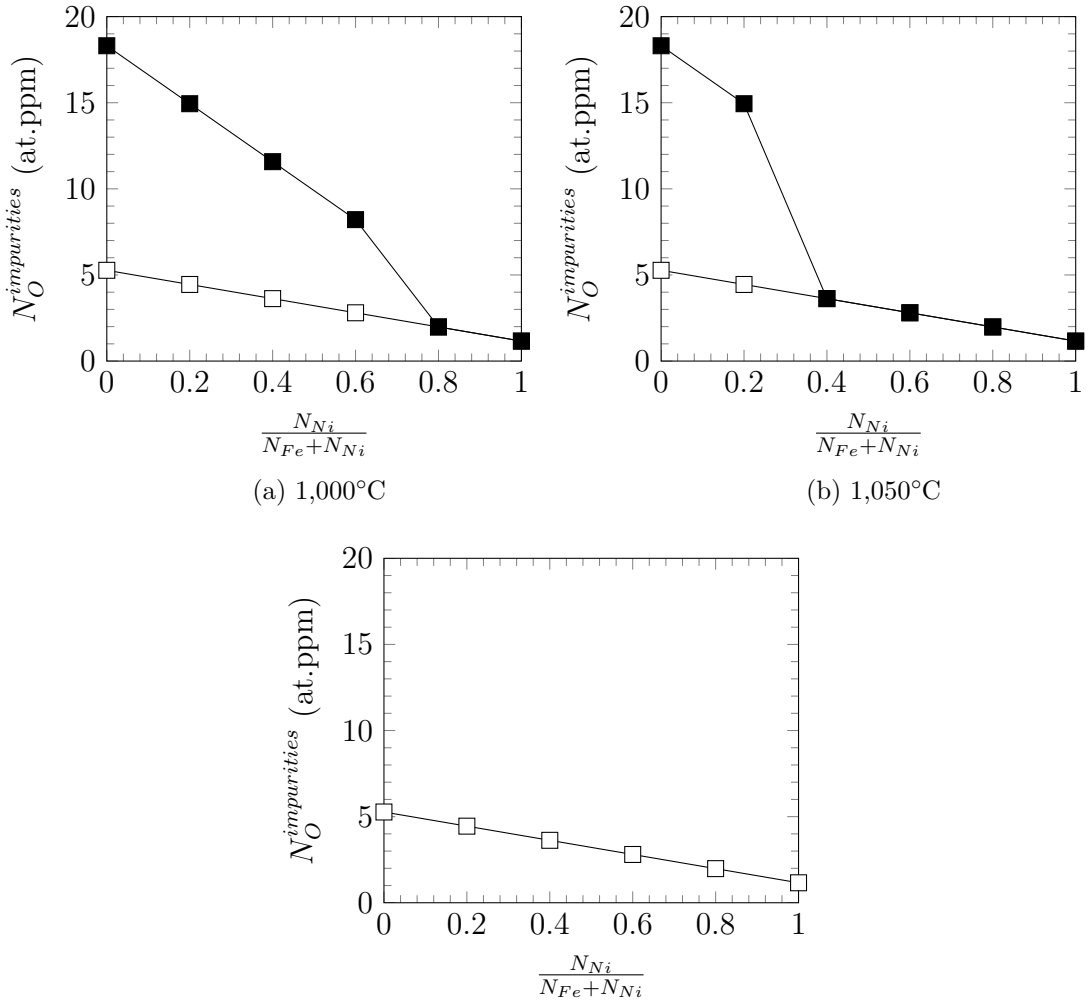

(a) 1,000°C

(b) 1,050°C

(c) 1,100°C & 1,150°C

Figure 2.14: Amount of oxygen from oxidised impurities, with Cr_2O_3(–■–),no Cr_2O_3 (–□–).

2.7 Internal oxidation zone characterisation

2.7.1 IOZ depth measurement

The depth of the internal oxidation zone was measured from optical microscopy of a cross-sectioned sample. Surfaces were polished down to 0.5 μm using diamond

paste and 10 penetration measurements were carried out to estimate the depth of the IOZ. One measurement was done per micrographs for estimation of the IOZ depth as illustrated in Figure 2.15. In addition, 5 micrographs were made on one side of the sample and the 5 following were made on the opposite side to check the homogeneity of the IOZ.

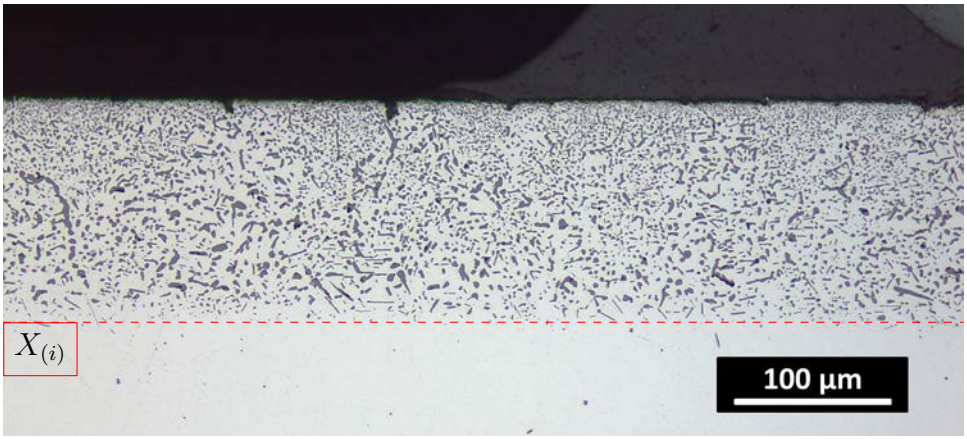

Figure 2.15: Measurement of the IOZ depth for alloy Fe-20Ni-7.5Cr reacted 60h at 1,000°C in H_2/H_2O with 3% water vapour content.

2.7.2 Volume fraction measurement

The internal oxide volume fraction was measured using optical microscopy with a magnification of x1000 using the software ImageJ. The images were binary processed as illustrated in Figure 2.16. The area fraction of internal oxide is given by

$$F_A = \frac{n_{blackpixel}}{n_{blackpixel} + n_{whitepixel}} \tag{2.16}$$

where $n_{blackpixel}$ and $n_{whitepixel}$ is the number of black and white pixels, respectively. In addition, Delesse showed that the area fraction is an estimate of the volume fraction [108] and yields

$$F_V = F_A \tag{2.17}$$

where F_V is the volume fraction. In addition, it was also demonstrated by Rosiwal [108] that the lineal oxide fraction, F_L, is equivalent to the internal oxide volume fraction. Thus, the variation of the internal oxide volume fraction with the IOZ

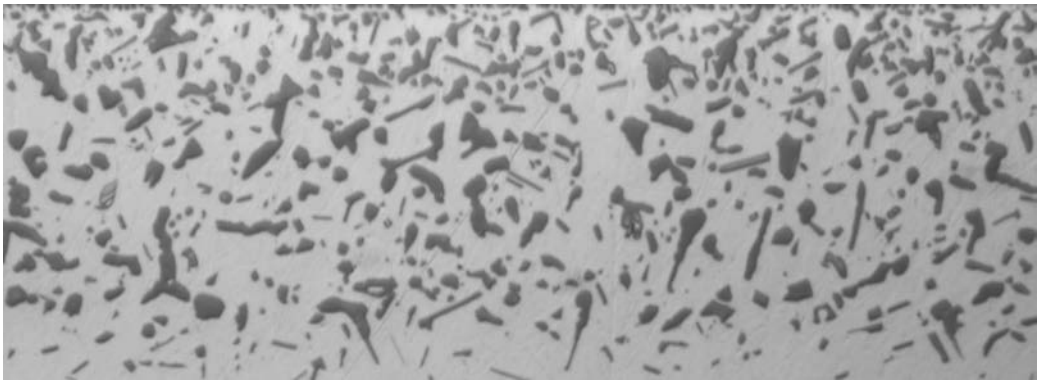

(a) Optical micrograph, x1000

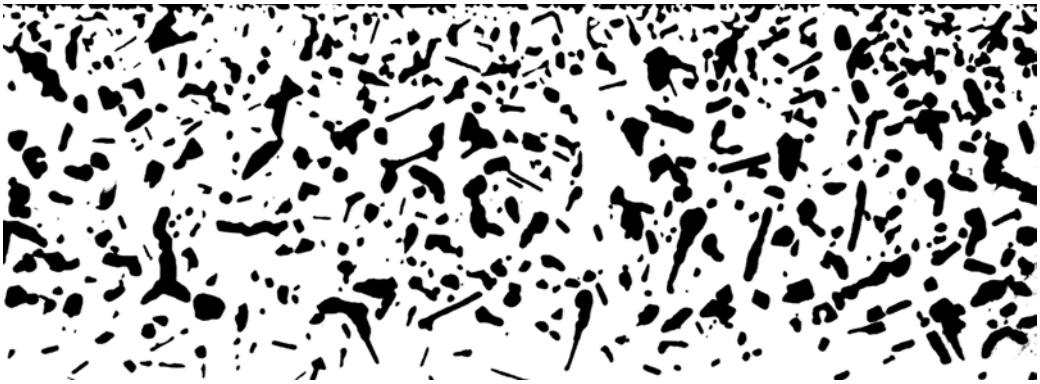

(b) Binary of micrograph

Figure 2.16: Optical micrograph, x1000, Fe-20Ni-7.5Cr exposed 4h at 1,150°C in H_2/H_2O gas with 13% water vapour.

depth was investigated by measuring the lineal oxide fraction at different depth in the binary image and plots similar to Figure 2.17 were obtained.

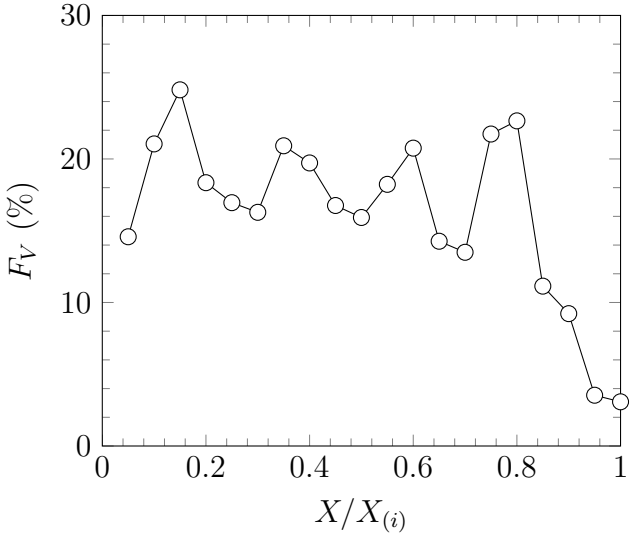

Figure 2.17: Internal oxide volume fraction as function of IOZ depth measured for Fe-20Ni-7.5Cr alloy exposed for 4h at 1,150°C in H_2/H_2O mixtures containing 13% of water vapour.

2.8 characterisation technique

2.8.1 Scanning Electron Microscopy/Energy Dispersive Spectroscopy (SEM/EDS)

Observation and chemical analysis of the internal oxidation zone were performed in a Hitachi S3400 SEM equipped with secondary and baskscatterred detector for imaging and a Bruker XFlash 6|30 detector for microanalysis. The majority of observations were carried out using the backscattered detector as it allows the identification of phases without EDS analysis. Indeed, a chemical contrast is observable with this detector and it gives information on the chemical composition of phases. Spectrum obtained from EDS measurement were analysed using the software Esprit developed by Bruker. Element quantification was carried out with the P/B-ZAF method and using internal standards provided by the manufacturer. The resolution of the probe was around 1μm with the conditions used.

2.8.2 X-Ray Diffraction (XRD)

Phase identification for powder or bulk material was performed with XRD in a PANalytical Empyrean X-ray diffractometer with a copper anode for nickel-rich alloys. However, for XRD on iron powder and iron-rich alloys, a cobalt anode was used in order to reduce the fluorescence of iron. Analysis of spectra and phase identification were carried out using X'Pert High Score plus software developed by PANanalytical.

Chapter 3

Oxygen solubility

This chapter is dedicated to the oxygen solubility measurement in iron, nickel and Fe-Ni alloys. In the first section, thermodynamic considerations for the calculation of the oxygen solubility are briefly described. In a subsequent section, values of oxygen solubility measured after exposure in Fe/FeO Rhines packs and H_2/H_2O gases are presented and compared. Finally, models to predict the oxygen solubility in binary Fe-Ni alloys reviewed in Section 1.5.3 of the literature survey are tested. It should be noted that all uncertainties given correspond to a 95% confidence interval.

3.1 Determination of the oxygen solubility

The oxygen solubility was measured after exposure in Fe/FeO Rhines packs [109] and H_2/H_2O gases. The measurement of the oxygen solubility was extremely sensitive to contamination because of the low oxygen concentrations in iron, nickel and Fe-Ni alloys. A few measurements failed, presumably due to contamination during sample preparation. Consequently, many experiments were repeated in order to increase the statistical reliability of the experimental results.

The oxygen solubility is related to the oxygen partial pressure (Section 1.5) by:

$$K^{(s)} = \frac{N_O}{p_{O_2}^{1/2}} \tag{3.1}$$

where $K^{(s)}$ is the Sievert constant, N_O the oxygen mole fraction and p_{O_2} the oxygen partial pressure. It was decided in the first place to focus on the excess Gibbs free energy related to the reaction of oxygen dissolution in a metal, rather than the value of the oxygen solubility. This choice is justified by the fact that the variation of N_O with temperature may be misleading, as was highlighted when the oxygen solubility in nickel, measured by several authors [71, 78, 80] was reviewed in Section 1.5.2. The problem is that oxygen partial pressure also varies with temperature (as controlled by the metal-metal oxide equilibrium) and this is handled by using Equation (3.1).

3.1.1 Evaluation of the excess Gibbs free energy of oxygen dissolution reaction

The reaction of oxygen dissolution in a metal is written

$$\frac{1}{2}\mathrm{O}_{2\left(g,\ p_{O_2}=1\ \mathrm{atm}\right)} \rightarrow \underline{\mathrm{O}}_{(N_O=1)} \tag{3.2}$$

Considering a standard state of 1 atm for the gas, a Raoultian standard state for oxygen dissolved in the material and γ_O the activity coefficient of oxygen dissolved in the metal, it was shown in Section 1.5 that the equilibrium condition for reaction 3.2 is

$$RT\ln\left(\gamma_O\right) + RT\ln\left(N_O\right) - \frac{1}{2}RT\ln\left(p_{O_2}\right) = 0 \tag{3.3}$$

In addition, the activity coefficient is given by the following relation

$$RT\ln\left(\gamma_O\right) = \overline{G}_O^{xs} = \overline{H}_O^{xs} - T\overline{S}_O^{xs} \tag{3.4}$$

where $\overline{G}_O^{xs}$ is the partial molar excess of Gibbs free energy, $\overline{H}_O^{xs}$ the partial molar excess enthalpy and $\overline{S}_O^{xs}$ the partial molar excess entropy. Combining, Equations (3.4) and (3.3) yields

$$\overline{G}_O^{xs} = \overline{H}_O^{xs} - T\overline{S}_O^{xs} = \frac{1}{2}RT\ln\left(p_{O_2}\right) - RT\ln\left(N_O\right) \tag{3.5}$$

Finally, substituting Equation (3.5) in (3.1), the following relation is found

$$\frac{-\overline{G}_O^{xs}}{RT} = \ln\left(K^{(s)}\right) \tag{3.6}$$

It has to be emphasised that in this section, firstly values of $\overline{G}_O^{xs}$ evaluated directly from oxygen concentration measured are presented. However, due to the scatter in the oxygen concentration measurement, it was decided to estimate excess enthalpy and entropy for oxygen dissolution from the measured oxygen solubility and then to recalculate the excess Gibbs energy and oxygen solubility from this

evaluation of $\overline{H}_O^{xs}$ and $\overline{S}_O^{xs}$. This facilitates the investigation of excess Gibbs free energy and oxygen solubility variation with alloy composition and temperature.

It is noted that the small interval of temperature used in the present study was due to experimental difficulties faced for oxygen solubility experiment. A few tentative Fe/FeO Rhines pack experiments at higher temperature were carried out but resulted in failure of the quartz capsule [109]. On the other hand, experiments at lower temperature in iron-rich alloys are not possible due to the $\gamma \rightarrow \alpha$ transformation. In addition, constraints on the weight and geometry of the sample for oxygen analysis fix the sample thickness. Therefore, the thickness of sample cannot be reduced, and the time to reach the equilibrium increases dramatically when the temperature decreases, making low temperature experiments very difficult.

3.1.2 Oxygen solubility in dry environment

To calculate the excess free energy of reaction 3.2 from Equations (3.1) and (3.6), the amount of oxygen dissolved is required. As previously described in Section 2.6, impurities less noble than iron like aluminium or chromium may form thermodynamically stable oxides under experimental conditions used in the present study. Therefore, the oxygen dissolved in a material is given by

$$N_O = N_O^{measured} - N_O^{impurities} \tag{3.7}$$

where $N_O^{measured}$ is the oxygen mole fraction measured with the technique described in Section 2.6 and $N_O^{impurities}$ the amount of oxygen coming from oxidised impurities. From thermodynamic calculations, it was clear that aluminium and titanium impurities, which form stable oxides at extremely low oxygen partial pressure, are oxidised during exposure at the Fe/FeO equilibrium pressure. However, the state of chromium impurities is uncertain in some alloys. At 1,000°C, it is impossible to state if chromium impurities were oxidised in alloys with nickel content lower than 80 at.% and a similar situation arises at 1,050°C for alloys with nickel content

lower than 40 at.% (Section 2.6). However, at higher temperatures, chromium impurities were considered to remain unoxidised for all compositions as presented in Section 2.6.

In Figure 3.1, found from Equations (3.1) and (3.6), $\overline{G}_O^{xs}$ is plotted as a function of the temperature. Values of $\overline{G}_O^{xs}$ were calculated from experimentally measured oxygen concentrations and oxygen partial pressures reported in Table 2.5. The multiple points plotted in Figure 3.1 represent the many replicate measurements. In addition, circle symbols correspond to $\overline{G}_O^{xs}$ assuming that no chromium is oxidised, while cross symbols represent values of this energy if the chromium was considered oxidised. Chromium impurity levels were assessed using chemical analysis provided by the manufacturer and presented in Appendix A. Figure 3.1 shows that excess Gibbs free energies calculated when the chromium formed a stable oxide are apparently similar to values when the chromium is considered to remain unoxidised. To estimate the difference between excess Gibbs free energies when the state of chromium impurities was unknown, the following ratio was calculated

$$\Delta E = 100 \times \left| \frac{\overline{\left(\overline{G}_O^{xs}\left(Cr\right)\right)} - \overline{\left(\overline{G}_O^{xs}\right)}}{\overline{\left(\overline{G}_O^{xs}\right)}} \right| \tag{3.8}$$

with $\overline{\left(\overline{G}_O^{xs}\left(Cr\right)\right)}$ is the average excess Gibbs free energy assuming that chromium impurities form Cr_2O_3 and $\overline{\left(\overline{G}_O^{xs}\right)}$ the average excess Gibss free energy when it is assumed that the chromium remains unoxidised. Average values were calculated for a given temperature from data presented in Figure 3.1. In Figure 3.2, values of ΔE are presented. Figure 3.2 shows that the difference in excess Gibbs free energy for reaction 3.2 if the chromium remains in solution or is oxidised is always lower than 8%. Therefore, as it was impossible to determine the state of the chromium under the experimental conditions, and because the difference between excess Gibbs free energy if chromium was oxidised or not is small, it was decided to assume that the chromium was never oxidised in any metals or Fe-Ni alloy, under all experimental conditions used, and only aluminium and titanium formed stable oxides. It should

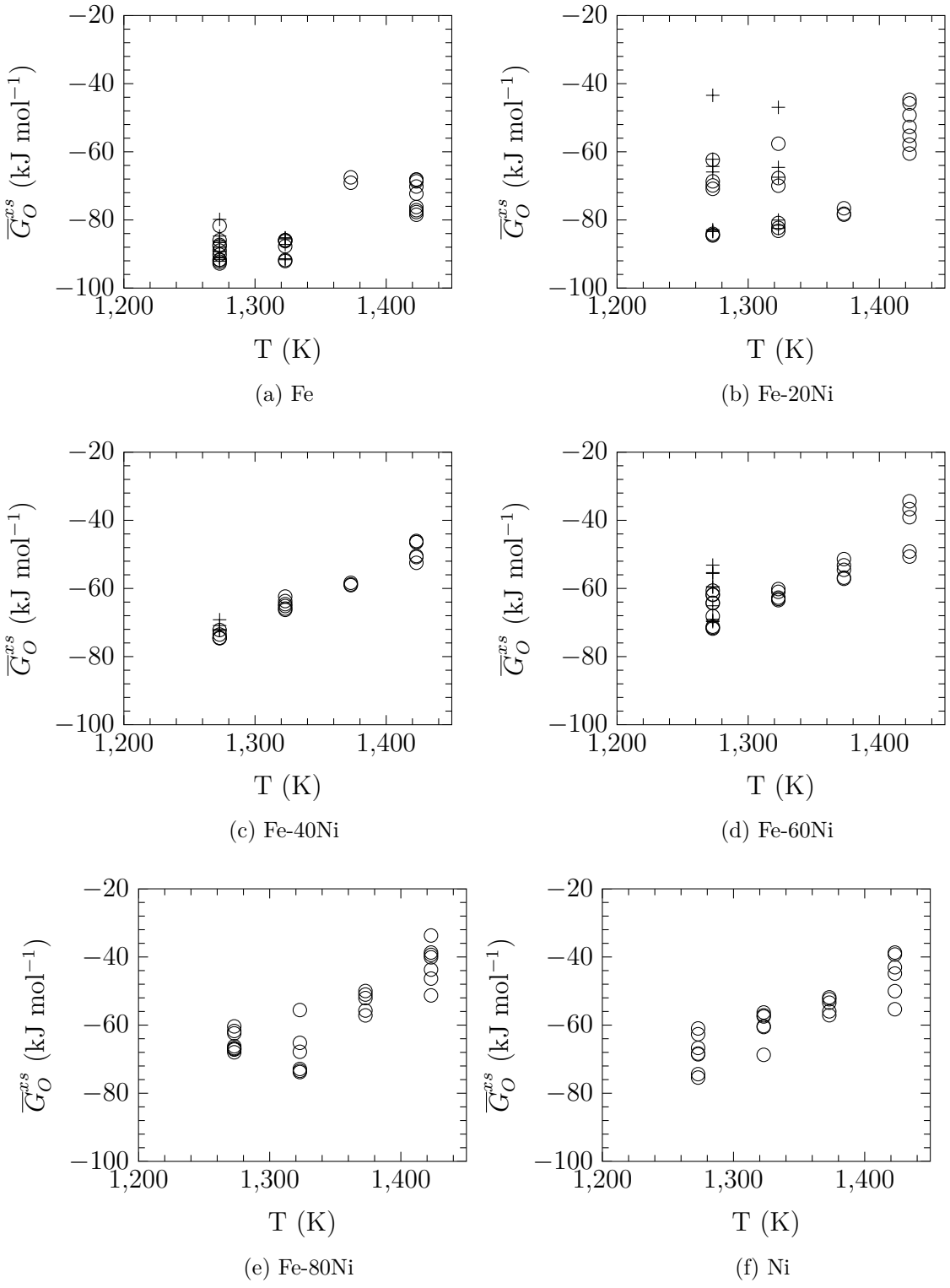

(a) Fe

(b) Fe-20Ni

(c) Fe-40Ni

(d) Fe-60Ni

(e) Fe-80Ni

(f) Ni

Figure 3.1: Excess Gibbs free energy evaluated from oxygen concentration measurement for different temperature after reaction in Fe/FeO packs, assuming no impurity Cr oxidation (○) and with Cr oxidation (+).

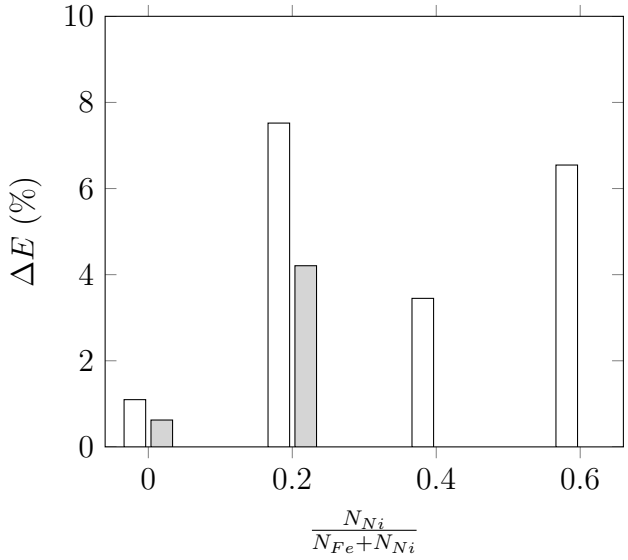

Figure 3.2: Difference between excess Gibbs free energy for oxygen dissolution if chromium impurities remains in solution or form Cr_2O_3: 1,000°C (▯▯), 1,050°C (▮▮).

be noted that this assumption yields the lowest estimation of excess Gibbs free energy.

At the equilibrium, substituting Equation (3.4) in (3.3) yields the following relation for the oxygen solubility.

$$N_O = p_{O_2}^{1/2} \exp\left(\frac{\overline{S}_O^{xs}}{R}\right) \exp\left(\frac{-\overline{H}_O^{xs}}{RT}\right) \tag{3.9}$$

Thus, the excess enthalpy and entropy of reaction were evaluated using a non linear fit of the data to Equation (3.9) employing the module SolverAid of Excel software [110]. This fitting method was chosen because it yields an error distribution close to a normal distribution. Values of $\overline{H}_O^{xs}$ and $\overline{S}_O^{xs}$ are presented in Table 3.1 along with the correlation factor, r, determined during the evaluation of these parameters. The correlation factor is defined by

$$r = \frac{COV\left(\overline{H}_O^{xs}, \overline{S}_O^{xs}\right)}{\sigma_{\overline{H}_O^{xs}} \sigma_{\overline{S}_O^{xs}}} \tag{3.10}$$

where COV is the covariance of the two parameters and σ the standard deviation. Here, the error was considered equal to two standard deviations. The correlation factor found when the excess enthalpy and entropy are evaluated is close to 1 for

every alloy, and indicates that $\overline{H}_O^{xs}$ and $\overline{S}_O^{xs}$ are strongly correlated. In addition, the large uncertainty evaluated on these parameters arise from the scatter in solubility measurement. The variations of $\overline{H}_O^{xs}$ and $\overline{S}_O^{xs}$ with the alloy composition are shown in Figure 3.3.

Table 3.1: Excess enthalpy and entropy determined by non-linear fitting of oxygen solubility (Eq.3.9) measured in Fe/FeO Rhines packs.

$\frac{N_{Ni}}{N_{Fe}+N_{Ni}}$	$\overline{H}_O^{xs}$ kJ mol^{-1}	$\overline{S}_O^{xs}$ J mol^{-1} K^{-1}	r
0	-238 ± 38	-116 ± 28	0.9989
0.2	-260 ± 84	-140 ± 63	0.9990
0.4	-280 ± 18	-162 ± 14	0.9991
0.6	-256 ± 39	-148 ± 29	0.9991
0.8	-273 ± 72	-159 ± 54	0.9991
1	-259 ± 50	-149 ± 37	0.9991

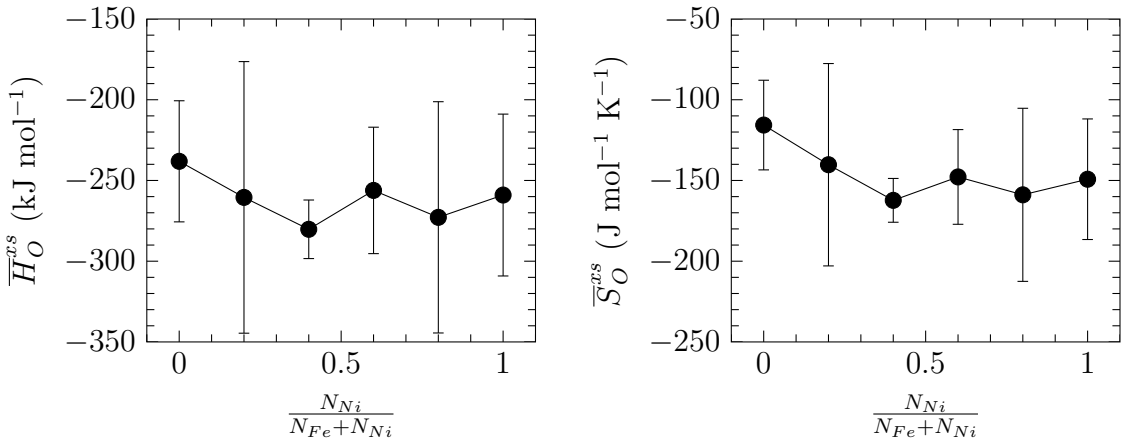

(a) $\overline{H}_O^{xs}$ (b) $\overline{S}_O^{xs}$

Figure 3.3: Variation of excess enthalpy and entropy with the alloy composition after exposure in Fe/FeO Rhines packs.

The excess enthalpy for oxygen dissolution is found to be between -300 and -200 kJ mol^{-1} while the excess entropy takes values between -200 and -100 J mol^{-1} K^{-1}. However, due to the large uncertainty in these values, their variation with alloy composition is difficult to asses. These values of excess enthalpy and entropy for oxygen dissolution allow the evaluation of $\overline{G}_O^{xs}$ according to Equation (3.4). Values of excess Gibbs free energy estimated from $\overline{H}_O^{xs}$ and $\overline{S}_O^{xs}$ in Table 3.1 are presented in Figure 3.4. It has to be emphasised that the error in the value of $\overline{G}_O^{xs}$ was estimated taking into account that $\overline{H}_O^{xs}$ and

$\overline{S}_O^{xs}$ are strongly correlated. The calculation of uncertainty in the case of correlated parameters is presented in Appendix E. Under the assumption that the error in the temperature is negligible, the uncertainty for $\overline{G}_O^{xs}$ is given by

$$\delta\left(\overline{G}_O^{xs}\right)^2 = \delta\left(\overline{H}_O^{xs}\right)^2 + T^2\delta\left(\overline{S}_O^{xs}\right)^2 - 2rT\delta\left(\overline{H}_O^{xs}\right)\delta\left(\overline{S}_O^{xs}\right) \tag{3.11}$$

where $\delta\left(\overline{G}_O^{xs}\right)$, $\delta\left(\overline{H}_O^{xs}\right)$ and $\delta\left(\overline{S}_O^{xs}\right)$ are uncertainties in the corresponding quantity. From Equation (3.11), it is seen that the strong correlation ($r = 1$) between $\overline{H}_O^{xs}$ and $\overline{S}_O^{xs}$ reduces the uncertainty for calculated values of $\overline{G}_O^{xs}$. This reduction of uncertainty in calculated values of $\overline{G}_O^{xs}$ arises from the fact that the relation between $\overline{G}_O^{xs}$, $\overline{H}_O^{xs}$ and $\overline{S}_O^{xs}$ is known (Eq.3.4). Therefore, one degree of freedom is removed from the calculated uncertainty, yielding lower uncertainty in calculated values of $\overline{G}_O^{xs}$ than the individual uncertainties on parameters $\overline{H}_O^{xs}$ and $\overline{S}_O^{xs}$.

The different values of excess Gibbs free energy measured at different temperatures are plotted for the different alloys in Figure 3.4. At all temperatures, the

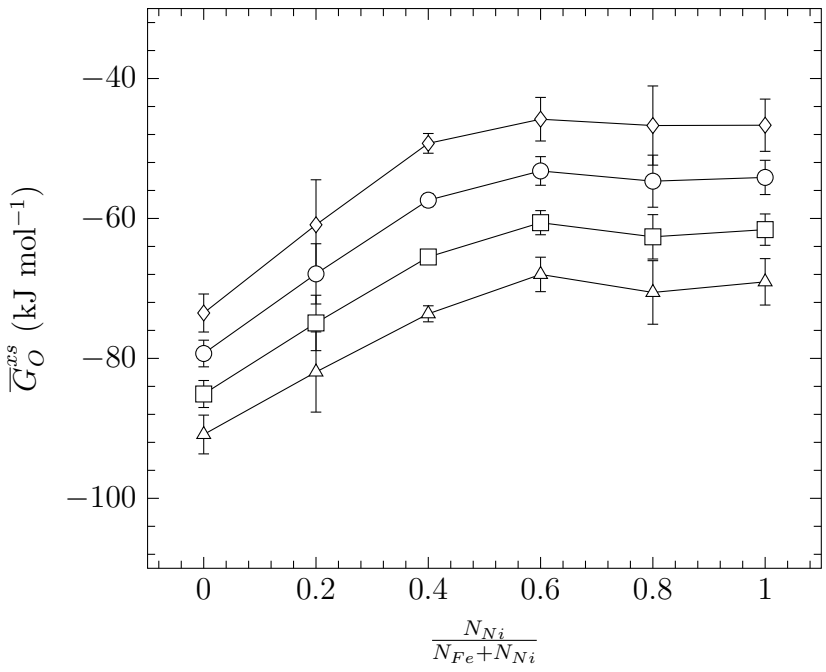

Figure 3.4: Excess Gibbs free energy measured after exposure in Fe/FeO Rhines packs at several temperatures, 1,000°C (–△–), 1,050°C (–□–), 1,100°C (–○–), 1,150°C (–◇–).

most negative value of $\overline{G}_O^{xs}$ is found for pure iron. It increases to reach a plateau for alloys with a nickel content larger than 60 at.%.

From values of $\overline{H}_O^{xs}$ and $\overline{S}_O^{xs}$ given in Table 3.1, the oxygen solubility was calculated with Equation (3.9) for the different compositions and temperatures, and the results are presented in Table 3.2 and plotted as a function of the alloy composition in Figure 3.5. In addition, as for the uncertainty in the excess Gibbs free energy, the uncertainty in oxygen solubility values calculated from $\overline{H}_O^{xs}$ and $\overline{S}_O^{xs}$ was calculated taking into account the strong correlation between the excess enthalpy and entropy. Thus, the uncertainty in N_O is given by

$$\delta\left(N_O\right)^2 = p_{O_2}\frac{1}{R^2}\exp\left(\frac{-2\overline{G}_O^{xs}}{RT}\right)\left[\frac{\delta\left(\overline{H}_O^{xs}\right)^2}{T^2} + \delta\left(\overline{S}_O^{xs}\right)^2 - \frac{2r\delta\left(\overline{H}_O^{xs}\right)\left(\overline{S}_O^{xs}\right)}{T}\right] \quad (3.12)$$

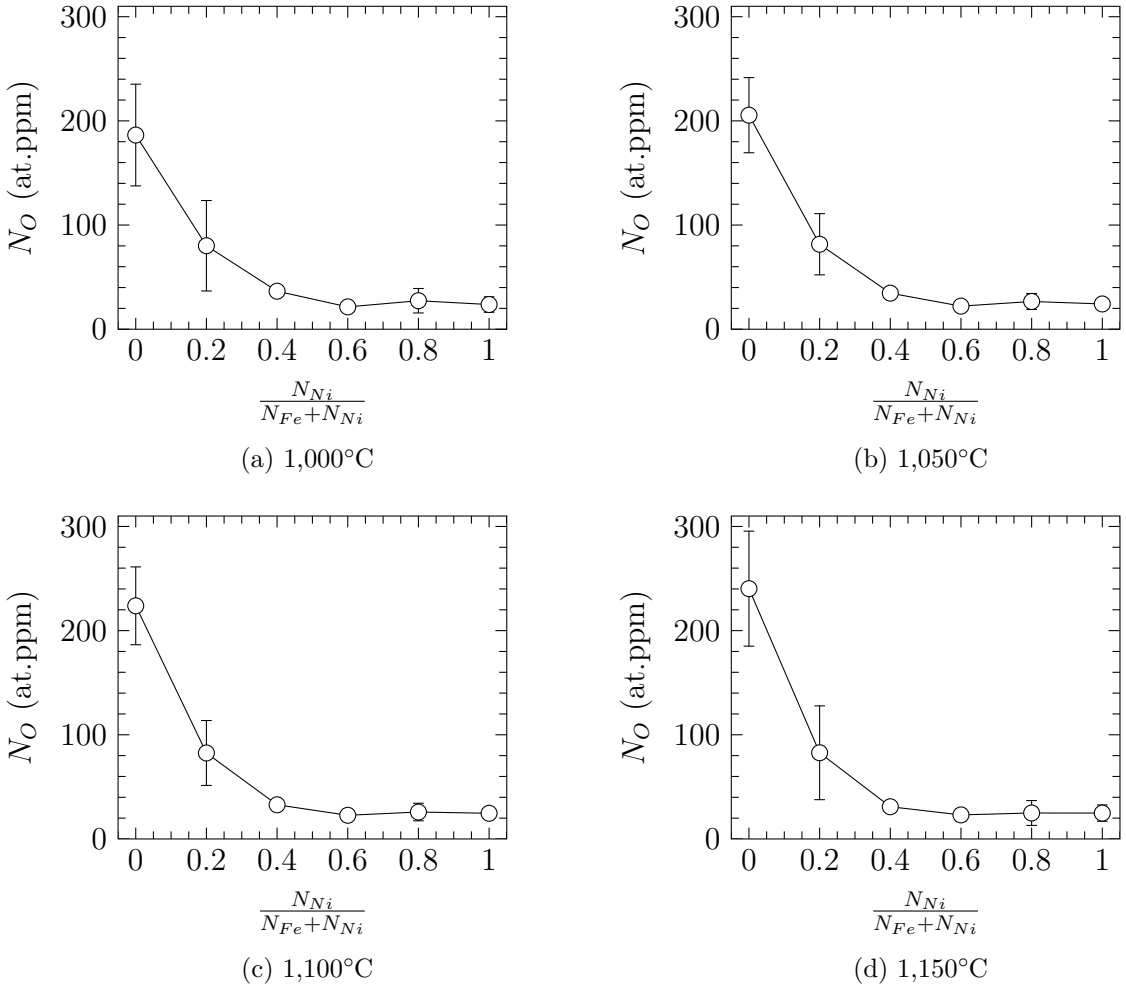

(a) 1,000°C (b) 1,050°C

(c) 1,100°C (d) 1,150°C

Figure 3.5: Variation of the oxygen solubility measured in Fe/FeO Rhines pack with the alloy composition.

Table 3.2: Oxygen solubility values calculated using Equation (3.9) with values of $\overline{H}_O^{xs}$ and $\overline{S}_O^{xs}$ determined in Fe/FeO Rhines packs.

$\frac{N_{Ni}}{N_{Fe}+N_{Ni}}$	N_O (at.ppm) 1,000°C	1,050°C	1,100°C	1,150°C
0	186 ± 49	205 ± 36	224 ± 37	240 ± 55
0.2	80 ± 43	82 ± 29	83 ± 31	83 ± 45
0.4	36 ± 4	35 ± 2	33 ± 3	31 ± 4
0.6	21 ± 5	22 ± 3	23 ± 4	23 ± 6
0.8	27 ± 12	27 ± 8	26 ± 8	25 ± 12
1	24 ± 7	24 ± 5	25 ± 5	25 ± 8

Figure 3.5 shows that the maximum in solubility is observed in pure iron at all temperatures. When nickel is added to the alloy composition, the oxygen solubility drops significantly to reach a plateau of 20 at.ppm for alloys with $\frac{N_{Ni}}{N_{Fe}+N_{Ni}} > 0.5$. A small increase in the oxygen solubility is found at 1,000, 1,050 and 1,100°C for the alloy with the composition $\frac{N_{Ni}}{N_{Fe}+N_{Ni}} = 0.8$. The overall variation of the oxygen solubility with the alloy composition is similar to variations observed for other interstitials like carbon [111] or nitrogen [112], as illustrated in Figure 3.6.

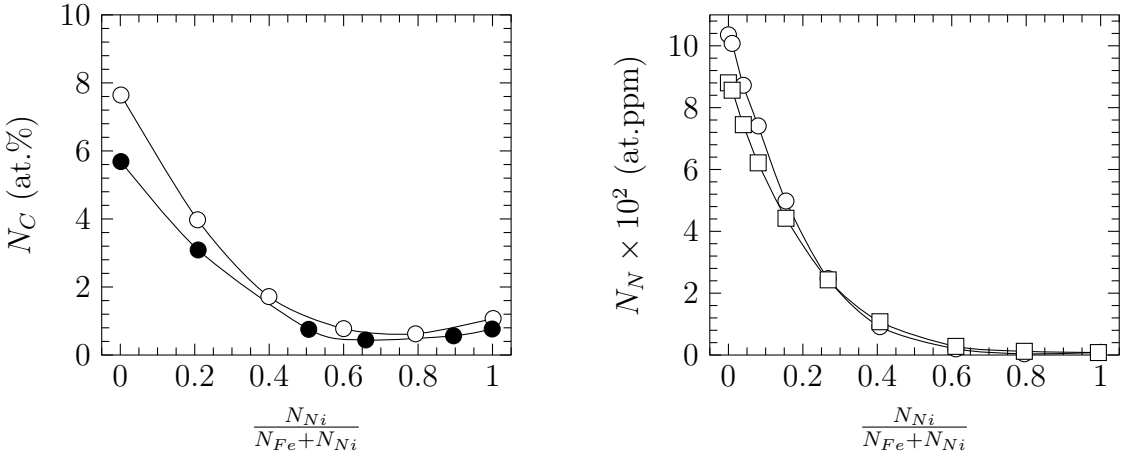

(a) Carbon solubility in Fe-Ni alloys at 1,000°C for gasses with different carbon activities: $a_c = 1$ (–○–), $a_c = 0.693$ (–●–)

(b) Nitrogen solubility in Fe-Ni alloys under 1 atm of N_2 at 1,000°C (–○–) and 1,217°C (–□–)

Figure 3.6: Solubility at high temperature of carbon [111] and nitrogen [112] in Fe-Ni alloys measured in various conditions.

3.1.3 Oxygen solubility measured in H_2/H_2O gases

The oxygen solubility in Fe, Ni and Fe-Ni alloys was measured in environments containing water vapour and hydrogen, with the oxygen partial pressure set at the Fe/FeO equilibrium. Measurements were carried out at 1,050, 1,100 and 1,150°C, however due to technical difficulties faced during the experiment at 1,000°C, no sample was obtained to carry out oxygen measurement. In addition, as with experiments carried out in Rhines packs, it was considered that only aluminium and titanium impurities formed thermodynamically stable oxides. In Figure 3.7, excess Gibbs free energy determined from oxygen concentration measurements and Equation (3.6) is presented. Figure 3.7 shows that the excess Gibbs free energy varies linearly with the temperature as predicted by Equation (3.4).

Values of $\overline{H}_O^{xs}$ and $\overline{S}_O^{xs}$ were determined using the non-linear fitting method presented in Section 3.1.2 with Equation (3.9), and values found are presented in Table 3.3 along with the correlation factor, r, determined during the fit. In addition, those values are plotted as a function of alloy composition in Figure 3.8.

Table 3.3: Excess enthalpy and Entropy for oxygen dissolution from H_2/H_2O gases containing 13% water vapour with the oxygen partial pressure set at the Fe/FeO dissociation pressure.

$\frac{N_{Ni}}{N_{Fe}+N_{Ni}}$	$\overline{H}_O^{xs}$ kJ mol^{-1}	$\overline{S}_O^{xs}$ J mol^{-1} K^{-1}	r
0	-276 ± 36	-139 ± 26	0.9996
0.2	-329 ± 62	-188 ± 46	0.9996
0.4	-331 ± 38	-196 ± 37	0.9996
0.6	-374 ± 68	-231 ± 50	0.9997
0.8	-262 ± 99	-155 ± 72	0.9996
1	-277 ± 77	-164 ± 56	0.9996

The excess enthalpy is found to decrease from -280 kJ mol^{-1}, measured in pure iron, to a minimum of about -400 kJ mol^{-1} found in the alloy of composition Fe-60Ni. When more nickel is added to the alloy composition, the excess enthalpy increases to reach a value of -280 kJ mol^{-1} in pure nickel. The excess entropy varies with the alloy composition in the same way as $\overline{H}_O^{xs}$. In iron the entropy found

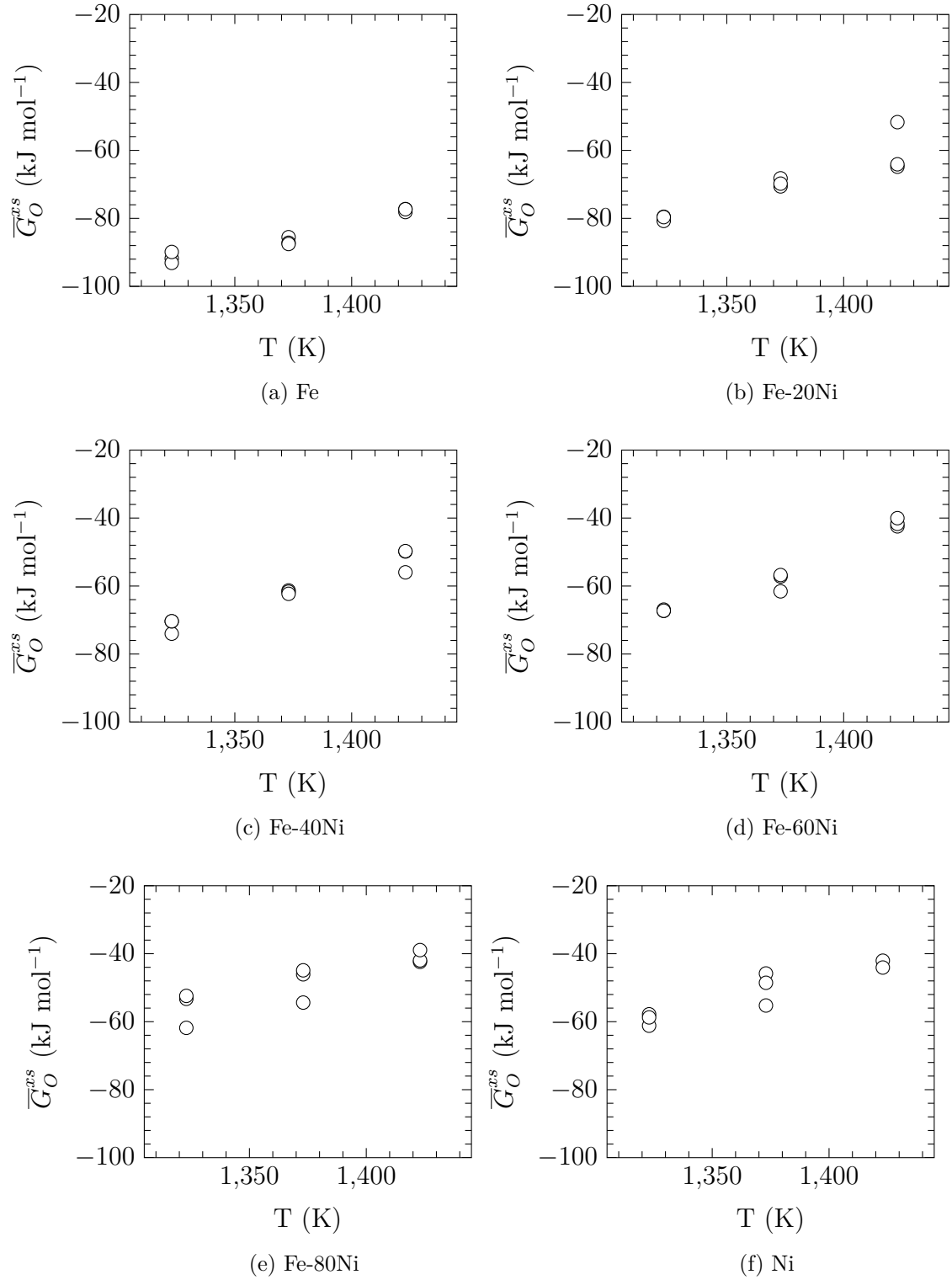

(a) Fe

(b) Fe-20Ni

(c) Fe-40Ni

(d) Fe-60Ni

(e) Fe-80Ni

(f) Ni

Figure 3.7: Excess Gibbs free energy evaluated from oxygen concentration measurement for different temperatures after reaction in H_2/H_2O gases containing 13% water vapour with the oxygen partial pressure set at the Fe/FeO equilibrium.

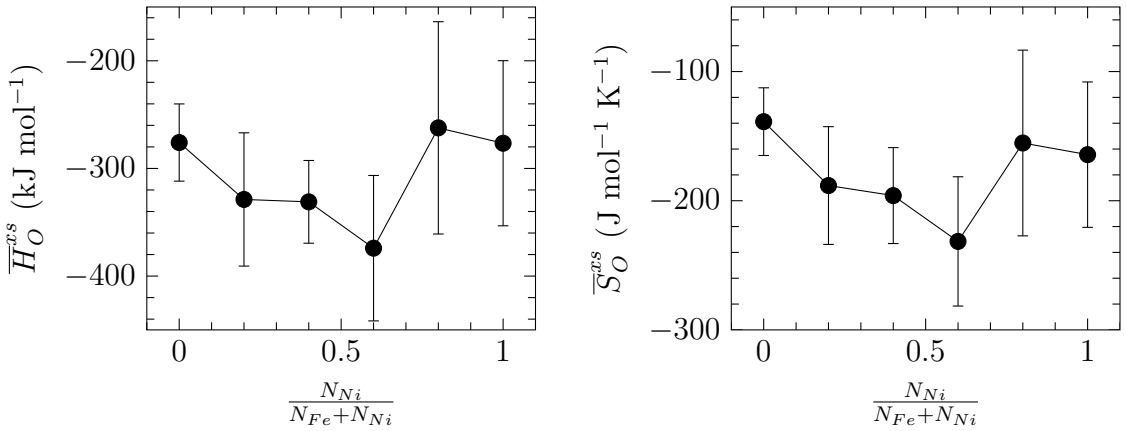

(a) $\overline{H}_O^{xs}$ (b) $\overline{S}_O^{xs}$

Figure 3.8: Variation of excess enthalpy and entropy with the alloy composition after exposure in H_2/H_2O gases containing 13% water vapour and the oxygen partial pressure set at the Fe/FeO dissociation pressure.

is around -140 J mol^{-1} K^{-1} and decreases to reach a minimum in Fe-60Ni alloys around -240 J mol^{-1} K^{-1}. Then, the excess entropy increases to reach a value of -160 J mol^{-1} K^{-1} in pure nickel.

Values of excess enthalpy and entropy reported in Table 3.3 , allows the calculation of the excess Gibbs free energy using Equation (3.4). However, values of the correlation factor in Table 3.3 show that $\overline{H}_O^{xs}$ and $\overline{S}_O^{xs}$ are strongly correlated when estimated with the non linear fit. Therefore uncertainties in calculated values of $\overline{G}_O^{xs}$ were estimated with Equation (3.11). Values of $\overline{G}_O^{xs}$ calculated for different alloy compositions and temperatures are presented in Figure 3.9. It should be noted that $\overline{H}_O^{xs}$ and $\overline{S}_O^{xs}$ were evaluated for temperature from 1,050 to 1,150°C. Therefore, for a temperature of 1,000°C, values of excess Gibbs free energy were extrapolated with Equation (3.4). These values were not checked experimentally, but they were calculated for purposes of comparison with excess Gibbs free energy measured in Fe/FeO Rhines pack at 1,000°C. Figure 3.9 shows that the minimum value of $\overline{G}_O^{xs}$ is found in pure iron, and this energy increases with nickel addition to arrive at a maximum in Fe-80Ni and then slightly decreases to meet the excess Gibbs free energy measured in pure nickel.

From values of $\overline{H}_O^{xs}$ and $\overline{S}_O^{xs}$ given in Table 3.3, the oxygen solubility for the

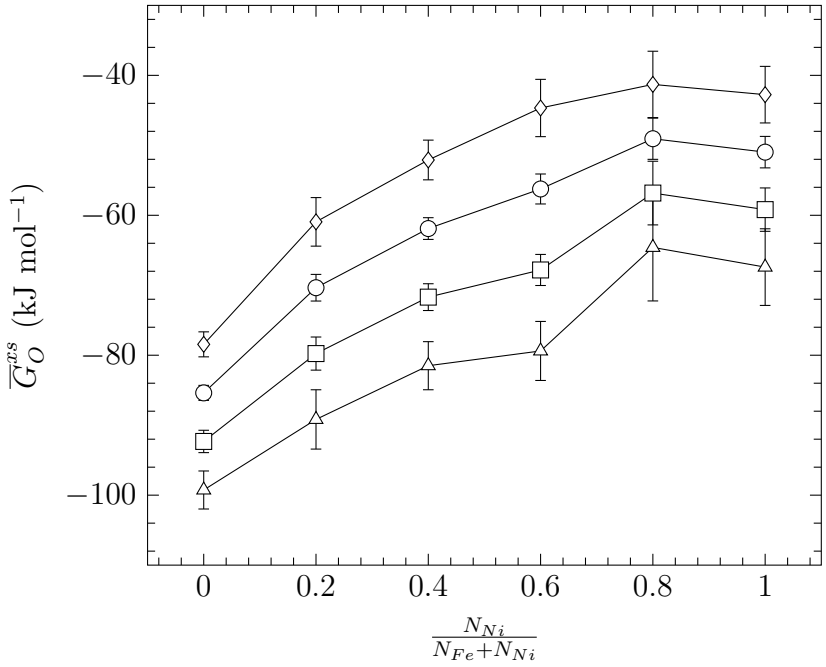

Figure 3.9: Variation of $\overline{G}_O^{xs}$ with the alloy composition, measured after exposure in H_2/H_2O gases containing 13% water vapour with the oxygen partial pressure set at the Fe/FeO equilibrium for several temperatures:
1,000°C (extrapolation) (–△–), 1,050°C (–□–), 1,100°C (–○–), 1,150°C (–◇–).

different alloys were calculated. It has to be noted that, as with the excess Gibbs free energy, values of oxygen solubility presented for 1,000°C are values calculated from higher temperature measurements and were not checked experimentally. Results of calculation are presented in Table 3.4 and plotted as a function of the alloy composition in Figure 3.10.

Table 3.4: Oxygen solubility values calculated using Equation (3.9) with values of $\overline{H}_O^{xs}$ and $\overline{S}_O^{xs}$ determined in H_2/H_2O gases containing 13% of water vapour and the oxygen partial pressure set at the Fe/FeO equilibrium pressure.

$\frac{N_{Ni}}{N_{Fe}+N_{Ni}}$	N_O (at.ppm) 1,000°C	1,050°C	1,100°C	1,150°C
0	412 ± 106	397 ± 58	381 ± 36	365 ± 55
0.2	159 ± 64	127 ± 27	102 ± 17	83 ± 24
0.4	77 ± 25	61 ± 11	49 ± 7	39 ± 9
0.6	63 ± 25	43 ± 9	30 ± 6	21 ± 7
0.8	16 ± 11	16 ± 6	16 ± 4	16 ± 6
1	20 ± 10	19 ± 5	19 ± 4	18 ± 6

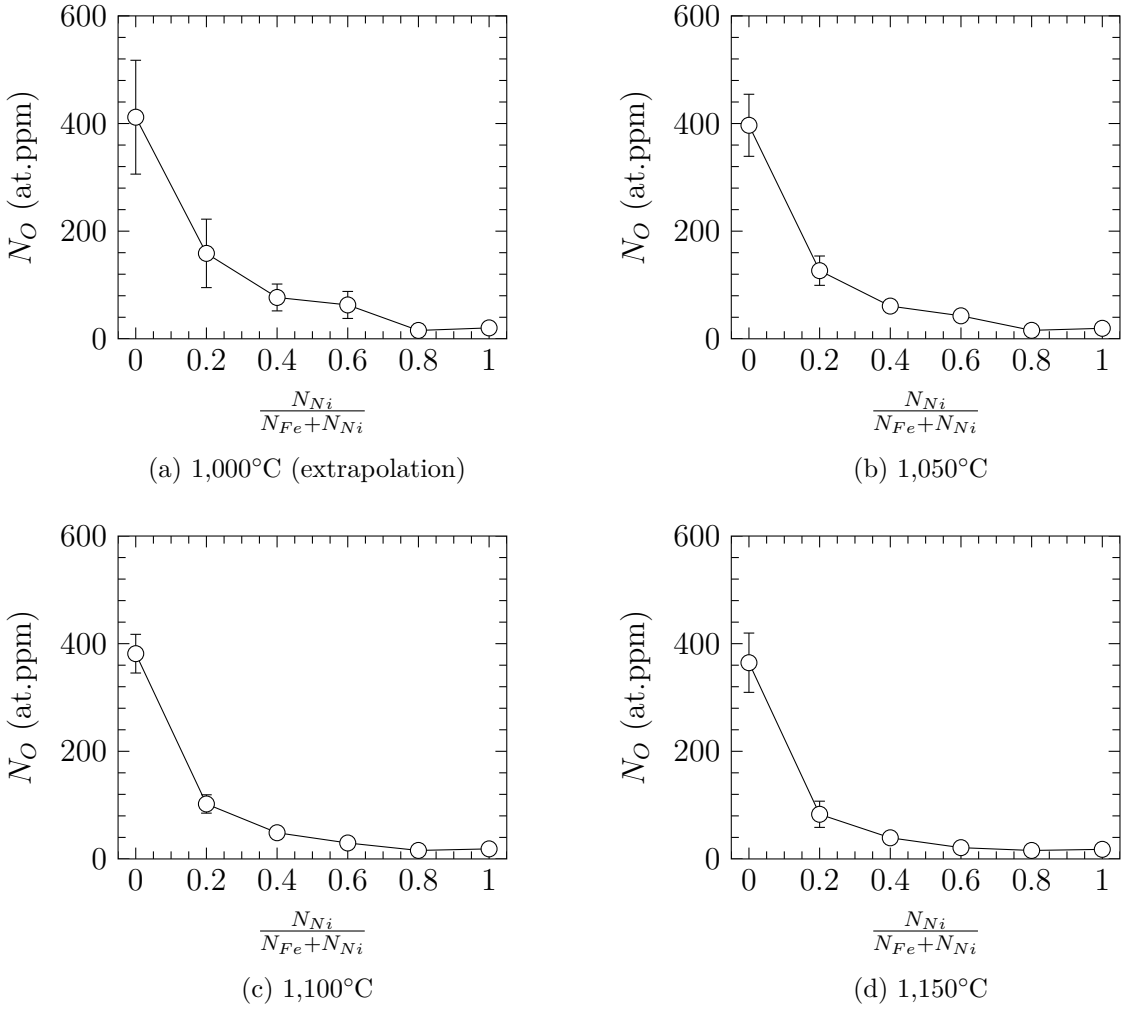

(a) 1,000°C (extrapolation)

(b) 1,050°C

(c) 1,100°C

(d) 1,150°C

Figure 3.10: Variation of the oxygen solubility with the alloy composition. Sample exposed to H_2/H_2O gases containing 13% water vapour and the oxygen partial pressure set at the Fe/FeO dissociation pressure.

As illustrated in Figure 3.10, the oxygen concentration decreases when the alloy composition changes from pure iron to pure nickel. The maximum of N_O is found in pure iron, and the minimum in pure nickel for all temperatures, with values of 400 and 20 at.ppm, respectively. Of particular note is a significant drop of 300 at.ppm observed between pure iron and the alloy Fe-20Ni.

3.2 Discussion on oxygen solubility in pure metals

No data for the oxygen solubility in Fe-Ni alloys are present in the literature but a few sets of data are available for pure iron and nickel.

3.2.1 Oxygen solubility in pure iron

The oxygen solubility in pure iron was measured by Swisher and Turkdogan [47] who carried out their experiments in H_2/H_2O gas mixtures with the oxygen partial pressure set slightly below the Fe/FeO equilibrium. In Figure 3.11, the excess Gibbs free energy calculated from the Swisher and Turkdogan measurement is plotted along with values measured in this study. In addition, values of $\overline{H}_O^{xs}$ and $\overline{S}_O^{xs}$ are given in Table 3.5. Figure 3.11 shows that the Gibbs free energies measured

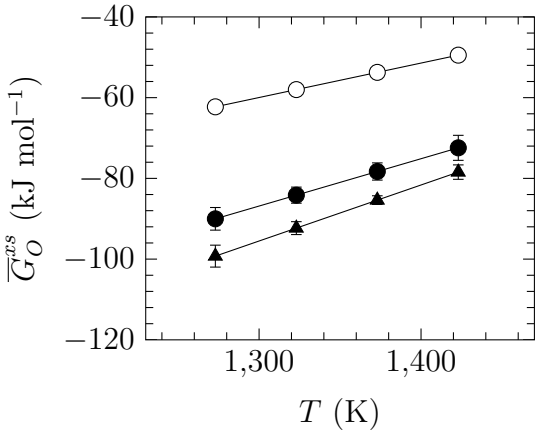

Figure 3.11: Excess Gibbs free energy for oxygen dissolution in pure Fe. [47] (–○–), this study RP (–●–), H_2/H_2O (–▲–).

Table 3.5: Excess enthalpy and entropy for oxygen dissolution in iron.

$\overline{H}_O^{xs}$ kJ mol^{-1}	$\overline{S}_O^{xs}$ J mol^{-1} K^{-1}	Ref.
-175	-87	[47]
-238 ± 38	-116 ± 28	RP
-276 ± 36	-139 ± 26	H_2/H_2O

in this study are found to be lower than $\overline{G}_O^{xs}$ measured by Swisher and Turkdogan. In addition, the largest difference appears to be between data measured in H_2/H_2O gases, although the environment used by Swisher and Turkdogan was similar. However, a few points are enigmatic in Swisher and Turkdogan's work. First of all, after their experiments, authors had to remove an oxide scale prior to analysing their samples for oxygen concentration. It is not clearly stated if this scale grew during the equilibration at high temperature or during the quenching. However, it is more likely that the scale formed during quenching, because oxygen partial pressures set by Swisher and Turkdogan in their experiments were slightly lower than the Fe/FeO equilibrium. The second questionable point is the time required for the equilibration of their sample. The authors used rods with a diameter of 7.6 mm as samples, and

exposed them to H_2/H_2O gas for 18h at 1,350°C and 1 week at 881°C. The time required for the equilibration of their samples is examined below.

Crank [103] derived Equation (3.13) to calculate the ratio of material diffused into a cylinder after time t, M_t, to the corresponding quantity after an infinite time, M_∞.

$$\frac{M_t}{M_\infty} = 1 - \sum_{n=1}^{\infty} \frac{4}{a^2 \alpha_n^2} \exp\left(-D_O \alpha_n^2 t\right) \tag{3.13}$$

Here a is the radius of the cylinder, D_O the oxygen diffusion coefficient and α_n are the roots of the Bessel function of the first kind of order zero given by

$$J_0\left(a\alpha_n\right) = 0 \tag{3.14}$$

To calculate the maximum time required for the equilibration of the cylinder, oxygen diffusion coefficient values measured by Takada *et al.* [40] in iron were employed. These authors evaluated the true oxygen diffusion coefficient in pure iron by taking into account the effect of the fast oxygen diffusion at internal matrix/oxide interfaces taking place during internal oxidation experiments. In addition, Takada *et al.* used Swisher and Turkdogan's solubility to calculate the oxygen diffusion coefficient from their own permeability experiments. However, the solubility measured in the present study is one order of magnitude higher than that measured by Swisher and Turkdogan. Therefore, Takada *et al.*'s diffusion coefficient estimated in their way was about 1 order of magnitude too high. In addition, the radius of the cylinder was taken equal at 0.38 cm and it yields $\alpha_1 = 16.7$ and $\alpha_2 = 38.2$. In Table 3.6, values used to calculate the ratio $\frac{M_t}{M_\infty}$ and results of the calculation are given.

Table 3.6: Calculation of $\frac{M_t}{M_\infty}$ with oxygen diffusion coefficient published by Takada *et al.* [40] and corrected for higher oxygen solubility. Times correspond to those used by Swisher and Turkdogan.

Temperature °C	D_O $cm^2\ s^{-1}$	time hour	$\frac{M_t}{M_\infty}$
1,350	6×10^{-7}	18	0.86
881	4×10^{-9}	168	0.3

Results of the calculation showed that even at the highest temperature, the exposure duration used to equilibrate samples in Swisher and Turkdogan's [47] experiments are insufficient. These authors did not report any diffusion calculation, and it is difficult to evaluate their choice of exposure times. What is known is that they measured oxygen permeability using Fe-Al alloys. As is now well known, this system exhibits enhanced oxygen diffusion resulting from aligned precipitate-matrix interfaces (Section 1.4). Values of D_O deduced in this way are consequently significantly higher than the alloy matrix oxygen diffusion coefficient which is required. Values of the pre-exponential factor and activation energy determined by Swisher and Turkdogan [47] to estimate the oxygen diffusion coefficient are given in Table 1.12. With their diffusion coefficient, Swisher and Turkdogan found that their experimental durations were long enough to reach the equilibrium in their sample, as shown in Table 3.7. From values of the oxygen diffusion coefficient shown in

Table 3.7: Calculation of $\frac{M_t}{M_\infty}$ with oxygen diffusion coefficient published by Swisher and Turkdogan [47].

Temperature °C	D_O $cm^2\ s^{-1}$	time hour	$\frac{M_t}{M_\infty}$
1,350	1.93×10^{-5}	18	1
881	1.4×10^{-6}	168	1

Tables 3.6 and 3.7, it is clear that Swisher and Turkdogan overestimated this parameter due to the low solubility they measured, and also because they measured the effective diffusion coefficient of oxygen instead of the true oxygen diffusion coefficient. This overestimation of the oxygen diffusion coefficient and the consequently inadequate exposition duration is a contributing factor to the low oxygen solubility measured in Swisher and Turkdogan's experiments.

3.2.2 Oxygen solubility in nickel

Oxygen solubility was also measured in pure nickel, and three sets of data exist in the literature. The first values were measured by Seybolt [78] who oxidised nickel to form a scale of a nickel oxide scale and then let the sample equilibrate under an inert atmosphere. Later, Alcock and Brown [71] measured the oxygen solubility by a thermogravimetric technique with a mixture of CO/CO_2 to fix the oxygen partial pressure at the Ni/NiO equilibrium pressure. More recently, Park and Alstetter [80] used an electrochemical method to measure the oxygen solubility with the oxygen activity equivalent to the Ni/NiO dissociation pressure. However, Park and Alstetter are the only authors to report values of $\overline{H}_O^{xs}$ and $\overline{S}_O^{xs}$, while only values of oxygen solubility were available from works of Seybolt [78] and Alcock and Brown [71]. Therefore, to estimate the excess enthalpy and entropy from solubility measurement carried out by Seybolt and Alcock and Brown, the non linear fitting of Equation (3.9) presented in Section 3.1.2 was used. Then, values of $\overline{G}_O^{xs}$ were calculated with Equation (3.4) from values of $\overline{H}_O^{xs}$ and $\overline{S}_O^{xs}$.

In Figure 3.12 and Table 3.8, the excess Gibbs free energy values measured in the different works are plotted versus temperature, and excess enthalpy and entropy are listed. Uncertainties in $\overline{H}_O^{xs}$ and $\overline{S}_O^{xs}$ for values from Seybolt and Alcock and Brown were determined during the non linear fit using the module SolverAid in Excel [110].

Figure 3.12 shows that $\overline{G}_O^{xs}$ measured in this study is lower than values measured by the previous authors [71, 78, 80]. To compare $\overline{H}_O^{xs}$ and $\overline{S}_O^{xs}$ it should be emphasised that due to the strong correlation of excess enthalpy and entropy, these values cannot be compared individually but they have to be considered as a solution couple. For example, the excess entropy measured in H_2/H_2O gases is in good agreement with the excess entropy measured by Seybolt and Aclcok and Brown. However, the average values of excess enthalpy measured in H_2/H_2O is almost 30 kJ mol^{-1} higher than values measured by Seybolt and Alcock and Brown. Therefore, values of $\overline{G}_O^{xs}$ are different when calculated from $\overline{H}_O^{xs}$ and $\overline{S}_O^{xs}$. However, comparing data

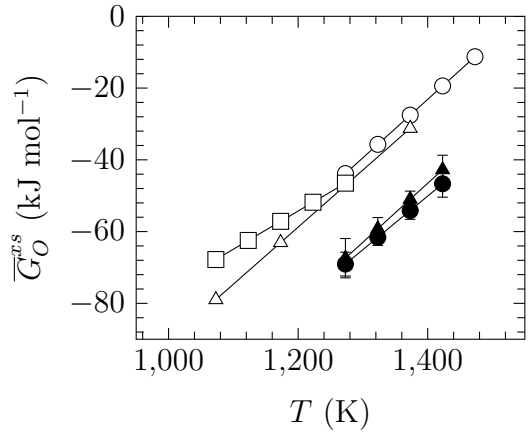

Figure 3.12: Excess free energy for oxygen dissolution in pure Ni, (open symbol) p_{O_2} =Ni/NiO, (filled symbol) p_{O_2} =Fe/FeO. [78] (–○–),[71] (–△–),[80] (–□–), this study RP (–●–), H_2/H_2O (–▲–).

Table 3.8: Excess enthalpy and entropy for oxygen dissolution in nickel.

$\overline{H}_O^{xs}$ kJ mol^{-1}	$\overline{S}_O^{xs}$ J mol^{-1} K^{-1}	Ref.
-250 ± 1	-159 ± 1	[78]
-251 ± 5	-163 ± 3	[71]
-182	-106	[80]
-259 ± 50	-149 ± 37	RP
-277 ± 77	-164 ± 56	H_2/H_2O

found from Seybolt and Alcock's experiments, good agreement is found between excess enthalpy and entropy and therefore values of $\overline{G}_O^{xs}$ are similar for these authors. It is difficult to assess the agreement of $\overline{H}_O^{xs}$ and $\overline{S}_O^{xs}$ between the different studies, and it is more useful to compare values of excess Gibbs free energy. The differences in excess Gibbs free energy are difficult to explain because the assumption of a dilute solution should be valid for all studies. However, the major difference between previous measurements and the present study is that experiments for oxygen solubility in nickel were carried out at the Ni/NiO dissociation pressure in the past, whereas the new data obtained were measured at the Fe/FeO equilibrium. In the range 1,000-1,150°C, the difference between the dissociation pressures of Ni/NiO and Fe/FeO is 4 orders of magnitude. In addition, difference in excess Gibbs free energy measured at the Ni/NiO and Fe/FeO dissociation pressure shown in Figure 3.12 suggests that the Sievert constant given by

$$K^{(s)} = \exp\left(\frac{-\overline{G}_O^{xs}}{RT}\right) \tag{3.15}$$

may not be independent of the oxygen partial pressure.

Furthermore, recent DFT calculations [93] show that the nature of defects

in pure nickel in equilibrium with O_2 depends of the temperature and the oxygen concentration, and therefore the oxygen partial pressure. Calculations show that at high temperature and low oxygen concentration all the oxygen dissolved in nickel is in interstitial position. However, if the oxygen partial pressure increases, defects composed of 1 vacancy and 1 oxygen start to form. Interstitial oxygen is stable in octahedral site and the formation energy is 44 kJ mol^{-1} while the insertion of one oxygen next to a vacancy required an energy of 72 kJ mol^{-1}. Therefore, excess enthalpy in the case of defect oxygen-vacancy (V-O) would be larger and may results in larger values of $\overline{G}_O^{xs}$. However, it has to be emphasised that the entropy associated with the defect is unknown. Therefore, the effect of the type of defect in nickel on the excess Gibbs free energy is difficult to assess but could be considered as one explanation for discrepancies between $\overline{G}_O^{xs}$ measured at the Fe/FeO and Ni/NiO equilibrium pressures and would require further study.

3.3 Effect of water vapour on the oxygen solubility

The oxygen solubility in various materials was measured in dry and wet atmospheres to investigate the effect of water vapour and/or hydrogen on the oxygen solubility. However, it should be noted that Fe/FeO Rhines packs (considered as the dry environment) are never completely free of water vapour (which comes from the silica) and therefore never free of hydrogen according to the following reaction

$$H_2 + \frac{1}{2}O_2 \rightarrow H_2O \tag{3.16}$$

with an equilibrium constant

$$K_{3.16} = \frac{p_{H_2O}}{p_{H_2} p_{O_2}^{1/2}} \tag{3.17}$$

In an Fe/FeO Rhines pack, the oxygen partial pressure is set by the equilibrium metal/metal oxide. Therefore for a given temperature, the ratio $\frac{p_{H_2O}}{p_{H_2}}$ is fixed. In Table 2.6 of Section 2.3, the standard free energy of reaction 3.16 is given and values of $\frac{p_{H_2O}}{p_{H_2}}$ were calculated with Equation (3.17).

The solubility of water in silica glass at high temperature and under low pressure has been investigated by Moulson *et al.* [113] and Shackelford *et al.* [114]. These authors observed that the water solubility varies with the square root of the water vapour partial pressure suggesting that water is incorporated to silica as a dissociate molecule. Therefore, the water solubility in silica glass follows Sievert's law. From solubility measurements carried out by Moulson *et al.* [113] and Shackelford *et al.* [114], the Sievert constant was evaluated and results showed that between 1,000 and 1,150°C, $K^{(s)}$ is almost constant at a value of 3.2×10^{-3}.

In the Fe/FeO Rhines pak, p_{H_2O} is fixed by the silica water content. Generally, silica contains around 100 at.ppm of water [115] and this value was used to estimate the water vapour partial pressure in the Fe/FeO Rhines. Using Sievert's law

$$K^{(s)} = \frac{N_{H_2O}}{p_{H_2O}^{1/2}} \tag{3.18}$$

with the value of the Sievert constant evaluated from Moulson and Shackelford's experiments and $N_{H_2O} = 100$ at.ppm for water dissolved in silica, the water vapour partial pressure found is $p_{H_2O} = 9.6 \times 10^{-4}$ atm. Finally, the hydrogen partial pressure was estimated using the value of p_{H_2O} in Equation (3.17). Results of the calculation are presented in the Table 3.9.

Table 3.9: Calculation of hydrogen partial pressure in Fe/FeO Rhines packs.

Temperature °C	$p_{O_2}^{Fe/FeO}$ atm	$\frac{p_{H_2O}}{p_{H_2}}$	$p_{H_2} \times 10^3$ atm
1,000	12×10^{-15}	0.64	1.5
1,050	8×10^{-15}	0.68	1.4
1,100	4.6×10^{-14}	0.72	1.3
1,150	2.3×10^{-13}	0.75	1.3

The lowest hydrogen partial pressure used for an experiment in flowing H_2/H_2O gas mixtures was 0.17 atm, 2 orders of magnitude larger than the hydrogen partial pressure in a Rhines packs, and the same difference was observed between water vapour partial pressure in Rhines packs and H_2/H_2O gas mixtures. Therefore, it was considered that water vapour and hydrogen partial pressure in Rhines packs has no effect on measurements carried out with this method.

The excess Gibbs free energy measured in Fe/FeO Rhines packs and H_2/H_2O gases are compared in Figure 3.13. The Figures shows that $\overline{G}_O^{xs}$ exhibits essen-

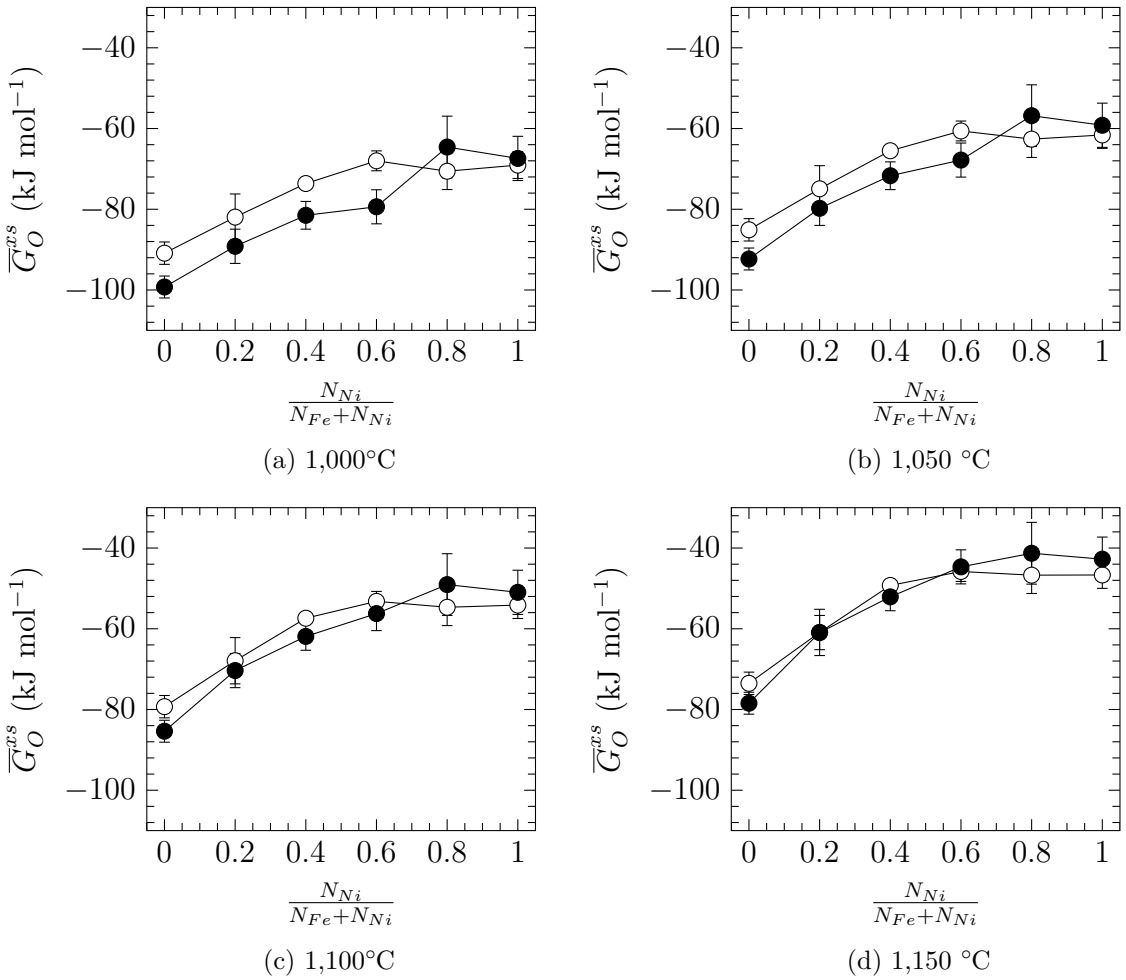

(a) 1,000°C (b) 1,050 °C

(c) 1,100°C (d) 1,150 °C

Figure 3.13: Comparison of the excess of Gibbs free energy for oxygen dissolution in pure Fe, Ni and several Fe-Ni alloys measured in Fe/FeO Rhines packs (–○–) and H_2/H_2O gases containing 13 % water vapour and oxygen partial pressure set at the Fe/FeO equilibrium (–●–).

tially the same change with the alloy composition whether it is measured in wet or dry environment. At 1,150°C, values of $\overline{G}_O^{xs}$ are similar in Fe/FeO Rhines Packs

and H_2/H_2O gases. However, in alloys with nickel content lower than 80 at.%, when the temperature decreases, $\overline{G}_O^{xs}$ measured in H_2/H_2O gases is found to be lower than values measured in Fe/FeO Rhines packs. In addition, the difference between excess Gibbs free energy values measured in both environments increases as the temperature decreases. These differences between $\overline{G}_O^{xs}$ found when alloys are exposed to dry or wet atmospheres correspond to different oxygen solubility as illustrated in Figure 3.14.

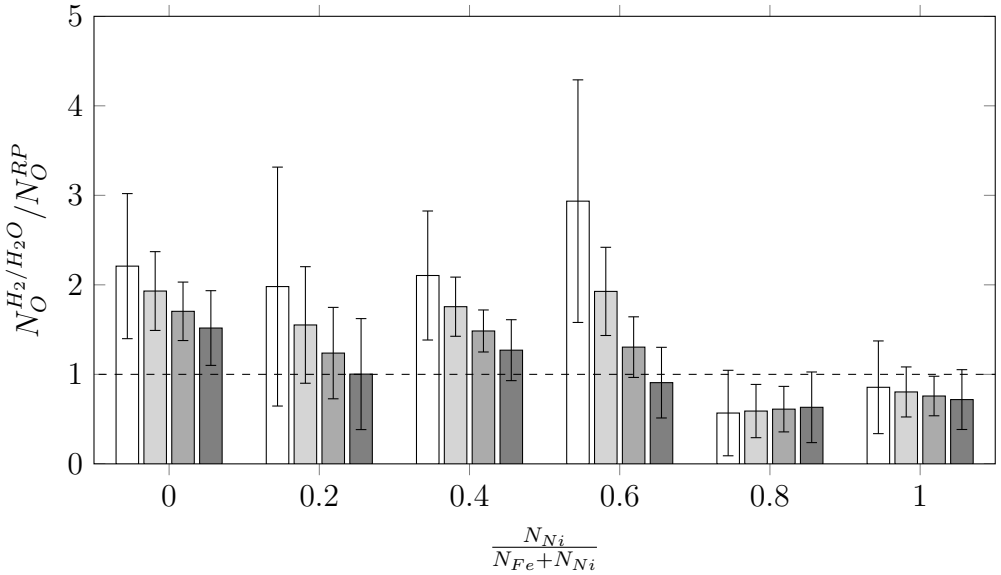

Figure 3.14: Comparison of oxygen solubility calculated from Gibbs free energy measured in Fe/FeO Rhines pack,N_O^{RP} and H_2/H_2O gas mixtures ,$N_O^{H_2/H_2O}$ at different temperature: 1,000°C (▯▯), 1,050°C (▯▯), 1,100°C (▮▮), 1,150°C (▮▮).

Figure 3.14 shows that for alloys with a nickel content lower than 80 at.%, the oxygen solubility is larger in H_2/H_2O gases than in Fe/FeO Rhines packs, and the difference between solubilities diminishes as the temperature increases. In pure nickel, the oxygen solubility measured in the dry environment is generally higher than values measured in wet conditions and the difference between solubility values increases with temperature. The oxygen solubility measured for the alloy with the composition Fe-80Ni does not exhibit any influence of the temperature on the ratio $N_O^{H_2/H_2O}/N_O^{RP}$. In addition, at this composition the oxygen solubility is always higher when measured after exposure in a dry environment than when samples were exposed to humid gases. Overall, the water vapour and/or hydrogen have an effect

on the excess Gibbs free energy of oxygen dissolution for alloys with a nickel content lower than 80 at.%. In addition, the effect of water vapour and/or hydrogen in iron-rich alloys appears to be more significant at lower temperature. In pure nickel, the presence of water vapour and hydrogen seems to slightly decrease the energy for the oxygen dissolution. However, it should be noted that the uncertainties in solubilities are large compared to the ratio charted in Figure 3.14, particularly for pure nickel.

3.4 Prediction of oxygen solubility in binary alloy

As reviewed in the first chapter of this thesis, two basic models to predict the oxygen solubility in binary alloy are available in the literature: the Quasichemical model of Alcock and Richardson [71] and a model proposed by Wagner [72]. The first authors gave the following expression to calculate the oxygen activity coefficient in a binary alloy

$$\gamma_O^{Fe-Ni} = \left[N_{Fe} \left(\frac{\gamma_{Fe}^{Fe-Ni}}{\gamma_O^{Fe}} \right)^{\frac{1}{Z}} + N_{Ni} \left(\frac{\gamma_{Ni}^{Fe-Ni}}{\gamma_O^{Ni}} \right)^{\frac{1}{Z}} \right]^{-Z} \tag{3.19}$$

where γ_O^{Fe-Ni}, γ_O^{Fe} and γ_O^{Ni} are the oxygen activity coefficient in the binary Fe-Ni, Fe and Ni. The parameters γ_{Fe}^{Fe-Ni} and γ_{Ni}^{Fe-Ni} are activity coefficients of iron and nickel in binary Fe-Ni and Z the coordination number taken equal to 6 for the oxygen interstitial solute in a FCC phase. To test this model, values of iron and nickel activity coefficients were taken from [116], and the activity coefficient of oxygen in pure iron and nickel was calculated using the relation

$$RT \ln \left(\gamma_O^{Fe-Ni} \right) = \overline{G}_O^{xs} \tag{3.20}$$

Finally, the oxygen solubility in Fe-Ni was calculated using the following relation

$$N_O = \frac{p_{O_2}^{1/2}}{\gamma_O^{Fe-Ni}} \tag{3.21}$$

The second model tested is that proposed by Wagner [72], who expressed the relationship between the different activity coefficients of the different species by the following equation

$$\gamma_O^{Fe-Ni} = \left\{ \sum_{i=0}^{i-Z} \binom{Z}{i} \left[\frac{(1-N_{Fe})}{(\gamma_O^{Ni})^{\frac{1}{Z}}} \right]^{Z-i} \times \left[\frac{N_{Fe}}{(\gamma_O^{Fe})^{\frac{1}{Z}}} \right]^{i} \exp\left[\frac{(Z-i)ih}{2RT} \right] \right\}^{-1} \tag{3.22}$$

where $\binom{Z}{i}$ is the binomial factor. Wagner's model is built on energetic consideration. Indeed, Wagner considered the move of one oxygen atom from an interstitial site surrounded by (Z-i) nickel and i iron atoms to an interstitial site surrounded by (Z-1-i) nickel and (i+1) iron. The change of enthalpy related to this jump is denoted $\Delta H(i \rightarrow i+1)$. It has to be emphasised that Wagner considered no thermal entropy in his model, therefore the variation in enthalpy is equivalent to variation of Gibbs free energy. In addition, Wagner considered that this variation of energy is increasing by a constant quantity,h, when one atom is changed in the solvation shell of the oxygen and the following relations are found for the successive enthalpy changes

$$\Delta H(i=0 \rightarrow i=1) < \Delta H(i=1 \rightarrow i=2) \text{ etc} \tag{3.23}$$

$$\Delta H(i+1 \rightarrow i+2) - \Delta H(i \rightarrow i+1) = h \tag{3.24}$$

As the parameter h is unknown, it is estimated by fitting oxygen solubility from experimental data to values calculated using the activity coefficient found from Equation (3.22). In Figures 3.15 and 3.16, oxygen solubility values calculated with both models are compared with experimental data obtained from Fe/FeO Rhines packs and H_2/H_2O gas experiments.

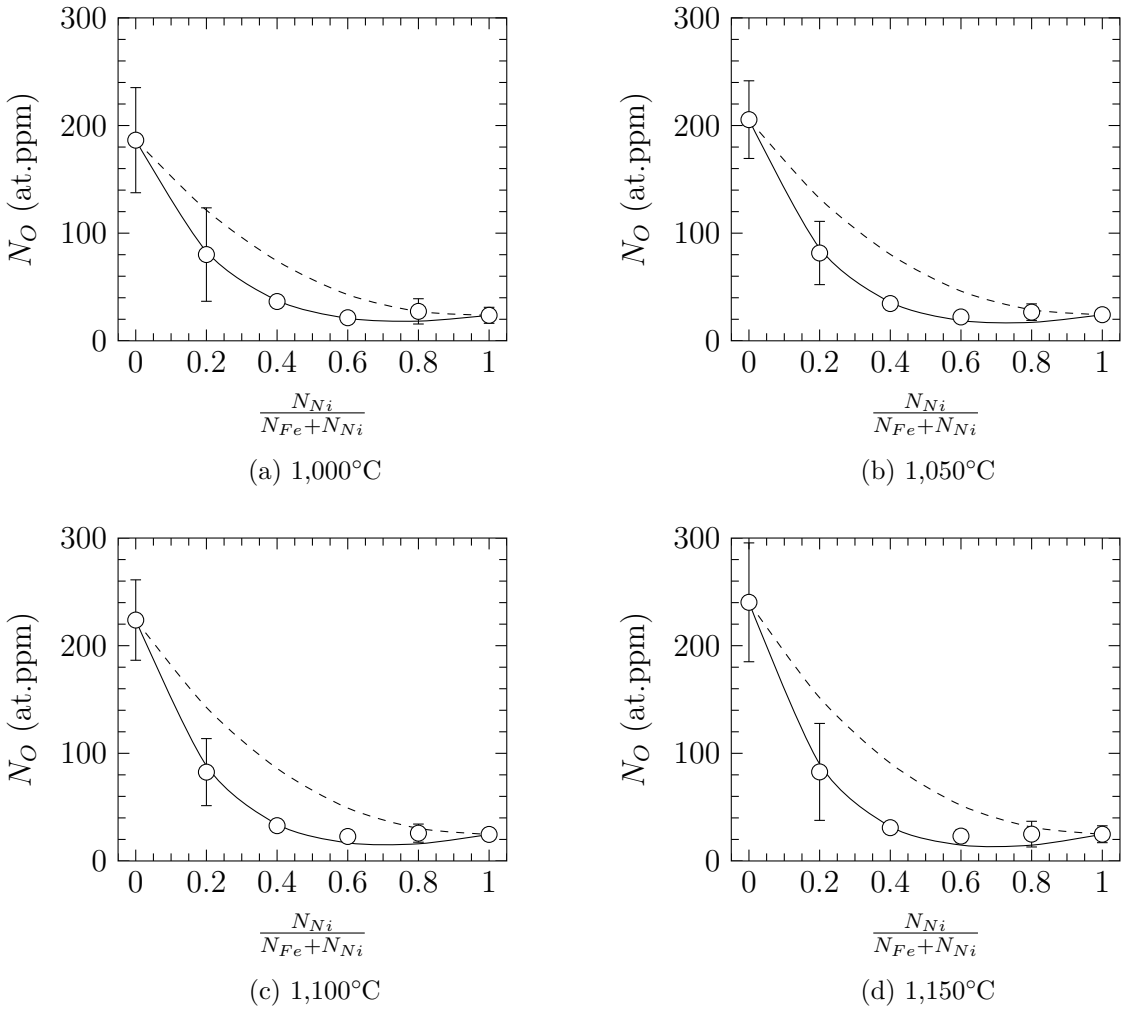

(a) 1,000°C (b) 1,050°C

(c) 1,100°C (d) 1,150°C

Figure 3.15: Oxygen solubility measured in Fe/FeO Rhines packs and calculated with Alcock and Richardson's model (- - -) and Wagner's model(——).

Figures 3.15 and 3.16 shows that in both environments the Alcock and Richardson model predicts the variation of oxygen solubility with the alloy composition reasonably well. However, the strong deviation from ideality observed in the experimental data is not well described by this model. On the other hand, Wagner's model with the adjustable parameter h describes very well the variation of oxygen solubility with alloy composition. Values of the parameter h found in the different environments and temperatures are presented in Table 3.10.

From the data in Table 3.10, it is observed that the parameter h decreases with increasing temperature. This variation is not predicted by Wagner's model because the author did not take into account the entropic term in his model [72], and h is defined as a difference of enthalpies and should be constant with the temperature,

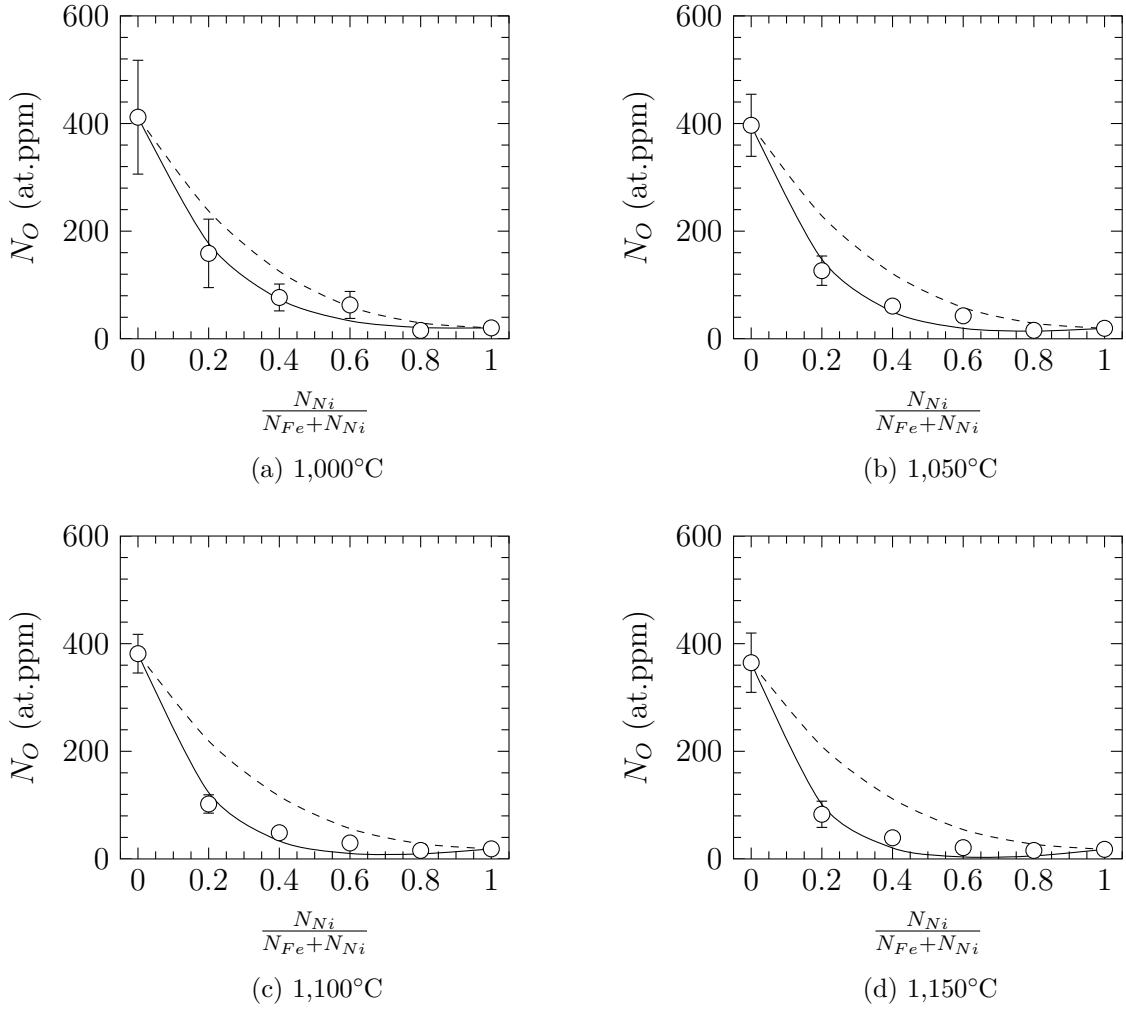

(a) 1,000°C (b) 1,050°C

(c) 1,100°C (d) 1,150°C

Figure 3.16: Oxygen solubility measured in H_2/H_2O gases and calculated with Alcock and Richardson model's (- - -) and Wagner's model(——).

under the assumption that enthalpies are independent of the temperature. In the present study, h was evaluated by fitting Equation (3.22) to γ_O^{Fe-Ni} values estimated from oxygen solubility measured with Equation (3.21). However, the activity coefficient γ_O^{Fe-Ni} has an entropic contribution as presented in Tables 3.1 and 3.3. Thus,

Table 3.10: Energetic parameter h (kJ mol^{-1}) evaluated by fitting solubility calculated with Eq.(3.22) to experimental solubility.

Temperature °C	Fe/FeO Rhines pack	H_2/H_2O
1,000	-3.1	-2.6
1,050	-3.7	-4.4
1,100	-4.4	-6.9
1,150	-5.2	-13.1

variation of h with the temperature, not predicted by Wagner's model, may results from the entropic contribution of γ_O^{Fe-Ni}, not considered in Wagner's development.

Values of h in Table 3.10 show that when the temperature increases, values measured in wet gases drop significantly compared to values found in Fe/FeO Rhines packs. Nevertheless, the value of h is strongly dependent on oxygen solubility measured in pure Fe and Ni. For Fe, the oxygen solubility in H_2/H_2O is larger than the solubility measured in Fe/FeO Rhines packs, while in nickel the oxygen solubility is equal in both environments. The large difference of solubility found in iron when samples are reacted in hydrogen-free atmosphere and H_2/H_2O gases reflects the disagreement observed for the energetic parameter h. It is seen from the results that an investigation of interactions among H, O and vacancies in iron could be useful.

3.5 Summary

Oxygen solubility in Fe-Ni alloys measured after reaction in Fe/FeO Rhines pack and H_2/H_2O gases containing 13% water vapour and the oxygen partial pressure set at the Fe/FeO equilibrium pressure, exhibits the same, non-ideal, dependency on alloy composition between 1,000 and 1,150°C. The maximum oxygen solubility is found in pure iron and decreases continuously to reach a minimum of solubility in pure nickel.

It was observed that oxygen solubility measured after exposure in dry and wet environments were similar at 1,150°C. However, when the temperature decreases, the oxygen solubility measured in alloys with nickel content less than 80 at.% is found to be higher after exposure in H_2/H_2O gases than in Fe/FeO Rhines pack. On the other hand, for pure nickel, no effect of water vapour on the oxygen solubility was observed at all temperatures investigated.

These results show that water vapour and/or hydrogen affect the oxygen solubility in alloys with nickel content up to 60 at.%, the effects being more significant at low temperature.

Oxygen solubility values measured in the present studies were compared to

values measured for iron and nickel in previous works. For iron, the only data available for oxygen solubility in the γ phase were measured by Swisher and Turkdogan, who used H_2/H_2O gas mixtures to set the oxygen partial pressure at the Fe/FeO equilibrium. However, their oxygen solubility is one order of magnitude lower than the oxygen solubility measured here. The low oxygen solubility reported by Swisher and Turkdogan is thought to be due to an insufficient time of exposure to equilibrate their samples.

For oxygen solubility in nickel, conclusions were made concerning values of the excess Gibbs free energy for oxygen dissolution, as previous studies were carried out at the Ni/NiO equilibrium pressure. Present results showed that the Gibbs free energy for oxygen dissolution measured at the Fe/FeO dissociation pressure is lower than when evaluated from experiment at the Ni/NiO equilibrium pressure. Therefore, the $\overline{G}_O^{xs}$ may be dependent of the oxygen partial pressure.

This hypothesis is supported by recent DFT calculations, showing that the type of defect in nickel is controlled by the temperature and the oxygen concentration in nickel, and thus the oxygen partial pressure. At high temperature and low oxygen partial pressure, the majority of oxygen atoms are in interstitial positions while if the oxygen partial pressure increases defects, composed of one oxygen atom and one vacancy start to form, and may change the energy for oxygen dissolution in metal.

For oxygen solubility measured in Fe-Ni alloys, two predictive models were tested. Results showed that Alcock and Richardson's model partially predicts the variation of the oxygen solubility with the alloy nickel content. However, Wagner's model predicts much better the variation of the oxygen solubility with the alloy composition, once the energetic parameter h is evaluated. The parameter h describes interactions of the interstitial oxygen with iron and nickel atoms. For this reason computational methods like first principle studies would be recommended to investigate variation of this parameter when hydrogen is present in the material, or the effect of vacancies on the oxygen solubility.

Chapter 4

Internal oxidation kinetics

This chapter has for its subject, the results of internal oxidation experiments carried out in Fe/FeO Rhines packs and under flowing H_2/H_2O gas. In the first part, internal oxidation kinetics determined by measuring the IOZ depth of samples reacted in Fe/FeO Rhines packs are presented.

The second part of this chapter is dedicated to internal oxidation kinetics measured in H_2/H_2O gases from IOZ depth or thermogravimetric analysis. It must be emphasized that, these different techniques were carried out in H_2/H_2O gases having different compositions, and special care is taken to compare kinetics measured in these different environments.

Finally, internal oxidation kinetics measured in water and hydrogen-free atmospheres are compared with data from flowing H_2/H_2O gas experiments. It must be noted that for all results stated here, the error given corresponds to two standard deviations.

4.1 Internal oxidation kinetics in Fe/FeO Rhines packs

4.1.1 Internal oxidation zone characterisation

The different microstructures observed in alloys reacted at 1,000°C in Fe/FeO Rhines packs are presented in Figure 4.1. The internal oxidation zone contained discrete oxide particles with no preferential orientation as shown in the Figure. In addition, grain boundaries are noticeable because they are totally oxidised as illustrated for Fe-20Ni-4Cr and Fe-20Ni-7.5Cr. However, for all compositions and temperatures, the IOZ depth under grain boundaries was equal to the depth of the IOZ within the grain. This observation suggests a type A kinetics regime for grain boundary diffusion. In that case, oxygen diffusion, which controls internal oxidation kinetics, is characterised by an effective diffusion coefficient. According to Hart [53]

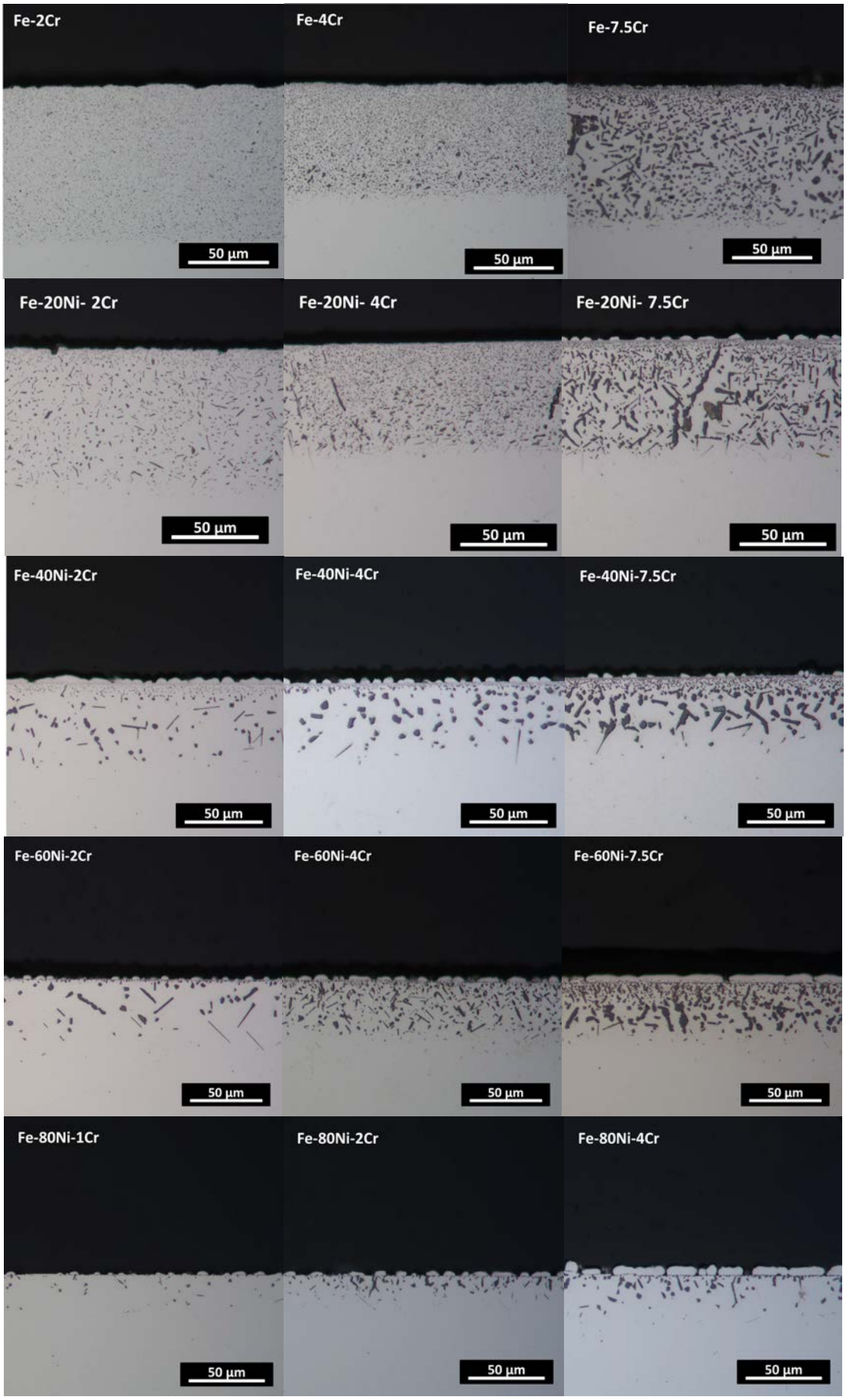

Figure 4.1: Micrographs of IOZ after exposure in Fe/FeO Rhines pack at 1,000°C: 48 h for Fe, Fe-20Ni, Fe-40Ni; 100 h for Fe-60Ni, Fe-80Ni.

this effective diffusivity is given by

$$D_O^{eff} = gD_O^{gb} + (1-g)D_O^g \tag{4.1}$$

which can be rewritten

$$\frac{D_O^{eff}}{D_O^g} = \frac{gD_O^{gb}}{D_O^g} + (1-g) \tag{4.2}$$

where D_O^{gb} is the oxygen diffusion coefficient at the grain boundary, D_O^g the oxygen diffusion coefficient within the grain and g a numerical factor equal to

$$g = \frac{\delta}{d} \tag{4.3}$$

with δ the width of a grain boundary and d the grain size. The smallest grain size observed after annealing was approximately 300 μm as reported in Table 2.4. In addition, considering that $\delta = 1$ nm it yields $g = 3 \times 10^{-6}$. The oxygen diffusion coefficient at the grain boundary and in the lattice for pure nickel was calculated by Nam *et al.* [89] using computational methods and the authors showed that oxygen diffusion coefficient at the grain boundary is 2 orders of magnitude higher than the oxygen diffusion coefficient for lattice diffusion. Using the previously estimated value of g yields

$$\frac{gD_O^{gb}}{D_O^g} = 3 \times 10^{-4} \tag{4.4}$$

Thus Equation (4.2) becomes

$$\frac{D_O^{eff}}{D_O^g} = 1 \tag{4.5}$$

and showed that the internal oxidation kinetics is controlled by the diffusion of oxygen within the grain and the contribution of oxygen diffusion at grain boundaries is negligible.

Oxide particle size and shape are seen to change with the alloy composition. It was observed that particles appear to be more spherical in low chromium and nickel content alloys. At a given temperature, it was always observed that the internal oxide size increases with increasing chromium and nickel alloy levels. However, no

effect of temperature on internal oxide shape and size was observed. It should also be noted that for a given composition, the internal oxide size changes with depth, as observed in Figure 4.1. Small spherical particles precipitate directly beneath the alloy surface and large particles are observed close to the internal oxidation front. This observation is in agreement with Böhm and Kahlweit [35], who predicted that the particle size increases with the IOZ depth. However, their model was developed assuming spherical particles, and they emphasised the fact that some deviations would be excepted after a certain depth because particles are more likely to have random shapes as they become larger.

In addition, for nickel-rich alloys, a discontinuous layer of material was noticed on the alloy surface, as observed for Fe-60Ni-7.5Cr and Fe-80Ni-4Cr alloys in Figure 4.1. Analysis with EDS showed that the discontinuous layer was made of pure matrix. The formation of a layer of pure matrix on alloy surface has already been observed by authors who carried out internal oxidation of Ni-Al/Cr alloys at high temperature in Ni/NiO Rhines packs.

The formation of this layer was investigated by Yi *et al.* [117] who proposed that the transport of matrix atoms to the alloy surface results from the large volume change taking place in the IOZ when internal oxides precipitate. The large volume change could enable Nabarro-Heering creep or diffusion of matrix atoms via dislocation pipes in the IOZ, resulting in the formation of a pure matrix layer on the alloy surface. For Fe-Ni-Cr alloys exposed to environments where the oxygen partial pressure is equal to the Fe/FeO equilibrium pressure, internal oxides likely to form are Cr_2O_3 or $FeCr_2O_4$, which have larger molar volumes (per unit Cr content) than Fe-Ni alloys. Therefore, a large volume expansion occurs when these oxides precipitates in the IOZ, and mechanisms proposed by Yi *et al.* explain the presence of the discontinuous matrix layer on the alloy surface.

Internal oxides in the IOZ were identified as $FeCr_2O_4$ and Cr_2O_3 using XRD and EDS measurements. The iron-chromium spinels were located beneath the alloy surface while chromium oxides were found close to the internal oxidation

front, as shown in Figure 4.2 where darker particles are chromium oxides and others iron-chromium spinel. The formation of two different oxides is due to the decrease of the oxygen activity through the IOZ.

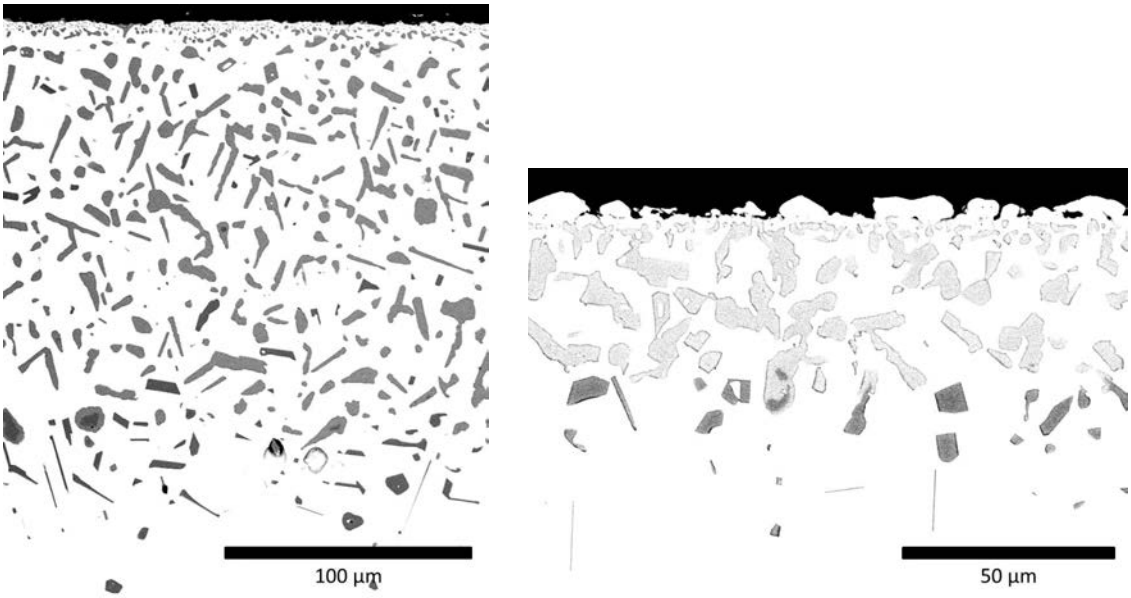

(a) Fe-7.5Cr (b) Fe-60Ni-7.5Cr

Figure 4.2: SEM observation of the IOZ after 48h of reaction at 1,150°C in Fe/FeO Rhines pack.

In addition, composite particles with an outer layer having the spinel composition and a core of Cr_2O_2, as illustrated in Figure 4.3, were observed in the IOZ. These particles show that the conversion of Cr_2O_3 into $FeCr_2O_4$ starts from the outside of the oxide particle. This has already been reported by Langelier *et al.* [118] for alloy 600 reacted at 480°C in H_2/H_2O gas with the oxygen partial pressure set below the Ni/NiO equilibrium.

The proportion of the two subzones, in each of which a specific oxide precipitates, was investigated by calculating the ratio f defined by

$$f = \frac{X_{(t)}}{X_{(i)}} \tag{4.6}$$

where $X_{(t)}$ is the depth where the transition between spinel and chromium oxide takes place. The depth $X_{(t)}$ was measured from SEM observations as illustrated in Figure 4.2.(b). However, f was only measured for alloys with 7.5 at.% of chromium because particles were large enough to be clearly identified as spinel or chromium

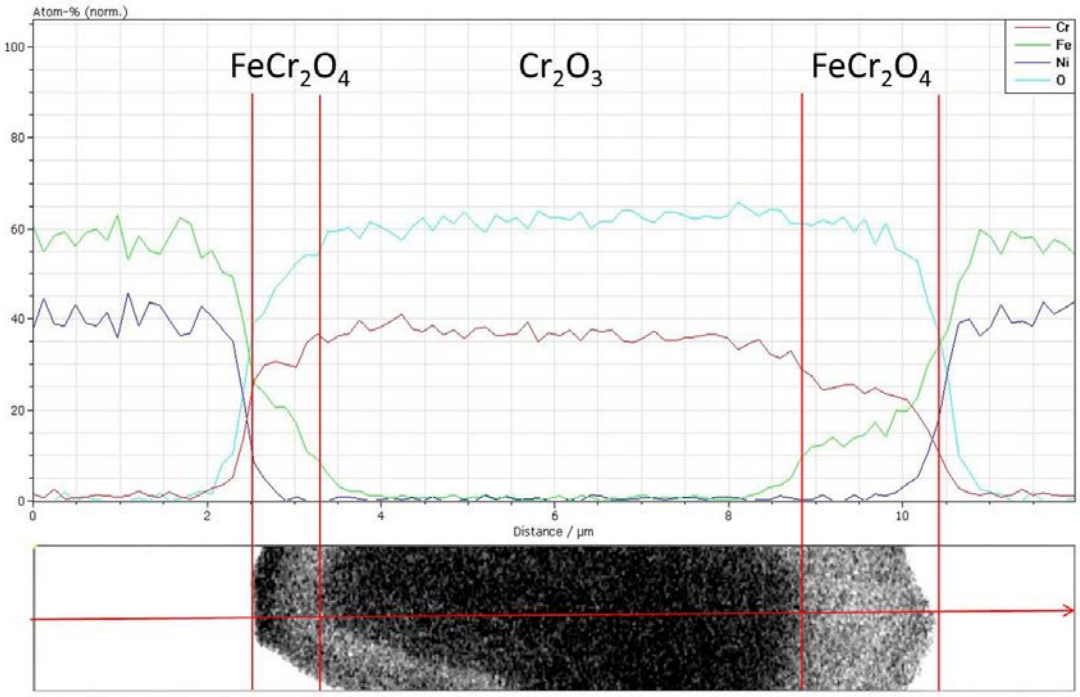

Figure 4.3: EDS scan in a composite oxide particle.

oxide. In addition, f was assumed independent of the time. In Table 4.1 measured values of f are presented. The error considered on these values was ±0.1. In

Table 4.1: f evaluated from measure of $X_{(t)}$ for alloys with 7.5 at.% Cr (4 at.% Cr for $\frac{N_{Ni}}{N_{Fe}+N_{Ni}}$=0.8) reacted in Fe/FeO Rhines packs. Error considered: ±0.1.

Temperature	$\frac{N_{Ni}}{N_{Fe}+N_{Ni}}$				
°C	0	0.2	0.4	0.6	0.8
1,000	0.87	0.83	0.65	0.69	0.40
1,050	0.89	0.86	0.67	0.67	0.40
1,100	0.86	0.73	0.66	0.73	0.41
1,150	0.86	0.73	0.69	0.70	0.42

Figure 4.4, values of f presented in Table 4.1 are plotted as a function of alloy composition. The Figure shows that f is not affected by the temperature except perhaps for alloys with a nickel content equal to 20 at.%. However, due to the large uncertainty in the evaluation of f, low values of f measured at 1,100 and 1,150°C for alloys with 20 at.% Ni were not considered as significant. It is clear that f decreases with the alloy nickel content suggesting that the iron-chromium spinel is less stable in nickel-rich alloys.

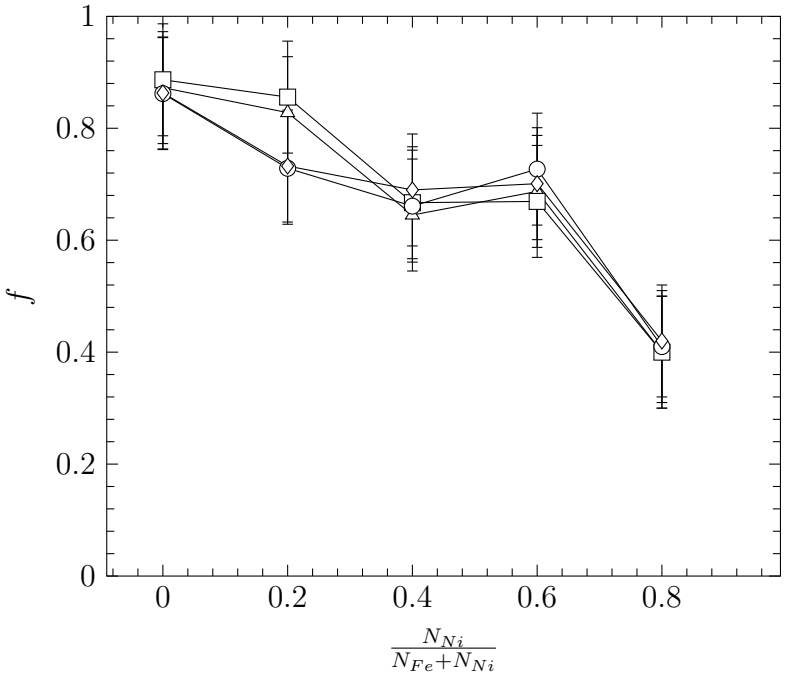

Figure 4.4: Variation of f with alloy nickel content. f measured for alloys with 7.5 at.% Cr reacted in Fe/FeO Rhines packs (4 at.% Cr for $\frac{N_{Ni}}{N_{Fe}+N_{Ni}}$=0.8). 1,000°C (–△–), 1,050°C (–□–), 1,100°C (–○–), 1,150°C (–◇–).

To investigate the variation of f with alloy composition, the formation reaction for iron-chromium spinel, taking place at $X = X_{(t)}$, was considered

$$Cr_2O_3 + Fe + \frac{1}{2}O_2 \rightarrow FeCr_2O_4 \tag{4.7}$$

Under the assumption that all chromium is present as oxide in the IOZ, the equilibrium expression for 4.7 is given by

$$K_{4.7} = \frac{1}{a_{Fe} p_{O_2}^{1/2}} \tag{4.8}$$

At the depth $X_{(t)}$, the oxygen partial pressure, denoted by $p_{O_2}^{(t)}$, is fixed by reaction 4.7. To calculate this oxygen partial pressure, the free energy of reaction 4.7 was taken from Kubaschewski [119] and is given below

$$\Delta G_{4.7}^0 = -275,044 + 51T \text{ (J mol}^{-1}\text{)} \tag{4.9}$$

To compute values of $p_{O_2}^{(t)}$ from Equation (4.8), knowledge of the iron activity is required. In order to calculate the iron activity for Fe-Ni alloys, the following relation was used

$$a_{Fe} = \gamma_{Fe} N_{Fe} \tag{4.10}$$

with γ_{Fe} the iron activity coefficient in Fe-Ni alloys. To estimate this quantity, the partial excess Gibbs free energy was calculated and the following relation used

$$RT \ln(\gamma_{Fe}) = \overline{G}_{Fe}^{xs} \tag{4.11}$$

where $\overline{G}_{Fe}^{xs}$ is the partial excess Gibbs free energy of iron in solution in Fe-Ni.

The thermodynamics of the Fe-Ni system were investigated at high temperature by Chuang *et al.* [120]. The authors gave the following expression to calculate the partial excess Gibbs free energy for iron in Fe-Ni alloys.

$$\overline{G}_{Fe}^{xs} = \frac{1}{2} RT N_{Ni}^2 \left[(w_{12}^{'} + w_{21}^{'}) + (w_{12}^{'} - w_{21}^{'})(1 - 4N_{Fe}) \right] \tag{4.12}$$

with

$$w_{12}^{'} = 0.688475 - \frac{3033.57}{T(\mathrm{K})} \tag{4.13}$$

$$w_{21}^{'} = 0.111726 - \frac{490.74}{T(\mathrm{K})} \tag{4.14}$$

Finally, using excess Gibbs free energy of iron in solution in Fe-Ni alloy determined with Equation (4.12) in (4.11) allows the evaluation of the iron activity coefficient, and therefore the iron activity in Fe-Ni alloys. In Table 4.2, values of a_{Fe} calculated for several temperatures are presented. From values of iron activity in Table 4.2 and the free energy of reaction 4.7 (Eq. 4.9), the equilibrium oxygen partial pressure, $p_{O_2}^{(t)}$, was estimated for various alloy compositions and temperatures. Results of calculation are presented in Table 4.3.

Table 4.2: Iron activity calculated using $a_{Fe} = N_{Fe}\gamma_{Fe}$ and activity coefficient computed from Equation (4.11).

Temperature	$\frac{N_{Ni}}{N_{Fe}+N_{Ni}}$				
°C	0	0.2	0.4	0.6	0.8
1,000	1	0.78234	0.52437	0.26667	0.08110
1,050	1	0.78327	0.52814	0.27248	0.08508
1,100	1	0.78414	0.53166	0.27798	0.08896
1,150	1	0.78494	0.53495	0.28319	0.09271

Table 4.3: Evaluation of the oxygen partial pressure, $p_{O_2}^{(t)}$ (atm), at the location $X = X_{(t)}$.

Temperature	$\frac{N_{Ni}}{N_{Fe}+N_{Ni}}$				
°C	0	0.2	0.4	0.6	0.8
1,000	5.6×10^{-18}	9.1×10^{-18}	2.0×10^{-17}	7.9×10^{-17}	8.5×10^{-16}
1,050	4.0×10^{-17}	6.5×10^{-17}	1.4×10^{-16}	5.4×10^{-16}	5.5×10^{-15}
1,100	2.5×10^{-16}	4.0×10^{-16}	8.7×10^{-16}	3.2×10^{-15}	3.1×10^{-14}
1,150	1.3×10^{-15}	2.2×10^{-15}	4.7×10^{-15}	1.7×10^{-14}	1.6×10^{-13}

For comparison, $p_{O_2}^{(t)}$ and f are plotted in Figure 4.5 as a function of alloy composition for temperatures of 1,000 and 1,150°C. As is seen, $p_{O_2}^{(t)}$ increases with

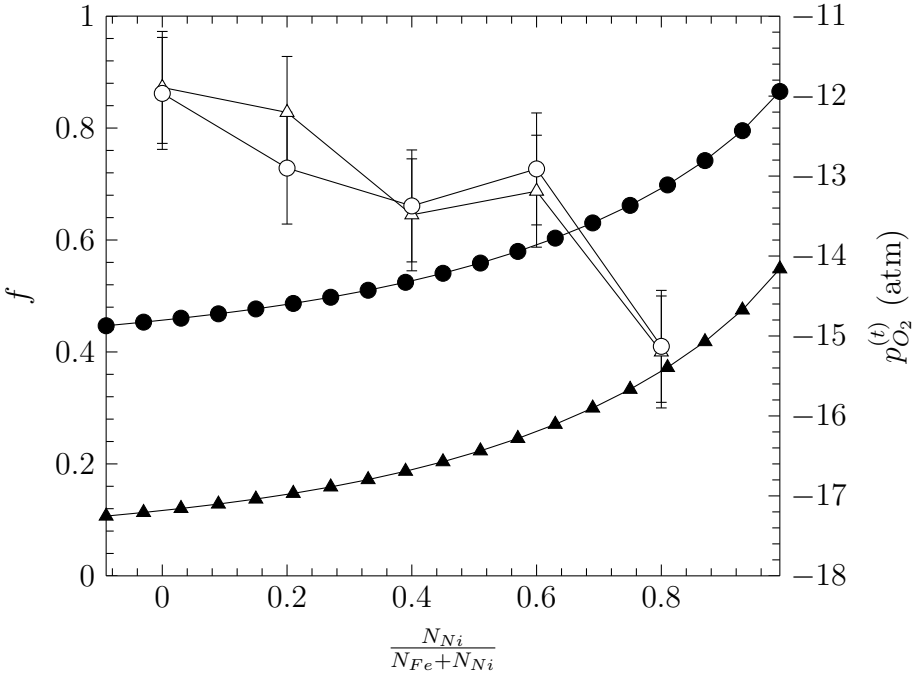

Figure 4.5: Variation of f (open symbols) and $p_{O_2}^{(t)}$ (filled symbols) with the alloy composition : 1,000°C (–△–,–▲–), 1,150°C (–◇–,–●–).

the alloy nickel content, indicating that the iron-chromium spinel is less stable in nickel-rich alloys due to the decrease of the iron activity with nickel addition. Thermodynamic predictions are in agreement with variations of f which showed that the subzone where iron-chromium spinel precipitates is smaller in nickel-rich alloys.

4.1.2 Internal oxidation kinetics

Recent data were obtained for internal oxidation kinetics measured in Fe/FeO Rhines pack [109]. In Figures 4.6 and 4.7 , IOZ depth measured in alloys after reaction in Fe/FeO Rhines pack are presented in plots of $X^2_{(i)}$ versus the time. Kinetics were found to be parabolic at all temperatures, and linear regression was used to calculate the internal oxidation rate constant given by the equation

$$X^2_{(i)} = 2k_p^{(i)}t \tag{4.15}$$

The resulting values of $k_p^{(i)}$ are presented in Table 4.4.

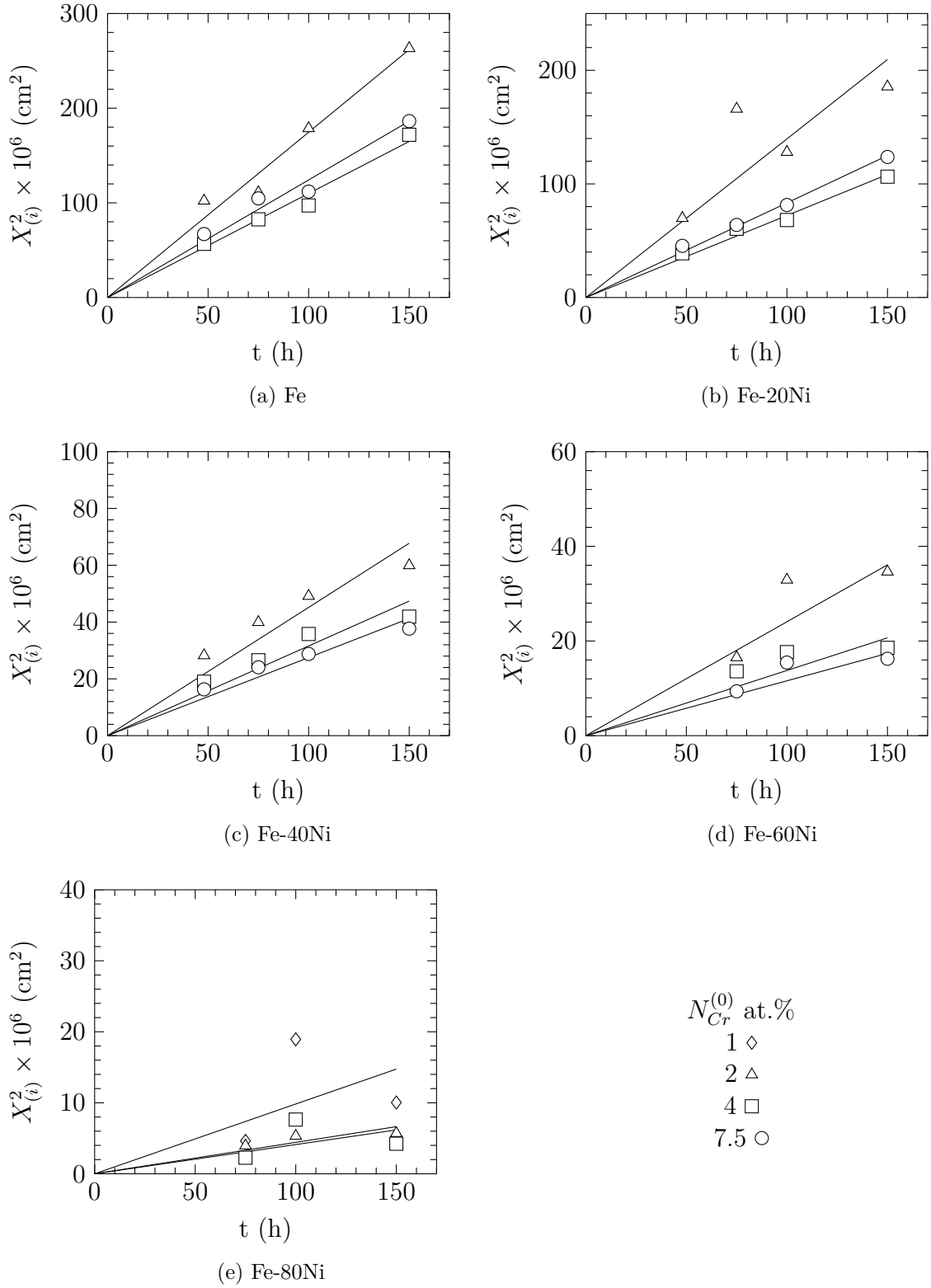

(a) Fe

(b) Fe-20Ni

(c) Fe-40Ni

(d) Fe-60Ni

(e) Fe-80Ni

Figure 4.6: Internal oxidation kinetics measured in Fe/FeO Rhines packs at 1,000°C, $p_{O_2} = (1.2 \pm 0.2) \times 10^{-15}$ atm.

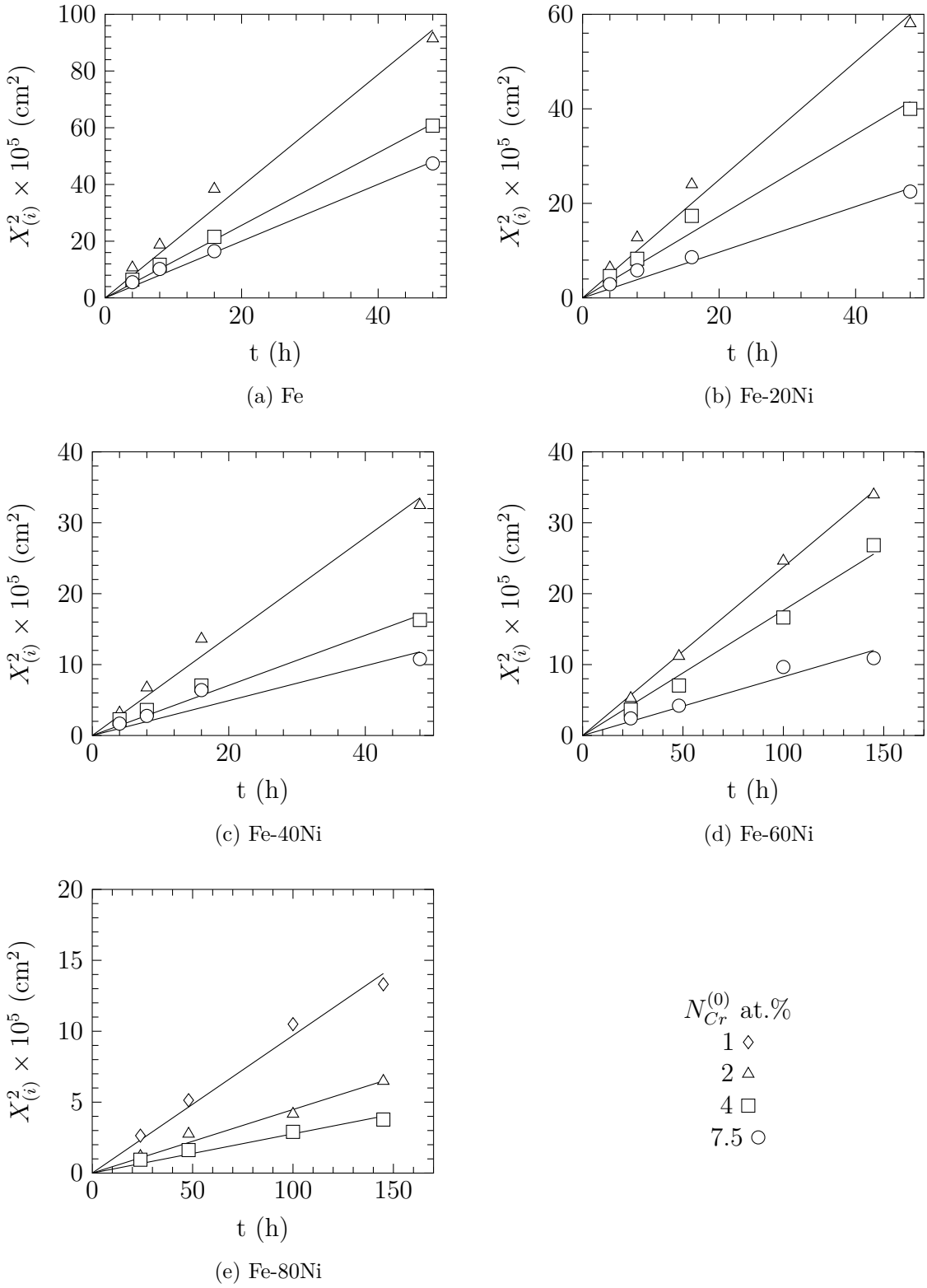

(a) Fe

(b) Fe-20Ni

(c) Fe-40Ni

(d) Fe-60Ni

(e) Fe-80Ni

Figure 4.7: Internal oxidation kinetics measured in Fe/FeO Rhines packs at 1,150°C, $p_{O_2} = (2.3 \pm 0.4) \times 10^{-13}$ atm.

Table 4.4: $k_p^{(i)}$ measured after exposure in Fe/FeO Rhines Pack.

N_{Cr} at.%	$\frac{N_{Ni}}{N_{Fe}+N_{Ni}}$	$k_p^{(i)}$ ($cm^2\ s^{-1}$) 1,000°C	1,050°C	1,100°C	1,150°C
1	0.8	$(1.4\pm1.4)\times10^{-11}$	$(2.5\pm0.4)\times10^{-11}$	$(6.0\pm1.3)\times10^{-11}$	$(1.3\pm0.2)\times10^{-10}$
2	0	$(2.4\pm0.3)\times10^{-10}$	$(5.6\pm0.4)\times10^{-10}$	$(1.4\pm0.2)\times10^{-9}$	$(2.7\pm0.4)\times10^{-9}$
	0.2	$(1.9\pm0.8)\times10^{-10}$	$(3.8\pm0.5)\times10^{-10}$	$(9.3\pm0.7)\times10^{-10}$	$(1.7\pm0.3)\times10^{-9}$
	0.4	$(6.3\pm1.6)\times10^{-11}$	$(1.7\pm0.6)\times10^{-10}$	$(4.5\pm1.2)\times10^{-10}$	$(9.7\pm1.5)\times10^{-10}$
	0.6	$(3.5\pm1.1)\times10^{-11}$	$(5.9\pm2.9)\times10^{-11}$	$(2.3\pm1.5)\times10^{-10}$	$(3.3\pm0.2)\times10^{-10}$
	0.8	$(6.1\pm1.9)\times10^{-12}$	$(1.5\pm0.2)\times10^{-11}$	$(2.7\pm0.4)\times10^{-11}$	$(6.2\pm1.0)\times10^{-11}$
4	0	$(1.5\pm0.2)\times10^{-10}$	$(3.2\pm0.2)\times10^{-10}$	$(9.3\pm0.6)\times10^{-10}$	$(1.8\pm0.1)\times10^{-9}$
	0.2	$(1.0\pm0.1)\times10^{-10}$	$(2.2\pm0.2)\times10^{-10}$	$(5.9\pm0.4)\times10^{-10}$	$(1.2\pm0.2)\times10^{-9}$
	0.4	$(4.4\pm1.1)\times10^{-11}$	$(1.1\pm0.4)\times10^{-10}$	$(3.9\pm0.3)\times10^{-10}$	$(4.9\pm1.0)\times10^{-10}$
	0.6	$(2.0\pm0.7)\times10^{-11}$	$(4.4\pm1.1)\times10^{-11}$	$(1.2\pm0.1)\times10^{-10}$	$(2.5\pm0.3)\times10^{-10}$
	0.8	$(5.7\pm5.4)\times10^{-12}$	$(9.5\pm8.0)\times10^{-12}$	$(2.1\pm0.9)\times10^{-11}$	$(3.8\pm0.7)\times10^{-11}$
7	0	$(1.7\pm0.2)\times10^{-10}$	$(3.3\pm0.3)\times10^{-10}$	$(7.1\pm0.4)\times10^{-10}$	$(1.4\pm0.1)\times10^{-9}$
	0.2	$(1.2\pm0.1)\times10^{-10}$	$(2.1\pm0.4)\times10^{-10}$	$(2.4\pm0.9)\times10^{-10}$	$(6.7\pm1.2)\times10^{-10}$
	0.4	$(3.8\pm0.8)\times10^{-11}$	$(1.0\pm0.4)\times10^{-10}$	$(1.9\pm0.4)\times10^{-10}$	$(3.4\pm1.4)\times10^{-10}$
	0.6	$(1.7\pm0.5)\times10^{-11}$	$(3.8\pm1.4)\times10^{-11}$	$(7.6\pm0.8)\times10^{-11}$	$(1.2\pm0.3)\times10^{-10}$

Results of internal oxidation experiment for various Fe-Cr and Fe-Ni-Cr alloys showed that for a given chromium content, the internal oxidation rate constant decreases when the alloy nickel content increases. This was observed at all temperatures as shown in Figure 4.8. However, at 1,000°C and 1,050°C for a given nickel concentration, the internal oxidation rate constant was found to be similar in alloys containing 4 and 7.5 at.% of chromium, while at higher temperatures, internal oxidation rate constants were found to decrease with chromium additions as predicted [26] by Equation (4.16).

$$k_p^{(i)} = \frac{N_O^{(s)} D_O}{\alpha \nu N_{Cr}^{(0)}} \tag{4.16}$$

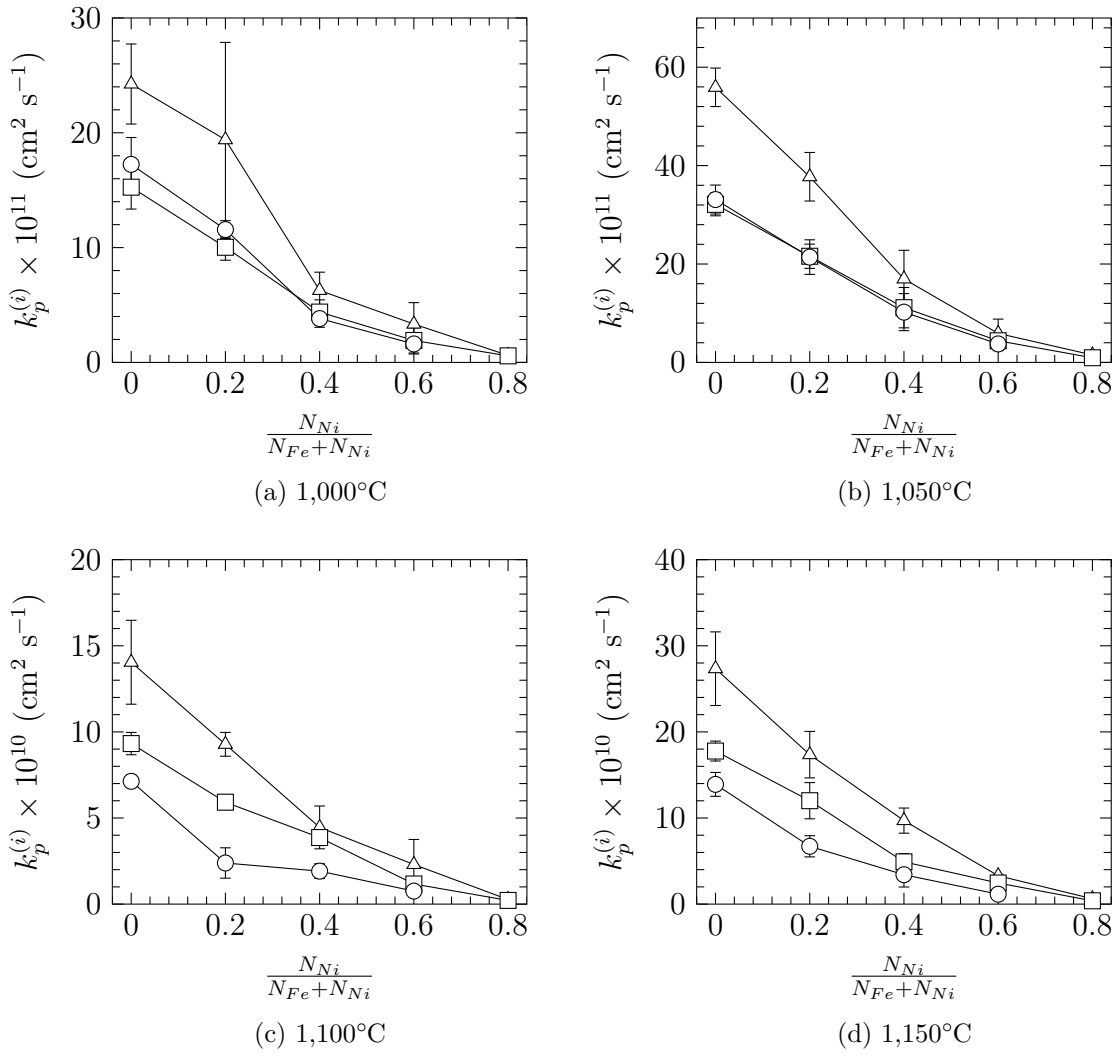

Figure 4.8: Variation of the internal oxidation constant measured in Fe/FeO Rhines pack with the alloy composition: 2 at.% Cr (–△–), 4 at.% Cr (–□–), 7.5 at.% Cr (–○–).

The temperature dependency of the internal oxidation rate constant is presented in Arrhenius plot (Figure 4.9). From this plot, the pre-exponential factor and the activation energy of the internal oxidation rate constant can be estimated using linear regression. Values of these parameters are given in Table 4.5.

Table 4.5: Pre-exponential factor and activation energy for internal oxidation rate constant: $k_p^{(i)} = k_p^{(0)} \exp(-Q/RT)$.

N_{Cr} at.%	$\frac{N_{Ni}}{N_{Fe}+N_{Ni}}$	$k_p^{(0)}$ cm^2 s^{-1}	Q kJ mol^{-1}
1	0.8	3.6×10^{-1}	257±21
2	0	1.1	234±23
	0.2	2.4×10^{-1}	221±24
	0.4	4.4	263±16
	0.6	1.0×10^{-2}	203±104
	0.8	5.5×10^{-2}	244±41
4	0	1.0	239±40
	0.2	1.5	248±27
	0.4	3.1×10^{-3}	184±117
	0.6	5.2×10^{-1}	254±20
	0.8	9.7×10^{-4}	202±22
7.5	0	1.4×10^{-1}	218±39
	0.2	8.4×10^{-2}	221±117
	0.4	5.5×10^{-3}	196±20
	0.6	2.6×10^{-4}	173±37

Pre-exponential factors and activation energies presented in Table 4.5 are plotted as functions of alloy composition in Figure 4.10. Regardless of the large uncertainness on the pre-exponential factor, which was evaluated to be close to a factor of 2, this parameter was found to decrease by several orders of magnitude from the iron-rich to the nickel-rich side as shown in Figure 4.10.a. On the other hand, values found for the activation energy were similar in the different alloys studied (Figure 4.10.b).

In order to investigate the effect of water vapour and/or hydrogen on internal oxidation kinetics, experiments were carried out in H_2/H_2O gas mixtures and results are presented in the following section.

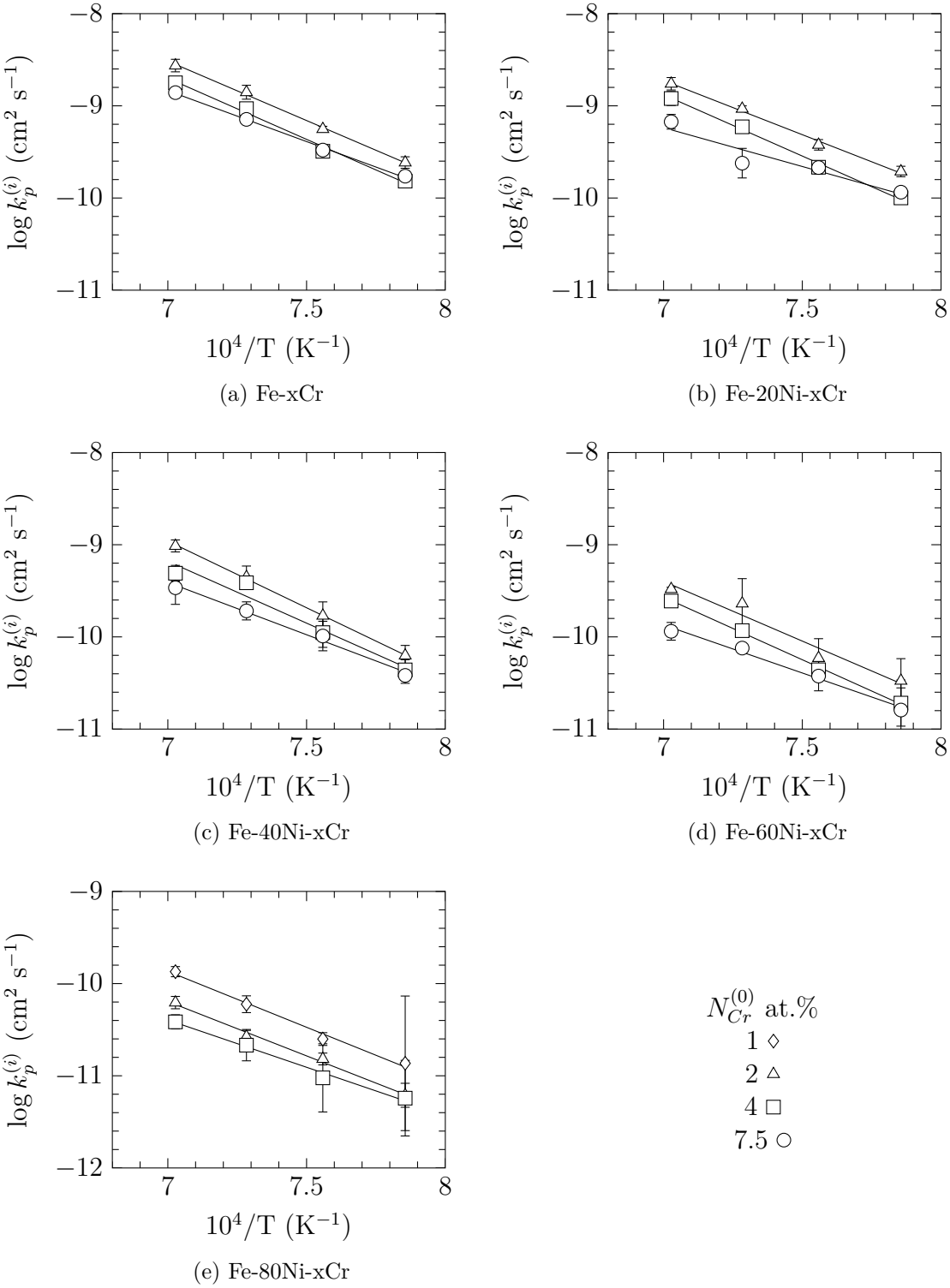

(a) Fe-xCr

(b) Fe-20Ni-xCr

(c) Fe-40Ni-xCr

(d) Fe-60Ni-xCr

(e) Fe-80Ni-xCr

Figure 4.9: Arrhenius plots of internal oxidation rate constant measured in Fe/FeO Rhines pack.

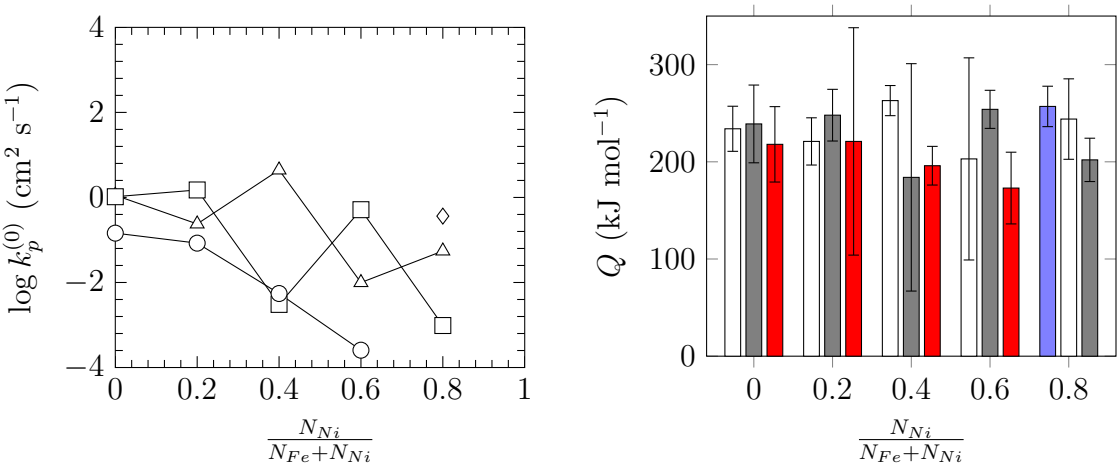

(a) Pre-exponential factor

(b) Activation energy

Figure 4.10: Pre-exponential factor and activation energy for the internal oxidation rate constant, $k_p^{(i)}$, measured in Rhines Pack: 1 at.% (–◇–,▮▮), 2 at.% (–△–,▯▯), 4 at.% (–□–,▮▮), 7.5 at.% (–○–,▮▮).

4.2 Internal oxidation in H_2/H_2O gas

In this section internal oxidation kinetics measured in H_2/H_2O gases with different water vapour contents and the oxygen partial pressure set at the Fe/FeO equilibrium pressure are presented. Firstly, the internal oxide zone microstructures observed are described, and kinetics measured are presented in a second part of this section.

4.2.1 Internal oxidation zone microstructure

After exposure in gases with 13% water vapour, samples were cross-sectioned and microstructure observed for experiments at 1,000°C are presented in Figure 4.11. Microstructures observed after reaction in Fe/FeO Rhines pack and H_2/H_2O gases were similar except for the alloy Fe-80Ni-4Cr, which exhibits internal and external oxidation when exposed to humid condition while exclusive internal oxidation was observed after exposure in Fe/FeO Rhines packs. No clear reason was found for this difference. However, the critical chromium concentration to observe the transition between internal and external oxidation, $N_{Cr}^{(0)*}$, under the oxygen partial pressure set at the Fe/FeO equilibrium was calculated from Croll and Wallwork's experi-

Figure 4.11: Micrographs of IOZ after exposure in H_2/H_2O gas with 13% water vapour at 1,000°C for 150h.

mental observations (Table 2.2). Results of calculation showed that for alloys with $\frac{N_{Ni}}{N_{Fe}+N_{Ni}} = 0.8$, $N_{Cr}^{(0)*}$ is approximately 6 at.%. Thus, Fe-80Ni-4Cr alloys have a chromium content close to the the critical chromium concentration to observe the transition between internal and external oxidation and the formation of a discontinuous chromia scale on the alloy surface during exposure at high temperature in H_2/H_2O gas may be due to slightly different experimental conditions between Rhines packs and H_2/H_2O gas experiments.

For other alloys exposed to humid gases, the particle size was found to increase with chromium and nickel content and nodules of pure matrix were observed on nickel-rich alloys, as was observed for samples reacted in Fe/FeO Rhines packs. Possible mechanisms for the formation of matrix nodules on the sample surface were presented in Section 4.1.1. In addition, no deeper oxidation was observed under grain boundaries as observed for Fe-7.5Cr or Fe-20Ni-7.5Cr. This was already reported in Section 4.1.1 for alloys reacted in Fe/FeO Rhines packs.

As reported for alloys reacted in Fe/FeO Rhines packs, the IOZ is composed of two subzones in which a specific oxide precipitates, as illustrated in Figure 4.12.

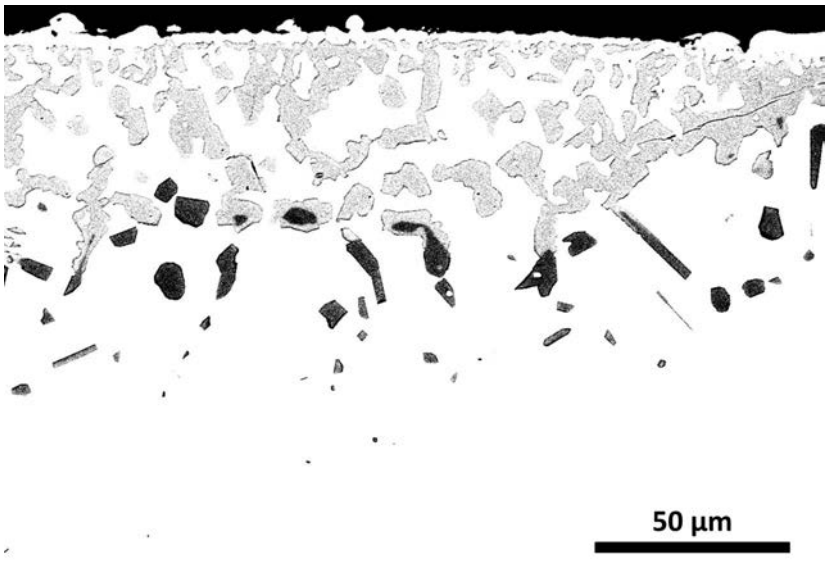

Figure 4.12: BSE osbervation of Fe-60Ni-7.5Cr exposed for 100h at 1,150°C in H_2/H_2O gases containing 13% water vapour and oxygen partial pressure set at Fe/FeO equilibrium.

Darker particles were identified by EDS as chromium oxide while light grey

oxides were iron-chromium spinel. In addition, as with alloys exposed in Fe/FeO Rhines pack, a few composite oxide particles can be observed in the IOZ, as seen in Figure 4.12. From SEM observations, the distribution of the two subzones was evaluated for alloys with 7.5 at.% Cr by measuring $f = X_{(t)}/X_{(i)}$. The depth $X_{(t)}$ is where chromium oxides are converted in iron-chromium spinels. Values of f estimated from SEM observations are given in Table 4.6 and they are plotted as a function of the alloy composition in Figure 4.13. As is seen, the temperature has a negligible effect on f. In addition, f decreases with alloy nickel content, as observed for alloys reacted in Fe/FeO Rhines packs. This variation is due to the reduction of the iron activity in nickel-rich alloys. As a result, the iron chromium spinel is less stable, and f decreases.

Table 4.6: f evaluated from measurements of $X_{(t)}$ for alloys with 7.5 at.% Cr (2 at.% Cr for $\frac{N_{Ni}}{N_{Fe}+N_{Ni}}$=0.8)reacted in H_2/H_2O gas with 13% of water vapour and oxygen partial pressure set at the Fe/FeO equilibrium. Error considered: ±0.1.

Temperature	$\frac{N_{Ni}}{N_{Fe}+N_{Ni}}$				
°C	0	0.2	0.4	0.6	0.8
1,000	0.98	0.80	0.74	0.70	0.35
1,050	0.85	0.86	0.75	0.70	0.30
1,100	0.84	0.80	0.74	0.60	0.40
1,150	0.90	0.80	0.74	0.74	0.40

Internal oxidation experiments were also carried out in a thermobalance using H_2/H_2O gas with 3% water vapour and the oxygen partial pressure set at the Fe/FeO equilibrium. Microstructures were similar to microstructures observed after exposure in humid gases containing 13% water vapour. However, the Fe-60Ni-7.5Cr alloy formed a Cr_2O_3 scale, as illustrated in Figure 4.14 where structures of alloys reacted in H_2/H_2O gases with 13% and 3% water vapour are compared. The difference in behaviour of the alloy Fe-60Ni-7.5Cr might be due to the different experimental protocol used for experiments in low water vapour content gases, which were carried out in a thermobalance.

As presented in Section 2.5.2, during the heating stage of the experiment in the thermobalance, the sample was held in the hot zone of the furnace under flowing

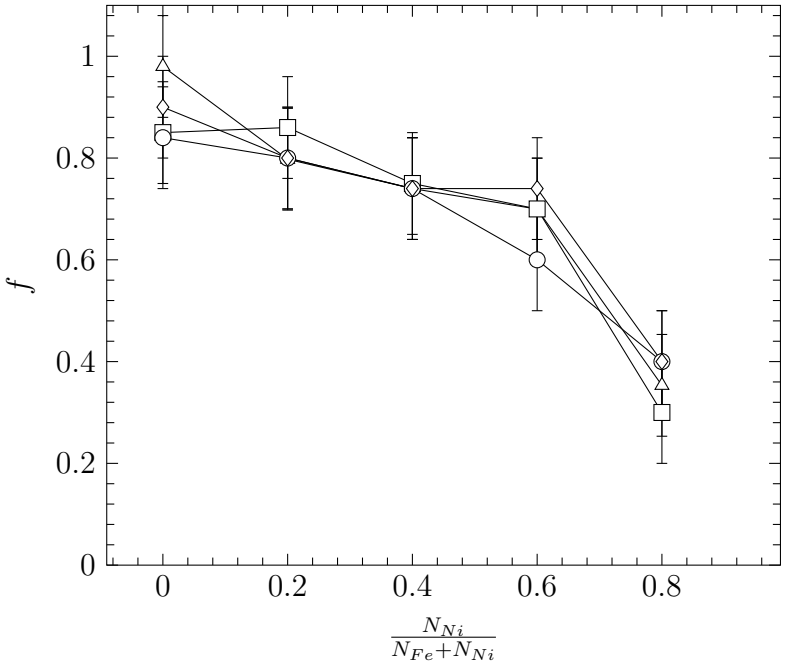

Figure 4.13: Variation of the parameter f with the alloy nickel content. f measured in alloy with 7.5 at.% Cr reacted in H_2/H_2O gases with 13% water vapour and oxygen partial pressure set at the Fe/FeO equilibrium. 1,000°C (–△–), 1,050°C (–□–), 1,100°C (–○–), 1,150°C (–◇–).

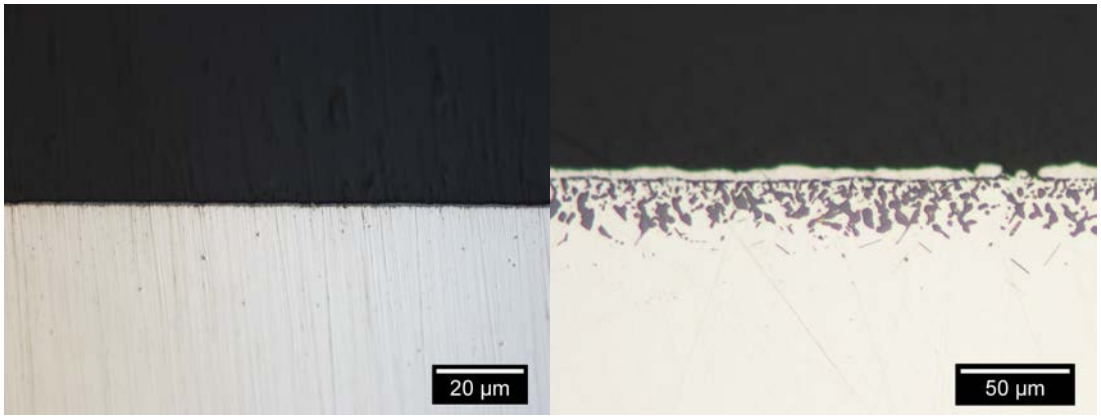

(a) Ar-4.8%H_2-3%H_2O
$p_{O_2} = (1.1 \pm 0.2) \times 10^{-15}$ atm

(b) Ar-20.3%H_2-13%H_2O
$p_{O_2} = (1.2 \pm 0.2) \times 10^{-15}$ atm

Figure 4.14: Fe-60Ni-7.5Cr after exposure at 1,000°C in Ar-H_2-H_2O for 24 h.

Ar-5%H_2. Under this atmosphere, chromium oxidises and passivation of the alloy may happen at this stage of the experiment. This explanation was suggested by a slower oxidation rate observed on weight gain curve at the beginning of the experiment (Section 4.2.3.1). Thus, if the alloy Fe-60Ni-7.5Cr is close to the transition between internal and external oxidation, a thin chromia scale may grow on the alloy surface during the heating stage. In addition, as presented in Section 1.3.1,

the minimum alloy chromium content required to sustain the growth of an external scale is

$$N_{Cr}^{(0)} > \frac{V_{alloy}}{V_{Cr_2O_3}} \left(\frac{\pi k_p}{2\tilde{D}} \right)^{\frac{1}{2}} \tag{4.17}$$

It was also reported [67] that the maximum of the chromium diffusion coefficient was observed for alloys with 60 at.% of nickel. At this nickel content, the critical chromium content to sustain the growth of an external oxide scale, given by Equation (4.17), is minimum. Therefore, for composition Fe-60Ni-7.5Cr, if a scale starts to grow during the heating stage, it is likely that no failure of the scale would be observed during the subsequent exposure and this results in no internal oxidation.

For alloys where internal oxidation was observed, f was measured for alloys reacted at 1,150°C. No measurement was carried out on samples reacted at lower temperature, because it is assumed that f is not affected by the temperature as observed from measurements of f carried out for alloys reacted in Fe/FeO Rhines packs or H_2/H_2O gases with 13% water vapour. Measurement results are presented in Table 4.7. It is seen the parameter f decreases with increasing alloy nickel content as predicted by thermodynamic calculations carried out in Section 4.1.1. values of f measured after experiments in the different environments are compared in Section 4.3.

Table 4.7: f evaluated from measurements of $X_{(t)}$ for alloys with 7.5 at.% Cr (2 at.% Cr for $\frac{N_{Ni}}{N_{Fe}+N_{Ni}}$=0.8) reacted in H_2/H_2O gas with 3% water vapour and oxygen partial pressure set at the Fe/FeO equilibrium. Error considered: ±0.1.

Temperature	$\frac{N_{Ni}}{N_{Fe}+N_{Ni}}$				
°C	0	0.2	0.4	0.6	0.8
1,150	0.88	0.84	0.7	0.7	0.4

4.2.2 Internal oxidation kinetics in H_2/H_2O gases with 13% water vapour

Internal oxidation kinetics of samples reacted in H_2/H_2O gases with 13% water vapour were estimated from measurement of IOZ depth and using the relation

$$X_{(i)}^2 = 2k_p^{(i)}t \tag{4.18}$$

or from discontinuous TGA and using the parabolic relation

$$\left(\frac{\Delta w}{S}\right)^2 = 2k_w^{(i)}t \tag{4.19}$$

4.2.2.1 Penetration measurement

Internal oxidation kinetics measured in H_2/H_2O gas containing 13% water vapour were found to be parabolic for all temperatures. An example of kinetics is given in Figure 4.15 for a temperature of 1,000°C. It should be noted that no penetration measurement was carried out for Fe-80Ni-4Cr alloys because this composition exhibited internal and external oxidation at all temperatures studied. Internal oxidation rate constants were evaluated using the same method as for kinetics in Rhines pack presented in Section 4.1.2. In Table 4.8, the resulting values are summarised, along with errors estimated as two standard deviations.

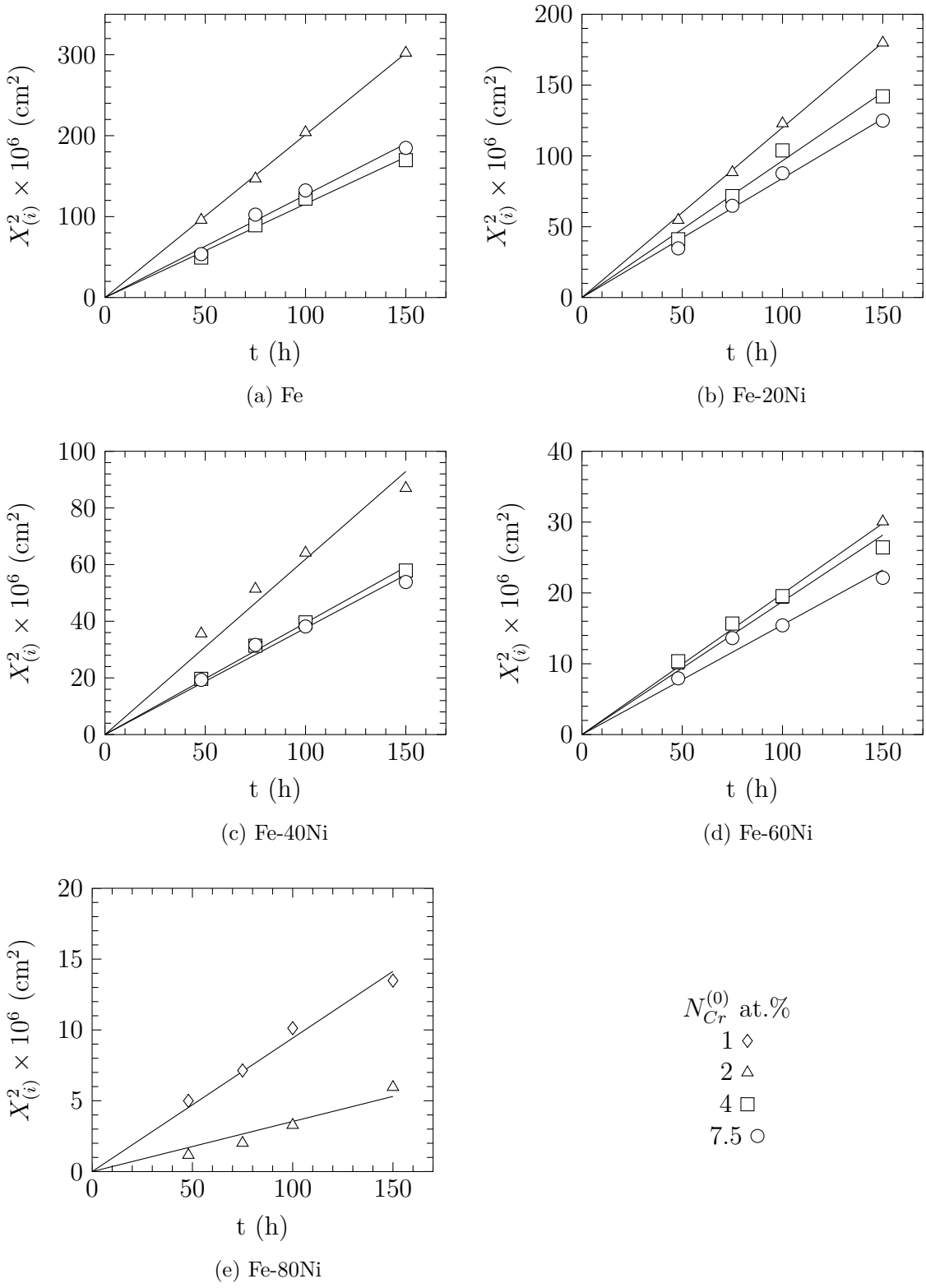

(a) Fe

(b) Fe-20Ni

(c) Fe-40Ni

(d) Fe-60Ni

(e) Fe-80Ni

Figure 4.15: Internal oxidation kinetics measured in H_2/H_2O gas at 1,000°C and oxygen partial pressure set at the Fe/FeO equilibrium.

Table 4.8: $k_p^{(i)}$ measured after exposure in flowing H_2/H_2O gas containing 13% H_2O and oxygen partial pressure set at the Fe/FeO equilibrium.

N_{Cr} at.%	$\frac{N_{Ni}}{N_{Fe}+N_{Ni}}$	$k_p^{(i)}$ ($cm^2\ s^{-1}$) 1,000°C	1,050°C	1,100°C	1,150°C
1	0.8	$(1.4\pm0.4)\times10^{-11}$	$(3.1\pm0.2)\times10^{-11}$	$(6.1\pm0.6)\times10^{-11}$	$(1.2\pm0.6)\times10^{-10}$
2	0	$(2.8\pm0.1)\times10^{-10}$	$(7.2\pm0.1)\times10^{-10}$	$(1.3\pm0.1)\times10^{-9}$	$(3.4\pm0.2)\times10^{-9}$
	0.2	$(1.7\pm0.1)\times10^{-10}$	$(4.2\pm0.2)\times10^{-10}$	$(9.5\pm0.5)\times10^{-10}$	$(2.2\pm0.1)\times10^{-9}$
	0.4	$(8.6\pm1.0)\times10^{-11}$	$(2.3\pm0.1)\times10^{-10}$	$(4.8\pm0.3)\times10^{-10}$	$(1.3\pm0.1)\times10^{-9}$
	0.6	$(2.8\pm0.1)\times10^{-11}$	$(7.2\pm0.1)\times10^{-11}$	$(1.5\pm0.1)\times10^{-10}$	$(2.7\pm0.1)\times10^{-10}$
	0.8	$(4.9\pm1.4)\times10^{-12}$	$(1.5\pm0.3)\times10^{-11}$	$(3.0\pm0.3)\times10^{-11}$	$(5.6\pm3.9)\times10^{-11}$
4	0	$(1.6\pm0.1)\times10^{-10}$	$(3.8\pm0.1)\times10^{-10}$	$(8.6\pm0.2)\times10^{-10}$	$(2.0\pm0.3)\times10^{-9}$
	0.2	$(1.3\pm0.1)\times10^{-10}$	$(3.1\pm0.1)\times10^{-10}$	$(6.5\pm0.1)\times10^{-10}$	$(1.4\pm0.1)\times10^{-9}$
	0.4	$(5.5\pm0.2)\times10^{-11}$	$(1.4\pm0.1)\times10^{-10}$	$(2.7\pm0.3)\times10^{-10}$	$(7.2\pm0.5)\times10^{-10}$
	0.6	$(2.6\pm0.4)\times10^{-11}$	$(5.3\pm0.1)\times10^{-11}$	$(1.0\pm0.1)\times10^{-10}$	$(1.6\pm0.1)\times10^{-10}$
7.5	0	$(1.8\pm0.2)\times10^{-10}$	$(3.7\pm0.2)\times10^{-10}$	$(6.5\pm0.1)\times10^{-10}$	$(1.4\pm0.1)\times10^{-9}$
	0.2	$(1.2\pm0.1)\times10^{-10}$	$(2.3\pm0.4)\times10^{-10}$	$(3.9\pm0.4)\times10^{-10}$	$(1.1\pm0.1)\times10^{-9}$
	0.4	$(5.2\pm0.4)\times10^{-11}$	$(1.1\pm0.2)\times10^{-10}$	$(1.9\pm0.1)\times10^{-10}$	$(4.3\pm0.5)\times10^{-10}$
	0.6	$(1.7\pm0.5)\times10^{-11}$	$(4.9\pm0.4)\times10^{-11}$	$(6.9\pm0.8)\times10^{-11}$	$(9.5\pm0.1)\times10^{-11}$

As with experiments carried out in Rhines packs, internal oxidation rate constants were plotted as a function of the alloy composition in Figure 4.16. Internal oxidation rate constants were found to decrease when nickel was added to the alloy composition just as it was observed for Rhines pack experiments. In addition, as noticed for experiments in Fe/FeO Rhines packs, internal oxidation rate constants measured for alloys with chromium contents of 4 and 7.5 at.% of chromium are similar at the lowest temperatures studied, and start to become different when the temperature increases.

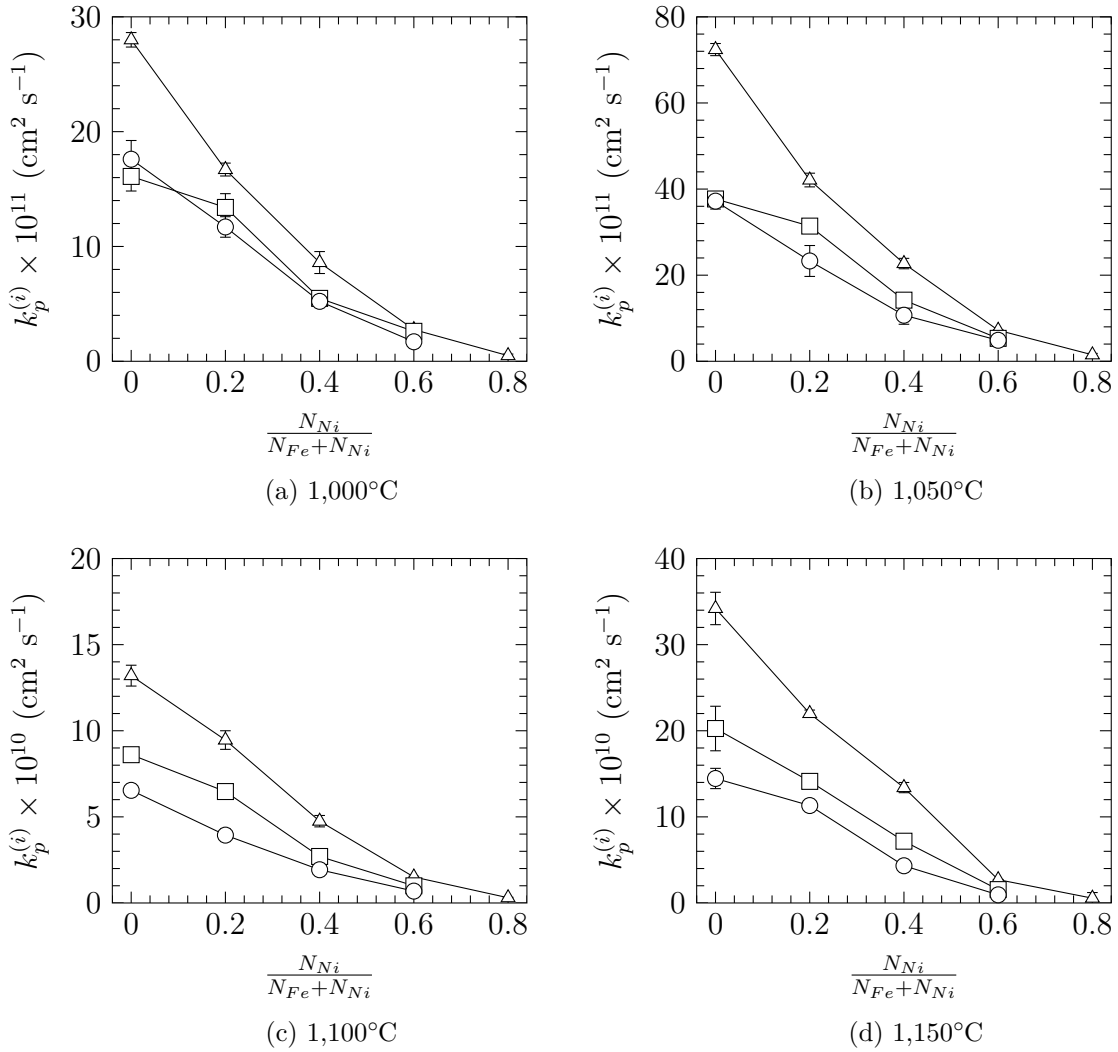

Figure 4.16: Internal oxidation rate constants measured in H_2/H_2O gas with 13% of water vapour and oxygen partial pressure set at the Fe/FeO equilibrium as a function of the alloy composition: 2 at.% Cr (–△–), 4 at.% Cr (–□–), 7.5 at.% Cr (–○–).

Arrhenius diagrams were plotted in Figure 4.17 for experiments in H_2/H_2O

to calculate the pre-exponential factor and the activation energy for the internal oxidation rate constant. These two parameters are reported in Table 4.9, along with errors in their estimations. Pre-exponential factors and activation energies are shown in Figure 4.18 as a function of alloy composition.

Table 4.9: Pre-exponential factor and activation energy for internal oxidation rate constant measured in H_2/H_2O gases with 13% water vapour and oxygen partial pressure set at the Fe/FeO equilibrium: $k_p^{(i)} = k_p^{(0)} \exp(-Q/RT)$.

N_{Cr} at.%	$\frac{N_{Ni}}{N_{Fe}+N_{Ni}}$	$k_p^{(0)}$ cm^2 s^{-1}	Q kJ mol^{-1}
1	0.8	7.8×10^{-3}	213±20
2	0	3.7×10^{1}	273±23
	0.2	1.2×10^{1}	265±24
	0.4	2.5×10^{2}	307±16
	0.6	1.1×10^{-2}	207±104
	0.8	3.0×10^{-3}	210±41
4	0	1.4×10^{1}	268±40
	0.2	1.1	242±27
	0.4	1.8×10^{1}	283±117
	0.6	2.0×10^{-4}	166±20
7.5	0	3.1×10^{-1}	227±39
	0.2	3.6×10^{1}	286±117
	0.4	1.4×10^{-1}	232±20
	0.6	3.2×10^{-6}	123±37

The pre-exponential factor was found to decrease in nickel-rich alloys as observed in Rhines pack experiments. However, a new trend seems to appear for the activation energy. In alloys with $\frac{N_{Ni}}{N_{Fe}+N_{Ni}} = 0$, 0.4 and 0.6, the activation energy decreases with chromium addition. This was already reported by Goto *et al.* [49] who observed a reduction of the activation energy for the internal oxidation rate constant in Ni-Cr alloys reacted in Ni/NiO Rhines pack. Goto proposed to explain this reduction that in high chromium content alloys, the volume fraction of internal oxide is higher and more interfaces for fast oxygen diffusion at matrix/oxide interface are available. In addition, the interfacial diffusion is considered to have a lower activation energy that the volume diffusion and this leads to an overall lower activation energy for the internal oxidation constant in high chromium content alloys.

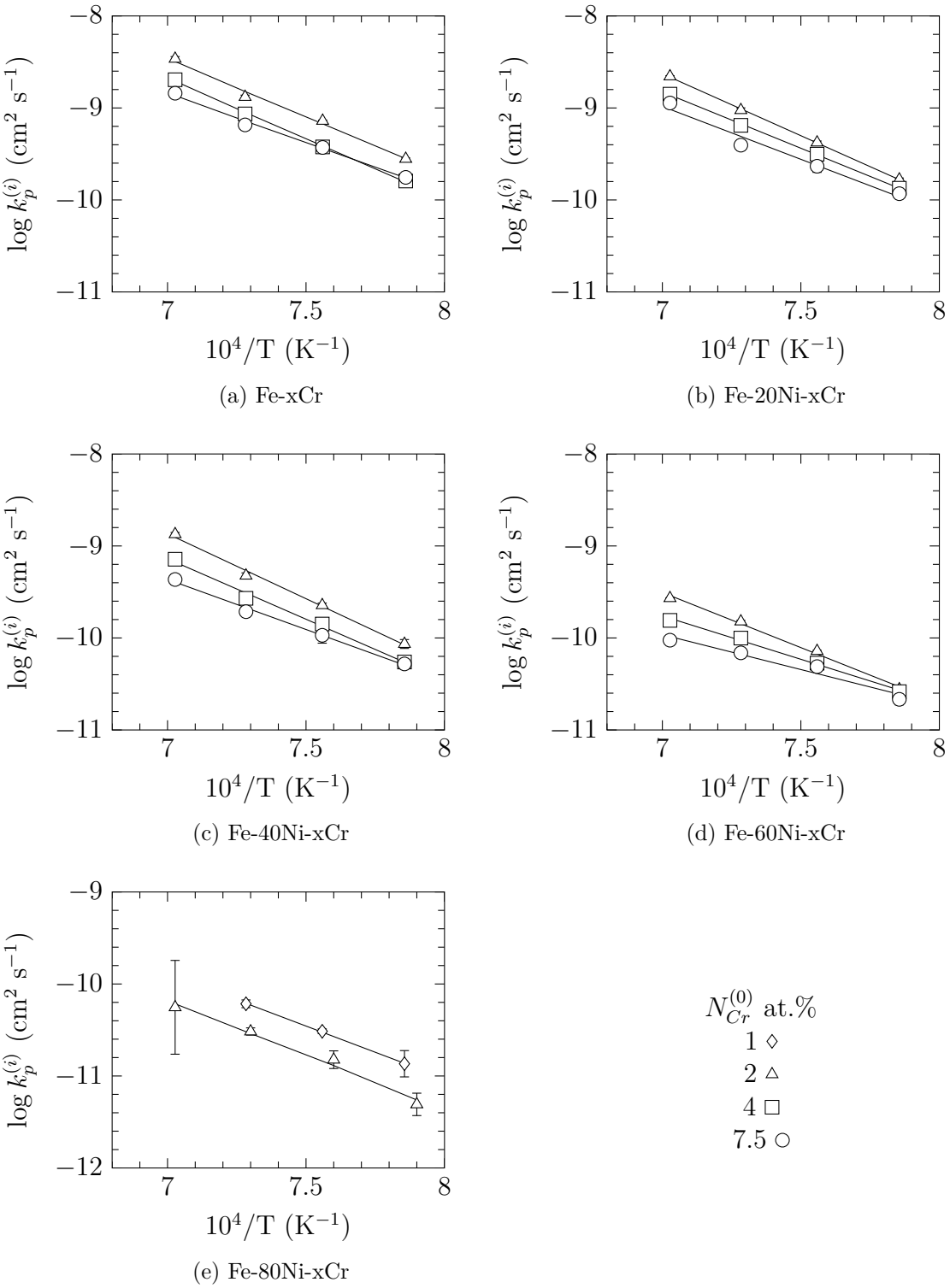

(a) Fe-xCr

(b) Fe-20Ni-xCr

(c) Fe-40Ni-xCr

(d) Fe-60Ni-xCr

(e) Fe-80Ni-xCr

Figure 4.17: Arrhenius plot of internal oxidation rate constant measured in H_2/H_2O gases with 13% water vapour and oxygen partial pressure set at the Fe/FeO equilibrium.

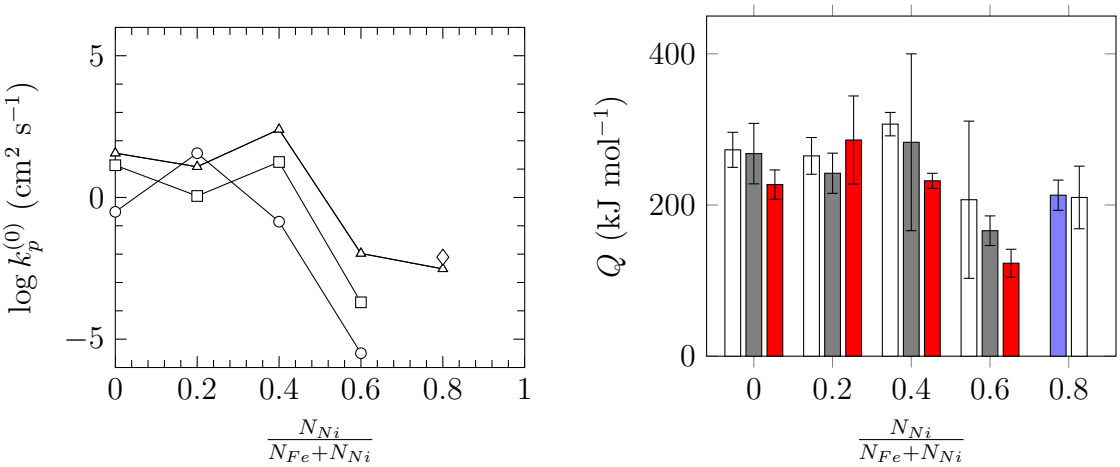

(a) Pre-exponential factor

(b) Activation energy

Figure 4.18: Pre-exponential factor and activation energy for $k_p^{(i)}$ measured in H_2/H_2O gases with 13% of water vapour and oxygen partial pressure set at the Fe/FeO equilibrium: 1 at.% (–◇–, ▮▮), 2 at.% (–△–, ▯▯), 4 at.% (–□–, ▮▮), 7.5 at.% (–○–, ▮▮).

4.2.2.2 Discontinuous TGA

For reactions at 1,000 and 1,050°C, weight change of samples were recorded to estimate the internal oxidation rate constant in term of weight change, $k_w^{(i)}$. To do so, $\left(\frac{\Delta w}{S}\right)^2$ was plotted as a function of t as illustrated in Figure 4.19 for experiments at 1,000°C, and Equation (4.19) was fitted to experimental data.

Kinetics were found to be parabolic which is in agreement with penetration measurements carried out at 1,000 and 1,050°C. Values of $k_w^{(i)}$ estimated are presented in Table 4.10.

Figure 4.20 shows that $k_w^{(i)}$ is decreasing with the alloy nickel content, consistent with variation of $k_p^{(i)}$ measured at 1,000 and 1,050°C as the two internal oxidation rate constants should be proportional according to Gesmundo [31] who gives he following relationship between the two internal oxidation rate constants

$$\frac{k_w^{(i)}}{k_p^{(i)}} = \left[\frac{M_O}{V_{alloy}}\alpha N_{Cr}^{(0)}\nu\right]^2 \tag{4.20}$$

where M_O is the oxygen atomic weight, V_{alloy} the alloy molar volume, α the enrichment factor $N_{Cr}^{(0)}$, the alloy chromium content and ν the internal oxide stoichiometry.

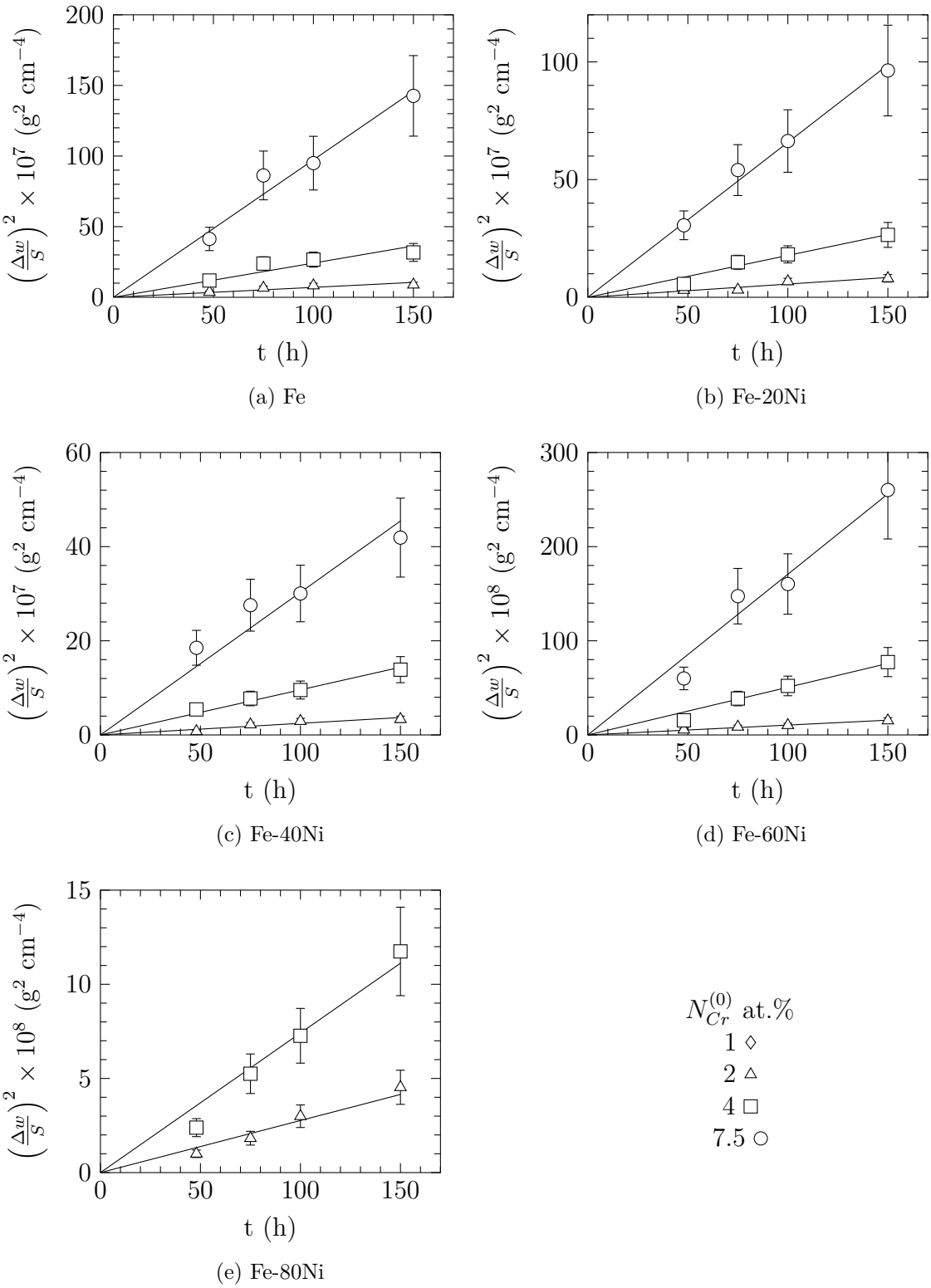

Figure 4.19: Weigh change of sample measured in H_2/H_2O gas with 13% water vapour at 1,000°C, $p_{O_2} = (1.2 \pm 0.2) \times 10^{-15}$ atm.

Table 4.10: $k_w^{(i)}$ measured by discontinuous TGA in H_2/H_2O gas with 13% water and the oxygen partial pressure set at the Fe/FeO equilibrium.

N_{Cr} at.%	$\frac{N_{Ni}}{N_{Fe}+N_{Ni}}$	$k_w^{(i)}$ ($g^2\ cm^{-4}\ s^{-1}$) 1,000°C	1,050°C
1	0.8	$(3.8\pm1.7)\times10^{-14}$	$(1.3\pm0.8)\times10^{-13}$
2	0	$(9.7\pm3.2)\times10^{-13}$	$(2.1\pm0.4)\times10^{-12}$
	0.2	$(7.8\pm2.1)\times10^{-13}$	$(1.7\pm0.3)\times10^{-12}$
	0.4	$(3.4\pm1.0)\times10^{-13}$	$(6.7\pm0.6)\times10^{-13}$
	0.6	$(1.5\pm0.1)\times10^{-13}$	$(3.8\pm1.3)\times10^{-13}$
	0.8	$(1.0\pm0.2)\times10^{-13}$	$(2.4\pm0.4)\times10^{-13}$
4	0	$(3.3\pm1.0)\times10^{-12}$	$(8.3\pm0.7)\times10^{-12}$
	0.2	$(2.5\pm1.0)\times10^{-12}$	$(5.8\pm0.6)\times10^{-12}$
	0.4	$(1.3\pm0.1)\times10^{-12}$	$(2.9\pm0.2)\times10^{-12}$
	0.6	$(7.0\pm1.0)\times10^{-13}$	$(1.4\pm0.1)\times10^{-12}$
7.5	0	$(1.4\pm0.2)\times10^{-11}$	$(2.6\pm0.3)\times10^{-11}$
	0.2	$(9.1\pm0.7)\times10^{-12}$	$(1.7\pm0.1)\times10^{-11}$
	0.4	$(4.2\pm0.9)\times10^{-12}$	$(8.3\pm1.0)\times10^{-12}$
	0.6	$(2.4\pm0.4)\times10^{-12}$	$(5.1\pm0.3)\times10^{-12}$

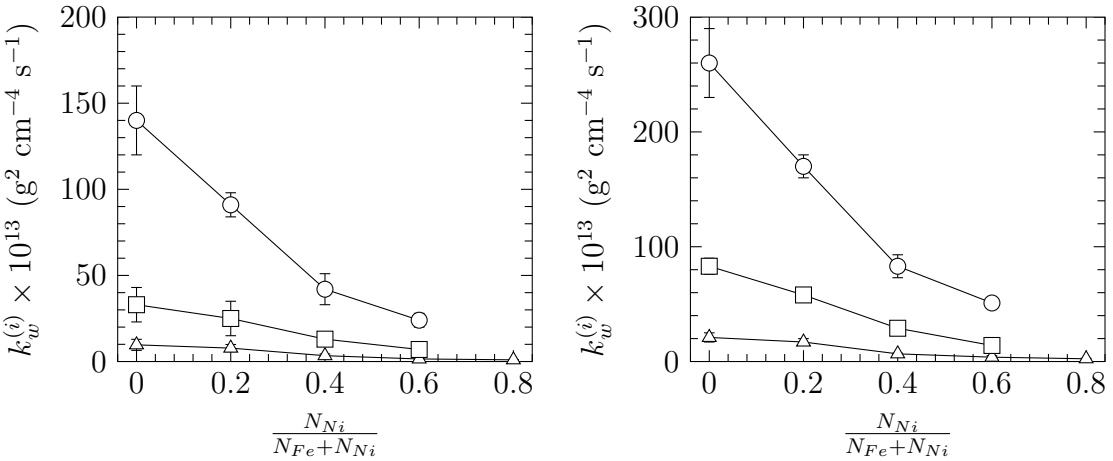

(a) 1,000°C (b) 1,050°C

Figure 4.20: $k_w^{(i)}$ measured in H_2/H_2O gas with 13% water vapour and oxygen partial pressure set at the Fe/FeO equilibrium as a function of the alloy composition: 2 at.% Cr (–△–), 4 at.% Cr (–□–), 7.5 at.% Cr (–○–).

In addition, $k_w^{(i)}$ is found to increase with the alloy chromium as excepted from Equation (4.21) developed by Gesmundo [31]

$$k_w^{(i)} = \left(\frac{M_O}{V_{alloy}}\right)^2 \alpha N_{Cr}^{(0)} \nu N_O^{(s)} D_O \tag{4.21}$$

with $N_O^{(s)} D_O$ the oxygen permeability. However, Figure 4.16 shows that $k_p^{(i)}$ is independent of the alloy chromium content for alloys with 4 and 7.5 at.% Cr while this is not observed for $k_w^{(i)}$ as seen in Figure 4.20. Investigation of this difference of behaviour would be addressed in a next section.

4.2.2.3 Comparison of kinetics in term of weight gain and penetration

According to Equation (4.20), the ratio of internal oxidation rate constants may be calculated. In Figure 4.21, Equation (4.20) was tested by calculating the ratio $\frac{k_w^{(i)}}{k_p^{(i)}}$ from internal oxidation rate constants evaluated from penetration and weight change measurements (Tables 4.8 and 4.10), and the right hand side term of Equation (4.20) was calculated assuming values of the different parameters. Firstly no enrichment was considered, yielding $\alpha = 1$. In addition, the IOZ is composed of 2 oxides with different stoichiometry: $Fe_{0.5}CrO_2$ and $CrO_{1.5}$, and the alloy molar volume varies from pure iron (7.3 cm^3 mol^{-1}) to pure nickel (6.6 cm^3 mol^{-1}). Therefore, an average molar volume of 7 cm^3 mol^{-1} was considered and calculations were carried out for the two oxides.

Figure 4.21 shows that the ratio $\frac{k_w^{(i)}}{k_p^{(i)}}$ is close to the value calculated if chromium oxide is considered as internal oxide for alloys with nickel content up to 40 at.% and all chromium contents. However, for alloys with 60 at.% of nickel and 2 at.% Cr, the ratio $\frac{k_w^{(i)}}{k_p^{(i)}}$ is close to the value calculated if chromium oxide is considered as an internal oxide and the ratio $\frac{k_w^{(i)}}{k_p^{(i)}}$ increases with temperature. The ratio calculated from measurements of weight gain and penetration for alloys with 80 at.% Ni and 2 at.% Cr is found to be higher by a factor of 2-3 than values calculated from alloy chromium content and effective stoichiometry.

Variation of $\frac{k_w^{(i)}}{k_p^{(i)}}$ calculated from measurements of internal oxidation rate constants disagree with the variation expected. Indeed, as previously described in Section 4.2.1, it was shown that the IOZ is mainly composed of iron-chromium spinel in iron-rich alloys, while in nickel-rich alloys more chromium oxide precipitates because of the less stable iron-chromium spinel. Therefore, one can expect that the

ratio $\frac{k_w^{(i)}}{k_p^{(i)}}$ would be close to the value calculated considering spinel as an internal oxide for iron-rich alloys. Then, the ratio $\frac{k_w^{(i)}}{k_p^{(i)}}$ is expected to decrease to reach the value calculated if chromium oxide precipitates in nickel-rich alloys. However, the opposite is observed in Figure 4.21. The unexpected variation of $\frac{k_w^{(i)}}{k_p^{(i)}}$ suggests that the assumption of no enrichment may not be verified and requires further investigation. Moreover, it is thoughtful to evaluate the bias on internal oxidation kinetics induced by the large volume expansion, due to internal oxides precipitation. These questions are addressed in Chapter 5.

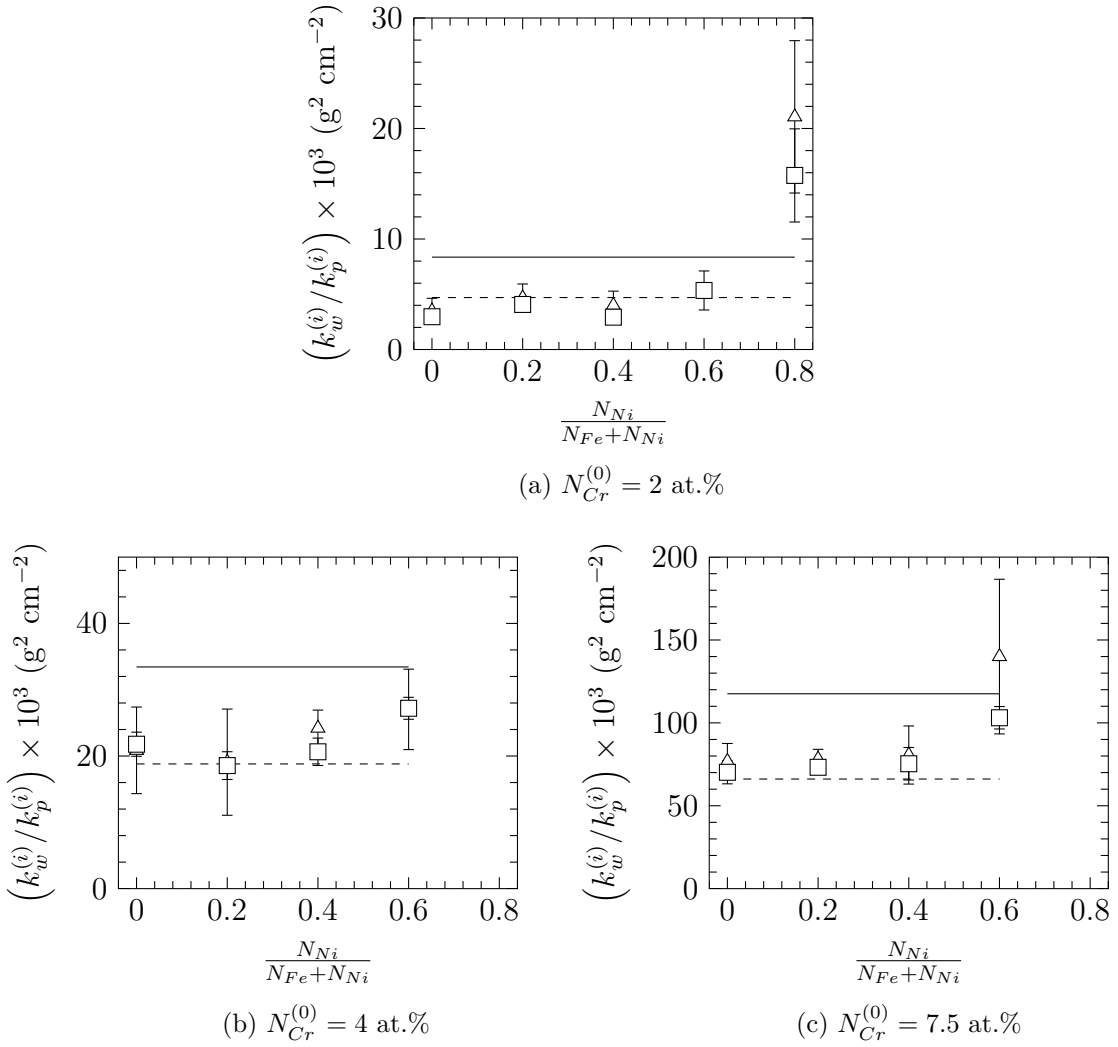

(a) $N_{Cr}^{(0)} = 2$ at.%

(b) $N_{Cr}^{(0)} = 4$ at.%

(c) $N_{Cr}^{(0)} = 7.5$ at.%

Figure 4.21: $\frac{k_w^{(i)}}{k_p^{(i)}}$ calculated from weight change and penetration: 1,000°C (△), 1,050°C (□) or calculated from $N_{Cr}^{(0)}$ and ν for two different internal oxides : $Fe_{0.5}CrO_2$ (——), $CrO_{1.5}$ (- - -).

4.2.3 Internal oxidation in H_2/H_2O gases with 3% water vapour

In this section, internal oxidation measured in H_2/H_2O gases containing 3% of water vapour and the oxygen partial pressure set at the Fe/FeO equilibrium are presented. It has to be noted that these experiments were carried out in a thermobalance to study internal oxidation kinetics by continuous TGA. In addition, after exposure sample were cross-sectioned and internal oxidation rate constants in term of penetration were evaluated.

4.2.3.1 Continuous TGA

Continuous TGA measurements were carried out at 1,000, 1,050 and 1,150°C for alloys with 2 and 7.5 at.% of chromium. In Figure 4.22, kinetics measured at 1,050°C are presented. Kinetics were found to be parabolic after a short transient oxidation at the beginning of the experiment for all temperatures studied. During this transient oxidation, rates were found to be slower than the long term parabolic behaviour. To estimate the internal oxidation constant, in term of weight gain, the fitting method proposed by Monceau *et al.* [6] over the entire duration of the experiment for external oxidation was applied for internal oxidation. As presented in Section 1.1.2, this technique allows the determination of the internal oxidation constant at the stationary regime, avoiding any influence of the transient oxidation in the early stage of the experiment. In Figure 4.23, examples of fitting data obtained from experiments on Fe-Cr alloys at 1,050°C are presented. Values of $k_w^{(i)}$ estimated by using the complete parabolic law are given in Table 4.11.

Values in Table 4.11 are used in Arrhenius plot in Figure 4.24 to determine the pre-exponential factor and activation energy for $k_w^{(i)}$. Values of pre-exponential factor and activation energy evaluated by linear regression of data in Figure 4.24 are presented in Table 4.12. It should be noted that no attempt was made to estimate the error on the pre experimental factor. In addition, no error for the activation energy was reported when only two temperatures were tested. However, it can

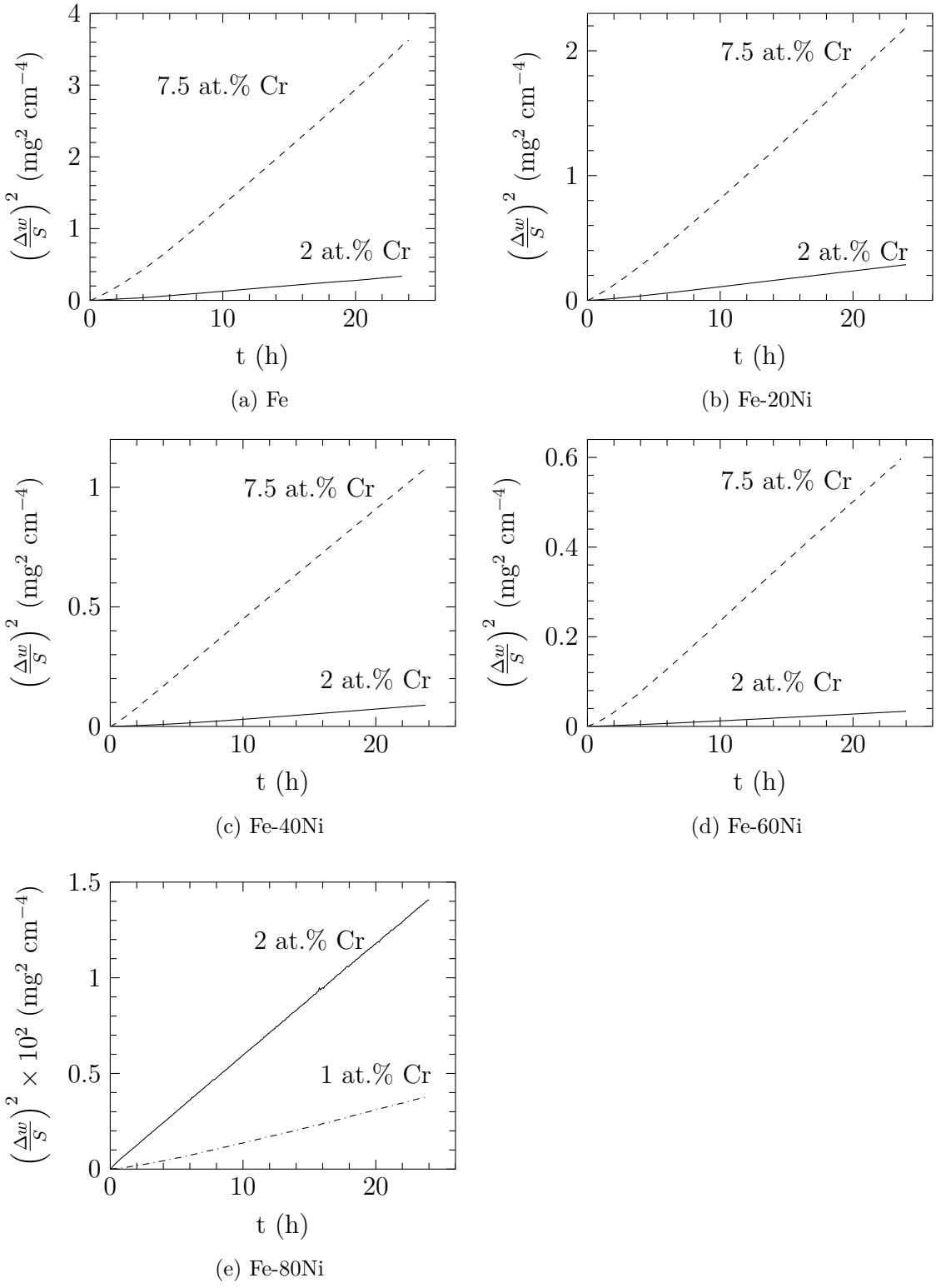

(a) Fe

(b) Fe-20Ni

(c) Fe-40Ni

(d) Fe-60Ni

(e) Fe-80Ni

Figure 4.22: Internal oxidation kinetics measured at 1,050°C in H_2/H_2O gas with 3% water vapour and oxygen partial pressure set at the Fe/FeO equilibrium, $p_{O_2} = (1.1 \pm 0.2) \times 10^{-15}$ atm.

be noticed that values of the pre-exponential factor are less scattered compared to values evaluated from IOZ depth measurement (Figures 4.10 and 4.18).

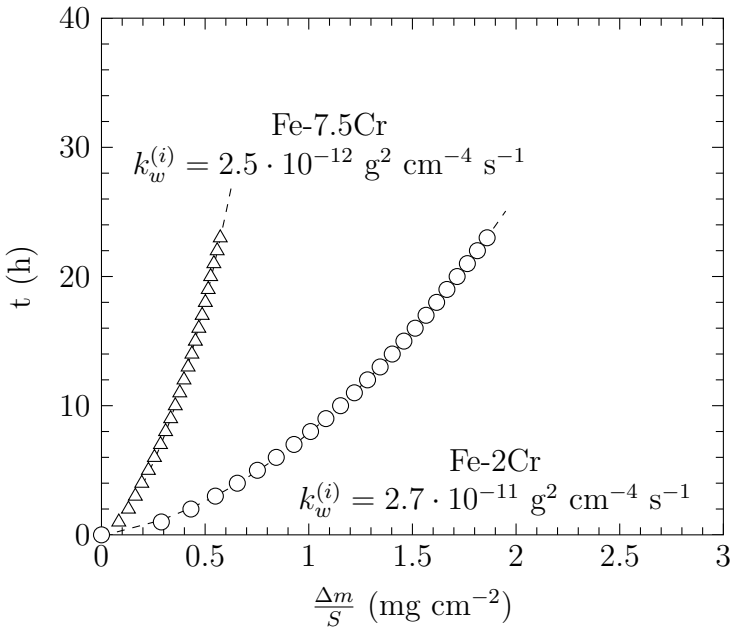

Figure 4.23: Determination of the internal oxidation constant using the complete parabolic law [6]: $t = C\left(\frac{\Delta w}{S}\right)^2 + B\frac{\Delta w}{S} + A$ and $k_w^{(i)} = 1/2C$ in g^2 cm^{-4} s^{-1}. Fe-Cr alloys reacted at 1,050°C.

Table 4.11: Internal oxidation constant measured by continuous TGA in H_2/H_2O gas with 3% water and oxygen partial pressure set at the Fe/FeO equilibrium.

N_{Cr} at.%	$\frac{N_{Ni}}{N_{Fe}+N_{Ni}}$	$k_w^{(i)}$ (g^2 cm^{-4} s^{-1}) 1,000°C	1,050°C	1,150°C
1	0.8	-	$(3.0\pm0.1)\times10^{-14}$	$(2.4\pm0.5)\times10^{-13}$
2	0	$(9.9\pm0.2)\times10^{-13}$	$(2.5\pm0.1)\times10^{-12}$	$(1.4\pm0.1)\times10^{-11}$
	0.2	$(8.0\pm0.2)\times10^{-13}$	$(2.0\pm0.1)\times10^{-12}$	$(9.7\pm0.2)\times10^{-12}$
	0.4	$(3.5\pm0.1)\times10^{-13}$	$(8.7\pm0.2)\times10^{-13}$	$(4.1\pm0.1)\times10^{-12}$
	0.6	$(2.1\pm0.1)\times10^{-13}$	$(2.6\pm0.1)\times10^{-13}$	$(1.3\pm0.1)\times10^{-12}$
	0.8	-	$(8.0\pm0.2)\times10^{-14}$	$(6.6\pm0.2)\times10^{-13}$
7.5	0	$(1.3\pm0.1)\times10^{-11}$	$(2.7\pm0.1)\times10^{-11}$	$(8.7\pm0.2)\times10^{-11}$
	0.2	$(8.2\pm0.2)\times10^{-12}$	$(1.6\pm0.1)\times10^{-11}$	$(6.6\pm0.1)\times10^{-11}$
	0.4	$(3.9\pm0.1)\times10^{-12}$	$(6.4\pm0.1)\times10^{-12}$	$(2.7\pm0.1)\times10^{-11}$
	0.6	-	$(4.0\pm0.1)\times10^{-12}$	$(1.3\pm0.1)\times10^{-11}$

Values in Table 4.12 where plotted as a function of the alloy composition in Figure 4.25.

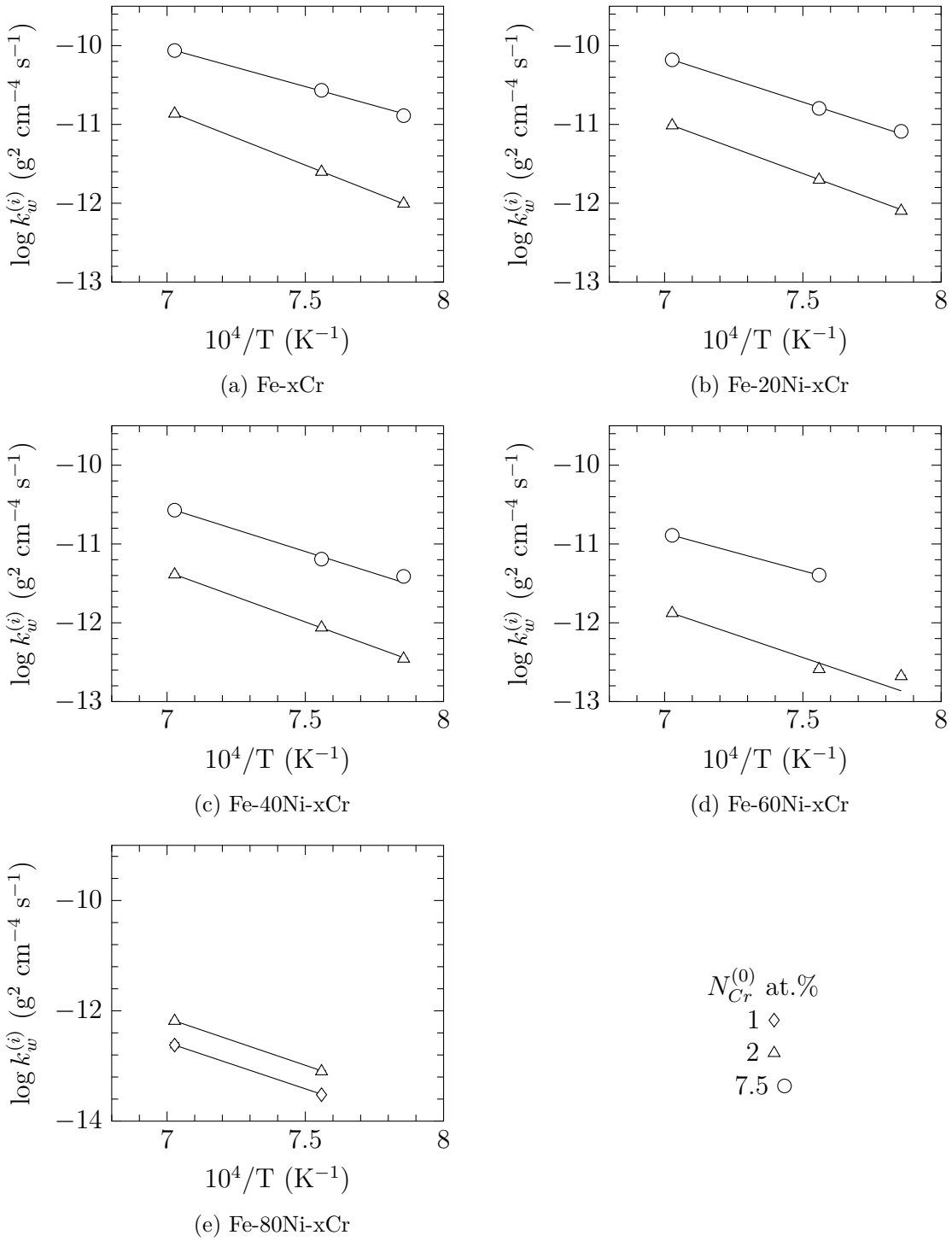

(a) Fe-xCr

(b) Fe-20Ni-xCr

(c) Fe-40Ni-xCr

(d) Fe-60Ni-xCr

(e) Fe-80Ni-xCr

Figure 4.24: Arrhenius plot of $k_w^{(i)}$ measured in H_2/H_2O gases with 3% water vapour and oxygen partial pressure set at the Fe/FeO equilibrium.

Table 4.12: Pre-exponential factor and activation energy for internal oxidation rate constant measured in H_2/H_2O gases with 3% of water vapour and oxygen partial pressure set at the Fe/FeO equilibrium: $k_w^{(i)} = k_w^{(0)} \exp(-Q/RT)$.

N_{Cr} at.%	$\frac{N_{Ni}}{N_{Fe}+N_{Ni}}$	$k_w^{(0)}$ g^2 cm^{-4} s^{-1}	Q kJ mol^{-1}
1	0.8	1.5×10^{-1}	321
2	0	7.1×10^{1}	264±3
	0.2	1.1×10^{-2}	247±3
	0.4	3.7×10^{-3}	244±6
	0.6	3.0×10^{-4}	228±10
	0.8	0.6×10^{-1}	325
7.5	0	5.5×10^{-4}	185±13
	0.2	6.2×10^{-3}	217±18
	0.4	1.7×10^{-3}	212±42
	0.6	6.4×10^{-5}	182

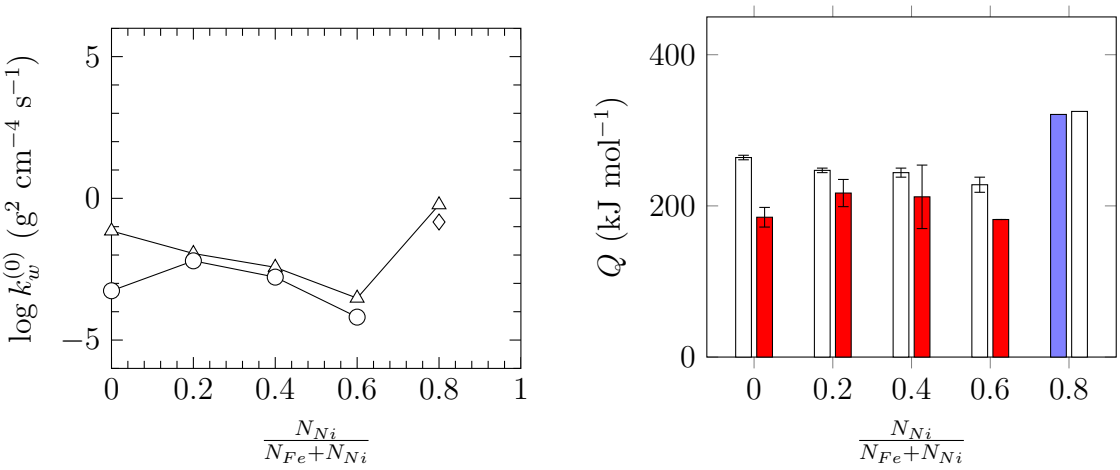

(a) Pre-exponential factor

(b) Activation energy

Figure 4.25: Pre-exponential factor and activation energy for $k_w^{(i)}$ measured in H_2/H_2O gases with 3% water vapour and oxygen partial pressure set at the Fe/FeO equilibrium: 1 at.% (–◇–,▮▮), 2 at.% (–△–,▯▯), 7.5 at.% (–○–,▮▮).

Figure 4.25 shows that the pre-exponential factor decreases with nickel addition for alloys with a nickel content lower than 80 at.%. In addition, pre-exponential factor measured in dilute alloys are slightly higher than values measured in chromium-rich alloys. The activation energy for alloys with a nickel content up to 60 at.% is found to be larger in alloys with 2 at.% of Cr than for alloys with higher chromium content. This is though to be due to fast oxygen diffusion at oxide/matrix interfaces

which decreases the activation energy for the internal oxidation rate constant as reported by Goto *et al.* [49]. However, similar values of Q are found between the different nickel contents. Alloys with nickel content of 80 at.% stand out as they exhibit the largest pre-exponential factor and activation energy for $k_w^{(i)}$. In addition, for this composition, pre-exponential factor and activation energy appears to be independent of the alloys chromium content.

4.2.3.2 Penetration measurement

After exposition in the thermobalance, sample were cross-sectioned and the IOZ depth was measured. Then, the internal oxidation rate constant in term of penetration was estimate using

$$X_{(i)} = 2k_p^{(i)}t \tag{4.22}$$

However, only a single penetration was used to estimate the internal oxidation rate constant. Therefore an uncertainty of 30% was considered for $k_p^{(i)}$ from experiment in thermobalance. In Table 4.13 values of $k_p^{(i)}$ are presented.

Table 4.13: $k_p^{(i)}$ measured after exposition in H_2/H_2O gas with 3% water and the oxygen partial pressure set at the Fe/FeO equilibrium

N_{Cr} at.%	$\frac{N_{Ni}}{N_{Fe}+N_{Ni}}$	$k_p^{(i)}$ (cm^2 s^{-1}) 1,000°C	1,050°C	1,150°C
1	0.8	-	$(2.2\pm0.7)\times10^{-11}$	$(9.1\pm2.7)\times10^{-11}$
2	0	$(1.9\pm0.6)\times10^{-10}$	$(4.2\pm1.3)\times10^{-10}$	$(2.8\pm0.8)\times10^{-9}$
	0.2	$(1.0\pm0.3)\times10^{-10}$	$(2.4\pm0.7)\times10^{-10}$	$(1.5\pm0.4)\times10^{-9}$
	0.4	$(7.0\pm2.1)\times10^{-11}$	$(1.3\pm0.4)\times10^{-10}$	$(6.5\pm1.9)\times10^{-10}$
	0.6	$(1.6\pm0.5)\times10^{-11}$	$(3.7\pm1.1)\times10^{-11}$	$(1.9\pm0.6)\times10^{-10}$
	0.8	-	$(4.7\pm1.4)\times10^{-12}$	$(5.0\pm1.5)\times10^{-11}$
7.5	0	$(1.4\pm0.4)\times10^{-10}$	$(2.4\pm0.7)\times10^{-10}$	$(1.2\pm0.4)\times10^{-9}$
	0.2	$(8.1\pm2.4)\times10^{-11}$	$(1.7\pm0.5)\times10^{-10}$	$(6.9\pm2.1)\times10^{-10}$
	0.4	$(4.2\pm1.3)\times10^{-11}$	$(7.5\pm2.3)\times10^{-11}$	$(2.6\pm0.8)\times10^{-10}$
	0.6	-	$(2.5\pm0.8)\times10^{-11}$	$(8.4\pm2.5)\times10^{-11}$

The pre-exponential factor and the activation energy for $k_p^{(i)}$ were determined for comparison with parameter estimated from experiment in Fe/FeO Rhines packs and H_2/H_2O gas mixtures with 13% water vapour. As it was done for pre-exponential factor and Q estimated for $k_w^{(i)}$ in Table 4.12, no attempt was made to estimate error on the pre-exponential factor. Values of $k_p^{(0)}$ and Q are presented in Table 4.14.

Table 4.14: Pre-exponential factor and activation energy for internal oxidation rate constant measured in H_2/H_2O gases with 3% water vapour and oxygen partial pressure set at the Fe/FeO equilibrium: $k_p^{(i)} = k_p^{(0)} \exp(-Q/RT)$.

N_{Cr} at.%	$\frac{N_{Ni}}{N_{Fe}+N_{Ni}}$	$k_p^{(0)}$ cm^2 s^{-1}	Q kJ mol^{-1}
1	0.8	1.3×10^{-2}	222
2	0	1.1×10^{2}	288±40
	0.2	3.6×10^{1}	283±21
	0.4	5.0×10^{-1}	242±41
	0.6	3.9×10^{-1}	254±11
	0.8	1.2×10^{3}	364
7.5	0	7.3×10^{-1}	239±52
	0.2	6.8×10^{-2}	218±6
	0.4	2.4×10^{-3}	190±17
	0.6	7.7×10^{-4}	190

4.2.3.3 Comparison between penetration and weight gain measurement

As performed for kinetics measured in gases with 13% water vapour, Equation (4.20) was tested by comparing the ratio $\frac{k_w^{(i)}}{k_p^{(i)}}$ calculated from weight change and penetration measurements and estimated from the alloy chromium content, and the internal oxide stoichiometry. As per calculations carried out in Section 4.2.2, no enrichment was assumed, $\alpha = 1$ and an average alloy molar volume of 7 cm^3 mol^{-1} was used. In addition, the calculation was carried out considering $Fe_{0.5}CrO_2$ or $CrO_{1.5}$ as internal oxides. Results of the calculation are presented in Figure 4.26 which shows that the ratio $\frac{k_w^{(i)}}{k_p^{(i)}}$ from measurements of weight gain and penetration increases with the alloy nickel content. This variation is unexpected as more chromium oxides pre-

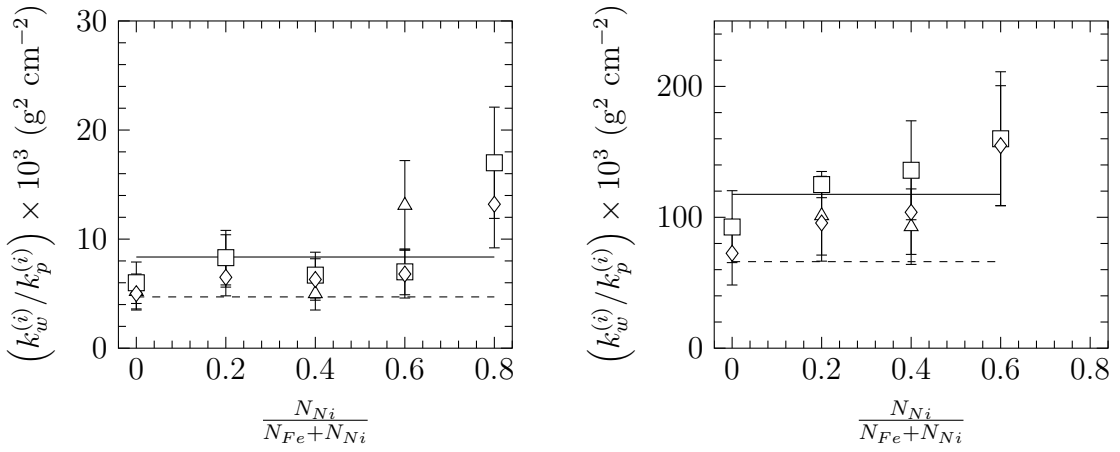

(a) $N_{Cr}^{(0)} = 2$ at.% (b) $N_{Cr}^{(0)} = 7.5$ at.%

Figure 4.26: $\frac{k_w^{(i)}}{k_p^{(i)}}$ calculated from weight change and penetration: 1,000°C (△), 1,050°C (□), 1,150°C (◊) or calculated from $N_{Cr}^{(0)}$ and ν for two different internal oxides: $Fe_{0.5}CrO_2$ (——), $CrO_{1.5}$ (- - -).

cipitate in nickel-rich alloys, the internal oxide stoichiometry should tend towards the chromium oxide stoichiometry, and therefore $\frac{k_w^{(i)}}{k_p^{(i)}}$ is expected to decreases with the alloy nickel content. However, it should be noted that when $k_w^{(i)}$ is estimated with the complete parabolic law, the transient stage at the beginning of the oxidation is not considered while $k_p^{(i)}$ estimated from penetration measurements takes into account this short transient stage which slightly reduce the value of $k_p^{(i)}$. Therefore, the two different methods used to estimate internal oxidation rate constants may yield a small overestimation of the ratio $\frac{k_w^{(i)}}{k_p^{(i)}}$. Nevertheless, the significant increase of the ratio $\frac{k_w^{(i)}}{k_p^{(i)}}$ in nickel-rich alloys suggests that the penetration corresponding to the weight change was underestimated by a factor of approximately 1.5, which is unlikely. However as suggested when this calculation was carried out for kinetics measured in H_2/H_2O gases with 13% water vapour (Section 4.2.2), the assumption that no enrichment takes place during internal oxidation may also not be verified for nickel-rich alloys. Methods to estimate the enrichment factor are presented in Chapter 5.

4.3 Effect of water vapour and hydrogen on internal oxidation rates

Internal oxidation reactions were carried out in various atmospheres to investigate the effect of water vapour and/or hydrogen on this type of oxidation. Firstly, the question of the effect of residual hydrogen present in the alloy due to sample preparation procedures (annealing under pure H_2) for internal oxidation experiments carried out in Fe/FeO Rhines packs has to be addressed. In Section 3.3, it was shown that in a Rhines pack, there is a small hydrogen partial pressure ($p_{H_2} \approx 1.4 \times 10^{-3}$ atm) set by the equilibrium between water vapour coming from the silica tube and the oxygen partial pressure fixed by the Fe/FeO buffer. Therefore, for a sample in a Rhines pack, it is considered that the sample contains a uniform hydrogen distribution and hydrogen mole fraction at sample surfaces is fixed at 0. Under these conditions, the mole fraction of hydrogen in the sample after a time t was calculated by Barrer [121] and is given by

$$N_H(t) = \sum_{n=0}^{\infty} \frac{8N_H^{(0)}}{(2n+1)^2\pi^2} \exp\left(\frac{-D(2n+1)^2\pi^2 t}{l^2}\right) \tag{4.23}$$

where $N_H^{(0)}$ is the initial mole fraction of hydrogen in the sample, D the solute diffusion coefficient and l the sheet thickness. To estimate the time required to diffuse out residual hydrogen, a reasonable value for $N_H^{(0)}$ has to be selected. However, only data for hydrogen solubility in pure Fe and Ni at high temperature are present in the literature [122, 123]. Values published showed that at 1,200°C and under 1 atm of hydrogen, pure nickel dissolved 600 at.ppm while the hydrogen solubility in pure iron is 400 at.ppm. Therefore, the value of 600 at.ppm was selected for $N_H^{(0)}$ as it gives the longest desorption time. In addition, the sample thickness was taken equal to 1.4 mm and hydrogen diffusion coefficients published by Yamanishi *et al.* [124] and Dus *et al.* [125] were used for Fe-Ni alloys and hydrogen diffusion coefficient in iron were taken from Bester *et al.* [126]. Finally, it was considered that residual hydrogen has left the sample if $N_H(t) = 1 \times 10^{-9}$.

The time required to diffuse out residual hydrogen was only calculated at 1,000°C because at this temperature the time for hydrogen to diffuse is the longest due to the slowest hydrogen diffusion. However, diffusion coefficients for Fe-Ni alloys were extrapolated to 1,000°C using the Arrhenius relation because the authors carried out their measurements at a maximum temperature of 850°C. In Table 4.15, the time required for residual hydrogen to diffuse out of the sample at 1,000°C is given along with hydrogen diffusion coefficients used in Equation 4.23. From the

Table 4.15: Time required to diffuse out of the sample residual hydrogen at 1,000°C

$\frac{N_{Ni}}{N_{Fe}+N_{Ni}}$	$D_H \times 10^5$ cm^2 s^{-1}	time min
0	16	3
0.2	12	4
0.4	4.4	10
0.6	11	4
0.8	7.0	6

values in Table 4.15, it seems that the time required to remove residual hydrogen from the sample is extremely small compared to the duration of internal oxidation experiment. It should be noted that for higher temperature than 1,000°C, the time to diffuse out residual hydrogen is smaller than values reported in Table 4.15. Therefore, it was considered that the possible residual hydrogen present in materials prior to experiment has no effect on internal oxidation kinetics measured in Rhines packs and, on the evaluation of the oxygen permeability

It is interesting to have a brief look at the effect of water vapour on the distribution of the two subzones where $FeCr_2O_4$ and Cr_2O_3 precipitate in the IOZ. Indeed, Ueda *et al.* [69] carried out internal oxidation of Fe-Ni-Cr alloys in dry and wet atmospheres with the oxygen partial pressure set at the Fe/FeO equilibrium at 800°C, and suggested that the under humid gases the solid state reaction to convert chromium oxide into iron chromium spinel is enhanced. To check this suggestion, values of f measured after exposure in Fe/FeO Rhines packs (Table 4.1) and H_2/H_2O with different water vapour contents but the oxygen partial pressure

set at the Fe/FeO equilibrium (Tables 4.6 and 4.7) are compared. In addition, as observed in Sections 4.1.1 and 4.2.1, the temperature seems to have no effect on the parameter f, and therefore only values measured at 1,150°C are compared.

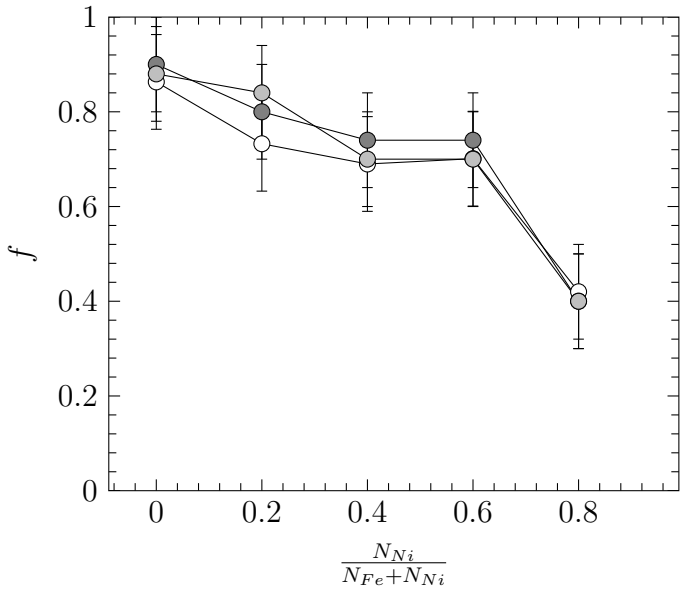

Figure 4.27: Values of f measured at 1,150°C in various environment with the oxygen partial set at the Fe/FeO equilibrium : Fe/FeO Rhines packs (–○–), 3% H_2O (–◍–), 13% H_2O (–●–).

Figure 4.27 shows that water vapour and/or hydrogen and the concentration of these species in the gas have no significant effect on the distribution of the two subzone in the IOZ. However, it should be noted that the uncertainty in the parameter f is large and a small effect of the presence of water vapour in the gas would not be observable. The difference between the present results and Ueda *et al.*'s observations may be due to the lower temperature used by the latter authors in their experiment. In addition, Ueda *et al.* used low partial pressures of water and hydrogen, 3.3×10^{-3} and 6.5×10^{-3} atm, respectively compared to 0.13 and 0.20 atm used in the present study.

Internal oxidation rate constants in terms of weight gain or penetration, were found to decrease with the increase of alloy nickel content in all environments, suggesting that the water vapour and/or hydrogen do not affect the dependency of internal oxidation kinetics on alloy nickel content. In particular, when $k_p^{(i)}$ is measured at 1,000 and 1,050°C, this parameter is found to be independent of the alloy

chromium content for alloys with 4 and 7.5 at.% of chromium. This was observed for alloys reacted in Fe/FeO Rhines packs and H_2/H_2O gas mixtures. Therefore, this unexpected behaviour seems not to be related to the environment. One possible explanation is based on the fast diffusion of oxygen at matrix/oxide interface. Setiawan *et al.* [43] and Takada *et al.* [40] proposed that the oxygen permeability measured is an effective permeability and it varies with the alloy chromium content in linear way. Thus, the effective oxygen permeability is expressed by

$$N_O D_O^{eff} = N_O^{(s)} D_O^{mat} + N_B^{(0)} \lambda \tag{4.24}$$

where $N_O^{(s)} D_O^{mat}$ is the oxygen permeability of the matrix and λ a constant reflecting the contribution of fast oxygen diffusion at matrix/oxide interface. Substituting Equation (4.24) in (4.16) yields

$$k_p^{(i)} = \frac{1}{\nu\alpha}\left(\frac{N_O^{(s)} D_O^{mat}}{N_{Cr}^{(0)}} + \lambda\right) \tag{4.25}$$

From Equation (4.25), the internal oxidation rate constant is independent of the alloy chromium content if the following relation is verified

$$\frac{N_O^{(s)} D_O^{mat}}{N_{Cr}^{(0)}} << \lambda \tag{4.26}$$

indicating that matrix/oxide interface diffusion is controlling the internal oxidation. Similar values of $k_p^{(i)}$ measured at 1,000 and 1,050°C for alloys with 4 and 7.5 at.% of chromium suggest that at these temperatures, oxygen diffusion at matrix oxide interface is preponderant. In addition, this is qualitatively supported by the fact this was observed at the lowest temperature investigated, and in alloys with the highest chromium content, and therefore oxide volume fraction, where the effect of fast oxygen diffusion at matrix oxide interface is enhanced, as reported by Goto *et al.* [49].

It is of interest to compare values of activation energy for the internal oxidation rate constants measured in the different environments. In Figure 4.28, values

of Q for $k_p^{(i)}$ evaluated in the different environments and reported in Tables 4.5, 4.9 and 4.14 are compared. As is seen, the activation energy values for internal oxidation rate constants estimated from experiments in the different environments are largely similar excepted for a few cases. For alloys with 2 at.% of chromium, alloys with 40 at.% of nickel exhibit the highest activation energy when exposed to H_2/H_2O gases with 13% water vapour.

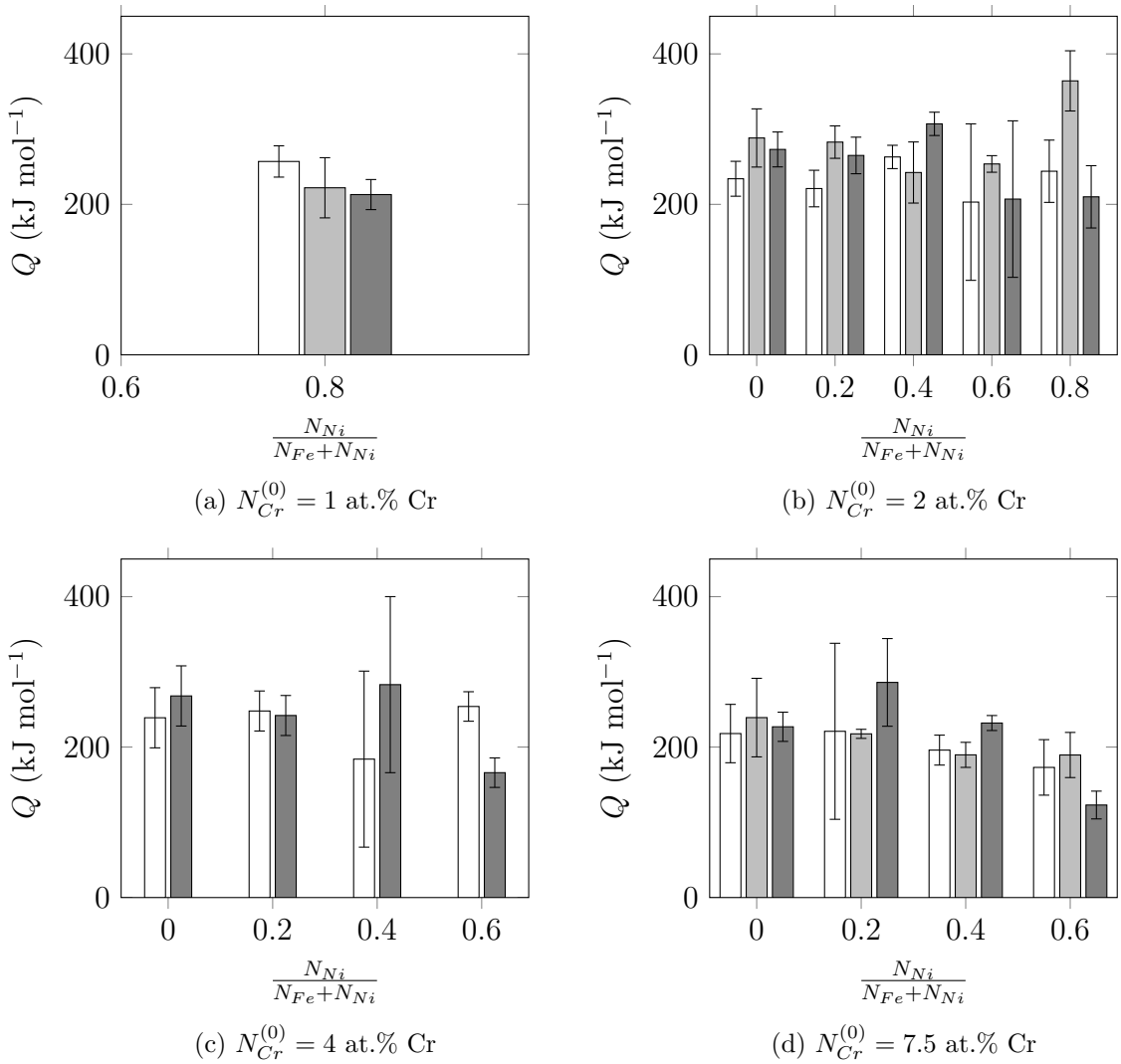

(a) $N_{Cr}^{(0)} = 1$ at.% Cr

(b) $N_{Cr}^{(0)} = 2$ at.% Cr

(c) $N_{Cr}^{(0)} = 4$ at.% Cr

(d) $N_{Cr}^{(0)} = 7.5$ at.% Cr

Figure 4.28: Comparison of activation energy for $k_p^{(i)}$ measured in various environment : Fe/FeO Rhines packs (▯▯), 3% H_2O (▮▯), 13% H_2O (▮▮)

A significant difference also is observed for alloys Fe-60Ni-4Cr for which the activation energy found after exposition in humid gases is lower than activation energy found after experiment in Fe/FeO Rhine packs. No explanation was found for these apparent differences.

It should be noted that $k_p^{(i)}$ for experiments in H_2/H_2O gas mixtures with 3% water vapour was estimated from a single penetration depth measurement at the end of exposure. Therefore, uncertainty in the internal oxidation rate constants estimated is significant and activation energies reported in Figure 4.28 for experiments in 3% H_2O are only considered as indicative.

Finally, it is interesting to compare directly the values of $k_p^{(i)}$ and $k_w^{(i)}$ measured in the various environments. In Figure 4.29, the ratio of internal oxidation rate constant in term of penetration measured in H_2/H_2O gases with 13% water vapour, $k_p^{(i)(13\%\ H_2O)}$, to the rate constant measured in Fe/FeO Rhines packs, $k_p^{(i)\ (RP)}$, is presented. It shows that overall, internal oxidation rate constant measured in H_2/H_2O and Fe/FeO Rhines packs are very similar. Some alloys exhibits low or high ratio, almost all are equal to 1, within the uncertainty limits. These differences in rates are therefore not considered as significant.

Some alloys do stand out: Fe-20Ni-7.5Cr at 1,150°C or Fe-40Ni-2Cr and Fe-40Ni-4Cr at the same temperature. No clear reason for these high ratios was identified and more experiments would be required to confirmed those high values. Overall, Figure 4.29 shows that the effect of water vapour on internal oxidation constant is not large and internal oxidation kinetics differ at the maximum by a factor of 2 at the uncertainty limits. However, it is possible that water vapour may have a small effect on internal oxidation rates. Observation of this would required determination of $k_p^{(i)}$ with an extremely high precision, as any effect of water vapour is obviously small. For this reason no comparison of internal oxidation rate constants evaluated from IOZ penetration for alloys reacted in H_2/H_2O gases with 3% H_2O with Rhines pack results was attempted. The large error in $k_p^{(i)}$ estimated from TGA experiments invalidates the comparison. Oxygen solubility measurement (Section 3.3) show that water vapour may have an effect at low temperature in iron-rich alloys. Therefore internal oxidation rate constant in term of weight change evaluated at 1,000 and 1,050°C for alloy reacted in H_2/H_2O with 13% water vapour, $k_w^{(i)(13\%H_2O)}$, was compared to the rate constant estimated in humid gases

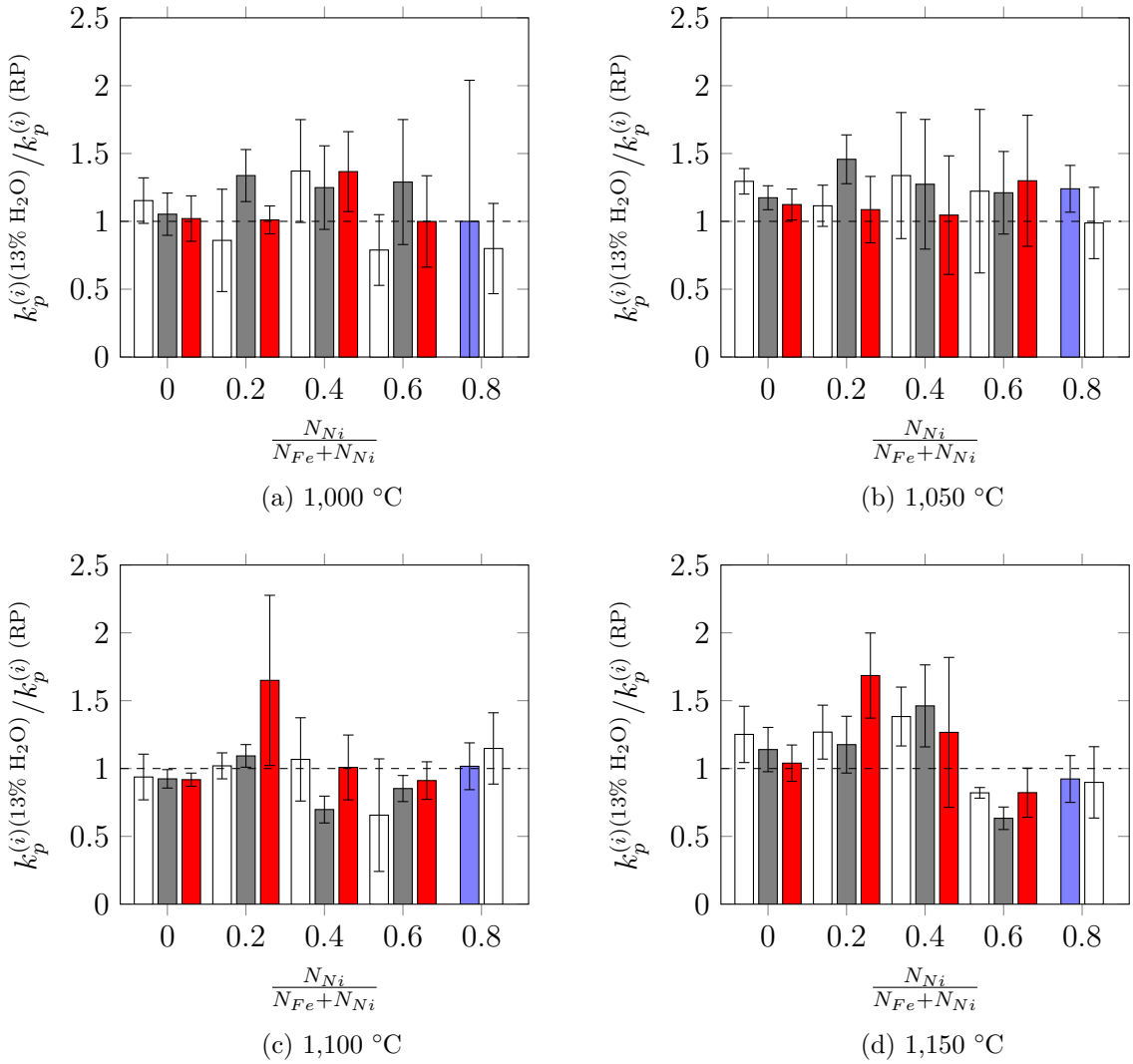

(a) 1,000 °C (b) 1,050 °C

(c) 1,100 °C (d) 1,150 °C

Figure 4.29: Comparison of internal oxidation constant evaluated by IOZ depth measurement in Rhines pack, $k_p^{(i)\ (RP)}$, and in flowing Ar-H_2-H_2O with 13% water vapour, $k_p^{(i)(13\%\ H_2O)}$: 1 at.% Cr (▮▮), 2 at.% Cr (▯▯), 4 at.% Cr (▮▮), 7.5 at.% Cr (▮▮).

with 3% water vapour, $k_w^{(i)(3\%H_2O)}$. Ratios of internal oxidation rate constant are presented in Figure 4.30.

It is seen that good agreement is found between internal oxidation rate constants determined in humid environment with different water vapour contents for alloys with nickel content up to 40 at.% of nickel. However, for alloys with 60 and 80 at.% of nickel, rate constants measured in low water content gases are found smaller than those measured in H_2/H_2O gases with 13% water vapour. This result is though to be due to the difference in experimental protocol for these experiments

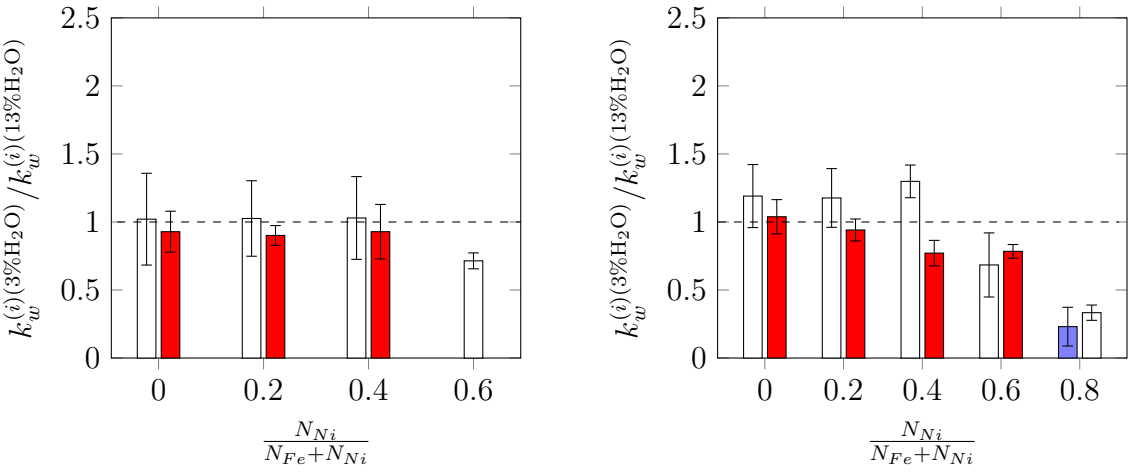

(a) 1,000 °C (b) 1,050 °C

Figure 4.30: Comparison of internal oxidation constant evaluated by weight gain measurement in H_2/H_2O gases with 3% water vapour, $k_w^{(i)(3\%H_2O)}$, and in H_2/H_2O gases with 13% water, $k_w^{(i)(13\%H_2O)}$. Oxygen partial pressure set at the Fe/FeO equilibrium in all environments: 1 at.% Cr (▮▮), 2 at.% Cr (▯▯), 7.5 at.% Cr (▮▮).

(Section 4.2.1). Low water vapour content gases were used in a thermobalance where the sample is held in the hot zone of the furnace, under flowing Ar-5%H_2, during the heating stage. In this step of the experiment , it is suggested that passivation of the alloy takes place and affects further internal oxidation. This idea is supported by the fact that at the low oxygen partial pressure, it is more favourable to form a chromia scale in nickel-rich alloys as shown in Section 2.1.2. Those results highlight the fact that initial conditions used to study internal oxidation are important.

4.4 Summary

In this Chapter, internal oxidation oxidation kinetics measured in various environments were presented, along with a brief description of IOZ microstructures. Firstly, it was shown that the internal oxidation zone is composed of 2 subzones in which $FeCr_2O_4$ spinel and Cr_2O_3 precipitate. In addition, the relative size of the two subzones varies with the alloy nickel content. In Fe-Cr alloys, the IOZ is mainly composed of iron-chromium spinel and the size of this subzone decreases with nickel addition while the size of the subzone containing chromium oxide was increasing.

This variation of the distribution of the two subzones is predicted by thermodynamics and results from the lower stability of the $FeCr_2O_4$ spinel in nickel-rich alloys. It should also be noted that the distribution of the two subzones was found to be independent of the temperature and the environment.

Internal oxidation kinetics were parabolic. Rates measured in Fe/FeO Rhines packs were close to those evaluated from experiments in H_2/H_2O gases with 13% water vapour with oxygen partial pressure set at the Fe/FeO equilibrium. This indicates no significant effect of the water vapour on kinetics. The same finding was arrived at for the activation energy for $k_p^{(i)}$, reinforcing the conclusion that water vapour has no effect on internal oxidation kinetics. However, the activation energy for the internal oxidation rate constant was found to decrease with increasing alloy chromium content, indicating that fast oxygen diffusion at matrix/oxide interface in the IOZ affect the internal oxidation kinetics. This conclusion is reinforced by the observation that $k_p^{(i)}$ becomes independent of alloy chromium content at the lowest temperature for chromium-rich alloys.

Internal oxidation measured by weight gain in humid gases with a different water vapour content at 1,000 and 1,050°C were found to be in agreement for iron-rich alloys, while discrepancies were observed in nickel-rich alloys. It is proposed that the different rates observed were due to the different experimental protocols used for experiment in low and high water vapour content gases. Therefore, it is concluded that the water vapour content has no effect on the internal oxidation kinetics, but that initial conditions used to study internal and external oxidation may have a strong effect on the kinetic observed subsequently.

Chapter 5

Oxygen permeability

This chapter is devoted to the calculation of the oxygen permeability from internal oxidation kinetics determined by penetration measurement and discontinuous/continuous TGA. According to Wagner [1], the oxygen permeability can be estimated from the internal oxidation rate constant using Equation 5.1.

$$k_p^{(i)} = \frac{N_O^{(s)} D_O}{\nu \alpha N_{Cr}^{(0)}} \tag{5.1}$$

where $N_O^{(s)} D_O$ is the oxygen permeability of the base metal, ν the effective stoichiometry, α the enrichment factor and $N_{Cr}^{(0)}$ the alloy mole fraction. Critically, this formulation ignores the volume change accompanying oxide precipitation, an issue addressed in this chapter. It is also possible to evaluate the oxygen permeability from weight gain measurement as derived by Gesmundo *et al.* [31], who gave the equation to calculate the oxygen permeability from the internal oxidation rate constant, $k_w^{(i)}$, expressed in terms of weight change:

$$k_w^{(i)} = \left(\frac{M_O}{V_{alloy}} \right)^2 \alpha \nu N_{Cr}^{(0)} N_O^{(s)} D_O \tag{5.2}$$

here M_O is the oxygen atomic weight, V_{alloy} the alloy molar volume and the other parameters have the same meaning as in Equation (5.1). However, Wagner did not consider volume expansion in his development while the presence of nodules, with the matrix composition, on nickel-rich alloy surface reveals that a large volume expansion takes place in the IOZ during internal oxidation. This volume change is due to internal oxide precipitation with higher molar volume than the alloy. Therefore, the expression of the internal oxidation rate constant was developed with consideration of volume expansion in the first section of this chapter. In addition, to compute values of oxygen permeability from internal oxidation kinetic measurements, knowledge of the enrichment factor and the effective stoichiometry is required. These parameters are evaluated in the second and third sections of this chapter, respectively. In the last section, oxygen permeability calculated from internal oxidation kinetics is presented.

5.1 $k_p^{(i)}$ with consideration of volume expansion

In Chapter 4, the internal oxidation kinetic rate constant was defined by

$$X^2 = 2k_p^{(i)}t \tag{5.3}$$

To relate the internal oxidation rate constant to the oxygen permeability it is assumed that the IOZ growth results from oxygen diffusion and volume expansion. At high temperature, it is assumed that the displacement of the internal oxidation front due to oxygen diffusion follows a parabolic behaviour. Thus, the small displacement of the internal oxidation front due to oxygen diffusion alone is given by

$$\delta X = \frac{2\gamma^2 D_O}{X}\delta t \tag{5.4}$$

where γ is a kinetic parameter introduced by Wagner [1] and D_O the oxygen diffusion coefficient. The incremental displacement of the internal oxidation front due to oxygen diffusion and volume expansion is given by

$$\delta X = \frac{2\gamma^2 D_O}{X}\delta t + \delta X\frac{\Delta v}{v} \tag{5.5}$$

where $\Delta v/v$ is the term of volume expansion. Rearranging Equation (5.5) yields

$$X\delta X = \frac{1}{\left(1-\frac{\Delta v}{v}\right)}2\gamma^2 D_O\delta t \tag{5.6}$$

By integration of the previous equation under the assumption that at $t = 0$, $X = 0$ gives the following relation for the IOZ depth as function of the time

$$X^2 = \frac{4\gamma^2 D_O t}{\left(1-\frac{\Delta v}{v}\right)} \tag{5.7}$$

Substituting Equation (5.7) in (5.3) yields

$$k_p^{(i)} = \frac{2\gamma^2 D_O}{\left(1-\frac{\Delta v}{v}\right)} \tag{5.8}$$

In addition, the kinetic parameter γ is given by [1]

$$\gamma^2 = \frac{N_O^{(s)}}{2\nu N_{Cr}^{(0)}\alpha} \tag{5.9}$$

and combining Equations (5.9) and (5.8) yields the following expression for the internal oxidation rate constant

$$k_p^{(i)} = \frac{N_O^{(s)} D_O}{\nu N_{Cr}^{(0)}\alpha} \frac{1}{\left(1 - \frac{\Delta v}{v}\right)} = \frac{N_O^{(s)} D_O}{\nu N_{Cr}^{(0)}\alpha}\Gamma \tag{5.10}$$

with

$$\Gamma = \frac{1}{\left(1 - \frac{\Delta v}{v}\right)} \tag{5.11}$$

The expression of the internal oxidation rate constant allows the determination of the oxygen permeability if the value of the enrichment factor and the stoichiometry of the internal oxide are known. The evaluation of these parameters is presented in the next sections of this chapter.

5.2 Enrichment factor

The oxidation morphology results from the competition between the inward flux of oxygen and the outward flux of chromium. If the flux of oxygen is extremely large compared to the flux of chromium, internal oxidation takes place but the chromium does not have enough time to diffuse. Then, the amount of chromium present as oxide in the internal oxidation zone is equal to the quantity originally present in the corresponding volume of the alloy and no enrichment is observed. In contrast, if the flux of oxygen is of the same order of magnitude as that of the chromium flux, internal oxidation still takes place but extra chromium coming from the alloy interior is found in the internal oxidation zone. This extra chromium represents the enrichment of the IOZ. The degree of enrichment is defined by

$$\alpha = \frac{N_{Cr}^{Ox}}{N_{Cr}^{(0)}} \tag{5.12}$$

with

$$N_{Cr}^{Ox} = \frac{n_{Cr}^{Ox}}{n_{Cr}^{(0)} + n_{Fe}^{(0)} + n_{Ni}^{(0)}} \tag{5.13}$$

$$N_{Cr}^{(0)} = \frac{n_{Cr}^{(0)}}{n_{Cr}^{(0)} + n_{Fe}^{(0)} + n_{Ni}^{(0)}} \tag{5.14}$$

where $n_{Cr}^{(0)}$, $n_{Fe}^{(0)}$ and $n_{Ni}^{(0)}$ are the initial numbers of mole of chromium, iron and nickel in the IOZ prior to internal oxidation, respectively and n_{Cr}^{Ox} the number of mole of chromium as oxide in the IOZ after internal oxidation. If extra chromium from the core of the material diffuses into the IOZ, then $N_{Cr}^{Ox} > N_{Cr}^{(0)} \Leftrightarrow \alpha > 1$. The enrichment factor is evaluated by two methods presented in this section: a diffusional approach using Wagner's model and the internal oxide volume fraction measurement.

5.2.1 Diffusional approach for enrichment factor calculation

In Wagner's theoretical treatment of internal oxidation [1], the author gave the following equation to estimate the enrichment factor

$$\alpha = \left[\sqrt{\pi} hc \exp(hc^2)\,\mathrm{erfc}(hc)\right]^{-1} \tag{5.15}$$

with

$$hc = \gamma\varphi^{1/2} = \gamma\sqrt{\frac{D_O}{\tilde{D}_{Cr}}} \tag{5.16}$$

Although, the value of D_O might be unknown. However, D_O and γ are related to the internal oxidation rate constant by Equation (5.8). Substituting the latter Equation in (5.16) yields a new expression of the variable hc

$$hc = \left[\frac{k_p^{(i)}}{2\Gamma\tilde{D}_{Cr}}\right]^{1/2} \tag{5.17}$$

However, to compute the value of the enrichment factor, the volume expansion has to be evaluated. The volume expansion calculation is carried out in the following

section.

5.2.1.1 IOZ expansion due to internal oxide precipitation

In order to evaluate the volume expansion due to the precipitation of an internal oxide, it was assumed that all the chromium contained in an initial volume oxidised and the resulting volume was calculated. However, the internal oxidation zone is composed of two subzones, in which a specific oxide precipitates in each of them, as illustrated in Figure 5.1.

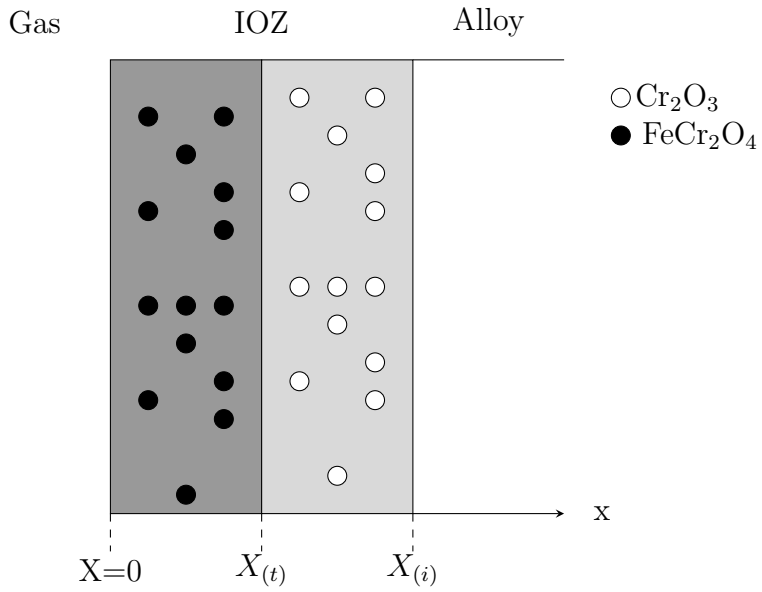

Figure 5.1: Internal oxide distribution in the internal oxidation zone.

Therefore, the volume expansion was calculated in the case of the formation of Cr_2O_3 or $FeCr_2O_4$. If a unit volume, v, of a ternary alloy Fe-Ni-Cr is considered, the number of mole of each species in this volume is given by

$$n_{Fe}^{(0)} = N_{Fe}^{(0)} \frac{v}{V_{alloy}} \tag{5.18}$$

$$n_{Ni}^{(0)} = N_{Ni}^{(0)} \frac{v}{V_{alloy}} \tag{5.19}$$

$$n_{Cr}^{(0)} = N_{Cr}^{(0)} \frac{v}{V_{alloy}} \tag{5.20}$$

where $N^{(0)}_{Fe/Ni/Cr}$ is the mole fraction of the corresponding species, respectively. In addition, the relation between the different mole fractions is given by

$$N^{(0)}_{Fe} + N^{(0)}_{Ni} + N^{(0)}_{Cr} = 1 \tag{5.21}$$

If all the chromium oxidises as chromium oxide and enrichment takes places during the oxidation process, the volume of chromium oxide is expressed by

$$v_{CrO_{1.5}} = v\alpha N^{(0)}_{Cr} \frac{V_{CrO_{1.5}}}{V_{alloy}} \tag{5.22}$$

where $V_{CrO_{1.5}}$ is the chromium oxide molar volume and the volume of matrix is given by

$$v_{matrix} = v\left(N^{(0)}_{Ni} + N^{(0)}_{Fe}\right)\frac{V_{matrix}}{V_{alloy}} \tag{5.23}$$

where V_{matrix} is the molar volume of the matrix, composed only of iron and nickel. However, on the assumption that the chromium has no effect on the alloy molar volume, $V_{matrix} = V_{alloy}$.

Combining Equations (5.21), (5.22) and (5.23), the difference of volume before and after the precipitation Cr_2O_3 is found to be given

$$\Delta v_{CrO_{1.5}} = (v_{CrO_{1.5}} + v_{matrix}) - v = v\alpha N^{(0)}_{Cr}\frac{V_{CrO_{1.5}}}{V_{alloy}} + v\left(1 - N^{(0)}_{Cr}\right) - v \tag{5.24}$$

This may be rewritten to find the fractional volume expansion

$$\frac{\Delta v_{CrO_{1.5}}}{v} = N^{(0)}_{Cr}\left[\alpha\frac{V_{CrO_{1.5}}}{V_{alloy}} - 1\right] \tag{5.25}$$

If an iron-chromium spinel precipitates, the volume of spinel is given by an expression similar to Equation (5.22) assuming again that all the chromium is oxidised.

$$v_{Fe_{0.5}CrO_2} = v\alpha N^{(0)}_{Cr}\frac{V_{Fe_{0.5}CrO_2}}{V_{alloy}} \tag{5.26}$$

In addition, iron is consumed to form the iron-chromium spinel. This amount of

material represents a volume which has to be subtracted from the volume of matrix. Therefore, the matrix volume is given by

$$v_{matrix} = v\left(N_{Ni}^{(0)} + N_{Fe}^{(0)}\right)\frac{V_{matrix}}{V_{alloy}} - 0.5v\alpha N_{Cr}^{(0)}\frac{V_{matrix}}{V_{alloy}} \tag{5.27}$$

Then the fractional volume expansion is given by

$$\frac{\Delta v_{Fe_{0.5}CrO_2}}{v} = N_{Cr}^{(0)}\left[\alpha\frac{V_{Fe_{0.5}CrO_2}}{V_{alloy}} - (1 + 0.5\alpha)\right] \tag{5.28}$$

In Table 5.1, the volume expansion is calculated for Fe-Cr and Ni-Cr alloys with different chromium content, assuming no enrichment ($\alpha = 1$), if $FeCr_2O_4$ spinel or Cr_2O_3 oxide precipitates. To calculate the fractional volume expansion, the alloy molar volume was considered equal to the molar volume of pure Fe and Ni, presented in Table 1.6, for the corresponding alloy.

Table 5.1: Fractional volume expansion calculated considering $Fe_{0.5}CrO_2$ or $CrO_{1.5}$ oxides in Fe-Cr or Ni-Cr alloys.

	$N_{Cr}^{(0)}$ at.%	$\frac{\Delta v_{Fe_{0.5}CrO_2}}{v}$	$\frac{\Delta v_{\mathrm{CrO_{1.5}}}}{v}$
Fe-Cr	2	4%	2%
	7.5	13%	8%
Ni-Cr	2	4%	2%
	7.5	16%	9%

Calculation of the fractional volume expansion showed that in alloys containing 7.5 at.% of chromium, if iron-chromium spinel precipitates, the expansion reaches value up to 16% in Ni-Cr alloys. At this stage of the calculation it is thoughtful to determine the total expansion of the IOZ when two different oxides precipitate. To evaluate the total IOZ expansion, it was assumed that the best estimate of the volume change is given by the weighted average of the two subzone expansions. Considering the ratio $f = X_{(t)}/X_{(i)}$, with $X_{(t)}$ the depth where chromium oxide is converted to iron-chromium spinel, the total volume expansion

is given by

$$\overline{\left(\frac{\Delta v}{v}\right)} = f\left(\frac{\Delta v_{Fe_{0.5}CrO_2}}{v}\right) + (1-f)\left(\frac{\Delta v_{CrO_{1.5}}}{v}\right) \tag{5.29}$$

Substituting Equations (5.25) and (5.28) in (5.29) yields

$$\overline{\left(\frac{\Delta v}{v}\right)} = N_{Cr}^{(0)}\left[f\alpha\frac{V_{Fe_{0.5}CrO_2}}{V_{alloy}} + (1-f)\,\alpha\frac{V_{CrO_{1.5}}}{V_{alloy}} - (1+0.5f\alpha)\right] \tag{5.30}$$

and the parameter Γ now given by

$$\Gamma = \frac{1}{1-\overline{\left(\frac{\Delta v}{v}\right)}} \tag{5.31}$$

At this stage of the calculation, it is useful to estimate the variation of Γ with f, $N_{Cr}^{(0)}$ and α. In Figure 5.2, Γ is plotted for different combinations of parameters previously cited. Figure 5.2 shows that the variation of f has a limited effect on

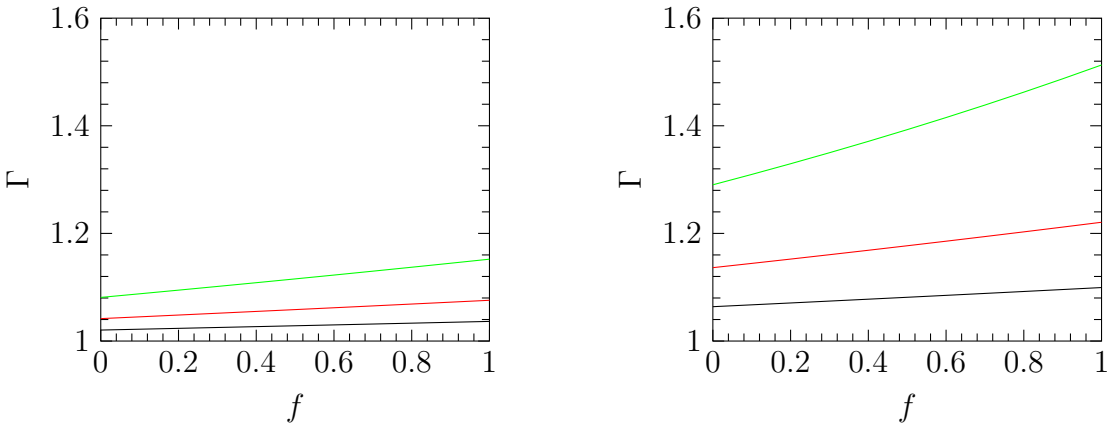

(a) $\alpha = 1$ (b) $\alpha = 2$

Figure 5.2: Variation of Γ calculated for different values of enrichment factor and chromium content : 2 at.% (—), 4 at.% (—), 7.5 at.% (—).

the value of Γ for alloys with 2 and 4 at.% of chromium, regardless of the value of the enrichment factor. However, for alloys with a chromium content of 7.5 at.%, the dependency of Γ on f is more important when the enrichment factor is high. Evaluation of Γ allows determination of the enrichment factor from Equation (5.15), using (5.16).

5.2.1.2 Enrichment factor calculated from diffusional approach

To calculate the enrichment factor from the diffusion of oxygen and chromium, the variable hc is estimated with the following equation

$$hc = \left[\frac{k_p^{(i)}}{2\Gamma\tilde{D}_{Cr}}\right]^{1/2} \tag{5.32}$$

The required value of Γ is obtained as a function of Δv from (5.31) and Δv is found as function of α from Equations (5.25), (5.28) and (5.29). These relationships are combined with Equation (5.15) to obtain an implicit function of α, which must be solved numerically. A MATLAB program was created for this purpose, evaluating α using a step by step method. It was considered that the program had converged when the difference between two successive values of α was lower than 10^{-3}. To compute values of enrichment factors, internal oxidation rate constants found from kinetic measurements presented in Chapter 4 were used along with chromium interdiffusion coefficients taken from the literature. For Fe-Cr alloy calculations, diffusion coefficients published by Bowen and Leak [57] were considered, while values measured by Duh and Dayananda [67] were used for ternary Fe-Ni-Cr alloys. However, the latter authors measured chromium diffusion coefficient in a large domain of composition but only at 1,100°C. To evaluate the interdiffusion of chromium at a specific composition another MATLAB routine was created. This program uses interdiffusion coefficients published by Duh and Dayananda to interpolate the interdiffusion coefficient at a precise composition. It has to be emphasised that for the interpolation, cross-effects were neglected.

In addition, the MATLAB program carries out an extrapolation with temperature using the activation energy measured by Rothman *et al.* [127] of 300 kJ mol^{-1} in the following relation

$$\tilde{D}_{Cr}(T(K)) = \tilde{D}_{Cr}(1,373K) * \exp\left(\frac{Q}{R}\left(\frac{1}{1373} - \frac{1}{T(K)}\right)\right) \tag{5.33}$$

where $\tilde{D}_{Cr}(1,373K)$ is the interdiffusion coefficient interpolated at the desired com-

position in the first part of the MATLAB routine and Q Rothman's activation energy. In Table 5.2, $\tilde{D}_{Cr}$ values calculated for alloy compositions used in internal oxidation experiments are presented. In the Table, the interdiffusion coefficient for

Table 5.2: Interdiffusion coefficient of chromium for Fe-Cr [57] and Fe-Ni-Cr [67] alloys.

$\frac{N_{Ni}}{N_{Fe}+N_{Ni}}$	$N_{Cr}^{(0)}$ at.%	$\tilde{D}_{Cr} \times 10^{12}$ (cm^2 s^{-1})			
		1,000°C	1,050°C	1,100°C	1,150°C
0	2, 4, 7.5	6.5 ± 1.7	19 ± 5	51 ± 13	128 ± 33
0.2	2	5.0 ± 1.3	15 ± 4	40 ± 10	100 ± 26
0.2	4	5.0 ± 1.3	15 ± 4	39 ± 10	99 ± 25
0.2	7.5	4.8 ± 1.3	14 ± 4	38 ± 10	95 ± 24
0.4	2	6.7 ± 1.8	20 ± 5	53 ± 13	133 ± 34
0.4	4	6.8 ± 1.8	20 ± 5	53 ± 14	134 ± 35
0.4	7.5	5.2 ± 1.4	15 ± 4	41 ± 11	104 ± 27
0.6	2	7.5 ± 2.0	22 ± 6	59 ± 15	149 ± 38
0.6	4	9.2 ± 2.5	27 ± 7	73 ± 19	184 ± 47
0.6	7.5	8.8 ± 2.3	26 ± 7	70 ± 18	175 ± 45
0.8	1	7.7 ± 2.0	22 ± 6	61 ± 15	152 ± 39
0.8	2	7.7 ± 2.0	22 ± 6	60 ± 15	152 ± 39
0.8	4	7.8 ± 2.1	23 ± 6	61 ± 16	155 ± 40

binary Fe-Cr alloys is considered independent of alloy chromium content, no effect of alloy composition on diffusion properties was reported by Bowen and Leak [57]. However, in ternary alloys, the chromium content has an effect on the interdiffusion coefficient. The effect is most marked in alloys with $\frac{N_{Ni}}{N_{Fe}+N_{Ni}} = 0.6$, as seen in Table 5.2. Diffusion coefficients in Table 5.2 were used for calculation of enrichment factor for alloys reacted in both Fe/FeO Rhines packs and H_2/H_2O gases, as it is unlikely that the presence of water vapour and/or hydrogen in the environment has an effect on the chromium diffusion. This was demonstrated at 800°C by Ani *et al.* [42] who measured the chromium interdiffusion coefficient in Fe-Cr alloys using the diffusion couple technique. The authors annealed their diffusion couple in an Fe/FeO Rhines pack and in H_2/H_2O gases, and measured the same interdiffusion coefficient after reaction in each environment.

In addition, the parameter f was taken from Table 4.1 for calculation for

Fe/FeO Rhines pack experiments. For experiments carried out in H_2/H_2O gases, the gas water content and temperature appear to have no effect on the parameter f, as presented in Section 4.3. Consequently, values measured in alloys exposed to H_2/H_2O gases containing 13% water vapour (Table 4.6) were used for calculation of enrichment factors for alloys exposed to gases with either 13 or 3% water vapour.

To compute values of the enrichment factor, alloy and oxide molar volumes are required. The molar volume of Fe-Ni-Cr alloys were calculated from lattice parameters of binary Fe-Ni alloys under the assumption that the effect of the small chromium content has no effect on the value of the molar volume. The molar volume of an alloy is given by

$$V_{alloy} = \frac{v_c N_A}{n} \tag{5.34}$$

where n is the number of atom per unit cell, v_c the volume of a unit cell and N_A Avogadro's number. To calculate the volume of a unit cell, lattice parameter for Fe-Ni alloys measured at room temperature by Swartzendruber and Alcock [128] were used. The γ phase has an FCC structure, $n = 4$. Using, $N_A = 6.023 \times 10^{23}$ atoms mol^{-1}, alloy lattice parameters from [128], molar volumes calculated from Equation (5.34) are given in Table 5.3.

Table 5.3: Alloy lattice parameters and molar volumes.

Alloy	lattice parameter (nm)	V_{alloy} (Eq. 5.34) (cm^3 mol^{-1})
Fe	0.3647	7.30
Fe-40Ni	0.3596	7.00
Fe-60Ni	0.3573	6.87
Fe-80Ni	0.3551	6.75
Ni	0.3524	6.59

Unfortunately, this calculation cannot be performed for the Fe-20Ni alloy because no lattice parameter for the FCC phase at room temperature is available due to the martensitic transformation taking place in this alloy. Therefore a molar volume of 7.1 cm^3 mol^{-1} was assumed for this alloy. The molar volume of chromium

oxide was calculated from molecular weight and density reported in [129] and it is found that $V_{CrO_{1.5}} = 14.6$ cm^3 mol^{-1}. The $FeCr_2O_4$ spinel has a density ranging from 4.3 to 5 g cm^{-3} [130] and a molecular weight of 223.835 g mol^{-1}. An average density of 4.65 g cm^{-3} was considered to calculate the spinel molar volume and yields $V_{Fe_{0.5}CrO_2} = 24$ cm^3 mol^{-1}.

Enrichment factors for alloys reacted in Fe/FeO Rhines packs were calculated using Equation (5.15) with $k_p^{(i)}$ values from Table 4.4, chromium interdiffusion coefficients and molar volumes presented above. Results of these calculations are presented in Table 5.4, and variations of the enrichment factor with temperature and alloy composition for alloys with 2 and 7.5 at.% of chromium are plotted in Figure 5.3.

Table 5.4: Enrichment factors calculated with Equation (5.15) from kinetics measured in Fe/FeO Rhines packs.

$\frac{N_{Ni}}{N_{Fe}+N_{Ni}}$	$N_{Cr}^{(0)}$	α			
	at.%	1,000°C	1,050°C	1,100°C	1,150°C
0	2	1.03 ± 0.01	1.03 ± 0.01	1.04 ± 0.01	1.05 ± 0.01
0	4	1.04 ± 0.01	1.06 ± 0.01	1.05 ± 0.01	1.07 ± 0.02
0	7.5	1.04 ± 0.01	1.06 ± 0.01	1.07 ± 0.02	1.09 ± 0.02
0.2	2	1.03 ± 0.01	1.04 ± 0.01	1.04 ± 0.01	1.05 ± 0.01
0.2	4	1.05 ± 0.01	1.06 ± 0.02	1.06 ± 0.01	1.08 ± 0.02
0.2	7.5	1.04 ± 0.01	1.07 ± 0.02	1.15 ± 0.05	1.13 ± 0.03
0.4	2	1.09 ± 0.03	1.10 ± 0.04	1.10 ± 0.03	1.12 ± 0.03
0.4	4	1.13 ± 0.04	1.15 ± 0.05	1.12 ± 0.03	1.22 ± 0.05
0.4	7.5	1.13 ± 0.03	1.14 ± 0.05	1.19 ± 0.05	1.25 ± 0.08
0.6	2	1.17 ± 0.06	1.26 ± 0.11	1.20 ± 0.10	1.31 ± 0.06
0.6	4	1.32 ± 0.10	1.41 ± 0.10	1.41 ± 0.07	1.47 ± 0.09
0.6	7.5	1.39 ± 0.10	1.48 ± 0.13	1.61 ± 0.10	1.89 ± 0.16
0.8	1	1.36 ± 0.26	1.50 ± 0.10	1.54 ± 0.12	1.58 ± 0.11
0.8	2	1.64 ± 0.17	1.71 ± 0.13	1.95 ± 0.17	2.00 ± 0.18
0.8	4	1.71 ± 0.42	2.05 ± 0.52	2.18 ± 0.31	2.48 ± 0.24

The enrichment factor is found to increase with the alloy nickel content as shown in Figure 5.3. This is due to slower internal oxidation kinetics and faster chromium diffusion in nickel-rich alloys. In addition, the enrichment factor is found

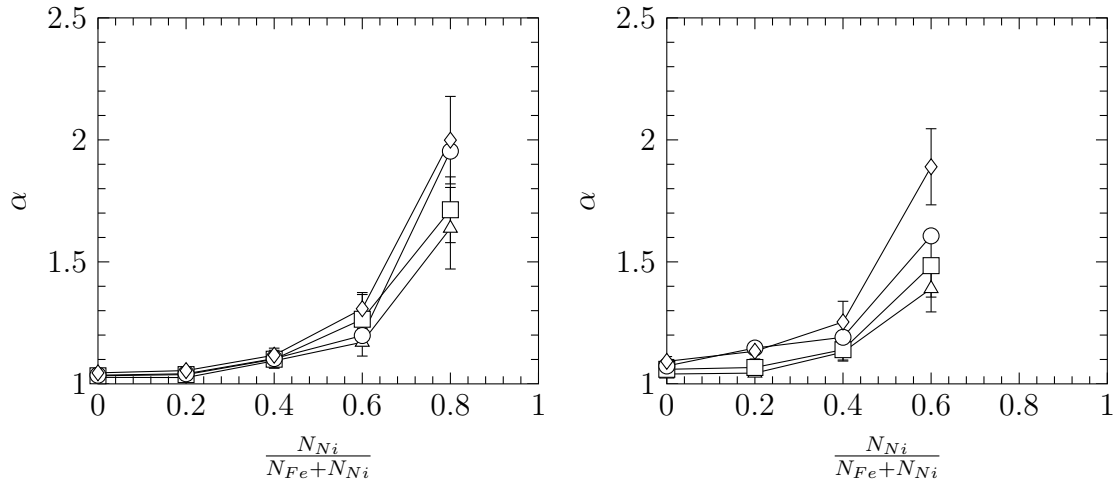

(a) $N_{Cr} =$ 2 at.% (b) $N_{Cr} =$ 7.5 at.%

Figure 5.3: Variation of the enrichment factor with alloy composition and temperature for alloys with 2 and 7.5 at.% of chromium.
1,000°C (–△–), 1,050°C (–□–), 1,100°C (–○–), 1,150°C (–◇–).

to increase with temperature. Enrichment of the IOZ takes place when the condition $N_O^{(s)} D_O >> N_{Cr}^{(0)} \tilde{D}_{Cr}$ is not verified. Considering, that oxygen and chromium diffusion coefficients follow an Arrhenius law, the ratio of oxygen and chromium flux is given by

$$\frac{N_O^{(s)} D_O}{N_{Cr}^{(0)} \tilde{D}_{Cr}} = \frac{N_O^{(s)} D_O^{(0)}}{N_{Cr}^{(0)} D_{Cr}^{(0)}} \exp\left(\frac{1}{RT}\left(Q_{Cr} - Q_O\right)\right) \tag{5.35}$$

where $D_O^{(0)}$ and $\tilde{D}_{Cr}^{(0)}$ are the pre-exponential factor for oxygen and chromium diffusion, respectively, and Q_O and Q_{Cr}, the activation energies for diffusion of the corresponding species. Oxygen diffuses through interstitial sites while chromium diffuses via substitutional mechanism. Thus, it is assumed that $Q_O < Q_{Cr}$ and it is found that the ratio $\dfrac{N_O^{(s)} D_O}{N_{Cr}^{(0)} D_{Cr}}$ decreases, therefore enrichment increases with temperature. This is in agreement with the variation of α presented in Figure 5.3.

It is also useful to estimate the effect of the volume expansion on the calculated value of the enrichment factor. To do so, the following ratio is introduced

$$\Delta\alpha(\%) = 100\frac{\alpha - \alpha'}{\alpha'} \tag{5.36}$$

where α' is the enrichment factor calculated when the variable hc is determined with

no volume expansion, as considered in Wagner's original model (Section 1.3.2.2), while α values (Table 5.4) reflect the volume expansion effect. In Figure 5.4, the parameter $\Delta\alpha$ calculated for the different alloys is presented. The effect of volume

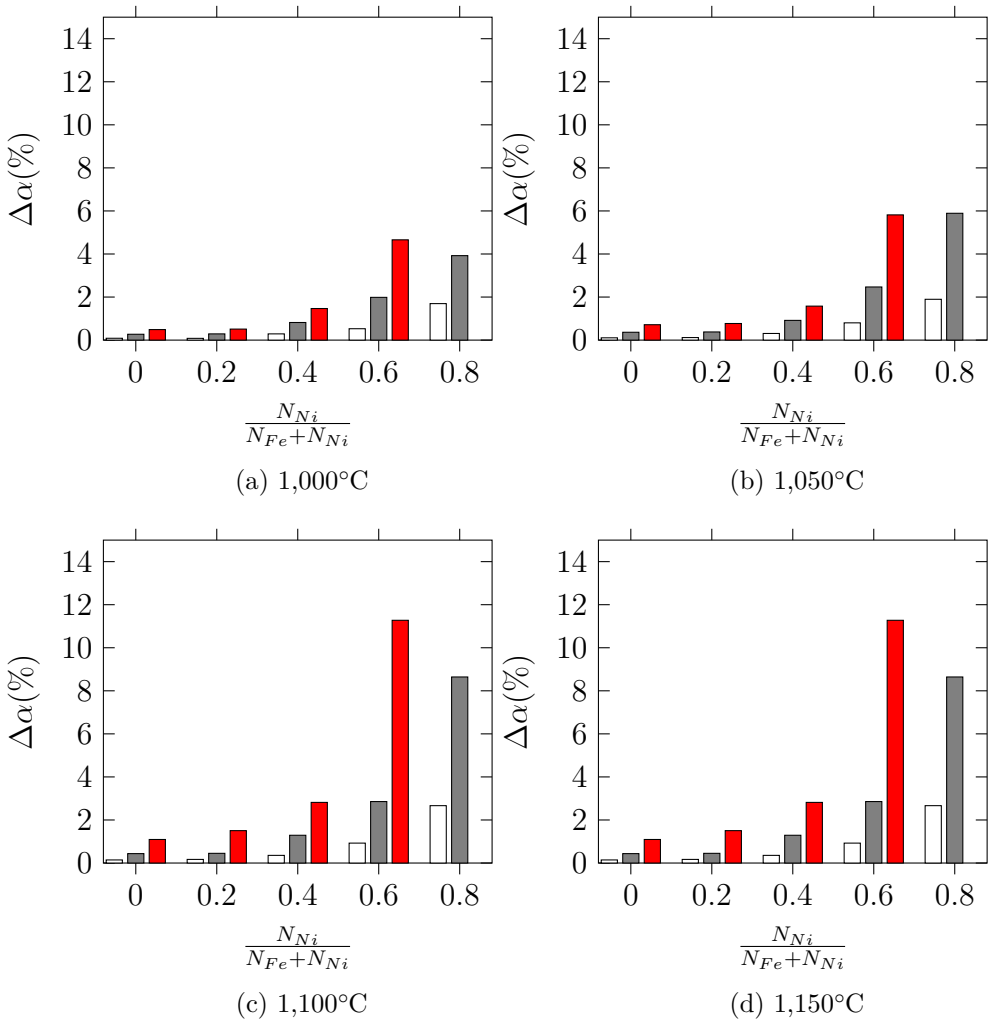

(a) 1,000°C (b) 1,050°C

(c) 1,100°C (d) 1,150°C

Figure 5.4: Effect of volume expansion on the value of the enrichment factor measured in Fe/FeO Rhines packs: 2 at.% (▯▯), 4 at.% (▮▮), 7.5 at.% (▮▮).

expansion on the calculation of the enrichment factor is negligible at all temperatures for alloys with a chromium content of 2 at.%. For alloys with 4 and 7.5 at.% Cr, the volume effect on calculated enrichment is significant in alloys with 60 and 80 at.% Ni. At 1,000 and 1,050°C the consideration of volume expansion increases the value of the enrichment factor by 5% compared to the value calculated if no volume expansion is considered for Fe-60Ni-7.5Cr and Fe-80Ni-4Cr alloys. At 1,100 and 1,150°C the difference between enrichment factors reaches 10% for the same alloys, as illustrated

in Figure 5.4.

Enrichment factors for alloys reacted in H_2/H_2O gases containing 13 and 3% of water vapour were calculated using $k_p^{(i)}$ from Tables 4.8 and 4.13. Results of this calculation are presented in Tables 5.5 and 5.6.

Table 5.5: Enrichment factors calculated with Equation (5.15) from kinetics measured in H_2/H_2O gases containing 13% water vapour.

$\frac{N_{Ni}}{N_{Fe}+N_{Ni}}$	$N_{Cr}^{(0)}$ at.%	α 1,000°C	1,050°C	1,100°C	1,150°C
0	2	1.02 ± 0.01	1.03 ± 0.01	1.04 ± 0.01	1.04 ± 0.01
0	4	1.04 ± 0.01	1.05 ± 0.01	1.06 ± 0.01	1.06 ± 0.01
0	7.5	1.04 ± 0.01	1.05 ± 0.01	1.08 ± 0.02	1.09 ± 0.02
0.2	2	1.03 ± 0.01	1.03 ± 0.01	1.04 ± 0.01	1.04 ± 0.01
0.2	4	1.04 ± 0.01	1.05 ± 0.01	1.06 ± 0.01	1.07 ± 0.01
0.2	7.5	1.04 ± 0.01	1.06 ± 0.02	1.10 ± 0.02	1.09 ± 0.02
0.4	2	1.07 ± 0.02	1.08 ± 0.02	1.10 ± 0.02	1.09 ± 0.02
0.4	4	1.11 ± 0.02	1.12 ± 0.03	1.17 ± 0.04	1.16 ± 0.03
0.4	7.5	1.10 ± 0.02	1.14 ± 0.03	1.19 ± 0.04	1.21 ± 0.04
0.6	2	1.21 ± 0.04	1.23 ± 0.04	1.28 ± 0.05	1.36 ± 0.07
0.6	4	1.27 ± 0.06	1.35 ± 0.06	1.46 ± 0.08	1.65 ± 0.10
0.6	7.5	1.32 ± 0.06	1.40 ± 0.07	1.64 ± 0.10	2.04 ± 0.13
0.8	1	1.35 ± 0.10	1.43 ± 0.08	1.53 ± 0.20	1.64 ± 0.24
0.8	2	1.74 ± 0.18	1.72 ± 0.15	1.87 ± 0.14	2.07 ± 0.47

Enrichment factors calculated for alloys exposed to wet gases exhibit the same variation with temperature and alloy composition as enrichment factors calculated for alloys reacted in Fe/FeO Rhines packs. In addition, the effect of volume expansion on enrichment factor evaluation for alloys exposed to gases with water vapour was similar to the effect presented in Figure 5.4 for alloys reacted in Fe/FeO Rhines packs. The very similar values found after reaction in Rhines packs and the two H_2/H_2O mixtures reflect the similarity of the observed rate constants.

In order to validate Wagner's diffusional approach for enrichment factor calculation, this parameter was evaluated by a second method based on the measurement of experimentally observed internal oxide volume fraction.

Table 5.6: Enrichment factors calculated with Equation (5.15) from kinetics measured in H_2/H_2O gases containing 3% of water vapour.

$\frac{N_{Ni}}{N_{Fe}+N_{Ni}}$	$N_{Cr}^{(0)}$ at.%	α 1,000°C	1,050°C	1,150°C
0	2	1.03 ± 0.01	1.05 ± 0.01	1.04 ± 0.01
0	7.5	1.05 ± 0.01	1.08 ± 0.02	1.11 ± 0.02
0.2	2	1.05 ± 0.01	1.06 ± 0.01	1.06 ± 0.02
0.2	7.5	1.06 ± 0.01	1.09 ± 0.02	1.13 ± 0.03
0.4	2	1.09 ± 0.02	1.10 ± 0.02	1.17 ± 0.04
0.4	7.5	1.12 ± 0.03	1.15 ± 0.03	1.31 ± 0.06
0.6	2	1.32 ± 0.06	1.38 ± 0.07	1.56 ± 0.10
0.6	7.5	-	1.65 ± 0.10	2.74 ± 0.23
0.8	1	-	1.53 ± 0.10	1.76 ± 0.13
0.8	2	-	2.52 ± 0.24	2.15 ± 0.19

5.2.2 Estimation of the enrichment factor by internal oxide volume fraction measurement

The second method proposed to estimate the enrichment factor is based on the evaluation of the volume fraction of oxide to determine the quantity of chromium in the IOZ. As previously described in Section 4.1.1, the internal oxidation zone is composed of two subzones, with a different oxide precipitated in each of them. In order to take into account the precipitation of the two different oxides for the enrichment factor estimation, relations between the different volumes used in the calculation are presented in the first part of this section. Then, the calculation of the enrichment factor is presented.

5.2.2.1 Definition of volume fractions in the case of the precipitations of 2 oxides for estimation of enrichment factor.

The IOZ is divided into two subzones as illustrated in Figure 5.5. The different subzones are defined as follows:

- Subzone 1 is the zone where iron-chromium spinel precipitates and the volume of this zone is defined by $v^{(1)} = AX_{(t)}$ with $X_{(t)}$ the depth where the transition

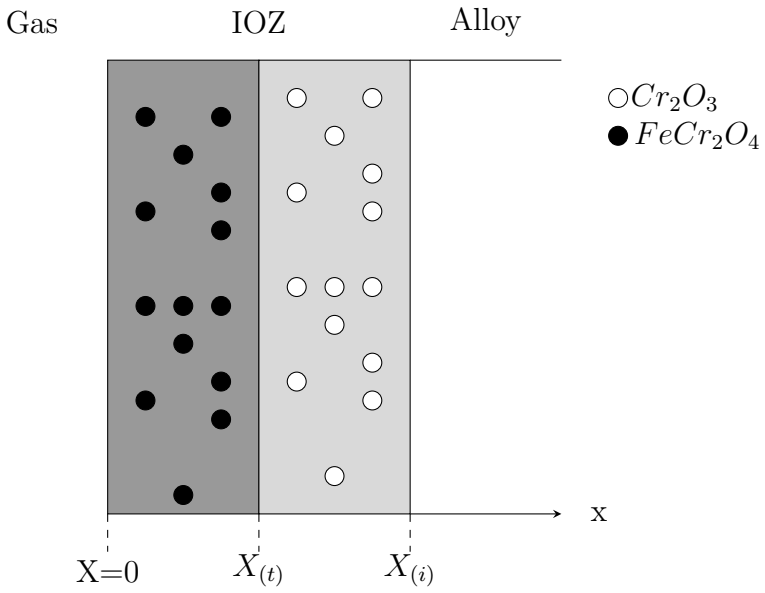

Figure 5.5: Internal oxide distribution in the internal oxidation zone.

between iron-chromium spinel and chromium oxide is observed and A a unit area. The volume fraction of oxide in this zone is given by

$$F_v^{(1)} = \frac{v_{Fe_{0.5}CrO_2}}{v^{(1)}} \tag{5.37}$$

with $v_{Fe_{0.5}CrO_2}$ the volume of iron-chromium spinel.

- The Subzone 2 is the zone where chromium oxide precipitates and the volume of the zone is defined by $v^{(2)} = A\left(X_{(i)} - X_{(t)}\right)$. The volume fraction of oxide in this zone is given by

$$F_v^{(2)} = \frac{v_{CrO_{1.5}}}{v^{(2)}} \tag{5.38}$$

with $v_{CrO_{1.5}}$ the volume of chromium oxide.

In addition, the global volume fraction is defined by

$$F_v = \frac{v_{Fe_{0.5}CrO_2} + v_{CrO_{1.5}}}{v_{IOZ}} \tag{5.39}$$

where $v_{IOZ} = AX_{(i)}$ is the IOZ volume. Substituting the relation $f = \frac{X_{(t)}}{X_{(i)}}$ in Equations (5.37) and (5.38), volumes of oxide in each zone are given by the following

equations

$$v_{Fe_{0.5}CrO_2} = F_v^{(1)} v_{IOZ} f \tag{5.40}$$

$$v_{CrO_{1.5}} = F_v^{(2)} v_{IOZ} (1 - f) \tag{5.41}$$

Combining equations (5.40), (5.41) and (5.39) yields the following relation between the different volume fractions

$$F_v = f F_v^{(1)} + (1 - f) F_v^{(2)} \tag{5.42}$$

Equation (5.42) was tested experimentally by measuring, with the technique presented in Section 2.7.2, the internal oxide volume fraction in the different zones and through the entire IOZ. These measurements were carried out for alloys with 7.5 at.% of chromium and nickel content up to 60 at.%, reacted in Fe/FeO Rhines packs and H_2/H_2O gases with 13% water vapour at 1,000 and 1,150°C. In addition, the parameter f required to define the different volumes in which internal oxide volume fractions have to be measured were taken from measurement in Tables 4.1 and 4.6. Results of volume fraction measurements are presented in Table 5.7 and 5.8.

Table 5.7: Volume fraction measured for alloys with 7.5 at.% Cr, after exposure at 1,000°C in Fe/FeO Rhines packs and H_2/H_2O gases containing 13% of water vapour.

$\frac{N_{Ni}}{N_{Fe}+N_{Ni}}$	$F_v^{(1)}$		$F_v^{(2)}$		F_v	
	RP	H_2/H_2O	RP	H_2/H_2O	RP	H_2/H_2O
0	23 ± 3	24 ± 1	11 ± 6	12 ± 5	21 ± 3	23 ± 2
0.2	22 ± 1	23 ± 1	14 ± 3	14 ± 7	20 ± 1	21 ± 0.4
0.4	27 ± 1	25 ± 2	16 ± 3	17 ± 10	24 ± 1	22 ± 4
0.6	34 ± 2	27 ± 1	17 ± 3	23 ± 9	28 ± 1	27 ± 0.1

Firstly, internal oxide volume fractions measured in alloys exposed to dry or wet conditions at 1,000 and 1,150 °C are in good agreement. To validate measurements of $F_v^{(1)}$ and $F_v^{(2)}$, the global volume fraction F_v was calculated with Equation (5.42) and compared to values measured, presented in Tables 5.7 and 5.8. In Figure 5.6, values of F_v calculated with Equation (5.42) and values measured are

Table 5.8: Volume fraction measured for alloys with 7.5 at.% Cr after exposure at 1,150°C in Fe/FeO Rhines packs and H_2/H_2O gases containing 13% water vapour.

$\frac{N_{Ni}}{N_{Fe}+N_{Ni}}$	$F_v^{(1)}$		$F_v^{(2)}$		F_v	
	RP	H_2/H_2O	RP	H_2/H_2O	RP	H_2/H_2O
0	23 ± 1	23 ± 1	4 ± 4	3 ± 1	21 ± 1	21 ± 2
0.2	26 ± 3	26 ± 1	15 ± 2	15 ± 3	23 ± 3	24 ± 1
0.4	30 ± 1	31 ± 2	15 ± 2	10 ± 2	25 ± 1	26 ± 1
0.6	41 ± 2	44 ± 2	13 ± 3	21 ± 4	34 ± 2	38 ± 3

compared and shows that they are in good agreement. Thus, the measurements of f and F_v are consistent because Equation (5.42) is verified.

5.2.2.2 Calculation of enrichment factor from volume fraction measurement

To estimate the enrichment factor, the amount of chromium in the IOZ is calculated from the volume fraction of oxide precipitated. To simplify the calculation, it is assumed that in the IOZ, all the chromium is present as oxide and the matrix surrounding internal particles is composed only of iron and nickel. In zone 1, where only iron-chromium spinel precipitates, the number of mole of chromium is given by

$$n_{cr}^{(1)} = F_v^{(1)} \frac{v^{(1)}}{V_{Fe_{0.5}CrO_2}} = f v_{IOZ} \frac{F_v^{(1)}}{V_{Fe_{0.5}CrO_2}} \tag{5.43}$$

and in zone 2 where exclusively chromium oxide precipitates, the amount of chromium is given by

$$n_{cr}^{(2)} = F_v^{(2)} \frac{v^{(2)}}{V_{CrO_{1.5}}} = (1-f)\, v_{IOZ} \frac{F_v^{(2)}}{V_{CrO_{1.5}}} \tag{5.44}$$

Finally, adding Equation (5.43) and (5.44), the total number of mole of chromium in the IOZ is expressed by

$$n_{Cr}^{ox} = n_{cr}^{(1)} + n_{cr}^{(2)} = v_{IOZ} \left[f \frac{F_v^{(1)}}{V_{Fe_{0.5}CrO_2}} + (1-f) \frac{F_v^{(2)}}{V_{CrO_{1.5}}} \right] \tag{5.45}$$

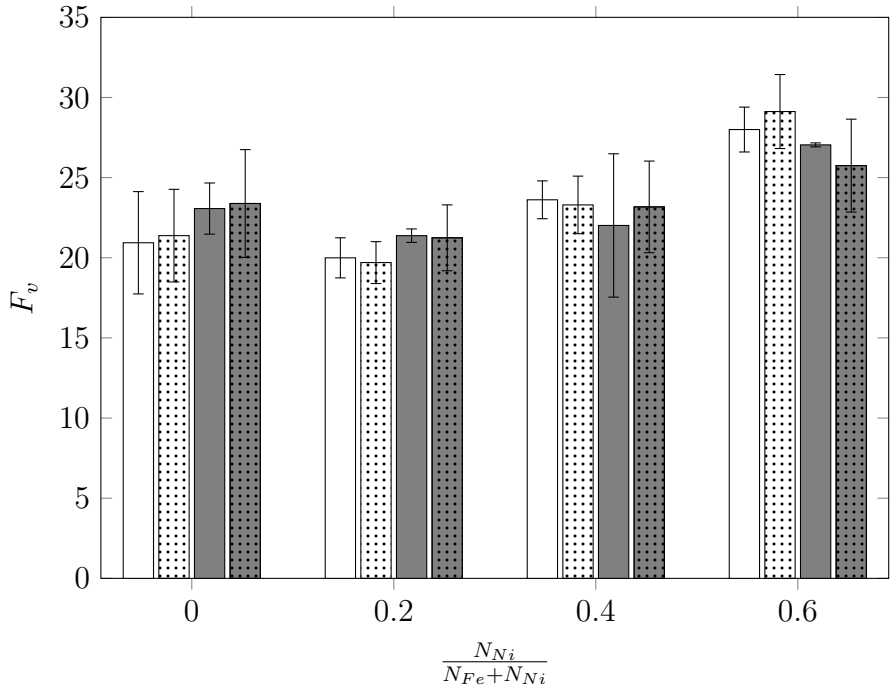

(a) 1,000°C

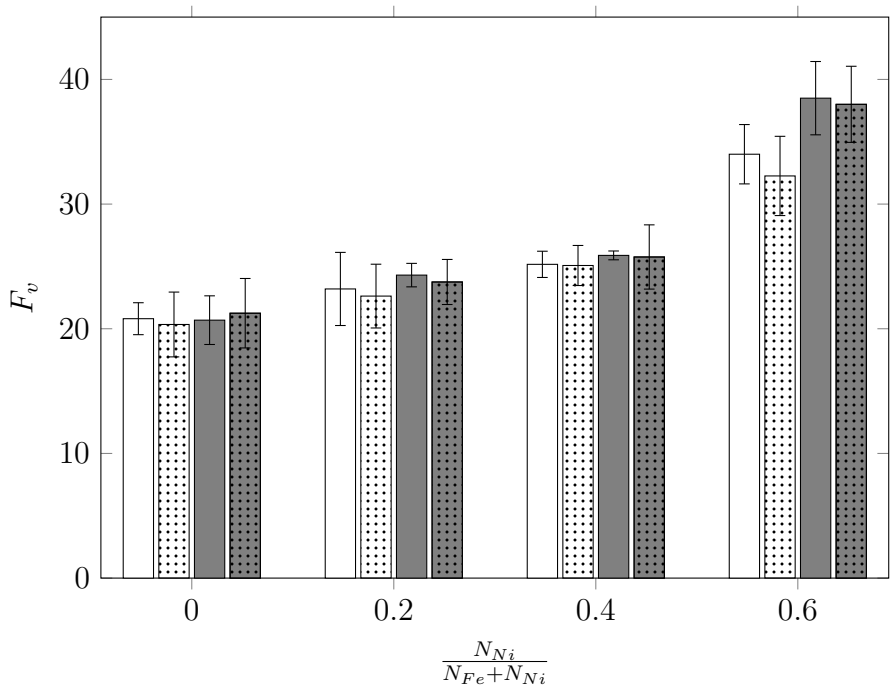

(b) 1,150°C

Figure 5.6: Comparison of total volume fraction measured by image analysis (□,■) and calculated with equation (5.42) (□,■) for alloys with 7.5 at.% Cr: Fe/FeO Rhines pack (□,□) and H_2/H_2O gases containing 13% of water vapour (■,■).

However, to estimate the enrichment factor, the amount of chromium in the IOZ prior to the internal oxidation,$n_{Cr}^{(0)}$ has to be evaluated.

Because the IOZ has expanded, it is necessary to calculate $n_{Cr}^{(0)}$ somewhat indirectly. By definition

$$N_{Cr}^{(0)} = \frac{n_{Cr}^{(0)}}{n_{Cr}^{(0)} + n_{Fe}^{(0)} + n_{Ni}^{(0)}} \tag{5.46}$$

Therefore, Equation (5.46) allows the determination of the initial quantity of chromium in the IOZ if the number of mole of iron and nickel is known. In zone 1, the number of mole of iron and nickel is given by

$$n_{Fe}^{(1)} + n_{Ni}^{(1)} = \left(1 - F_v^{(1)}\right) \frac{v^{(1)}}{V_{matrix}} = f v_{IOZ} \frac{\left(1 - F_v^{(1)}\right)}{V_{matrix}} \tag{5.47}$$

However, it has to be noted that a part of the iron is consumed to form the iron-chromium spinel and it has to be added to the total number of mole of iron and nickel. The mole of iron consumed to form the spinel is given by

$$n_{Fe}^{(1)'} = 0.5 n_{cr}^{(1)} = 0.5 f v_{IOZ} \frac{F_v^{(1)}}{V_{Fe_{0.5}CrO_2}} \tag{5.48}$$

For the subzone 2, equivalent equations are found, except that no iron is consumed to form the chromium oxide.

$$n_{Fe}^{(2)} + n_{Ni}^{(2)} = \left(1 - F_v^{(2)}\right) \frac{v^{(2)}}{V_{matrix}} = (1 - f)\, v_{IOZ} \frac{\left(1 - F_v^{(2)}\right)}{V_{matrix}} \tag{5.49}$$

Adding Equations (5.47), (5.48) and (5.49), employing again the assumption that $V_{matrix} = V_{alloy}$, the total number of mole of iron and nickel in the IOZ is found to be

$$n_{Fe}^{(0)} + n_{Ni}^{(0)} = \frac{v_{IOZ}}{V_{alloy}} \left[0.5 F_v^{(1)} f \frac{V_{alloy}}{V_{Fe_{0.5}CrO_2}} + (1 - F_v) \right] \tag{5.50}$$

Substituting Equation (5.50) in (5.46) yields

$$n_{Cr}^{(0)} = \frac{N_{Cr}^{(0)}}{1 - N_{Cr}^{(0)}} \frac{v_{IOZ}}{V_{alloy}} \left[0.5 F_v^{(1)} f \frac{V_{alloy}}{V_{Fe_{0.5}CrO_2}} + (1 - F_v) \right] \tag{5.51}$$

Finally, the enrichment factor is calculated using the relation

$$\alpha = \frac{N_{Cr}^{ox}}{N_{Cr}^{(0)}} = \frac{n_{Cr}^{ox}}{n_{Cr}^{(0)}} \tag{5.52}$$

Combining Equations (5.45), (5.51) in (5.52) yields

$$\alpha = V_{alloy} \frac{1 - N_{Cr}^{(0)}}{N_{Cr}^{(0)}} \frac{\left[f \frac{F_v^{(1)}}{V_{Fe_{0.5}CrO_2}} + (1-f) \frac{F_v^{(2)}}{V_{CrO_{1.5}}} \right]}{\left[0.5 F_v^{(1)} f \frac{V_{alloy}}{V_{Fe_{0.5}CrO_2}} + (1 - F_v) \right]} \tag{5.53}$$

Enrichment factors at 1,000 and 1,150°C were evaluated from volume fraction measurement for alloys with 7.5 at.% of chromium reacted in Fe/FeO Rhines packs and H_2/H_2O gas mixtures containing 13% of water vapour using Equation (5.53). To calculate enrichment factor values, volume fractions presented in Tables 5.7 and 5.8 were used, and the parameter f was taken from Table 4.1 for alloys reacted in Fe/FeO Rhines packs. For enrichment factors in alloys reacted with H_2/H_2O gases, values of f given in Table 4.6 were employed. In Figures 5.7 and 5.8, enrichment factors calculated from the diffusional approach and estimated by volume fraction measurements are compared.

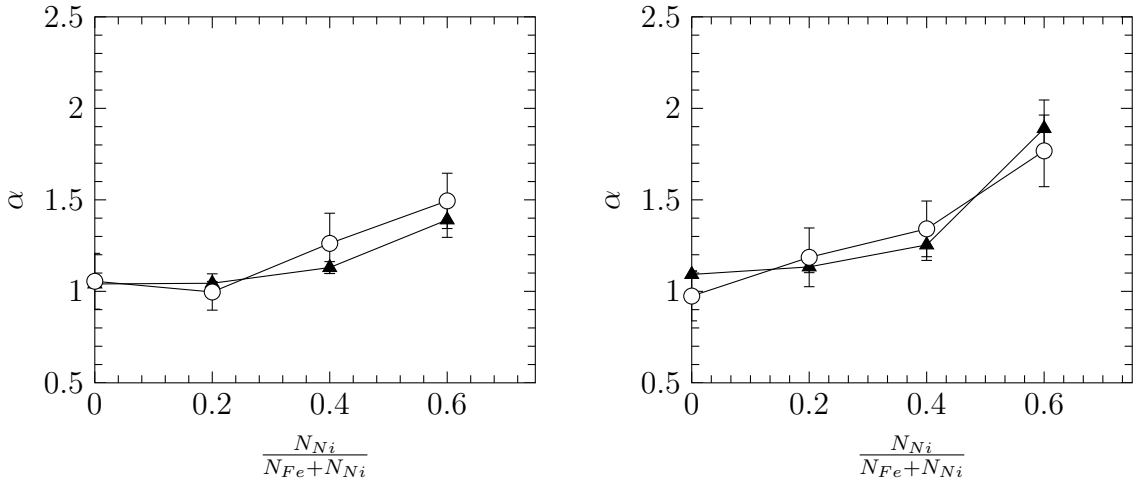

(a) 1,000°C (b) 1,150°C

Figure 5.7: Comparison of enrichment factor calculated from the diffusional approach (Eq.5.15,–▲–) and from volume fraction measurement (Eq.5.53,–○–) for alloys containing 7.5 at.% Cr reacted in Fe/FeO Rhines packs .

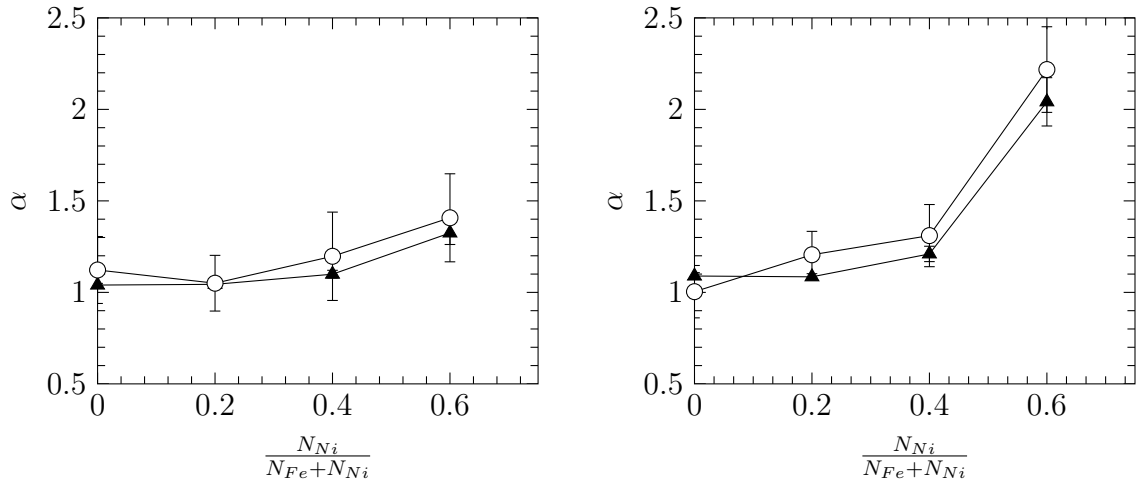

(a) 1,000°C (b) 1,150°C

Figure 5.8: Comparison of enrichment factor calculated from the diffusional approach (Eq.5.15,–▲–) and from volume fraction measurement (Eq.5.53,–○–) for alloys containing 7.5 at.% Cr reacted H_2/H_2O gases containing 13% water vapour.

Figures 5.7 and 5.8 show that enrichment factors determined by the two techniques are in good agreement. Therefore, it is concluded that the diffusional approach gives a good estimate of the enrichment factor and values presented in the tables of Section 5.2.1 are used for the determination of the oxygen permeability.

5.3 Determination of internal oxide stoichiometry

In Section 4.2.1, it was reported that the IOZ is composed of two subzones, where in each of them a specific oxide, $FeCr_2O_4$ or Cr_2O_3 precipitates. However, the presence of different oxides required the definition of an effective stoichiometry coefficient to calculate the oxygen permeability. In the further development, the effective stoichiometry was determined by different techniques presented in this section.

5.3.1 Definition of the effective stoichiometry

As a first approach, it was considered that the effective stoichiometry reflects the amount of iron-chromium spinel compared to the quantity of chromium oxide

in the IOZ. Therefore, the effective stoichiometry was considered as the average of the spinel and chromium oxide stoichiometry but weighted by the relative size of the subzone in which each oxide precipitates and the expression of ν_{eff} is given by

$$\nu_{eff} = f\nu_1 + (1 - f)\nu_2. \tag{5.54}$$

where $\nu_1 = 2$ and $\nu_2 = 1.5$ are the stoichiometry of the chromium oxide and the spinel, respectively, and $f = X_{(t)}/X_{(i)}$ with $X_{(t)}$ the depth where conversion of chromium oxide to spinel takes place and $X_{(i)}$ the IOZ depth. Values of effective stoichiometry were calculated from f measured in alloys with 7.5 at.% of chromium reacted in Fe/FeO Rhines packs and H_2/H_2O gas mixtures containing 13% of water vapour (Tables 4.1 and 4.6). Results are presented in Tables 5.9 and 5.10.

Table 5.9: Effective stoichiometric coefficient for alloys with 7.5 at.% Cr reacted in Fe/FeO Rhines packs calculated with the mixing law (Eq.5.54) with f measured in Rhines packs.

Temperature			$\frac{N_{Ni}}{N_{Fe}+N_{Ni}}$		
°C	0	0.2	0.4	0.6	0.8
1,000	1.94 ± 0.06	1.91 ± 0.06	1.87 ± 0.05	1.80 ± 0.05	1.70 ± 0.03
1,050	1.94 ± 0.06	1.93 ± 0.05	1.87 ± 0.05	1.80 ± 0.05	1.70 ± 0.03
1,100	1.93 ± 0.06	1.85 ± 0.05	1.83 ± 0.05	1.86 ± 0.05	1.71 ± 0.03
1,150	1.93 ± 0.06	1.85 ± 0.05	1.84 ± 0.05	1.85 ± 0.05	1.71 ± 0.03

Table 5.10: Effective stoichiometric coefficient for alloys with 7.5 at.% Cr reacted in H_2/H_2O gases containing 13% of water vapour calculated with the mixing law (Eq.5.54) with f measured in alloys reacted in H_2/H_2O gases.

Temperature			$\frac{N_{Ni}}{N_{Fe}+N_{Ni}}$		
°C	0	0.2	0.4	0.6	0.8
1,000	1.99 ± 0.07	1.90 ± 0.06	1.87 ± 0.05	1.80 ± 0.05	1.70 ± 0.02
1,050	1.93 ± 0.06	1.93 ± 0.06	1.87 ± 0.05	1.80 ± 0.05	1.70 ± 0.02
1,100	1.92 ± 0.06	1.90 ± 0.06	1.87 ± 0.05	1.80 ± 0.04	1.70 ± 0.03
1,150	1.95 ± 0.06	1.90 ± 0.06	1.87 ± 0.05	1.87 ± 0.05	1.70 ± 0.03

The values obtained with Equation (5.54) showed that the reaction environment and the temperature have no observable effect on the effective stoichiometry

measured in chromium-rich alloys. However, the effective stoichiometry is decreased when the alloy nickel content increases. This variation is expected due to the decrease of iron activity in nickel-rich alloys. Consequently, the iron-chromium spinel is less stable when the nickel alloy content increases.

Direct measurement of the parameter f with SEM observation was difficult in alloys with chromium content lower than 7.5 at.% due to the small size of internal oxide particles. However, to estimate the effective stoichiometry in dilute alloys, it is possible to calculate its value by coupling results of internal oxidation kinetics measured by penetration and weight gain. Use of this method to evaluate the effective stoichiometric coefficient is presented in the next section.

5.3.2 Determination of the effective stoichiometric coefficient by coupling TGA and penetration measurement

Evaluation of the effective oxide stoichiometry in dilute alloys was carried out with the method used by Gesmundo *et al.* to evaluate the stoichiometry of internal oxides after internal oxidation of alloys containing niobium [30]. Gesmundo developed Equation (5.55) to relate internal oxidation rate constant in term of penetration and weight change:

$$\frac{k_w^{(i)}}{k_p^{(i)}} = \left(\frac{M_O}{V_{alloy}} \alpha \nu_{eff} N_{Cr}^{(0)} \right)^2 \tag{5.55}$$

where $k_w^{(i)}$ and $k_p^{(i)}$ are the internal oxidation rate constants in term of weight change and penetration respectively, M_O the atomic weight of oxygen, V_{alloy} the molar volume of the alloy, α the enrichment factor, $N_{Cr}^{(0)}$ the alloy mole fraction of chromium, ν_{eff} the effective stoichiometry and $N_O^{(s)} D_O$ the oxygen permeability. Gesmundo assumed that no volume change takes place during internal oxidation and used the expression of $k_p^{(i)}$ developed by Wagner. However, as presented in Section 5.2.1.1, the assumption of no volume change is correct for sufficiently dilute alloys but is no longer valid in chromium-rich alloys. Consequently, an extra term was added to Wagner's expression of the internal oxidation rate (Section 5.1) and $k_p^{(i)}$ is given by

$$k_p^{(i)} = \frac{N_O^{(s)} D_O}{\alpha \nu N_{Cr}^{(0)}} \Gamma \tag{5.56}$$

If the ratio $\frac{k_w^{(i)}}{k_p^{(i)}}$ is recalculated with $k_p^{(i)}$ given by Equation (5.56), the following expression is found

$$\frac{k_w^{(i)}}{k_p^{(i)}} = \frac{1}{\Gamma} \left(\frac{M_O}{V_{alloy}} \alpha N_{Cr}^{(0)} \nu_{eff} \right)^2 \tag{5.57}$$

Thermogravimetric and penetration studies were carried out on samples reacted in the thermobalance and in the horizontal furnace.

Firstly, results obtained by discontinuous TGA on samples reacted in a horizontal furnace at 1,000 and 1,050°C are investigated. It should be recalled that experiments in a horizontal furnace used H_2/H_2O gas mixtures containing 13% of water vapour, with the oxygen partial pressure set at the Fe/FeO equilibrium. To compute values of the effective stoichiometry, enrichment factors from Table 5.5, calculated using the diffusional approach, are used. In addition, the parameter f, required to estimate Γ, was only measured in chromium-rich alloys. It was assumed that f is constant for a given alloy chromium content in evaluating the volume expansion in dilute alloys. However as shown in Figure 5.2, the value of f has a negligable effect on the volume expansion term for dilute chromium alloy. Consequently, even if f is different in low chromium alloys, using values of this parameter measured in chromium-rich alloys would yield a negligable difference in the evaluation of Γ.

Results of the calculation of ν_{eff} are presented in Figure 5.9. It shows that effective stoichiometry values measured by coupling thermogravimetric measurement and penetration measurement are found to increase with the alloy chromium content. The variation of ν_{eff} with $N_{Cr}^{(0)}$ suggests that the following reaction is affected by the alloy chromium content.

$$Fe + Cr_2O_3 + \frac{1}{2}O_2 \rightarrow FeCr_2O_4 \tag{5.58}$$

The Gibbs free energy of reaction 5.58 was taken from Kubaschewski [119] and is

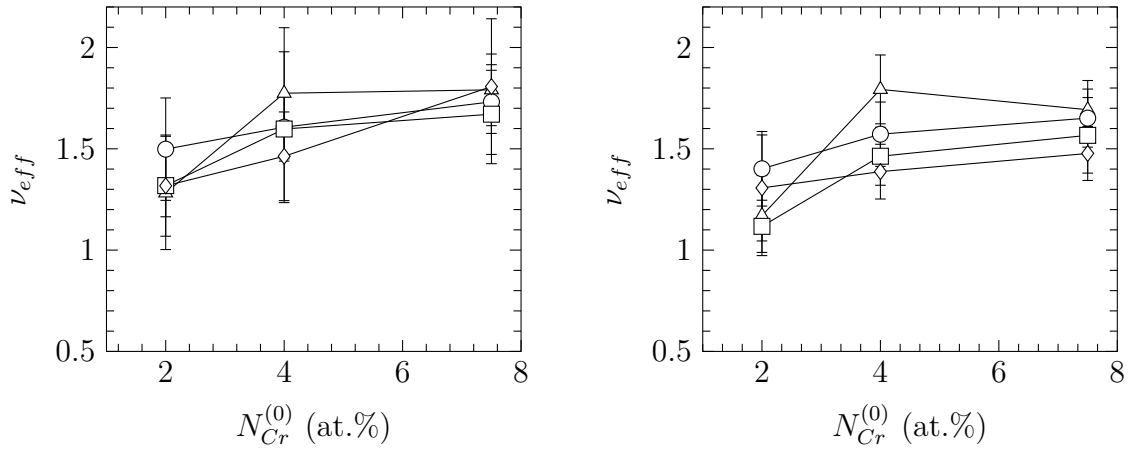

(a) 1,000°C (b) 1,050°C

Figure 5.9: Effective stoichiometry calculated from internal oxidation rate (Eq.5.57) measured in H_2/H_2O gases containing 13% of water vapour as a function of the alloy chromium content. Fe (–△–), Fe-20Ni (–○–), Fe-40Ni (–□–), Fe-60Ni (–◇–).

given below

$$\Delta G^0_{5.58} = -275,044 + 51T \text{ (J mol}^{-1}\text{)} \tag{5.59}$$

In addition, the reaction constant of 5.58 is given by

$$K_{5.58} = \frac{1}{a_{Fe} p_{O_2}^{1/2}} \tag{5.60}$$

Equation (5.60) shows that the stability of the iron-chromium spinel depends of iron activity. Low values of ν_{eff} in dilute chromium alloys suggest that at the location $X = X_{(t)}$ a large amount of chromium remains unoxidised in the matrix and decreases the iron activity. However, determination of the quantity of chromium in the matrix at the location $X = X_{(t)}$ required the evaluation of chromium oxide solubility product, $K_{sp}^{(Cr_2O_3)}$. In addition, values of $\nu_{eff} < 1.5$ calculated with Equation (5.57) for alloys with 2 and 4 at.% Cr are in disagreement with Wagner's model. Indeed, the lowest stoichiometry possible is 1.5, corresponding to an internal oxidation zone where only Cr_2O_3 precipitates, and in this case $f = 0$. These low values of ν_{eff} might be though to arise from the fact that Γ, which represents the volume expansion, was calculated with f measured in chromium-rich alloys, and assumed

independent of the alloy chromium content. However, as previously mentioned, in dilute alloys, Γ is close to 1 and independent of the value of f as shown in Figure 5.2. Therefore, Γ has a negligible effect on the evaluation of the effective stoichiometry in dilute alloys. To investigate low effective stoichiometric coefficient measured in dilute alloys and the variation of this parameter with the alloy chromium content, thermodynamic calculations to determine the chromium oxide solubility product are presented in the next section.

Nevertheless, it should be noted that for alloys with chromium contents of 4 and 7.5 at.%, the effective stoichiometry calculated from internal oxidation rate constant decreases with nickel addition. This variation is in agreement with variations of ν_{eff} observed when this parameter is estimated from values of the parameter f measured by SEM as illustrated in Figure 5.10 where ν_{eff} estimated from SEM observations (Table 5.10) or kinetic measurements (Eq.5.57) are compared for alloys with 7.5 at.% Cr. Figure 5.10 shows that the effective stoichiometry calculated from coupling kinetic measurements are lower than values estimated from SEM observations.

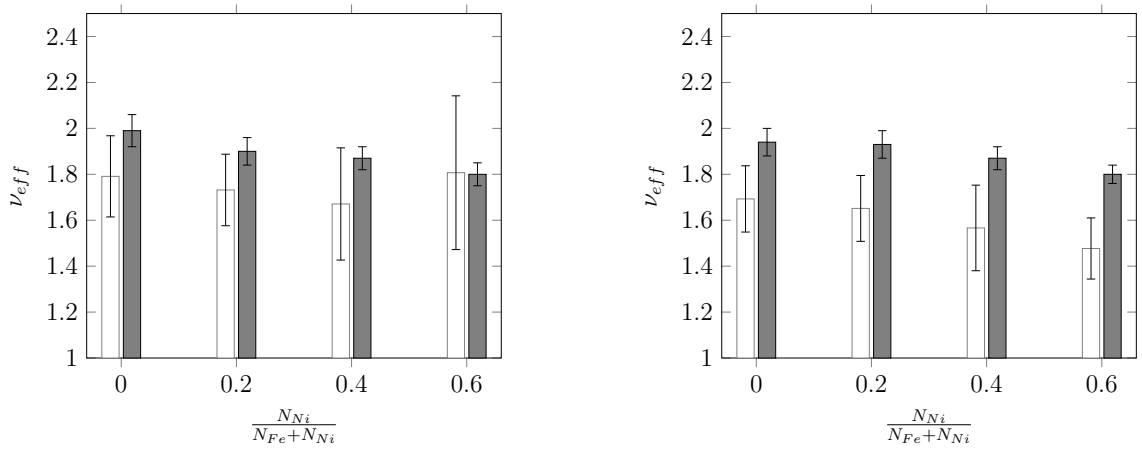

(a) 1,000 °C (b) 1,050 °C

Figure 5.10: Comparison of effective stoichiometric coefficient evaluated by kinetic measurements (Eq.5.57,□□)and SEM observations (Eq.5.54,▮▮) in alloys with 7.5 at.% Cr exposed to H_2/H_2O gases with 13% of water vapour.

The high values of effective stoichiometry measured by SEM observations may arise from the fact that the depth $X_{(t)}$ represents the depth where the oxidation of

chromium oxide in iron-chromium spinel starts. In reality, as seen in Figure 4.2, a part of the IOZ is composed of a mixture of spinel, chromium oxide and internal oxide particles with a core of chromium oxide and an outer layer of iron-chromium spinel. Because $X_{(t)}$ is defined as the depth where the transformation of chromium oxide into spinel starts, a systematic overestimation of the parameter f, therefore ν_{eff}, results because for a range of depths smaller than $X_{(t)}$ all particles are assumed to be oxidised as iron-chromium spinel, whereas in fact some combined oxides exist. Nonetheless, the trend that the effective stoichiometry decreases with nickel addition is observable in both sets of data except in alloy with 60 at.% of nickel reacted at 1,000°C. However, due to the large uncertainty in this particular measurement, it is possible that the effective stoichiometry in this alloy was lower than ν_{eff} measured in the 40 at.% Ni alloy. The variation of ν_{eff} with the alloy nickel content is predicted by the thermodynamics. Indeed, the iron-chromium spinel is less stable in nickel-rich alloys due to the reduction of the iron activity with nickel addition (Eq. 5.60). Therefore, when the alloy nickel content increases, the size of the subzone with $FeCr_2O_4$ spinel decreases while the subzone where Cr_2O_3 precipitates increases (Section 4.2.1). Thus, the parameter f, therefore ν_{eff} decreases.

5.3.3 Matrix chromium content at $X = X_{(t)}$

In Section 5.3.2, it appears that ν_{eff} increases with the alloy chromium content and it was proposed to explain this variation that at the the location $X = X_{(t)}$ all the chromium was not oxidised, which decreases the iron activity, thus the stability of the iron chromium spinel. To determine the chromium content of the matrix at the location $X = X_{(t)}$, the solubility product of chromium oxide given by

$$K_{sp}^{(Cr_2O_3)} = N_O^3 N_{Cr}^2 \tag{5.61}$$

is used. If the oxygen solubility at $X = X_{(t)}$ is known, Equation (5.61) allows the determination of the chromium mole fraction of the matrix at this location. The

calculation of chromium oxide solubility product is first presented for Fe-Cr alloys.

5.3.3.1 Chromium oxide solubility product in Fe-Cr alloys

To estimate the chromium oxide solubility product, the reaction of formation of chromium oxide from elements in solution is given by

$$2\underline{\mathrm{Cr}} + 3\underline{\mathrm{O}} \rightarrow \mathrm{Cr_2O_3} \tag{5.62}$$

Taken pure condensed phase as the reference state for solid and a pressure of 1 atm for gas phase, the free energy of reaction 5.62 is

$$\Delta G_{5.62} = G^0_{Cr_2O_3} - 2\overline{G}_{Cr} - 3\overline{G}_O \tag{5.63}$$

where $G^0_{Cr_2O_3}$ is the standard free energy of pure chromium oxide and, $\overline{G}_{Cr}$ and $\overline{G}_O$ the partial free energy of chromium and oxygen in solution, respectively. To evaluate $K_{sp}^{(Cr_2O_3)}$, firstly the following reaction is considered

$$2\mathrm{Cr} + \frac{3}{2}\mathrm{O_2} \rightarrow \mathrm{Cr_2O_3} \tag{5.64}$$

with the standard free energy of reaction taken from [3] and given by

$$\Delta G^0_{5.64} = G^0_{Cr_2O_3} - 2G^0_{Cr} - \frac{3}{2}G^0_{O_2} = -1,120,260 + 258T \text{ (J mol}^{-1}) \tag{5.65}$$

Then, assuming a Raoultian standard state for species in solution, the free energy of chromium in solution in iron is given by

$$\overline{G}_{Cr} = G^0_{Cr} + \overline{G}^{xs}_{Cr} + RT\ln(N_{Cr}) \tag{5.66}$$

where the excess Gibbs free energy of chromium in solution in iron is given by

$$\overline{G}^{xs}_{Cr} = \overline{H}^{xs}_{Cr} - T\overline{S}^{xs}_{Cr} = RT\ln(\gamma_{Cr}) \tag{5.67}$$

where γ_{Cr} is the chromium activity coefficient in iron. This coefficient was measured at high temperature in Fe-Cr alloys by Mazandarany and Pehlke [131]. From their measurements, the authors estimated the activity coefficient of chromium in solution in iron at infinite dilution ,γ^0_{Cr}. These values are presented in Table 5.11. From

Table 5.11: Activity coefficient for chromium in iron at infinite dilution.

Temperature (°C)	900	1,000	1,100	1,200
γ^0_{Cr}	4.89	3.99	3.35	2.9

activity coefficient values presented in Table 5.11 and using Equation (5.67), the excess enthalpy and entropy were evaluated using linear regression and it was found that at infinite dilution of chromium in solution in iron, $\overline{H}^{xs}_{Cr} = 25,031$ J mol^{-1} and $\overline{S}^{xs}_{Cr} = 8.2$ J mol^{-1} K^{-1}.

Finally, the free energy of oxygen in solution in iron is given by

$$\overline{G}_O = G^0_O + \overline{G}^{xs}_O + RT\ln(N_O) \tag{5.68}$$

where $\overline{G}^{xs}_O$ is calculated with $\overline{H}^{xs}_O$ and $\overline{S}^{xs}_O$ measured from oxygen solubility measurements in H_2/H_2O gases. These values reported in Table 3.3 yield

$$\overline{G}_O = G^0_O - 276,000 + 139T + RT\ln(N_O) \ \text{(J mol}^{-1}\text{)} \tag{5.69}$$

Combining Equations (5.63), (5.66) and (5.69) and using the assumption that the alloy chromium content has no effect on the energy for oxygen dissolution in iron, the following relation is found

$$\Delta G_{5.62} = G^0_{Cr_2O_3} - 2\left[G^0_{Cr} + \overline{G}^{xs}_{Cr} + RT\ln(N_{Cr})\right] - 3\left[G^0_O + \overline{G}^{xs}_O + RT\ln(N_O)\right] \tag{5.70}$$

In addition, in Chapter 3 it was shown that assuming a Raoultian standard state

for the oxygen dissolved and 1 atm for oxygen in the gas phase yields

$$\frac{1}{2}G^0_{O_2} = G^0_O \tag{5.71}$$

Substituting Equation (5.71) in (5.70) gives

$$\Delta G_{5.62} = \Delta G^0_{5.64} - 2\overline{G}^{xs}_{Cr} - 3\overline{G}^{xs}_{O} - RT\ln\left(N^3_O N^2_{Cr}\right) \tag{5.72}$$

$$\Delta G_{5.62} = -342,322 - 142.7T - RT\ln\left(N^3_O N^2_{Cr}\right)\ (\text{J mol}^{-1}) \tag{5.73}$$

At the equilibrium, $\Delta G_{5.62} = 0$, which allows calculation of the solubility product. Results of calculation for different temperatures are given in Table 5.12.

Table 5.12: Solubility product of chromium oxide in iron.

Temperature (°C)	$K_{sp}^{(Cr_2O_3)}$
1,000	3.1×10^{-22}
1,050	1.0×10^{-21}
1,100	3.3×10^{-21}
1,150	9.4×10^{-21}

A similar calculation was carried out for the solubility product of chromium oxide in Ni-Cr and is developed in the next section.

5.3.3.2 Chromium oxide solubility product in Ni-Cr alloys

The solubility product of chromium oxide in nickel was determined with a calculation similar to that presented for Fe-Cr alloys (Section 5.3.3.1). However, the excess enthalpy and entropy for oxygen dissolution have to be replaced by values measured for nickel. These values were taken from Table 3.3 and yield

$$\overline{G}_O = G^0_O - 277,000 + 164T + RT\ln\left(N_O\right)\ (\text{J mol}^{-1}) \tag{5.74}$$

To calculate $\overline{G}^{xs}_{Cr}$ for Ni-Cr alloys, the activity coefficient for infinite dilution of chromium in solution in nickel measured by Mazandarany and Pehlke [131] was con-

sidered. However, the authors reported a constant value of 0.47 for the chromium activity coefficient between 1,000 and 1,300°C. As with Fe-Cr alloys, using this activity coefficient and Equation (5.67), the excess enthalpy and entropy for chromium in solution in nickel were estimated using a linear regression. It is found that the excess enthalpy is 0 and $\overline{S}_{Cr}^{xs} = 6.7$ J mol^{-1} K^{-1}. Thus combining Equations (5.65), (5.67) and (5.74) one obtains

$$\Delta G_{5.62} = -289,260 - 221.4T - RT \ln\left(N_O^3 N_{Cr}^2\right) \text{ (J mol}^{-1}\text{)} \tag{5.75}$$

At the equilibrium $\Delta G_{5.62} = 0$, and $K_{sp}^{(Cr_2O_3)}$ values are computed and presented in Table 5.13.

Table 5.13: Solubility product of chromium oxide in nickel

Temperature (°C)	$K_{sp}^{(Cr_2O_3)}$
1,000	3.6×10^{-24}
1,050	1.0×10^{-23}
1,100	2.6×10^{-23}
1,150	6.4×10^{-23}

From values of $K_{sp}^{(Cr_2O_3)}$ in Table 5.12 for Fe-Cr alloys and Table 5.13 for Ni-Cr alloys, it appears that chromium oxide is more stable in Ni-Cr alloys than in Fe-Cr. With those solubility product values, the amount of chromium at the location $X = X_{(t)}$ in the IOZ can be evaluated and this calculation is presented in the next section.

5.3.3.3 Calculation of the matrix chromium content at $X = X_{(t)}$

In Section 5.3.2, the hypothesis was advanced that the low effective stoichiometry observed in dilute chromium alloy is due to the fact that chromium remains unoxidised at $X = X_{(t)}$, thereby decreasing the iron activity and thus the stability of the spinel. The estimation of chromium remaining in the matrix at $X = X_{(t)}$, $N_{Cr}^{(t)}$ was carried out for Fe-Cr alloys and Fe-80Ni alloys. To estimate $N_{Cr}^{(t)}$, the oxygen concentration at this location is required. The depth $X_{(t)}$ is where chromium oxide

is converted to iron-chromium spinel according to the following reaction

$$\mathrm{Fe} + \mathrm{Cr_2O_3} + \frac{1}{2}\mathrm{O_2} \rightarrow \mathrm{FeCr_2O_4} \tag{5.76}$$

Therefore, at $X = X_{(t)}$, the oxygen partial pressure is equal to the equilibrium pressure of reaction 5.76. This oxygen partial pressure was calculated in Section 4.1.1 and values are presented in Table 4.3. However, it should be noted that this oxygen partial pressure was calculated under the assumption that all the chromium is oxidised in the IOZ and therefore hence $a_{Fe} = 1$ in Fe-Cr alloys, and iron activity in a Fe-80Ni alloy was calculated for different temperatures, and values are given in Table 4.2. Those calculation showed that iron acitivy in Fe-80Ni alloy range from 0.08 at 1,000°C to 0.09 at 1,150°C. Then, Sievert's law can be used to estimate the oxygen concentration at $X = X_{(t)}$, $N_O^{(t)}$. Finally, knowing the oxygen concentration and the solubility product of chromium oxide, the mole fraction of chromium in the matrix at $X = X_{(t)}$ can be calculated thanks to Equation (5.61).

In Table 5.14, the oxygen partial pressure , oxygen solubility and the mole fraction of chromium in the matrix, $N_{Cr}^{(t)}$, at $X_{(t)}$ are given with solubility products used for the calculation. For calculation in the nickel-rich alloy, chromium oxide solubility products determined for Ni-Cr alloys were considered.

Table 5.14: Evaluation of the matrix chromium content at $X = X_{(t)}$.

Alloy	Temperature °C	$p_{O_2}^{(t)}$ atm	$N_O^{(t)}$ at.ppm	$K_{sp}^{(Cr_2O_3)}$	$N_{Cr}^{(t)}$ at.ppm
Fe-Cr	1,000	5.6×10^{-18}	28	3.1×10^{-22}	119
	1,050	4.0×10^{-17}	28	1.0×10^{-21}	213
	1,100	2.5×10^{-16}	28	3.3×10^{-21}	388
	1,150	1.3×10^{-15}	27	9.4×10^{-21}	691
Fe-80Ni-Cr	1,000	8.5×10^{-16}	13	3.6×10^{-24}	40
	1,050	5.5×10^{-15}	13	1.0×10^{-23}	67
	1,100	3.1×10^{-14}	13	2.6×10^{-23}	109
	1,150	1.6×10^{-13}	13	6.4×10^{-23}	171

Results presented in Table 5.14 show that at $X = X_{(t)}$, the amount of chromium dissolved in the matrix is extremely low and the assumption that all

chromium is oxidised is verified. Therefore, this result disproves the idea that low effective stoichiometry found in dilute alloys is due to chromium dissolved in the matrix at $X = X_{(t)}$ reducing the activity of iron and destabilising the iron-chromium spinel. Therefore another explanation must be sought.

5.3.4 Distribution of volume fraction through the IOZ

One of the major assumptions made by both Wagner and Gesmundo in treating internal oxidation is that all chromium is oxidised in the IOZ, thus internal oxide volume fraction is constant through the IOZ. This assumption allows derivation of the following equation

$$\frac{k_w^{(i)}}{k_p^{(i)}} = \frac{1}{\Gamma}\left(\frac{M_O}{V_{alloy}}\alpha N_{Cr}^{(0)}\nu_{eff}\right)^2 \tag{5.77}$$

However, Equation (5.77) yields low values of effective stoichiometry in dilute alloys as presented in Figure 5.9. To test if the hypothesis of a constant volume fraction through the IOZ is true, the internal oxide volume fraction was measured as a function of depth in alloys with 2 and 7.5 at.% Cr reacted at 1,000°C in H_2/H_2O gases with 13% of water vapour. The measurement of internal oxide volume fraction is described in Section 2.7.2. Results are presented in Figure 5.11. In addition, in this Figure, the gray rectangle represents the value of the parameter f and its uncertainty. Thus, this rectangle is centred on the value of $X_{(t)}$, where the transition chromium oxide-spinel is observed.

Figure 5.11 shows the internal oxide volume fraction is relatively constant for $x < X_{(t)}$ while it drops significantly for $x > X_{(t)}$ to reach values close to zero at the internal oxidation front. The constant value of internal oxide volume fraction measured for penetrations lower than $X_{(t)}$ suggests that all chromium is oxidised in this subzone and is in agreement with the calculation of the amount of chromium left in the matrix at $X_{(t)}$, carried out in Section 5.3.3. However, in the subzone where chromium oxide precipitates, the decrease in volume fraction increasing depth

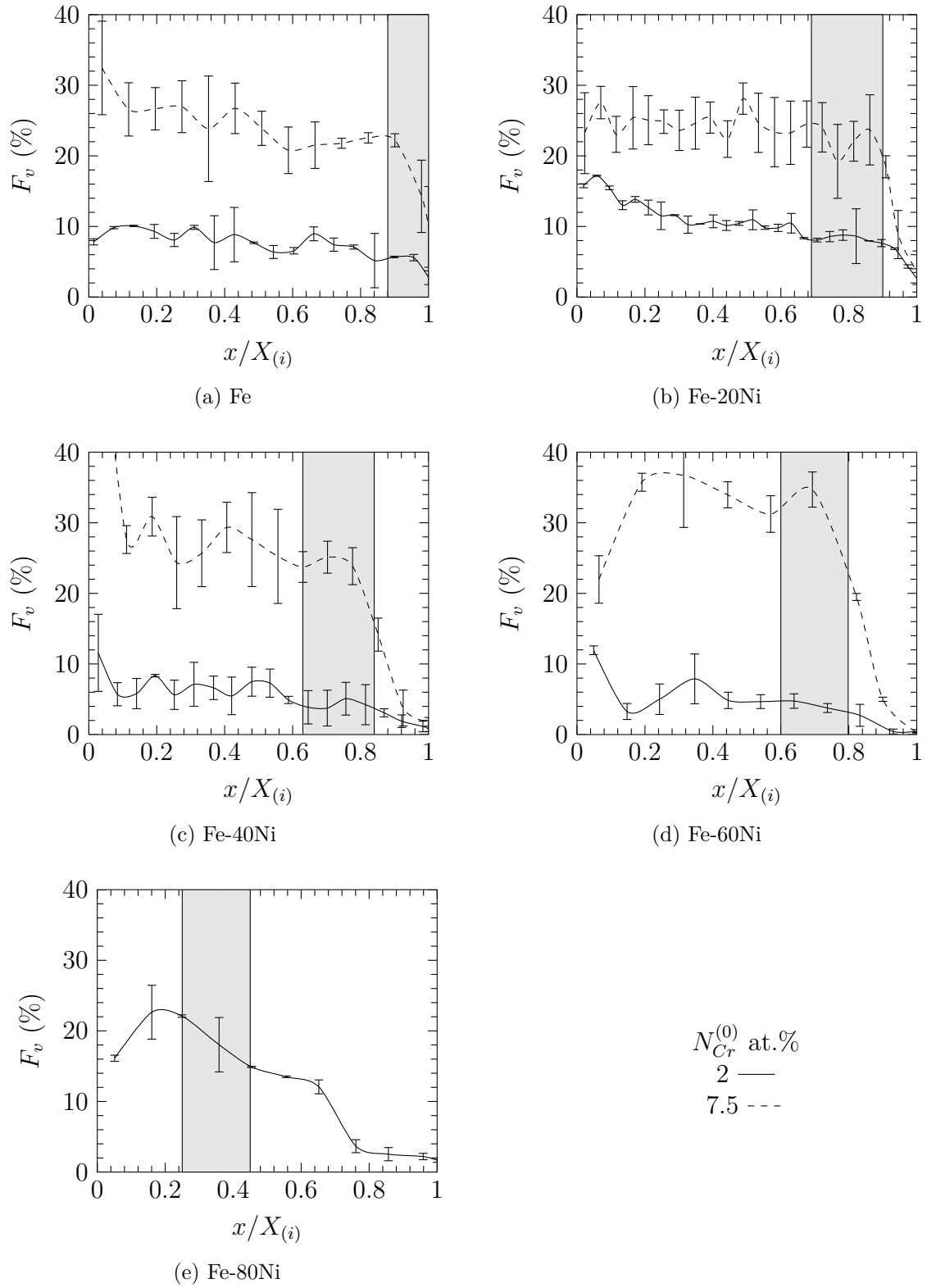

(a) Fe

(b) Fe-20Ni

(c) Fe-40Ni

(d) Fe-60Ni

(e) Fe-80Ni

Figure 5.11: Internal oxide volume fraction as function of the IOZ depht for alloys reacted at 1,000°C in H_2/H_2O gases with 13% of water vapour.

indicates that all chromium is not oxidised in this subzone.

In Section 5.2.2, relationship to evaluate the amount of chromium oxidised and present in a subzone prior to internal oxidation were developed and are used here. The amount of chromium present as oxide in subzone 2 is given by

$$n_{Cr}^{(2)} = F_v^{(2)} \frac{v^{(2)}}{V_{CrO_{1.5}}} = (1-f)\, v_{IOZ} \frac{F_v^{(2)}}{V_{CrO_{1.5}}} \tag{5.78}$$

where $F_v^{(2)}$ is the volume fraction of oxide in subzone 2. However, if enrichment of the subzone 2 takes place the amount of chromium oxidised may be overestimated. Thus, Equation (5.79) was formulated as below to remove the effect of enrichment

$$n_{Cr}^{ox(2)} = (1-f)\, v_{IOZ} \frac{F_v^{(2)}}{\alpha V_{CrO_{1.5}}} \tag{5.79}$$

The amount of chromium present in subzone 2 prior to internal oxidation was calculated in Section 5.2.2.2 and is given by

$$n_{Cr}^{(0)(2)} = \frac{N_{Cr}^{(0)}}{1-N_{Cr}^{(0)}} \frac{(1-f)\, v_{IOZ}}{V_{alloy}} \left(1 - F_v^{(2)}\right) \tag{5.80}$$

Subtracting Equation (5.79) from (5.80) yields the number of mole of chromium unoxidised in zone 2:

$$n_{Cr}^{(2)} = (1-f)\, v_{IOZ} \left[\frac{N_{Cr}^{(0)}}{1-N_{Cr}^{(0)}} \frac{\left(1 - F_v^{(2)}\right)}{V_{alloy}} - \frac{F_v^{(2)}}{\alpha V_{CrO_{1.5}}} \right] \tag{5.81}$$

In addition, to estimate the average matrix chromium mole fraction of subzone 2, Equation (5.81) is divided by the total number of mole of matrix metal in subzone 2 given by

$$n_t^{(2)} = \frac{(1-f)\, v_{IOZ}}{V_{alloy}} \left(1 - F_v^{(2)}\right) \tag{5.82}$$

and yields

$$N_{Cr}^{(2)} = \frac{N_{Cr}^{(0)}}{1-N_{Cr}^{(0)}} - \frac{F_v^{(2)}}{\left(1 - F_V^{(2)}\right)} \frac{V_{alloy}}{\alpha V_{CrO_{1.5}}} \tag{5.83}$$

The measurement of $F_V^{(2)}$ was already carried out in Section 5.2.2.1 for alloys

with 7.5 at.% of chromium reacted at 1,000°C in H_2/H_2O gases with 13% of water vapour and results are reported in Table 5.7. However, these measurements exhibit large uncertainties and it was preferred to evaluate $F_V^{(2)}$ as the average of volume fractions measured at different depth in subzone 2. The same method was used for alloys with a chromium content of 2 at.%. In addition, using enrichment factors presented in Table 5.5, the mole fraction of chromium unoxidised in subzone 2 was evaluated and results are reported in Table 5.15.

Table 5.15: Mole fraction of chromium unoxidised in subzone 2 for alloys reacted at 1,000°C in H_2/H_2O gases with 13% of water vapour.

$N_{Cr}^{(0)}$ at.%	$\frac{N_{Ni}}{N_{Fe}+N_{Ni}}$	α	$F_V^{(2)}$	$N_{Cr}^{(2)}$ at.%	$\frac{N_{Cr}^{(2)}}{N_{Cr}^{(0)}}$
2	0	1.02	0.03	0.6	0.3
	0.2	1.03	0.05	-0.4	-
	0.4	1.07	0.02	1.0	0.5
	0.6	1.21	0.02	1.3	0.7
	0.8	1.74	0.06	0.4	0.2
7.5	0	1.04	0.12	1.1	0.17
	0.2	1.04	0.14	0.5	0.08
	0.4	1.1	0.14	0.8	0.13
	0.6	1.32	0.20	-0.8	-

They show that some values of $N_{Cr}^{(2)}$ are negative. However, these negative values are likely due to uncertainty in volume fraction measurement. To verify this hypothesis, the volume fraction required to obtain $N_{Cr}^{(2)} = 0$, noted $F_v^{(2)*}$, was evaluated for alloys Fe-20Ni-2Cr and Fe-60Ni-7.5Cr using Equation (5.83). Results of calculation are presented in Table 5.16.

Table 5.16: Comparison of $F_v^{(2)}$ required for $N_{Cr}^{(2)} = 0$ and the volume fraction measured.

Alloy	$F_v^{(2)*}$ %	$F_v^{(2)}$ %
Fe-20Ni-2Cr	4.1	5 ± 2
Fe-60Ni-7.5Cr	18.5	20 ± 3

The volume fraction required to observe $N_{Cr}^{(2)} = 0$ is within the uncertainty of volume fraction measured and negative values reported in Table 5.15 are due to uncertainty on volume fraction measurements. The maximum value of $N_{Cr}^{(2)}$ was evaluated considering the minimum of $F_v^{(2)}$. Values found are 0.6 and 0.8 at.% for Fe-20Ni-2Cr and Fe-60Ni-7.5Cr, respectively. Overall, it is considered that the mole fraction of unoxidised chromium in subzone 2 is approximately 1 at.% for dilute and chromium-rich alloys. Therefore, in a qualitative sense, chromium-rich alloys conformed more closely to the assumption that all chromium is oxidised in the IOZ than did dilute alloys, as shown by the ratio $\frac{N_{Cr}^{(2)}}{N_{Cr}^{(0)}}$. In chromium-rich alloys, the amount of chromium left in the matrix represents 10% of the original amount, while in dilute alloys, chromium unoxidised represents 50% of $N_{Cr}^{(0)}$.

The distribution of internal oxide in this case of relatively low stability oxide was investigated by Orhiner and Morral and their model is presented in the next section.

5.3.5 Orhiner and Morral model for distribution of internal oxide in subzone 2

Orhiner and Morral [46] developed a model to consider the precipitation of particles with a low stability, as is observed here for chromium oxide in subzone 2. According to the lever rule the fraction of precipitate in subzone 2 is given by

$$F_p = \frac{N_{Cr}^{(0)} - N_{Cr}}{N_{Cr}^{p} - N_{Cr}} \tag{5.84}$$

where N_{Cr} is the local chromium mole fraction and N_{Cr}^{p} the mole fraction of chromium in the precipitate. In addition, assuming that the solution is dilute yields $N_{Cr}^{p} >> N_{Cr}$ and Equation (5.84) becomes

$$F_p = \frac{N_{Cr}^{(0)} - N_{Cr}}{N_{Cr}^{p}} \tag{5.85}$$

Equation (5.85) can be rewritten at the alloy sample surface and is given by

$$F_p^{(s)} = \frac{N_{Cr}^{(0)} - N_{Cr}^{(s)}}{N_{Cr}^{p}} \tag{5.86}$$

Dividing Equation (5.85) by (5.86) yields the expression for the fraction of precipitate normalized to its value at the surface

$$r = \frac{F_p}{F_p^{(s)}} = \frac{N_{Cr}^{(0)} - N_{Cr}}{N_{Cr}^{(0)} - N_{Cr}^{(s)}} \tag{5.87}$$

In the IOZ, the local equilibrium is given by [46]

$$\frac{N_{Cr}}{N_{Cr}^{(0)}} = 1 - \alpha r \tag{5.88}$$

where α is a solubility parameter given by

$$\alpha = 1 - \frac{K_{sp}^{1/2}}{N_{Cr}^{(0)} \left(N_O^{(s)}\right)^{3/2}} \tag{5.89}$$

Under Wagner's assumption, the internal oxide precipitation is complete and homogeneous, therefore the fraction of internal oxide at any depth in the IOZ should be equal to the fraction of precipitate at the surface and thus $r = 1$. In addition, if all chromium is oxidised, $N_{Cr} \approx 0$ and Equation (5.88) shows that this is only possible if $\alpha = 1$.

In order to check for deviation from Wagner's model the subzone 2, values of α calculated for different alloys at 1,000°C are presented in Table 5.17. For these calculations, the $K_{sp}^{(Cr_2O_3)}$ values in iron (Table 5.12) was used for alloys with nickel content lower than 50 at.%, and $K_{sp}^{(Cr_2O_3)}$ evaluated in nickel (Table 5.13) was used for alloys with nickel content higher than 50 at.%. In addition, the oxygen solubility at the sample surface $N_O^{(s)}$ was replaced by $N_O^{(t)}$ in Equation (5.89).

Values of α are close to 1 and therefore indicates that most chromium should be oxidised in subzone 2. However, it is difficult to assess the effect of subzone 1,

Table 5.17: Evaluation of the solubility parameter α in various alloys reacted at 1,000°C.

$N_{Cr}^{(0)}$ at.%	$\frac{Ni}{N_{Fe}+N_{Ni}}$	$N_O^{(t)}$ at.ppm	K_{sp}	α
2	0	28	3.1×10^{-22}	0.9944
	0.2	14	3.1×10^{-22}	0.9829
	0.4	10	3.1×10^{-22}	0.9718
	0.6	16	3.6×10^{-24}	0.9985
	0.8	13	3.6×10^{-24}	0.9980
7.5	0	28	3.1×10^{-22}	0.9984
	0.2	14	3.1×10^{-22}	0.9954
	0.4	10	3.1×10^{-22}	0.9923
	0.6	16	3.6×10^{-24}	0.9996

where iron-chromium spinel precipitates, on the oxygen supply of the subzone 2. If the boundary value concentration, $N_O^{(t)}$, is lower than the value estimated from the thermodynamic approach, the parameter α should decrease according to Equation (5.89). In addition, the latter Equation predicts that deviations from Wagner's model are more likely to arise in dilute alloys when $N_{Cr}^{(0)}$ approaches 0. This observation is in agreement with the qualitative analysis made in Section 5.3.4 from estimates of the mole fraction of chromium unoxidised in subzone 2.

The estimation of chromium unoxidised in subzone 2 from volume fraction measurements and from Orhriner and Morral's model for precipitation of low stability internal oxide yield the same conclusions. In the subzone where chromium oxide precipitates, the internal oxide volume fraction decreases with increasing depth due to the relatively low stability of this oxide. In addition, the usual approximation of complete precipitation of chromium is less likely to be achieved in dilute alloys. For this reason, when the effective stoichiometry is evaluated by coupling internal oxidation kinetics measured by weight gain and penetration, the low values estimated for dilute alloys arise because not all chromium is oxidised in subzone 2. This results in a small overestimation of the penetration. However in chromium-rich alloys the assumption that all the chromium is oxidised is approximately correct.

To quantify the deviation from Wagner's model, Orhriner and Morral [46]

proposed the plot in Figure 5.12, where curves were determined by solving several differential equations and defining a kinetic parameter given by

$$y = \frac{X}{2\sqrt{\frac{N_O^{(s)} D_O t}{\nu N_{Cr}^{(0)}}}} \tag{5.90}$$

Assuming no enrichment, Equation (5.90) is rewritten

$$y = \frac{X}{2\sqrt{k_p^{(i)} t}} = \frac{X}{\sqrt{2}\sqrt{2k_p^{(i)} t}} \tag{5.91}$$

Finally the relation between penetration and $k_p^{(i)}$ is

$$X = y\sqrt{2}\sqrt{2k_p^{(i)} t} \tag{5.92}$$

and the term $y\sqrt{2}$ represents the deviation from Wagner's model. Under Wagner's conditions, $\alpha = 1$ and Orhriner and Morral estimated that $y = \frac{1}{\sqrt{2}}$ [46] as seen

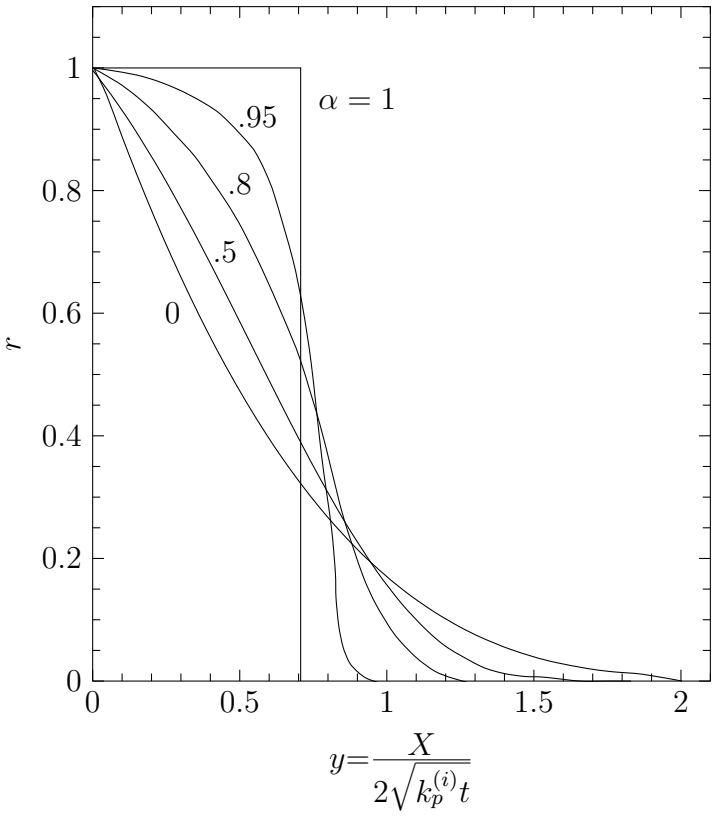

Figure 5.12: Estimation of y for different values of α [46].

in Figure 5.12. Substituting y in Equation (5.92) yields the classic parabolic relationship between penetration and time. However, if the value of $\alpha < 1$, indicating incomplete precipitation of the solute element in the IOZ, Figure 5.12 shows that $y > \frac{1}{\sqrt{2}}$, thus the penetration is greater than is predicted from Wagner's model.

It should be noted that Orhriner and Morral's model [46] was developed for an IOZ composed of a single oxide while in the present study, the IOZ is composed of 2 subzones where different oxides precipitate (Section 4.1.1). In addition, the incomplete precipitation of chromium is observed only in the subzone next to the internal oxidation front (subzone 2) where chromium oxide precipitates. In order to investigate the effect of the incomplete precipitation in subzone 2 on the overall internal oxidation kinetics the geometry presented in Figure 5.13 was considered with $\nu_1 = 2$ and $\nu_2 = 1.5$. For simplicity in the following development, no enrichment and constant oxygen concentration gradients in the IOZ were assumed.

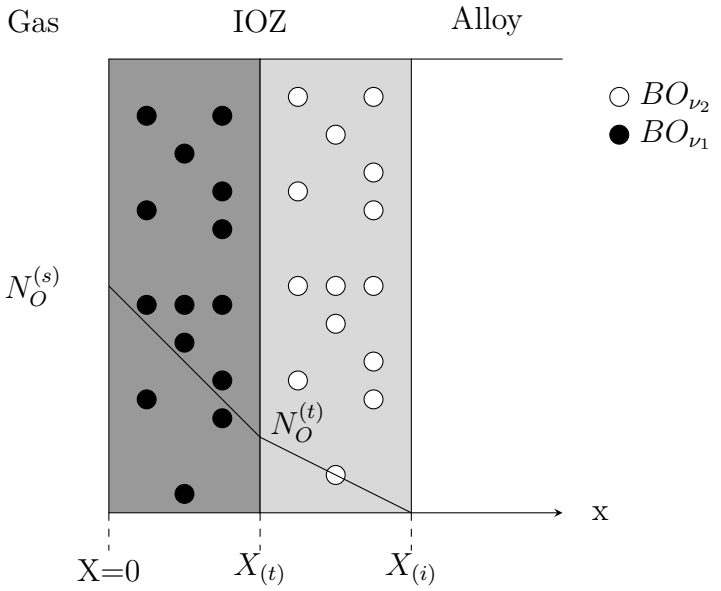

Figure 5.13: Schematic representation of internal oxide distribution in the IOZ when multiple internal oxides precipitate.

For growth of subzone 2, the following relation one has

$$2y^2 \frac{D_O N_O^{(t)}}{X_{(i)} - X_{(t)}} = \nu_2 N_{Cr}^{(0)} \frac{dX_{(i)}}{dt} \tag{5.93}$$

where $2y^2$ is the corrective factor introduced by Orhiner and Morral to take into

account the incomplete precipitation of chromium in subzone 2. This equation can be rewritten

$$D_O N_O^{(t)} = \frac{X_{(i)} - X_{(t)}}{2y^2} \nu_2 N_{Cr}^{(0)} \frac{dX_{(i)}}{dt} \tag{5.94}$$

A second relation is found with boundary conditions at the depth $X = X_{(t)}$. At this depth a part of the oxygen flux coming from subzone 1 is used to convert chromium oxide into iron-chromium spinel and the remaining oxygen flux (Eq. 5.93) enters the subzone 2 to sustain IOZ growth. Therefore, in subzone 1, the following relation is found

$$\frac{D_O \left(N_O^{(s)} - N_O^{(t)} \right)}{X_{(t)}} = \frac{\nu_2}{2y^2} N_{Cr}^{(0)} \frac{dX_{(i)}}{dt} + (\nu_1 - \nu_2) N_{Cr}^{(0)} \frac{dX_{(t)}}{dt} \tag{5.95}$$

Substituting Equation (5.94) in (5.95) yields

$$\frac{D_O N_O^{(s)}}{X_{(t)}} - \left(\frac{X_{(i)}}{X_{(t)}} - 1 \right) \frac{1}{2y^2} \nu_2 N_{Cr}^{(0)} \frac{dX_{(i)}}{dt} = \frac{\nu_2}{2y^2} N_{Cr}^{(0)} \frac{dX_{(i)}}{dt} + (\nu_1 - \nu_2) N_{Cr}^{(0)} \frac{dX_{(t)}}{dt} \tag{5.96}$$

Using the relation $f = X_{(t)}/X_{(i)}$ in (5.96) and under the assumption that f is independent of time, it is found that

$$\frac{D_O N_O^{(s)}}{X_{(i)}} = \frac{\nu_2}{2y^2} N_{Cr}^{(0)} \frac{dX_{(i)}}{dt} + (\nu_1 - \nu_2) f^2 N_{Cr}^{(0)} \frac{dX_{(i)}}{dt} \tag{5.97}$$

Finally, the rate equation for the overall IOZ is given by

$$\frac{D_O N_O^{(s)}}{X_{(i)}} = N_{Cr}^{(0)} \left[\frac{\nu_2}{2y^2} + (\nu_1 - \nu_2) f^2 \right] \frac{dX_{(i)}}{dt} \tag{5.98}$$

Equation (5.98) was first tested in limiting cases to check its validity. If it is considered that the IOZ is only composed of iron-chromium spinel, thus $f = 1$. However, when iron-chromium spinel forms, chromium is totally oxidised which yields $y = \frac{1}{\sqrt{2}}$ and Equation (5.98) gives

$$\frac{D_O N_O^{(s)}}{X_{(i)}} = N_{Cr}^{(0)} \nu_1 \frac{dX_{(i)}}{dt} \tag{5.99}$$

The classic relation for the growth of internal oxidation zone developed by Wagner

is found, which is consistent with the fact that all chromium is oxidised when spinel precipitates. It should be noted that this case is not realistic as chromium oxide is more stable than iron-chromium spinel, Cr_2O_3 oxides always precipitate at the internal oxidation front and yields $f < 1$. If now it is assumed that the IOZ is only composed of chromium oxide, $f = 0$ and Equation (5.98) becomes

$$\frac{D_O N_O^{(s)}}{X_{(i)}} = N_{Cr}^{(0)} \frac{\nu_2}{2y^2} \frac{dX_{(i)}}{dt} \tag{5.100}$$

which is a relation equivalent to Equation (5.92). In addition, the factor $2y^2$ which is the reflection of incomplete precipitation of chromium is present in Equation (5.100) reflecting the possibility that precipitation of chromium can be incomplete when chromium oxide formed. However, if it is assumed that the precipitation was complete then $y = \frac{1}{\sqrt{2}}$ and Equation (5.100) becomes

$$\frac{D_O N_O^{(s)}}{X_{(i)}} = N_{Cr}^{(0)} \nu_2 \frac{dX_{(i)}}{dt} \tag{5.101}$$

which is Wagner's expression for the growth of IOZ when all chromium is oxidised.

The study of limiting cases shows that Equation (5.98) describes well the internal oxidation kinetics if incomplete precipitation takes place in one of the subzones which makes up the IOZ. Therefore, Equation (5.98) was integrated and rewritten

$$X_{(i)}^2 = 2 \frac{N_O^{(s)} D_O t}{\nu_{eff} N_{Cr}^{(0)}} \tag{5.102}$$

with

$$\nu_{eff} = \left[\frac{\nu_2}{2y^2} + (\nu_1 - \nu_2) f^2 \right] \tag{5.103}$$

In Figure 5.14, ν_{eff} as a function of f is plotted for different values of y. The Figure shows that for Wagner's model ($y = \frac{1}{\sqrt{2}}$), ν_{eff} varies between 1.5 and 2 as expected. However, ν_{eff} exhibits a parabolic dependency on f, while a linear model (Eq.5.54) was considered in Section 5.3.1. Difference between Equations (5.103) and (5.54) may result from assumptions required to develop Equations (5.93) and (5.95), such

as linear oxygen concentration in the IOZ.

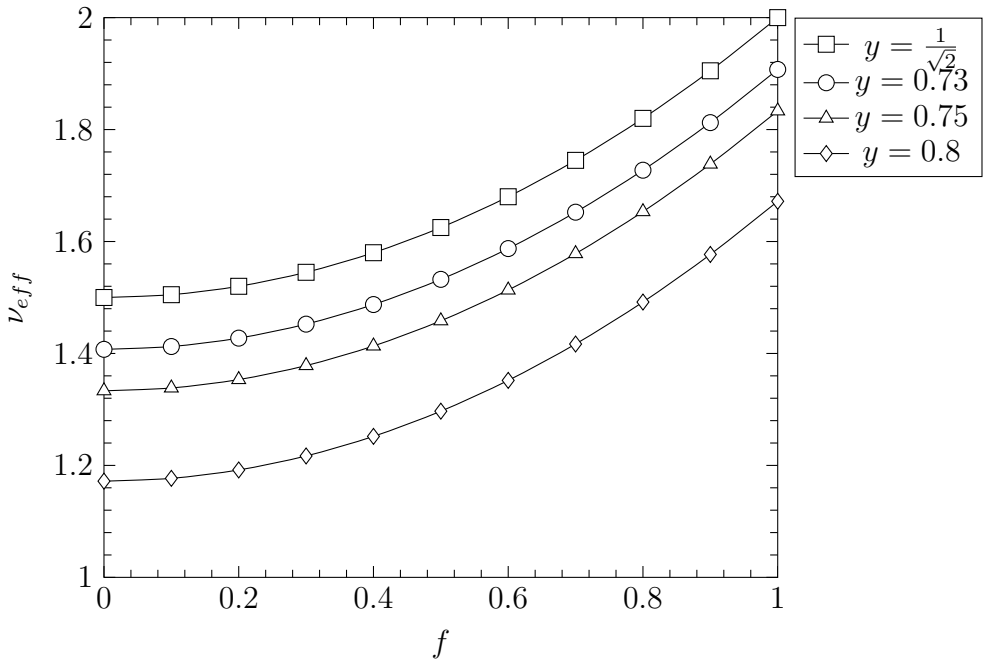

Figure 5.14: Variation of ν_{eff} in the case of incomplete precipitation in subzone 2 with f calculated for different values of y.

In addition, if incomplete precipitation takes place in subzone 2, the value of y increases and, for a given f, a smaller effective stoichiometry is expected. Variation of ν_{eff} with the parameter y is consistent with the fact that in dilute chromium alloys, chromium is not totally oxidised and smaller effective stoichiometry was measured, see Figure 5.9. However, to relate internal oxidation in term of penetration and weight gain, an extra corrective term has to be added to Equation (5.77) but no attempt to carry out this calculation was made.

It is useful to estimate the difference between effective stoichiometry calculated with Equation (5.54) or Equation (5.103). As shown in Table 5.17, it was estimated that the solubility product α defined by Orhriner reaches a minimum equal to 0.97 for Fe-40Ni-2Cr alloys at 1,000°C. This value of α roughly corresponds to $y = 0.73$ according to Figure 5.12. However, in nickel-rich alloys, the chromium oxide solubility product is smaller than in iron-rich alloys. Therefore α is closer to 1 in alloy with nickel content larger than 50 at.%, corresponding to y approaching $\frac{1}{\sqrt{2}} \approx 0.7$ for alloys with this composition. To estimate the difference between effective stoi-

chiometry calculated with Equation (5.54) or Equation (5.103), the following ratio was introduced

$$\Delta\nu_{eff} = \frac{\nu_{eff}^{Eq.5.54}}{\nu_{eff}^{Eq.5.103}} \tag{5.104}$$

where $\nu_{eff}^{Eq.5.54}$ is given by Equation (5.54) and $\nu_{eff}^{Eq.5.103}$ by Equation (5.103).

This quantity is shown in Figure 5.15, plotted as a function of f. For calculation of ν_{eff} with Equation (5.103), two values of the parameter y were considered: $y = 0.71$ for nickel-rich alloys and $y = 0.73$ for iron-rich alloys. Figure 5.15 shows

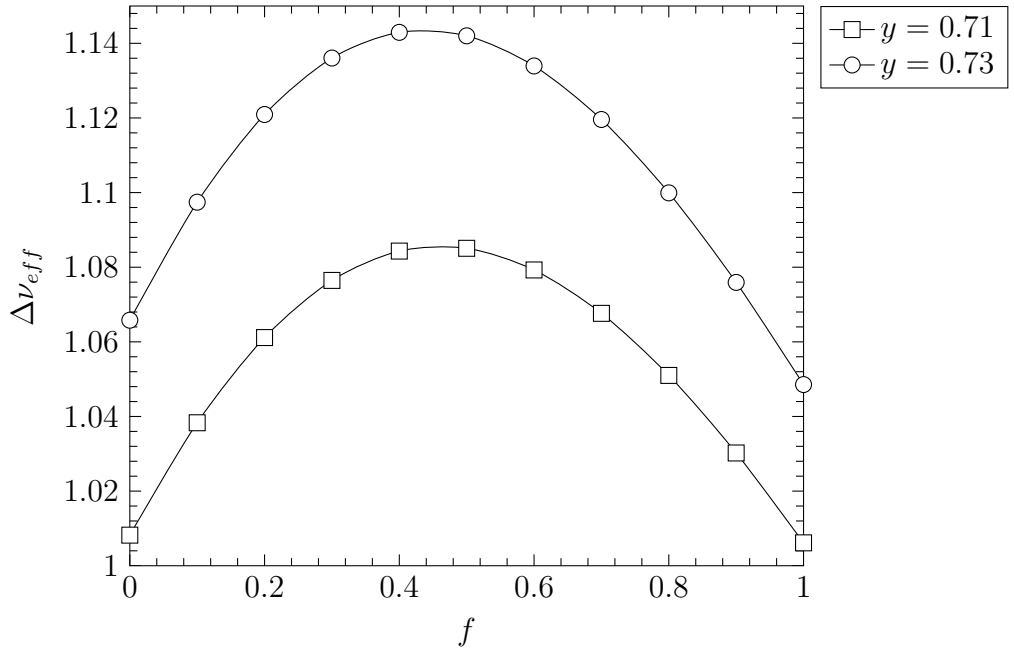

Figure 5.15: Comparison of ν_{eff} calculated with Equation (5.54) or (5.103).

that for iron-rich alloys ($y = 0.73$), the maximum of $\Delta\nu_{eff}$ is for $f = 0.5$ and equal to $\Delta\nu_{eff} = 1.14$. However, for these alloys, when rich in chromium, it was observed that $f > 0.7$, therefore $\Delta\nu_{eff} < 1.12$. For nickel-rich alloys, the maximum of $\Delta\nu_{eff}$ is observed for $f = 0.5$ and equals 1.08. These differences were considered as negligible. Moreover, strong assumptions are made to derive Equation (5.103), and the effect of the strong enrichment in nickel-rich alloys on that equation is difficult to estimate, and was not taken into account. Therefore, it was decided,using an effective stoichiometry calculated from Equation (5.103) which is approximated as independent of the alloy chromium content. Values estimated for chromium-rich alloys from SEM observations are used for dilute chromium alloys.

5.3.6 Effect of water content on the effective stoichiometry

In the previous section, the effective stoichiometry was calculated from weight change and penetration measured in alloys reacted in H_2/H_2O gases containing 13% of water vapour. In this section, the effective stoichiometry measured for alloys exposed in H_2/H_2O gases with 3% of water is evaluated and compared to results obtained for alloys exposed to gases with a high water vapour content. However, this comparison was only carried out for alloys with 7.5 at.% of chromium because as developed in the previous Section 5.3.4 that these alloys verified more closely the assumption that all chromium is oxidised in the IOZ. In Figures 5.16, effective stoichiometry measured after exposure in gases with different water vapour contents are presented. At 1,000°C, the same values of the effective stoichiometry is found for

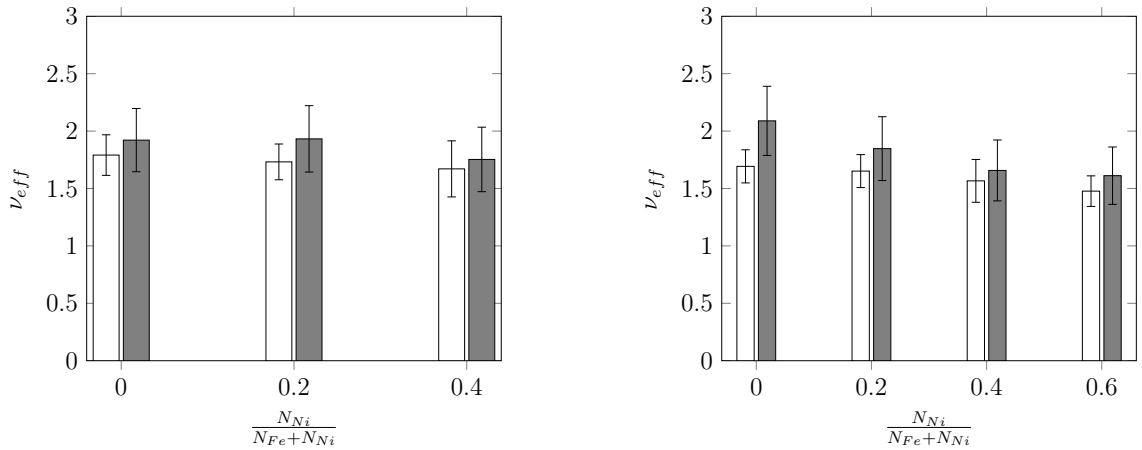

(a) 1,000°C (b) 1,050°C

Figure 5.16: Comparison of effective stoichiometry calculated from kinetics measured for alloys with 7.5 at.% Cr in flowing H_2/H_2O gases containing 13% ( )and 3% ( ) water vapour.

alloys exposed in gases with 3 and 13% of water vapour while at 1,050°C similar stoichiometries are observed for the alloy with $\frac{N_{Ni}}{N_{Fe}+N_{Ni}} \geq 0.2$. For Fe-Cr alloys, a higher value of effective stoichiometry was found at 1,050°C when the alloy is exposed to gases with a low water vapour content. However, the uncertainty of the effective stoichiometry measured is large and it is difficult to achieve a conclusion on a possible effect of the gas water content on the effective stoichiometry in Fe-Cr alloys. Continuous TGA was also carried out at 1,150°C and results of effective stoichiom-

etry calculated for chromium-rich alloys using internal oxidation rate constants in Equation (5.57) are compared in Figure 5.17 to effective stoichiometry measured by SEM observations in chromium-rich alloys reacted in humid gases with 13 % of water vapour. A good agreement is found between values measured by SEM observations

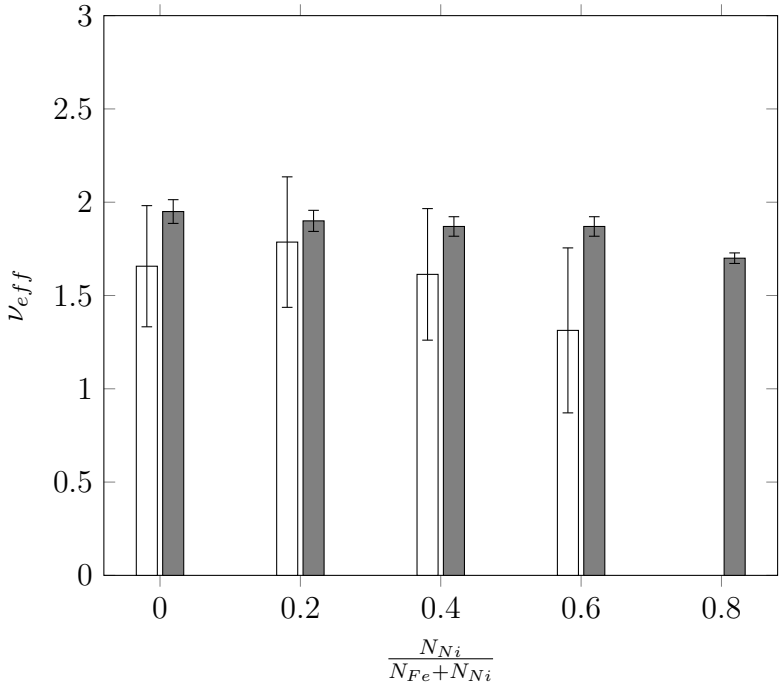

Figure 5.17: Comparison of effective stoichiometric coefficient evaluated by kinetics measurement (Eq.5.57,▯▯) in alloys exposed to humid gas with 3% water vapour and SEM observation (Eq.5.54,▮▮) carried out in alloys exposed to wet gases with 13% water vapour both at 1,150°C.

on alloys reacted in H_2/H_2O gases containing 13% of water vapour and effective stoichiometry calculated from internal oxidation rate constants measured on alloys exposed to humid gases with 3% of water vapour for alloys with $\frac{N_{Ni}}{N_{Fe}+N_{Ni}} < 0.6$. The large value of effective stoichiometry measured by SEM observations in alloys with $\frac{N_{Ni}}{N_{Fe}+N_{Ni}} = 0.6$, may be due to overestimation of $X_{(t)}$ as described in section 5.3.2.

Overall it was found that between 1,000 and 1,150°C, the effective stoichiometry appears to be independent of the water vapour content of the gas. In addition, as presented in Section 5.3.1, effective stoichiometry measured in chromium-rich alloys reacted in Fe/FeO Rhines packs are similar to values found in alloys exposed to H_2/H_2O gases with 13% or 3% of water vapour. All results suggest that the presence and quantity of water vapour do not have a significant effect on the effec-

tive stoichiometry.

5.4 Oxygen permeability

Evaluation of the enrichment factor, α, the effective stoichiometry, ν_{eff} and the volume expansion allows the calculation of the oxygen permeability from values of internal oxidation rate constants measured by penetration or weight gain. Oxygen permeabilities evaluated from penetration measurements for alloys reacted in Fe/FeO Rhines packs and H_2/H_2O gases with 13 and 3% of water vapour are presented in this section. No oxygen permeability was evaluated by weight gain measurement because to compute values of the oxygen permeability from TGA, the distribution of internal oxide in the IOZ has to be known. However, this parameter is difficult to estimate with precision. Therefore, it was preferred to estimate the oxygen permeability from penetration measurement.

5.4.1 Oxygen permeability measured in Fe/FeO Rhines packs

The oxygen permeability is related to the internal oxidation rate constant by the following equation

$$k_p^{(i)} = \frac{N_O^{(s)} D_O}{\nu_{eff} \alpha N_{Cr}^{(0)}} \Gamma \tag{5.105}$$

with

$$\Gamma = \frac{1}{1 - \overline{\left(\frac{\Delta v}{v}\right)}} \tag{5.106}$$

$$\overline{\left(\frac{\Delta v}{v}\right)} = N_{Cr}^{(0)} \left[f\alpha \frac{V_{Fe_{0.5}CrO_2}}{V_{alloy}} + (1-f)\,\alpha \frac{V_{CrO_{1.5}}}{V_{alloy}} - (1 + 0.5 f\alpha) \right] \tag{5.107}$$

In order to simplify the notation, the new variable $k_p^{(i)'}$ is introduced and defined by

$$k_p^{(i)'} = \frac{k_p^{(i)} \nu_{eff} \alpha}{\Gamma} = \frac{N_O^{(s)} D_O}{N_{Cr}^{(0)}} \tag{5.108}$$

To calculate the oxygen permeability in dry environments, enrichment factors are taken from Table 5.4, effective stoichiometric coefficients from Table 5.9 and f from Table 4.1. In addition, to compute values of oxygen permeability, it is assumed that the effective stoichiometry and the factor f are independent of the alloy chromium content, as demonstrated in Section 5.3.

To estimate the oxygen permeability, the variable $k_p^{(i)\prime}$ is plotted versus the inverse of the alloy chromium content according to Equation (5.108). However, it was reported in Chapter 4, that internal oxidation kinetics seem to become independent of the alloy chromium content at 1,000 and 1,050°C. In order to investigate this observation, it was decided to present the permeability in two parts. Firstly, oxygen permeability estimated from kinetic measurements obtained at 1,000 and 1,050°C is presented, and oxygen permeability calculated from kinetics measured at 1,100 and 1,150°C are introduced in a second section.

5.4.1.1 Determination of oxygen permeability at 1,000 and 1,050°C

In Figure 5.18, the variable $k_p^{(i)\prime}$ measured at 1,000 and 1,050°C is plotted versus the inverse of the alloy chromium concentration. Figure 5.18 shows that for alloys with a nickel content equal to or larger than 40 at.% nickel, the quantity $k_p^{(i)\prime}$ varies linearly with the inverse of the alloy chromium content, as predicted by Equation (5.108). However, the latter Equation also predicts that extrapolations should pass through the origin, but this is not observed in Figure 5.18. For alloys with nickel content lower than 40 at.%, at 1,000°C the variable $k_p^{(i)\prime}$ exhibits a high value in alloys with a chromium content of 2 at.% and then decreases to reach a plateau, and $k_p^{(i)\prime}$ is found to be similar in alloys with 4 and 7.5 at.% of chromium. This unexpected variation is also observed at 1,050°C for Fe-Cr alloys while in Fe-20Ni-Cr alloys the variation of $k_p^{(i)\prime}$ is close to linear. As suggested in Chapter 4, the observation of similar values of $k_p^{(i)\prime}$ for some alloys with 4 and 7.5 at.% of chromium may be due to fast oxygen diffusion at matrix/oxide interfaces. In addition, deviations from Equation (5.108) for alloys with nickel content larger than 20 at.% are also

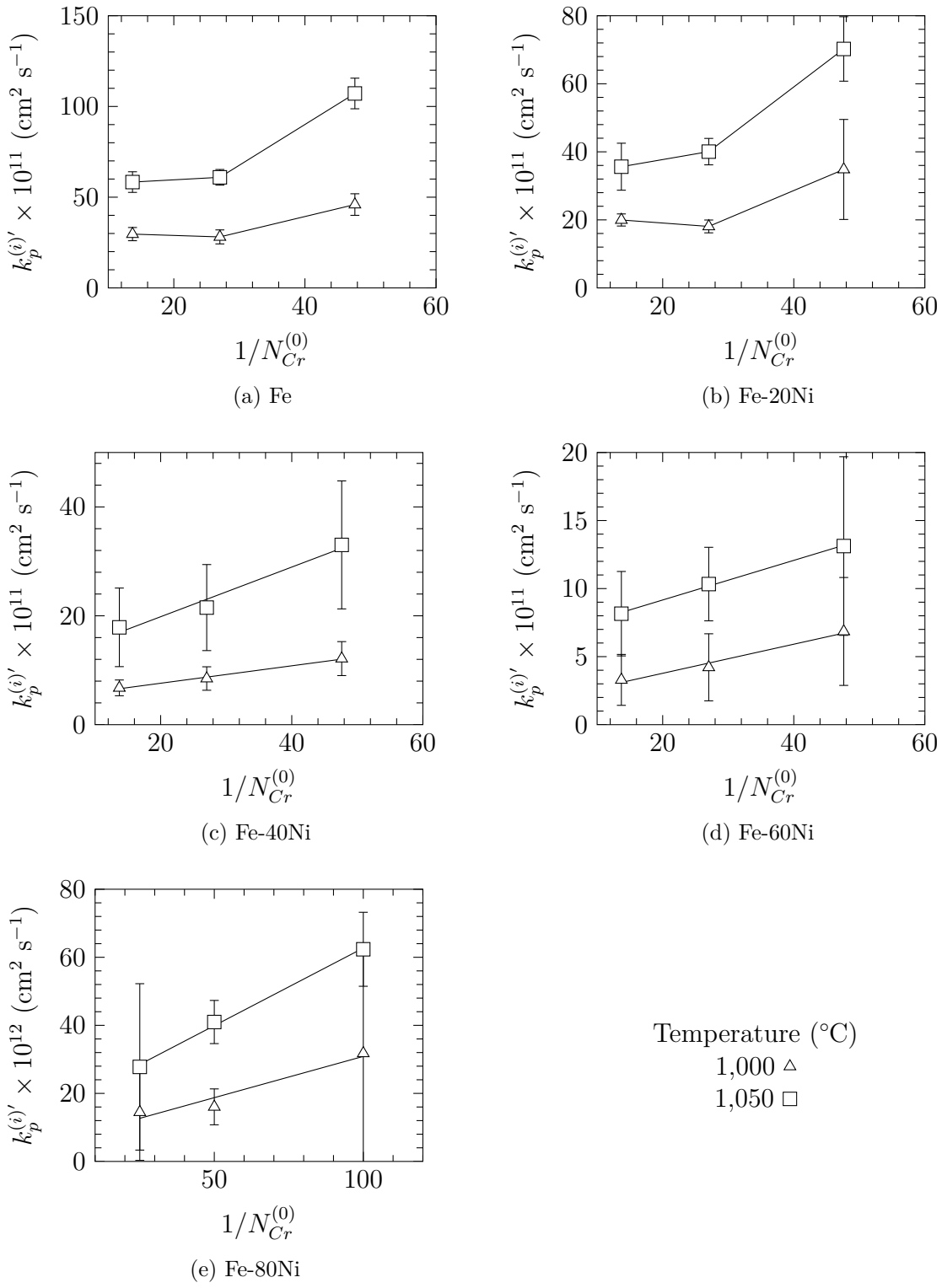

Figure 5.18: Plot of the parameter $k_p^{(i)\prime}$ measured at 1,000 and 1,050°C in Fe/FeO Rhines packs versus the inverse of the alloy chromium concentration.

attributed to fast oxygen diffusion at matrix/oxide interfaces, as reported by several authors [40, 41, 49, 52]. To estimate the contribution of the fast oxygen diffusion at matrix/oxide interfaces when spherical particles precipitate, a calculation similar to Stott's development for rod-shape internal oxides [51] was carried out.

According to Hart's equation [53], the effective oxygen diffusion coefficient is a linear combination of diffusivities of oxygen in the matrix, in the oxide and at the oxide/matrix interface. Therefore, these diffusivities are weighted by the area fraction of each diffusion medium. The effective oxygen diffusion coefficient is expressed by the following equation

$$D_O^{eff} = F_A^{mat} D_O^{mat} + F_A^{int} D_O^{int} + F_A^{ox} D_O^{oxide} \tag{5.109}$$

where

- F_A^{mat} is the area fraction of matrix available for oxygen diffusion.
- F_A^{int} is the area fraction of interface available for oxygen diffusion.
- F_A^{ox} is the area fraction of oxide available for oxygen diffusion.
- D_O^{mat} is the oxygen diffusion coefficient in the matrix.
- D_O^{int} is the oxygen diffusion coefficient at the interface oxide/matrix interface.
- D_O^{oxide} is the oxygen diffusion coefficient in the oxide

The oxygen diffusion in the oxide is extremely slow compared to the oxygen diffusion in the matrix and at the metal/oxide interface [132, 133]. Therefore, Equation (5.109) is adequately approximated by

$$D_O^{eff} = F_A^{mat} D_O^{mat} + F_A^{int} D_O^{int} \tag{5.110}$$

In addition, the area fraction of matrix is given by

$$F_A^{mat} = 1 - F_A^{int} - F_A^{ox} \tag{5.111}$$

To estimate the value of the effective diffusion coefficient, interface and oxide area fractions have to be estimated.

In the subsequent development, it is considered that internal oxides are spherical with a constant radius, R_p, and they are randomly distributed in the internal oxidation zone. Therefore, a plane at a depth z would section spheres at different locations. However, sectioning a volume containing spheres of the same size and randomly distributed is equivalent to sectioning a single sphere, with the same radius, at all locations z. Therefore, all calculations to estimate area fraction of matrix and interface were carried out on a single spherical particle, as illustrated in Figure 5.19. Under the assumption that the single sphere is sectioned at all locations, z, with equal probability, it was decided that best estimates of F_A^{ox} and F_A^{int} are their average values when calculated from $z = 0$ to $z = R_p$. The calculations of F_A^{ox} and F_A^{int} are presented in the next section.

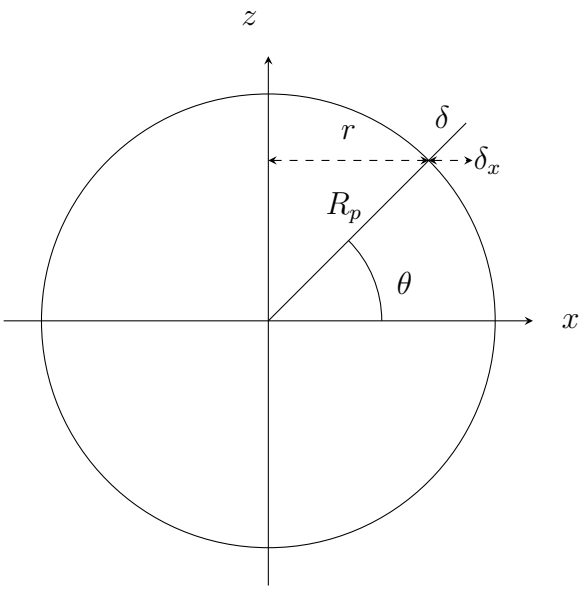

Figure 5.19: Geometry for area calculation.

Calculation of F_A^{ox} and F_A^{int}

To calculate the interface area fraction, the following relation was used

$$F_A^{int} = F_A^{ox} \frac{< A_{int} >}{< A_{ox} >} \tag{5.112}$$

where $< A_{int} >$ is the area of average sections made by the intersection of a plane

with the interfacial zone around the sphere, and $< A_{ox} >$ is the area of average sections made by the intersection of a plane with the sphere. In addition, under the assumption that particles are spherical and randomly distributed in the internal oxidation zone, the oxide area fraction is taken to be the internal oxide volume fraction at each depth.

$$F_A^{ox} = F_V \tag{5.113}$$

In the sphere, the relation between r and z is given by

$$R_p^2 = z^2 + r^2 \tag{5.114}$$

and yields the following relation for A_{ox} at the location z

$$A_{ox}(z) = \pi r^2 = \pi(R_p^2 - z^2) \tag{5.115}$$

Therefore, the area of the average section of oxide is given by

$$< A_{ox} >= \frac{1}{R_p} \int_0^{R_p} A_{ox}(z) dz \tag{5.116}$$

$$< A_{ox} >= \frac{1}{R_p} \int_0^{R_p} \pi(R_p^2 - z^2) dz = \frac{2}{3} \pi R_p^2 \tag{5.117}$$

To calculate $< A_{int} >$ the same development as for $< A_{ox} >$ was used. It is considered that the interface has a thickness of δ. However, to calculate the component of δ perpendicular to the oxygen flux, a length δ_x is defined as the projection of δ on the x-axis

$$\delta_x = \delta \cos(\theta) \tag{5.118}$$

where θ is defined in Figure 5.19. Using the trigonometric relation yields

$$\cos(\theta) = \frac{r(z)}{R_p} \tag{5.119}$$

and combining Equations (5.118) and (5.119), yields the following equation for δ_x

as a function of z

$$\delta_x(z) = \delta \frac{r(z)}{R_p} \tag{5.120}$$

The interface area at one location z is given by

$$A_{int}(z) = 2\pi\delta_x r(z) = 2\pi\delta \frac{r(z)^2}{R_p} \tag{5.121}$$

The area of the average interfacial section around the particle is found by integrating over z

$$< A_{int} >= \frac{1}{R_p} \int_0^{R_p} A_{int}(z) dz \tag{5.122}$$

$$< A_{int} >= \frac{1}{R_p} \int_0^{R_p} 2\frac{\pi\delta}{R_p}(R_p^2 - z^2) = \frac{4}{3}\pi\delta R_p \tag{5.123}$$

Combining Equations (5.113), (5.117) and (5.123), the area fraction of interface is found to be

$$F_A^{int} = \frac{< A_{int} >}{< A_{ox} >} F_A^{ox} = \frac{2\delta}{R_p} F_V \tag{5.124}$$

Calculation of F_A^{int} and F_A^{ox} allows the development of an expression for the effective oxygen diffusion coefficient.

Effective oxygen diffusion coefficient

The effective oxygen diffusion coefficient is given by

$$D_O^{eff} = F_A^{mat} D_O^{mat} + F_A^{int} D_O^{int} \tag{5.125}$$

Substituting Equation (5.111) in (5.125) yields

$$D_O^{eff} = D_O^{mat} \left[1 + F_A^{int} \left(\frac{D_O^{int}}{D_O^{mat}} - 1 \right) - F_A^{ox} \right] \tag{5.126}$$

Combining Equations (5.113), (5.124) and (5.126) yields the expression for the ef-

fective diffusion coefficient.

$$D_O^{eff} = D_O^{mat}\left\{1 + F_v\left[\frac{2\delta}{R_p}\left(\frac{D_O^{int}}{D_O^{mat}} - 1\right) - 1\right]\right\} \tag{5.127}$$

In addition, the oxygen diffusion at the interface oxide/matrix is expected to be much faster than oxygen diffusion in the matrix. Therefore, Equation (5.127) is rewritten as

$$D_O^{eff} = D_O^{mat}\left[1 + F_v\left(\frac{2\delta}{R_p}\frac{D_O^{int}}{D_O^{mat}} - 1\right)\right] \tag{5.128}$$

If the internal oxide volume fraction is considered constant through the IOZ, it is given by the following expression

$$F_v = \alpha N_{Cr}^{(0)}\frac{V_{oxide}}{V_{alloy}} \tag{5.129}$$

where α is the enrichment factor, $N_{Cr}^{(0)}$ the mole fraction of chromium in the alloy, V_{oxide} the internal oxide molar volume and V_{alloy} the alloy molar volume. Here, expansion of the IOZ accompanying precipitation has been ignored. Finally, under the assumption that the oxygen solubility at the sample surface is independent of the alloy chromium content, the effective permeability is given by

$$N_O^{(s)}D_O^{eff} = N_O^{(s)}D_O^{mat}\left[1 + \alpha N_{Cr}^{(0)}\frac{V_{oxide}}{V_{alloy}}\left(\frac{2\delta}{R_p}\frac{D_O^{int}}{D_O^{mat}} - 1\right)\right] = N_O^{(s)}D_O^{mat}\left(1 + \lambda N_{Cr}^{(0)}\right) \tag{5.130}$$

with

$$\lambda = \alpha\frac{V_{oxide}}{V_{alloy}}\left(\frac{2\delta}{R_p}\frac{D_O^{int}}{D_O^{mat}} - 1\right) \tag{5.131}$$

Equation (5.130) shows that the effective oxygen permeability follows a linear relationship with the alloy chromium content, but also that a critical radius, R_p' exists for which the effective oxygen permeability becomes lower than the matrix permeability. The critical radius is given by

$$R_p' = \frac{2\delta D_O^{int}}{D_O^{mat}} \tag{5.132}$$

If internal oxides have a radius greater than R'_p, these particles block the inward flux of oxygen and slow down internal oxidation kinetics.

Determination of this critical radius requires knowledge of the ratio $\frac{D_O^{int}}{D_O^{mat}}$ and δ. Stott *et al.* [51] reported ranges of the ratio $\frac{D_O^{int}}{D_O^{mat}}$ for dilute Ni-Cr alloys assuming $\delta = 1$ nm. However, the evaluation of the ratio of oxygen diffusion coefficients depends on the particle size, which is not constant through the IOZ. For this reason, the authors reported a lower and an upper bound of the ratio $\frac{D_O^{int}}{D_O^{mat}}$, corresponding to the smallest and the largest particles size observable. They found ratios ranging from 10^4 to 2×10^4 at 1,000°C and from 0.2×10^4 to 0.9×10^4 at 1,100°C. These authors also reported that $\frac{D_O^{int}}{D_O^{mat}}$ decreases with increasing temperature. The temperature dependency of the ratio $\frac{D_O^{int}}{D_O^{mat}}$ is related to the activation energy of each diffusion mechanism. Equation (5.135) illustrates this statement. If one considers

$$D_O^{mat} = D_O^{(0),mat} \exp\left(\frac{-Q^{mat}}{T}\right) \tag{5.133}$$

$$D_O^{int} = D_O^{(0),int} \exp\left(\frac{-Q^{int}}{T}\right) \tag{5.134}$$

where $D_O^{(0),mat}$ and $D_O^{(0),int}$ are pre-exponential factors for diffusion in the matrix and at the matrix/oxide interface, respectively and Q^{mat} and Q^{int} the activation energy of each mechanism.

$$\frac{D_O^{int}}{D_O^{mat}} = \frac{D_O^{(0),int}}{D_O^{(0),mat}} \exp\left(\frac{-(Q^{int} - Q^{mat})}{T}\right) \tag{5.135}$$

- If $Q^{int} > Q^{mat}$, the ratio $\frac{D_O^{int}}{D_O^{mat}}$ increases when the temperature increases but it is unlikely.
- If $Q^{int} < Q^{mat}$, the ratio $\frac{D_O^{int}}{D_O^{mat}}$ decreases when the temperature increases. This behaviour is expected as the activation energy for diffusion at interfaces is commonly smaller than the activation energy for matrix diffusion. In addition, this assumption is in agreement with Stott's observationsfor Ni-Cr and Ni-Al alloys [51].

To investigate the effects of $\frac{D_O^{int}}{D_O^{mat}}$, R_p and F_V on the effective diffusion coefficient, a parametric study of the ratio $\frac{D_O^{eff}}{D_O^{mat}}$ was carried out. First of all, Equation (5.128) is valid for $R_p \in [2\delta\ ; +\infty[$. In Figure 5.20, the variation of the ratio $\frac{D_O^{eff}}{D_O^{mat}}$ is plotted versus the particle radius, R_p, for several internal oxide volume fractions. To plot curves in Figure 5.20, the ratio $\frac{D_O^{int}}{D_O^{mat}}$ was considered equal to 10^4 and $\delta = 1$ nm. These parameter yields a critical radius R_p' equal 20 μm (Eq.5.132). The critical radius also appears in Figure 5.20. Indeed, if $R_p > R_p'$ the ratio $\frac{D_O^{eff}}{D_O^{mat}}$

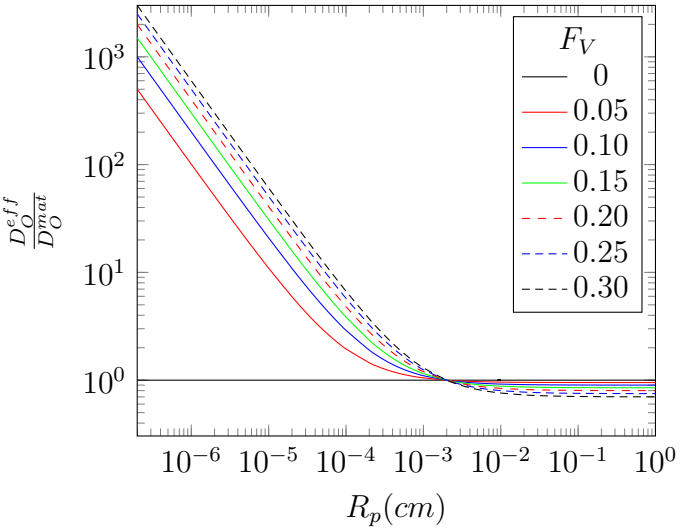

(a) All R_p

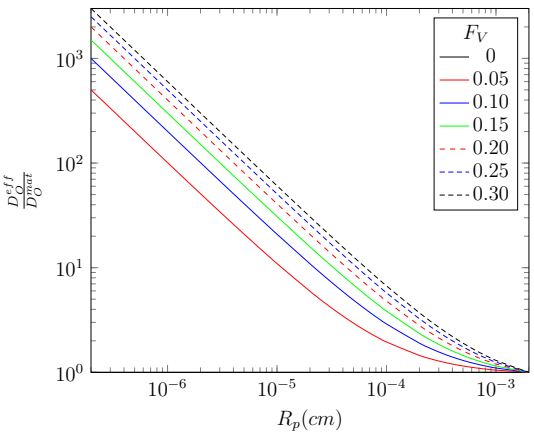

(b) $R_p < R_p'$

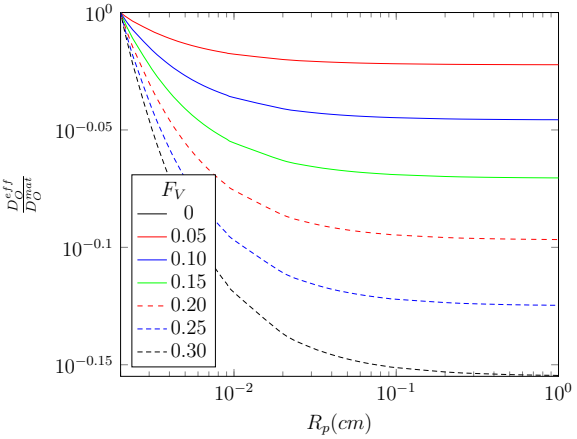

(c) $R_p > R_p'$

Figure 5.20: Ratio $\frac{D_O^{eff}}{D_O^{mat}}$ calculated for different internal oxide volume fractions.

becomes lower than 1. In Figure 5.20, it is clear that for a particle radius from 0 to 20 μm, the larger the particles are, the less is oxygen diffusion enhanced. In addition, for a fixed particle size, if the volume fraction increases, the effective

oxygen diffusion coefficient also increases, because more interfaces are available for fast oxygen diffusion. However, for particle radius larger than R'_p, the blocking effect is stronger if particles are larger or if the volume fraction increases. In addition, Figure 5.20 shows that for a given volume fraction, all curves exhibit one asymptote.

- If $R_p \to +\infty$, the minimum of the ratio $\frac{D_O^{eff}}{D_O^{mat}}$ is reached and Equation (5.128) becomes

$$\frac{D_O^{eff}}{D_O^{mat}} = 1 - F_v \tag{5.136}$$

On the other hand, if the $R_p \to 0$, Equation (5.130) shows that $\frac{D_O^{eff}}{D_O^{mat}}$ tends to infinity. However, the smallest value of R_p is obviously non-zero but its value is difficult to estimate. The minimum R_p could be considered as the minimum particle size, R_p^* for the growth of a particle as described in Section 1.3.2.7 or as the size of clusters composed of oxygen and chromium atoms. Nevertheless, for $R_p > 0$, $\frac{D_O^{eff}}{D_O^{mat}}$ is equal to a high finite value.

In addition, it was reported in Chapter 4 that the particle size increases with the IOZ depth. According to Equation (5.130), the change in particle size reduces the oxygen flux within the IOZ and should yield non parabolic internal oxidation kinetics. However, all kinetics were found to be parabolic suggesting that the change in particle size does not have a significant effect on the oxygen flux. The average particle size, $\overline{R}_p$ was measured by the intercept method at 3 locations in the IOZ: just beneath the alloy surface $\frac{X}{X_{(i)}} = 0$, at the middle of the IOZ, $\frac{X}{X_{(i)}} = 0.5$ and next to the internal oxidation front, $\frac{X}{X_{(i)}} = 1$. Measurements were carried out in alloys with 7.5 at.% Cr reacted at 1,000°C because the effect of fast oxygen diffusion at the matrix/oxide interface should be more significant at this composition and temperature. Measurements are presented in Table 5.18.

Results of Table 5.18 show that the particle size beneath the alloy surface is smaller than the internal oxide size in the middle of the IOZ and slightly decrease next to the internal oxidation front. During the conversion of a chromium oxide particle into iron-chromium spinel, the particle is expected to expand due to the

Table 5.18: Average particle size, $\overline{R}_p$ (μm), measured at 3 locations in the IOZ.

$\frac{X}{X_{(i)}}$	$\frac{N_{Ni}}{N_{Fe}+N_{Ni}}$ 0	0.2	0.4	0.6	0.8
0	0.5 ± 0.1	0.5 ± 0.1	0.4 ± 0.1	0.6 ± 0.1	0.4 ± 0.1
0.5	0.9 ± 0.1	0.8 ± 0.2	1.3 ± 0.3	1.2 ± 0.1	0.6 ± 0.1
1	0.7 ± 0.1	0.7 ± 0.2	1.1 ± 0.4	0.6 ± 0.2	0.5 ± 0.1

larger molar volume of $FeCr_2O_4$ compared to Cr_2O_3. Therefore, the decrease in $\overline{R}_p$ close to the internal oxidation front may be due to the size change when chromium oxide is converted to iron-chromium spinel.

The ratio of $\lambda^{\frac{X}{X_{(i)}}=0}$ to $\lambda^{\frac{X}{X_{(i)}}=0.5}$ was calculated with particle size measured at $\frac{X}{X_{(i)}} = 0$ and $\frac{X}{X_{(i)}} = 0.5$ to estimate the effect of particle size on oxygen permeability. For this calculation it was considered that $\frac{D_O^{int}}{D_O^{mat}} = 10^4$ and $\delta = 1$ nm as reported by Stott *et al.* [51]. The calculations are presented in Table 5.19.

Table 5.19: Ratio of parameters λ calculated for different particle sizes.

$\frac{N_{Ni}}{N_{Fe}+N_{Ni}}$	0	0.2	0.4	0.6	0.8
$\lambda^{\frac{X}{X_{(i)}}=0} / \lambda^{\frac{X}{X_{(i)}}=0.5}$	2.0	1.6	3.2	2.2	1.6

Results of the calculation showed that the oxygen flux beneath the alloy surface should be larger than the oxygen flux in the middle of the IOZ by a factor of 2-3. However, the ratio of $\lambda^{\frac{X}{X_{(i)}}=0}$ to $\lambda^{\frac{X}{X_{(i)}}=0.5}$ gives the maximum value of the difference between the flux enhanced by small particles beneath the alloy surface and the flux of oxygen in the middle of the IOZ. However, the global effect of enhanced oxygen diffusion on internal oxidation kinetics integrates the different values of λ through the IOZ.

In the zone between $\frac{X}{X_{(i)}} = 0$ and $\frac{X}{X_{(i)}} = 0.5$, the particle size is increasing and yields lower values of λ than $\lambda^{\frac{X}{X_{(i)}}=0}$. In addition, in the other half of the IOZ, the internal particle size may be considered almost constant and the parameter λ in this zone is equal to $\lambda^{\frac{X}{X_{(i)}}=0.5}$ for all depths. Therefore, it is likely that the effect of the changing particle size with depth induces a transient stage at the beginning of

internal oxidation. However, in the present study, the IOZ depth was measured on samples where the particle size was already large and it is likely that the transient stage at the beginning of oxidation was not observable.

Calculation of oxygen permeability

The model previously developed shows that Equation (5.108) gives access to the value of the effective stoichiometry, and is rewritten

$$k_p^{(i)'} = \frac{k_p^{(i)} \nu_{eff} \alpha}{\Gamma} = \frac{N_O^{(s)} D_O^{eff}}{N_{Cr}^{(0)}} \tag{5.137}$$

However, to estimate the matrix oxygen permeability, Equations (5.108) and (5.130) were combined to obtain a new expression for the variable $k_p^{(i)'}$

$$k_p^{(i)'} = \frac{N_O^{(s)} D_O^{mat}}{N_{Cr}^{(0)}} \left[1 + \alpha N_{Cr}^{(0)} \frac{V_{oxide}}{V_{alloy}} \left(\frac{2\delta}{R_p} \frac{D_O^{int}}{D_O^{mat}} - 1 \right) \right] = \frac{N_O^{(s)} D_O^{mat}}{N_{Cr}^{(0)}} \left(1 + \lambda N_{Cr}^{(0)} \right) \tag{5.138}$$

with

$$\lambda = \alpha \frac{V_{oxide}}{V_{alloy}} \left(\frac{2\delta}{R_p} \frac{D_O^{int}}{D_O^{mat}} - 1 \right) \tag{5.139}$$

which takes into account interfacial diffusion and enrichment of the IOZ. In addition, Equation (5.138) shows that an extrapolation for $\frac{1}{N_{cr}^{(0)}} = 0$ yields

$$k_p^{(i)'} = N_O^{(s)} D_O^{mat} \lambda \tag{5.140}$$

a value which may be different of 0. Therefore, Equation (5.138) describes more successfully the variation of $k_p^{(i)'}$ with the inverse of the alloy chromium content presented in Figure 5.18 as extrapolation to $\frac{1}{N_{Cr}^{(0)}} = 0$ may not go through the origin. However, the linear behaviour of $k_p^{(i)'}$ with $\frac{1}{N_{Cr}^{(0)}}$ is only observed for alloys with nickel contents larger than 20 at.% while variation of $k_p^{(i)'}$ observed for Fe-Cr and Fe-20Ni-Cr alloys at 1,000 and 1,050°C in Figure 5.18 are not predicted by Equation (5.138). According to Equation (5.138) the parameter $k_p^{(i)'}$ becomes inde-

pendent of the alloy chromium content if the following relation is satisfied

$$\frac{1}{N_{Cr}^{(0)}} << \lambda \tag{5.141}$$

First of all, the left hand side of Equation (5.141) is minimum in the present dataset for alloys with 7.5 at.% of chromium. The right hand side of Equation (5.141) depends on many parameters like the temperature, the particle size or the enrichment factor as shown in Section 5.4.1.1. As numerical data required to evaluate the parameter λ are difficult to assess with precision, the variation of λ is described below in a qualitative way based on general observations:

- If the temperature and the ratio $\frac{N_{Ni}}{N_{Fe}+N_{Ni}}$ are fixed and the chromium content of the alloy increases, the parameter λ decreases due to the increasing particle size.

- If the temperature and the alloy chromium content are fixed and the nickel alloy content increases, the parameter λ decreases due to the increasing particle size (Section 4.1.1).

- If the alloy composition is fixed and the temperature increases, the parameter λ decreases due to the large decrease of the ratio $\frac{D_O^{int}}{D_O^{mat}}$. The variation of the enrichment factor with temperature was neglected because it is extremely small compared with the variation of $\frac{D_O^{int}}{D_O^{mat}}$.

According to variations in the parameter λ listed above, the best conditions to verify Equation (5.141) are met for the lowest temperature, in alloys with high chromium and iron contents. This is in agreement with experimental observations from Figure 5.18. Therefore, the fast oxygen diffusion at matrix/oxide interface is presumably responsible for deviations from the linear behaviour of the variable $k_p^{(i)'}$ with the inverse of the chromium content observed in Fe-Cr and Fe-20Ni-Cr alloys.

To determine the matrix oxygen permeability at 1,000 and 1,050°C, for alloys with nickel contents larger than 20 at.% of nickel, experimental data was fitted

to Equation (5.138) and matrix oxygen permeabilities evaluated by this method are presented in Table 5.20. This technique was also used to evaluate the matrix oxygen permeability for Fe-20Ni alloys reacted at 1,050°C as $k_p^{(i)'}$ is almost linear with the inverse of the alloy chromium content.

For Fe-Cr alloys exposed at 1,000 and 1,050°C and Fe-20Ni-Cr alloys exposed at 1,000°C, it is obvious that $k_p^{(i)'}$ values obtained from alloys with 7.5 at.% of chromium are biased by the fast oxygen diffusion at matrix/oxide interfaces. In addition, $k_p^{(i)'}$ values measured in alloys with 4 at.% of chromium are difficult to assess. It is impossible to know if its value is reliable or extremely high due to the fast oxygen diffusion. Therefore, it was decided that the best estimate of the oxygen permeability at 1,000 and 1,050°C for Fe and at 1,000°C for Fe-20Ni alloys, was obtained by calculating the effective permeability with Equation (5.137) and approximating this value as the matrix oxygen permeability for alloys with 2 at.% of chromium (because the effect of enhanced oxygen diffusion is small for these alloys due to the small internal oxide volume fraction).

To estimate the contribution of fast oxygen, the parameter λ was evaluated using Equation (5.139) for Fe and Fe-20Ni alloys. For this calculation the enrichment factor was considered equal to 1 as the enrichment is small for iron-rich alloys as shown in Section 5.2. In addition, in those alloys, the internal oxidation zone is mainly composed of spinel thus the spinel molar volume of 24 cm^3 mol^{-1} was considered for V_{oxide}, and the molar volume of Fe and Fe-20Ni alloys are similar and considered equal to 7 cm^3 mol^{-1}. According to values presented in Table 5.18 the internal particle size measured in the middle of the IOZ was similar for Fe and Fe-20Ni alloys. Therefore, $R_p = 1$ μm was used for the calculation. Finally, the ratio $\frac{D_O^{int}}{D_O^{mat}}$ was considered equal to 10^4 as reported by Stott *et al.* [51]. The calculation gives $\lambda = 65$.

In Figure 5.21, the variable $k_p^{(i)'}$ calculated from experimental data for Fe at 1,000 and 1,050°C and Fe-20Ni at 1,000°C are plotted versus the inverse of the alloy chromium concentration. Under the assumption that the fast oxygen diffusion at

matrix/oxide interface does not affect alloys with 2 and 4 at.% Cr, values of $k_p^{(i)'}$ for higher chromium content can be extrapolated as shown in Figure 5.21 by the dashed line. Values of $k_p^{(i)'}$ measured for chromium-rich alloys are corrected using Equation (5.138) to only consider matrix diffusion. The value of $\lambda = 65$ previously calculated was used for the correction. Figure 5.21 shows that corrected values are lower than the extrapolation based on $k_p^{(i)'}$ measured for alloys with 2 and 4 at.% Cr and assuming that fast oxygen diffusion was negligible in those alloys. However, the latter assumption may not be verified for alloys with 4 at.% Cr and $k_p^{(i)'}$ for these alloys should be slightly lower. It is likely that the extrapolation carried out using data obtained from alloys with 2 and 4 at.% chromium overestimates the value calculated for alloys with 7.5 at.% Cr. This result supports the choice to estimate the matrix oxygen permeability of Fe reacted at 1,000 and 1,050°C and Fe-20Ni exposed at 1,000°C with a direct calculation using Equation (5.137) and $k_p^{(i)'}$ measured in alloy with 2 at.% Cr.

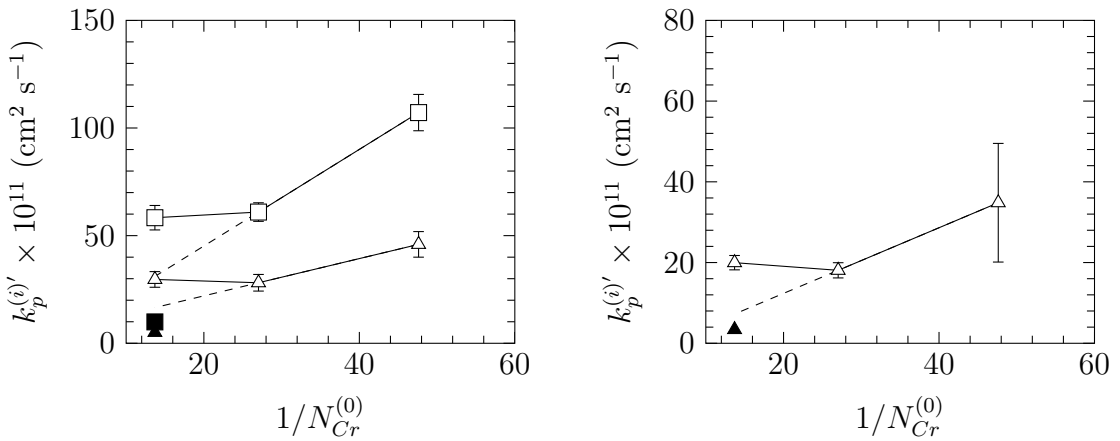

(a) Fe (b) Fe-20Ni

Figure 5.21: Plot of the parameter $k_p^{(i)'}$ measured at 1,000 and 1,050°C in Fe/FeO Rhines packs versus the inverse of the alloy chromium concentration. Values corrected for chromium-rich alloys using Equation (5.138) (–▲–,–■–).

5.4.1.2 Determination of oxygen permeability at 1,100 and 1,150°C

In Figure 5.22, the variable $k_p^{(i)'}$ measured at 1,100 and 1,150°C is plotted versus the inverse of the alloy chromium content. Figure 5.22 shows that at high

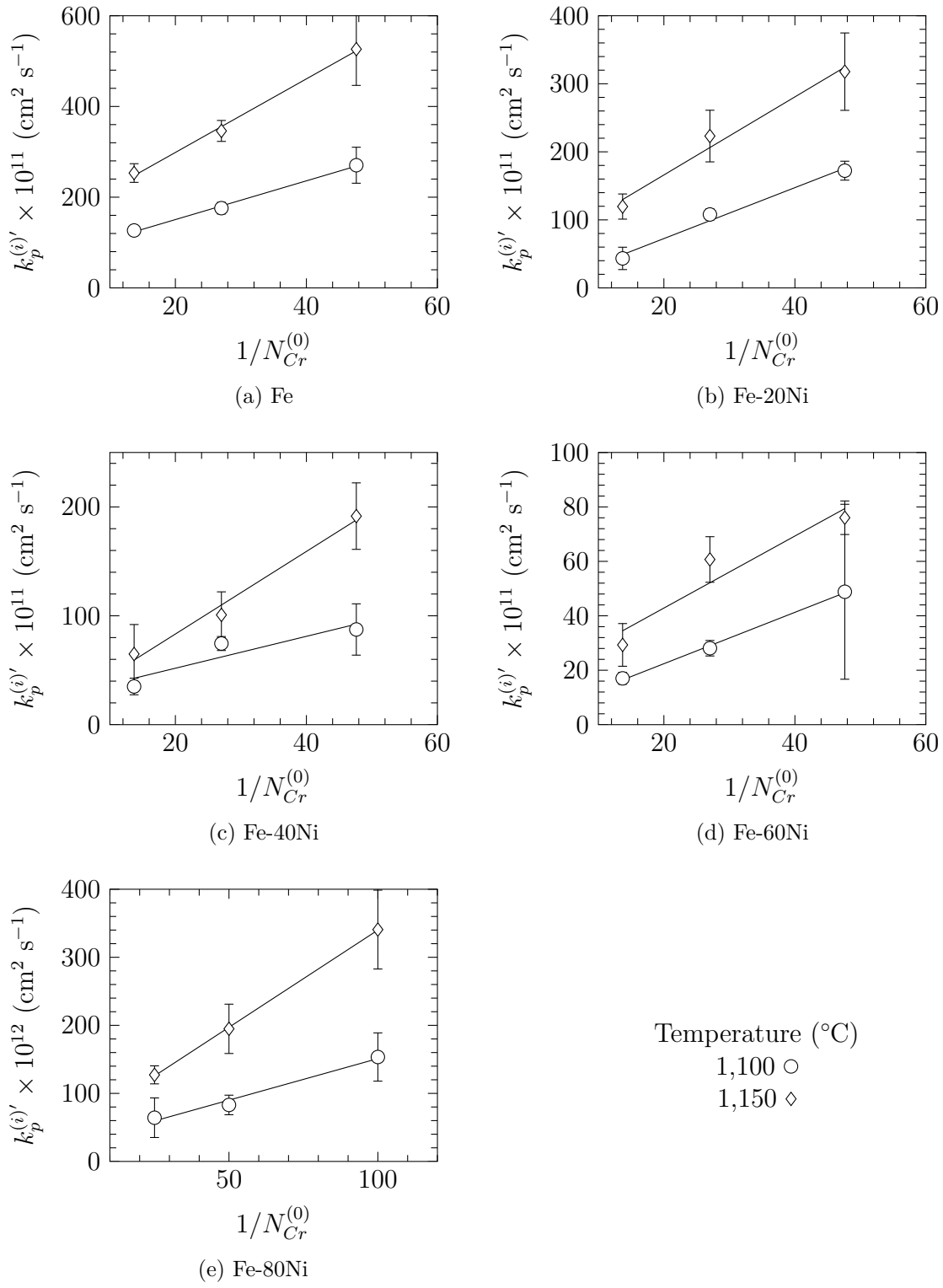

Figure 5.22: Plot of the parameter $k_p^{(i)\prime}$ measured at 1,100 and 1,150°C in Fe/FeO Rhines packs versus the inverse of the chromium.

temperature, $k_p^{(i)'}$ varies linearly with the inverse of the chromium content for all alloys studied. This is expected as soon as the condition for independence from interfacial diffusion effects

$$\frac{1}{N_{Cr}^{(0)}} >> \lambda \tag{5.142}$$

is easier to meet, because the ratio $\frac{D_O^{int}}{D_O^{mat}}$ decreases, therefore λ decreases, when the temperature increases. However, even at these higher temperatures, extrapolation of the data in Figure 5.22 does not pass through the origin. This implies fast oxygen diffusion at matrix/oxide interfaces. Therefore, matrix oxygen permeability was determined using Equation (5.138) to fit experimental data presented in Figure 5.22. Matrix oxygen permeabilities estimated in this way are presented in Table 5.20.

5.4.1.3 Matrix oxygen permeability

In Table 5.20, matrix oxygen permeability values are presented.

Table 5.20: Matrix oxygen permeability measured in Fe/FeO Rhines packs.

$\frac{N_{Ni}}{N_{Fe}+N_{Ni}}$	$N_O^{(s)} D_O^{mat} \times 10^{13}$ (cm^2 s^{-1})			
	1,000°C	1,050°C	1,100°C	1,150°C
0	96 ± 27	225 ± 58	427 ± 49	811 ± 97
0.2	73 ± 36	106 ± 61	374 ± 93	574 ± 172
0.4	16 ± 3	46 ± 16	146 ± 127	379 ± 93
0.6	11 ± 3	15 ± 2	94 ± 10	132 ± 87
0.8	2.4 ± 1.2	4.6 ± 0.5	12 ± 3	29 ± 1

In Figure 5.23, matrix oxygen permeability as function of the alloy composition is plotted. In order to add a point for pure nickel, the oxygen permeability measured by Guo *et al.* with Ni-Cr alloys in Ni/NiO Rhines packs was considered [50]. To estimate the oxygen permeability at the Fe/FeO equilibrium pressure from Guo's measurements the following relation was used

$$\left(N_O^{(s)} D_O^{mat}\right)^{(Fe/FeO)} = \frac{N_O^{Fe/FeO}}{N_O^{Ni/NiO}} \left(N_O^{(s)} D_O^{mat}\right)^{(Ni/NiO)} \tag{5.143}$$

where $\left(N_O^{(s)} D_O^{mat}\right)^{(Fe/FeO)}$ and $\left(N_O^{(s)} D_O^{mat}\right)^{(Ni/NiO)}$ are the oxygen permeability

at the Fe/FeO and Ni/NiO equilibrium pressures, respectively, and $N_O^{Fe/FeO}$ and $N_O^{Ni/NiO}$ the oxygen solubility in nickel measured at the equilibrium pressure indicated. It was decided not to extrapolate from O_2 pressure to the other using Sievert's law because the Sievert constant may not be constant when extrapolation spans such a large range of oxygen partial pressure (see Chapter 3). Instead of using the Sievert's law, it was preferred to directly use the value of oxygen solubility measured by Alcock and Brown [79] for $N_O^{Ni/NiO}$ and values presented in Chapter 3 for $N_O^{Fe/FeO}$.

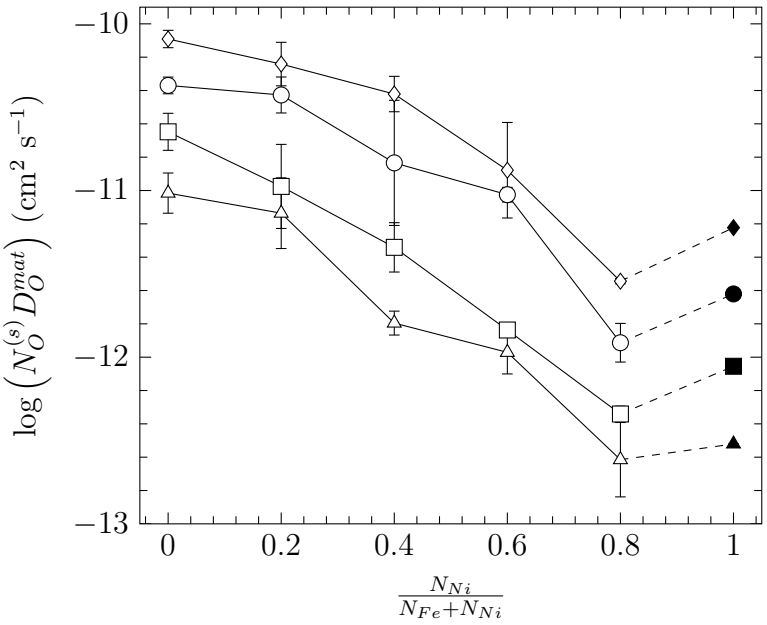

Figure 5.23: Matrix oxygen permeability measured in Fe/FeO Rhines packs at different temperature: 1,000°C (△), 1,050°C (□), 1,100°C (○), 1,150°C (◇). Values in pure nickel extrapolated with equation (5.143) from data published by Guo *et al.* [50] (filled symbols). Note log scale.

Figure 5.23 shows that the oxygen permeability increases when the temperature increases, and variations with the alloy composition are similar at the different temperatures studied. A logarithmic scale is used to encompass the large range of values. The maximum oxygen permeability is found for pure iron. From this maximum the oxygen permeability decreases as the alloy nickel content is increased, to reach a minimum for alloys with $\frac{N_{Ni}}{N_{Fe}+N_{Ni}} = 0.8$. It has to be emphasised that it is difficult to assess the reliability of the change in oxygen permeability from alloys with 80 at.% nickel to pure nickel.

The difficulty arises because the calculation using Equation (5.143) depends on values selected for $N_O^{(s)}$ measured at the Ni/NiO equilibrium pressure. Values presented in Figure 5.23 were calculated with the oxygen solubility measured by Alcock and Brown [79] in the temperature range 1,050-1,200°C in CO/CO_2 gas mixtures. These values were chosen instead of values measured by Park and Alstetter [80] because the latter authors carried out their measurements at temperatures lower than 1,000°C, and recent calculations [93] have showm that the temperature may have an effect on the type of defect present in pure nickel. Therefore, temperature extrapolation may result in incorrect values of the Sievert constant, and consequently it seems preferable to use experimental values measured. Alcock and Brown [79] measured the oxygen solubility in CO/CO_2 gases. Recent work [109] has shown that the carbon has no effect on the oxygen solubility, which supports the choice of Alcock and Brown's values to calculate the oxygen permeability. However, given all the assumptions made in calculating oxygen permeability in nickel, values presented in Figure 5.23 for nickel must be considered with prudence.

The oxygen permeability could be rewritten as in the equation below

$$N_O^{(s)} D_O^{mat} = p_{O_2}^{1/2} \exp\left(\frac{-\overline{G}_O^{xs}}{RT}\right) D_O^{(0)} \exp\left(\frac{-Q}{RT}\right) = p_{O_2}^{1/2} D_O^{(0)} \exp\left[\frac{-\left(\overline{G}_O^{xs} + Q\right)}{RT}\right] \tag{5.144}$$

where p_{O_2} is the oxygen partial pressure and $D_O^{(0)}$ the pre-exponential factor for the oxygen diffusion coefficient. Therefore, the variation of oxygen permeability with temperature follows an Arrhenius relationship. Figure 5.24 shows the permeability data plotted according to Equation (5.144), demonstrating its applicability. In Chapter 3 and 6, $\overline{G}_O^{xs}$ and Q, respectively, were estimated.

Figure 5.24 shows that the oxygen permeability of the matrix measured in the different alloys follows an Arrhenius law as expected. In particular, the oxygen permeability of the matrix determined for Fe-Cr at 1,000 and 1,050°C and for Fe-20Ni-Cr at 1,000°C conform with Arrhenius plots for higher temperature data. Therefore, the choice made earlier to consider that for these alloys the effective per-

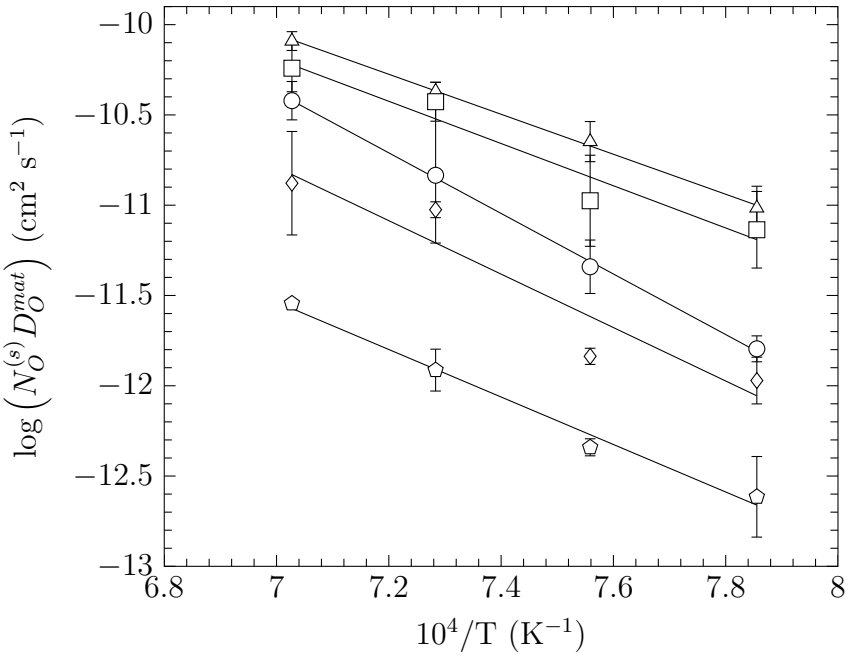

Figure 5.24: Arrhenius plots of matrix permeability evaluated in Fe/FeO Rhines pack. Fe (△), Fe-20Ni (□), Fe-40Ni (□), Fe-60Ni (◇), Fe-80Ni (⬠).

meability calculated with Equation (5.108) for alloys with 2 at.% of chromium is similar to the matrix permeability appears to be reasonable.

Values of λ resulting from the determination of $N_O^{(s)} D_O^{mat}$ with the linear fit of Equation (5.130) to experimental data are given in Table 5.21. For Fe reacted at 1,000 and 1,050°C and Fe-20Ni exposed at 1,000°C, no values are reported as Equation (5.130) does not apply. Some values of λ exhibit extremely large uncertainties

Table 5.21: Values of λ for alloys reacted in Fe/FeO Rhines packs.

$\frac{N_{Ni}}{N_{Fe}+N_{Ni}}$	λ			
	1,000°C	1,050°C	1,100°C	1,150°C
0	-	-	15 ± 2	17 ± 2
0.2	-	16 ± 9	0 ± 8	9 ± 7
0.4	28 ± 1	23 ± 3	15 ± 15	2 ± 7
0.6	15 ± 5	43 ± 1	4 ± 3	12 ± 13
0.8	27 ± 20	37 ± 3	24 ± 11	19 ± 2

due to the limited number of data points and also the calculation of λ. During the fitting procedure the product noted $C = N_O^{(s)} D_O^{mat} \lambda$ is estimated and the value of λ is obtained with the ratio $\frac{C}{N_O^{(s)} D_O^{mat}}$. The uncertainty of λ was calculated assuming

that C and $N_O^{(s)} D_O^{mat}$ are strongly correlated, $r = 1$, which is likely. Therefore, uncertainty of λ was calculated with the following equation

$$(\delta\lambda)^2 = \left(\frac{(\delta C)}{N_O^{(s)} D_O^{mat}}\right)^2 + \left(\frac{-C\left(\delta N_O^{(s)} D_O^{mat}\right)}{\left(N_O^{(s)} D_O^{mat}\right)^2}\right)^2 - 2\frac{C}{\left(N_O^{(s)} D_O^{mat}\right)^3}(\delta C)\left(\delta N_O^{(s)} D_O^{mat}\right) \tag{5.145}$$

where $(\delta\lambda)$, $\left(\delta N_O^{(s)} D_O^{mat}\right)$ and (δC) are the uncertainties of indicated values. In addition, negative values of λ may arise from experimental uncertainties and have to be considered with care. From values in Table 5.21 no clear conclusion on the variation of λ with alloy composition or temperature was possible.

The oxygen permeability was also evaluated from internal oxidation kinetics measured in H_2/H_2O gases to investigate the effect of water vapour and/or hydrogen, and results are presented in the following section.

5.4.2 Oxygen permeability in H_2/H_2O gases

Internal oxidation experiment were carried out in gases containing 13% or 3% water vapour with the oxygen partial pressure set at the Fe/FeO equilibrium in both environments. Results obtained in gases with 13% water vapour are presented first and oxygen permeability measured in gases with 3% water vapour are presented in a second section.

5.4.2.1 Oxygen permeability measured in gases with 13% water vapour

In this section oxygen permeability values measured in gases with 13% water vapour are presented. To evaluate the oxygen permeability, f values and effective stoichiometric coefficients presented in Tables 4.6 and 5.10 were employed. It was assumed that these factors are independent of the alloy chromium content. Enrichment factors considered for the oxygen permeability evaluation were taken from Table 5.5. In addition, results obtained from internal oxidation kinetic measurements at 1,000 and 1,050°C are presented first. Then results at 1,100 and 1,150°C are given in a second section.

Determination of oxygen permeability at 1,000 and 1,050°C

In Figure 5.25, the reduced variable $k_p^{(i)'}$ is plotted for alloys reacted in H_2/H_2O gas mixtures containing 13% water vapour. The Figure 5.25 shows that for all binary Fe-Ni alloys, the variable $k_p^{(i)'}$ varies linearly with the inverse of the alloy chromium concentration. However, extrapolations do not pass through the origin, presumably due to the fast oxygen diffusion at matrix/oxide interfaces as presented in Section 5.4.1.1. For Fe-Cr alloys reacted at 1,000°C, the variable $k_p^{(i)'}$ exhibits the same deviations from linearity as observed for Fe-Cr alloys reacted in Fe/FeO Rhines packs. Therefore, for Fe-Cr alloys exposed to the lowest temperature, the matrix oxygen permeability was estimated with the method presented in Section 5.4.1.1 for Fe/FeO Rhines packs at 1,000 and 1,050°C. For binary Fe-Ni alloys and Fe-Cr alloys exposed at 1,050°C, Equation (5.138) was fitted to experimental data to determine the matrix oxygen permeability. All matrix oxygen permeability values are presented in Table 5.22.

Determination of oxygen permeability at 1,100 and 1,150°C

In Figure 5.26, the variable $k_p^{(i)'}$ is plotted versus the inverse of the alloy chromium content The Figure 5.26 shows that at 1,100 and 1,150°C for all alloys, $k_p^{(i)'}$ exhibits a linear variation with the inverse of the chromium concentration. In addition, the effect of the fast oxygen diffusion at matrix/oxide interface is still observable, because extrapolations do not pass trough the origin. Therefore, the matrix oxygen permeability was evaluated by using a linear fit of Equation (5.138) to experimental data and matrix oxygen permeability evaluated are reported in Table 5.22.

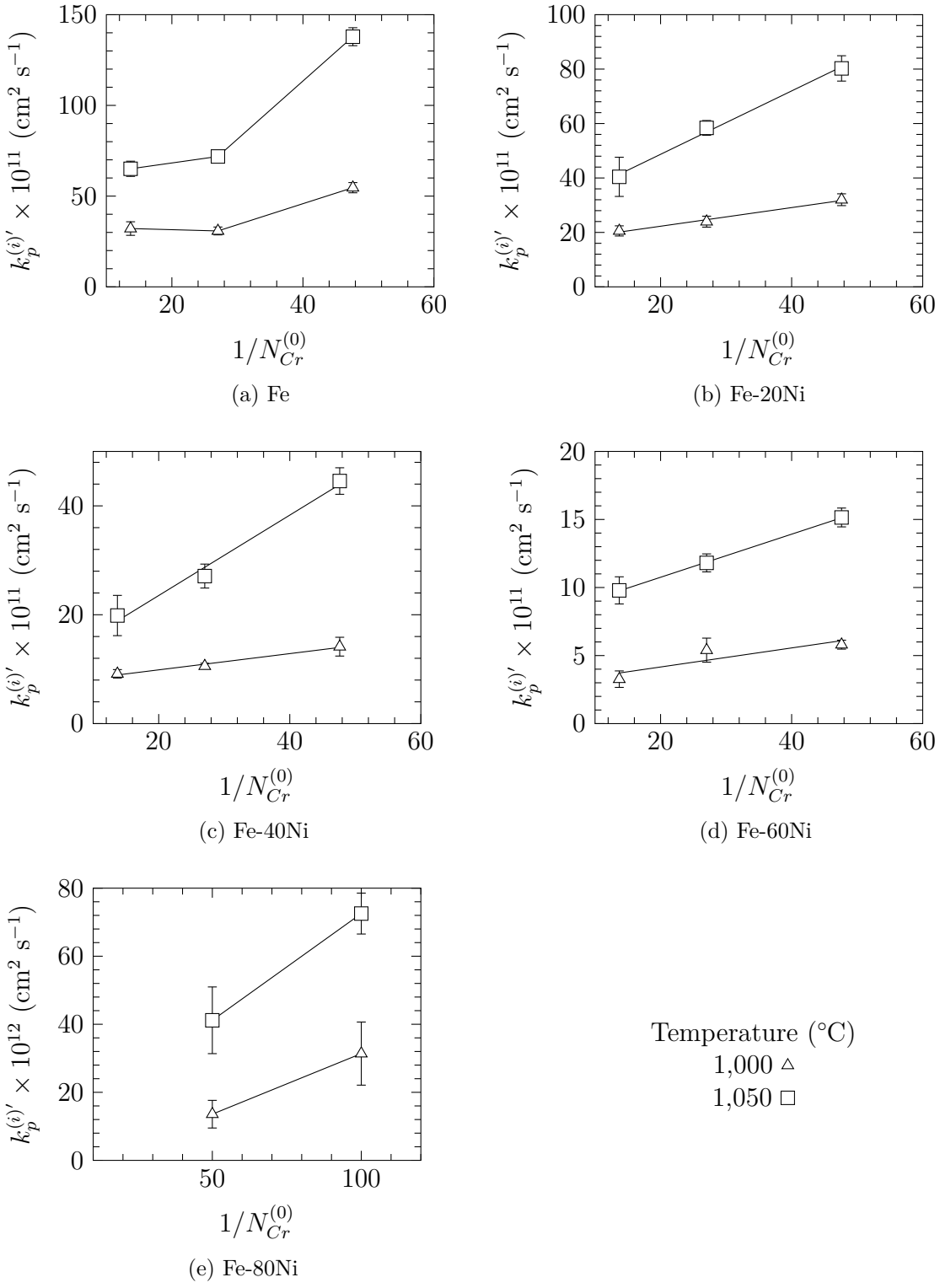

Figure 5.25: Plot of the parameter $k_p^{(i)'}$ measured at 1,000 and 1,050°C in H_2/H_2O gases containing 13% water vapour and the oxygen partial pressure set at the Fe/FeO equilibrium versus the inverse of the chromium.

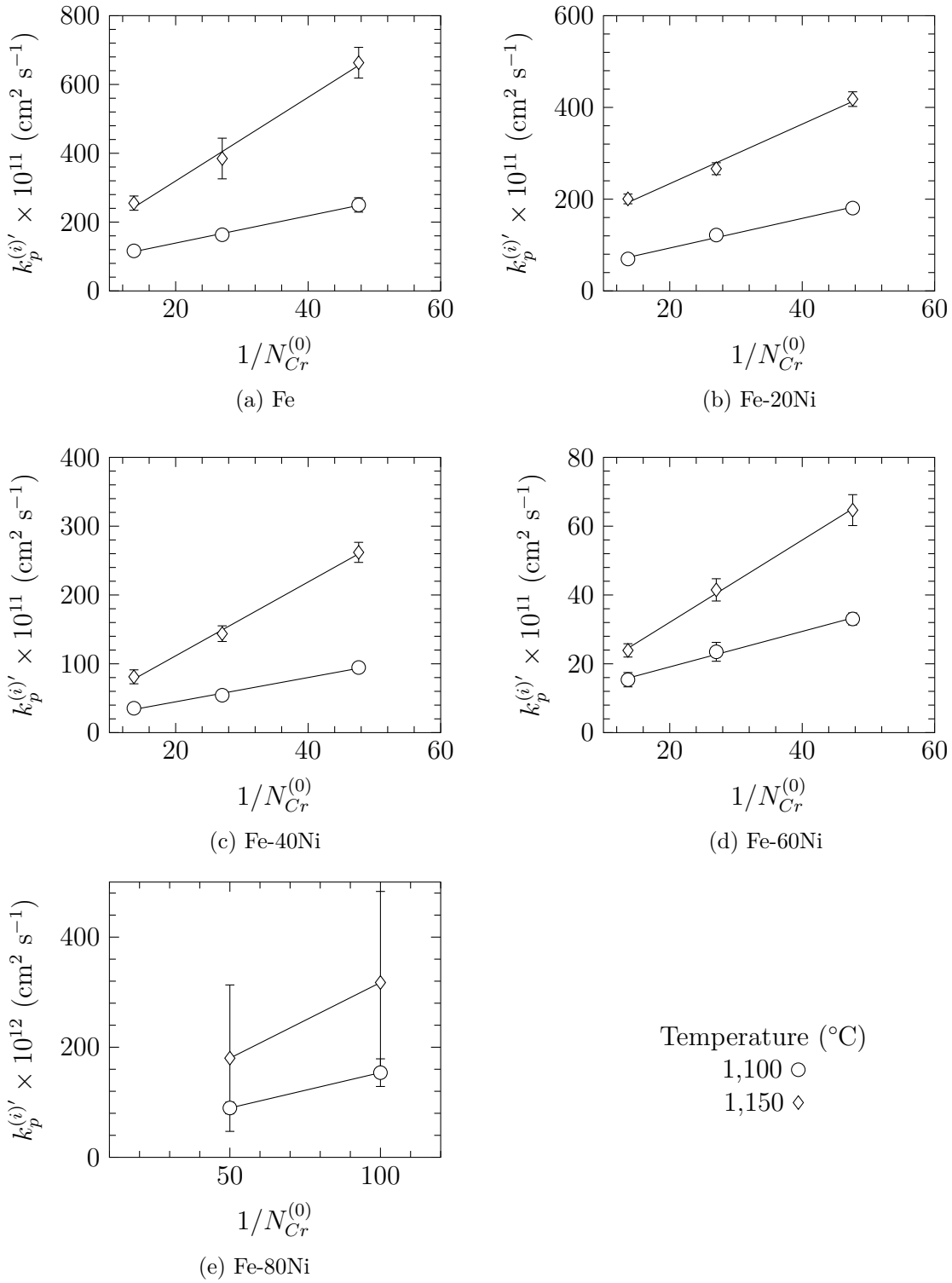

Figure 5.26: Plot of the parameter $k_p^{(i)'}$ measured at 1,100 and 1,150°C in H_2/H_2O gases containing 13% water vapour and the oxygen partial pressure set at the Fe/FeO equilibrium versus the inverse of the chromium.

Matrix oxygen permeability

In Table 5.22 matrix oxygen permeability evaluated at several temperatures for different alloys exposed in H_2/H_2O gases with 13% water vapour are presented.

Table 5.22: Matrix oxygen permeability measured in H_2/H_2O gases containing 13% of water vapour and the oxygen partial pressure set at the Fe/FeO equilibrium

$\frac{N_{Ni}}{N_{Fe}+N_{Ni}}$	$N_O^{(s)} D_O^{mat} \times 10^{13}$ (cm^2 s^{-1})			
	1,000°C	1,050°C	1,100°C	1,150°C
0	115 ± 29	224 ± 146	396 ± 38	1216 ± 206
0.2	26 ± 3	116 ± 16	323 ± 57	649 ± 131
0.4	15 ± 4	74 ± 17	176 ± 29	537 ± 56
0.6	7 ± 8	16 ± 1	52 ± 8	120 ± 11
0.8	3.6 ± 0.7	6.3 ± 1.3	13 ± 3	27 ± 5

In Figure 5.27, the variation of the oxygen permeability with alloy composition is presented. Again, a logarithmic scale is used to encompass the wide range of data. Figure 5.27 shows that matrix oxygen permeability decreases continuously from pure iron to alloy with $\frac{N_{Ni}}{N_{Fe}+N_{Ni}} = 0.8$. Oxygen permeability for pure nickel measured by

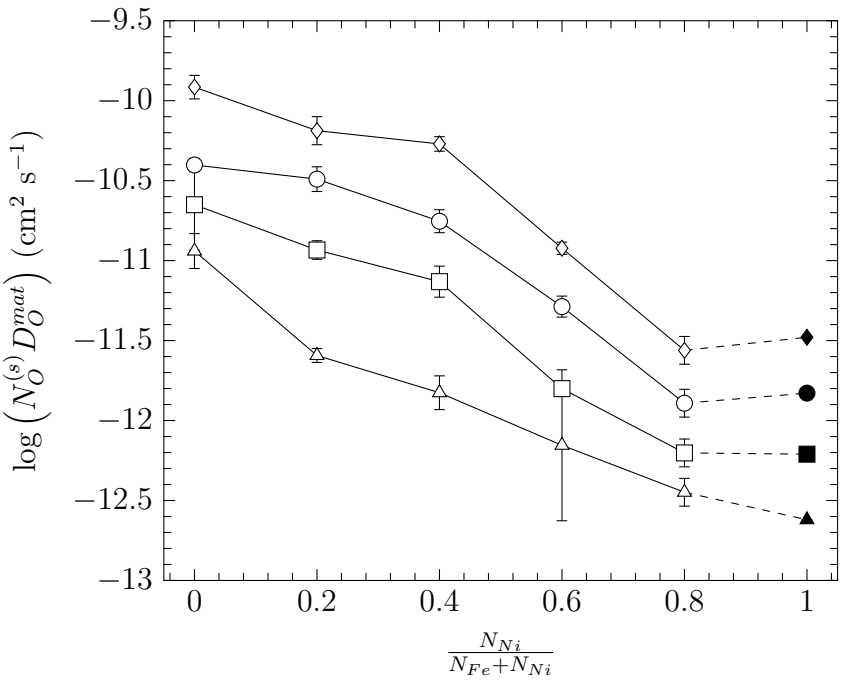

Figure 5.27: Matrix oxygen permeability measured in H_2/H_2O gases containing 13% water vapour and the oxygen partial pressure set at Fe/FeO equilibrium: 1,000°C (△), 1,050°C (□), 1,100°C (○), 1,150°C (◊). Values in pure nickel extrapolated with equation (5.143) from data published by Guo *et al.* [50] (filled symbols). Note log scale.

Guo *et al.* [50] in H_2/H_2O gas mixture with the oxygen partial pressure set at the Ni/NiO dissociation pressure and extrapolated to the Fe/FeO equilibrium pressure were added to the Figure. This permeability was extrapolated to the Fe/FeO dissociation pressure using Equation (5.143). However, as pointed out in Section 5.4.1.3, these values of oxygen permeability are extremely dependent on the oxygen solubility considered for the extrapolation. Therefore, the change in the oxygen permeability from Fe-80Ni alloys to pure nickel has to be considered with care.

The oxygen permeability temperature dependency is also shown in Figure 5.28 with an Arrhenius plot. Figure 5.28 shows that oxygen permeability measured in H_2/H_2O gases with 13% water vapour verified the Arrhenius relation. However, as with data presented for oxygen permeability measured in Fe/FeO Rhines packs, no energy or pre-exponential factor was determined from Figure 5.28. Values of Q are estimated in Chapter 6.

The value of the parameter λ was estimated from the fit of Equation (5.138) to data obtained from experiments in Fe/FeO Rhines packs. Values of λ were reported in Table 5.23. No value of λ was evaluated for Fe and Fe-20Ni alloys reacted at 1,000°C as values of $k_p^{(i)'}$ do not show a linear variation with the inverse of the alloy chromium concentration. As observed with values of λ determined from experi-

Table 5.23: Values of λ for alloys reacted in H_2/H_2O gas mixture containing 13% water vapour and oxygen partial pressure set at the Fe/FeO equilibrium.

$\frac{N_{Ni}}{N_{Fe}+N_{Ni}}$	λ			
	1,000°C	1,050°C	1,100°C	1,150°C
0	-	12 ± 14	15 ± 2	6 ± 4
0.2	-	22 ± 2	9 ± 4	16 ± 3
0.4	46 ± 3	12 ± 5	5 ± 4	1 ± 3
0.6	39 ± 7	48 ± 1	17 ± 2	7 ± 2
0.8	-12 ± 8	16 ± 5	20 ± 7	16 ± 5

ments in Fe/FeO Rhines packs, some values in Table 5.23 exhibit large uncertainty. The uncertainty in λ values was evaluated with Equation (5.145). In addition, negative values are thought to arise from experimental uncertainties and have to be considered as insignificant. No particular trend with the alloy composition is ob-

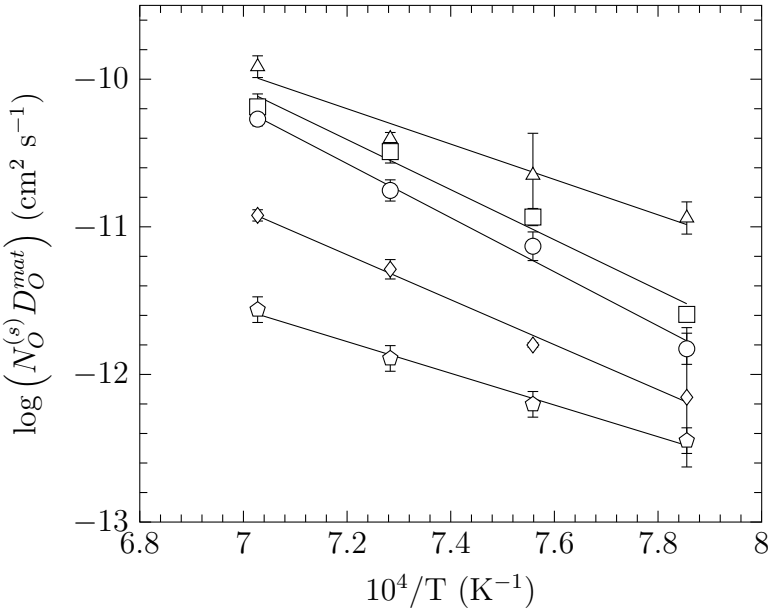

Figure 5.28: Arrhenius plots of matrix oxygen permeability measured in H_2/H_2O gases containing 13% water vapour and the oxygen partial pressure set at the Fe/FeO equilibrium.Fe (△), Fe-20Ni (□), Fe-40Ni (□), Fe-60Ni (◇), Fe-80Ni (⬠).

served from value in Table 5.23. However, for alloys with $\frac{N_{Ni}}{N_{Fe}+N_{Ni}} = 0.4$ and 0.6, it seems that λ decreases with temperature. For other alloys no firm conclusion was achieved due to large uncertainties.

5.4.2.2 Oxygen permeability measured in gases with 3% water vapour by penetration measurement

Continuous TGA was carried out with a thermobalance in which samples were exposed to H_2/H_2O gases with 3% water vapour. After exposure, samples were cross sectioned, the internal oxidation zone depth was measured, and $k_p^{(i)}$ calculated from this single measurement. In this Section, matrix oxygen permeability evaluated from these penetration measurements are presented. Only alloys with 2 and 7.5 at.% of chromium were used for these experiments, and 3 temperatures were investigated 1,000, 1,050 and 1,150°C.

In Figure 5.29, the variable $k_p^{(i)'}$ is plotted versus the alloy chromium content. The Figure shows that even at the highest temperature investigated, the effect of fast oxygen diffusion at matrix/oxide interfaces is observable, because extrapolations do not pass through the origin. Values of matrix permeability were estimated by a fit

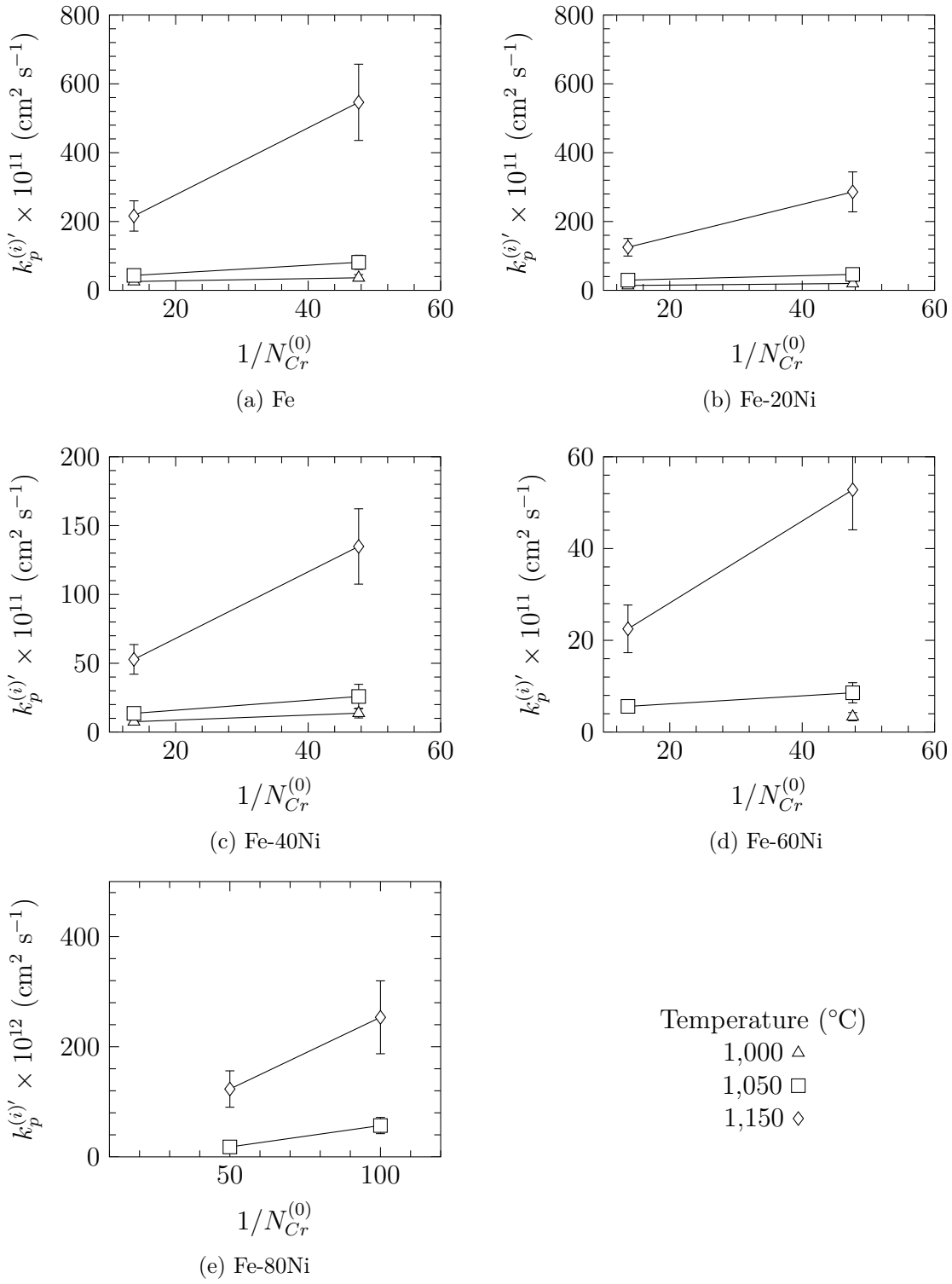

Figure 5.29: $k_p^{(i)'}$ measured at different temperatures in H_2/H_2O gases containing 3% water vapour and oxygen partial pressure set at the Fe/FeO equilibrium.

of Equation (5.138) to experimental data for different Fe-Ni alloy bases. However, the alloy Fe-60Ni-7.5Cr exposed to humid gases at 1,000°C exhibited transition between internal and external oxidation, and no internal oxidation rate constant was measured at this temperature for this alloy. Therefore, for this alloy the effective permeability was estimated from Equation (5.108) with internal oxidation kinetic rate constant measured for Fe-60Ni-2Cr. This permeability was considered to be closely similar to the matrix permeability because the oxygen diffusion is enhanced to only a small extent in low chromium alloys. In addition, for Fe-Cr alloys, it as observed that at 1,000 and 1,050°C, fast oxygen diffusion at matrix oxide interface has a strong effect on the value of $k_p^{(i)'}$ for alloys with 7.5 at.%, regardless the environment. Therefore, the iron matrix oxygen permeability at 1,000 and 1,050°C using Equation (5.108) and the internal oxidation oxidation rate measured for Fe-2Cr. Errors in the matrix permeability values presented in Table 5.24 were estimated to be 30%.

Table 5.24: Matrix oxygen permeability measured in alloys exposed to H_2/H_2O gases with 3% water vapour. Error in oxygen permeability estimated at 30%.

$\frac{N_{Ni}}{N_{Fe}+N_{Ni}}$	$N_O^{(s)} D_O^{mat} \times 10^{13}$ (cm^2 s^{-1})		
	1,000°C	1,050°C	1,150°C
0	77	171	974
0.2	17	49	474
0.4	18	36	242
0.6	7	9	89
0.8	-	8	38

From the data in Table 5.24, the matrix oxygen permeability is seen to decrease when the alloy nickel content increases. In addition, the oxygen permeability increases when temperature increases, as expected. No attempt to determine λ was carried out as only alloys with two different chromium contents were tested. In addition, $k_p^{(i)}$ was estimated from a single penetration measurement. Therefore values of $k_p^{(i)'}$ are of a limited reliability and values of λ would exhibit large uncertainties that no conclusion would be possible from those values.

5.4.3 Effect of H_2/H_2O gases on matrix oxygen permeability

To investigate the effect of water vapour and/or hydrogen on the matrix oxygen permeability, values of this property evaluated in previous sections are plotted versus the alloy composition for each temperature. Again, logarithmic scales are used to encompass the large range of values.

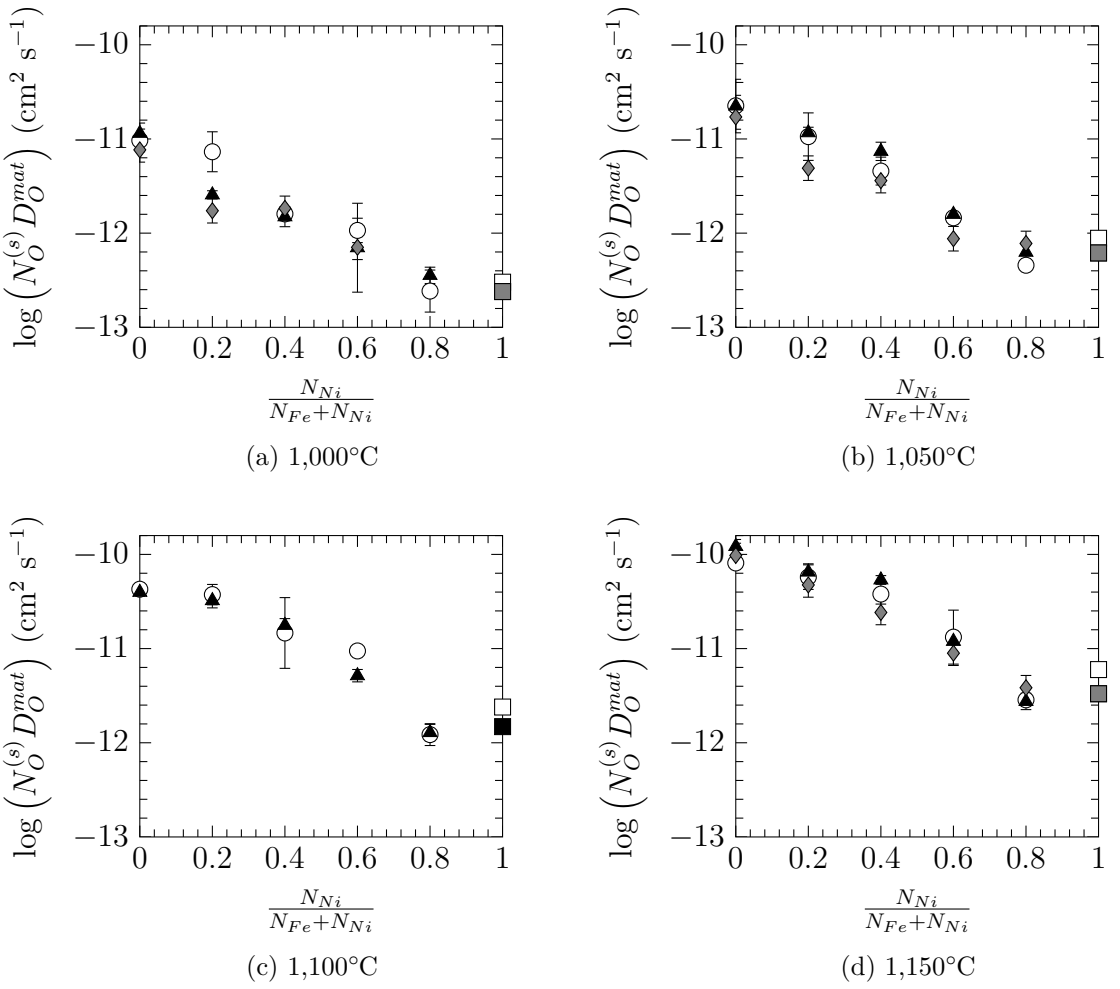

(a) 1,000°C (b) 1,050°C

(c) 1,100°C (d) 1,150°C

Figure 5.30: Comparison of matrix oxygen permeability measured in Fe/FeO Rhines packs (○), H_2/H_2O gases with 13% water vapour (▲) and H_2/H_2O gases with 3% water vapour (♦). Values in pure nickel extrapolated with Equation (5.143) from data published by Guo *et al.* [50] (□, ■, ■). Note log scale.

Figure 5.30 shows that the variation of the matrix oxygen permeability with alloy composition is similar in the different environments studied. In addition, the temperature dependency of the matrix oxygen permeability is not affected by the presence of water vapour and hydrogen in the environment. The matrix oxygen

permeability values measured after exposure in wet gases with 3% water vapour are usually slightly smaller than values measured in Fe/FeO Rhines packs or H_2/H_2O gases with 13% water vapour, for alloys with nickel content lower than 60 at.%. This results suggest that the composition of H_2/H_2O gas mixtures has an effect on the oxygen permeability for these alloys. However, experiments with 13% and 3% water vapour were carried out in very different apparatus types. Moreover, results obtained from experiments in H_2/H_2O gases with 3% water vapour are derived from a single exposure time, and are of low reliability. More experiments are required before a conclusion can be reached on this matter.

5.4.4 Effect of water vapour on the parameter λ

The parameter λ, which reflects the contribution of interfacial diffusion to the oxygen permeability, was estimated from experiments carried out in Fe/FeO Rhines packs (Table 5.21) and in H_2/H_2O gas containing 13% water vapour and the oxygen partial pressure set at the Fe/FeO equilibrium (Table 5.23). In Figure 5.31 values of λ measured in both atmospheres are compared. It should be noted that negative values of λ are not display in the figure.

Figure 5.31 shows that the effect of water vapour on λ is difficult to assess due to large uncertainty in values estimated. Differences between λ measured in the different environments are not considered as statistically significant regarding the scatter of data evaluated. It is possible that water vapour may have a small effect on λ but its evaluation would require additional work using a larger number of alloys with different chromium contents to obtain a precise evaluation of λ using Equation (5.138).

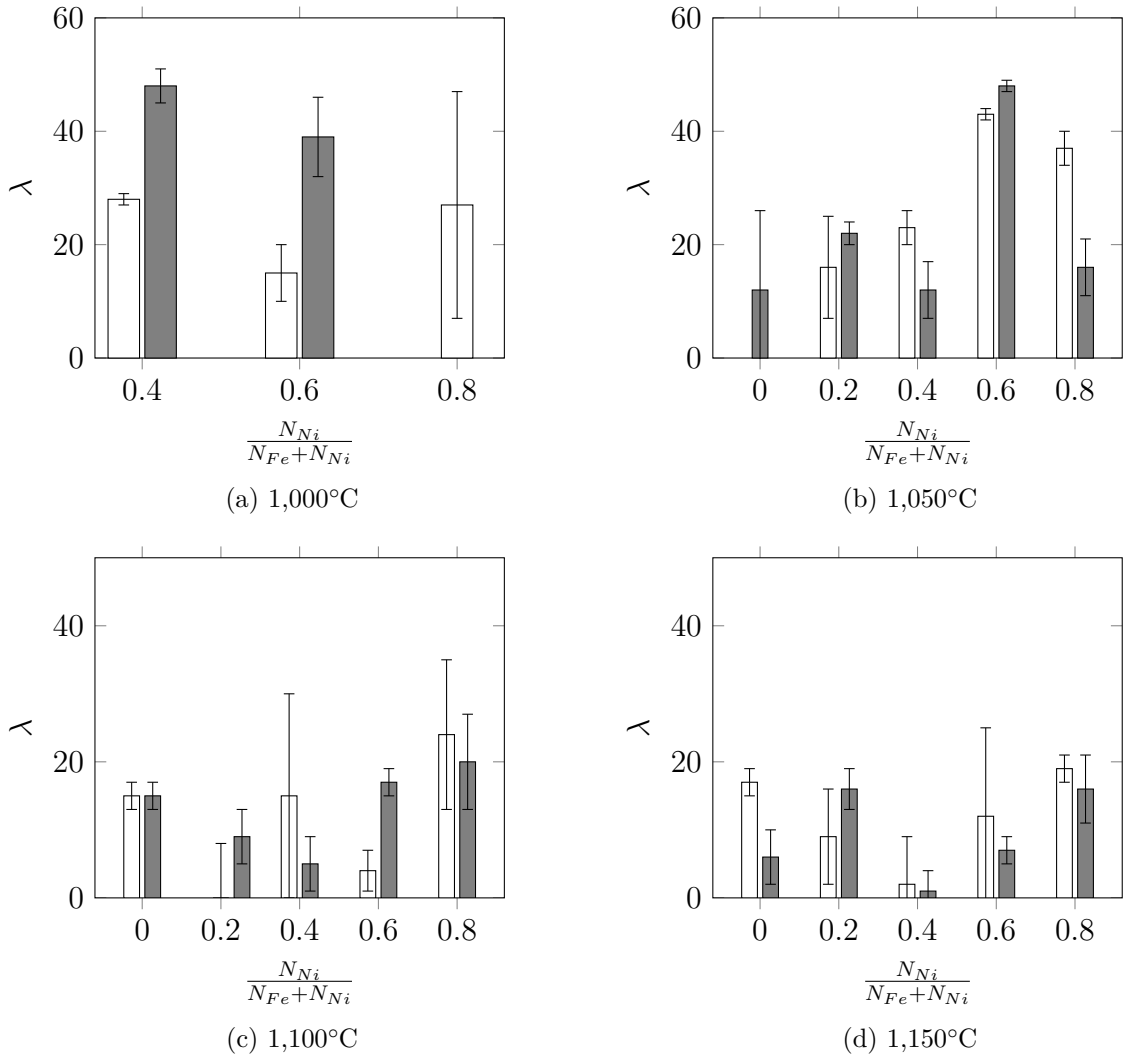

(a) 1,000°C (b) 1,050°C

(c) 1,100°C (d) 1,150°C

Figure 5.31: Comparison of λ estimated from experiments carried out in Fe/FeO Rhines packs ( ) and H_2/H_2O ( ) gas with 13% of water vapour.

5.4.5 Iron Oxygen permeability

Oxygen permeability in iron has been measured by several authors using Fe/FeO Rhines packs or H_2/H_2O gas mixtures with the oxygen partial pressure set at the Fe/FeO equilibrium. As previously demonstrated, the water vapour and/or hydrogen has a negligible effect on the matrix oxygen permeability. Therefore, data for iron obtained from measurement in the 3 environments investigated were considered as a single set of data as illustrated in Figure 5.32.

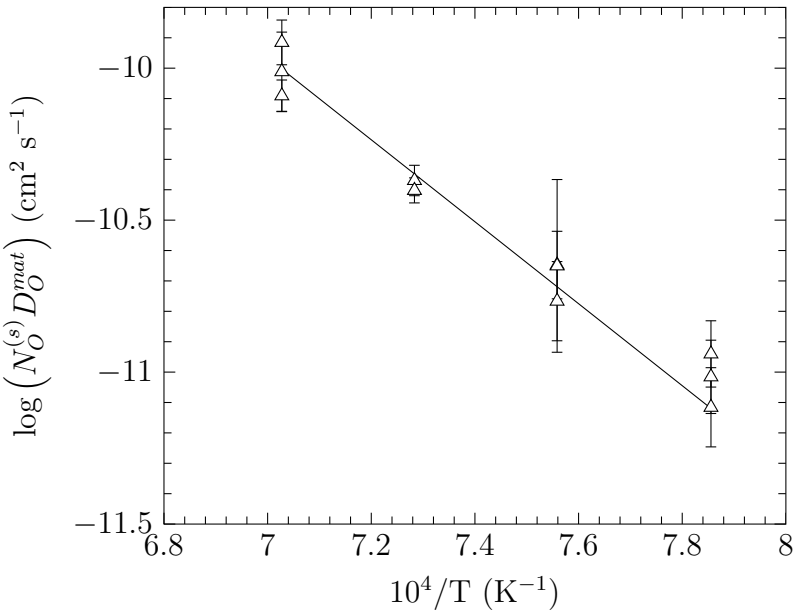

Figure 5.32: Arrhenius plots for iron matrix permeability with data from Fe/FeO Rhines pack and H_2/H_2O gas mixtures with 13 and 3% water vapour considered as a single set of data

In addition, the oxygen permeability can be expressed by

$$N_O^{(s)} D_O^{mat} = U^{(0)} \exp\left(\frac{-Q}{RT}\right) \tag{5.146}$$

where $U^{(0)}$ is a constant pre-exponential factor containing p_{O_2} and Q the activation energy for the oxygen permeability. These parameters were evaluated using a non linear fit of Equation (5.146) to experimental data presented in Figure 5.32. The activation energy found is 258 ± 34 kJ mol^{-1}. This value is in perfect agreement with the activation energy of 258 kJ mol^{-1} reported in previous work [40, 41, 45, 47]. Using the estimated parameters $U^{(0)}$ and Q, the oxygen permeability was recalculated with Equation (5.146) and plotted in Figure 5.33, along with oxygen permeability measured in previous studies. When parameters $U^{(0)}$ and Q are estimated, a correlation factor of 1 is found between these parameters. Therefore, to estimate the uncertainty in the oxygen permeability calculated with Equation (5.146), the correlation between $U^{(0)}$ and Q has to be considered. The calculation of error with consideration of correlation is given in Appendix E.

Figure 5.33 shows that values measured in this study are in good agreement

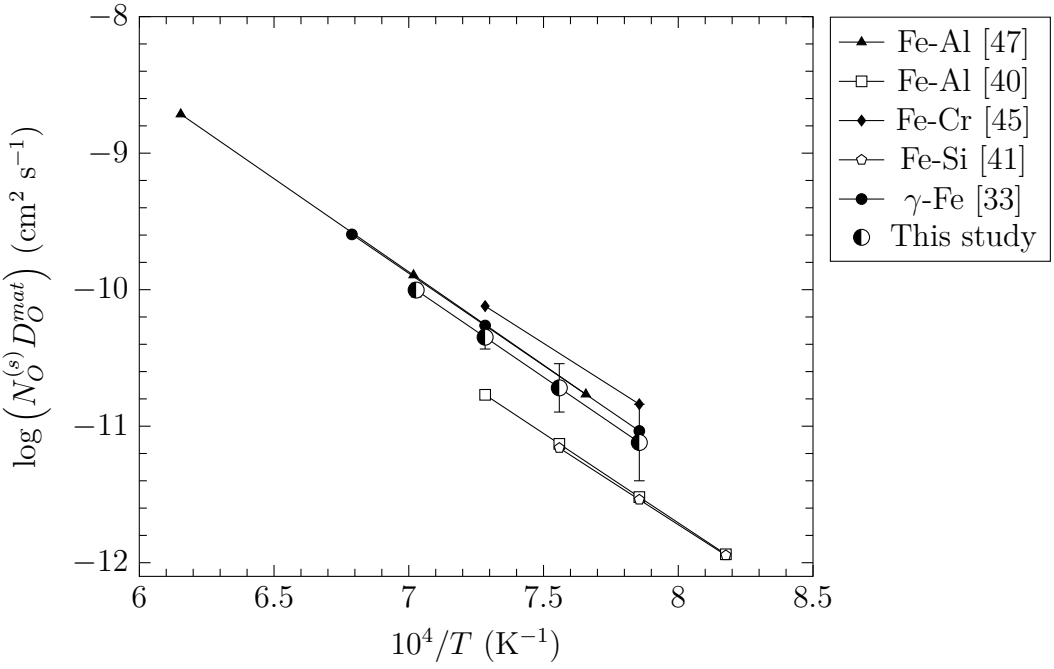

Figure 5.33: Oxygen permeability of γ-iron measured in different atmospheres, Fe/FeO Rhines pack (open symbols), H_2/H_2O gas mixtures (filled symbols), ◐ combined data RP+H_2/H_2O.

with oxygen permeability measured by Meijering [33] and Swisher and Turkdogan [47] in H_2/H_2O gas mixtures with the oxygen partial pressure set at the Fe/FeO equilibrium pressure. These authors used Fe-Al alloys to measure the oxygen permeability by internal oxidation. It is known that the specific rod-like shape of internal aluminium oxides enhances the oxygen diffusion through the IOZ, and usually leads to high values of oxygen permeability. However, the authors used extremely dilute alloys with a maximum aluminium content of 125 wt.ppm. As was shown in Section 5.4.1.1, the contribution of fast oxygen diffusion is proportional to the alloy solute content. Therefore, the contribution of fast oxygen diffusion at matrix/oxide interfaces may have been negligible in their experiments [33, 47].

The oxygen permeability was measured in Fe/FeO Rhines pack by Takada *et al.* [40, 41] These authors used dilute Fe-Al and Fe-Si alloys to measure the oxygen permeability, and took into account the fast oxygen diffusion at matrix oxide interfaces in estimating the matrix oxygen permeability. No obvious reason was found for the low oxygen permeability measured by Takada *et al.* The only apparent difference was that in their experiments, those authors used Fe/FeO/Al_2O_3

powder mixtures in their Rhines packs. In addition, the authors identified internal oxides as $FeAl_2O_4$ in the IOZ of Fe-Al alloys [40] indicating that this spinel was thermodynamically stable under conditions in the pack. Thus, it is likely that $FeAl_2O_4$ forms within the powder mixture. The formation of the iron-aluminium spinel consumes oxygen and may reduce the oxygen partial pressure in the pack. This lower oxygen partial pressure than the Fe/FeO equilibrium would explain the lower oxygen permeability found by Takada *et al.* [40, 41] compared to other authors [33, 45, 47] as shown in Figure 5.33.

5.4.6 Oxygen permeability of Fe-Ni alloys from internal/external oxidation transition

In Chapter 1 of this study, the oxygen permeability of Fe-Ni alloys at 1,000°C was estimated from the work of Croll and Wallwork [66] who investigate the transition between internal and external oxidation. The critical alloy chromium concentration for the transition between internal and external oxidation is given by Wagner

$$N_{Cr}^{(0)^*} = \left(\frac{F_v^* \pi V_{alloy} N_O^{(s)} D_O}{2\nu V_{oxide} D_{Cr}} \right)^{\frac{1}{2}} \tag{5.147}$$

where F_v^* is the critical volume fraction of oxide required to observe the transition between internal and external oxidation, V_{alloy} and V_{oxide} the molar volume of the alloy and oxide considered, respectively, ν the internal oxide stoichiometry, D_{Cr} the chromium interdiffusion coefficient and $N_O^{(s)} D_O^{mat}$ the oxygen permeability. Equation (5.147) allows the determination of oxygen permeability if the critical chromium content required to observe the transition is known (see Section 1.4.4). Oxygen permeability values estimated in this way from $N_{Cr}^{(0)^*}$ values [66] are given in Figure 5.34, along with oxygen permeability measured in the present study by internal oxidation.

Figure 5.34 shows that good agreement is found between values calculated from the transition between internal and external oxidation observed by Croll and Wallwork, and oxygen permeability measured by internal oxidation. The largest

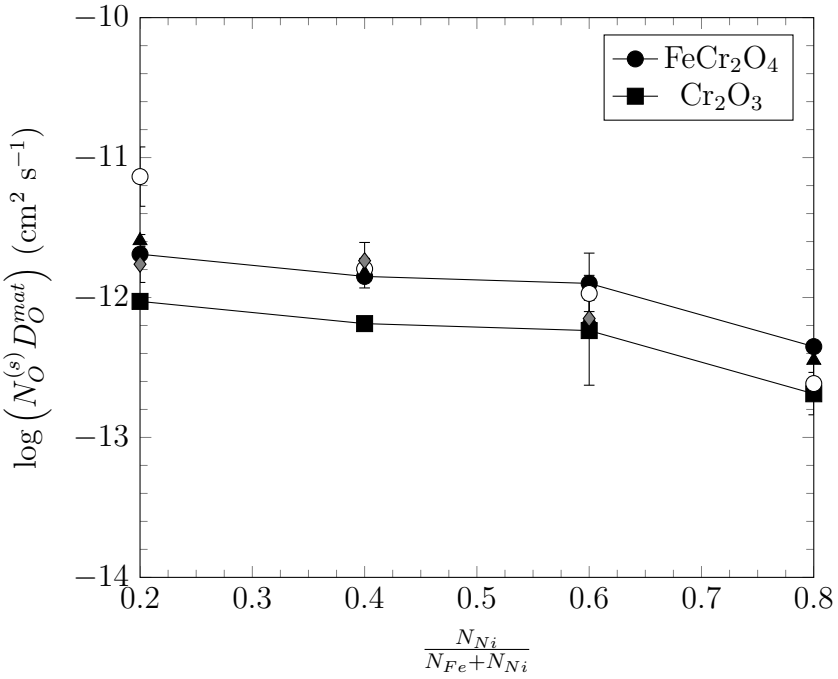

Figure 5.34: Permeability measured from the chromium critical content for transition between internal and external oxidation observed by Croll and Wallwork at 1,000°C and calculated for the Fe/FeO dissociation pressure (–●–,–■–). Oxygen permeability measured by internal oxidation in Fe/FeO Rhines pack (○), H_2/H_2O with 13% water vapour (▲), H_2/H_2O with 3% water vapour (♦).

difference is observed for alloy with $\frac{N_{Ni}}{N_{Fe}+N_{Ni}} = 0.2$ reacted in Fe/FeO Rhines pack while oxygen permeability measured in gas containing water vapour are in good agreement.

Calculation of oxygen permeability from the data of Croll and Wallwork was performed on the basis of either spinel or chromium oxide as the internal oxide. Figure 5.34 shows that in iron-rich alloys, permeability measured by internal oxidation is in agreement with permeability calculated from the transition when iron-chromium spinel is considered as the internal oxide. However, in nickel-rich alloys oxygen permeability from internal oxidation becomes closer to the permeability estimated when chromium oxide is considered as the internal oxide. This is consistent with the known destabilisation of the iron-chromium spinel nickel-rich alloys.

5.5 Summary

Oxygen permeability has been estimated from values of the internal oxidation rate constant presented in Chapter 4. However, to compute values of oxygen permeability, evaluation of the enrichment factor and stoichiometry of the internal oxide is required.

The enrichment factor was evaluated by 2 different methods: the diffusional approach developed by Wagner [1] and internal oxide volume fraction measurement. Comparison between enrichment factors values estimated by each technique showed that the volume expansion of the IOZ due to internal oxide precipitation cannot be neglected for alloys with 7.5 at.% Cr. Taking into account the volume expansion in chromium-rich alloys, good agreement is found between enrichment factor values evaluated by the diffusional approach or the internal oxide volume fraction measurement. In addition, water vapour and/or hydrogen appears to have no significant effect on IOZ enrichment. For calculation of the oxygen permeability, it was decided to use enrichment factors evaluated from Wagner's diffusional approach.

In Chapter 4, it was reported that the IOZ is composed of two subzones in which a specific oxide precipitates: $FeCr_2O_4$ spinel are found in the subzone beneath the alloy surface while Cr_2O_3 are found in the subzone adjacent to the internal oxidation front. To take into account the stoichiometry of each oxide an effective stoichiometry was defined. The effective stoichiometry was considered as the average of the spinel and chromium oxide stoichiometry but weighted by the relative size of the subzone in which each oxide precipitated. The size of each subzone was determined with SEM observations of chromium-rich alloys.

Attempt to calculate the effective stoichiometry by coupling weight gain and penetration measurements reveals that in dilute chromium alloys, chromium was not completely precipitated in the subzone where chromium oxide forms. This incomplete precipitation is due to the low stability of chromium oxide under experimental conditions used in the present study. On the other hand, for chromium-rich alloys, the assumption of a complete precipitation of chromium was acceptable. The ef-

fect of incomplete chromium precipitation on estimation of oxygen permeability was considered negligible compared to experimental uncertainties. However, additional work is required to relate penetration and weight gain measurements for internal oxidation.

For evaluation of oxygen permeability, values of ν_{eff} calculated using the weighted average were considered. However, these value were estimated from measurements of subzone size for chromium-rich alloys. Therefore it was approximated that effective stoichiometry was independent of the alloy chromium content and values estimated for chromium-rich alloys were used for dilute alloys. In addition, it should be noted that no effect of water vapour and/or hydrogen on the value of ν_{eff} was observed.

The oxygen permeability was calculated from internal oxidation rate constants estimated from penetration measurements and taking into account the IOZ expansion due to internal oxide penetration. Results showed that oxygen diffusion at matrix/oxide interfaces cannot be neglected to estimate the matrix oxygen permeability even at the highest temperature studied. Variation of the matrix oxygen permeability with the alloy composition is found to not be affected by the presence of water vapour in the atmosphere. In addition, values of matrix oxygen permeability estimated from experiments in Fe/FeO Rhines packs and H_2/H_2O gas are similar indicating no significant effect of water vapour and/or hydrogen on $N_O^{(0)} D_O^{mat}$. The highest matrix oxygen permeability is measured in pure iron and then decreases in a non-ideal manner with the alloy nickel content to reach its minimum value in pure nickel. The difference between the maximum and minimum value is approximately 2 orders of magnitude.

The oxygen permeability for iron measured in the present study was compared to values present in the literature. Good agreement is found with values reported in previous studies [33, 45, 47], only oxygen permeability measured by Takada *et al.* [40, 41] are significantly different. However, it is thought that their experiments were carried out at an oxygen partial pressure lower than the Fe/FeO equilibrium

due to the use of Al_2O_3 in their powder mixtures. Indeed, alumina and iron may form $FeAl_2O_4$ which consumes oxygen, and therefore reduces the oxygen partial pressure inside the pack.

Matrix oxygen permeabilities measured for Fe-Ni alloys were compared to values estimated from Croll and Wallwork's work [66] who evaluated the critical alloy chromium content to observe the transition between internal and external oxidation. These critical chromium contents estimated in various Fe-Ni-Cr alloys yield values of oxygen permeability which are in agreement with values of $N_O^{(s)} D_O^{mat}$ found in the present study.

The parameter λ reflecting fast oxygen diffusion at matrix/oxide interfaces was also evaluated from experiments in dry and humid environments. However, the uncertainty in λ value is large and it is difficult to achieve a conclusion on a possible effect of the water vapour and/or hydrogen on this parameter. Overall, values measured in dry and humid environments are not extremely different which suggest that water vapour and/or hydrogen has no significant effect on λ. However, further investigation is required to confirm this conclusion.

Chapter 6

Oxygen Diffusion

Estimation of the oxygen diffusion coefficient from oxygen permeability is possible once an independent evaluation of oxygen solubility is available. This is concerned with the calculation of oxygen diffusion coefficient from oxygen solubility and oxygen permeability values, presented in Chapters 3 and 5, respectively. In the first section, oxygen diffusion coefficient values was estimated from Fe/FeO Rhines packs experiments. Then, the oxygen diffusion coefficient is calculated with data obtained from experiments in H_2/H_2O gas mixtures. In the last section of this chapter, the effect of water vapour and/or hydrogen on the oxygen diffusion is investigated by comparing values measured in dry and wet conditions.

6.1 Oxygen diffusion coefficient measured in Rhines pack

This section is devoted to the evaluation of oxygen diffusion coefficients from oxygen solubility and permeability values measured in Fe/FeO Rhines packs. The value of the matrix oxygen diffusion coefficient is easily calculable as it only requires division of matrix oxygen permeability by oxygen solubility. To carry out this calculation, values of oxygen solubility presented in Table 3.2 and oxygen permeability from Table 5.20 were used. Results of the calculation are given in Table 6.1.

Table 6.1: Matrix oxygen diffusion coefficient measured in Fe/FeO Rhines packs.

$\frac{N_{Ni}}{N_{Fe}+N_{Ni}}$	$D_O^{mat} \times 10^9$ (cm^2 s^{-1})			
	1,000°C	1,050°C	1,100°C	1,150°C
0	52 ± 20	110 ± 35	191 ± 42	338 ± 92
0.2	91 ± 67	130 ± 89	453 ± 209	693 ± 435
0.4	44 ± 9	132 ± 48	447 ± 390	1226 ± 350
0.6	50 ± 19	66 ± 14	415 ± 93	573 ± 410
0.8	9.0 ± 6.0	17 ± 6	47 ± 20	115 ± 56

Before going any further in the development, it has to be verified that D_O^{mat} evaluated with oxygen solubility measured in Chapter 3 agrees with the assumption that when oxygen analysis were carried out, samples were in equilibrium with

Fe/FeO. To estimate if the equilibrium was reached in the sample, Equation (6.1) was used

$$\frac{M_t}{M_\infty} = 1 - \sum_{n=0}^{\infty} \frac{8}{(2n+1)^2\pi^2} \exp\left(\frac{-D_O^{mat}(2n+1)^2\pi^2 t}{4l^2}\right) \tag{6.1}$$

where M_t and M_∞ is the amount of solute in the material after a time t and after an infinite time, respectively. In addition, l is the half sheet thickness, equal to 0.07 cm in the present study. From Table 6.1, the lowest alloy oxygen diffusion coefficient was found for Fe-80Ni alloys at all temperatures. Therefore, values of D_O^{mat} measured at this composition were used in Equation (6.1). Results of this calculation are presented in Table 6.2.

Table 6.2: Determination of $\frac{M_t}{M_\infty}$ to verify saturation of samples used for solubility experiment in Fe/FeO Rhines packs.

Temperature °C	Experimental duration hours	$\frac{M_t}{M_\infty}$
1,000	480	0.9997
1,050	240	0.9997
1,100	120	1.0000
1,150	72	1.0000

Values of $\frac{M_t}{M_\infty}$ in Table 6.2 show that samples used for oxygen solubility measurement were saturated when they were analysed, and confirm the validity of the oxygen solubility measurement. In Figure 6.1, values of oxygen diffusion coefficient presented in Table 6.1 are plotted as a function of alloy composition. The oxygen diffusion coefficient for nickel was calculated from oxygen permeability measured by Guo *et al.* [50] and the oxygen solubility reported by Alcock and Brown [79] both measured at the Ni/NiO dissociation pressure. However, recent calculations [93] have shown that the oxygen concentration in nickel may change the type of defect present in this material. Thus, for an oxygen concentration corresponding to the oxygen partial pressure for Fe/FeO equilibrium and a temperature of 1200°C, Connetable *et al.* [93] showed that approximately 70% of oxygen atoms are located in interstitial sites and 30% form clusters composed of 1 oxygen atom and 1 vacancy. However, if the oxygen concentrations in nickel increases to reach values

measured under the Ni/NiO equilibrium pressure, calculations showed that approximately 80% of oxygen atoms are located in clusters and only 20% are in interstitial position. Therefore, the determination of oxygen diffusion coefficient may be dependent on the oxygen partial pressure at which it is measured due to the change of defect present in nickel. For this reason, values presented in Figure 6.1 for nickel have to be considered with care because experiments were carried out at the Fe/FeO equilibrium pressure in the present study.

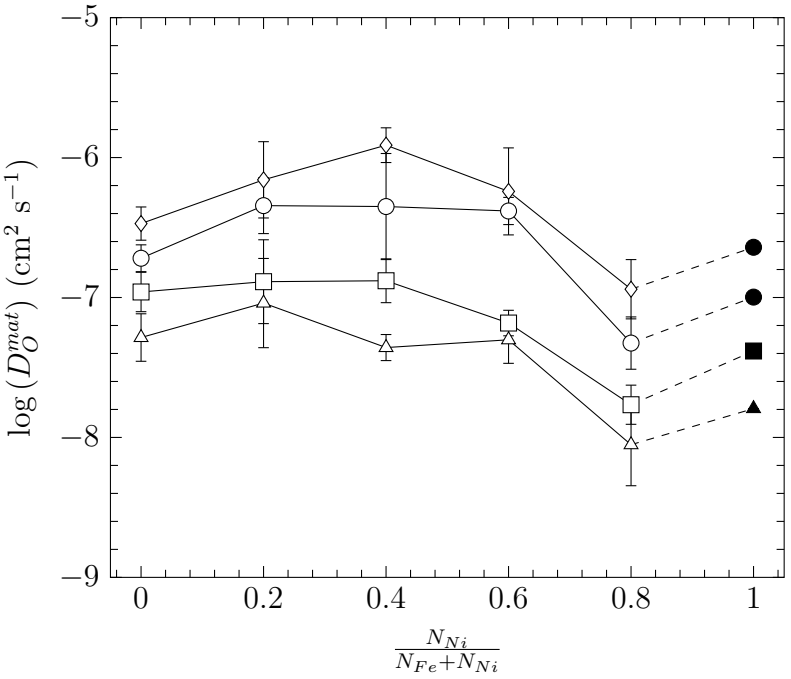

Figure 6.1: Matrix oxygen diffusion coefficient measured in Fe/FeO Rhines packs at different temperature:
1,000°C (–△–), 1,050°C (–□–), 1,100°C (–○–), 1,150°C (–◇–).
Values for pure nickel extrapolated with Equation (5.143) from data published by Guo *et al.* [50] (filled symbols).

In addition, it should be noted that large uncertainty in the oxygen diffusion coefficient arises from the calculation of D_O^{mat} from oxygen permeability and solubility. If the oxygen permeability is noted P for the following calculation, the oxygen diffusion coefficient is given by

$$D_O^{mat} = \frac{P}{N_O^{(s)}} \tag{6.2}$$

Therefore, under the assumption that P and $N_O^{(s)}$ are not correlated, the fractional uncertainty in the oxygen diffusion coefficient is

$$\left(\frac{(\delta D_O^{mat})}{D_O^{mat}}\right)^2 = \left(\frac{(\delta P)}{P}\right)^2 + \left(\frac{\delta N_O^{(s)}}{N_O^{(s)}}\right)^2 \tag{6.3}$$

where (δD_O^{mat}), (δP) and $\left(\delta N_O^{(s)}\right)$ are uncertainties of oxygen diffusion coefficient, oxygen permeability and oxygen solubility, respectively. Equation (6.3) shows that the uncertainty in oxygen diffusion coefficient is the addition of uncertainty in P and $N_O^{(s)}$ which are large. Thus, uncertainty in the calculated value of D_O^{mat} from oxygen permeability and solubility is significant.

Figure 6.1 shows that at 1,000 and 1,050°C, the matrix oxygen diffusion coefficient is approximately constant for alloys with nickel content up to 60 at.%, and then decreases to reach its minimum value for alloys with 80 at.% of nickel. At higher temperatures, changes in the variation of the oxygen diffusion coefficient with the alloy composition are observed. At 1,100°C, from pure iron, the oxygen diffusion coefficient increases with nickel additions to reach a plateau for the composition Fe-20Ni. Oxygen diffusion coefficient is found to be similar in alloys with 20, 40 and 60 at.% of nickel before decreasing to reach a minimum value in alloys with a nickel content of 80 at.%. At 1,150°C oxygen diffusion coefficient variations with the alloy composition are similar to those observed at 1,100°C, excepted that a maximum is observed for alloys with 40 at.% of nickel. Similar variations for the diffusion coefficient of carbon in Fe-Ni alloys were reported by Bose and Grabke [134].

Those authors measured carbon diffusion coefficients for Fe-Ni alloys with a fixed carbon concentration of 1×10^3 at.ppm. Results of their measurements are presented in Figure 6.2. It is seen that the carbon diffusion coefficient exhibits a maximum for alloys with a nickel content between 40 and 60 at.%, and this maximum increases when the temperature increases, just as observed for oxygen in Figure 6.1.

According to Wert and Zener [135], who theorised on the basis of interstitial diffusion, the pre-exponential factor, $D^{(0)}$, is proportional to the lattice parameter, a.

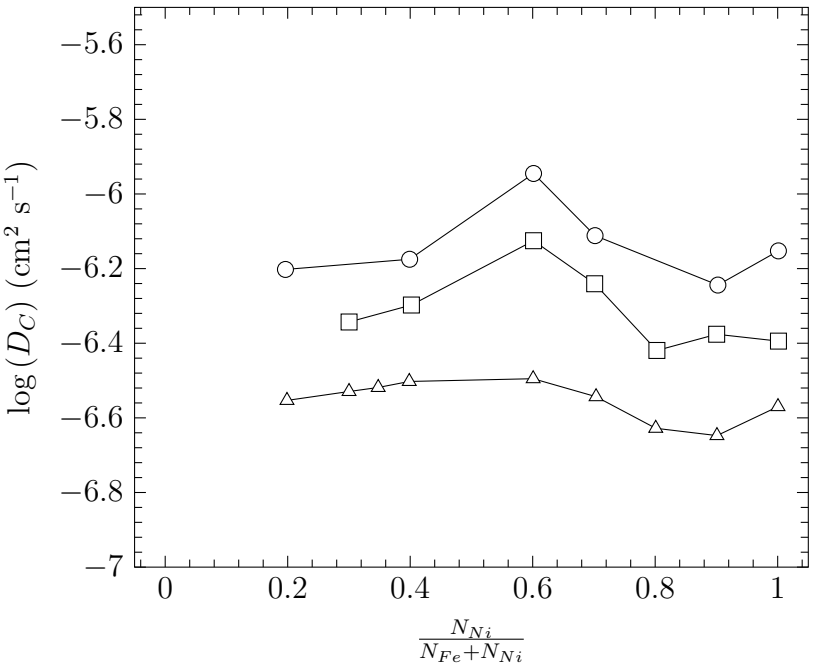

Figure 6.2: Carbon diffusion coefficient in Fe-Ni alloys with a fix concentration $N_C^{(0)} = 1 \times 10^3$ at.ppm [134]: 1,000°C (–△–), 1,050°C (–□–), 1,100°C (–○–).

Therefore, Bose and Grabke [134] measured the lattice parameter of various Fe-Ni alloys at high temperature, and their results are presented in Figure 6.3.

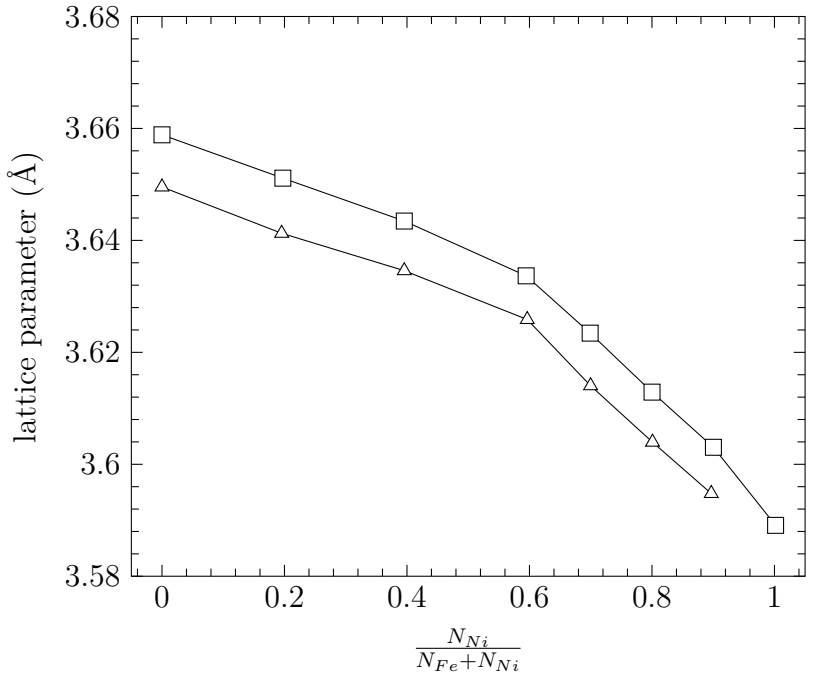

Figure 6.3: Lattice parameter at high temperature for Fe-Ni alloys [134] : 950°C (–△–); 1,050°C (–□–).

It shows that the lattice parameter for Fe-Ni alloys is continuously decreasing

as the alloy nickel content rises. This is similar to the continuous decrease in the oxygen diffusion coefficient observed at 1,000 and 1,050°C in Figure 6.1 for alloys with nickel content larger than 40 at.%. However, the reason for the maximum observed at temperatures above 1,000°C for alloys with 40 at.% of nickel remains unexplained.

Bose and Grabke [134] proposed to use Wagner's model, presented in Chapter 3 to predict the oxygen solubility in binary Fe-Ni alloys, to investigate the presence of the maximum. In this model, under the assumption of no entropic contribution, Wagner expressed the partial molar enthalpy of dissolution for one atom of solute in an interstitial site surrounded by (Z-i) atoms of nickel and i atoms of irons by

$$\Delta\overline{H}_i^{xs} = \frac{Z-i}{Z}\Delta\overline{H}_{Ni}^{xs} + \frac{i}{Z}\Delta\overline{H}_{Fe}^{xs} - \frac{1}{2}(Z-i)\,ih \tag{6.4}$$

where, $Z = 6$ is the coordination number of a solute atom in an octahedral site, $\Delta\overline{H}_{Ni}^{xs}$ and $\Delta\overline{H}_{Fe}^{xs}$ are the partial excess enthalpy for oxygen dissolution in pure nickel and iron given in Table 3.1 for experiment in Fe/FeO Rhines packs and h the energetic parameter presented in Table 3.10. It should be noted that Equation (6.4) is sightly different from the equation used by Bose and Grabke, probably due to a mistake of the authors. Indeed, Wagner in his model specified that the excess enthalpy multiplied by the term $\frac{Z-i}{i}$ in Equation (6.4) should correspond to the metal with the smallest solute solubility and the excess enthalpy of the other pure metal should be multiplied by $\frac{i}{Z}$. In the present study, the oxygen solubility is lower in nickel than in iron, but this is also observed for carbon. However, Bose and Grabke [134] multiplied $\frac{Z-i}{i}$ by the excess enthalpy of iron and $\frac{i}{Z}$ by the excess enthalpy of nickel, the opposite of Wagner's description.

The excess enthalpy $\Delta\overline{H}_i^{xs}$ was calculated at a temperature of 1,150°C using h values presented in Table 3.10 for the different configurations (Z varying from 0 to 6), and results are presented in Figure 6.4.

From Figure 6.4, the maximum of $\Delta\overline{H}_i^{xs}$ appears to be for an interstitial site surrounded by 3 iron atoms and 3 atoms of nickel, suggesting that for this config-

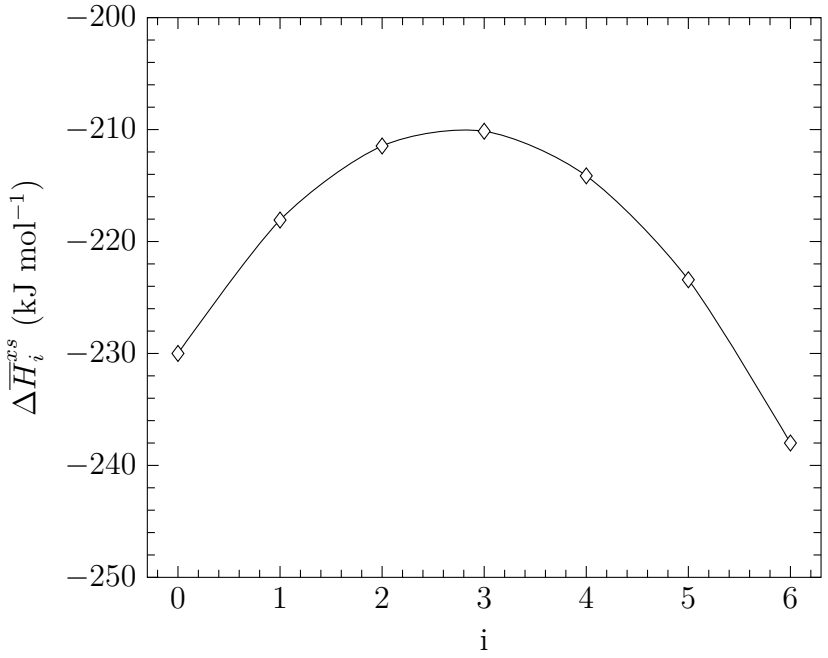

Figure 6.4: Excess enthalpy as a function of the number of iron atoms surrounding an octahedral site.

uration, interactions between iron, nickel and oxygen atoms are at the minimum. Thus, the movement of oxygen atoms between interstitial sites is easier and should result in a low activation energy for oxygen diffusion and high oxygen diffusion coefficient. Wagner provided Equation (6.5) to estimate the probability to find one specific configuration as a function of the alloy composition

$$P(i) = \binom{Z}{i} N_{Fe}^{i} N_{Ni}^{Z-i} \tag{6.5}$$

where $\binom{Z}{i}$ is the binomial factor. It is straightforward that the highest probability to observe site surrounded by 3 atoms of each metallic species is achieved for the composition Fe-50Ni. This composition is slightly higher than the composition for which the maximum of the oxygen diffusion coefficient is observed. However, the combined effect of the lattice parameter decreasing with the alloy nickel content and small interactions between atoms for a composition Fe-50Ni may result in a shift in the maximum of the oxygen diffusion coefficient toward the iron-rich alloy side. Study of the lattice parameter variations and energetic considerations seem to reasonably describe the variation of the oxygen diffusion coefficient with the alloy

composition for Fe-Ni alloys.

The diffusion coefficient is related to the temperature via an Arrhenius relationship

$$D_O^{mat} = D_O^{(0)} \exp\left(\frac{-Q}{RT}\right) \tag{6.6}$$

where $D_O^{(0)}$ is a constant pre-exponential factor and Q the oxygen diffusion activation energy. In Figure 6.5, oxygen diffusion coefficients presented in Table 6.1 are plotted as a function of the inverse temperature.

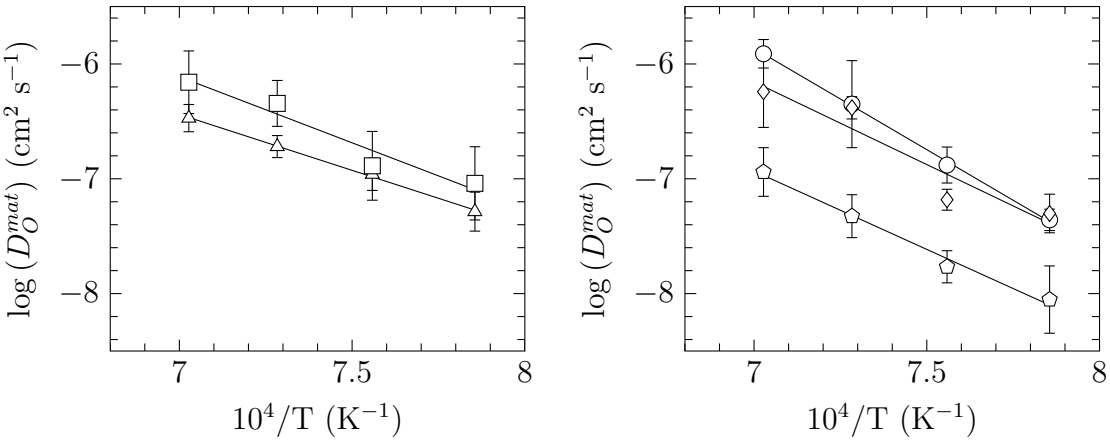

(a) Fe (△), Fe-20Ni (□)

(b) Fe-40Ni (○), Fe-60Ni (◇), Fe-80Ni (⬠)

Figure 6.5: Arrhenius plots of internal oxidation rate constant measured in Fe/FeO Rhines pack.

Figure 6.5 shows that the oxygen diffusion coefficient conforms with the Arrhenius relationship for all alloy compositions. In addition, the pre-exponential factor $D_O^{(0)}$ and the activation energy Q were determined. A non-linear fit of Equation (6.6) was used as this technique yields a distribution of error for $D_O^{(0)}$ and Q close to the normal distribution. To estimate the uncertainty of the two latter parameters, the module SolverAid of Excel software [110] was used.

When $D_O^{(0)}$ and Q were estimated, it appears that these values were strongly correlated as shown by values of correlation factors, r, close to 1 reported in Table 6.3. In addition, the uncertainty estimated for the pre-exponential factor was extremely large, due to the small temperature interval used in the present study and the limited number of experimental points available for the fit of Equation (6.6).

Therefore, no uncertainty is reported for the pre-exponential factor in Table 6.3. Instead, the average uncertainty expected if D_O^{mat} is calculated from $D_O^{(0)}$ and Q in the temperature range 1,000 to 1,150°C is reported in Table 6.3. This uncertainty was calculated with Equation (6.7) .

$$\left(\delta D_O^{mat}\right)^2 = \exp\left(\frac{-2Q}{RT}\right)\left[\left(\delta D_O^{(0)}\right)^2 + \left(D_O^{(0)}\left(\frac{-\delta Q}{RT}\right)\right)^2 + 2rD_O^{(0)}\left(\frac{-\delta Q}{RT}\right)\left(\delta D_O^{(0)}\right)(\delta Q)\right] \tag{6.7}$$

where (δD_O^{mat}), $\left(\delta D_O^{(0)}\right)$ and (δQ) are uncertainties in the corresponding parameter. However, Equation (6.7) shows that the uncertainty depends of the temperature. Therefore, the uncertainty calculated is the average between uncertainties estimated at each temperature.

Table 6.3: Pre-exponential factor and activation energy for oxygen diffusion measured in Fe/FeO Rhines pack.

$\frac{N_{Ni}}{N_{Fe}+N_{Ni}}$	$D_O^{(0)}$ cm^2 s^{-1}	Q kJ mol^{-1}	r	$\delta(D_O^{mat})/D_O^{mat}$ %
0	1.0	178 ± 3	0.7865	11
0.2	2.0×10^1	203 ± 81	0.9997	40
0.4	2.1×10^6	333 ± 12	0.9999	7
0.6	4.5×10^1	214 ± 145	0.9997	72
0.8	3.6×10^3	286 ± 20	0.9999	10

The activation energy reported for oxygen diffusion in iron in Table 6.3 is in good agreement with the activation energy expected [33, 40, 41, 44, 47] for interstitial diffusion in austenitic iron, approximately 160 kJ mol^{-1}. For other alloys, the activation energy for oxygen diffusion is always higher than 200 kJ mol^{-1}. However for Fe-20Ni and Fe-60Ni alloys, the uncertainty in the activation energy is large, and no clear conclusion can be made. On the other hand, for Fe-40Ni and Fe-80Ni alloys, the estimated activation energies are subject to small uncertainties, but values estimated are high compared to Q for interstitial diffusion. The question of the high activation energy measured in nickel-rich alloys is addressed later in this chapter, in Section 6.3.

6.2 Oxygen diffusion coefficient measured in H_2/H_2O

The oxygen permeability was measured in H_2/H_2O gases containing 3 and 13% water vapour. In the first part of this section oxygen diffusion coefficient values estimated from permeability and solubility measured in gases containing 13% water vapour are presented. Then, oxygen diffusion coefficients estimated from permeability measured in humid gases with 3% water vapour are presented. However, in Chapter 3, it was observed that water vapour has an effect on the oxygen solubility for temperatures around 1,000°C but not at 1,150°C. Therefore the calculation of oxygen diffusion coefficient from permeability measured in gases with 3% water vapour was only carried out for a temperature of 1,150°C, using the oxygen solubility measured in H_2/H_2O gases containing 13% water vapour.

6.2.1 Gases with 13% of water vapour

In Figure 6.6, values of the oxygen diffusion coefficient estimated for alloys exposed to H_2/H_2O gases with 13% water vapour and presented in Table 6.4 are plotted as a function of the alloy base composition.

Table 6.4: Matrix oxygen diffusion coefficient measured in H_2/H_2O gases with 13% of water vapour and oxygen partial pressure set at the Fe/FeO equilibrium.

$\frac{N_{Ni}}{N_{Fe}+N_{Ni}}$	$D_O^{mat} \times 10^9$ (cm^2 s^{-1})			
	1,000°C	1,050°C	1,100°C	1,150°C
0	28 ± 10	56 ± 38	104 ± 14	333 ± 76
0.2	16 ± 7	92 ± 23	316 ± 77	783 ± 279
0.4	19 ± 8	122 ± 34	362 ± 78	1366 ± 358
0.6	11 ± 13	37 ± 8	174 ± 42	570 ± 204
0.8	23 ± 17	40 ± 18	81 ± 27	174 ± 78

As with oxygen diffusion coefficient estimated from Fe/FeO Rhines packs in Section 6.1, it was verified that samples used to measured oxygen solubility in H_2/H_2O gases were at equilibrium for oxygen analysis. To do so Equation (6.1) was

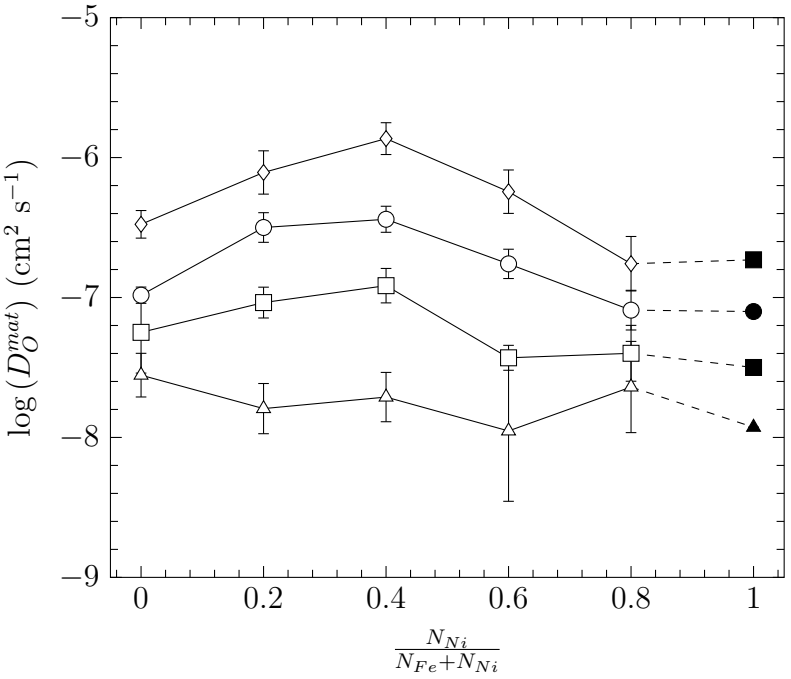

Figure 6.6: Matrix oxygen diffusion coefficient measured in H_2/H_2O gases containing 13% water vapour and oxygen partial pressure set at the Fe/FeO equilibrium pressure at different temperature:
1,000°C (–△–), 1,050°C (–□–), 1,100°C (–○–), 1,150°C (–◇–).
Values in pure nickel extrapolated with Equation (5.143) from data published by Guo *et al.* [50] (filled symbols).

used, with $l = 0.07$ cm. In addition, from values in Table 6.4, the minimum oxygen diffusion coefficient measured at 1,000°C is equal to 11×10^{-9} cm^2 s^{-1}, while at higher temperature oxygen diffusion coefficients measured for Fe-80Ni were considered. Results of calculation are presented in Table 6.5.

Table 6.5: Determination of $\frac{M_t}{M_\infty}$ to verify saturation of samples used for solubility experiment in H_2/H_2O gases.

Temperature °C	Experimental duration hours	$\frac{M_t}{M_\infty}$
1,000	480	0.9999
1,050	240	1.0000
1,100	120	1.0000
1,150	72	1.0000

Results of calculation in Table 6.5 show that samples were saturated when oxygen analysis was carried out, and confirm the validity of the oxygen solubility measurement.

Figure 6.6 shows that variations of D_O^{mat} with the alloy composition are similar after exposure in Fe/FeO Rhines packs and H_2/H_2O gas with 13% water vapour with oxygen partial pressure set at the Fe/FeO equilibrium pressure. At 1,000°C, the oxygen diffusion coefficient seems to be approximately independent of the alloy nickel content. However, when the temperature increases, the oxygen diffusion coefficient is found to increase from its value in pure iron, and exhibits a maximum for alloys with about 40 at.% of nickel. Then, for alloys with nickel content larger than 40 at.%, the oxygen diffusion coefficient decreases. This variation of the diffusion coefficient with the alloy composition is thought to be due to smaller interactions between oxygen and iron and nickel atoms in alloys with 40 at.% Ni, and also to the continuous decrease of the lattice parameter with the alloy nickel content, as described in Section 6.1.

In Figure 6.7 the oxygen diffusion coefficients presented in Table 6.4 are plotted according to the Arrhenius equation. As is seen, for all compositions the oxygen

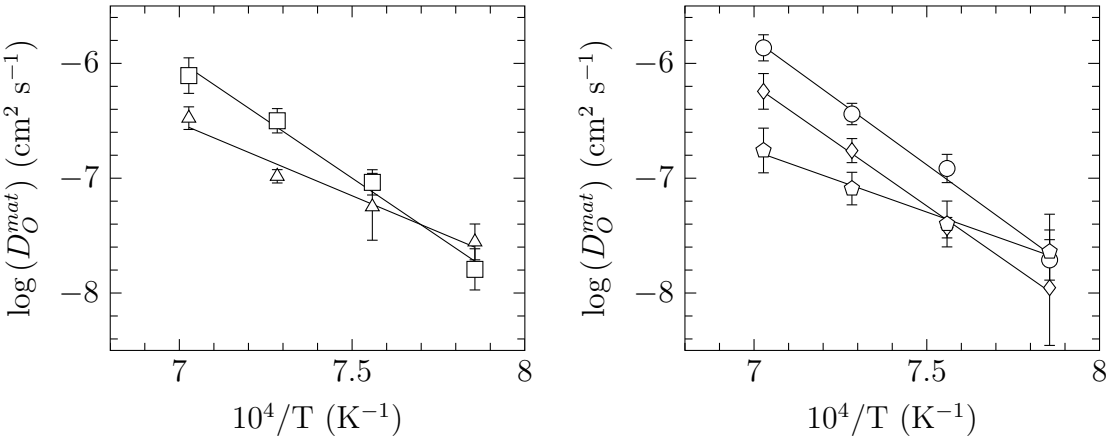

(a) Fe (△), Fe-20Ni (□)

(b) Fe-40Ni (○), Fe-60Ni (◇), Fe-80Ni (⬠)

Figure 6.7: Arrhenius plots of internal oxidation rate constant measured in H_2/H_2O gases containing 13% water vapour and oxygen partial pressure set at the Fe/FeO equilibrium pressure.

diffusion coefficient follows an Arrhenius law. The pre-exponential factor and activation energy for oxygen diffusion were estimated, and are presented in Table 6.6. To determine those parameters, a non-linear fit to Equation (6.6) was carried out. The correlation factor between $D_O^{(0)}$ and Q, estimated during the fitting procedure

is also given in Table 6.6. Just, as with $D_O^{(0)}$ and Q estimated from experiments in Fe/FeO Rhines packs (Section 6.1), the uncertainty in the pre-exponential factor was extremely large, and it was preferred to give the resulting uncertainty for the oxygen diffusion coefficient when calculated from $D_O^{(0)}$ and Q values reported in Table 6.6. The error for the calculated value of D_O^{mat} was estimated by taking the average of uncertainty values determined for each temperature using Equation (6.7). Activation energies for oxygen diffusion at all compositions tested in the present

Table 6.6: Pre-exponential factor and activation energy for oxygen diffusion measured in H_2/H_2O gases with 13% water vapour and oxygen partial pressure set at the Fe/FeO equilibrium.

$\frac{N_{Ni}}{N_{Fe}+N_{Ni}}$	$D_O^{(0)}$ $cm^2\ s^{-1}$	Q $kJ\ mol^{-1}$	r	$\delta(D_O^{mat})/D_O^{mat}$ %
0	3.3×10^5	327 ± 88	0.9999	43
0.2	2.5×10^5	313 ± 37	0.9999	18
0.4	2.3×10^9	415 ± 34	0.9999	17
0.6	1.5×10^8	393 ± 24	0.9999	12
0.8	4.8×10^1	230 ± 27	0.9998	13

study found from experiments in H_2/H_2O are higher than the value of 150 kJ mol^{-1} characteristic for interstitial diffusion.

6.2.2 Gases with 3% water vapour

In Table 6.7, the oxygen diffusion coefficient estimated at 1,150°C from oxygen permeability measured in gases with 3% water vapour (Table 5.24) and oxygen solubility measured in humid gases containing 13% water vapour (Table 3.4) are presented. Values in Table 6.7 are plotted as a function of alloy composition in Figure 6.8. This Figure shows that the variation of oxygen diffusion coefficient with the alloy composition is similar to that seen for diffusion coefficients measured in Fe/FeO Rhines packs or H_2/H_2O gases with 13% water vapour.

Table 6.7: Matrix oxygen diffusion coefficient measured in H_2/H_2O gases with 3% water vapour and oxygen partial pressure set at the Fe/FeO equilibrium.

$\frac{N_{Ni}}{N_{Fe}+N_{Ni}}$	0	0.2	0.4	0.6	0.8
$D_O^{mat} \times 10^9$ (cm^2 s^{-1})	267 ± 91	571 ± 171	615 ± 150	426 ± 145	244 ± 100

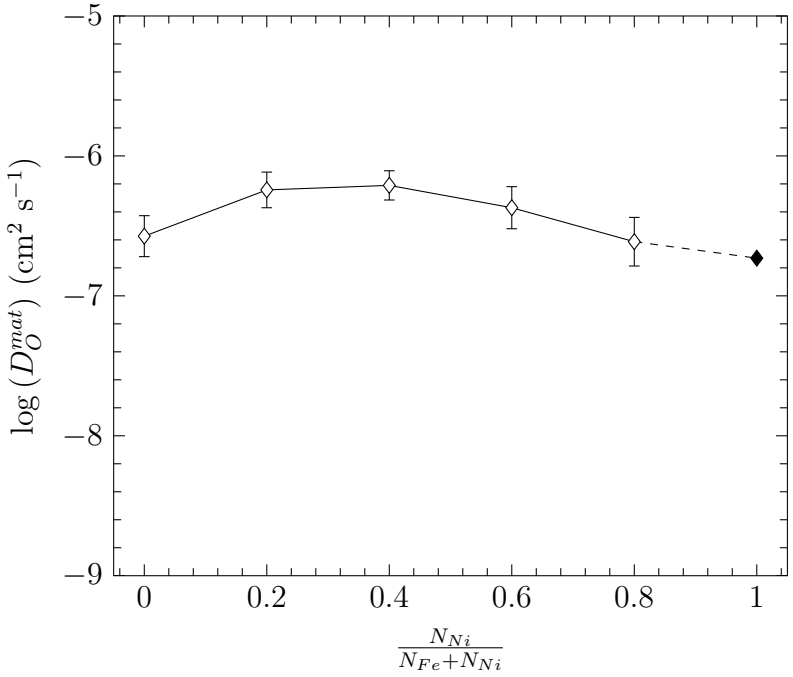

Figure 6.8: Matrix oxygen diffusion coefficient measured in H_2/H_2O gases with 3% water vapour at 1,150°C (–◇–). Values in pure nickel extrapolated with Equation (5.143) from data published by Guo *et al.* [50] (filled symbols).

6.3 Effects of water vapour and hydrogen on the oxygen diffusion coefficient

In Sections 6.1 and 6.2, calculation of oxygen diffusion coefficients from oxygen permeability values measured by internal oxidation was carried out. The values obtained under dry and wet conditions are compared in this Section to investigate the effect of water vapour and/or hydrogen on the oxygen diffusion coefficient.

In Figure 6.9, oxygen diffusion coefficients estimated at different temperatures in the various environments are compared. The Figure shows that at 1,150°C, a good agreement is found between values of oxygen diffusion coefficient measured in Fe/FeO Rhines packs and H_2/H_2O gases containing 13% water vapour. From

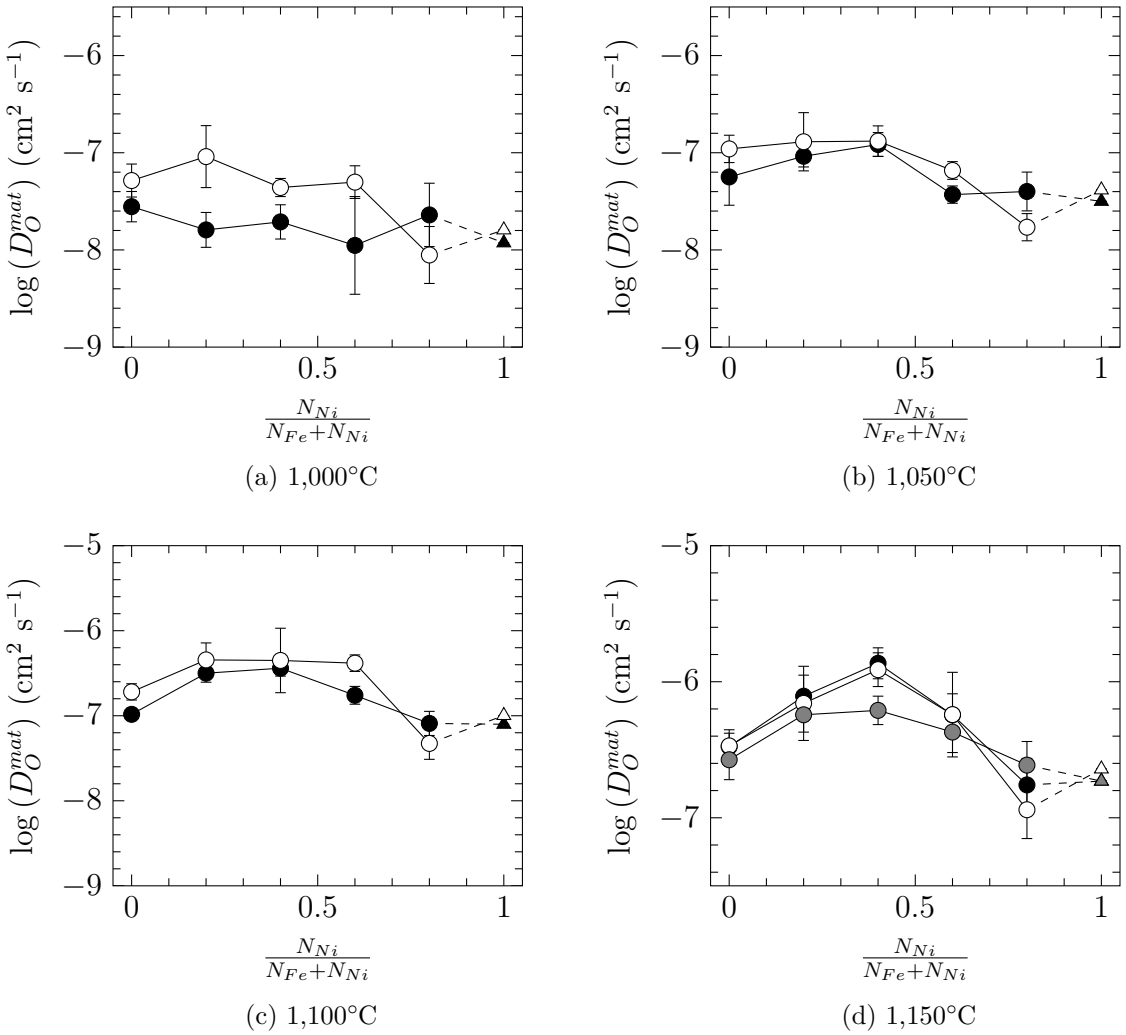

(a) 1,000°C (b) 1,050°C

(c) 1,100°C (d) 1,150°C

Figure 6.9: Comparison of matrix oxygen diffusion coefficient measured in Fe/FeO Rhines packs (–○–), H_2/H_2O gas with 3% water vapour (–●–), H_2/H_2O gas with 13% water vapour (–●–). Values in pure nickel extrapolated with Equation (5.143) from data published by Guo *et al.* [50] (–△–,–▲–,–▲–). Note log scale.

values measured in both environments, the largest difference is observed for alloys with $\frac{N_{Ni}}{N_{Fe}+N_{Ni}} = 0.8$. However, values are within experimental uncertainties, and therefore measurements for this composition were considered consistent.

Oxygen diffusion coefficients measured in H_2/H_2O with 3% water vapour are lower than oxygen diffusion coefficients measured in other environments. However, oxygen diffusion coefficients estimated from experiments carried out in H_2/H_2O gases with 3% water vapour were deduced from oxygen permeability estimated from a single penetration measurement, as presented in Section 5.4.2.2. In addition, kinetics measured in humid gases with 3% water vapour exhibit a short transient

stage at the beginning of the internal oxidation (Section 4.2.3). During this transient stage, internal oxidation kinetics are slower. This would affect permeability value estimates, and thus the oxygen diffusion coefficient. Therefore, results obtained from experiments in gases with 3% water vapour were considered as of indicative values only.

For a temperature of 1,100°C, good agreement is found between oxygen diffusion coefficients measured in alloys with $\frac{N_{Ni}}{N_{Fe}+N_{Ni}} = 0.2, 0.4$. For the alloy with 80% nickel, measurement was considered consistent because of the large uncertainty at this composition. It should be noted that the same qualitative behaviour is observed for lower temperature. Oxygen diffusion coefficients for pure Fe and Fe-60Ni alloy are smaller when measured in humid gases by a factor of 2. At 1,050°C agreement between values measured after exposure in dry and wet atmosphere is found for all compositions except the alloy with 60 at.% nickel, where the oxygen diffusion measured in H_2/H_2O gases was lower by a factor of 2.

At the lowest temperature studied in this study, 1,000°C, oxygen diffusion coefficient values measured in H_2/H_2O are smaller by a factor of 3 to 4 for alloys with nickel content between 20 and 60 at.%. For pure iron and Fe-80Ni, it is considered that results are consistent due to the significant measurement uncertainty estimated at those composition. Low values of oxygen diffusion coefficient observed at 1,000°C result from the higher oxygen solubility found at this temperature when alloys are exposed to H_2/H_2O gases.

No explanation was found for the discrepancies between values measured for Fe-60Ni at 1,050 and 1,100°C or for Fe at 1,100°C. These difference could arise from the inaccurate evaluation of the enrichment factor or the effective stoichiometry, which are difficult to estimate with precision as reported in Chapter 5. In general, it can be concluded that for temperatures above 1,000°C, the water vapour effect has no significant effect on the oxygen diffusion. However, at 1,000°C, oxygen diffusion is slower when water vapour and hydrogen are present in the atmosphere and possible mechanisms increasing the solubility in humid atmosphere may also

affect the oxygen diffusion.

It is also of interest to compare values of the activation energy for the oxygen diffusion coefficient estimated from experiments in different environments. In Figure 6.10, activation energy values presented in Tables 6.3 and 6.6 are compared.

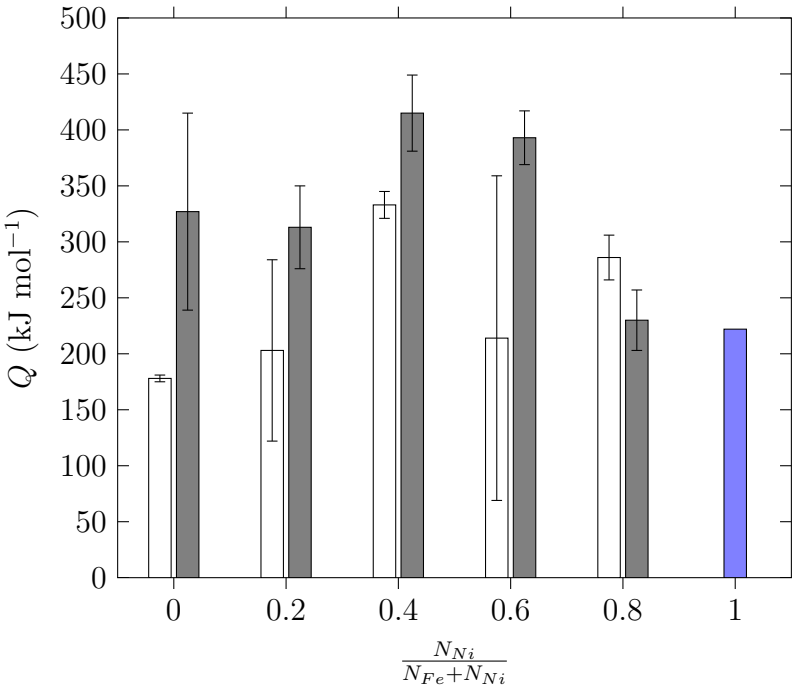

Figure 6.10: Activation energy for oxygen diffusion coefficient measured in Fe/FeO Rhines packs ( ) and H_2/H_2O gases containing 13% of water vapour with the oxygen partial pressure set at the Fe/FeO equilibrium pressure ( ). Value for nickel determined in Section 1.6.2 from several internal oxidation experiments at Ni/NiO dissociation pressure ( ).

The activation energy for the oxygen diffusion coefficient measured in H_2/H_2O is found to be higher than Q estimated for oxygen diffusion coefficient in Rhines packs, apart from the alloy with $\frac{N_{Ni}}{N_{Fe}+N_{Ni}} = 0.8$, as shown in Figure 6.10. In addition, it should be noted that Q is maximum for alloys with nickel between 40 and 60 at.% in both dry and humid atmospheres.

In nickel-rich alloys, the activation energy is found to be higher than 200 kJ mol^{-1}. This is in agreement with the activation energy of 222 kJ mol^{-1} for oxygen diffusion in nickel, estimated in Chapter 1 from several studies in which the oxygen diffusion coefficient was measured from oxygen permeability determined by internal oxidation. Computational studies [91, 92] showed that in pure nickel,

oxygen moves from one octahedral site to another through a tetrahedral site, and the migration energy corresponding to this displacement is approximately 90 kJ mol^{-1}, well below the activation energy found in the present study for oxygen diffusion in Fe-80Ni alloys. However, Fang *et al.* [91] observed that oxygen atoms and vacancies have strong interaction in nickel. In addition, those authors calculated the migration energy required by one atom of oxygen to move away from a vacancy and found a value of 162 kJ mol^{-1}. The latter value is in agreement with the value of Q =164 kJ mol^{-1} for oxygen diffusion in pure nickel measured by Park and Altstetter [80] with an electrochemical technique, but still lower than Q measured by internal oxidation as shown in Figure 6.10.

Fang's calculation indicates that vacancies slow down oxygen diffusion in nickel resulting in high activation energy. This result suggests that a similar mechanism affects oxygen diffusion in Fe-80Ni alloys. In addition, the probability of interaction between oxygen atoms and vacancies at elevated temperature is high due to the large vacancy concentration, which is approximately equal to the oxygen solubility. In addition, in Section 6.1, it was reported that DFT calculations [93] predict that at the Fe/FeO equilibrium 70% of oxygen atoms are located in interstitial sites and 30% form clusters of one oxygen atoms and one vacancy. Then, vacancies may have an effect on the oxygen diffusion even for experiments carried out at the Fe/FeO equilibrium.

Furthermore, it should be noted that diffusion is dependent on the pressure. During internal oxidation a large volume change takes place in the IOZ due to internal oxide precipitation and the internal oxidation front is under compressive stress. Thus, the diffusion path of oxygen is compressed in this region and may result in an increase of the activation energy for oxygen diffusion.

In addition nodules of pure matrix were observed on the alloy surface for nickel-rich alloys (Section 4.1.1). According to Yi [117], the formation of these nodules may result from Nabarro-Herring creep or diffusion through dislocation pipe. The mechanism involving Nabarro-Herring creep is interesting because it

involves the diffusion of vacancies through the IOZ from the alloy surface to the internal oxidation front. As stated previously, a large volume change takes place in the IOZ causing the internal oxidation front to undergo a state of compressive stress. Therefore, the vacancy concentration at the internal oxidation front is close to zero, and results in a vacancy concentration gradient through the IOZ. Thus vacancies diffuse from the alloy surface to the internal oxidation front where they are annihilated. A transport mechanism of oxygen by metallic vacancy was suggested by Perusin *et al.* [94] who observed the formation of voids due to vacancy coalescence beneath the alloy surface when they oxidised pure nickel to measure the oxygen diffusion coefficient. In addition, void walls were oxidised suggesting that oxygen is transported from the alloy surface to the void via vacancies.

The strong interaction between oxygen atoms and vacancies found by computational studies, the large volume expansion taking place on the IOZ due to the precipitation of internal oxides and the probable Nabarro-Herring creep mechanism taking place in nickel-rich alloys are mechanisms which may affect the oxygen diffusion. Therefore, evaluation of the activation energy for oxygen diffusion from internal oxidation experiments may yield systematically higher values due to the interference of acting mechanisms previously listed. This might also be a reason for the lower activation energy measured by Park and Altstetter [80] who measured the oxygen diffusion coefficient with an electrochemical technique, where no volume expansion or Nabarro-Herring creep takes place.

In addition, the pre-exponential factor reported in Table 6.3 varies by few orders of magnitude. According to Wert and Zener [135], the pre-exponential factor is given by the following expression

$$D_O^{(0)} = g a^2 \nu \exp\left(\frac{\Delta S^M}{R}\right) \tag{6.8}$$

where $g = 1$ for FCC lattice, a is the lattice parameter, ν the jump frequency and ΔS^M is the migration entropy. If the oxygen diffusion is affected by the presence of defects such as vacancies in the material, the migration entropy may also be affected,

thereby changing the value of the pre-exponential factor. However, calculation of entropy by computational techniques is difficult, and no study of the entropy of a defect composed of vacancy and oxygen atoms is available in the literature. For oxygen diffusion in iron, activation energy and pre-exponential factor estimated from experiment in Fe/FeO Rhines packs (Table 6.3) agree with values expected for interstitial, diffusion while $D_O^{(0)}$ and Q measured in H_2/H_2O disagree with this type of diffusion mechanism. However, as suggested in the preceding discussion of for activation energy and pre-exponential factor in nickel-rich alloys, high values of $D_O^{(0)}$ and Q may result from strong interactions between vacancies and oxygen atoms. In addition, as high values are measured under humid condition, it is likely that H or OH play a role affecting interaction between defects and oxygen atoms. Unfortunately, no study of interactions between oxygen atoms and metal vacancies is available in the literature for FCC iron.

It is noted that no comparison with oxygen diffusion coefficient estimated from oxygen permeability measured in previous work has been carried out. Indeed, the authors [33, 38–41, 43, 45, 47] used Swisher and Turkdogan [47] oxygen solubility to calculate the oxygen diffusion coefficient. However, as demonstrated in Section 3.2.1, it is likely that the oxygen solubility measured by Swisher and Turkdogan [47] is underestimated because their samples were not saturated when they carried out their oxygen analysis. Therefore, oxygen diffusion should be recalculated from oxygen permeability.

However, in Section 5.4.5 it was observed that oxygen permeability measured in the present study agree with values reported in previous works except for experiments carried out by Takada *et al.* [40, 41] who measured lower permeability, thought to be due to a lower oxygen partial pressure than the Fe/FeO equilibrium in their Rhines packs. Nevertheless, as values of oxygen permeability agree, calculation of the oxygen diffusion coefficient using oxygen solubility measured in the present study will necessarily yield a good agreement for oxygen diffusion coefficient values. Concerning Fe-Ni alloys, a similar variation of the activation energy with the alloy

composition is observed, suggesting that specific properties of binary Fe-Ni alloys have an influence on the oxygen diffusion, as described in Section 6.1. However, the presence of water vapour and hydrogen appears to amplify the effect of alloy composition on oxygen diffusion.

6.4 Summary

Oxygen diffusion coefficients estimated from oxygen permeability and solubility values measured in Fe/FeO Rhines packs and H_2/H_2O gases containing 13% water vapour with oxygen partial pressure set at the Fe/FeO oxygen partial pressure, are in good agreement for temperatures above 1,000°C. In both atmospheres, the oxygen diffusion coefficient exhibits a maximum for alloys with a nickel content of 40 at.%. This maximum is thought to be due to the combined effects of smaller interactions between oxygen, iron and nickel atoms at this composition and the continuous decrease of the alloy lattice parameter with increasing nickel alloy content. In contrast, at 1,000°C, oxygen diffusion coefficients measured in H_2/H_2O gases are smaller than those estimated from Fe/FeO Rhines packs experiments, by a factor of 2 to 4. This disagreement reflects the higher solubility measured under humid conditions at this temperature, while the oxygen permeability is not affected by the environment.

The activation energy for oxygen diffusion in pure Fe estimated from experiments in Fe/FeO Rhines pack is found to be in agreement with values expected for interstitial diffusion in pure iron. However, Q exhibits a maximum for alloys with nickel content of 40 at.% and is well above 200 kJ mol^{-1} in Fe-80Ni alloys. The high activation energy value found in nickel-rich alloys is thought to be due to interaction between oxygen atoms and defect such as vacancies which slow down the oxygen diffusion. Therefore, it is likely that high values of Q evaluated in Fe-Ni alloys may be due to interactions of oxygen atoms with defects present in the alloy lattice.

Comparison of activation energy values for oxygen diffusion coefficients estimated from reactions in dry and wet atmosphere showed higher values are found

in the H_2/H_2O atmosphere for alloys with nickel content lower than 80 at.%. This result suggests strong interactions between O, H atoms and vacancies which may affect oxygen diffusion. Although, computational studies to investigate these sorts of interactions were carried out in nickel but none are available for FCC iron.

The oxygen diffusion coefficient at the matrix/oxide interface could be determined using the expression of the parameter λ given by Equation (5.139). However, values of λ exhibit large uncertainties as reported in Chapter 5 and no result for interfacial diffusion allows a clear conclusion to be obtained from values of λ. The parameter λ is given by

$$\lambda = \alpha \frac{V_{oxide}}{V_{alloy}} \left(\frac{2\delta}{R_p} \frac{D_O^{int}}{D_O^{mat}} - 1 \right) \tag{6.9}$$

and it was observed that the water vapour and/or hydrogen has no significant effect on its value (Section 5.4.4). In addition, it was shown that the enrichment factor (Section 5.2) and the distribution of the two subzones where iron-chromium spinel and chromium oxide precipitates (Section 4.3) are also not affected by water vapour and hydrogen. Therefore, the product $\alpha \frac{V_{oxide}}{V_{alloy}}$ is not affected by humid gas. In addition, as suggested by results obtained for oxygen solubility and diffusivity, water vapour and/or hydrogen seem to have an effect on those properties at 1,000°C. Therefore, the average particle size was measured for chromium-rich alloys reacted in H_2/H_2O gas with 13% water vapour at 1,000°C for 48h. These measurements were compared to values presented in Table 5.18 measured for alloys reacted in Fe/FeO Rhines packs at the same temperature and duration. Comparisons were only made on particle size measured in the middle of the internal oxidation zone ($X/X_{(i)} = 0.5$). It should be noted that alloys with $\frac{N_{Ni}}{N_{Fe}+N_{Ni}} = 0.8$ and 4 at.% Cr formed an external scale when exposed to humid gas. Thus, no particle size measurement is available for comparison. Results of measurement in dry and humid conditions are presented in Table 6.8. Values in Table 6.8 show that water vapour and/or hydrogen has no significant effect on the internal particle size at 1,000°C. This result in addition with previous observation that the product $\alpha \frac{V_{oxide}}{V_{alloy}}$ and λ are not significantly affected by

Table 6.8: Comparison of internal particle size measured at $X/X_{(i)} = 0.5$ after exposure in Fe/FeO Rhines packs and H_2/H_2O gas with 13% water vapour. Alloy exposed 48h at 1,000°C.

$\frac{N_{Ni}}{N_{Fe}+N_{Ni}}$	$\overline{R}_p$ (μm) at $X/X_{(i)} = 0.5$	
	RP	H_2/H_2O
0	0.9 ± 0.1	0.7 ± 0.1
0.2	0.8 ± 0.2	0.9 ± 0.2
0.4	1.3 ± 0.3	1.5 ± 0.1
0.6	1.2 ± 0.1	1.2 ± 0.2

water vapour and/or hydrogen suggests that the ratio $\frac{D_O^{int}}{D_O^{mat}}$ is also unaffected by the presence of water vapour and/or hydrogen. However, additional work is required to estimate the parameter λ with better precision to achieve a firm conclusion. One solution to do so would be to use a larger number of alloys with different chromium contents as done by Stott *et al.* [51] who estimated the interfacial oxygen diffusion coefficient in Ni-Cr alloys using 7 different chromium contents for their alloys. In the present study only 3 different chromium contents were used and which resulted in a large uncertainty when λ is evaluated.

Chapter 7

Conclusions

Design of new austenitic alloys based on the Fe-Ni-Cr system for high temperature application requires knowledge of the alloy oxygen permeability to ensure the growth of a chromia scale. When alloys are exposed to high temperature and oxidising conditions, this chromia scale acts as a barrier to protect the underlying alloys. In addition, water vapour is usually present in high temperature processes and its effect on the oxygen permeability has to be assessed to optimise the design of new alloys. Determination of the oxygen permeability also allows the estimation of the oxygen diffusion coefficient in the base metal, if an independent solubility measurement is available. However, in the past those properties were measured only for pure metal Fe and Ni, and no data for Fe-Ni alloys are available in the literature.

The aims of this project were to measure oxygen solubility, permeability and diffusivity for Fe, Ni and Fe-Ni alloys. In addition, it should be emphasised that to obtain the most accurate results for oxygen solubility, permeability and diffusivity, the growth of an oxide scale of the base metal has to be avoided during an experiment. Therefore, in previous work, experiments were carried out in atmospheres where the oxygen partial pressure was set at the Fe/FeO or Ni/NiO equilibrium for experiment with iron and nickel based alloys, respectively. In the present study the oxygen partial pressure was set at the Fe/FeO equilibrium for all alloys, using the Rhines pack technique and H_2/H_2O gas mixtures. These two atmospheres avoid the formation of an oxide scale on alloys when exposed at high temperature and allow the investigation of the effect of water vapour on oxygen properties.

The oxygen solubility values measured in Fe, Ni and Fe-Ni alloys after exposure in either Rhines packs or H_2/H_2O gas mixtures exhibit identical dependency on the alloy composition. The maximum oxygen solubility was found in pure iron, and it continuously decreases with alloy nickel content. However, the variation with alloy composition is non-ideal, and two models to predict the oxygen solubility in Fe-Ni alloys were tested. It was found that Wagner's model [72] described the variation of oxygen solubility with composition of Fe-Ni alloys very well. For p_{O_2} fixed at the Fe/FeO equilibrium value, the oxygen solubility was sensitive to small additions of Ni

to iron, but relatively constant over a range of nickel-rich alloy compositions. Thus, for example, at 1,100°C in H_2/H_2O, the solubility decreases from about 400 at.ppm in pure iron to about 100 at.ppm in Fe-20Ni, 50 at.ppm in Fe-40Ni and is about 20 at.ppm in both Fe-80Ni and pure Ni. Comparison of results in Fe/FeO Rhines packs and H_2/H_2O gas mixtures showed that the oxygen solubility value in nickel-rich alloys is not affected by water vapour and/or hydrogen. On the other hand, for iron-rich alloys, the oxygen solubility measured after exposure under humid gases was higher by a factor of 2 than oxygen solubility measured in Rhines packs. These results suggest that interactions between O and H alter the oxygen solubility. It is proposed that defects such as vacancies in iron may have a more significant effect on oxygen solubility when hydrogen is present, by modifying interactions between O, H, OH and vacancies.

In the literature, only 4 reliable datasets are available for oxygen solubility in austenitic material, 1 for pure iron and 3 for pure nickel. For iron, Swisher and Turkdogan [47] carried out their experiments between 900 and 1,300°C in H_2/H_2O gases with the oxygen partial pressure set at the Fe/FeO equilibrium. The oxygen solubility measured under the previous experimental conditions was approximately 20 at.ppm at 1,050°C. However, in the present study, where experiments were carried out at the identical oxygen partial pressure in Fe/FeO Rhines packs and H_2/H_2O gas mixtures, the oxygen solubility was found to be higher by 1 order of magnitude than values previously reported. Oxygen solubility measured by Swisher and Turkdogan [47] is thought to be an underestimation, as diffusion calculations show it is likely that their samples were not fully saturated due to the limited time of their experimental exposures.

The oxygen solubility measured in nickel was measured at the Ni/NiO dissociation pressure by three different groups of authors who agreed on oxygen solubility values [78–80]. Here, oxygen solubility was measured at the Fe/FeO oxygen partial pressure and yields values of approximately 30 at.ppm in the temperature range 1,000-1,150°C. However, if values measured at the Fe/FeO equilibrium pressure are

extrapolated using Sievert's equation to the Ni/NiO oxygen partial pressure, which is several orders of magnitude higher than the Fe/FeO equilibrium pressure, values are larger by a factor of 2 compared to oxygen solubility measured at the Ni/NiO equilibrium pressure [78–80]. This result suggests that Sievert's law might not be applicable for such a large range of oxygen partial pressures. This idea is supported by recent DFT calculations [93], which showed that for temperatures above 1,000°C and oxygen concentrations lower than 50-70 at.ppm, which corresponds to oxygen solubility measured at the Fe/FeO oxygen partial pressure, oxygen atoms are mainly located at interstitial sites. However, for oxygen concentrations of 100-200 at.ppm, corresponding to oxygen solubility measured at the Ni/NiO oxygen partial pressure, oxygen in nickel is principally present as a cluster composed of one oxygen atom and one vacancy. This change in the type of defect as a function of the oxygen concentration in nickel has an impact on how the oxygen solubility varies with the oxygen partial pressure. Therefore, extrapolation using Sievert's law might only be valid for a small range of oxygen partial pressures.

The second oxygen property measured was the oxygen permeability of Fe and Fe-Ni alloys by internal oxidation of Fe-Cr and Fe-Ni-Cr alloys. It was shown experimentally that the IOZ was composed of two subzones, in each of which a specific oxide precipitates. In the subzone beneath the alloy surface, internal oxides were identified as $FeCr_2O_4$ while the subzone adjacent to the internal oxidation front was made of Cr_2O_3 oxides. Results from experiments in dry and humid conditions showed that the distribution of the two subzones is not affected by the presence of water vapour. As the internal oxidation zone is composed of two oxides with different stoichiometry, an effective stoichiometric coefficient was defined based on the distribution of the two subzones, and used in mass balance calculations.

Internal oxidation kinetics for alloys reacted in Fe/FeO Rhines packs and H_2/H_2O gas were found to be parabolic at all temperatures investigated. Values of $k_p^{(i)}$ measured in humid condition were close to values measured in Fe/FeO Rhines packs suggesting that water vapour and/or hydrogen have no significant effect on

internal oxidation rate. The internal oxidation rate constant was found to continuously decrease with nickel addition and increase with the temperature. For alloys with 2 at.% Cr, at 1,150°C, $k_p^{(i)}$ varies from 3×10^{-9} cm^2 s^{-1} for Fe alloys to 6×10^{-11} cm^2 s^{-1} for Fe-80Ni alloys. In addition, it was observed that for all compositions, a rise of temperature from 1,000 to 1,150°C increases the value of $k_p^{(i)}$ by approximately 1 order of magnitude.

However, at temperatures of 1,100 and 1,150°C, $k_p^{(i)}$ decreases when the alloy chromium content increases as predicted by Wagner's model [1] while for temperature below 1,100°C, this behaviour was only observed for alloys with a nickel content larger than 20 at.%. For Fe and Fe-20Ni alloys, the internal oxidation rate constants measured in alloys with chromium contents of 4 and 7.5 at.% were similar. The constant values of $k_p^{(i)}$ for different chromium contents is thought to be due to fast oxygen diffusion at matrix/oxide interfaces within the IOZ.

Results of internal oxidation measurements also showed that enrichment of chromium in the IOZ was taking place in nickel-rich alloys. The enrichment factor required to estimate the oxygen permeability was determined using Wagner's diffusional approach and from volume fraction measurements. Good agreement was found between the two techniques. However, these calculations reveal that the volume change of the IOZ due to internal oxide precipitation cannot be neglected in chromium-rich alloys.

In addition, study of the distribution of the internal oxide in the IOZ showed that for dilute chromium alloys, Wagner's assumption that all chromium was oxidised was not verified in the subzone where chromium oxide precipitates. This incomplete precipitation of chromium is due to the relatively high solubility product of chromium oxide, which was estimated from thermodynamic calculations in the present study. Nevertheless, it was shown that the discrepancy in Wagner's assumption has a negligible effect on the determination of the oxygen permeability using Wagner's model for internal oxidation.

From values of the internal oxidation rate constant, effective stoichiometry

and enrichment factor, the oxygen permeability of Fe and Fe-Ni alloys were calculated. Results showed that fast oxygen diffusion at matrix/oxide interfaces cannot be neglected, even for temperatures above 1,000°C. To deal with this, a model to relate oxygen diffusion to parameters such as particle size and distribution was developed in order to separate the contribution of interfacial and matrix oxygen diffusion to measured oxygen permeability, and therefore estimate the matrix oxygen permeability.

The model developed allows the evaluation of the matrix oxygen permeability with an acceptable uncertainty. However, parameters reflecting the fast oxygen diffusion at matrix/oxide interfaces were difficult to estimate with precision. Therefore, no clear trend for the variation of those parameters with the alloy composition and temperature were observed, and additional work is required to estimate the interfacial diffusion.

The matrix oxygen permeability was found to decrease with alloy nickel content in a non-ideal manner. In addition, no significant effect of water vapour and/or hydrogen on oxygen permeability was observed. The matrix oxygen permeability is found to vary by several orders of magnitude from its value in iron to the matrix oxygen permeability measured in Fe-80Ni alloys. For a temperature of 1,000°C, the matrix permeability of iron is close to 1×10^{-11} cm^2 s^{-1} and the value for Fe-80Ni alloys is around 3×10^{-13} cm^2 s^{-1}. In addition, matrix oxygen permeability increases with increasing temperature. For all compositions, an increase of temperature from 1,000 to 1,150°C increases the value of $N_O^{(s)} D_O^{mat}$ by one order of magnitude.

Oxygen permeability obtained for iron was compared with literature values, and good agreement was found between values measured in the present study and permeability reported in previous work. Only oxygen permeability reported by Takada *et al.* [40, 41] is lower by a factor of 2 than oxygen permeability reported by other authors. However, it is thought that the oxygen partial pressure in Takada's [40, 41] experiments was lower than the Fe/FeO equilibrium and thus yields lower values of oxygen permeability.

The last oxygen property measured in this study was the oxygen diffusion coefficient from oxygen permeability and solubility. The oxygen diffusion coefficient measured in Fe/FeO Rhines packs and H_2/H_2O gases exhibit the same dependency on the alloy composition. At 1,000°C, the oxygen diffusion coefficient appears to be constant with varying nickel content of the alloy. In addition at this temperature the oxygen diffusion coefficient for alloys with nickel content up to 60 at.% is affected by the presence of water vapour. Values of oxygen diffusion coefficient are approximately 59×10^{-9} cm^2 s^{-1} and 18×10^{-9} cm^2 s^{-1} for experiments in Fe/FeO Rhines packs and H_2/H_2O gas, respectively. These discrepancies arise from the high oxygen solubility when measured in H_2/H_2O compared to the value measured in Fe/FeO Rhines packs for alloys with nickel content lower than 80 at.%.

For higher temperatures, no effect of water vapour and hydrogen was observed and the oxygen diffusion coefficient exhibits a maximum for alloys with 40 at.% of nickel. The appearance of this maximum is to thought be due to a combined effect of weaker bonds between oxygen, iron and nickel atoms at this composition and the continuous decrease of the lattice parameter with the alloy nickel content.

Comparison of the activation energy for oxygen diffusion showed that for Fe-80Ni alloys, the activation energy for oxygen diffusion is not affected by water vapour and/or hydrogen but is significantly higher than the characteristic activation energy of interstitial diffusion. This difference might be explained by interactions between vacancies and oxygen atoms in nickel-rich alloys, as suggested by DFT calculations. In addition, the large volume expansion taking place during internal oxidation may affect the activation energy for oxygen diffusion. For alloys with nickel content up to 60 at.%, the activation energy measured after exposure under humid conditions was found to be higher by a maximum of a factor 2, compared to the activation energy calculated for oxygen diffusion measured from Fe/FeO Rhines packs experiments, suggesting strong interaction between O, H and defects such as vacancies.

Overall, water vapour and/or hydrogen do not affect the variation of the oxygen solubility and diffusivity with alloy composition. However, it appears that they

change the oxygen solubility and diffusivity values for iron-rich alloys at temperatures around 1,000°C. Therefore, it may be expected that the effects of water vapour and/hydrogen on oxygen solubility or diffusivity are stronger at temperatures below 1,000°C. First principle calculations in pure Ni demonstrated that oxygen and vacancies have strong interactions at high oxygen activities, and this affects oxygen diffusion and solubility. Unfortunately no such study was carried out for FCC iron. Thus, the results of the present study suggest that research into the interactions between O, H and vacancies, could be useful in understanding and explaining the effect of water vapour observed here.

Appendices

Appendix A

Analysis certificate from raw materials

SIGMA-ALDRICH®
sigma-aldrich.com
3050 Spruce Street, Saint Louis, MO 63103, USA
Website: www.sigmaaldrich.com
Email USA: techserv@sial.com
Outside USA: eurtechserv@sial.com

Certificate of Analysis

Product Name:
Iron – chips, 99.98% trace metals basis

Fe

Product Number:	**267945**
Lot Number:	**MKBJ4567V**
Brand:	ALDRICH
CAS Number:	7439-89-6
MDL Number:	MFCD00010999
Formula:	Fe
Formula Weight:	55.85 g/mol
Quality Release Date:	10 NOV 2011

Test	Specification	Result
Appearance (Color) Grey to Black	Conforms to Requirements	Grey
Appearance (Form) Shiny Chips	Conforms to Requirements	Solid
X-Ray Diffraction	Conforms to Structure	Conforms
ICP Major Analysis Confirms Iron Component	Confirmed	Conforms
Trace Metal Analysis	≤ 300.0 ppm	66.3 ppm
Aluminum (Al)		1.7 ppm
Arsenic (As)		2.4 ppm
Chromium (Cr)		8.1 ppm
Copper (Cu)		3.8 ppm
Magnesium (Mg)		0.1 ppm
Manganese (Mn)		23.8 ppm
Nickel (Ni)		3.5 ppm
Sodium (Na)		7.1 ppm
Tin (Sn)		15.6 ppm
Purity 99.98% Purity Based On Trace Metals Analysis	Conforms	Conforms

Jamie Gleason, Manager
Quality Control

Alfa Aesar

Certificate of analysis

Product No.: 42333

Product: Nickel slug, 3.175mm (0.125in) dia x 3.175mm (0.125in) length, Puratronic®, 99.995% (metals basis)

Lot No: I30Z076

Ni 99.998 %

Ag	0.06	Al	0.07	As	< 0.01	Au	< 0.05
B	< 0.001	Ba	< 0.001	Be	< 0.001	Bi	< 0.005
Br	< 0.01	C	9	Ca	< 0.05	Cd	< 0.01
Ce	< 0.001	Cl	< 0.05	Co	0.55	Cr	0.19
Cs	0.002	Cu	0.145	F	< 0.01	Fe	2.35
Ga	< 0.01	Ge	< 0.05	H	1	Hf	< 0.005
Hg	< 0.05	I	< 0.005	In	< 0.005	Ir	0.2
K	< 0.05	La	< 0.001	Li	< 0.001	Mg	< 0.005
Mn	0.006	Mo	0.02	N	< 1	Na	< 0.011
Nb	< 0.01	Nd	< 0.001	O	6.5	Os	0.185
P	0.03	Pb	0.043	Pd	< 0.05	Pt	< 0.05
Re	0.12	Rh	< 0.01	Ru	< 0.01	S	1.5
Sb	1.065	Se	< 0.01	Si	< 0.16	Sn	< 0.01
Sr	< 0.01	SC	< 0.001	Te	< 0.005	Th	< 0.0001
Tl	< 0.01	U	< 0.0001	Ti	0.38	W	0.015
Zn	0.01	Zr	< 0.005	Y	0.011	V	0.002

Values given in ppm unless otherwise noted
Carbon, hydrogen, nitrogen, oxygen and sulfur determined by LECO
All other elements determined by GDMS

This document has been electronically generated and does not require a signature.

Appendix B

Etchants

In this appendix, a list of etchants used in this study and their compositions are listed

Nital 5% : 5 ml nitric acid
95 ml ethanol

Marble : 50 ml water
50 ml chloridric acid
10g $CuSO_4$

Etchant 1 : 5 ml Nitric acid
95 ml acetic acid

Appendix C

LECO analyser parameters

The company LECO published a note [105] to measure very low oxygen content in steel and nickel base alloys. This note was approved by the ASTM E-1019 of 2003. During measurements these parameters were used. Some of them had to be adjusted to adapt the method to our equipment. Below all parameters used in the measurement method are listed

Analysis parameters:

Outgas cycles:	2
Analysis delay:	15 second
Analysis delay comparator:	1.0
auto analyse:	on

Element parameters:

Minimum analysis time:	35
Significant digits:	6
Conversion factor:	1.0
Integration Delay:	0
Comparator level:	0.2

Furnace parameters:

Furnace control mode:	power
Purge time:	15 second
Outgas time:	16 second
Outgas cool time:	8 second
Outgas Low and High:	6000H 6000L
Analysis Low and High:	5000H 5000L

Appendix D

Standards for oxygen analysis

List of standards for oxygen analysis calibration provided by LECO

LECO 501-644 Certified value: 67 ± 6 wt.ppm

LECO 502-457 Certified value: 47 ± 4 wt.ppm

LECO 501-550 Certified value: 23 ± 4 wt.ppm

LECO 502-197 Certified value: 10 ± 3 wt.ppm

LECO 502-144 Certified value: 2 ± 0.4 wt.ppm

List of standards provided by China National Analysis Center

NS11037 Certified value: 66 ± 3 wt.ppm

NS11022 Certified value: 38 ± 2 wt.ppm

NS11021 Certified value: 6.2 ± 0.6 wt.ppm

Appendix E

Error for functions of 2 variables

If a function $z = f(x, y)$ is considered and each variable has an error δx and δy. If measurement and therefore errors in x and y are independent and random the error in z is given by

$$\delta z = \sqrt{\left(\frac{\partial f}{\partial x}\delta x\right)^2 + \left(\frac{\partial f}{\partial y}\delta y\right)^2} \tag{E.1}$$

However if the measurement of x and y is not independent, therefore errors in x and y are correlated and the correlation factor defined by

$$r = \frac{COV\,(x, y)}{\sigma_x \sigma_y} \tag{E.2}$$

where COV is the covariance of the two parameters and σ the standard deviation. In addition the error in z is now given by

$$\delta z = \sqrt{\left(\frac{\partial f}{\partial x}\delta x\right)^2 + \left(\frac{\partial f}{\partial y}\delta y\right)^2 + 2r\frac{\partial f}{\partial x}\frac{\partial f}{\partial y}\sigma_x \sigma_y} \tag{E.3}$$

From Equation (E.3) it is obvious that if errors in x and y are independent and random, therefore those parameters are not correlated and $r = 0$. Then Equation (E.3) becomes identical to Equation (E.2).

Résumé étendu

1 Introduction

Les systèmes permettant de produire de l'énergie tels que les turbines à gaz ou les centrales à charbon font face aujourd'hui à un véritable défi. La demande croissante d'énergie oblige ces installations à augmenter leur production tout en respectant les normes environnementales appelant à une réduction des émissions des gaz à effet de serre notamment le CO_2. Pour relever ce défi, l'efficacité des unités de production d'énergie doit être améliorée. L'une des solutions envisagée pour atteindre cet objectif est d'augmenter la température de fonctionnement des installations. Cependant, cela nécessite le développement de nouveaux alliages austénitiques basés sur le système Fe-Ni.

Les alliages utilisés dans les unités de production d'énergie utilisant le charbon ou le gaz comme combustibles sont exposés, en plus des températures élevées, à des environnements corrosifs contenant des gaz tels que CO, CO_2, H_2O, SO_2 etc. Ceux-ci proviennent de la combustion ou sont introduits volontairement dans le but d'augmenter les performances comme c'est le cas pour la vapeur d'eau dans les turbines à gaz [136]. Par conséquent, les matériaux doivent présenter une excellente résistance contre l'oxydation à haute température dans ces environnements. Cette propriété est généralement obtenue par la formation d'une couche d'oxyde de chrome (ou d'alumine) à la surface du matériau qui agit comme une barrière protégeant l'alliage sous-jacent des gaz corrosifs. Face à ces exigences, le système Fe-Ni-Cr demeure le système de référence pour le développement de nouveaux alliages réfractaires. Néanmoins, la formation d'une couche d'oxyde externe de chromine permettant de protéger le matériau nécessite que la composition de l'alliage réponde à certains critères énoncés par Carl Wagner [1].

Lorsqu' un alliage Fe-Ni-Cr est exposé à haute température dans un milieu oxydant, si le flux de chrome provenant de l'intérieur du matériau est suffisamment grand, celui-ci permet la formation et la croissance d'une couche d'oxyde de chrome en surface. Cependant, si le flux de chrome n'est pas suffisant, l'oxygène pénétrant le matériau réagit avec le chrome contenu dans l'alliage pour former des oxydes

internes. De manière générale, l'oxydation interne doit être évitée lors de l'utilisation des alliages. Afin d'empêcher ce phénomène, une solution consiste à augmenter le flux de chrome provenant de l'intérieur du matériau et se dirigeant vers sa surface ce qui peut être facilement réalisé en augmentant la concentration en chrome de l'alliage. De ce fait, il existe une concentration minimum de chrome pour observer la transition entre oxydation interne et externe. Wagner [1] démontra, lors de son étude de l'oxydation interne, que cette quantité minimum peut être calculée dès lors que la perméabilité de l'oxygène, définie comme le produit de la solubilité et de la diffusivité de l'oxygène dans le matériau, est connue.

Carl Wagner montra également que la cinétique d'oxydation interne est proportionnelle à la perméabilité de l'oxygène. Cette propriété fut mesurée pour le fer et le nickel purs en étudiant les cinétiques d'oxydation interne d'alliages Fe-Al/Cr [33, 38, 45, 47] et Ni-Al/Cr [50–52, 54]. De plus, la mesure de la perméabilité de l'oxygène permet l'évaluation du coefficient de diffusion de l'oxygène à partir du moment où une mesure indépendante de la solubilité de l'oxygène est disponible. Néanmoins, il n'existe que 4 travaux dans la littérature qui fournissent des valeurs de solubilité de l'oxygène dans le fer et le nickel pur et aucune donnée n'est disponible dans les alliages Fe-Ni.

Dans ce travail, les mesures de solubilité, perméabilité, et diffusivité de l'oxygène ont été effectuées dans fer pur et dans plusieurs alliages Fe-Ni (Fe, Fe-20Ni, Fe-40Ni, Fe-60Ni, Fe-80Ni, Ni). Il faut noter que la détermination de la perméabilité de l'oxygène nécessite l'évaluation de paramètres annexes tels que la stoechiométrie des oxydes internes ainsi que l'enrichissement en chrome de la zone d'oxydation interne. De plus, la perméabilité, la solubilité et la diffusivité de l'oxygène ont été mesurées dans deux environnements, sec et humide, afin de déterminer les effets de l'hydrogène et/ou de la vapeur d'eau sur les différentes propriétés de l'oxygène. Afin d'obtenir les meilleurs résultats possibles, aucune couche d'oxyde ne doit se former sur la surface des matériaux durant leur réaction à haute température. Pour se faire, l'atmosphère sèche a été obtenue grâce à la méthode des « packs de Rhines » [37].

Les échantillons ont été encapsulés sous vide dans une ampoule en silice contenant également un mélange de poudre Fe/FeO pour fixer la pression partielle d'oxygène. L'atmosphère humide a été, quant à elle, réalisée avec des mélanges gazeux H_2/H_2O contenant 13% de vapeur d'eau. Ces mélanges avaient le ratio $\frac{p_{H_2O}}{p_{H_2}}$ approprié afin de fixer la pression partielle d'oxygène à la pression d'équilibre Fe/FeO. Cela a permis de comparer les résultats obtenus dans cet environnement aux résultats des expériences réalisées avec les « packs de Rhines ».

Ce manuscrit est composé de 7 chapitres. Le premier chapitre consiste en une revue bibliographique sur l'oxydation interne à haute température du fer, du nickel et des alliages Fe-Ni. Les travaux sur la solubilité de l'oxygène dans le fer et le nickel pur sont également présentés dans ce chapitre. Le Chapitre 2 décrit les méthodes expérimentales et les techniques de caractérisation utilisées durant cette étude. Les résultats des mesures de solubilité de l'oxygène et une discussion sur les effets possibles de l'hydrogène et/ou de la vapeur d'eau sont présentés dans le Chapitre 3. Le Chapitre 4 est dédié à la mesure des cinétiques d'oxydation interne dans les différents environnements utilisés. Les valeurs de perméabilité de l'oxygène estimées à partir des cinétiques d'oxydation interne sont présentées dans le cinquième chapitre avec les méthodes utilisées pour déterminer la stœchiométrie des oxydes internes et l'enrichissement en chrome de la zone d'oxydation interne. La question de l'effet de la vapeur d'eau et/ou de l'hydrogène sur la perméabilité de l'oxygène est également abordée dans ce chapitre. Le Chapitre 6 est dédié au calcul du coefficient de diffusion de l'oxygène, à partir de la solubilité et de la perméabilité de l'oxygène mesurées durant ce travail. Finalement un dernier chapitre résume les différents résultats obtenus et les conclusions énoncées durant cette étude.

Dans ce résumé, seuls les principaux résultats des Chapitres 3, 4, 5 et 6 sont développés.

2 Solubilité de l'oxygène

Afin de mesurer la solubilité de l'oxygène dans le fer, le nickel et les alliages Fe-Ni, des échantillons parallélépipédiques ayant une épaisseur de 1,4 mm et pesant 1 g ont été exposés durant une durée précise permettant de les saturer en oxygène. De plus, ces échantillons ont été équilibrés dans les atmosphères sèche et humide pour étudier les effets possibles de l'hydrogène et/ou de la vapeur d'eau sur la solubilité de l'oxygène.

La fraction molaire d'oxygène, N_O, a été mesurée grâce à un doseur d'oxygène LECO TCH600 utilisant la technique de fusion sous gaz inerte. L'instrument a été spécialement calibré grâce à des standards fournis par LECO afin de mesurer des niveaux d'oxygène extrêmement bas (10-200 at.ppm). Les informations relatives à la calibration sont présentées dans le Chapitre 2. La mesure de la solubilité de l'oxygène a également permis de déterminer l'énergie d'excès de Gibbs pour l'oxygène en solution dans les différents matériaux utilisés. De plus, des modèles de la littérature permettant de prédire la solubilité de l'oxygène dans des alliages binaires ont été testés.

Les solubilités de l'oxygène mesurées dans les alliages Fe-Ni après réaction dans les « packs de Rhines » et dans les mélanges gazeux H_2/H_2O contenant 13% de vapeur d'eau présentent la même dépendance avec la composition de l'alliage entre 1000 et 1150°C. Le maximum de solubilité est observé dans le fer pur, puis elle décroit avec l'ajout de nickel à la composition de l'alliage pour finalement atteindre un minimum dans le nickel pur. Il faut noter que cette dépendance est non idéale.

Les valeurs de solubilité obtenues à 1150°C grâce aux expériences réalisées en « pack de Rhines » et dans les mélanges H_2/H_2O sont similaires alors que pour des températures inférieures, la solubilité de l'oxygène mesurée dans les alliages contenant moins de 80 at.% de nickel est plus élevée après réaction dans l'environnement contenant de la vapeur d'eau. De plus, la différence entre les valeurs de N_O mesurées dans l'atmosphère sèche et humide augmente quand la température diminue. La plus grande différence est observée dans le fer pur à 1000°C où la solubilité mesurée après

réaction dans l'environnement contenant de la vapeur d'eau est deux fois plus grande que la solubilité de l'oxygène mesurée après réaction dans le « pack de Rhines ». Le nickel pur présente un comportement différent car la solubilité de l'oxygène mesurée dans les deux environnements est identique et ceci a été observé à toutes les températures étudiées. Ce résultat indique que la vapeur d'eau et/ou l'hydrogène n'ont aucun effet sur la solubilité de l'oxygène pour ce matériau au-dessus de 1000°C.

La mesure de la solubilité de l'oxygène dans le fer, le nickel et les alliages Fe-Ni a montré que la vapeur d'eau et/ou l'hydrogène semble avoir un effet sur cette propriété dans les alliages contenant jusqu'à 60% de nickel. Il a également été observé que cet effet est important aux plus basses températures.

Les valeurs de solubilité de l'oxygène, obtenues durant cette étude, ont été comparées aux valeurs de la littérature. Concernant le fer pur, les uniques valeurs de solubilité de l'oxygène dans le fer gamma ont été mesurées par Swisher et Turkdogan [47]. Ces auteurs ont utilisé des mélanges H_2/H_2O avec une pression partielle d'oxygène fixée à la pression d'équilibre Fe/FeO pour saturer leurs échantillons en oxygène. Leur protocole expérimental est similaire au protocole utilisé dans ce travail. Néanmoins, les valeurs de solubilité rapportées par Swisher et Turkdogan sont de l'ordre de 20 à 50 at.ppm pour des températures variant de 950 à 1250°C alors que dans notre étude, pour des températures variant de 1000 à 1150°C, des valeurs proches de 200 et 400 at.ppm ont été mesurées après réaction dans les « packs de Rhines » et les mélanges H_2/H_2O respectivement.

Les équations de diffusion, permettant de déterminer le temps requis pour atteindre la saturation en oxygène des échantillons, nous ont permis de montrer que les faibles valeurs de solubilité de l'oxygène, rapportées par Swisher et Turkdogan, pouvaient être dues à des durées d'exposition trop courtes pour que leurs échantillons soient totalement équilibrés.

Pour la solubilité de l'oxygène dans le nickel pur à la pression d'équilibre Fe/FeO, il a été décidé de comparer les valeurs d'énergie de la réaction de dissolution de l'oxygène dans la nickel, $\Delta\overline{G}^{xs}$, plutôt que de faire une comparaison sur les valeurs

de N_O. En effet, les solubilités de l'oxygène dans le nickel ont été mesurées à la pression d'équilibre Ni/NiO dans les travaux antérieurs [78–80]. Les valeurs de $\Delta\overline{G}^{xs}$ estimées, d'après les valeurs de N_O mesurées dans les environnements avec la pression partielle d'oxygène fixée à la pression d'équilibre Fe/FeO, sont plus basses que $\Delta\overline{G}^{xs}$ mesurées par les auteurs ayant réalisés leurs expériences à la pression d'équilibre Ni/NiO [78–80]. Ce résultat suggère que la mesure de $\Delta\overline{G}^{xs}$ pourrait dépendre de la pression partielle d'oxygène à laquelle la mesure est effectuée et indique que la loi de Sievert est très probablement uniquement valide sur un domaine restreint de pression partielle d'oxygène. Cette hypothèse est supportée par de récents calculs en Théorie de la Fonctionnelle de la Densité (DFT) [93] qui ont montré que des défauts ponctuels tels que des lacunes ou des défauts composés d'une lacune et d'un ou plusieurs atomes d'oxygène peuvent se former dans le nickel et que la concentration respective de ces défauts dépend de la température et de la concentration en oxygène dans le nickel.

Les calculs DFT [93] ont montré que pour des températures de l'ordre de 1200°C et à la pression d'équilibre Fe/FeO, la majorité des atomes d'oxygène sont en position interstitielle alors qu'à la pression d'équilibre Ni/NiO les atomes d'oxygène sont principalement localisés dans des défauts composés d'une lacune et d'un atome d'oxygène, VO_1. Les calculs DFT ont également montré que l'énergie d'insertion d'un atome d'oxygène dans un site interstitiel octaédrique est de 44 kJ mol^{-1} alors que l'énergie de formation d'un défaut VO_1 est de l'ordre de 72 kJ mol^{-1}. Cette différence dans l'énergie de formation des défauts dans le nickel peut expliquer les différences observées entre les valeurs de $\Delta\overline{G}^{xs}$ mesurées lors d'expériences à la pression d'équilibre Fe/FeO et Ni/NiO. Les mesures de solubilité de l'oxygène dans les alliages Fe-Ni ont permis de tester deux modèles permettant de prédire N_O en fonction de la composition de l'alliage. Il a été observé que le modèle d'Alcock et Richardson [71] prédit la variation de la solubilité de l'oxygène avec la composition de l'alliage. Cependant, les valeurs calculées grâce à ce modèle sont en désaccord avec les valeurs de N_O que nous avons mesurées. Le modèle de Wagner [72] permet

quant à lui de prédire avec un excellent accord les valeurs de solubilité de l'oxygène dans les alliages Fe-Ni. Toutefois, l'utilisation du modèle de Wagner nécessite la définition du paramètre énergétique h. Ce paramètre représente l'énergie nécessaire pour échanger un atome de nickel entourant le site interstitiel où l'oxygène se situe avec un atome de fer. Le calcul des interactions entre atomes grâce à des méthodes numériques pourrait permettre d'évaluer le paramètre énergétique h avec précision mais également de déterminer si H ou OH jouent un rôle sur les interactions entre les atomes de fer, de nickel et d'oxygène et également entre les atomes d'oxygène et les lacunes.

3 Oxydation interne

Les cinétiques d'oxydation interne ont été mesurées en évaluant la taille de la zone d'oxydation interne grâce à la microscopie optique. Elles ont aussi été évaluées par thermogravimétrie. De plus, une étude de la microstructure de la zone d'oxydation interne a été réalisée. Il faut également noter que les expériences d'oxydation interne ont été réalisées dans les atmosphères sèche et humide afin d'étudier les potentiels effets de la vapeur d'eau et/ou de l'hydrogène sur les cinétiques et sur les microstructures.

3.1 Microstructure de la zone d'oxydation interne

L'étude de la microstructure de la zone d'oxydation interne a révélé que celle-ci est constituée de précipités bien répartis et n'ayant aucune orientation préférentielle. De plus, du fait de la très grande taille de grains des alliages, les effets de diffusion aux joints de grains ont été considérés comme négligeables.

La taille et la forme des précipités semblent dépendre de la composition de l'alliage. Il a été observé que les particules d'oxyde interne ont une forme sphérique dans les alliages pauvres en chrome et nickel. De plus, pour une température donnée, il a été observé que la taille des précipités augmente dans les alliages riches en chrome

et nickel. Il faut également noter que pour les différentes compositions, la taille des précipités augmente avec la profondeur de la zone d'oxydation interne comme prédit par Böhm and Kahlweit [35]. Néanmoins, aucun effet significatif de l'environnement sur la taille ou la forme des oxydes internes n'a été observé. Dans les alliages riches en nickel, des nodules métalliques ayant la composition de la matrice ont été observés sur la surface des matériaux après oxydation interne. La formation de ces nodules a été étudiée par Yi *et al.* [117]. Leur formation a été expliquée par les contraintes induites par le changement de volume se produisant lorsque des oxydes internes, ayant des volumes molaires plus élevés que la matrice, précipitent.

Des observations en microscopie électronique à balayage (MEB) ont montré que la zone d'oxydation interne est constituée de deux sous-zones distinctes. A l'intérieur de chacune d'entre elles, un oxyde particulier, $FeCr_2O_4$ ou Cr_2O_3, précipite. La formation de ces deux sous-zones est due à la diminution de l'activité de l'oxygène à l'intérieur de la zone d'oxydation interne. En effet, l'activité de l'oxygène diminue avec la pénétration d'où la présence du spinel $FeCr_2O_4$ directement sous la surface du matériau, alors que Cr_2O_3 précipite dans la sous-zone adjacente au front d'oxydation interne. Il faut également noter que la taille relative des deux zones varie en fonction de la concentration en nickel dans l'alliage. Dans les alliages Fe-Cr, la zone d'oxydation interne est principalement constituée du spinel fer-chrome, alors que dans les alliages Fe-Ni-Cr, lorsque la taille de la zone contenant $FeCr_2O_4$ diminue au profit de la zone contenant Cr_2O_3, la concentration en nickel augmente. La variation de la taille des deux sous-zones est en accord avec les prévisions thermodynamiques et est due à la réduction de l'activité du fer quand la concentration en nickel augmente. Le spinel $FeCr_2O_4$ étant moins stable dans les alliages riches en nickel. Il a également été observé que la taille relative des deux sous-zones n'était pas affectée de façon significative par la température ou la présence de vapeur d'eau dans l'environnement.

3.2 Cinétique d'oxydation interne

Les cinétiques d'oxydation interne ont été évaluées d'après la mesure de la taille de la zone d'oxydation interne ou par mesure du gain de masse. De plus, les expériences utilisant des mélanges gazeux H_2/H_2O ont été réalisées dans un four horizontal pour les gaz contenant 13% de vapeur d'eau, alors que les expériences utilisant seulement 3% de vapeur d'eau furent réalisées dans une thermobalance.

Premièrement, toutes les cinétiques ont été trouvées paraboliques dans les différents environnements à toutes les températures étudiées dans la présente étude. Les cinétiques d'oxydation mesurées durant les expériences en « pack de Rhines » Fe/FeO sont similaires aux vitesses d'oxydation observées lors des expériences utilisant des mélanges de gaz H_2/H_2O contenant 13% de vapeur d'eau. Ce résultat indique que la présence de vapeur d'eau et d'hydrogène n'a qu'un effet limité sur les cinétiques d'oxydation interne. Il a également été observé que la valeur de la constante d'oxydation interne, $k_p^{(i)}$, diminue de façon continue avec l'ajout de nickel et augmente avec la température. A 1150°C, $k_p^{(i)}$ varie de 3×10^{-9} cm^2 s^{-1} pour Fe-2Cr jusqu'à 6×10^{-11} cm^2 s^{-1} pour Fe-80Ni-2Cr. De plus, il a été observé que pour une augmentation de température de 1000 à 1150°C, $k_p^{(i)}$ augmente d'un ordre de grandeur.

L'énergie d'activation pour $k_p^{(i)}$ a également été déterminée à partir des valeurs de $k_p^{(i)}$ estimées grâce aux expériences en « packs de Rhines » et en atmosphère H_2/H_2O. Cette énergie a été trouvée identique dans les deux environnements étudiés soutenant l'idée que l'hydrogène et/ou la vapeur d'eau n'a pas d'effet significatif sur les cinétiques d'oxydation interne. Néanmoins, il a été observé que l'énergie d'activation de $k_p^{(i)}$ diminue lorsque que la concentration en chrome de l'alliage augmente, suggérant que la diffusion rapide de l'oxygène aux interfaces matrice/oxyde interne affecte la cinétique d'oxydation interne comme proposé par Goto *et al.* [49].

Les cinétiques d'oxydation interne ont également été évaluées par gain de masse à 1000 et 1050°C dans des environnements H_2/H_2O contenant différents pourcentages de vapeur d'eau (3% et 13%) et avec la pression partielle d'oxygène fixée à

la pression d'équilibre Fe/FeO. Les résultats obtenus ont montré que les cinétiques d'oxydation étaient similaires dans les alliages riches en fer alors que des cinétiques différentes étaient observées pour les alliages riches en nickel. Ces différences dans les cinétiques d'oxydation interne ont été attribuées à des différences dans les protocoles expérimentaux utilisés pour les expériences dans les gaz contenant 3% et 13% de vapeur d'eau. En effet, les expériences impliquant les mélanges H_2/H_2O ayant la plus faible teneur en vapeur d'eau ont été réalisées dans une thermobalance alors que les expériences utilisant des mélanges H_2/H_2O contenant 13% de vapeur d'eau ont été conduites dans un four horizontal. La montée en température dans les deux protocoles a été effectuée sous un flux continu d'Ar-5%H_2. Cependant, durant les expériences utilisant la thermobalance, l'échantillon était suspendu dans la zone chaude du four pendant la montée en température et une passivation de la surface de l'échantillon a pu se produire durant cette étape. Pour les expériences dans le four horizontal, les échantillons étaient insérés dans la zone chaude du four lorsque celui-ci avait atteint la température de consigne et le gaz réactif introduit rapidement après afin d'éviter la passivation des échantillons.

L'hypothèse d'une fine couche de passivation de la surface de l'échantillon lors des expériences réalisées avec une thermobalance est supportée par l'observation d'un régime transitoire d'oxydation sur les courbes de gain de masse en fonction du temps. En effet, durant cette période transitoire, la cinétique d'oxydation est plus lente que durant le régime d'oxydation permanent. De plus, les différences de cinétique ont été observées dans les alliages riches en nickel qui ont une concentration en chrome proche de celle nécessaire à la formation d'une couche externe d'oxyde d'après les travaux de Croll et Wallwork [66] ce qui appuie l'hypothèse d'une passivation des échantillons durant la montée en température.

Néanmoins, les cinétiques d'oxydation interne, en termes de gain de masse, étant similaires dans les alliages riches en fer, il fut conclu que la concentration en vapeur d'eau du gaz ne semble pas avoir d'effet significatif sur les cinétiques d'oxydation interne.

4 Perméabilité de l'oxygène

La perméabilité de l'oxygène $N_O^{(s)} D_O^{mat}$, ou $N_O^{(s)}$ correspond à la solubilité de l'oxygène en surface, considérée égale à la valeur de solubilité $N_O^{(s)}$ évaluée dans le Chapitre 3 et D_O^{mat} le coefficient de diffusion de l'oxygène, a été estimée à partir des valeurs de $k_p^{(i)}$ rapportées dans le Chapitre 4. Le calcul de la perméabilité de l'oxygène requiert l'évaluation de paramètres annexes tels que le facteur d'enrichissement, α, et la stœchiométrie de l'oxyde interne ν.

4.1 Facteur d'enrichissement

Le facteur d'enrichissement, α, est défini comme le ratio $\frac{N_{Cr}^{ox}}{N_{Cr}^{(0)}}$ ou N_{Cr}^{ox} est la fraction molaire de chrome présent sous forme d'oxyde dans la zone d'oxydation interne et $N_{Cr}^{(0)}$ la concentration en chrome initiale de l'alliage. Dans le cas où le flux d'oxygène dans le métal est très grand par rapport au flux de chrome ($N_O^{(s)} D_O^{mat} >> N_{Cr}^{(0)} \tilde{D}_{Cr}$), le chrome n'a pas le temps de diffuser et α=1. Cependant, si les flux d'oxygène et de chrome sont semblables ($N_O^{(s)} D_O^{mat} \approx N_{Cr}^{(0)} \tilde{D}_{Cr}$), une partie du chrome présent dans le cœur de l'alliage peut diffuser vers la zone d'oxydation interne et la concentration de chrome à l'intérieur de celle-ci devient plus élevée que la concentration en chrome initiale de l'alliage, et α devient supérieur à 1.

Pour évaluer ce paramètre, deux méthodes différentes ont été utilisées. La première méthode fut développée par Wagner [1] et consiste à calculer le facteur d'enrichissement grâce aux équations de la diffusion. La seconde technique permet d'évaluer α à partir de la mesure de la fraction volumique d'oxyde interne. La comparaison des valeurs du facteur d'enrichissement estimées par chacune des techniques a mis en évidence que l'expansion de la zone d'oxydation interne, due à la précipitation d'oxyde interne, ne peut être négligée pour le calcul du facteur d'enrichissement et de la perméabilité de l'oxygène pour les alliages ayant une concentration en chrome de 7,5 at.%. En prenant en compte l'expansion de la zone d'oxydation interne dans les alliages riches en chrome pour le calcul du paramètre α, il a été montré que l'approche basée sur les équations de la diffusion et celle

utilisant la mesure de la fraction volumique d'oxyde donne des résultats équivalents.

De plus, la vapeur d'eau et/ou l'hydrogène semblent n'avoir aucun effet sur l'enrichissement de la zone d'oxydation interne. De ce fait, il a été décidé d'utiliser les facteurs d'enrichissement évalués à partir de l'approche proposée par Wagner [1] pour calculer la perméabilité de l'oxygène.

4.2 Stoechiométrie effective

Au chapitre 4, l'étude de la microstructure de la zone d'oxydation interne a montré que celle-ci est composée de deux sous-zones dans lesquelles un oxyde spécifique précipite: le spinel $FeCr_2O_4$ précipite dans la sous-zone se trouvant directement en dessous de la surface de l'alliage tandis que Cr_2O_3 se situe dans la sous-zone adjacente au front d'oxydation interne. Afin d'estimer la perméabilité de l'oxygène de façon précise, la stœchiométrie des deux oxydes doit être considérée. Cependant, les deux oxydes présents dans la zone d'oxydation interne ont une stœchiométrie différente. Le spinel présente une stœchiométrie de 2 alors que celle de l'oxyde de chrome est de 1,5. De ce fait une stœchiométrie effective, ν_{eff}, a dû être utilisée. Le paramètre ν_{eff} a été défini comme la moyenne pondérée de la stœchiométrie du spinel $FeCr_2O_4$ et de celle de Cr_2O_3, chaque stœchiométrie étant pondérée par la taille relative de la sous-zone dans laquelle chaque oxyde précipite. L'évaluation de la taille de chaque sous-zone a été réalisée grâce à des observations MEB comme décrit dans le Chapitre 4. Il faut également noter que dans le Chapitre 4, il a été conclu que l'hydrogène et/ou la vapeur d'eau n'avaient aucun effet sur la taille des différentes sous-zones. Ce résultat suggère que la stœchiométrie effective n'est pas affectée par la présence de vapeur d'eau et d'hydrogène dans l'environnement.

Il a également été tenté d'évaluer la stœchiométrie effective en couplant les mesures de cinétique d'oxydation interne en termes de pénétration et de gain de masse. Malheureusement, ces calculs n'ont pas permis l'évaluation du paramètre ν_{eff}.

En effet, la relation quantitative entre gain de masse et profondeur d'oxydation

interne a été établie pour une précipitation complète du chrome dans la zone d'oxydation interne. Or, dans les alliages ayant une faible concentration en chrome, nous avons montré que cette hypothèse n'est pas complétement vérifiée. Cette précipitation incomplète est due à la faible stabilité de l'oxyde de chrome dans les conditions expérimentales utilisées. Néanmoins, dans les alliages riches en chrome, l'hypothèse de la précipitation complète du chrome est vérifiée. Il a donc été décidé de comparer les valeurs de ν_{eff} estimées d'après les observations MEB aux valeurs calculées en couplant les mesures de cinétique d'oxydation interne en termes de pénétration et de gain de masse pour les alliages ayant une concentration en chrome de 7,5 at.%. Cette comparaison a montré que les valeurs de stœchiométrie effective estimées grâce aux différentes méthodes étaient en bon accord.

L'erreur induite par la précipitation incomplète du chrome sur l'évaluation de la perméabilité de l'oxygène pour les alliages dilués en chrome fut estimée en utilisant le modèle d'Orhiner and Morral [46]. L'utilisation de ce modèle a permis de montrer que l'erreur sur la valeur de la perméabilité de l'oxygène, due à la précipitation incomplète du chrome dans la zone d'oxydation interne, est négligeable par rapport aux erreurs sur les autres paramètres requis pour évaluer $N_O^{(s)} D_O^{mat}$.

Afin d'évaluer la perméabilité de l'oxygène, la stœchiométrie effective définie par la moyenne pondérée de la stœchiométrie des différents oxydes a été utilisée. Il faut noter que ces valeurs furent calculées grâce à des mesures de la taille relative des différentes sous-zones dans des alliages riches en chrome et il a été considéré que ν_{eff} est indépendant de la concentration en chrome de l'alliage. Les valeurs estimées grâce aux mesures réalisées sur des alliages ayant une concentration en chrome de 7,5 at.% ont ainsi pu être utilisées pour les alliages dilués.

4.3 Calcul de la perméabilité de l'oxygène

La perméabilité de l'oxygène a été calculée à partir des valeurs de $k_p^{(i)}$ évaluées grâce aux mesures de la taille de la zone d'oxydation interne (Chapitre 4) mais en prenant en considération la dilatation de celle-ci due à la précipitation d'oxyde interne. L'évaluation de la perméabilité de l'oxygène a mis en évidence que la diffusion rapide de l'oxygène aux interfaces matrice/oxyde interne contribue de façon significative à la cinétique d'oxydation interne. Un coefficient de diffusion effectif permettant de découpler la diffusion de l'oxygène aux interfaces et dans le réseau a dû être défini afin d'estimer la perméabilité de l'oxygène dans la matrice. Il a été montré que la contribution de la diffusion rapide aux interfaces matrice/oxyde interne à la perméabilité de l'oxygène observée peut être estimée uniquement si des paramètres tels que la taille et la géométrie des particules sont connus.

Les valeurs de perméabilité de l'oxygène évaluées d'après les cinétiques d'oxydation interne mesurées dans l'atmosphère sèche et humide sont similaires, ce qui indique que la vapeur d'eau et/ou l'hydrogène n'a pas d'effet sur $N_O^{(s)} D_O^{mat}$. La perméabilité de l'oxygène décroit de façon continue et de manière non idéale quand la concentration en nickel de l'alliage augmente. De plus, $N_O^{(s)} D_O^{mat}$ varie de plusieurs ordres de grandeurs depuis sa valeur maximale mesurée dans le fer jusqu'au minimum trouvé dans les alliages Fe-80Ni. Pour une température de 1000°C, la perméabilité de l'oxygène dans le fer est approximativement de 1×10^{-11} cm^2 s^{-1} et la valeur de perméabilité pour l'alliage Fe-80Ni est de l'ordre de 3×10^{-13} cm^2 s^{-1}. Il faut également noter que la perméabilité de l'oxygène augmente avec la température. Pour une augmentation de température de 1000 à 1150°C, il a été observé que la perméabilité de l'oxygène augmente d'environ un ordre de grandeur.

Les valeurs de perméabilité de l'oxygène mesurées pour le fer ont été comparées aux valeurs de la littérature. Les valeurs de $N_O^{(s)} D_O^{mat}$ estimées dans notre étude sont en excellent accord avec la plupart des valeurs mesurées précédemment [33, 45, 47] mais en désaccord avec les valeurs publiées par Takada *et al.* [38] qui ont trouvé des valeurs de perméabilité plus basses d'un facteur 2 dans leurs travaux. Cependant,

Takada *et al.* ont utilisé la technique des « packs de Rhines » avec un mélange de poudre $Fe/FeO/Al_2O_3$ pour réaliser leurs expériences. Or, à haute température et avec la pression partielle d'oxygène fixée à l'équilibre Fe/FeO, le spinel $FeAl_2O_4$ est thermodynamiquement stable. Si durant leurs expériences, $FeAl_2O_4$ s'est formé dans le mélange de poudre, cette réaction a consommé de l'oxygène et a pu réduire la pression partielle d'oxygène à l'intérieur du « pack de Rhines » et conduire à des valeurs de perméabilité de l'oxygène plus basses. Les valeurs de $N_O^{(s)} D_O^{mat}$ trouvées pour les alliages Fe-Ni ont été comparées aux valeurs calculées à partir des expériences menées par Croll et Wallwork [66]. En effet, ces auteurs ont déterminé la concentration minimale de chrome pour pouvoir observer la transition entre oxydation interne et oxydation externe à 1000°C. D'après cette valeur critique de chrome, la perméabilité de l'oxygène a pu être déterminée. Les valeurs de $N_O^{(s)} D_O^{mat}$, estimées d'après les travaux de Croll et Wallwork, sont en accord avec les valeurs calculées à partir de l'oxydation interne d'alliages Fe-Ni-Cr réalisés dans la présente étude.

5 Diffusion de l'oxygène

Le coefficient de diffusion de l'oxygène a été estimé grâce aux valeurs de perméabilité et de solubilité que nous avons mesurées. Pour des températures supérieures à 1000°C, le coefficient de diffusion de l'oxygène ne dépend pas de la présence de H_2 et H_2O dans l'atmosphère. Dans les environnements sec et humide, le coefficient de diffusion de l'oxygène présente un maximum dans les alliages avec une teneur en nickel de 40 at.%. La présence de ce maximum semble être le résultat d'un effet combiné de plus faibles interactions entre les atomes d'oxygène, de fer et de nickel à cette composition, ainsi que de la diminution du paramètre de maille quand la concentration en nickel dans l'alliage augmente.

A 1000°C, la situation est différente. Le coefficient de diffusion de l'oxygène est constant quel que soit la concentration en nickel dans l'alliage. De plus, D_O^{mat} semble être affecté par la présence de vapeur d'eau dans l'environnement pour les alliages ayant une concentration en nickel jusqu'à 60 at.%. Les valeurs du

coefficient de diffusion de l'oxygène mesurée en « pack de Rhines » et dans des mélanges gazeux H_2/H_2O pour ces alliages sont respectivement $5,9 \times 10^{-8}$ cm^2 s^{-1} et $1,8 \times 10^{-8}$ cm^2 s^{-1}. Néanmoins, pour l'alliage Fe-80Ni, le coefficient de diffusion mesuré dans les deux environnements ne semble pas être affecté par la présence de vapeur d'eau et/ou d'hydrogène.

La différence entre les valeurs de D_O^{mat} mesurées dans les environnements sec et humide pour les alliages avec moins de 80 at.% de nickel reflète la plus grande solubilité de l'oxygène mesurée dans l'atmosphère contenant de la vapeur d'eau pour les alliages riches en fer, alors que les valeurs de perméabilité sont quant à elles similaires dans les deux environnements.

L'énergie d'activation pour la diffusion de l'oxygène dans le fer estimé d'après les expériences en « pack de Rhines » (Q=168 kJ mol^{-1}) est en accord avec la valeur caractéristique de la diffusion interstitielle aux alentours de 150 kJ mol^{-1}. Cependant, dans cet environnement, l'énergie d'activation estimée pour la diffusion de l'oxygène dans les alliages Fe-Ni est bien au-dessus de 200 kJ mol^{-1} et elle présente même un maximum à 333 kJ mol^{-1} pour l'alliage contenant 40 at.% de nickel. Ces valeurs élevées d'énergie d'activation pour la diffusion semblent être dues aux interactions qui existent entre les atomes d'oxygène et les défauts présents dans le matériau, comme les lacunes.

La comparaison des valeurs de Q mesurées dans l'atmosphère sèche et humide a montré que des valeurs d'énergie d'activation plus élevées étaient mesurées après exposition dans une atmosphère contenant de la vapeur d'eau et de l'hydrogène pour des alliages contenant moins de 80 at.% de nickel. Ce résultat suggère que les interactions entre O, OH et les défauts tels que les lacunes peuvent modifier la diffusivité des atomes d'oxygène.

6 Conclusion

Durant ce travail, il a été montré que la présence de vapeur d'eau et/ou d'hydrogène n'affecte pas la façon dont la solubilité, la perméabilité et la diffu-

sivité de l'oxygène varient avec la composition des alliages Fe-Ni. Cependant, il a été observé que les valeurs de solubilité et de diffusivité de l'oxygène, dans les alliages riches en fer, sont modifiées par la présence de vapeur et d'hydrogène à 1000°C alors que les valeurs de N_O et D_O^{mat} sont similaires dans les environnements sec et humide à plus haute température. Ce résultat suggère que les effets de la vapeur d'eau et/ou de l'hydrogène pourraient être plus importants pour des températures en dessous de 1000°C. Des méthodes de calcul numérique ont mis en évidence, que dans le nickel, les atomes d'oxygène et les lacunes ont une forte interaction et que cela affecte la diffusion de l'oxygène dans le nickel. Cependant, aucune étude de ce genre n'est disponible pour le fer gamma. Les résultats obtenus dans notre travail suggèrent que des investigations sur les interactions O, H, et les lacunes pourraient être utiles afin de comprendre et d'expliquer les effets de la vapeur d'eau et/ou de l'hydrogène observés.

Bibliography

[1] C. Wagner, "Reaktionstypen bei der oxydation von legierungen," *Zeitschrift für Elektrochemie, Berichte der Bunsengesellschaft für physikalische Chemie*, vol. 63, no. 7, pp. 772–782, 1959.

[2] H. J. T. Ellingham, "Reducibility of oxides and sulfides in metallurgical processes," *J Soc Chem Ind*, vol. 63, pp. 125–133, 1944.

[3] D. J. Young, *High temperature oxidation and corrosion of metals*, vol. 1. Elsevier, 2008.

[4] C. Wagner, "Z. physik," *Chem.(Leipzig) B*, vol. 21, p. 25, 1933.

[5] R. E. Bedworth and N. B. Pilling, "The oxidation of metals at high temperatures," *J INST MET*, vol. 29, no. 3, pp. 529–582, 1923.

[6] D. Monceau and B. Pieraggi, "Determination of parabolic rate constants from a local analysis of mass-gain curves," *Oxidation of metals*, vol. 50, no. 5-6, pp. 477–493, 1998.

[7] R. Peraldi, D. Monceau, and B. Pieraggi, "Correlations between growth kinetics and microstructure for scales formed by high-temperature oxidation of pure nickel. II. growth kinetics," *Oxidation of Metals*, vol. 58, no. 3-4, pp. 275–295, 2002.

[8] M. H. Davies, M. T. Simnad, and C. E. Birchenall, "On the mechanism and kinetics of the scaling of iron," *J Met-T AIME*, vol. 3, pp. 889–896, 1951.

[9] J. Païdassi, "Sur la cinetique de l'oxydation du fer dans l'air dans l'intervalle 700–1250°C," *Acta Metallurgica*, vol. 6, no. 3, pp. 184–194, 1958.

[10] A. G. Goursat and W. W. Smeltzer, "Kinetics and morphological development of the oxide scale on iron at high temperatures in oxygen at low pressure," *Oxidation of Metals*, vol. 6, no. 2, pp. 101–116, 1973.

[11] J. S. Sheasby, W. E. Boggs, and E. T. Turkdogan, "Scale growth on steels at 1200°C: rationale of rate and morphology," *Metal Science*, vol. 18, no. 3, pp. 127–136, 1984.

[12] R. Y. Chen and W. Y. D. Yeun, "Review of the high-temperature oxidation of iron and carbon steels in air or oxygen," *Oxidation of Metals*, vol. 59, no. 5-6, pp. 433–468, 2003.

[13] A. Rahmel and J. Tobolski, "Einfluss von wasserdampf und kohlendioxyd auf die oxydation von eisen in sauerstoff bei hohen temperaturen," *Corrosion Science*, vol. 5, no. 5, pp. 333–346, 1965.

[14] C. W. Tuck, M. Odgers, and K. Sachs, "The oxidation of iron at 950°C in oxygen/water vapour mixtures," *Corrosion Science*, vol. 9, no. 4, pp. 271–285, 1969.

[15] A. E. Fick, "Laws of diffusion," *Annals of Physics (Leipzig, Germany)*, vol. 170, p. 59, 1855.

[16] L. Onsager, "Reciprocal relations in irreversible processes. i.," *Phys. Rev.*, vol. 37, pp. 405–426, 1931.

[17] L. C. Brown and J. S. Kirkaldy, "Carbon diffusion in dilute ternary austenites," *Trans Met Soc AIME*, vol. 230, no. 1, p. 223, 1964.

[18] C. Wagner and J. H. Westbrook, *Thermodynamics of alloys*, vol. 19. Addison-Wesley Reading, MA, 1952.

[19] L. S. Darken, "Diffusion, mobility and their interrelation through free energy in binary metallic systems," *Trans. Aime*, vol. 175, no. 1, pp. 184–201, 1948.

[20] W. A. Johnson, "Diffusion experiments on a gold-silver alloy by chemical and radioactive tracer methods," *Trans. Am. Inst. Min. Metall. Eng*, vol. 147, pp. 331–346, 1942.

[21] G. R. Wallwork, "The oxidation of alloys," *Reports on Progress in Physics*, vol. 39, no. 5, p. 401, 1976.

[22] C. Wagner, "Theoretical analysis of the diffusion processes determining the oxidation rate of alloys," *Journal of the Electrochemical Society*, vol. 99, no. 10, pp. 369–380, 1952.

[23] L. J. Bonis and N. J. Grant, "Structure and properties of dispersion strengthened internally oxidized nickel alloys," *Trans Met Soc AIME*, vol. 224, no. 2, p. 308, 1962.

[24] I. Anzel, A. C. Kneissl, A. Krizman, and R. Rudolf, "Dispersion strengthening of copper by internal oxidation of rapidly solidified Cu–Re alloys: Part I: The microstructure and stability of rapidly solidified ribbons," *Zeitschrift für Metallkunde*, vol. 94, no. 2, pp. 127–133, 2003.

[25] I. Anzel, A. C. Kneissl, L. Kosec, R. Rudolf, and L. Gusel, "Dispersion strengthening of copper by internal oxidation of rapidly solidified Cu-Re alloys: Part II: Experimental study of internal oxidation," *Zeitschrift für Metallkunde*, vol. 94, no. 9, pp. 993–1000, 2003.

[26] R. A. Rapp, "Kinetics, microstructures and mechanism of internal oxidation-its effect and prevention in high temperature alloy oxidation," *Corrosion*, vol. 21, no. 12, pp. 382–401, 1965.

[27] F. Maak, "Investigations on the oxidation of copper beryllium alloys at high temperature," *Journal Name: Z. Metallk.*, Aug 1961.

[28] F. N. Rhines, W. A. Johnson, and W. A. Anderson, "Rates of high-temperature oxidation of dilute copper alloys," *The American Institute of Mining, Metallurgical, and Petroleum Engineers*, pp. 205–221, 1942.

[29] S. Guruswamy, S. Park, J. Hirth, and R. Rapp, "Internal oxidation of ag-in alloys: stress relief and the influence of imposed strain," *Oxidation of Metals*, vol. 26, no. 1, pp. 77–100, 1986.

[30] F. Gesmundo, Y. Niu, F. Viani, and F. Rizzo, "An analysis of the internal oxidation of binary M-Nb alloys under low oxygen pressures at 600-800°C," *Oxidation of metals*, vol. 46, no. 5, pp. 441–463, 1996.

[31] F. Gesmundo, F. Viani, Y. Niu, and D. L. Douglass, "The relation between the parabolic rate constants for the internal oxidation of binary alloys in terms of weight gain or thickness," *Oxidation of Metals*, vol. 42, no. 3-4, pp. 239–247, 1994.

[32] R. A. Rapp, "The transition from internal to external oxidation and the formation of interruption bands in silver-indium alloys," *Acta Metallurgica*, vol. 9, no. 8, pp. 730 – 741, 1961.

[33] J. L. Meijering, "Advances in material research 5," 1971.

[34] J. Megusar and G. H. Meier, "Internal oxidation of dilute Co-Ti alloys," *Metallurgical Transactions A*, vol. 7, pp. 1133–1140, Aug 1976.

[35] G. Böhm and M. Kahlweit, "On internal oxidation of metallic alloys," *Acta. Metall*, vol. 12, pp. 641–648, 1964.

[36] D. L. Wood, "Internal oxidation of copper-aluminum alloys," tech. rep., General Electric Co. Research Lab., Schenectady, NY, 1958.

[37] F. N. Rhines, "A metallographic study of internal oxidation in the alpha solid solutions of copper," *AIME TRANS*, vol. 137, pp. 246–286, 1940.

[38] J. Takada, S. Yamamoto, S. Kikuchi, and M. Adachi, "Internal oxidation of Fe-Al alloys in the α-phase region," *Oxidation of Metals*, vol. 25, no. 1-2, pp. 93–105, 1986.

[39] J. Takada and M. Adachi, "Determination of diffusion coefficient of oxygen in α-iron from internal oxidation measurements in Fe-Si alloys," *Journal of Materials Science*, vol. 21, no. 6, pp. 2133–2137, 1986.

[40] J. Takada, S. Yamamoto, S. Kikuchi, and M. Adachi, "Determination of diffusion coefficient of oxygen in γ-iron from measurements of internal oxidation in Fe-Al alloys," *Metallurgical Transactions A*, vol. 17, no. 2, pp. 221–229, 1986.

[41] J. Takada, K. Kashiwagi, and M. Adachi, "Internal oxidation of Fe-Si alloys in γ-phase region," *Journal of Materials Science*, vol. 19, no. 10, pp. 3451–3458, 1984.

[42] M. H. B. Ani, T. Kodama, M. Ueda, K. Kawamura, and T. Maruyama, "The Effect of Water Vapor on High Temperature Oxidation of Fe-Cr Alloys at 1073°K," *Materials Transactions*, vol. 50, no. 11, pp. 2656–2663, 2009.

[43] A. R. Setiawan, M. Hanafi Bin Ani, M. Ueda, K. Kawamura, and T. Maruyama, "Oxygen permeability through internal oxidation zone in Fe-Cr alloys under dry and humid conditions at 973 and 1 073°K," *ISIJ international*, vol. 50, no. 2, pp. 259–263, 2010.

[44] O. Ahmed, D. J. Young, M. J. McNallan, E. J. Opila, T. Maruyama, and T. Narita, "High temperature corrosion and materials chemistry II, The Electrochemical Society," *Inc., Pennington, NJ*, p. 77, 2000.

[45] D. J. Young and O. Ahmed, "Kinetic and morphological development of internal precipitates in iron-chromium alloys," in *Materials science forum*, vol. 369, pp. 93–100, Trans Tech Publ, 2001.

[46] E. K. Ohriner and J. E. Morral, "Precipitate distribution in subscales," *Scripta Metallurgica*, vol. 13, no. 1, pp. 7 – 10, 1979.

[47] J. H. Swisher and E. T. Turkdogan, "Solubility permeability and diffusivity of oxygen in solid iron," *Trans Met Soc AIME*, vol. 239, no. 4, pp. 426–431, 1967.

[48] K. Bohnenkamp and H. J. Engell, "Uber die innere oxidation von eisenlegierungen," *Arch. Eisenhüttenwes*, vol. 35, pp. 1011–1018, 1964.

[49] S. Goto, K. Nomaki, and S. Koda, "Internal oxidation of nickel alloys containing a small amount of chromium," *JAP INST METALS J*, vol. 31, no. 4, pp. 600–606, 1967.

[50] P. Guo, J. Zhang, D. J. Young, and C. H. Konrad, "Oxygen permeability measurements in Ni using H_2/H_2O, CO/CO_2 and Ni/NiO Rhines pack atmospheres," *Oxidation of Metals*, vol. 83, no. 3-4, pp. 223–235, 2015.

[51] F. H. Stott and G. C. Wood, "Internal oxidation," *Materials Science and Technology*, vol. 4, no. 12, pp. 1072–1078, 1988.

[52] D. P. Whittle, Y. Shida, G. C. Wood, F. H. Stott, and B. D. Bastow, "Enhanced diffusion of oxygen during internal oxidation of nickel-base alloys," *Philosophical Magazine A*, vol. 46, no. 6, pp. 931–949, 1982.

[53] E. W. Hart, "On the role of dislocations in bulk diffusion," *Acta Metallurgica*, vol. 5, no. 10, p. 597, 1957.

[54] W. M. Schwarzkopf, "Beitrag zur inneren oxydation von nickel-legierungen," *Zeitschrift für Elektrochemie, Berichte der Bunsengesellschaft für physikalische Chemie*, vol. 63, no. 7, pp. 830–832, 1959.

[55] R. Moore. PhD thesis, Sheffield University, 1971.

[56] P. J. Alberry and C. W. Haworth, "Interdiffusion of Cr, Mo, and W in iron," *Metal Science*, vol. 8, no. 1, pp. 407–412, 1974.

[57] A. W. Bowen and G. M. Leak, "Solute diffusion in α-and γ-iron," *Metallurgical Transactions*, vol. 1, no. 6, pp. 1695–1700, 1970.

[58] J. Ruzickova and B. Million, "Self-diffusion of the components in the fcc phase of binary solid solutions of the Fe-Ni-Cr system," *Materials Science and Engineering*, vol. 50, no. 1, pp. 59–64, 1981.

[59] S. B. Jung, T. Yamane, Y. Minamino, K. Hirao, H. Araki, and S. Saji, "Interdiffusion and its size effect in nickel solid solutions of Ni-Co, Ni-Cr and Ni-Ti systems," *Journal of Materials Science Letters*, vol. 11, no. 20, pp. 1333–1337, 1992.

[60] K. Monma, H. Suto, and H. Oikawa, "Diffussion of Ni63 and Cr51 in nickel chromium alloys," *J Jpn Inst Met*, vol. 28, pp. 188–192, 1964.

[61] A. Davin, V. Leroy, D. Coutsouradis, and L. Habraken, "Diffusion de quelques éléments de substitution dans le fer, le nickel et le cobalt," *Memoires Scientifiques Rev Metall*, vol. 60, pp. 275–83, 1963.

[62] Y. E. Ugaste, "Interdiffusion in the Ni–Cr system," *Fiz. Met. Metalloved*, vol. 24, no. 3, pp. 442–449, 1967.

[63] E. Essuman, G. H. Meier, J. Żurek, M. Hänsel, and W. J. Quadakkers, "The Effect of Water Vapor on Selective Oxidation of Fe-Cr Alloys," *Oxidation of Metals*, vol. 69, no. 3-4, pp. 143–162, 2008.

[64] E. Essuman, G. H. Meier, J. Zurek, M. Hänsel, T. Norby, L. Singheiser, and W. J. Quadakkers, "Protective and non-protective scale formation of Ni-Cr alloys in water vapour containing high- and low-p_{O_2} gases," *Corrosion Science*, vol. 50, no. 6, pp. 1753–1760, 2008.

[65] C. S. Giggins and F. S. Pettit, "Oxidation of Ni-Cr alloys between 800 and 1200°C," *Trans Met Soc AIME*, vol. 245, no. 12, pp. 2495–2507, 1969.

[66] J. E. Croll and G. R. Wallwork, "The design of iron-chromium-nickel alloys for use at high temperatures," *Oxidation of Metals*, vol. 1, no. 1, pp. 55–71, 1969.

[67] J. G. Duh and M. A. Dayananda, "Interdiffusion in Fe-Ni-Cr alloys at 1100°C," in *Defect and Diffusion Forum*, vol. 39, p. 1, Trans Tech Publ, 1985.

[68] A. D. Dalvi and R. Sridhar, "Thermodynamics of the Fe-Ni-O and Fe-Ni systems at 1065°K to 1380°K," *Canadian Metallurgical Quarterly*, 2013.

[69] M. Ueda, Y. Inoue, H. Ochiai, M. Takeyama, and T. Maruyama, "The Effect of Water Vapor on the Transition from Internal to External Oxidation of Austenitic steels at 1,073°K," *Oxidation of Metals*, vol. 79, no. 5-6, pp. 485–494, 2013.

[70] C. B. Alcock and F. D. Richardson, "Dilute solutions in molten metals and alloys," *Acta Metallurgica*, vol. 6, no. 6, pp. 385 – 395, 1958.

[71] C. B. Alcock and F. D. Richardson, "Dilute solutions in alloys," *Acta Metallurgica*, vol. 8, no. 12, pp. 882 – 887, 1960.

[72] C. Wagner, "The activity coefficient of oxygen and other nonmetallic elements in binary liquid alloys as a function of alloy composition," *Acta Metallurgica*, vol. 21, no. 9, pp. 1297 – 1303, 1973.

[73] J. A. Kitchener, J. O. Bockris, M. Gleiser, and J. W. Evans, "The solubility of oxygen in γ-iron," *Acta Metallurgica*, vol. 1, no. 1, pp. 93 – 101, 1953.

[74] A. U. Seybolt, "Solubility of oxygen in α-iron," *Transactions Of The American Institute Of Mining And Metallurgical Engineers*, vol. 200, no. 5, pp. 641–644, 1954.

[75] J. L. Meijering, "On the diffusion of oxygen through solid iron," *Acta Metallurgica*, vol. 3, no. 2, pp. 157–162, 1955.

[76] E. S. Tankins and N. A. Gokcen, "Solubility of oxygen in δ-iron," *Trans. ASM*, vol. 53, pp. 843–852, 1961.

[77] M. T. Hepworth, R. P. Smith, and E. T. Turkdogan, "Permeability, Solubility, and Diffusivity of Oxygen in BCC Iron," *Aime Met Soc Trans*, vol. 236, no. 9, pp. 1278–1283, 1966.

[78] W. F. Gale and T. C. Totemeier, eds., *Smithells Metals Reference Book (Eighth Edition)*. Oxford: Butterworth-Heinemann, eighth edition ed., 2004.

[79] C. B. Alcock and P. B. Brown, "Physicochemical factors in the dissolution of thoria in solid nickel," *Metal Science*, vol. 3, no. 1, pp. 116–120, 1969.

[80] J. Park and C. J. Altstetter, "The diffusion and solubility of oxygen in solid nickel," *Metallurgical Transactions A*, vol. 18, no. 1, pp. 43–50, 1987.

[81] T. Chiang and Y. A. Chang, "The activity coefficient of oxygen in binary liquid metal alloys," *Metallurgical Transactions B*, vol. 7, no. 3, pp. 453–467, 1976.

[82] W. Fischer and M. Haussmann, "The direct electrochemical determination of the oxygen content of iron baths. pt. 3. effect of cobalt, nickel, chromium and vanadium on the activity of oxygen in iron baths," *ARCH EISENHUTTENW*, vol. 37, no. 12, 1966.

[83] W. Fischer, D. Janke, and W. Ackermann, "Thermodynamics of the dissolution of oxygen in fe-co, fe-ni, fe-cu, and co-ni melts," *ARCH. EISENHUTTENWESEN*, vol. 41, no. 4, pp. 361–367, 1970.

[84] S. Matoba and T. Kuwana, "Activity of oxygen in liquid steel," *Tetsu-to-Hagané Overseas*, vol. 5, no. 3, pp. 187–195, 1965.

[85] H. A. Wriedt and J. Chipman, "Oxygen in liquid iron-nickel alloys," *JOM*, vol. 8, no. 9, pp. 1195–1199, 1956.

[86] Y. A. Chang and D. C. Hu, "On the gibbs energy interaction parameters of oxygen and nitrogen in liquid alloys," *Metallurgical Transactions B*, vol. 10, no. 1, pp. 43–48, 1979.

[87] S. Goto and S. Koda, "Diffusion behaviour of oxygen during the internal oxidation of Ni-Al and Ni-Cr alloys," *J JAPAN INST METALS*, vol. 34, no. 3, pp. 319–326, 1970.

[88] G. J. Lloyd and J. W. Martin, "The diffusivity of oxygen in nickel determined by internal oxidation of dilute Ni–Be alloys," *Metal Science*, vol. 6, no. 1, pp. 7–11, 1972.

[89] H. O. Nam, I. S. Hwang, K. H. Lee, and J. H. Kim, "A first-principles study of the diffusion of atomic oxygen in nickel," *Corrosion Science*, vol. 75, pp. 248–255, 2013.

[90] J. J. Kim, S. H. Shin, J. A. Jung, K. J. Choi, and J. H. Kim, "First-principles study of interstitial diffusion of oxygen in nickel chromium binary alloy," *Applied Physics Letters*, vol. 100, no. 13, p. 131904, 2012.

[91] H. Z. Fang, S. L. Shang, Y. Wang, Z. K. Liu, D. Alfonso, D. E. Alman, Y. K. Shin, C. Y. Zou, A. C. T. van Duin, Y. K. Lei, *et al.*, "First-principles studies on vacancy-modified interstitial diffusion mechanism of oxygen in nickel, associated with large-scale atomic simulation techniques," *Journal of Applied Physics*, vol. 115, no. 4, p. 043501, 2014.

[92] D. Connétable, É. Andrieu, and D. Monceau, "First-principles nickel database: Energetics of impurities and defects," *Computational Materials Science*, vol. 101, pp. 77–87, 2015.

[93] D. Connétable, M. David, A. Prillieux, D. Young, and D. Monceau, "Impact of the clusterization on the solubility of oxygen and vacancy concentration in nickel: A multi-scale approach," *Journal of Alloys and Compounds*, vol. 708, pp. 1063–1072, 2017.

[94] S. Perusin, D. Monceau, and E. Andrieu, "Investigations on the Diffusion of Oxygen in Nickel at 1000°C by SIMS Analysis," *Journal of The Electrochemical Society*, vol. 152, no. 12, pp. E390–E397, 2005.

[95] W. Zhao and B. Gleeson, "Steam effects on the oxidation behaviour of Al_2O_3-scale forming Ni-based alloys," *Oxidation of Metals*, vol. 79, no. 5-6, pp. 613–625, 2013.

[96] W. Zhao and B. Gleeson, "Assessment of the detrimental effects of steam on Al_2O_3-scale establishment," *Oxidation of Metals*, vol. 83, no. 5-6, pp. 607–627, 2015.

[97] T. Ustad and H. Sørum, "Interdiffusion in the Fe-Ni, Ni-Co, and Fe-Co systems," *physica status solidi (a)*, vol. 20, no. 1, pp. 285–294, 1973.

[98] T. Ericsson, L. G. Liljestrand, S. Sehlstedt, and H. Sterner, "Some observations on interdiffusion in the Fe-Cr-Ni system," *J IRON STEEL INST*, vol. 208, no. 12, pp. 1109–1110, 1970.

[99] B. Million, J. Růžičková, J. Velíšek, and J. Vřešťál, "Diffusion processes in the Fe-Ni system," *Materials Science and Engineering*, vol. 50, no. 1, pp. 43–52, 1981.

[100] L. Kaufman and M. Cohen, "The martensitic transformation in the iron-nickel system," *Transactions of the American Institute of Mining and Metallurgical Engineers*, vol. 206, no. 10, pp. 1393–1401, 1956.

[101] M. W. Chase Jr, C. A. Davies, J. R. Downey Jr, D. J. Frurip, R. A. McDonald, A. N. Syverud, and N. Tables, "Version 1.0, NIST Standard Reference Database 13," 1985.

[102] A. Wexler, "Vapor pressure formulation for water in range 0 to 100°C. A revision," *J. Res. Natl. Bur. Stand. A*, vol. 80, pp. 775–785, 1976.

[103] J. Crank, *The mathematics of diffusion*. Oxford university press, 1979.

[104] R. Lamoreaux, D. Hildenbrand, and L. Brewer, "High-Temperature Vaporization Behavior of Oxides II. Oxides of Be, Mg, Ca, Sr, Ba, B, Al, Ga, In, Tl,

Si, Ge, Sn, Pb, Zn, Cd, and Hg," *Journal of physical and chemical reference data*, vol. 16, no. 3, pp. 419–443, 1987.

[105] LECO, "Ultra Low Nitrogen and Oxygen in Iron, Steel, Nickel-Base, and Cobalt-base Alloys," 2007.

[106] *LECO TCH600 Instruction manual*.

[107] N. S. Jacobson, K. Savadkouei, C. Morin, J. Fenstad, and E. H. Copland, "Combustion methods for measuring low levels of carbon in nickel, copper, silver, and gold," *Metallurgical and Materials Transactions B*, pp. 1–11, 2016.

[108] G. F. Vander Voort, *Metallography, principles and practice*. ASM International, 1984.

[109] D. Jullian. PhD thesis, University of New South Wales, 2017.

[110] R. de Levie, "Estimating parameter precision in nonlinear least squares with excel's solver," *J. Chem. Educ*, vol. 76, no. 11, p. 1594, 1999.

[111] T. Wada, H. Wada, J. Elliott, and J. Chipman, "Thermodynamics of the Fcc Fe-Ni-C and Ni-C alloys," *Metallurgical and Materials Transactions B*, vol. 2, no. 8, pp. 2199–2208, 1971.

[112] H. Wriedt and O. Gonzalez, "The solubility of nitrogen in solid iron-nickel alloys near 1,000 degrees C," *Transactions of the metallurgical society of AIME*, vol. 221, no. 3, pp. 532–535, 1961.

[113] A. Moulson and J. Roberts, "Water in silica glass," *Transactions of the Faraday Society*, vol. 57, pp. 1208–1216, 1961.

[114] J. F. Shackelford and J. S. Masaryk, "The thermodynamics of water and hydrogen solubility in fused silica," *Journal of Non-Crystalline Solids*, vol. 21, no. 1, pp. 55–64, 1976.

[115] N. P. Bansal and R. H. Doremus, *Handbook of glass properties*. Elsevier, 2013.

[116] B. Conard, T. McAneney, and R. Sridhar, "Thermodynamics of iron-nickel alloys by mass spectrometry," *Metallurgical Transactions B*, vol. 9, no. 3, pp. 463–468, 1978.

[117] H. Yi, S. Guan, W. Smeltzer, and A. Petric, "Internal oxidation of Ni-Al and Ni-Al-Si alloys at the dissociation pressure of NiO," *Acta Metallurgica et Materialia*, vol. 42, no. 3, pp. 981–990, 1994.

[118] B. Langelier, S. Persaud, R. Newman, and G. Botton, "An atom probe tomography study of internal oxidation processes in alloy 600," *Acta Materialia*, vol. 109, pp. 55–68, 2016.

[119] O. Kubaschewski, E. L. Evans, and E. A. Gulbransen, "Metallurgical thermochemistry," *Journal of The Electrochemical Society*, vol. 104, no. 1, pp. 22C–23C, 1957.

[120] Y.-Y. Chuang, K.-C. Hsieh, and Y. A. Chang, "A thermodynamic analysis of the phase equilibria of the Fe-Ni system above 1200°K," *Metallurgical Transactions A*, vol. 17, no. 8, pp. 1373–1380, 1986.

[121] R. M. Barrer, "Diffusion in and through solids," 1951.

[122] R. B. McLellan and P. Sutter, "Thermodynamics of the hydrogen-nickel system," *Acta Metallurgica*, vol. 32, no. 12, pp. 2233–2239, 1984.

[123] A. San-Martin and F. Manchester, "The Fe-H (iron-hydrogen) system," *Journal of Phase Equilibria*, vol. 11, no. 2, pp. 173–184, 1990.

[124] Y. Yamanishi, T. Tanabe, and S. Imoto, "Hydrogen Permeation and Diffusion through Pure Fe, Pure Ni and Fe-Ni Alloys," *Transactions of the Japan institute of metals*, vol. 24, no. 1, pp. 49–58, 1983.

[125] R. Dus and M. Smialowski, "Diffusion of hydrogen in FCC alloys of nickel with iron," *Acta Metallurgica*, vol. 15, no. 10, pp. 1611–1616, 1967.

[126] H. Bester and K. W. Lange, "Abschätzung mittlerer werte für die diffusion von kohlenstoff, sauerstoff, wasserstoff, stickstoff und schwefel in festem und flüssigem," *steel research international*, vol. 43, no. 3, pp. 207–213, 1972.

[127] S. Rothman, L. Nowicki, and G. Murch, "Self-diffusion in austenitic Fe-Cr-Ni alloys," *Journal of Physics F: Metal Physics*, vol. 10, no. 3, p. 383, 1980.

[128] L. Swartzendruber, V. Itkin, and C. Alcock, "The Fe-Ni (iron-nickel) system," *Journal of phase equilibria*, vol. 12, no. 3, pp. 288–312, 1991.

[129] S. L. Phillips and D. L. Perry, *Handbook of inorganic compounds*. Boca Raton : CRC Press, 1995. Includes indexes.

[130] J. Guertin, J. A. Jacobs, and C. P. Avakian, *Chromium (VI) handbook*. CRC press, 2016.

[131] F. Mazandarany and R. Pehlke, "Thermodynamic properties of solid alloys of chromium with nickel and iron," *Metallurgical and Materials Transactions B*, vol. 4, no. 9, pp. 2067–2076, 1973.

[132] A. Sabioni, A. Huntz, F. Millot, and C. Monty, "Self-diffusion in Cr_2O_3 II. oxygen diffusion in single crystals," *Philosophical Magazine A*, vol. 66, no. 3, pp. 351–360, 1992.

[133] A. Sabioni, A. Huntz, F. Millot, and C. Monty, "Self-diffusion in Cr_2O_3 III. chromium and oxygen grain-boundary diffusion in polycrystals," *Philosophical Magazine A*, vol. 66, no. 3, pp. 361–374, 1992.

[134] S. Bose and H. Grabke, "Diffusion coefficient of carbon in Fe-Ni austenite in the temperature range 950-1100°C," *Zeitschrift für Metallkunde*, vol. 69, pp. 8–15, 1978.

[135] C. Wert and C. Zener, "Interstitial atomic diffusion coefficients," *Physical Review*, vol. 76, no. 8, p. 1169, 1949.

[136] A. Poullikkas, "An overview of current and future sustainable gas turbine technologies," *Renewable and Sustainable Energy Reviews*, vol. 9, no. 5, pp. 409–443, 2005.